MAR 1 5 1949

THE PHYSICAL REVIEW

VOLU[illegible] Second Series NUMBER 5

MA[illegible]H 1, 1949

Published for the

AMERICAN PHYSICAL SOCIETY

by the

AMERICAN INSTITUTE OF PHYSICS

Lancaster [illegible] New York, N. Y.

THE PHYSICAL REVIEW

A journal of experimental and theoretical physics established by E. L. Nichols in 1893

Published by the American Institute of Physics
for the
AMERICAN PHYSICAL SOCIETY

Officers

President

F. W. Loomis
University of Illinois
Urbana, Illinois

Vice-President

I. I. Rabi
Columbia University
New York, New York

Secretary

K. K. Darrow
Bell Telephone Laboratories
Office:
Columbia University
New York 27, New York

Treasurer

G. B. Pegram
Columbia University
New York 27, New York

Local Secretary
for the Pacific Coast

J. Kaplan
University of California at Los
Angeles
Los Angeles, California

Managing Editor

John T. Tate
University of Minnesota
Minneapolis, Minnesota

The Physical Review
Entered as second-class matter
Acceptance for mailing at special

BOARD OF EDITORS

E. Tate

Associate Editors

H. A. Bethe
L. A. Ridenour
W. H. Zachariasen

for publication should be submitted to
of Minnesota, Minneapolis, Minnesota. The authors
an page publication charge of $4 per page which
them to 100 free reprints. Instructions will be sent
and all correspondence concerning papers in the group
by published by the Publication Manager, American
57 East 55 Street, New York 22, New York.

Subscription Price

United States and Canada . . . . . .
. . . . . .

Back Numbers

Series 2,] Vol. 1, 1913–Vol. 74, 1948—
rates
each, prior to July, 1929;
each, July, 1929–December, 1941;
each, January, 1942–December,
each.

orders for back numbers should be
Lancaster, Pennsylvania, or to the
57 East 55 Street, New York 22, New York.

case of members of the
to the Treasurer; in the case of
American Institute of Physics.

Physics Department, Cornell University

Lemon Streets, Lancaster, Pennsylvania.
Lancaster, Pennsylvania, under the
, section 538, P. L. & R., authorized

THE
PHYSICAL REVIEW

A journal of experimental and theoretical physics established by E. L. Nichols in 1893

SECOND SERIES, VOL. 75, No. 5 MARCH 1, 1949

Neutron-Proton and Neutron-Neutron Scattering at High Energies*

F. ROHRLICH** AND J. EISENSTEIN***
Lyman Laboratory of Physics, Harvard University, Cambridge, Massachusetts
(Received September 20, 1948)

The phase method and the Born approximation is used to calculate the cross sections of high energy neutrons scattered by protons and neutrons. Various exchange theories are considered for both, central and tensor forces of rectangular and Yukawa well shape.

For the tensor case the phase method leads to general formulas for the differential and total cross sections in terms of *real* phase shifts. The reality of the phase shifts is a direct consequence of the use of the asymptotic form of the eigenfunctions of the tensor force Hamiltonian. The differential cross section in this case also contains the "amounts of admixture" which measure the coupling of states of different orbital angular momentum which have the same total angular momentum and the same parity. The real phase shifts and the amounts of admixture are derived from a variational principle. The total cross sections thus obtained are within a few percent of the exact values. The Born approximation is not satisfactory at 100 Mev.

At this energy, tensor forces of a rectangular well shape with Rarita-Schwinger constants yield 0.2113, 0.1497, and 0.1271 barns for the n-p cross section, and 0.2566, 0.1381, and 0.0359 barns for the n-n cross section, in the neutral, charged, and symmetrical exchange theory, respectively. The observed n-p cross section at 90 Mev, 0.083 ± 0.004 barns, agrees best with the theoretical value of $\sim$0.080 barns at 100 Mev, derived from a tensor interaction potential of equal amounts of neutral and charged exchange. It is concluded, however, that a Yukawa tensor potential of the symmetrical exchange type can be in agreement with the experiments, if relativistic corrections of the n-p cross section at 100 Mev are negative and of the order of 5–10 percent. The differential cross section needs considerably larger corrections unless a different tensor force range is used.

INTRODUCTION

THE phenomenological theories of nuclear forces could be compared until recently only with scattering data up to about 10 Mev. Neutron-proton and neutron-neutron scattering in this energy range is practically spherically symmetrical. No conclusion could, therefore, be reached about the exchange character of nuclear forces. Similarly, it was possible to fit the observed data with central and with tensor forces, and with a variety of different potential well shapes.[1] Recently, Sleator[2] measured the total n-p cross section at energies between 6 and 22 Mev. He found that six different theories are in fair agreement with the experiments at least on some part of the energy range, but that only the charged and the symmetrical tensor theory fit within the whole range considered. Proton-proton scattering experiments[3] at 14.5 Mev show a negative P-wave contribution to the angular distribution which indicates exchange forces. Neu-

* This work is based on parts of the theses submitted by the authors to the Graduate School of Arts and Sciences, Harvard University, in partial fulfilment of the requirements for the degree of Doctor of Philosophy.

** Now at the Institute for Advanced Study, Princeton, New Jersey.

*** National Research Council Predoctoral Fellow. Now at the University of Wisconsin, Madison, Wisconsin.

[1] D. Bohm and C. Richman, Phys. Rev. 71, 567 (1947).
[2] W. Sleator, Phys. Rev. 72, 207 (1947).
[3] Wilson, Lofgren, Richardson, Wright, and Shankland, Phys. Rev. 71, 560 and 72, 1132 (1947).

tron-proton scattering experiments[4] at 12–13 Mev are in agreement with symmetrical tensor forces, but do not compare with the results obtained for a tensor force of the neutral or charged type.

Scattering experiments of 90-Mev neutrons by protons and deuterons were recently carried out in Berkeley.[5, 6a] These data should enable one to still further eliminate phenomenological theories which are consistent with low energy scattering data. It should be mentioned here that the analysis of high energy scattering cross sections suffers from the serious drawback that, while relativistic effects may be important at energies as high as 100 Mev, the corresponding corrections of the non-relativistic calculations are yet unknown.[6b]

The present investigation pursues a twofold aim. Firstly, cross sections for high energy scattering are calculated for rectangular and Yukawa well shapes. The constants employed fit the binding energy of the deuteron, the epithermal *n-p* cross section, and the low energy *p-p* cross sections. This involves the assumption that *p-p* and *n-p* forces are essentially the same. It is investigated how the results change when different constants are assumed.[7] The first part deals with central forces, the second part with tensor forces. Actually, only tensor forces have significance, since it is not possible to account for the electric quadrupole moment of the deuteron under the assumption of central forces. Numerical results are obtained for various energies, including 100 Mev, and are compared with the Berkeley experiments.

Secondly, the phase method is applied to *n-p* and *n-n* scattering with tensor forces and—as in the case of central forces—the cross sections are given in terms of *real* phase shifts. The first calculations of scattering cross sections for tensor forces[8] and all those published since[9, 10] yielded complex phase shifts, because the asymptotic form postulated for the eigenfunctions did not correspond to the partial waves which are characterized by constants of motion. The formulation in terms of real phase shifts appears to be more satisfactory from a theoretical point of view. Together with real phase shifts, it is necessary to introduce the amounts of admixture which measure the coupling between two states of different orbital angular momentum, but same total angular momentum and same parity. This coupling is due to the non-central character of tensor forces, and is introduced in a natural way by a unitary transformation from the LSM_LM_S scheme, in which the central force Hamiltonian is diagonal, to the $(-1)^L SJM$ scheme, in which the tensor force Hamiltonian is diagonal.

The phase shifts and the amounts of admixture are found by a variational procedure, since it is not possible to solve the occurring simultaneous differential equations in a closed form. The variational principle for the phase shifts was first given by Schwinger in his course on nuclear physics[11] where it was applied to S and D wave scattering.

We published some of our numerical results previously.[12] Meanwhile, a number of papers have appeared which deal with scattering by central[13, 14] or tensor forces,[15, 10] some of which overlap partly with our own calculations. This enables us to shorten certain parts of this report.[16] In particular, we refer to Ashkin and Wu[10] for the derivation of the scattering cross-section formulas for tensor forces in Born approximation.

The first part deals with central forces. The exact results which are obtained from the phase method (Section IA), are compared with the Born approximation (Section IB). The second

[4] J. S. Laughlin and P. G. Kruger, Phys. Rev. **73**, 197 (1948).

[5] Cook, McMillan, Peterson, and Sewell, Phys. Rev. **72**, 1264 (1948)L.

[6a] Hadley, Kelly, Leith, Segrè, Wiegand, and York, Phys. Rev. **73**, 1114 (1948)L.

[6b] For an estimate see: H. Snyder and R. E. Marshak, Phys. Rev. **72**, 1253 (1947).

[7] This is important, because recent experiments on the scattering of slow neutrons by ortho- and parahydrogen (R. B. Sutton *et al.* Phys. Rev. **72**, 1147 (1947)) and by hydrogen in crystals (C. G. Shull *et al.* Phys. Rev. **73**, 842 (1948)) indicate that the ranges of singlet and triplet forces may be much shorter than was commonly accepted, and may also be unequal to each other. See also: J. M. Blatt, Phys. Rev. **74**, 92 (1948).

[8] W. Rarita and J. Schwinger, Phys. Rev. **59**, 436 and 556 (1941).

[9] J. Jauch, Phys. Rev. **67**, 125 (1945).

[10] J. Ashkin and T. Y. Wu, Phys. Rev. **73**, 972 (1948).

[11] See also: J. Schwinger, Phys. Rev. **72**, 742 (1947)A.

[12] J. Eisenstein and F. Rohrlich, Phys. Rev. **73**, 641 and 1411 (1948).

[13] M. Camac and H. A. Bethe, Phys. Rev. **73**, 191 (1948).

[14] T. Y. Wu, Phys. Rev. **73**, 934, and 1132L (1948).

[15] H. S. W. Massey, E. H. S. Burhop, and T. M. Hu, Phys. Rev. **73**, 1403 (1948)L.

[16] For full details we refer to our theses (see the first note of this paper).

TABLE I. Total cross sections for neutron-proton scattering at 100 Mev. Central forces, exact calculations. (All values are in barns, i.e., 10^{-24} cm².)

Theory	$\sigma_{np}^{(s)}$	$\sigma_{np}^{(t)}$	σ_{np}
Neutral	0.0645	0.1939	0.1616
Charged	0.0552	0.1582	0.1325
Symmetric	0.1692	0.0921	0.1114*

* The value 0.094 obtained by Ta-You Wu (see reference 14, Table III) is due to a numerical error.

TABLE II. Total cross sections for neutron-neutron scattering at 100 Mev. Central forces, exact calculations. (All values are in barns, i.e., 10^{-24} cm².)

Theory	$\sigma_{nn}^{(s)}$	$\sigma_{nn}^{(t)}$	σ_{nn}
Neutral	0.0464	0.2289	0.1832
Charged	0.0464	0.1575	0.1297
Symmetric	0.0464	0.0252	0.0305

part is devoted to tensor forces. The results in Born approximation (Section IIA) are discussed, and the formulas for the differential and total cross section of *n-p* and *n-n* scattering are derived with the phase method (Section IIB). Numerical results are obtained by the aid of the variational principle for real phase shifts (Section IIC), and the comparison with the experiments is summarized. A list of formulas for *n-p* and *n-n* cross sections according to different theories is given in the appendix.

I. CENTRAL FORCES

A. The Phase Method

The assumption of central forces permits the direct application of the method of partial waves[17,18] or phase method. For each of the two spin states the space dependent part of the wave function can be written as the sum of the wave functions of fixed orbital angular momentum L. These functions are the solutions of a Schrödinger equation which, after separation of variables

$$\psi_L=\frac{u_L(r)}{r}P_L(\cos\theta) \tag{1}$$

lead to the radial equations

$$\left(\frac{d^2}{dr^2}+k^2-\frac{M}{\hbar^2}V(r)-\frac{L(L+1)}{r^2}\right)u_L(r)=0$$
$$(L=0,\,1,\,2\cdots), \tag{2}$$

where

$$k^2=ME/\hbar^2. \tag{3}$$

M is the mass of the nucleon, E is the total energy in the center of mass system, and $V(r)$ is the potential energy. With a rectangular potential well of depth V_0 and range r_0 we can introduce the dimensionless quantities

$$x=r/r_0,\quad \kappa^2=MEr_0^2/\hbar^2=(kr_0)^2,$$
$$\lambda=MV_0r_0^2/\hbar^2 \tag{4}$$

and find for the wave function interior and exterior of the well,

$$\left(\frac{d^2}{dx^2}+\kappa^2\pm\lambda-\frac{L(L+1)}{x^2}\right)u_L^{(i)}(x)=0\quad(x<1), \tag{5}$$

$$\left(\frac{d^2}{dx^2}+\kappa^2-\frac{L(L+1)}{x^2}\right)u_L^{(e)}(x)=0\quad(x>1). \tag{6}$$

The $\pm$ sign corresponds to attractive and repulsive potential, respectively. The boundary conditions

$$u_L^{(i)}(0)=0,\quad u_L^{(e)}(\infty)\sim\sin\left(\kappa x+\frac{\pi L}{2}+\delta_L\right) \tag{7}$$

are fulfilled by the solutions

$$u_L^{(i)}(x)=xj_L(\kappa_1 x), \tag{8}$$

$$u_L^{(e)}(x)=Ax[j_L(\kappa x)-\tan\delta_L n_L(\kappa x)], \tag{9}$$

where

$$\kappa_1=(\kappa^2\pm\lambda)^{\frac{1}{2}}, \tag{10}$$

and

$$j_L(\kappa x)=\left(\frac{\pi}{2\kappa x}\right)^{\frac{1}{2}}J_{L+\frac{1}{2}}(\kappa x)\sim\frac{\sin(\kappa x-\pi L/2)}{\kappa x},$$
$$n_L(\kappa x)=\left(\frac{\pi}{2\kappa x}\right)^{\frac{1}{2}}N_{L+\frac{1}{2}}(\kappa x)\sim-\frac{\cos(\kappa x-\pi L/2)}{\kappa x} \tag{11}$$

are the spherical Bessel and Neumann functions,[19] respectively. Smoothness of the wave functions at the edge of the well requires the

[17] H. Faxen and J. Holtsmark, Zeits. f. Physik. **45**, 307 (1927).

[18] N. F. Mott and H. S. W. Massey, *Theory of Atomic Collisions* (The Clarendon Press, Oxford, 1935).

[19] See for example: J. Stratton, *Electromagnetic Theory* (McGraw-Hill Book Company, Inc., New York, 1941).

equality of the logarithmic derivatives

$$\left[\frac{d}{dx}\log u_L^{(t)}(x)\right]_{x=1}=\left[\frac{d}{dx}\log u_L^{(s)}(x)\right]_{x=1}. \quad (12)$$

Introducing (8) and (9) into (12), we find easily

$$\tan\delta_L=(-1)^L\frac{j_{L-1}(\kappa)-\frac{\kappa_1}{\kappa}\frac{j_{L-1}(\kappa_1)}{j_L(\kappa_1)}j_L(\kappa)}{j_{-L}(\kappa)+\frac{\kappa_1}{\kappa}\frac{j_{L-1}(\kappa_1)}{j_L(\kappa_1)}j_{-L-1}(\kappa)}, \quad (13)$$

where we made use of the identity

$$n_L(x)=(-1)^{L+1}j_{-L-1}(x).$$

The phase shifts can be evaluated from (13) by means of the tables[20] for j_L and j_{-L}. For strongly repulsive potentials as occur in the exchange theories, κ_1 of Eq. (10) may become imaginary. In this case (13) has to be replaced by

$$\tan\delta_L=(-1)^L\frac{j_{L-1}(\kappa)-\frac{|\kappa_1|}{\kappa}\frac{I_{L-\frac{1}{2}}(|\kappa_1|)}{I_{L+\frac{1}{2}}(|\kappa_1|)}j_L(\kappa)}{j_{-L}(\kappa)+\frac{|\kappa_1|}{\kappa}\frac{I_{L-\frac{1}{2}}(|\kappa_1|)}{I_{L+\frac{1}{2}}(|\kappa_1|)}j_{-L-1}(\kappa)}, \quad (14)$$

where[21]

$$I_L(\kappa)=i^{-L}J_L(ix).$$

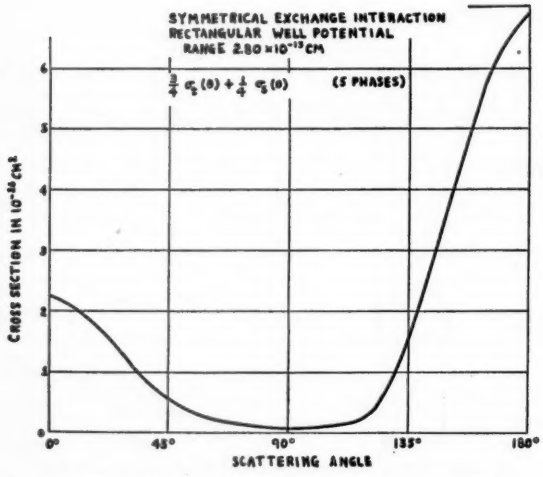

FIG. 1. Differential scattering cross section at 100 Mev.

[20] National Bureau of Standards, Mathematical Tables Project, *Tables of Spherical Bessel Functions*, Vol. I and II (Columbia University Press, New York, 1947).

[21] G. N. Watson, *Theory of Bessel Functions* (The Macmillan Company, New York, 1944).

The Eqs. (13) and (14) seem to us somewhat more convenient to use than the corresponding Eqs. (12) and (13) of Camac and Bethe.[13]

For the given well depths V_0 and for the even singlet and triplet states, we obtain from (4) two values, λ_s and λ_t, respectively. The value of κ_1 in (10) will in general depend on the parity $(-1)^L$ of the state and on the spin,

$$\kappa_1^{(s)}=(\kappa^2+\lambda_L^{(s)})^{\frac{1}{2}}, \quad \kappa_1^{(t)}=(\kappa^2+\lambda_L^{(t)})^{\frac{1}{2}}. \quad (15)$$

For the neutral theory[8]

$$\lambda_L^{(s)}=\lambda_s, \quad \lambda_L^{(t)}=\lambda_t, \quad (16)$$

for the charged theory

$$\lambda_L^{(s)}=(-1)^L\lambda_s, \quad \lambda_L^{(t)}=(-1)^L\lambda_t, \quad (17)$$

and for the symmetrical theory

$$\lambda_L^{(s)}=-(1-2(-1)^L)\lambda_s, \qquad \lambda_L^{(t)}=\tfrac{1}{3}(1+2(-1)^L)\lambda_t. \quad (18)$$

The phase shifts for these theories can now be calculated from (13) and (14). The differential cross section for n-p scattering is given by the well-known formula[17,18]

$$\sigma_{np}(\vartheta)=\left|\frac{1}{k}\sum_{L=0}^{\infty}(2L+1)e^{i\delta_L}\sin\delta_L P_L(\cos\vartheta)\right|^2, \quad (19)$$

and the total cross section by

$$\sigma_{np}=2\pi\int_0^{\pi}\sigma_{np}(\vartheta)\sin\vartheta d\vartheta =\frac{4\pi}{k^2}\sum_{L=0}^{\infty}(2L+1)\sin^2\delta_L. \quad (20)$$

From these equations the n-n cross sections are obtained by the aid of the exclusion principle

$$\sigma_{nn}^{(s)}(\vartheta)=\left|\sum_{L=0}^{\infty}\frac{1+(-1)^L}{k}(2L+1) \times\exp(i\delta_L^{(s)})\sin\delta_L^{(s)}P_L(\cos\vartheta)\right|^2 \quad (21)$$

$$\sigma_{nn}^{(t)}(\vartheta)=\left|\sum_{L=0}^{\infty}\frac{1-(-1)^L}{k}(2L+1) \times\exp(i\delta_L^{(t)})\sin\delta_L^{(t)}P_L(\cos\vartheta)\right|^2, \quad (21)$$

and

$$\sigma_{nn}=\tfrac{1}{2}\cdot 2\pi\int_0^\pi \sigma_{nn}(\vartheta)\sin\vartheta d\vartheta \qquad (22)$$

since only half the number of deviated neutrons are scattered neutrons, the other half being recoil neutrons. When the two spin states are taken into account, one finds from (19) or (21) the two angular distributions $\sigma^{(s)}(\vartheta)$ and $\sigma^{(t)}(\vartheta)$. They combine in their respective weight 1:3 to give the total cross section

$$\sigma(\vartheta)=\tfrac{1}{4}\sigma^{(s)}(\vartheta)+\tfrac{3}{4}\sigma^{(t)}(\vartheta),\quad \sigma=\tfrac{1}{4}\sigma^{(s)}+\tfrac{3}{4}\sigma^{(t)}, \qquad (23)$$

with $\sigma^{(s)}$ and $\sigma^{(t)}$ from (20) or (22).

We adopted the ranges and well depths $r_s=2.80\times10^{-13}$ cm, $V_0{}^s=11.904$ Mev, and $r_t=2.80\times10^{-13}$ cm, $V_0{}^t=21.213$ Mev. For neutrons of 100-Mev energy in the laboratory system we find the total scattering cross sections as tabulated in Table I for n-p collisions and in Table II for n-n collisions. The angular distribution for n-p scattering in the symmetrical theory is plotted in Fig. 1. Its triplet part can be seen from Fig. 3.

It can be seen from Tables I and II that the magnitude of the potential influences the cross section much more than does its sign. In Table II only odd phases enter the triplet cross sections.

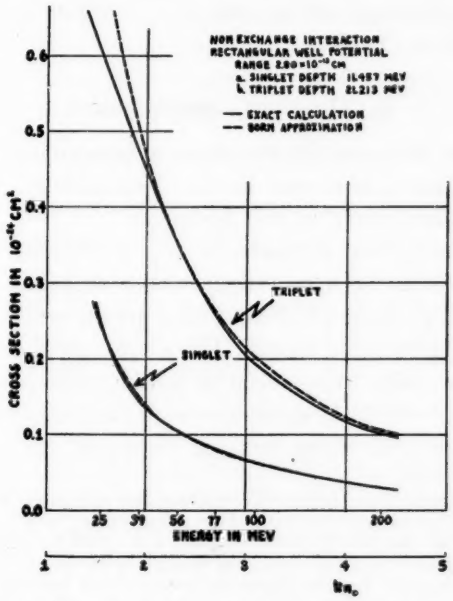

FIG. 2. Variation of singlet and triplet cross sections with energy.

TABLE IIIa. Variation of triplet n-p cross section with range at 25 Mev (central forces, exact calculations).

r_t (10^{-13} cm)	Neutral	Charged (barns)	Symmetric
1.8	0.4250	0.4130	0.4111
2.3	0.4657	0.4014	0.3931
2.8	0.6042	0.3891	0.3656

TABLE IIIb. Variation of triplet n-p cross section with range at 100 Mev (central forces, exact calculations).

r_t (10^{-13} cm)	Neutral	Charged (barns)	Symmetric
1.8	0.1351	0.0749	0.0613
2.8	0.1939	0.1582	0.0921

In the neutral and charged theory the magnitude of the potential is the same, but the odd states of the latter are repulsive rather than attractive. This causes a decrease of $\sigma_{nn}{}^{(t)}$ by one third, approximately. On the other hand, the charged and the symmetric theory have both repulsive odd states, but the magnitude of the potential in the latter is by two thirds smaller. This causes a decrease of $\sigma_{nn}{}^{(t)}$ by more than 80 percent. Qualitatively, the same behavior can be seen from $\sigma_{np}{}^{(t)}$ in Table I. In this case, however, it is less pronounced, because of the presence of even states which contribute equally in all three theories. As expected, the charged theory gives a somewhat smaller singlet cross section, $\sigma_{np}{}^{(s)}$, than does the neutral theory. The strong increase in $\sigma_{np}{}^{(s)}$ as we pass from the neutral to the symmetrical theory is due to the competition between a factor three and a minus sign. The repulsive P-state contributes 85 percent of the singlet n-p cross section in the symmetrical theory.

The total singlet and triplet n-p cross sections were calculated in the neutral theory for various energies between 25 and 200 Mev. They are plotted[22] in Fig. 2 and are in agreement with the results of Camac and Bethe.[13]

When we decrease the triplet range the triplet depth has to be increased correspondingly in order to account for the binding energy of the deuteron. We used Wiedenbeck and Marhoefer's

[22] It should be noted here that the singlet cross sections given in Fig. 2 were calculated with a potential well of 11.457 Mev rather than 11.904 Mev. The difference is practically negligible.

TABLE IV. Total cross sections for neutron-proton scattering at 100 Mev for central forces in Born approximation (rectangular well). All values are in barns (10^{-24} cm^2).

Theory	$\sigma_{np}^{(s)}$	$\sigma_{np}^{(t)}$	σ_{np}
Neutral and charged	0.0641	0.2034	0.1686
Symmetric	0.3872	0.0894	0.1639*

* The value 0.140 obtained by Ta-You Wu (see reference 14, Table III) is due to a numerical error (private communication of Dr. Wu).

value[23] of 2.185 Mev. The well depths for three different triplet ranges are as follows:

r_t	$V_0^{(t)}$	
1.80×10^{-13} cm	43.476 Mev	
2.30×10^{-13} cm	28.963 Mev	(24)
2.80×10^{-13} cm	21.213 Mev.	

The variation of the triplet cross section with range is shown in Table IIIa for 25 Mev and in Table IIIb for 100 Mev.

Tables IIIa and IIIb show that the neutral theory leads to a smaller cross section when the range is reduced, independent of the energy. The charged and the symmetrical theory also give smaller cross sections for a reduced range, but only at higher energies (e.g., 100 Mev); at lower energies (e.g., 25 Mev) they lead to larger values. These results are in agreement with those obtained by Camac and Bethe (Table III).[13] The combined singlet and triplet cross section is seen from their table to increase with decreasing

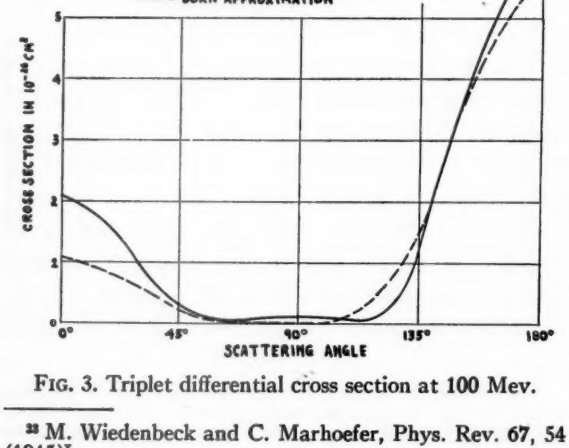

FIG. 3. Triplet differential cross section at 100 Mev.

[23] M. Wiedenbeck and C. Marhoefer, Phys. Rev. 67, 54 (1945)L.

TABLE V. Variation of triplet n-p cross section with range for central forces in Born approximation (rectangular well). All values are in barns.

Energy r_t	25 Mev. neutral and charged	100 Mev neutral and charged	Symmetric
1.8×10^{-13} cm	0.3578	0.1351	0.1121
2.3×10^{-13} cm	0.5522		0.0945
2.8×10^{-13} cm	0.7449	0.2034	0.0894

range ($r_s=r_t$) for energies below ~50 Mev for the charged theory and below ~60 Mev for the symmetrical theory.[24]

Equation (15) shows that the decrease of the cross section due to the presence of exchange forces (charged or symmetric type) is relatively smaller the higher the energy. This effect can be so large that the cross section may even increase with energy. For example, the triplet n-p cross section in the charged theory is 0.155 barn at 80 Mev ($r_t=2.80\times10^{-13}$ cm), as calculated from the phase shifts of Camac and Bethe,[13] but is 0.158 barn at 100 Mev (Table I). On the other hand, the symmetrical theory increases the contribution to the singlet cross section of the odd states. Where an increase in energy leads to a strong increase in the contribution from an odd state, this may again lead to an increase of the cross section with energy. Thus we find $\sigma_{np}^{(s)}=0.164$ barn at 80 Mev (Camac and Bethe's phase shifts) and $\sigma_{np}^{(s)}=0.169$ barn at 100 Mev (Table I).

B. The Born Approximation

The formulas for the Born approximation are well known and need not be derived here. They are summarized in the Appendix.

Total cross sections for n-p scattering were calculated for a rectangular well with the constants given in IA. The results are shown in Fig. 2 for the neutral theory. The singlet cross section above ~25 Mev and the triplet cross section above ~40 Mev agree well with the exact calculations. At these neutron energies the total

[24] For 80 Mev Ta-You Wu obtained an apparent increase in the cross section with decreasing range in the symmetrical theory. (Phys. Rev. 73, 1132 (1948)L, Table I.) His values 0.84 and 1.17×10^{-25} cm^2, however, should be interchanged. For the Gaussian potential the increase from 0.95 to 1.08×10^{-25} cm^2 is very probably only apparent, and is due to the use of the Born approximation (see Part I B, Table V).

TABLE VI. Total cross sections for n-p scattering at 100 Mev for central forces (Yukawa well, Born approximation). All values are in barns.

Theory	$\sigma_{np}^{(s)}$	$\sigma_{np}^{(t)}$	σ_{np}
Neutral or charged	0.0604	0.1309	0.1133
Symmetric	0.1545	0.0932	0.1086

energy in the center of mass system becomes comparable with the respective well depths, and the Born approximation ceases to hold. The curves for the Born approximation do not approach the curves for the exact calculations in a monotonic fashion, but oscillate and even cross the exact curves in the singlet case. This peculiar behavior is due to the sharp cut-off of the rectangular well.

In the Born approximation the total cross section in the charged theory is the same as in the neutral theory. At high energies (above ~40 Mev) the charged theory leads actually to much smaller values than does the neutral theory. The situation is even worse for the symmetrical theory. For a range of 2.80×10^{-13} cm the triplet cross section is still in fair agreement with the exact value, but the singlet cross section is too large by a factor of two, even at 100 Mev. These relations are evident from a comparison between Table IV and Table I.

It follows from these remarks that the Born approximation is in general not reliable at 100 Mev. One obtains reasonably good approximate values, however, if one uses the combination

$$\sigma=\tfrac{1}{4}\sigma^{(s)}(\text{exact})+\tfrac{3}{4}\sigma^{(t)}(\text{Born}) \qquad (25)$$

for the symmetrical theory. If we decrease the triplet range, the well depth increases (see (24)), and for $r_t=1.8\times10^{-13}$ cm becomes nearly equal to the total energy in the center of mass system at 100-Mev neutron energy. The Born approximation will, therefore, not give good values. This is exhibited in Table V from which we drew first the erroneous conclusion that the cross section increases with decreasing range in the symmetrical theory at 100 Mev[12]. (See also reference 24.) On the other hand, the oscillatory character of the curves for the Born approximation (Fig. 2) may lead to relatively good agreement for energies as low as 25 Mev, as can be seen from a comparison of Table V with Table IIIa.

TABLE VII. Variation of triplet n-p cross section with range for central forces in Born approximation (Yukawa well) (energy: 100 Mev).

r_t 10^{-13} cm	$V_0^{(t)}$ Mev	Neutral or charged (barns)	Symmetric
1.089	78.070	0.110	0.0896
1.183	67.450	0.131	0.0932
2.177	24.203	0.191	0.1285
4.355	8.339	0.374	0.2241

Although the total triplet cross section at 100 Mev, symmetrical theory, is in Born approximation not very far off the exact value, the triplet differential cross section may lead to entirely erroneous quantitative conclusions. A fair qualitative agreement can be seen from Fig. 3. We find a ratio of backward to sideward scattering $R^{(t)}(\text{Born})=\sigma^{(t)}(\pi)/\sigma^{(t)}(\pi/2)=900$, whereas the exact value is $R^{(t)}(\text{exact})=78$.

It is of interest to examine how the assumption of different well shapes influences the cross section. A Yukawa potential of the type

$$V=V_0(e^{-x}/x), \quad (x=r/r_y), \qquad (26)$$

was, therefore, assumed, where r_Y is the "range" of the Yukawa potential. An analysis of proton-proton scattering[25] leads to a singlet range of $0.42\ e^2/mc^2=1.183\times10^{-13}$ cm, and to a singlet depth $V_0^{(s)}=89.65\ mc^2=45.80$ Mev. The triplet depths for various ranges follow from the binding energy of the deuteron by the use of a variational procedure.[26] They are listed in Table VII. If one assumes the triplet and singlet ranges to be equal, and chooses the above value of 1.183×10^{-13} cm, one finds in Born approximation the cross sections of Table VI.

For this Yukawa well the reduction of the neutral cross section due to symmetrical exchange forces is much smaller than for a rectangular well of ranges 2.80×10^{-13} cm. The Born approximation for the neutral theory will not be far off the exact value. From calculations by Chew and Goldberger[27] we may conclude that

[25] L. E. Hoisington, S. S. Share, and G. Breit, Phys. Rev. 56, 884 (1939).

[26] L. Hulthen, Arkiv. f. Mat., Astr. o. Fys. 28A, No. 5 (1942).

[27] G. F. Chew and M. L. Goldberger, Phys. Rev. 73, 1409 (1948)L. For 80 Mev the Born approximation for a Yukawa well gives 0.131 barn; their value of 0.150 barn is due to an error (private communication).

TABLE VIII. Total n-p cross sections for a rectangular well at 100 Mev (tensor forces, Born approximation). All values in barns.

Theory	$\sigma_{\text{Born}}^{(0)}$	σ_{Born}	$\frac{1}{4}\sigma_{\text{Born}}^{(0)}+\frac{3}{4}\sigma_{\text{Born}}^{(1)}$	$R=\frac{\sigma(\pi)}{\sigma(\pi/2)}$
Neutral or charged	0.2516	0.2047	0.2048	0.30 or 3.75
Symmetric	0.0939	0.1672	0.1127	7.9

TABLE IX. Variation of triplet n-p cross section with range for 100 Mev (tensor forces, Born approximation, rectangular well).

r_t 10^{-13} cm	γ	V_0 Mev	Q 10^{-27} cm^2	D-state percent	Neutral barns	Symmetric barns
2.80	0.775	13.89	2.73	3.9	0.2516	0.0939
2.30	1.564	15.92	2.73	6.9	0.4216	
2.30	1.292	13.55	2.16	4.0	0.1835	0.102

the cross section in the symmetrical theory is at 100 Mev smaller than the exact value by about 6 percent or less. It follows that this well leads to considerably smaller neutral cross sections than the rectangular well ($r_s=r_t=2.80\times10^{-13}$ cm) at 100 Mev, and to about equal or somewhat larger values for the symmetrical theory. At 80 Mev the symmetrical theory leads to much larger cross sections with a Yukawa well,[27] 0.140 barns instead of 0.111 barn.

As in the case of a rectangular well a range reduction causes a decrease of the cross section. Since the error made in the Born approximation for the symmetrical theory is much smaller for a Yukawa well than it is for a rectangular well, we can be sure that the qualitative behavior exhibited by the Born approximation is correct; the various triplet cross sections are given in Table VII.

II. TENSOR FORCES

A. The Born Approximation

The inclusion of tensor forces in the nucleon interaction effects only the triplet states, since the tensor operator

$$S_{12}=3(\sigma_1\cdot r,\ \sigma_2\cdot r/r^2)-\sigma_1\cdot\sigma_2 \tag{27}$$

vanishes for singlet states. The triplet potential is

$$V(r)=f(\sigma_1\cdot\sigma_2,\ \tau_1\cdot\tau_2)[J(r)+\gamma S_{12}K(r)], \tag{28}$$

where γ is a constant and $f(\sigma_1\cdot\sigma_2,\ \tau_1\cdot\tau_2)$ is for the neutral theory

$$f=-1, \tag{29}$$

for the charged theory

$$f=(1+\sigma_1\cdot\sigma_2/2)(1+\tau_1\cdot\tau_2/2), \tag{30}$$

and for the symmetrical theory

$$f=\tfrac{1}{3}\sigma_1\cdot\sigma_2,\ \tau_1\cdot\tau_2. \tag{31}$$

Let

$$R=(-1)^L,\quad S=\frac{1+\sigma_1\cdot\sigma_2}{2},\quad T=\frac{1+\tau_1\cdot\tau_2}{2} \tag{32}$$

be the space, spin, and isotopic spin symmetry operator, respectively. Then the exclusion principle requires that the wave function be anti-

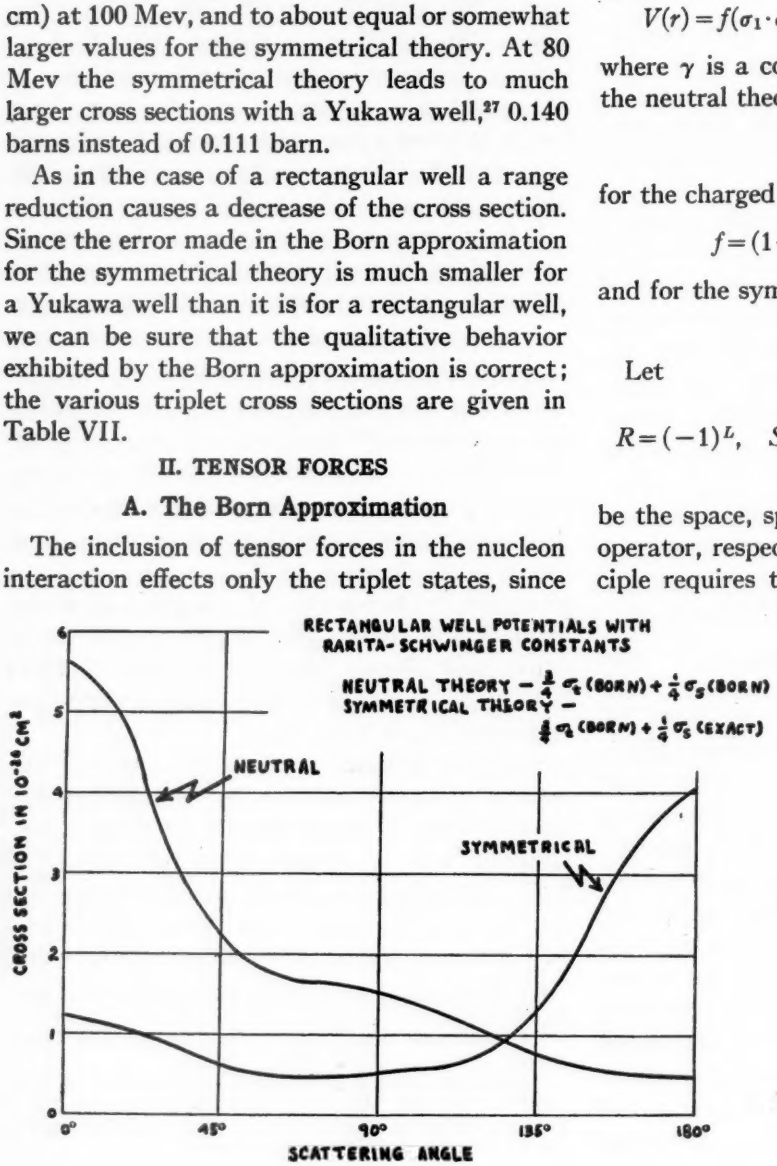

FIG. 4. Differential cross sections at 100 Mev for tensor force theories.

symmetric in the operator RST, i.e.,

$$\mathrm{RST}=-1. \tag{33}$$

If, furthermore, the particles are identical, i.e., they are two neutrons or two protons, $T=1$. These relations determine $f(\sigma_1\cdot\sigma_2, \tau_1\cdot\tau_2)$ uniquely and in agreement with Eqs. (16)–(18).

The constant γ can be so determined that

$$J(r)=V_0F(x), \quad K(r)=V_0G(x), \quad x=r/r_0. \tag{34}$$

With this potential the differential and total cross section can easily be derived in Born approximation.[10] The results are given in the appendix.

In what follows we will assume that the two shape factors $F(x)$ and $G(x)$ are equal. For this case and a rectangular well shape

$$F(x)=1 \quad (x<1), \quad F(x)=0 \quad (x>1),$$

the constants were determined by Rarita and Schwinger:[8] $r_0=2.80\times10^{-13}$ cm, $V_0=13.89$ Mev, $\gamma=0.775$. The triplet cross sections obtained with these constants are shown in Table VIII. The singlet cross sections are, of course, the same as without tensor forces, and are known exactly (Table I) and in Born approximation (Table IV). It is, therefore, easy to obtain the combination (25) for the total cross section which is much closer to the exact solution, especially for the symmetrical theory. This is also given in Table VIII.

The results in column 2 of Table VIII are in agreement with those of Ashkin and Wu.[10] The differential cross section in Born approximation was also given by these authors. Since the combination (25), however, gives much better results than the actual Born approximation, we have plotted the angular distribution for this combination (Fig. 4). We observe an appreciable increase of the scattering at right angles as a result of the tensor force. (Compare Figs. 1 and 4.) The backward scattering in the symmetrical theory decreased strongly. The total cross sections are larger for tensor forces than for central forces.

In order to examine the effect of a reduced triplet range we proceed as follows. Since it is not possible to fit both, the quadrupole moment of the deuteron and the amount of D-state, with

TABLE X. Constants for a Yukawa tensor potential.*

	r_1(central) 10^{-13} cm	Meson mass electron masses	r_1(tensor) 10^{-13} cm	Meson mass electron masses	$V_0^{(1)}$ Mev	γ
(I)	1.202	321	1.400	276	30.817	1.459
(II)	1.202	321	1.556	248	45.286	0.618

* See reference 28.

TABLE XI. Total n-p cross section for a Yukawa well and a symmetrical theory at 100 Mev (tensor forces, Born approximation). All values are in barns.

Constants	$\sigma^{(1)}$	σ	$R=\sigma(\pi)/\sigma(\pi/2)$
(I)	0.0674	0.0892	9.08
(II)	0.0760	0.0956	12.2

other constants than those given by Rarita and Schwinger,[8] we evaluated two sets of constants, one that fits the quadrupole moment and another that fits the D-state. We assumed a reduced range of 2.3×10^{-13} cm and used a variational procedure to determine the constants. The results are given in the following Table IX. Since a reduced range makes the angular distribution more isotropic (less contributions from higher angular momenta), it is clear that more D-state is required to fit the same quadrupole moment. The constant γ increases very strongly with decreasing range. As was pointed out in our Letter,[12] this effectively decreases the ratio of backward to sideward scattering. The cross section, however, reduces strongly in the neutral theory only, and increases even there if we try to fit the quadrupole moment.

For a Yukawa tensor potential constants were calculated by Feshbach, Eisenstein, and

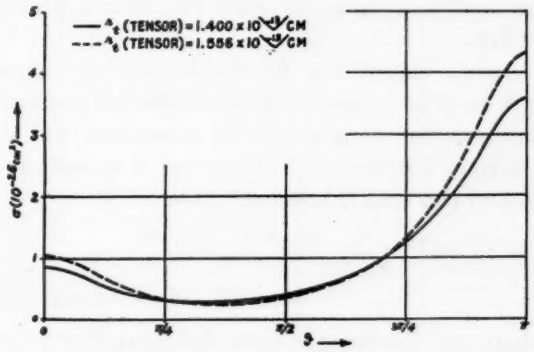

FIG. 5. Differential cross sections at 100 Mev for tensor forces and a Yukawa potential (symmetrical theory).

Schwinger.[28] They assumed a Yukawa well shape (26) for both shape functions (34), but different ranges, r_t(central) and r_t(tensor), for the central and tensor part of the triplet potential, respectively. They found two different sets of constants which fit the quadrupole moment of the deuteron (Table X). The singlet range and depth are the same as in the non-tensor case. Using the Born approximation one obtains from these constants the differential cross sections of Fig. 5 and the total cross sections as given in Table XI above. These total cross sections are smaller than those obtained for a rectangular tensor potential or for a Yukawa non-tensor potential. The ratios R are about the same as for the rectangular tensor potential, but they cannot be trusted too much because of the Born approximation.

B. The Phase Method for Tensor Forces

In the case of central forces the spin and the orbital angular momentum are constants of motion. One uses, therefore, the representation which is characterized by the four quantum numbers LSM_LM_S. When tensor forces are present the magnitude and the z-component of the orbital angular momentum are no longer constants of motion; neither is the z-component of the spin angular momentum. Only the square of the spin angular momentum commutes with the tensor Hamiltonian. It follows that a transformation to the $LSJm$ scheme, where J and m characterize the magnitude and the z-component of the total angular momentum, will not diagonalize the tensor Hamiltonian. A further transformation to the $(-1)^L SJm$ scheme is required. The parity operator, whose eigenvalues are $(-1)^L$, commutes with the tensor Hamiltonian.

Again, the tensor force operator S_{12} enters only in triplet states. In the LSM_LM_S scheme the angular dependence is described by the spherical harmonics $Y_L{}^{M_L}(\vartheta, \varphi)$. A transformation to the $LSJM$ scheme yields

$$\phi_{L,J}{}^m(\vartheta, \varphi) = \sum_{M_L, M_S} Y_L{}^{M_L}(\vartheta, \varphi)\chi_S{}^{M_S} \times (LSM_LM_S/LSJm), \quad (35)$$

where $\chi_S{}^{M_S}$ is the spin wave function. For triplet states the function $\phi_{LJ}{}^m$ can be regarded as a vector, $\Phi_{L,J}{}^m$ in the three-dimensional orthonormal space spanned by the vectors

$$\frac{1}{\sqrt{2}}(\chi_1{}^1+\chi_1{}^{-1}), \quad \frac{i}{\sqrt{2}}(\chi_1{}^1-\chi_1{}^{-1}), \quad \chi_1{}^0.$$

The vector $\Phi_{L,J}{}^m$ was discussed in detail by Corben and Schwinger[29] and by Rarita and Schwinger.[8]

In complete analogy to the case of central forces we separate the Schrödinger equation

$$\left[\nabla^2+\frac{M}{\hbar^2}(E-V)\right]\Psi=0, \quad (36)$$

into partial waves, according to the $LSJm$ scheme, first,

$$\Psi=\sum_{J,m} c_J{}^m\psi_J{}^m, \quad \psi_J{}^m=\sum_J c_L\psi_{L,J}{}^m \quad (L=J-1, J, J+1). \quad (37)$$

Separation of variables can now be achieved by putting

$$\psi_{J-1,J}=\frac{u_J(r)}{r}\Phi_{J-1,J}, \quad \psi_{J,J}{}^m=\frac{v_J(r)}{r}\Phi_{J,J}{}^m, \quad \psi_{J+1,J}{}^m=\frac{w_J(r)}{r}\Phi_{J+1}{}^m. \quad (38)$$

The operator S_{12} will couple states of equal parity[8]

$$\begin{aligned} S_{12}\Phi_{J-1,J}{}^m &= -2\frac{J-1}{2J+1}\Phi_{J-1,J}{}^m + 6\frac{[J(J+1)]^{\frac{1}{2}}}{2J+1}\Phi_{J+1,J}{}^m, \\ S_{12}\Phi_{J+1,J}{}^m &= 6\frac{[J(J+1)]^{\frac{1}{2}}}{2J+1}\Phi_{J-1,J}{}^m - 2\frac{J+2}{2J+1}\Phi_{J+1,J}{}^m, \\ S_{12}\Phi_{J,J}{}^m &= 2\Phi_{J,J}{}^m. \end{aligned} \quad (39)$$

When we introduce (37) and (38) into the Schrödinger equation (36) and observe (39), we

[28] H. Feshbach, J. Eisenstein, and J. S. Schwinger, Phys. Rev. 74, 1223 (1948).

[29] H. C. Corben and J. S. Schwinger, Phys. Rev. 58, 953 (1940).

obtain three radial equations for each value of J. The case $J=0$ is a trivial exception. With the potential (28) we find with the dimensionless quantities (4) and (34)

$$\begin{aligned}
&\left(\frac{d^2}{dx^2}+\kappa^2-\frac{J(J-1)}{x^2}\right)u_J(x)\\
&\quad=f(\sigma_1\cdot\sigma_2,\ \tau_1\cdot\tau_2)\\
&\qquad\times\lambda(f_J(x)u_J(x)+g_J(x)w_J(x)),\\
&\left(\frac{d^2}{dx^2}+\kappa^2-\frac{(J+1)(J+2)}{x^2}\right)w_J(x)\\
&\quad=f(\sigma_1\cdot\sigma_2,\ \tau_1\cdot\tau_2)\\
&\qquad\times\lambda(g_J(x)u_J(x)+h_J(x)w_J(x)),\\
&\left(\frac{d^2}{dx^2}+\kappa^2-\frac{J(J+1)}{x^2}\right)v_J(x)\\
&\quad=f(\sigma_1\cdot\sigma_2,\ \tau_1\cdot\tau_2)\lambda l(x)v_J(x),
\end{aligned}\tag{40}$$

where

$$\begin{aligned}
f_J(x)&=F(x)-2\frac{J-1}{2J+1}\gamma G(x),\\
g_J(x)&=6\frac{[J(J+1)]^{\frac{1}{2}}}{2J+1}\gamma G(x),\\
h_J(x)&=F(x)-2\frac{J+2}{2J+1}\gamma G(x),\\
l(x)&=F(x)+2\gamma G(x).
\end{aligned}\tag{41}$$

The first two differential equations are coupled, the third one is uncoupled. They are equivalent to the three integral equations

$$\begin{aligned}
u_J(x)&=A_J\kappa x j_{J-1}(\kappa x)-f\lambda\int_0^\infty G_J{}^u(x,x')\\
&\qquad\times[f_J(x')u_J(x')+g_J(x')w_J(x')]dx',\\
w_J(x)&=C_J\kappa x j_{J+1}(\kappa x)-f\lambda\int_0^\infty G_J{}^w(x,x')\\
&\qquad\times[g_J(x')u_J(x')+h_J(x')w_J(x')]dx',\\
v_J(x)&=B_J\kappa x j_J(\kappa x)-f\lambda\int_0^\infty G_J{}^v(x,x')\\
&\qquad\times l(x')v_J(x')dx',
\end{aligned}\tag{42}$$

where

$$\begin{aligned}
G_J{}^u(x,x')&=-\frac{1}{\kappa}\cdot\kappa x_<j_{J-1}(\kappa x_<)\cdot\kappa x_>n_{J-1}(\kappa x_>),\\
G_J{}^w(x,x')&=-\frac{1}{\kappa}\cdot\ \ j_{J+1}(\kappa x_<)\cdot\kappa x_>n_{J+1}(\kappa x_>),\\
G_J{}^v(x,x')&=-\frac{1}{\kappa}\cdot\kappa x_<j_J(\kappa x_<)\cdot\kappa x_>n_J(\kappa x_>).
\end{aligned}\tag{43}$$

are the appropriate symmetrical Green's functions. They satisfy the equations

$$\left(\frac{d}{dx^2}+\kappa^2-\frac{J(J-1)}{x^2}\right)G_J{}^u(x,x')=-\delta(x-x'),\quad\text{etc.}\tag{44}$$

and vanish at $x_<=0$. The notation $x_<$ and $x_>$ is convenient to designate respectively the smaller and the larger of x and x'.

It follows from the asymptotic relations (11) that for large x the Eqs. (42) become

$$\begin{aligned}
u_J(x)&\sim A_J\sin\left(\kappa x-(J-1)\frac{\pi}{2}\right)\\
&\quad-\frac{\lambda}{\kappa}f\cos\left(\kappa x-(J-1)\frac{\pi}{2}\right)\int_0^\infty\kappa x' j_{J-1}(\kappa x')\\
&\qquad\times(f_Ju_J+g_Jw_J)dx',\\
w_J(x)&\sim C_J\sin\left(\kappa x-(J+1)\frac{\pi}{2}\right)\\
&\quad-\frac{\lambda}{\kappa}f\cos\left(\kappa x-(J+1)\frac{\pi}{2}\right)\int_0^\infty\kappa x' j_{J+1}(\kappa x')\\
&\qquad\times(g_Ju_J+h_Jw_J)dx',\\
v_J(x)&\sim B_J\sin\left(\kappa x-\frac{J\pi}{2}\right)\\
&\quad-\frac{\lambda}{\kappa}f\cos\left(\kappa x-\frac{J\pi}{2}\right)\int_0^\infty\kappa x' j_J(\kappa x')l_Jv_Jdx'.
\end{aligned}\tag{45}$$

The asymptotic form required for our solutions may be written†

† In this form the phase shifts will in general also depend on m (see reference 30b).

$$u_J(x)\sim\frac{A_J}{\cos\delta_J^u}\sin\left(\kappa x-(J-1)\frac{\pi}{2}+\delta_J^u\right)$$
$$=A_J\sin\left(\kappa x-(J-1)\frac{\pi}{2}\right)$$
$$+A_J\tan\delta_J^u\cos\left(\kappa x\quad(J-1)\frac{\pi}{2}\right),\quad(46)$$
$$w_J(x)\sim\frac{C_J}{\cos\delta_J^w}\sin\left(\kappa x-(J+1)\frac{\pi}{2}+\delta_J^w\right),$$
$$v_J(x)\sim\frac{B_J}{\cos\delta_J^v}\sin\left(\kappa x-\frac{J\pi}{2}+\delta_J^v\right).$$

A comparison of (45) and (46) yields to the determination of the constants

$$A_J=-\cot\delta_J^u\cdot f\lambda\int_0^\infty j_{J-1}(\kappa x')[f_J(x')u_J(x')$$
$$+g_J(x')w_J(x')]x'dx',$$
$$C_J=-\cot\delta_J^w\cdot f\lambda\int_0^\infty j_{J+1}(\kappa x')[g_J(x')u_J(x')\quad(47)$$
$$+l(x')w_J(x')]x'dx',$$
$$B_J=-\cot\delta_J^v\cdot f\lambda\int_0^\infty j_J(\kappa x')l(x')v_J(x')x'dx'.$$

With the aid of these equations we can express the formal solutions (42) in terms of the phase shifts

$$u_J(x)=-\cot\delta_J^u f\lambda\cdot\kappa x j_{J-1}(\kappa x)$$
$$\times\int_0^\infty j_{J-1}(\kappa x')[f_J u_J+g_J w_J]x'dx'$$
$$-f\lambda\int_0^\infty G_J^u(x,x')[f_J u_J+g_J w_J]dx',$$
$$w_J(x)=-\cot\delta_J^w f\lambda\cdot\kappa x j_{J+1}(\kappa x)$$
$$\times\int_0^\infty j_{J+1}(\kappa x')[g_J u_J+h_J w_J]x'dx'\quad(48)$$
$$-f\lambda\int_0^\infty G_J^w(x,x')[g_J u_J+h_J w_J]dx',$$
$$v_J(x)=-\cot\delta_J^v f\lambda\cdot\kappa x j_J(\kappa x)$$
$$\times\int_0^\infty j_J(\kappa x')lv_J(x')x'dx'$$
$$-f\lambda\int_0^\infty G_J^v(x,x')lv_J dx'.$$

Since L can take on the values $J-1$, J, and $J+1$, the wave functions in the $(-1)^L SJm$ scheme will either be the same as those in the $LSJm$ scheme, namely when $L=J$, or they will be linear combinations of $\psi_{J-1,J}^m$ and $\psi_{J+1,J}^m$, which have the same parity. In the latter case there will be two independent wave functions for each value of J. We denote them by $\psi_{J,m}^\alpha$ and $\psi_{J,m}^\gamma$, respectively.

$$\psi_{J,m}^\alpha=\frac{1}{x}u_J^\alpha(x)\overset{m}{\Phi}_{J-1,J}-\frac{1}{x}w_J^\alpha(x)\overset{m}{\Phi}_{J+1,J},$$
$$\psi_{J,m}^\gamma=\frac{1}{x}u_J^\gamma(x)\overset{m}{\Phi}_{J-1,J}-\frac{1}{x}w_J^\gamma(x)\overset{m}{\Phi}_{J+1,J},\quad(49)$$
$$\psi_{J,m}^\beta=\frac{1}{x}v_J(x)\Phi_{J,J}^m=\psi_{J,J}^m.$$

These are the three eigenfunctions of the tensor Hamiltonian in the $(-1)^L SJm$ representation. If we want to write the total wave function Ψ of (36) as the sum of partial waves which are all "eigenwaves," as in the case of central forces, we have to replace the second sum in (37) by

$$\psi_J^m=c_\alpha\psi_{J,m}^\alpha+c_\beta\psi_{J,m}^\beta+c_\gamma\psi_{J,m}^\gamma.\quad(37')$$

Each of these partial waves is, therefore, defined by J, m, and one of the three indices α, β, γ. The wave function ψ_{total} which is the sum of the wave functions for the incident and the scattered wave, will also be the sum of partial waves defined by these quantum numbers. For any one of these waves we now require that its radial part differ asymptotically from the radial part of the corresponding incoming partial wave only by a phase shift. In other words, the asymptotic forms (46) have to be chosen such that (49) becomes—apart from constant factors

$$\psi_{J,m}^\alpha\sim\frac{1}{x}\sin(\kappa x-(J-1)\pi/2+\delta_J^\alpha)$$
$$\times(\overset{m}{\Phi}_{J-1,J}+\eta_J^\alpha\overset{m}{\Phi}_{J+1,J}),$$
$$\psi_{J,m}^\gamma\sim\frac{1}{x}\sin(\kappa x-(J+1)\pi/2+\delta_J^\gamma)\quad(50)$$
$$\times(\overset{m}{\Phi}_{J-1,J}+\eta_J^\gamma\overset{m}{\Phi}_{J+1,J}),$$
$$\psi_{J,m}^\beta\sim\frac{1}{x}\sin(\kappa x-J\pi/2+\delta_J^\beta)\Phi_{J,J}^m.$$

The function $v_J(x)$ is, therefore, not effected ($\delta_J{}^\beta=\delta_J{}^\gamma$). For $u_J(x)$ and $w_J(x)$, however, $\delta_J{}^u$ equals $\delta_J{}^w$ for each set α and γ, respectively.

$$u_J{}^{\alpha,\gamma}(x)\sim\sin(\kappa x-(J-1)\pi/2+\delta_J{}^{\alpha,\gamma}),$$
$$w_J{}^{\alpha,\gamma}(x)\sim\eta_J{}^{\alpha,\gamma}\sin(\kappa x-(J+1)\pi/2+\delta_J{}^{\alpha,\gamma}). \quad (46')$$

The eigenfunctions $\psi_{J,m}{}^\alpha$ and $\psi_{J,m}{}^\gamma$ of (49) are uniquely determined by this requirement of equal phase shifts for $u_J(x)$ and $w_J(x)$. It corresponds to a diagonalization of the scattering matrix which would otherwise be diagonal only for the states $L=J$, i.e., for the wave functions $\psi_{J,m}{}^\beta$. The phase shifts $\delta_J{}^\alpha$, $\delta_J{}^\beta$, and $\delta_J{}^\gamma$, which are defined by (46′) and (50) are all real.

The constants η_J follow from (46) and (46′) with $\delta_J{}^u=\delta_J{}^w$,

$$\eta_J=\text{asymptotic form of}\left(-\frac{w_J(x)}{u_J(x)}\right)=\frac{C_J}{A_J}, \quad (51)$$

and can easily be evaluated from (47) as will be shown in Section C. Since the orthogonality integrals of the wave functions (49) exist only in the limit

$$\lim_{x\to\infty}\left(\int_0^x u_\alpha(x)u_\gamma(x)dx\right)\Big/\left(\int_0^x u_\alpha{}^2(x)dx\right)^{\frac{1}{2}}\left(\int_0^x u_\gamma{}^2(x)dx\right)^{\frac{1}{2}},$$

only the asymptotic forms (50) will contribute, and one finds that the constants η_J satisfy the identity

$$\eta_J{}^\alpha\eta_J{}^\gamma=-1. \quad (52)$$

These constants are called the amounts of admixture. For definiteness we shall always denote the numerically smaller of them by $\eta_J{}^\alpha$. In the limit, as the tensor part of the potential goes to zero, $\eta_J{}^\alpha\to\pm 0$ and $\eta_J{}^\gamma\to\mp\infty$; the eigenfunctions, $\psi_{J,m}{}^\alpha$ and $\psi_{J,m}{}^\gamma$, become identical with $\psi_{J-1,J}{}^m$ and $\psi_{J+1,J}{}^m$, respectively, in this limit.†† It follows that $\eta_J{}^\alpha$ measures the amount of admixture of the state $L=J+1$ to the state $L=J-1$, and that $1/\eta_J{}^\gamma=-\eta_J{}^\alpha$ is the amount of admixture of the state $L=J-1$ to the state $L=J+1$.

We may now derive the formulas for the differential and total triplet cross section. For this purpose we transform the incident plane wave into the $LSJm$ representation which is the same as the $(-1)^LSJm$ scheme in the absence of a potential. In the LSM_LM_S representation

$$\psi_{\text{inc}}{}^{M_S}=\sum_L(2L+1)i^Lj_L(\kappa x)P_L(\cos(\hat{\kappa}\hat{\mathbf{x}}))\chi_1{}^{M_S}.$$

The inverse of the transformation (35) with the appropriate normalization factor gives

$$\psi_{\text{inc}}{}^m=(4\pi)^{\frac{1}{2}}\sum_L(2L+1)^{\frac{1}{2}}i^Lj_L(\kappa x)\times\sum_J\Phi_{LJ}{}^m(L1Jm|L10m)$$
$$\sim\frac{(4\pi)^{\frac{1}{2}}}{\kappa x}\sum_J\sum_L(2L+1)^{\frac{1}{2}}i^L\times\sin\left(\kappa x-\frac{\pi L}{2}\right)\Phi_{LJ}{}^m(L1Jm|L10m), \quad (53)$$

where we used again the vector notation $\Phi_{L,J}{}^m$. Since $m=M_L+M_S$ is a constant of motion and $M_L=0$ for the plane wave, one has always $m=M_S{}^{\text{inc}}$. The transformation matrix $(L1JM|L10m)$ is given in Table XII.[30a]

The asymptotic form of the total wave, i.e., the incident wave and the scattered wave will contain the tensor force eigenfunctions (49) in their asymptotic form (50)

$$\overset{m}{\psi}_{\text{total}}\sim\frac{(4\pi)^{\frac{1}{2}}}{\kappa x}\sum_J\{\alpha_J{}^m\exp(i\delta_J{}^\alpha)[i^{J-1}\sin(\kappa x-(J-1)\pi/2+\delta_J{}^\alpha)\overset{m}{\Phi}_{J-1,J}$$
$$+\eta_J{}^\alpha i^{J+1}\sin(\kappa x-(J+1)\pi/2+\delta_J{}^\alpha)\overset{m}{\Phi}_{J+1,J}]+\beta_J{}^m\exp(i\delta_J{}^\beta)i^J\sin(\kappa x-J\pi/2+\delta_J{}^\beta)\Phi_{J,J}{}^m$$
$$+\gamma_J{}^m\exp(i\delta_J{}^\gamma)[i^{J-1}\sin(\kappa x-(J-1)\pi/2+\delta_J{}^\gamma)\overset{m}{\Phi}_{J-1,J}$$
$$+\eta_J{}^\gamma i^{J+1}\sin(\kappa x-(J+1)\pi/2+\delta_J{}^\gamma)\overset{m}{\Phi}_{J+1,J}]. \quad (55)$$

†† Actually, $\eta_J{}^\alpha$ is always positive or zero.

[30a] E. U. Condon and G. H. Shortley, *Theory of Atomic Spectra* (The Macmillan Company, New York, 1935), p. 76. Note, however, that the table is written in terms of J rather than L, and that the phases are chosen different in order to comply with the choice of phases in the definitions of $\Phi_{LJ}{}^m$ (reference 29).

TABLE XII. $(2L+1)^{\frac{1}{2}}(L1Jm|L10m)$.

$L \backslash m$	± 1	0
$J-1$	$\mp((J-1)/2)^{\frac{1}{2}}$	$J^{\frac{1}{2}}$
J	$((2J+1)/2)^{\frac{1}{2}}$	0
$J+1$	$\pm(J/2)^{\frac{1}{2}}$	$(J+1)^{\frac{1}{2}}$

(54)

The constants,[30b] $\alpha_J{}^m$, $\beta_J{}^m$, and $\gamma_J{}^m$ are found by comparing this expression for vanishing potential $(\delta_J{}^\alpha=\delta_J{}^\beta=\delta_J{}^\gamma=0)$ with the plane wave (53)

$$\alpha_J{}^{\pm 1}=\mp\frac{(J+1)^{\frac{1}{2}}-\eta_J{}^\alpha J^{\frac{1}{2}}}{\sqrt{2}[1+(\eta_J{}^\alpha)^2]},\quad \alpha_J{}^0=\frac{J^{\frac{1}{2}}+\eta_J{}^\alpha(J+1)^{\frac{1}{2}}}{1+(\eta_J{}^\alpha)^2},$$

$$\beta_J{}^m=|m|\left(\frac{2J+1}{2}\right)^{\frac{1}{2}},\qquad (56)$$

$$\gamma_J{}^{\pm 1}=\mp\frac{(J+1)^{\frac{1}{2}}-\eta_J{}^\gamma J^{\frac{1}{2}}}{\sqrt{2}[1+(\eta_J{}^\gamma)^2]},\quad \gamma_J{}^0=\frac{J^{\frac{1}{2}}+\eta_J{}^\gamma(J+1)^{\frac{1}{2}}}{1+(\eta_J{}^\gamma)^2}.$$

The factors $e^{i\delta_J}$ in (55) have been chosen such that the scattered wave is a purely outgoing wave. It is found by subtracting the incident wave (53) from the total wave (55),

$$\begin{aligned}\overset{m}{\psi}_{\text{scatt}}\sim\frac{e^{ikr}}{r}\frac{(4\pi)^{\frac{1}{2}}}{k}\sum_J[&\alpha_J{}^m\exp(i\delta_J{}^\alpha)\\&\times\sin\delta_J{}^\alpha(\overset{m}{\Phi}_{J-1,J}+\eta_J{}^\alpha\overset{m}{\Phi}_{J+1,J})\\&+\beta_J{}^m\exp(i\delta_J{}^\beta)\sin\delta_J{}^\beta\overset{m}{\Phi}_{J,J}\\&+\gamma_J{}^m\exp(i\delta_J{}^\gamma)\sin\delta_J{}^\gamma\\&\times(\overset{m}{\Phi}_{J-1,J}+\eta_J{}^\gamma\overset{m}{\Phi}_{J+1,J})].\end{aligned}\qquad (57)$$

The differential cross section for polarized beams of neutrons and protons (fixed m) is the square of the absolute value of the coefficient of e^{ikr}/r of the scattered wave (57)

$$\sigma_i{}^m(\vartheta)=4\pi/k^2|\textstyle\sum_J[\cdots]|^2.\qquad (58)$$

If the incident neutrons are unpolarized we have to average over m

$$\sigma_i(\vartheta)=(4\pi/3k^2)\textstyle\sum_m|\sum_J[\cdots]|^2.\qquad (59)$$

The total cross section is found by integration over all the angles. The cross terms vanish, because of the orthogonality of the $\Phi_{L,J}{}^m$ and because of (52), and one finds with (56) after summation over m for the triplet total cross section

$$\sigma_{np}{}^{(t)}=\frac{4\pi}{k^2}\sum_J\frac{2J+1}{3}(\sin^2\delta_J{}^\alpha+\sin^2\delta_J{}^\beta+\sin^2\delta_J{}^\gamma).\qquad (60)$$

The triplet differential and total cross sections for tensor forces are completely analogous to the well-known formulas for central forces.[18] The differential cross section contains the phase shifts and the amounts of admixture, the total cross section contains the phase shifts only. In the following section we will derive these quantities from a variational principle.

C. Variational Principle for Phase Shifts

We start with the formal solutions (48), and consider first the phase shifts $\delta_J{}^\beta$ of the uncoupled states. Multiplication of the third equation by

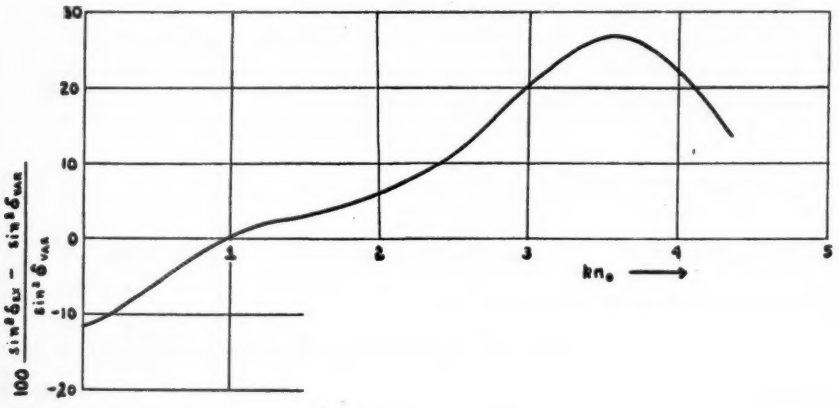

FIG. 6. Comparison of phase shifts: exact and variational calculations.

[30b] The dependence on m of these constants permits one to assume the boundary conditions (46′) with $\delta_J{}^\alpha$ and $\delta_J{}^\gamma$ independent of m.

$l(x)v_J(x)$ and integration leads readily to

$$-\cot\delta_J{}^\beta=\frac{\int l(x)v_J{}^2(x)dx+f\lambda\int l(x)v_J(x)dxG_J{}^v(x,x')dx'l(x')v_J(x')}{f\lambda\kappa\left(\int j_J(\kappa x)l(x)v_J(x)xdx\right)^2}, \tag{61}$$

which is easily seen to be stationary with respect to variations of the radial function $v_J(x)$. The resulting phase shift will have an error of the second order for any first order error in a trial function $\bar{v}_J(x)$.

In a similar way the phase shifts for coupled states are obtained. Multiplication of the first Eq. (48) by $f_J(x)u_J(x)+g_J(x)w_J(x)$, and of the second by $g_J(x)u_J(x)+h_J(x)w_J(x)$, addition and integration yields because of $\delta_J{}^u=\delta_J{}^w=\delta_J$,

$$-\cot\delta_J=(a_J+2b_J+c_J)/(\alpha_J+2\beta_J+\gamma_J), \tag{62}$$

where we used the following abbreviations:

$$\begin{aligned}
a_J&=(1/f\lambda)\int h_Jw_J{}^2dx\\
&\quad+\int g_Jw_Jdx G_J{}^udx'g_Jw_J\\
&\quad+\int h_Jw_Jdx G_J{}^wdx'h_Jw_J,\\
b_J&=(1/f\lambda)\int g_Ju_Jw_Jdx\\
&\quad+\int f_Ju_Jdx G_J{}^udx'g_Jw_J\\
&\quad+\int h_Jw_Jdx G_J{}^wdx'g_Ju_J,\\
c_J&=(1/f\lambda)\int f_Ju_J{}^2dx\\
&\quad+\int g_Ju_Jdx G_J{}^wdx'g_Ju_J\\
&\quad+\int f_Ju_Jdx G_J{}^udx'f_Ju_J\\
\alpha_J&=\kappa\left(\int xj_{J-1}(\kappa x)g_Jw_Jdx\right)^2\\
&\quad+\kappa\left(\int xj_{J+1}(\kappa x)h_Jw_Jdx\right)^2,
\end{aligned} \tag{63}$$

$$\begin{aligned}
\beta_J&=\kappa\left(\int xj_{J-1}(\kappa x)f_Ju_Jdx\right)\left(\int xj_{J-1}g_Jw_Jdx\right)\\
&\quad+\kappa\left(\int xj_{J+1}g_Ju_Jdx\right)\\
&\quad\times\left(\int xj_{J+1}h_Jw_Jdx\right),\\
\gamma_J&=\kappa\left(\int xj_{J-1}(\kappa x)f_Ju_Jdx\right)^2\\
&\quad+\kappa\left(\int xj_{J+1}(\kappa x)g_Ju_Jdx\right)^2.
\end{aligned}$$

The expression (62) for $\cot\delta_J$ is stationary with respect to variations of $u_J(x)$ and $w_J(x)$. Both variational principles, (61) and (62), were first given by Schwinger.[11]

Equation (62) is homogeneous in $u_J(x)$ and $w_J(x)$, i.e., it depends only on the ratio of any constant factors multiplying these functions. Suppose we choose trial functions $\bar{u}_J(x)$ and $\xi_J\bar{w}_J(x)$, where ξ_J is a yet undetermined constant. The integrals (63) can then be evaluated with $\bar{u}_J(x)$ and $\bar{w}_J(x)$ replacing $u_J(x)$ and $w_J(x)$, respectively, and one finds from (62)

$$-\cot\delta_J=(\xi_J{}^2\bar{a}_J+2\xi_J\bar{b}_J+\bar{c}_J)/(\xi_J{}^2\bar{\alpha}_J+2\xi_J\bar{\beta}_J+\bar{\gamma}_J). \tag{62'}$$

TABLE XIIIa. Triplet phase shifts and amounts of admixture at 15.3 Mev. (Tensor forces, rectangular well, variational calculation of coupled phases.)

J		$\delta_J{}^\alpha$	$\delta_J{}^\beta$	$\delta_J{}^\gamma$	$\eta_J{}^\alpha$
0	neutral			−0.1030	
	charged			0.5378	—
	symmetric			0.0751	
1	neutral		1.008		
	charged	−1.4129	0.1153	0.0086	0.0712
	symmetric		−0.0549		
2	neutral	0.1390		−0.0004	0.0600
	charged	−0.0200	0.0145	0.0015	0.2645
	symmetric	−0.0142		0.0002	0.1259

TABLE XIIIb. Triplet phase shifts and amounts of admixture at 100 Mev. (Tensor forces, rectangular well, variational calculation of coupled phases.)

J		$\delta_J{}^\alpha$	$\delta_J{}^\beta$	$\delta_J{}^\gamma$	$\eta_J{}^\alpha$
0	neutral			−0.6567	
	charged			0.8450	0
	symmetric			0.3024	
1	neutral		0.9795		
	charged	0.4031	−0.7428	−0.1794	0.1984
	symmetric		−0.3222		
2	neutral	0.5820		−0.0794	0.3320
	charged	−0.2196	0.6812	0.2231	0.9754
	symmetric	−0.1118		0.0504	0.6478
3	neutral		0.1071		
	charged	0.1918	−0.0555	−0.0147	0.3016
	symmetric		−0.0221		
4	any		0.0098		

This expression has now to be stationary with respect to ξ_J. We find

$$\xi_J = -(\bar{\beta}_J \cot\delta_J + \bar{b}_J)/(\bar{a}_J \cot\delta_J + \bar{a}_J). \quad (64)$$

From (62′) and (64)

$$(\bar{a}_J\bar{\gamma}_J - \bar{\beta}_J{}^2)\cot^2\delta_J + (\bar{a}_J\bar{\gamma}_J + \bar{a}_J\bar{c}_J - 2\bar{b}_J\bar{\beta}_J) \times\cot\delta_J + \bar{a}_J\bar{c}_J - \bar{b}_J{}^2 = 0. \quad (65)$$

The two solutions of this equation give the two phase shifts $\delta_J{}^\alpha$ and $\delta_J{}^\gamma$. The constants $\xi_J{}^\alpha$ and $\xi_J{}^\gamma$ follow then from (64), and the amounts of admixture from (51) and (47), where one puts $\delta_J{}^u = \delta_J{}^w = \delta_J{}^{\alpha,\gamma}$ and replaces $u_J(x)$ and $w_J(x)$ by $\bar{u}_J(x)$ and $\xi_J{}^{\alpha,\gamma}\bar{w}_J(x)$. The identity (52) provides for a valuable check of the calculations.

We used this variational procedure to calculate the cross sections for a rectangular well with the constants of Rarita and Schwinger[8] at 15 and 100 Mev. The trial functions were those which correspond to the Born-approximation

$$\bar{u}_J(x) = \kappa x j_{J-1}(\kappa x), \quad \bar{v}_J(x) = \kappa x j_J(\kappa x), \quad \bar{w}_J(x) = \kappa x j_{J+1}(\kappa x). \quad (66)$$

These trial functions will give better results the higher the energy and the higher the value of J. In order to obtain an estimate of the error we calculated the phase shift for the S-state in the non-tensor case with these trial functions ($\bar{v}_0(x)$) and the variational principle (61). One finds

$$-\cot\delta_0 = \left(\frac{2\kappa}{f\lambda} - \frac{\cos^2\kappa}{\kappa}\right)/(1-j_0(2\kappa)) + j_1(2\kappa)/(1-j_0(2\kappa))^2. \quad (67)$$

The exact solution is

$$-\cot\delta_0 = \left(1+\frac{\kappa'}{\kappa}\cot\kappa'\cot\kappa\right)\Big/ \left(\cot\kappa - \frac{\kappa'}{\kappa}\cot\kappa'\right). \quad (68)$$

Figure 6 shows how the results compare for the triplet state at various energies. The error vanishes near 10 Mev ($\kappa\sim1$) where the S-phase shift passes through $-90°$. It has a maximum near 130 Mev ($\kappa\sim3.5$) and decreases for higher energies as expected. The variational value of $|\delta_0|$ is always larger than the exact value, and, therefore, the difference of the squares of $\sin\delta_0$ has to change sign near $-90°$. The small error below 40 Mev ($\kappa\sim2$) is due to the fact that the first term of the expansion of the trial function with respect to κx becomes more and more important, and that this term is the same as in the exact solution. At zero energy the exact and variational phase shifts are zero, and the function plotted in Fig. 6 becomes indeterminate; it approaches the finite limit -11.37 percent.

A great number of the integrals (63) could be evaluated analytically, when the trial functions (66) were used. The results for the phase shifts and the amounts of admixture for n-p scattering at 15 and 100 Mev are shown in Tables XIIIa and XIIIb. Since the phase shifts for the uncoupled states can also be found by the exact formulas (13) and (14), it is easy to find the error of the variational procedure. A comparison of the exact and the variational $^3P_0$ and $^3P_1$ phases is made in Table XIV.

The singlet, triplet, and total cross sections at 15 and 100 Mev for n-p scattering are tabulated in Table XV. The cross sections at 100 Mev for n-n scattering are given in Table XVI.

Since the partial wave $\psi_{1,m}{}^\alpha$ is mainly an S-state as can be seen from the amounts of admixture, we will expect its contribution to the triplet

TABLE XIV. Comparison of P-phases.

Energy Mev	Theory	$^3P_0$ Exact	$^3P_0$ Var.	$^3P_1$ Exact	$^3P_1$ Var.
15.3	neutral	−0.1030	−0.1023	1.0081	0.9151
	charged	0.5378	0.5104	0.1153	0.1141
	symmetric	0.07514	0.07496	−0.05489	−0.05483
100.3	neutral	−0.6567	−0.6422	0.9795	0.9328
	charged	0.8450	0.8149	−0.7428	−0.7219
	symmetric	0.3024	0.3009	−0.3222	−0.3205

cross sections to be off the exact value by about the same amount as the S-state of the corresponding non-tensor case (Fig. 6). For 15 Mev ($\kappa\sim1.2$) and 100 Mev ($\kappa=3.08$) this error is 2 percent and 22 percent, respectively. It amounts to a maximum correction of 0.01 barn and 0.0025 barn for the total cross sections at these two energies (Table XV). The total cross sections at 15.3 Mev are in excellent agreement with the exact calculations of Rarita and Schwinger[8] which obtained 0.621, 0.666, and 0.983 barn for the symmetrical, charged, and neutral theory, respectively. Exact calculations at 100 Mev by Ashkin and Wu[10] give 0.129 barn for the total n-p cross section which is to be compared with our value of 0.1271(+0.0025 max.) barn of the symmetrical theory. All three theories give n-p cross sections at 100 Mev which compare well with the calculations at 83 Mev of Massey, Burhop, and Hu,[15] namely 0.1410, 0.1577, and 0.2388 barn for the symmetrical, charged, and neutral theory, respectively.

CONCLUSIONS

Recent experiments[5, 6a] on neutron-proton scattering at 90 Mev gave a cross section $\sigma_{np}=0.083\pm0.004$ barn. The angular distribution in the center of mass system seems to be symmetrical around 90° and yields a ratio $R=\sigma_{np}(\pi)/\sigma_{np}(\pi/2)$ of about 3. None of the phenomenological theories discussed so far in this paper yield these results. Qualitatively, the neutral theory is ruled out, because it leads to $R<1$; the charged theory leads to too large values of R; closest to the observations comes the symmetrical theory. The non-tensor theory leads to practically no sideward scattering, in contradiction to the experiments. A large increase of $\sigma(\pi/2)$ is obtained by the addition of a tensor part to the potential (compare Fig. 1 with Figs. 4 and 5.)

At 100 Mev in the symmetrical theory, the tensor force increases the total cross section for a rectangular well, but decreases it for a Yukawa well. The latter yields $\sigma_{np}(\text{Born})=0.089$ barn with the better set of constants (Table X); the exact value may be larger by an error of the order of 5 percent. The Born approximation value of R is three times too large. A decrease of the tensor range could sufficiently decrease the total cross section and would make the angular distribution more isotropic. On the other hand, a relativistic correction would have to account for a decrease in the total cross section by 5–10 percent; this is not impossible.[6b] It would also have to account for a large decrease of R. *We conclude, that the symmetrical tensor theory with a Yukawa well may be in agreement with the experiments, if the relativistic corrections at 100 Mev are taken into account and the tensor range is reduced.*

Under the assumption that the symmetry of the angular distribution around 90° can be experimentally established, a new type of exchange force suggests itself. It would consist of equal amounts of neutral and charged exchange potential, such that only even states contribute to the cross section.[31] The exchange operator in (28) would be in this case, as follows from (33),

$$f(\sigma_1\cdot\sigma_2,\ \tau_1\cdot\tau_2)=-\frac{1}{2}\left(1-\frac{1+\sigma_1\cdot\sigma_2}{2}\frac{1+\tau_1\cdot\tau_2}{2}\right)$$
$$=-\tfrac{1}{2}(1+(-1)^L). \quad (69)$$

From our exact and variational calculations we find for a rectangular well of ranges 2.80×10^{-13} cm the n-p cross sections at 100 Mev as shown in Table XVII. The total tensor cross section

TABLE XV. Cross sections for n-p scattering at 15 and 100 Mev. (Tensor forces, rectangular well potential, variational calculation of phases.)

Theory	15 Mev $\sigma_{np}^{(s)}$	15 Mev $\sigma_{np}^{(t)}$	15 Mev σ_{np}	100 Mev $\sigma_{np}^{(s)}$	100 Mev $\sigma_{np}^{(t)}$	100 Mev σ_{np}
Neutral	0.4369	1.1145	0.9833	0.06455	0.2602	0.2113
Charged	0.4236	0.7262	0.6657	0.05523	0.1812	0.1497
Symmetric	0.4445	0.6663	0.6108	0.16916	0.1131	0.1271

TABLE XVI. Cross sections for n-n scattering at 100 Mev. (Tensor forces, rectangular well, variational calculation of coupled states.)

	$\sigma_{nn}^{(s)}$	$\sigma_{nn}^{(t)}$	σ_{nn}
Neutral	0.04636	0.32661	0.25655
Charged	0.04636	0.16864	0.13807
Symmetric	0.04636	0.03239	0.03588

TABLE XVII. Neutron-proton cross sections at 100 Mev for an even interaction potential. (Rectangular well, phase method.)

Force	$\sigma_{np}^{(s)}$	$\sigma_{np}^{(t)}$	σ_{np}
Central	0.02318	0.06543	0.05487
Tensor	0.02318	0.09688	0.07831

[31] Ashkin and Wu (reference 10) quote Serber on this point.

may again be too small by less or about 0.0025 barn. Since the odd states do not contribute much to the scattering at 90°, the differential cross section at this angle will be not much smaller than in the symmetrical tensor theory, where the odd states are reduced to one third in their potential. This will be close to the observed value. From the symmetry and the strongly reduced total cross section it then follows that R will be much smaller than in the symmetrical tensor theory.

Two neutrons interact only in odd triplet and even singlet states. With the exchange force (69) they will interact only in singlet states. We find from (22): $\sigma_{nn}=2\sigma_{np}{}^{(s)}=0.04636$ barn. The symmetrical tensor theory gives (Table XV) $\sigma_{nn}=0.03588$ barn. The experimental value of the difference between the *n-d* and the *n-p* cross section at 90 Mev is[6a] 0.034 ± 0.003 barn. However, Wu and Ashkin[32] have shown that the *n-n* cross section may be appreciably larger than this difference. Therefore, either theory can be correct.

Finally, one should mention that a potential of the exchange type (69) is also in agreement with the measurements of Laughlin and Kruger.[4] The ratio $R=1.05$ which follows from the calculations of Rarita and Schwinger[8] for 15 Mev is certainly within the experimental error.

We conclude, therefore, that, *if relativistic corrections at 100 Mev are negligible, the scattering experiments are consistent with a nucleon tensor force which acts only in even states.*

ACKNOWLEDGMENT

We are grateful to Professor Julian Schwinger for helpful discussions of many aspects of this problem. One of us (F. R.) would also like to acknowledge the support he has received during this work from a Bayard Cutting Fellowship for Research in Physics.

APPENDIX: FORMULAS FOR THE DIFFERENTIAL AND TOTAL CROSS SECTIONS

A. Born Approximation

a. N-P Cross Sections

With the notation used in this paper and the symbols

$$\xi=2\kappa\sin\vartheta/2,\quad \chi=2\kappa\cos\vartheta/2,$$

the cross sections are found to have the following convenient forms:

For central forces and a rectangular well:

Differential cross section,

neutral: $$\sigma_{np}(\vartheta)=\lambda^2r_0^2j_1^2(\xi)/\xi^2 \quad \text{(singlet or triplet)}, \tag{A2}$$

charged: $$\sigma_{np}(\vartheta)=\lambda^2r_0^2j_1^2(\chi)/\chi^2 \quad \text{(singlet or triplet)}, \tag{A3}$$

symmetric:

$$\sigma_{np}{}^{(s)}(\vartheta)=\lambda_s^2r_0^2[j_1(\xi)/\xi-2j_1(\chi)/\chi]^2, \tag{A4}$$

$$\sigma_{np}{}^{(t)}(\vartheta)=\lambda_t^2r_0^2[j_1(\xi)/\xi+2j_1(\chi)/\chi]^2. \tag{A5}$$

Total cross section,

neutral and charged:

$$\sigma_{np}=\frac{\pi}{2k^2}\lambda^2[1-j_0^2(2\kappa)-j_1^2(2\kappa)] \quad \text{(singlet or triplet)}, \tag{A6}$$

symmetric:

$$\sigma_{np}{}^{(s)}=\frac{2\pi}{k^2}\lambda_s^2\{(5/4)[1-j_0^2(2\kappa)-j_1^2(2\kappa)]-R_0(\kappa)\}, \tag{A7}$$

$$\sigma_{np}{}^{(t)}=\frac{1}{9}\frac{2\pi}{k^2}\lambda_t^2\{(5/4)[1-j_0^2(2\kappa)-j_1^2(2\kappa)]+R_0(\kappa)\}, \tag{A8}$$

where

$$R_0(\kappa)=\int_0^\pi j_1(\xi)j_1(\chi)d\vartheta$$

$$=\kappa^2\sum_{L=0}^{\infty}(-1)^L(2L+1)[j_L^2(\kappa)-j_{L-1}(\kappa)j_{L+1}(\kappa)]. \tag{A9}$$

For central forces and a Yukawa well:

neutral: $$\sigma_{np}(\vartheta)=\lambda^2r_y^2/(1+\xi^2)^2 \quad \text{(singlet or triplet)}, \tag{A10}$$

charged: $$\sigma_{np}(\vartheta)=\lambda^2r_y^2/(1+\chi^2)^2 \quad \text{(singlet or triplet)}, \tag{A11}$$

symmetric:

$$\sigma_{np}{}^{(s)}(\vartheta)=\lambda_s^2r_y^2[1/(1+\xi^2)^2-2/(1+\chi^2)^2], \tag{A12}$$

$$\sigma_{np}{}^{(t)}(\vartheta)=\tfrac{1}{9}\lambda_t^2r_y^2[1/(1+\xi^2)^2+2/(1+\chi^2)^2]. \tag{A13}$$

Total cross section,

neutral and charged:

$$\sigma_{np}=\frac{\pi}{k^2}\lambda^2(2\kappa)^2/[1+(2\kappa)^2] \quad \text{(singlet or triplet)}, \tag{A14}$$

symmetric:

$$\sigma_{np}{}^{(s)}=\frac{\pi}{k^2}\lambda_s^2\left[5\frac{(2\kappa)^2}{1+(2\kappa)^2}-\frac{4}{1+2\kappa^2}\ln[1+(2\kappa)^2]\right], \tag{A15}$$

$$\sigma_{np}{}^{(t)}=\frac{1}{9}\frac{\pi}{k^2}\lambda_t^2\left[5\frac{(2\kappa)^2}{1+(2\kappa)^2}+\frac{4}{1+2\kappa^2}\ln[1+(2\kappa)^2]\right]. \tag{A16}$$

For tensor forces and a rectangular well:

Differential cross section,

neutral

$$\sigma_{np}{}^{(t)}=\lambda_t^2r_0^2[j_1^2(\xi)/\xi^2+8\gamma^2r_2^2(\xi)], \tag{A17}$$

[32] T. Y. Wu and J. Ashkin, Phys. Rev. **73**, 986 (1948).

charged: same with ξ replaced by χ.

symmetric:

$$\sigma_{np}^{(t)}=\tfrac{1}{8}\lambda_t^2r_0^2\{[j_1(\xi)/\xi+2j_1(\chi)/\chi]^2+8\gamma^2[r_2^2(\xi)-2r_2(\xi)r_2(\chi)+4r_2^2(\chi)]\},\quad\text{(A18)}$$

where

$$r_2(\xi)=\int_0^1 j_2(\xi x)x^2dx=(3Si\xi-4\sin\xi+\xi\cos\xi)/\xi^3.\quad\text{(A19)}$$

Total cross section,

neutral and charged:

$$\sigma_{np}^{(t)}=\frac{\pi}{k^2}\lambda_t^2\{\tfrac{1}{2}[1-j_0^2(2\kappa)-j_1^2(2\kappa)]+8\gamma^2R_2(2\kappa)\},\quad\text{(A20)}$$

symmetric:

$$\sigma_{np}^{(t)}=\frac{1}{9}\frac{2\pi}{k^2}\lambda_t^2\left\{\frac{5}{4}[1-j_0^2(2\kappa)-j_1^2(2\kappa)]+R_0(\kappa)+8\gamma^2\left[5R_2(2\kappa)-\int_0^\pi r_2(\xi)r_2(\chi)\xi\chi d\vartheta\right]\right\},\quad\text{(A21)}$$

where

$$R_2(2\kappa)=\int_0^{2\kappa}r_2^2(\xi)\xi d\xi.\quad\text{(A22)}$$

The integral over the cross term and the integral $R_2(2\kappa)$ of (A22) can be evaluated analytically, but the resulting expressions are too complicated to be given here.

For tensor forces and a Yukawa well:

Differential cross section,

neutral:

$$\sigma_{np}^{(t)}=\lambda_t^2r_y^2[1/(1+\xi^2)^2+8\gamma^2y_2^2(\xi)],\quad\text{(A23)}$$

charged: same with ξ replaced by χ.

symmetric:

$$\sigma_{np}^{(t)}=\tfrac{1}{8}\lambda_t^2r_y^2\{[1/(1+\xi^2)+2/(1+\chi^2)]^2+16\gamma^2[y_2^2(\xi)-2y_2(\xi)y_2(\chi)+4y_2^2(\chi)]\},\quad\text{(A24)}$$

where

$$y_2(\xi)=\int_0^\infty j_2(\xi x)e^{-x}xdx=\frac{3}{\xi^2}(1-\tan^{-1}\xi/\xi)-1/(1+\xi^2),\quad\text{(A25)}$$

Total cross section,

neutral and charged:

$$\sigma_{np}^{(t)}=\frac{\pi}{k^2}\lambda_t^2\left[\frac{(2\kappa)^2}{1+(2\kappa)^2}+16\gamma^2Y_2(2\kappa)\right],\quad\text{(A26)}$$

symmetric:

$$\sigma_{np}^{(t)}=\frac{1}{9}\frac{\pi}{k^2}\lambda_t^2\left\{5\frac{(2\kappa)^2}{1+(2\kappa)^2}+\frac{4}{1+2\kappa^2}\ln[1+(2\kappa)^2]+16\gamma^2\left[5Y_2(2\kappa)-\int_0^\pi y_2(\xi)y_2(\chi)\xi\chi d\vartheta\right]\right\},\quad\text{(A27)}$$

where

$$Y_2(2\kappa)=\int_0^{2\kappa}y_2^2(\xi)\xi d\xi=2-\tfrac{1}{2}1/[1+(2\kappa)^2]-(9/4)1/(2\kappa)^2-\tfrac{3}{4}(\tan^{-1}2\kappa)^2(1+3/(2\kappa)^4)-\tfrac{3}{2}\tan^{-1}2\kappa(1-3/(2\kappa)^2)/2\kappa.\quad\text{(A28)}$$

b. N-N Cross Section

The singlet cross section is the same for all exchange theories, central or tensor forces. It is for a rectangular well

$$\sigma_{nn}^{(s)}(\vartheta)=\lambda_s^2r_0^2[j_1(\xi)/\xi+j_1(\chi)/\chi]^2,\quad\text{(A29)}$$

$$\sigma_{nn}^{(s)}=\frac{\pi}{2k^2}\lambda_s^2[1-j_0^2(2\kappa)-j_1^2(2\kappa)+2R_0(\kappa)],\quad\text{(A30)}$$

and for a Yukawa well

$$\sigma_{nn}^{(s)}(\vartheta)=\lambda_s^2r_y^2[1/(1+\xi^2)+1/(1+\chi^2)],\quad\text{(A31)}$$

$$\sigma_{nn}^{(s)}=\frac{\pi}{k^2}\lambda_s^2\left[\frac{(2\kappa)^2}{1+(2\kappa)^2}+\frac{1}{1+2\kappa^2}\ln[1+(2\kappa)^2]\right].\quad\text{(A32)}$$

The triplet cross section in the charged theory is the same as in the neutral theory, and in the symmetrical theory it is $\frac{1}{8}$th of that in the neutral theory. The neutral triplet cross section is—

for central forces and a rectangular well:

$$\sigma_{nn}^{(t)}(\vartheta)=\lambda_t^2r_0^2[j_1(\xi)/\xi-j_1(\chi)/\chi]^2,\quad\text{(A33)}$$

$$\sigma_{nn}^{(t)}=\frac{\pi}{2k^2}\lambda_t^2[1-j_0^2(2\kappa)-j_1^2(2\kappa)-2R_0(\kappa)],\quad\text{(A34)}$$

for central forces and a Yukawa well:

$$\sigma_{nn}^{(t)}(\vartheta)=\lambda_t^2r_y^2[1/(1+\xi^2)-1/(1+\chi^2)]^2,\quad\text{(A35)}$$

$$\sigma_{nn}^{(t)}=\frac{\pi}{k^2}\lambda_t^2\left[\frac{(2\kappa)^2}{1+(2\kappa)^2}-\frac{1}{1+2\kappa^2}\ln[1+(2\kappa)^2]\right];\quad\text{(A36)}$$

for tensor forces and a rectangular well:

$$\sigma_{nn}^{(t)}(\vartheta)=\lambda_t^2r_0^2\{[j_1(\xi)/\xi-j_1(\chi)/\chi]^2+8\gamma^2[r_2^2(\xi)+r_2(\xi)r_2(\chi)+r_2^2(\chi)]\},\quad\text{(A37)}$$

$$\sigma_{nn}^{(t)}=\frac{\pi}{2k^2}\lambda_t^2\left\{1-j_0^2(2\kappa)-j_1^2(2\kappa)-2R_0(\kappa)+8\gamma^2\left[4R_2(2\kappa)+\int_0^\pi r_2(\xi)r_2(\chi)\xi\chi d\vartheta\right]\right\},\quad\text{(A38)}$$

where R_0, r_2, and R_2 are defined in (A9), (A19), and (A22);

for tensor forces and a Yukawa well:

$$\sigma_{nn}^{(t)}(\vartheta)=\lambda_t^2r_y^2\{[1/(1+\xi^2)-1/(1+\chi^2)]^2+8\gamma^2[y_2^2(\xi)+y_2(\xi)y_2(\chi)+y_2^2(\chi)]\},\quad\text{(A39)}$$

$$\sigma_{nn}^{(t)}=\frac{\pi}{k^2}\lambda_t^2\left\{\frac{(2\kappa)^2}{1+(2\kappa)^2}+\frac{1}{1+2\kappa^2}\ln[1+(2\kappa)^2]+8\gamma^2\left[2Y_2(2\kappa)+\frac{1}{2}\int_0^\pi y_2(\xi)y_2(\chi)\xi\chi d\vartheta\right]\right\},\quad\text{(A40)}$$

where y_2 and Y_2 are defined in (A25) and in (A28).

B. Phase Method for Tensor Forces

The differential cross section (59) can be written

$$\sigma^{(1)}(\vartheta)=\frac{1}{k^2}\sum_n c_n\cos^n\vartheta. \tag{A41}$$

When all the S, P, and D states are taken into account, but the coupling to higher angular momenta is neglected, one obtains for n-p scattering

$$\begin{aligned}
c_0=&\tfrac{1}{3}({}^3P_0)+\left[1-\frac{\left(1+\frac{1}{(8)^{\frac{1}{2}}}e^{-\zeta_1}\right)^2}{2\cosh^2\zeta_1}\right]({}^3S_1)\\
&+\tfrac{3}{4}({}^3P_1)+\tfrac{13}{12}({}^3P_2)+\left[1-\frac{\left(1-\frac{1}{(8)^{\frac{1}{2}}}e^{\zeta_1}\right)^2}{2\cosh^2\zeta_1}\right]({}^3D_1)\\
&+\tfrac{25}{12}({}^3D_2)+\tfrac{19}{12}({}^3D_3)-\frac{(\sinh\zeta_1+1/(8)^{\frac{1}{2}})^2}{2\cosh^2\zeta_1}\\
&\times({}^3S_1+{}^3D_1)-\tfrac{1}{3}({}^3P_0+{}^3P_2)-\tfrac{3}{4}({}^3P_1+{}^3P_2)\\
&+\tfrac{5}{12}({}^3D_2+{}^3D_3)-\frac{5e^{\zeta_1}(1+\sqrt{2}e^{-\zeta_1})^2}{24\cosh\zeta_1}({}^3D_1+{}^3D_2)\\
&+\frac{-\frac{7}{6}e^{\zeta_1}-\frac{\sqrt{2}}{12}+\frac{11}{12}e^{-\zeta_1}}{2\cosh\zeta_1}({}^3S_1+{}^3D_1)\\
&-\frac{5e^{-\zeta_1}(1-\sqrt{2}e^{\zeta_1})^2}{24\cosh\zeta_1}({}^3S_1+{}^3D_2),\\
c_1=&\frac{e^{-\zeta_1}(e^{\zeta_1}+\sqrt{2})^2}{6\cosh\zeta_1}({}^3S_1+{}^3P_0)+\frac{e^{-\zeta_1}(1-\sqrt{2}e^{\zeta_1})^2}{4\cosh\zeta_1}\\
&\times({}^3S_1+{}^3P_1)+\frac{10e^{\zeta_1}-16e^{-\zeta_1}}{12\cosh\zeta_1}({}^3S_1+{}^3P_2)\\
&+\frac{e^{\zeta_1}(e^{-\zeta_1}-\sqrt{2})^2}{6\cosh\zeta_1}({}^3P_0+{}^3D_1)-\tfrac{3}{2}({}^3P_0+{}^3D_3)\\
&+\frac{e^{\zeta_1}(1+\sqrt{2}e^{-\zeta_1})^2}{4\cosh\zeta_1}({}^3P_1+{}^3D_1)-3({}^3P_1+{}^3D_3)\\
&+\frac{5e^{-\zeta_1}-8e^{\zeta_1}}{6\cosh\zeta_1}({}^3P_2+{}^3D_1)-\tfrac{5}{2}({}^3P_2+{}^3D_2)\\
&+({}^3P_2+{}^3D_2),
\end{aligned}\tag{A42}$$

$$\begin{aligned}
c_2=&\tfrac{3}{2}\frac{\left(1+\frac{1}{(8)^{\frac{1}{2}}}e^{-\zeta_1}\right)^2}{\cosh^2\zeta_1}({}^3S_1)+\tfrac{3}{4}({}^3p_1)\\
&+\tfrac{3}{2}\frac{\left(1-\frac{1}{(8)^{\frac{1}{2}}}e^{\zeta_1}\right)^2}{\cosh^2\zeta_1}({}^3D_1)+\tfrac{7}{4}({}^3P_2)-\tfrac{25}{4}({}^3D_2)\\
&-\tfrac{1}{2}({}^3D_3)+\tfrac{3}{2}\frac{(\sin\zeta_1+1/(8)^{\frac{1}{2}})^2}{\cosh^2\zeta_1}({}^3S_1+{}^3D_1)\\
&+({}^3P_0+{}^3P_2)+\tfrac{9}{4}({}^3P_1+{}^3P_2)-\tfrac{15}{2}({}^3D_2+{}^3D_3)\\
&+\frac{5}{8}\frac{e^{\zeta_1}(1+\sqrt{2}e^{-\zeta_1})^2}{\cosh\zeta_1}({}^3D_1+{}^3D_2)\\
&+\frac{\frac{7}{2}e^{-\zeta_1}-\sqrt{2}-\frac{19}{2}e^{\zeta_1}}{2\cosh\zeta_1}({}^3D_1+{}^3D_3)\\
&+\frac{5}{8}\frac{e^{-\zeta_1}(1-\sqrt{2}e^{\zeta_1})^2}{\cosh\zeta_1}({}^3S_1+{}^3D_3)\\
&+\frac{\frac{7}{2}e^{\zeta_1}+\sqrt{2}-\frac{19}{2}e^{-\zeta_1}}{2\cosh\zeta_1}({}^3S_1+{}^3D_3),\\
c_3=&\frac{9e^{-\zeta_1}}{4\cosh\zeta_1}({}^3S_1+{}^3P_2)+\tfrac{5}{2}({}^3P_0+{}^3D_3)+\tfrac{5}{2}({}^3P_1+{}^3D_2)\\
&+5({}^3P_1+{}^3D_3)+\frac{9e^{\zeta_1}}{4\cosh\zeta_1}({}^3P_2+{}^3D_1)\\
&+5({}^3P_2+{}^3D_2)+3({}^3P_2+{}^3D_3)\},\\
c_4=&\tfrac{25}{3}({}^3D_2)+\tfrac{55}{12}({}^3D_3)+\tfrac{125}{12}({}^3D_2+{}^3D_3)\\
&+\frac{45e^{\zeta_1}}{8\cosh\zeta_1}({}^3D_1+{}^3D_3)+\frac{45e^{-\zeta_1}}{8\cosh\zeta_1}({}^3S_1+{}^3D_3),
\end{aligned}$$

where

$$\zeta_1=-\ln\eta_1{}^\alpha,$$

$$({}^3L_J)=\sin^2\delta_J{}^{\alpha,\beta,\gamma}\quad\begin{matrix}\alpha\to L=J-1\\ \beta\to L=J\\ \gamma\to L=J+1\end{matrix}, \tag{A43}$$

$$({}^3L_J+{}^3L'_{J'})=2\sin\delta_J{}^{\alpha,\beta,\gamma}\sin\delta_{J'}{}^{\alpha',\beta',\gamma'}\cos(\delta_J-\delta_{J'}).$$

The n-n cross section is obtained from this by omission of all the even phases and multiplication by a factor of four.

Particle Groups from the Bombardment of Aluminum by Deuterons

E. C. POLLARD, V. L. SAILOR, AND L. D. WYLY
Sloane Physics Laboratory, Yale University, New Haven, Connecticut*
(Received November 12, 1948)

Targets of aluminum leaf 30 kev thick have been bombarded by deuterons and found to emit protons in 14 groups and alpha-particles in four groups. These correspond to levels in Al^{28} and Mg^{25}. The level spacing in Al^{28} appears to become somewhat less at excitation energies of 5 Mev, and the population of the highly excited states is greater. There appear to be five major groupings, each having a finer structure. Observation at 90° and 0° with respect to the incident deuterons shows a considerable variation in relative yield. In comparison with neutron scattering levels for the same nucleus, the spacing here observed is greater. This may be due to the adverse selection of groups of high angular momentum on account of the Coulomb barrier. The level spacing in Mg^{25} is approximately 0.8 Mev. From the maximum energy of the protons and alpha-particles the mass difference between Al^{28} and Al^{27} is found to be 1.00073 ± 0.00008, and between Mg^{25} and Al^{27} is 1.99619 ± 0.00006 mass units.

INTRODUCTION

A STUDY of particle groups produced in the bombardment of elements between Ne and A[1] shows that they possess group structure corresponding to deep energy levels in the product nucleus. In the case of Al^{27} it was observed by Schultz, Davidson, and Ott[2] that the proton groups correspond to a level separation which is small so that no actual values for the nuclear energy changes could be given. More recent work by Allan and Wilkinson[3] using deuterons of much lower energy shows the presence of four well marked groups with a total excitation energy of a little over 2 Mev.

For the emission of protons the product nucleus is Al^{28}. Evidence regarding the level structure of this nucleus has been gained by Allen, Burcham, and Wilkinson[4] and Seagondollar and Barschall[5] by observing the variation in the total neutron cross section of aluminum as a function of neutron energy. These experiments show the presence of levels at excitation energies above 7 Mev. It would be interesting to try to observe proton groups of short range and at high bombarding energies to attempt to observe the same levels as found in the neutron scattering work. Our experiments do not permit this direct comparison to be made but show a trend which enables energy spacings to be estimated roughly.

EXPERIMENTAL METHOD AND RESULTS

The beam of the cyclotron is brought out through a deflecting magnet into a bombardment chamber as described by Martin.[6] Since the proton spectrum is known to be complicated, it is essential to remove any possible source of contamination by high yield elements. To aid this, the target of aluminum was suspended across a large C-shaped support so that no protons could emerge through the proton port unless they originate in the leaf. In this way any backing material is eliminated from the target. Observation was made at 90° to the deuteron beam by this method. For 0° observation the target was placed in the end of the bombardment chamber and backed by sufficient gold to stop the beam. The end of the bombardment chamber was made vacuum tight by an aluminum foil.

At these bombarding energies the cross section of aluminum is comparable with, or greater than, that of lighter elements. Therefore, there is no reason to expect larger yields from contaminants than from aluminum. A possible exception is oxygen, which has a high cross section and which is present as a thin oxide layer on the surface of the leaf. Groups having Q values close to those of oxygen were accordingly suspected, and a special

* Assisted by the Joint Program of the Office of Naval Research and the Atomic Energy Commission.

[1] Elder, Motz, and Davison, Phys. Rev. **71**, 917 (1947); P. W. Davison, in course of publication; E. Pollard and P. W. Davison, Phys. Rev. **73**, 1241 (1948).

[2] Schultz, Davidson, and Ott, Phys. Rev. **58**, 1043 (1940).

[3] H. R. Allan and Mrs. C. A. Wilkinson, Proc. Roy. Soc. (in course of publication).

[4] Allen, Burcham, and Wilkinson, Proc. Roy. Soc. **A192**, 114 (1947).

[5] L. W. Seagondollar and H. H. Barschall, Phys. Rev. **72**, 439 (1947).

[6] Albert B. Martin, Phys. Rev. **71**, 127 (1947).

TABLE I. Beam energy determination.

Scattered deuterons	Direct beam range	Proton range variation
3.74±0.05	3.79±0.05	3.80±0.07

series of bombardments was undertaken to investigate the possibility of oxygen contamination.

The energy and homogeneity of the beam were measured by three methods. The first was by scattering the deuterons from a gold leaf and observing their range using a proportional counter for detection. The results are shown in Fig. 1 as the full curve. A second series of measurements were made on the direct beam using a galvanometer to detect the deuterons and a small gas cell to introduce variable absorption into the beam. A third check on the beam energy was obtained from reduced energy bombardment of the target. A foil of 9.50-cm air equivalent was placed in the path of the beam. The maximum energy of the protons in the reaction $Al^{27}(dp)Al^{28}$ then fell from 89.0 cm to 54.0 cm. Table I shows the beam energy as derived in the three ways. The direct beam measurement is to be preferred. The individual measurements by this method are considerably better than indicated by the errors given, but because the beam energy is not completely homogeneous across the target, a larger estimate of error has been taken. A value of 3.79 Mev has been used in our calculations.

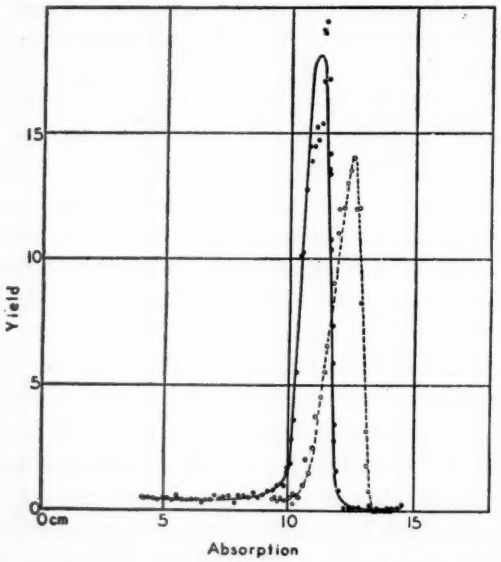

FIG. 1. Scattered deuterons and differential curve of beam. The full curve shows the variation of yield of deuterons scattered from a thin gold leaf as the thickness of absorber is increased. The dashed curve is derived from range measurements made on the direct beam using a galvanometer for detection.

The beam homogeneity can be inferred from Fig. 1. There is a certain amount of low energy beam, which will account for very small yields between proton groups. This is probably due to scattering as the beam emerges from the cyclotron. The half-width of the great majority of the beam is 1.20 cm, the theoretical half-width caused by straggling in the absorption cell is 0.4 cm, so that the spread of energy of the beam is ±0.083 Mev.

In the measurement of ranges aluminum foils were used. These were corrected by the calibration curve of Livingston and Bethe to air equivalent. A correction was applied for the effective depth of the proportional counter; however, it is not too precise a correction as the value depends on the bias of the counters. For scattering measurements and alpha-particle range determination a helium-filled counter was used, which greatly reduces this correction. The equivalent counter depth was taken to consist of two parts, the first the drift space before the discharge region is reached, and the second the depth of gas required to give the detected pulse. The drift space corresponded closely with the distance from the front of the counter to the axial wire.

The ranges were read as extrapolated numbers range. There is a small error involved in so doing as the target is not infinitely thin. However, the same procedure was applied to the measurement of the beam range and repeated comparisons have shown that the error introduced is smaller than other experimental errors. The Cornell 1937 range energy relations were used.

Proton Group Observation

The results of a typical run, of which ten were taken, at 90° to the incident beam are shown in Fig. 2. The bias level of the counting circuit was set so that only particles very close to the end of their path would record. It can be seen that five broad sets of particle groups are present. Careful observation led us to consider that the group of maximum energy is single or, if a doublet, cannot be resolved with our equipment.

The second pair of groups appear to be single. This is then followed by a set of three groups of decreasing yield as excitation increases and a set of two and perhaps three groups follows it. The highest yield set consists of five imperfectly resolved groups again falling off in yield as the excitation increases. The Q values for all these groups are given in Table II. Of these groups Q_7 and Q_{10} are possibly due to oxygen contamination. This is further discussed later.

Since the region of greatest interest is that of high excitation, a series of runs was taken in which the particles of ranges between 13 cm (the elastically scattered deuterons) and 30 cm were carefully examined. For this a low solid angle arrangement with a thinner target and an air absorption cell was used. The results are shown in Fig. 3. Five groups are believed to be present. Four can definitely be seen, and the presence of the fifth is deduced from the excessive width of the group at 24 cm.

Independent information on group structure can be obtained by varying both the angle of observation and the beam energy. A run taken at 0° with respect to the beam is shown in Fig. 4. Six groups are clearly seen, of which two, those ending at 58 cm and 42 cm, are abnormally wide. The angular resolution in this run was not so good as the 90° case which accounts for the poorer resolution. It can be seen that the relative yield of the groups is greatly different, a fact that has been observed in other reactions.[7] In this set of runs it was necessary to stop the beam in gold foil. This gold foil has a varying air equivalent for different energies. This variation is discussed in Bethe and Livingston's review article but the precision they claim is not very high. In order to enable the calculation of Q values from these data, we made a calibration of the gold foil by inserting it in the 90° absorption path and making a direct comparison with aluminum absorbers. The results we obtained

TABLE II. Q values.

	Al^{28} (90°)	0°	Mg^{25} (90°)
Q_0	5.45±0.05 Mev	5.38 Mev	6.52±0.06 Mev
Q_1	4.42±0.05	4.36	5.71±0.08
Q_2	3.88±0.10	3.74	4.94±0.08
Q_3	3.29±0.07	3.28	3.98±0.08
Q_4	2.84±0.08	2.72	
Q_5	2.48±0.10		
Q_6	2.04±0.08	1.98	
Q_7	1.55±0.10		
Q_8	0.98±0.12	0.96	
Q_9	0.73±0.05		
Q_{10}	0.57±0.10		
Q_{11}	0.29±0.08		
Q_{12}	0.01±0.08		
Q_{13}	−0.31±0.08		

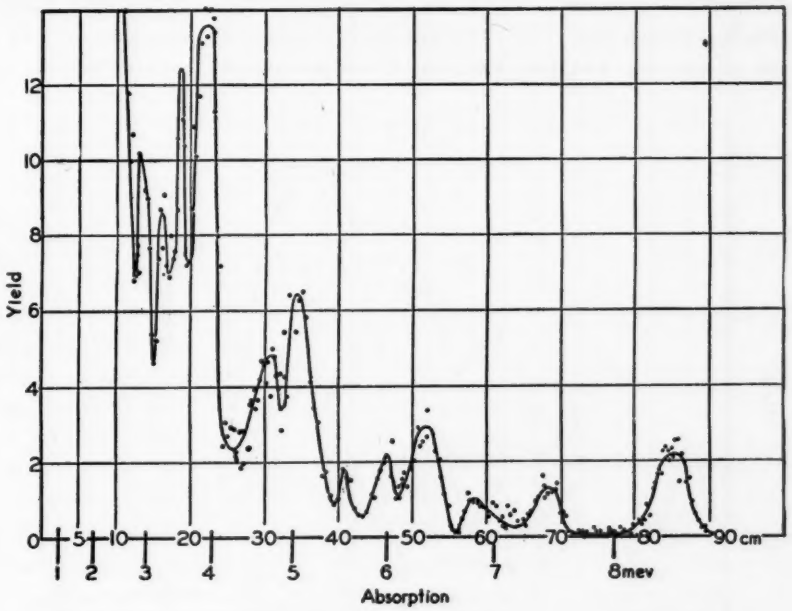

FIG. 2. Typical run at 90°. Absorption curve for the protons emitted at 90° to the deuteron beam. Five sets of groups can be seen, and 13 total groups at least are present. The yield is higher for high excitation.

[7] Powell and co-workers, unpublished; N. P. Heydenburg and D. R. Inglis, Phys. Rev. **73**, 230 (1948); P. W. Davison (in course of publication).

TABLE III.

Av. proton energy in 12.5 cm of gold	Measured range correction needed using 3.77 mg/cm² per cm of air	Range correction using Bethe and Livingston data
8.23 Mev	3.5 cm	3.26 cm
7.22	3.0	3.09
6.72	3.3	2.92
6.07	3.10	2.81
4.90	2.3	2.48

are given in Table III. Such a procedure is not highly precise unless extreme care is taken; however, our results are in good agreement with Bethe and Livingston.

Using this calibration the Q values given in Table II, second column, were calculated. Agreement with the 90° data is reasonable when allowance is made for the poorer geometrical conditions.

Some groups appear to be missing at 0°. Thus Q_5 and Q_6 appear definitely in the 90° run, but only Q_6 is apparent at 0°. This is surprising because the vanishing of $\cos\theta$ at 90° would be expected to modify the yield at that angle and reduce the intensity of some groups. It is surprising to find the 90° spectrum apparently richer.

The results of bombardment at different beam energies are shown in Fig. 5. The general appearance of the spectrum does not change very much, though the yield does diminish gradually for all groups. The fact that the cross section in the $O^{16}(dp)O^{17}$ reaction should be higher at this energy enables some estimate of the proportion of oxygen contaminant present. At a 1.5-Mev bombarding energy the actual yield of a suspected oxygen group is one-half that at full energy. Therefore, it is unlikely that more than half this suspected group is due to oxygen. We feel that Q_7 represents a mixture of yield from aluminum and oxygen but is not purely due to either.

Apart from the question of oxygen contamination, this curve shows that no considerable resonances occur except in the Q_6-Q_8 region.

An integral curve, in which all protons were counted, was plotted. From this approximate values for the cross sections of each group were estimated. These are shown on the energy level diagram, Fig. 7.

Alpha-Particle Group Observation

An attempt was made to observe proton groups of range less than that of the scattered deuterons. It was found that groups of highly ionizing particles existed, of greatest range somewhat less than the maximum range of the deuterons. By increasing the counter bias it was found possible to avoid counting deuterons entirely and detect only these groups of particles. Their ionization density checked with that of ThC′ alpha-particles, and we conclude that they are due to the reaction $Al^{27}(d\alpha)Mg^{25}$.

The results of a measurement of yield *versus*

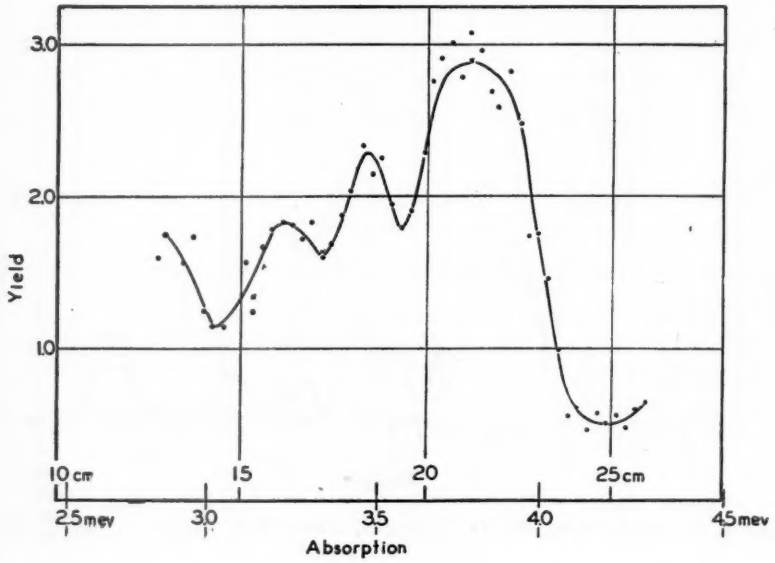

FIG. 3. Detail of proton groups at high excitation. Absorption curve in the high energy region showing the multiplicity of proton groups at low energy.

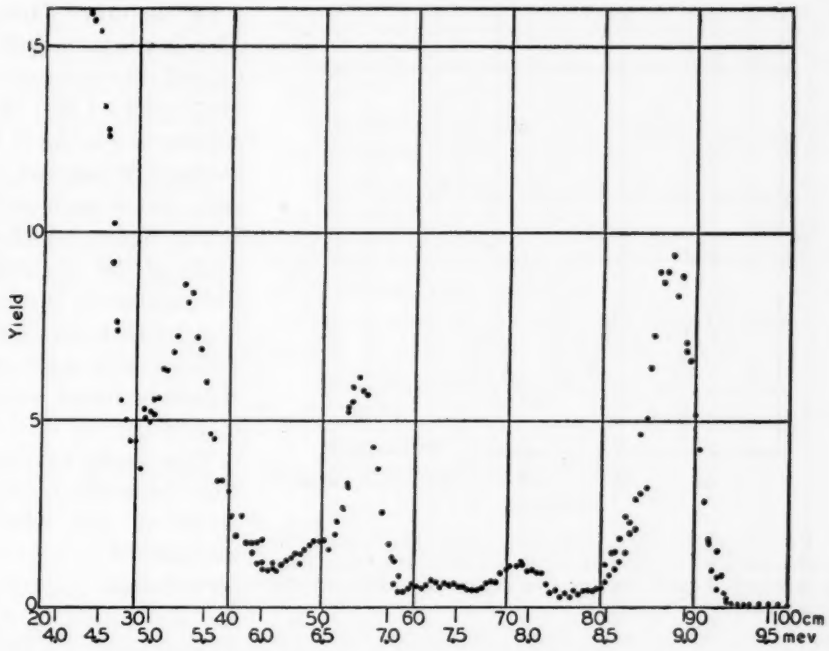

FIG. 4. Protons at 0°. Absorption curve for the protons emitted at 0° to the deuteron beam. Six groups can be seen, of which two are multiple. The relative yields are different from the 90° case.

absorption are shown in Fig. 6. Four groups of alpha-particles are observed. The Q values are given in Table II, and the cross sections are shown in Fig. 7.

The fact that the use of biasing methods was successful is due to the high resolution attained by the counters and amplifiers. We wish to give full credit for this design to Dr. H. L. Schultz of this laboratory.

DISCUSSION

Energy level diagrams for Al^{28} and Mg^{25} are given in Fig. 7 with the cross sections of each group based on observations at 90°. For comparison the levels found by Allen, Burcham, and Wilkinson, and by Seagondollar and Barschall are shown. The degree of excitation in the neutron scattering work can be accurately inferred from our data. Thus the maximum Q value sets the energy difference due to mass between the sum of a deuteron and Al^{27} and of a proton and Al^{28} as 5.45 Mev. The energy difference due to mass between the sum of Al^{27} and a neutron and Al^{28} can then be found to be 7.62 Mev. This makes use of the accepted values for the mass of deuteron, neutron, and proton. Accordingly, the minimum excitation energy in the neutron scattering experiments is 7.62 Mev. Our data do not quite overlap this work, but approach it so nearly that the trend can be inferred. It appears definitely that the level spacing we observe is

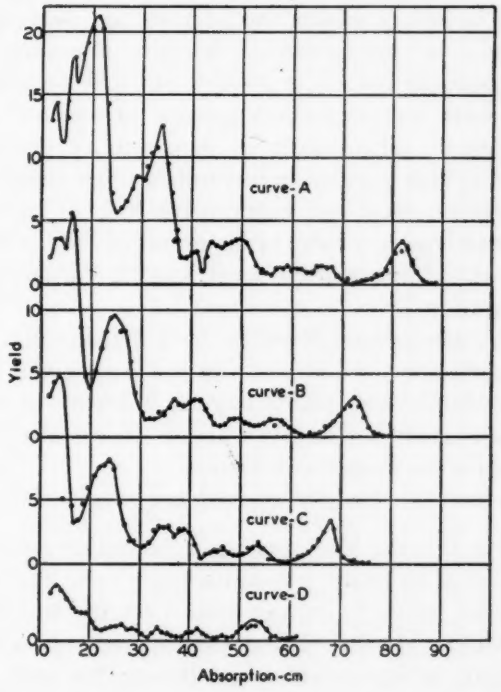

FIG. 5. Protons at different bombarding energies. Absorption curve for protons emitted at 90° to the beam for four bombarding energies. No great change in relative yield is observed except for the region Q_6-Q_8.

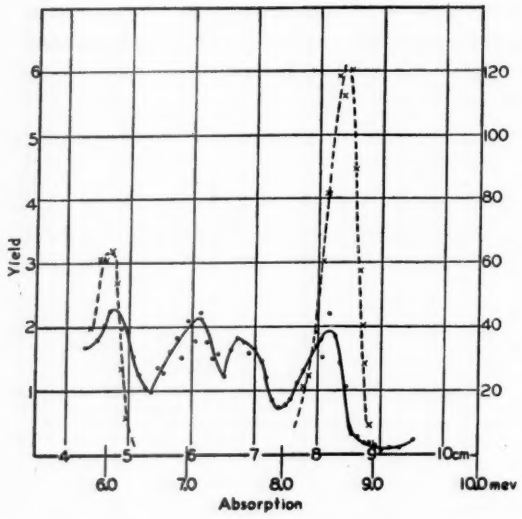

FIG. 6. Alpha-particle groups. Absorption curve for alpha-particles emitted at 90° to the deuteron beam with a superposed curve for the two groups of alpha-particles from ThC′.

larger than that found by Seagondollar and Barschall.

A possible explanation for this can be found in the condition affecting the emergence of protons. The region of high excitation, say from Q_4 up to Q_{13}, is one in which the protons are near the energy of the potential barrier. Penetration through the barrier is possible but will diminish the cross section for any groups for which it is necessary. This factor is increased for groups having high angular momentum, and we suggest, therefore, that our experiments fail to detect groups having a value of l in excess of 2. This will increase the apparent level spacing for higher excitation.

A consideration of energy level spacings and of the relative yield of particles has been given by Weisskopf,[8] who points out the influence of the potential barrier as given above. If we take the relation he suggests, namely,

$$D = A \exp[-BE^{\frac{1}{2}}],$$

where D is the level spacing at excitation energy E and A and B are constants for any one nuclear species, we find from our data $A = 1.48$ Mev and $B = 0.77$ (Mev)$^{-\frac{1}{2}}$. These values predict a level spacing in Seagondollar and Barschall's work of 0.16 Mev, whereas the observed spacing is more nearly 0.06 Mev.

[8] Victor F. Weisskopf, Phys. Rev. **52**, 295 (1937).

On the other hand, if our level spacing at 1.9 Mev is taken together with the value 0.06 just quoted, the resulting values for A and B are 4.0 Mev and 1.48 (Mev)$^{-\frac{1}{2}}$, respectively. This requires a spacing at 5.15 Mev of 0.14 Mev which is about 50 percent of our observed value. However, if it is supposed that these values of A and B are right and that in our experiments only levels of low angular momentum are observed, the agreement is not so bad. If this supposition is right then for bombarding energies of 7 Mev and up, with good resolution in detection, there should be found several more levels between our Q_6 and Q_{13}.

This same line of reasoning makes it likely that the levels Q_0 to Q_5 are the actual deep energy levels of Al^{28}. This is made the more likely because of the close agreement between our experiments and those of Allan and Wilkinson for the values Q_0 to Q_3. If actually there are several levels not found due to selection rules, it is to be expected that at higher bombarding energies at least one would show up. Our experiments were at four times their bombarding energy.

The most striking features of the proton ab-

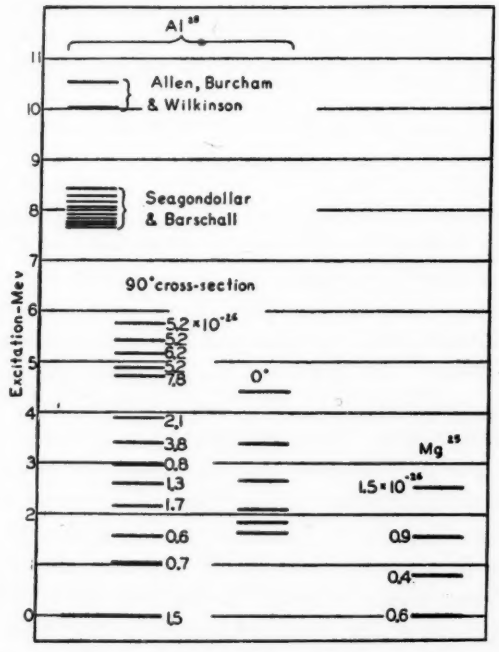

FIG. 7. Level schemes and cross sections. Energy level diagrams for Al^{28} and Mg^{25} as derived from our work. For comparison the levels derived from scattering are shown.

sorption curve are the two "sawtooth" sets of groups. It may be that this is due to the effect of the barrier on groups of increasing angular momentum, in which case the highest local peaks would be S levels.

The three excited states of Mg^{25} are shown in Fig. 7. These should agree with levels found from other reactions, such as $Mg^{24}(dp)Mg^{25}$. The fact that three isotopes of Mg exist renders the correct assignment of Q values difficult, so no comparison can be made at present with our values.

The mass differences $Al^{28}-Al^{27}$ and $Al^{27}-Mg^{25}$ are 1.000735 and 1.99619, respectively.

We wish to thank Professor R. F. Humphreys for much valuable discussion and Professor Howard L. Schultz for design of and assistance with the counting circuits.

PHYSICAL REVIEW VOLUME 75, NUMBER 5 MARCH 1, 1949

The Emission of Radiation in the Disintegration of Mesons*

DANIEL B. FEER**
Jefferson Physical Laboratory, Harvard University, Cambridge, Massachusetts
(Received October 25, 1948)

The probability has been calculated that a meson of integral spin disintegrates into an electron, a neutrino, and a photon. This is essentially a classical process, the radiation being regarded as caused by the acceleration of charge in the disintegration. Because of the classical nature of the problem, the result is independent of the quantum mechanical properties (spin, coupling) of the meson field. For definiteness, the non-radiative decay is taken as being a two-body process in accordance with the original Yukawa theory, but several different types of couplings are used. The quantum mechanical probability for emission of one photon diverges at the low frequency end of the spectrum; this difficulty is avoided by using as a measure of the process the ratio of mean energy emitted to mean energy available for the process per unit time. This is of order $e^2/\hbar c$; the energy spectrum also is in agreement with the classical result.

I. INTRODUCTION

THE nature of the products of decay of the ordinary cosmic-ray mesons (μ-mesons) is still unsettled. Recent experiments[1] however, have established that the decay does not result in the emission of a 50-Mev photon, as would be expected if the process involves simply the emission of two bodies, and the μ-meson has a spin of one-half. From the theoretical point of view, there is another possibility for the emission of electromagnetic radiation in the decay, which is of interest since it can occur regardless of the nature of the other particles emitted and is one of the few processes involving mesons which is essentially classical in nature. If the meson is at rest before disintegrating, and the decay electron has a high velocity, the sudden acceleration of charge should produce radiation. Quantum mechanically, this corresponds to a higher order process, in which a photon is emitted as well as the ordinary decay products. Similar calculations for radiative beta-decay of nuclei have been performed by Bloch and by Knipp and Uhlenbeck.[2]

Because of the classical nature of the problem, the quantum mechanical details of meson spin, and type of interaction between the meson and electron fields, which are not known from experimental evidence, should not affect the results. Some calculations for different types of interactions will be indicated, however, since they afford an interesting example of the way in

* Summary of a thesis presented in partial fulfillment of the requirements for the degree of Doctor of Philosophy at Harvard University.

** Now at Institute for Advanced Study, Princeton, New Jersey.

[1] E. Hincks and B. Pontecorvo, Phys. Rev. **73**, 257 (1948); R. Sard and E. Althaus, Phys. Rev. **73**, 1251 (1948); O. Piccioni, Phys. Rev. **74**, 1236 (1948).

[2] F. Bloch, Phys. Rev. **50**, 272 (1936); J. Knipp and G. Uhlenbeck, Physica **3**, 425 (1936).

which the classical nature of the problem can be used to simplify the quantum mechanical results. Since our primary purpose is merely to indicate this relation between classical and quantum mechanical results, for definiteness the original idea of Yukawa, that the decay products are an electron, and a neutrino will be used, although there is evidence that the process involves the emission of three bodies.[3]

II. CLASSICAL TREATMENT

The qualitative classical ideas given above can be extended to give a quantitative estimate of the probability of the process. The acceleration of the charged particle can be taken as caused by a finite pulse, say of form,

$$a(t)=c\alpha/(\alpha^2+t^2).$$

(Since this argument is concerned only with the order of magnitude of the effect, we omit the factor $2/\pi$ needed to make this approach c times a delta-function.) The "width" α can be determined by the uncertainty relation,

$$\alpha\Delta\omega\sim 1,$$

$\Delta\omega$ being the frequency band-width of the emitted spectrum. In order of magnitude, $\Delta\omega$ is roughly the same as the frequency of the quantum of maximum energy which can be emitted,

$$\hbar\omega_{\max}=\tfrac{1}{2}\mu c^2,$$

μ being the meson mass. Thus,

$$\Delta\omega\cong\mu c^2/\hbar.$$

This mixing of quantum properties with a classical theory is essential, since the basic process of meson decay is non-classical in nature.

The classical total energy emitted during such an acceleration is then,

$$E\sim\mu c^2(e^2/\hbar c).$$

The energy available for the process is of order μc^2, so less than one percent of the energy should be emitted in the form of radiation. The fact that the effect is of order of the fine-structure constant of course is a quantum mechanical result also.

The form of the energy spectrum can be found by taking the fourier transform of the acceleration pulse. This spectrum remains finite at the low frequency end, and must be cut off at the upper limit determined by energy and momentum requirements. The first fact corresponds quantum mechanically to the so-called "infra-red catastrophe" which results from an unjustified calculation of the probability of emission of a finite number of photons, and the second fact means that the spectrum must fall rapidly to zero near its upper limit.

III. QUANTUM MECHANICAL TREATMENT

For simplicity, we consider the meson initially at rest, and later indicate the results if the decay occurs while it is in motion. Only a negative meson will be considered, since the results are identical for both signs of charge. Further, the process will be described in the usual manner as involving the creation of an anti-neutrino, rather than a neutrino, both electron and neutrino then being regarded as two states of the same particle with different isotopic spin.

For the fields of vector and pseudoscalar types, there exist matrix elements for the direct transition from the initial state to the final state in which the electron and photon are present. However, such first-order processes do not give rise to low frequency divergences characteristic of the radiative corrections, and hence are negligible in comparison with the second-order terms at the low frequency end. Since the contributions to the cross section from all terms vanish at the high frequency end of the spectrum, these first-order terms do not give appreciable contributions to the cross section at any part of the spectrum, and hence may be neglected. For the pseudoscalar field, this neglect is further justified by the fact that the direct interaction vanishes if the coupling is of the pseudoscalar type. Because of the relation between the pseudoscalar and pseudovector couplings in the weak coupling approximation,[4] this further justifies the neglect of the direct term for the general pseudoscalar field.

There then exist the following types of possible second-order transitions:

[3] J. Steinberger, Phys. Rev. **74**, 500 (1948).

[4] E. C. Nelson, Phys. Rev. **60**, 830 (1941); F. J. Dyson, Phys. Rev. **73**, 929 (1948).

1. The meson is virtually annihilated, creating an electron and an anti-neutrino; the electron then virtually emits the photon.
2. An electron-positron pair is created with emission of a photon; the meson is then annihilated by absorbing the positron and emitting an anti-neutrino.
3. The meson first virtually emits the photon and then decays with the creation of an electron and an anti-neutrino.

The necessary matrix elements are all either well-known or obtainable from previous literature,[5] and will not be derived here. The apparent complexity due to the large number of possible intermediate states can be considerably reduced as follows.

The second type of virtual transition is due to the requirements of the hole theory of the Dirac electron, which forbids transitions into filled negative energy intermediate states. However, the same results are obtained if we do not use the hole picture, but use only the first process, and sum over both positive and negative energy intermediate states.

The third process need not be considered at all for the scalar or pseudoscalar fields, for a spinless particles at rest cannot interact with the electromagnetic field. The interaction term is,

$$H'_{MR}=-(iec/\hbar)\int[\mathbf{A}\cdot(\phi\nabla\phi^*-\phi^*\nabla\phi)]d\tau,$$

$\mathbf{A}$ being the transverse vector potential and ϕ the meson wave function. In a momentum space representation of this term, the gradient operator produces terms of the form $\hat{\mathbf{f}}\cdot\mathbf{k}'$, $\hat{\mathbf{f}}$ being the photon polarization, and $\mathbf{k}'$ the momentum of the meson in the intermediate state. However, if the meson is initially at rest,

$$\mathbf{k}'=-\boldsymbol{\kappa},$$

where $\boldsymbol{\kappa}$ is the photon wave vector, so $\hat{\mathbf{f}}\cdot\mathbf{k}'=0$.

The meson-radiation interaction does not vanish for particles of non-zero spin at rest (Dirac electron, vector meson). However, a direct calculation of terms resulting from this process shows that they do not give the low frequency divergence, and hence may be neglected. This is again understandable from the classical model. In the process in which the electron emits the radiation, the interacting particle has been accelerated, hence classically is capable of emitting radiation, whereas if the meson interacts with the radiation first it has not been accelerated, and hence classically will not radiate.

With the above simplifications, the transition probability can be calculated in a straightforward manner. One must be careful, however, not to make the approximation of neglecting the terms of order (electron mass/meson mass)^2 which arise in the energy denominators, or the integrals over the directions of the emitted particles will diverge. This again follows from the classical model, since in the decay of an infinitely heavy meson, the electron would be accelerated to the velocity of light instantaneously since $\Delta\omega$ would be infinite, and hence infinite radiation would be produced. Although the integrals which occur can all be evaluated in terms of elementary functions, it is convenient and of some interest to make use of the relation between the two pseudoscalar theories to avoid having to evaluate the integrals for the vector meson separately.

The probability per unit time of emitting a photon of frequency ω can be written as,

$$w(\omega)d\omega=\frac{1}{2\pi\hbar}\frac{e^2}{\hbar c}\left[\mu c^2-2\hbar\omega-\frac{(mc^2)^2}{\mu c^2}\right]\frac{d\omega}{\omega}$$

$$\times\begin{cases}\dfrac{G_1^2}{\hbar c}\cdot I_1(\omega)\text{; scalar meson; pseudoscalar meson with pseudoscalar coupling.} & \text{(a)}\\[2ex] \dfrac{F_1^2}{\hbar c}\cdot I_2(\omega)\text{; pseudoscalar meson with pseudovector coupling.} & \text{(b)}\\[2ex] \dfrac{1}{3}\left[\dfrac{F_2^2}{\hbar c}(I_1+2I_2)+\dfrac{G_2^2}{\hbar c}(2I_1+I_2)\right] & \\ \qquad\text{vector meson,} & \text{(c)}\end{cases}$$

where I_1 and I_2 are certain functions of ω obtained by integration over the relative angles of emission of the electron and anti-neutrino. Now from the relation between the two pseudoscalar theories,[4] we must get the same result from (a) as from (b) if we make the replacement,

$$G_1\rightarrow-(m/\mu)F_1.$$

[5] H. A. Bethe and L. W. Nordheim, Phys. Rev. **57**, 998 (1940); T. S. Chang, Kgl. Danske Vid. Sels. Math-fys. Medd. **19**, No. 10 (1942).

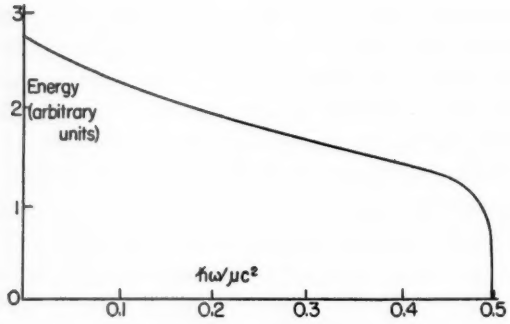

FIG. 1. Energy spectrum of emitted radiation; $\mu=200$ m. For different couplings the ordinates should be multiplied by the appropriate constant factor.

But therefore,

$$I_2=\left(\frac{m}{\mu}\right)^2 I_1,$$

so that we can neglect I_2 in the vector meson formula.

Evaluating I_1 we get, with $\kappa=\hbar\omega/\mu c^2$,

$$w(\omega)d\omega=\frac{1}{\pi}\frac{e^2}{\hbar c}\frac{\mu c^2}{\hbar}\left(1-\frac{m^2/\mu^2}{1-2\kappa}\right)^2$$

$$\times\left\{[(1-\kappa)^2+\kappa^2]\ln\left(\frac{1-2\kappa}{m^2/\mu^2}\right)-2(1-\kappa)\right\}\frac{d\omega}{\omega}$$

$$\times\begin{cases}G^2/\hbar c\text{; scalar meson.}\\ \left(\dfrac{G_1}{(\hbar c)^{\frac{1}{2}}}-\dfrac{m}{\mu}\dfrac{F_1}{(\hbar c)^{\frac{1}{2}}}\right)^2\text{; pseudoscalar meson.}\\ \left(\dfrac{1}{3}\dfrac{F_2^2}{\hbar c}+\dfrac{2}{3}\dfrac{G_2^2}{\hbar c}\right)\text{; vector meson.}\end{cases}$$

The energy spectrum is obtained by multiplying these expressions by $\hbar\omega$. It shows the same characteristics as the classical result (Fig. 1).

As predicted, the cross section diverges logarithmically at the low frequency end, so that the lifetime calculated by integrating $w(\omega)$ over-all frequencies is zero. A meaningful estimate for the probability of the process can be calculated by the method used by Bloch for the radiative beta-decay of nuclei.[2] We use the ratio of the mean energy emitted in radiation per unit time to the mean energy available for the process per unit time, which is essentially the non-radiative (first order) lifetime times the meson rest-energy. Because the interaction constants for the various theories of non-radiative decay[5,†] always occur in the same combination as here given, the result is,

$$R=\frac{1}{4\pi}\frac{e^2}{\hbar c}\left[\frac{8}{3}\ln\left(\frac{\mu}{m}\right)-\frac{31}{9}\right]$$

for all interactions. This result also holds for mixed theories of meson fields. For a meson mass of 200 electron masses, $R=0.84e^2/\hbar c=0.6$ percent.

IV. CONCLUSION

The essential features of the quantum mechanical result all have analogs in the classical treatment. The final result can be transformed to a moving system to consider possible changes that occur if the meson decays while in motion.

The results of such a Lorentz transformation are four in number: the relativistic mass increase, aberration and Doppler shift of the radiation, as well as the time dilatation which alone occurs for non-radiative decay. If the angular distribution of the emitted radiation is isotropic in the rest system, then from a system in motion relative to it the radiation appears bunched along the direction of travel.[6] However, although more energy is emitted by a moving meson because of the mass increase, the time dilatation just compensates this effect, and both the mean energy and the relative mean energy emitted per unit time are independent of the motion.

I wish to thank Professor W. H. Furry for suggesting this problem, and for much helpful discussion during its solution.

† Note that in Chang's paper the sign of f_1 should be reversed in the formula for the lifetime, if the usual choice for the Dirac Hamiltonian,

$$H=-c\boldsymbol{\alpha}\cdot\mathbf{p}-\beta mc^2$$

is used.

[6] This well-known result is derived, for example, by L. Janossy, *Cosmic Rays* (Oxford University Press, London, 1948), Section 152.

PHYSICAL REVIEW VOLUME 75, NUMBER 5 MARCH 1, 1949

The Interaction of Nuclear Electric Quadrupole Moments with Molecular Rotation in Asymmetric Top Molecules. II. Approximate Methods for First-Order Coupling

J. K. BRAGG
Cornell University, Ithaca, New York

AND

S. GOLDEN
Hydrocarbon Research, Inc., New York City, New York

(Received November 29, 1948)

An expression is developed for the rotational dependence of $\langle \partial^2 V/\partial z^2 \rangle_{Av}$ for asymmetric top molecules. The expression is valid for all rotational energy levels, and requires only a knowledge of the reduced energy spectrum as a function of asymmetry of the rotor.

The application of three distinct methods of approximating the energy of the asymmetric rotor to the expression for $\langle \partial^2 V/\partial z^2 \rangle_{Av}$ is described. This permits the calculation of quadrupolar interactions for certain rotational states (in particular, those of high J) for which energies have not yet been tabulated.

The expressions which are derived will usually prove to be at least as accurate as the first-order approximation to the quadrupolar interaction, in which $\langle \partial^2 V/\partial z^2 \rangle_{Av}$ is involved.

I. INTRODUCTION

IN the first paper of this series,[1] hereinafter referred to as I, the general theory of nuclear quadrupole coupling in asymmetric top molecules was outlined. The only part of the first-order problem which differs significantly from previous treatments for linear molecules[2] and symmetric top molecules[3] is the evaluation of the rotational dependence of $\langle \partial^2 V/\partial z^2 \rangle_{Av}$. In this quantity V is the electrostatic potential at the quadrupolar nucleus, z is a space-fixed axis, and the average is taken in the representation which diagonalizes the rotational energy of the molecule in question. In I, two expressions were given for $\langle \partial^2 V/\partial z^2 \rangle_{Av}$ in asymmetric top problems; one, Eq. (8), makes use of published line strengths of pure rotation transitions[4] of the asymmetric rotor for $J \leq 12$, and the other, Eq. (10), involves explicity the coefficients of the transformation from a symmetric rotor basis to one which diagonalizes the energy of the rotor in question.

It is the purpose of the present work to provide an expression which is applicable for all J, the use of which involves little labor.* The method is based on a suggestion of J. H. Van Vleck, and its essential result is that the dependence upon rotational state of the quadrupole coupling can, to first order, be obtained from a knowledge of the reduced energy spectrum of the asymmetric rotor as a function of the asymmetry of the rotor.

Tables of the reduced energies for $J \leq 10$ have been published:[5] the method is extended to all J in the regions of asymmetry for which certain approximations to the reduced energies have been developed.[6–8]

II. GENERAL DEVELOPMENT OF THE METHOD

It may be verified by reference to Eq. (10) of I that $\langle \partial^2 V/\partial z^2 \rangle_{Av}$ may be expressed in terms of the average values of the angular momentum operators $\mathbf{P}_a$, $\mathbf{P}_b$, and $\mathbf{P}_c$ about the principal axis of inertia, a, b, and c. As is customary, a, b, and c are chosen so that the moments of inertia satisfy $I_a \leq I_b \leq I_c$. Matrices of these operators are given, for example, in reference 5 (see Eq. (6)).

[1] J. K. Bragg, Phys. Rev. **74**, 533 (1948).
[2] J. M. P. Kellogg, I. I. Rabi, N. F. Ramsey, Jr., and J. R. Zacharias, Phys. Rev. **57**, 677 (1940); J. Bardeen and C. H. Townes, Phys. Rev. **73**, 97 (1948).
[3] B. P. Dailey, R. L. Kyhl, M. W. P. Strandberg, J. H. Van Vleck, and E. B. Wilson, Jr., Phys. Rev. **70**, 984 (1946); D. K. Coles and W. E. Good, Phys. Rev. **70**, 979 (1946).
[4] P. C. Cross, R. M. Hainer, and G. W. King, J. Chem. Phys. **12**, 219 (1944).

* A method applicable to slightly asymmetric tops has been described by Knight and Feld, Phys. Rev. **74**, 354 (1948).
[5] G. W. King, R. M. Hainer, and P. C. Cross, J. Chem. Phys. **11**, 27 (1943).
[6] G. W. King, J. Chem. Phys. **15**, 820 (1947).
[7] S. Golden, J. Chem. Phys. **16**, 78 (1948).
[8] S. Golden and J. K. Bragg, to be published.

TABLE I.*

quantity \ representation	I^r	I^l	III^r	III^l
F	$\frac{1}{2}(\kappa-1)$	$\frac{1}{2}(\kappa-1)$	$\frac{1}{2}(\kappa+1)$	$\frac{1}{2}(\kappa+1)$
$G-F$	$-\frac{1}{2}(\kappa-3)$	$-\frac{1}{2}(\kappa-3)$	$-\frac{1}{2}(\kappa+3)$	$-\frac{1}{2}(\kappa+3)$
$H/(G-F)$	$(\kappa+1)/(\kappa-3)$	$(\kappa+1)/(3-\kappa)$	$(1-\kappa)/(\kappa+3)$	$(\kappa-1)/(\kappa+3)$
$(d/d\kappa)[H/(G-F)]$	$-4/(\kappa-3)^2$	$4/(\kappa-3)^2$	$-4/(\kappa+3)^2$	$4/(\kappa+3)^2$

* This table has been derived from Table III of reference 5. The various representations are identified in Table II of that paper.

The expression is:

$$\langle\partial^2 V/\partial z^2\rangle_{Av}=A\langle\mathbf{P}_a^2\rangle+B\langle\mathbf{P}_b^2\rangle+C\langle\mathbf{P}_c^2\rangle. \quad (1)$$

The angular brackets indicate an average taken in the basis in which the energy of the rotor is diagonal. A, B, and C are the aa, bb, and cc components of the dyadic $\nabla\mathbf{E}$, multiplied by $2/(J+1)(2J+3)$.

Equation (1) makes possible the expression of $\langle\partial^2 V/\partial z^2\rangle_{Av}$ in terms of the energy and one of the quantities $\langle\mathbf{P}_c^2\rangle$ alone. The energy of the rotor is given by:

$$E=a\langle\mathbf{P}_a^2\rangle+b\langle\mathbf{P}_b^2\rangle+c\langle\mathbf{P}_c^2\rangle; \quad (2)$$

in this equation the averages are indicated only for comparison with (1). a, b, and c are the rotational constants $\hbar^2/2I_a$, $\hbar^2/2I_b$, and $\hbar^2/2I_c$.

Using the relation $\langle\mathbf{P}_a^2\rangle+\langle\mathbf{P}_b^2\rangle+\langle\mathbf{P}_c^2\rangle=J(J+1)$ and substituting Eq. (2), one may write for Eq. (1),

$$\begin{aligned}\langle\partial^2 V/\partial z^2\rangle_{Av}=&[(B-A)/(b-a)]E\\&+[[A(b-a)-a(B-A)]/(b-a)]\\&\times J(J+1)+[[(C-A)(b-a)\\&-(c-a)(B-A)]/(b-a)]\langle\mathbf{P}_c^2\rangle. \quad (3)\end{aligned}$$

The quantity $\langle\mathbf{P}_c^2\rangle$ may be set equal to $(\partial E/\partial c)$;[9] this relation is justified in the appendix. The energy may be expressed as[5]

$$E=[(a+c)/2]J(J+1)+[(a-c)/2]E_\tau^J(\kappa), \quad (4)$$

leading to:

$$\begin{aligned}\langle\mathbf{P}_c^2\rangle=&(1/2)J(J+1)-(1/2)E(\kappa)\\&+[(a-c)/2](\partial E(\kappa)/\partial c). \quad (5)\end{aligned}$$

$E(\kappa)$ is the reduced energy of the rotor; κ is Ray's asymmetry parameter, defined by

$$\kappa=(2b-a-c)/(a-c).$$

Equation (5) may thus be rewritten as

$$\begin{aligned}\langle\mathbf{P}_c^2\rangle=&(1/2)J(J+1)-(1/2)E(\kappa)\\&+(1/2)(\kappa-1)(\partial E(\kappa)/\partial\kappa). \quad (6)\end{aligned}$$

Substitution of (4) and (6) into (3), and simplification, leads to:

$$\begin{aligned}\langle\partial^2 V/\partial z^2\rangle_{Av}=&(A/2)[J(J+1)+E(\kappa)\\&-(\kappa+1)(\partial E(\kappa)/\partial\kappa)]+B(\partial E(\kappa)/\partial\kappa)\\&+(C/2)[J(J+1)-E(\kappa)\\&+(\kappa-1)(\partial E(\kappa)/\partial\kappa)]. \quad (7)\end{aligned}$$

Equation (7) may be obtained in a variety of forms by use of the relation $A+B+C=0$, stemming from $\nabla^2 V=0$. In particular, one of the parameters A, B, C may be eliminated.

The problem thus reduces to that of determining $E(\kappa)$ and $(\partial E(\kappa)/\partial\kappa)$. The accuracy with which these quantities may be calculated by present methods determines, therefore, the accuracy with which $\langle\partial^2 V/\partial z^2\rangle_{Av}$ may be evaluated. For $J\leq 10$, Eq. (7), together with the reduced energy tables of reference (5), should prove more accurate, in most cases, than Eq. (8) of I.

In the following section the use of approximation methods will be discussed.

III. APPROXIMATION METHODS[10]

In this section equations for $E(\kappa)$ and $(\partial E(\kappa)/\partial\kappa)$ will be given, as derived from the approximation methods of references 6, 7, and 8. The range of applicability of each is indicated. The accuracy of the results is at least what is warranted by the first-order nature of the quadrupole calculation involving $\langle\partial^2 V/\partial z^2\rangle_{Av}$ and

[9] This substitution, suggested by J. H. Van Vleck, is also applicable to the determination of the proportionality factor arising in electron spin multiplets in polyatomic molecules. (R. S. Henderson and J. H. Van Vleck, Phys. Rev. 74, 106 (1948).) This application will be discussed by Henderson in a forthcoming publication.

[10] Since the space required to summarize the three distinct approximation methods to asymmetric rotor energies here used would be prohibitive, a familiarity with the notation and results of these methods will be assumed.

by present precision in measurements of quadrupole effects of asymmetric rotors.

A. The Mathieu Function Approximation

This method is applicable for those levels whose energies are lowest for a given J (near-prolate rotor) or highest (near-oblate rotor). The computation of $E(\kappa)$ is described in detail in reference (7). A first approximation to the reduced energies is given by

$$E(\kappa)=FJ(J+1)+(G-F)\alpha, \tag{8}$$

where α is the characteristic value of Mathieu's equation appropriate to the level and value of κ in question, and F and $G-F$ are constants which depend on κ in a manner determined by the way in which a, b, and c are identified with molecule-fixed cartesian axes x', y', z'. Then:

$$\partial E(\kappa)/\partial\kappa=(dF/d\kappa)J(J+1)+(d(G-F)/d\kappa)\alpha +(G-F)(\partial\alpha/\partial\kappa). \tag{9}$$

By reference to Table I, which gives H, $G-F$, $H/(G-F)$, and $(d/d\kappa)[H/(G-F)]$ for the pertinent ways of assigning a, b, c to x', y', z', it may be seen that $dF/d\kappa=\frac{1}{2}$ and $d(G-F)/d\kappa=-\frac{1}{2}$ regardless of axis choice. Furthermore, one has $(\partial\alpha/\partial\kappa)=(\partial\alpha/\partial\theta)(d\theta/d\kappa)$, where θ is the constant appearing in Mathieu's equation:

$$(d^2y/dx^2)+(\alpha-2\theta\cos 2x)y=0,$$

given, for this approximation method, closely enough by

$$\theta=[H/(G-F)][J(J+1)/2]. \tag{10}$$

Equation (9) becomes, finally,

$$\partial E(\kappa)/\partial\kappa=\tfrac{1}{2}[J(J+1)-\alpha+(G-F)J(J+1) \times(\partial\alpha/\partial\theta)(d/d\kappa)[H/(G-F)]]. \tag{11}$$

In order to use this method, one determines θ from Eq. (10) and Table I. From tables of characteristic values of Mathieu's equation,[11] α and an approximate value of $\partial\alpha/\partial\theta$ may be obtained. $E(\kappa)$ and $\partial E(\kappa)/\partial\kappa$ may then be computed, and inserted in Eq. (7).

It is wise, in using Eq. (8) for $E(\kappa)$, to investigate whether sufficient accuracy is attained. First- and second-order corrections are tabulated in reference (7), and may be used if necessary. The value of $\partial E(\kappa)/\partial\kappa$ given by Eq. (11) should be sufficiently accurate for the present purpose without inclusion of these corrections.

B. The "Harmonic Oscillator Approximation"

This method, and the one to follow, the "correspondence principle" approach, are valid for those energy levels which are essentially degenerate in the sign of the limiting symmetric rotor quantum number K; i.e., those levels which are highest for a given J (near-prolate rotor) or lowest (near-oblate rotor). The present method yields an explicit expression for both $E(\kappa)$ and $\partial E(\kappa)/\partial\kappa$, which is, however, rather cumbersome, whereas the correspondence principle approach involves tabulated quantities from which computations are easily made. Therefore, each method should prove useful in certain cases.

The reduced energy $E(\kappa)$ is, up to and including first-order terms (see reference 8),

$$E_\tau{}^J(\kappa)=FJ(J+1)+(G-F)E'_\tau{}^J(\kappa)$$

where

$$E'_\tau{}^J(\kappa)=(J+\tfrac{1}{2})^2+(m+\tfrac{1}{2})^2-2J(m+\tfrac{1}{2})W -(6\beta/W^2)[\beta-\beta'(1+(1/2J))] \times(m^2+m+\tfrac{1}{2}). \tag{12}$$

Here $m=J-K_{-1}$ for a type I representation, $m=J-K_1$ for a type III representation, and K_{-1} and K_1 refer to the limiting K of the prolate and oblate symmetric tops, respectively. Also

$$W=[(1+(1/2J))^2-4\beta^2]^{\frac{1}{2}};$$
$$\beta=(1/2)[H/(G-F)][1+(1/2J) -(1/32J^2)+(1/64J^3)];$$
$$\beta'=(1/2)[H/(G-F)][1+(1/32J^2)].$$

The expressions for F, $G-F$, etc., in terms of κ are those of Table I. With sufficient accuracy for the present purpose,

$$\beta[\beta-\beta'[1+(1/2J)]]\cong-[1/64J^2][H/(G-F)]^2,$$

and

$$W\cong[1+(1/2J)][1-\tfrac{1}{2}[H/(G-F)]^2].$$

[11] *Tables of Characteristic Values of Mathieu's Differential Equation*, a report prepared for the Applied Mathematics Panel, NDRC, by the Mathematical Tables Project, National Bureau of Standards, AMP report 165.1R. In these tables certain differences in notation occur: the characteristic values b are given in terms of a parameter s; these are related to α and θ by $\theta=\frac{1}{4}s$ and $\alpha=b-\frac{1}{2}s$. Therefore, $\partial\alpha/\partial\theta=4(\partial b/\partial s)-2$.

Then

$$\partial E(\kappa)/\partial\kappa \cong \tfrac{1}{2}[J(J+1)-E'(\kappa)] + (2J+1)(m+\tfrac{1}{2})H(d/d\kappa)(H/(G-F)) + \frac{3(m^2+m+(1/2))H[(d/d\kappa)(H/(G-F))]}{16J^2(1+(1/2J))^2(1-[H/(G-F)]^2)^2}. \quad (13)$$

The results of Eqs. (12) and (13) are to be substituted in Eq. (7).

C. The Correspondence Principle Approximation

The result of reference (6) of primary interest in the present work is the tabulation (Table I) of a "reduced energy ratio," η, as a function of a quantum number ratio λ, and κ. η and λ are defined by

$$\eta(\kappa)_{J,K}=E(\kappa)_{J,K}/J(J+1), \quad \lambda=K/[J(J+1)]^{\frac{1}{2}}.$$

K here is the limiting (prolate or oblate) symmetric top quantum number. $\eta(\kappa)$ and $\partial\eta(\kappa)/\partial\kappa$ can be taken from the table, and

$$\partial E(\kappa)/\partial\kappa = J(J+1)[\partial\eta(\kappa)/\partial\kappa]. \quad (14)$$

The derivative $\partial\eta(\kappa)/\partial\kappa$ is evaluated for constant λ, and must not be confused with the derivative $\partial\eta/\partial\lambda$ which is given, together with η, in the table.

APPENDIX

Let

$$\mathbf{H}_0=a\mathbf{P}_a^2+b\mathbf{P}_b^2+c\mathbf{P}_c^2, \quad (15)$$

$$\mathbf{H}'=\delta c\mathbf{P}_c^2. \quad (16)$$

Then, if $E(a, b, c)$ is an eigenvalue of the unperturbed problem (15), and E' the first-order energy correction due to (16), $E'=\delta c\langle \mathbf{P}_c^2\rangle$, where the angular brackets denote an average over the (unperturbed) eigenstate corresponding to $E(a, b, c)$.

Let $E(a, b, c+\delta c)$ be the corresponding eigenvalue of the Hamiltonian,

$$\mathbf{H}=a\mathbf{P}_a^2+b\mathbf{P}_b^2+(c+\delta c)\mathbf{P}_c^2,$$

and define ϵ such that $E(a, b, c+\delta c)=E(a, b, c)+E'+\epsilon$. Then

$$\frac{\partial E(a, b, c)}{\partial c}=\lim_{\delta c\to 0}\frac{E'+\epsilon}{\delta c},$$

but $\epsilon=0(\delta c^2)$, so $\partial E(a, b, c)/\partial c=\langle \mathbf{P}_c^2\rangle$.

PHYSICAL REVIEW VOLUME 75, NUMBER 5 MARCH 1, 1949

On the Space Distribution of Slow Neutrons

G. C. WICK
University of California, Berkeley, California

(Received October 26, 1948)

The behavior of the neutron density about a plane- or point-source of fast neutrons within a homogeneous slowing-down medium has been re-investigated. For the case of constant mean free path a known analytical expression for the neutron density has been reduced to a form, which is valid for slow neutrons and *for any distance* from the source. The feasibility of a numerical evaluation of the formula is demonstrated for $M=1$ (hydrogen). In particular, the asymptotic behavior at very large distances has been studied. For the more realistic example of a medium in which the mean free path decreases with decreasing energy of the neutrons, formulae are presented describing the asymptotic density and the asymptotic energy spectrum at large distances from the source.

1. INTRODUCTION

THE present paper is an extension, in two directions, of previous work[1] on the transport equation for the diffusion and slowing-down of neutrons about a point source in an infinite homogeneous medium. First, the formal solution for the case of constant mean free path has been reduced to a numerically manageable form for sufficiently slow neutrons at all distances from the source. Secondly, for the case of a mean free path that decreases as the energy of the neutrons decreases, an asymptotic formula valid at large distances from the source has been derived.

A partial result for the first case, namely the asymptotic form of the constant-mean-free-path solution at very large distances was communi-

[1] M. Verde and G. C. Wick, Phys. Rev. **71**, 852 (1947), henceforward referred to as "A."

cated by the author to Dr. Marshak, who kindly included it in his general report on neutron slowing down.[2] For the convenience of the reader we shall adhere as far as possible to Marshak's notation, which is not very different from that in "A." Thorough familiarity with Parts I and III-D of Marshak's report will be assumed and those parts of our argument that have already been reproduced in the report will be treated summarily. Reference to "M" also allows us to generalize immediately our formulae to the case of an arbitrary mass number M of the slowing down element. For simplicity we shall omit the generalization for the case of a mixture, which is fairly obvious; we shall also neglect neutron capture and inelastic scattering.

The spatial distribution of neutrons about a point source can be easily derived from the distribution about a plane source, see "M" Eq. (62). We shall therefore limit ourselves to the latter case, which is slightly simpler. Our distribution function ψ will thus be a function of z, the perpendicular distance from the plane source, of u the logarithmic energy variable ($u=0$ for the primary fast neutrons of velocity v_0) and of μ the cosine of the angle between the velocity and the z axis. Integrating over the solid angle we obtain $\psi_0(z, u)$, which is the main function we wish to determine. Specifically the density of neutrons at the distance z (we shall always assume $z>0$, since the density is an even function of z) within the energy internal du is

$$v^{-1}l(u)\psi_0(z, u)du, \tag{1}$$

where $l(u)$ is the mean free path and v is the velocity ($=v_0e^{-u/2}$).

2. THE CASE OF CONSTANT MEAN FREE PATH ($l=1$)

2.1 Outline of the Procedure

The classical method, which was independently adopted in "A" and in the various papers summarized in "M", is to reduce the transport equation to a problem of the "one-velocity" type, see "A" Eq. (2′), by means of a Laplace transformation with respect to the energy variable u, η being the new variable. In this reduced problem the mean free path is the same as before ($=1$ by definition) and the variable η substituting u appears simply as a constant parameter, that determines the scattering probability per unit solid angle: $g(\mu_0, \eta)$, μ_0 being the cosine of the scattering angle. In the general case of mass number M of the scattering atoms, this function is given by Eq. (140b) in "M" or

$$g(\mu, \eta)=\frac{\alpha}{\pi}(M^2-1+\mu^2)^{-\frac{1}{2}}[G(\mu)]^{2\eta+2}. \tag{2}$$

Here

$$\alpha=(M+1)^2/4M; \tag{3}$$

and

$$G(\mu)=\frac{\mu+(\mu^2+M^2-1)^{\frac{1}{2}}}{M+1}.$$

$G(\mu)$ is the ratio v/v' of the velocities after and before scattering through an angle $\arccos\mu$.[3] We shall need later the Legendre coefficients $g_n(\eta)$ of $g(\mu, \eta)$

$$g_n(\eta)=2\pi\int_{-1}^{+1}d\mu P_n(\mu)g(\mu, \eta) \tag{4}$$

for instance

$$g_0(\eta)=\alpha(1+\eta)^{-1}[1-e^{-q(1+\eta)}],$$

$$g_1(\eta)=\alpha(\eta+\tfrac{1}{2})^{-1}(\eta+\tfrac{3}{2})^{-1}$$

$$\times[\eta+1-\tfrac{1}{2}M+(\eta+1+\tfrac{1}{2}M)e^{-q(1+\eta)}], \tag{5}$$

where $q=2\ln[(M+1)/(M-1)]$. For $M=1$ see also Eq. (32) below. It can be seen from Eq. (2) that if $M>1$ the functions $g_n(\eta)$ are holomorphic in the whole complex plane of the η variable, and satisfy the condition

$$\lim_{n\to\infty} g_n(\eta)=0. \tag{6}$$

If $M=1$ these statements hold true in the half-plane $\Re(\eta)>-1$, $\Re$ meaning real part.

After the transport equation has been further reduced by means of a Fourier transformation with respect to z, y being the new variable in Marshak's notation (we use instead $k=iy$ as in

[2] R. E. Marshak, Rev. Mod. Phys. 19, 185 (1947). This paper will be referred to as "M."

[3] The general form of Eq. (2) is easily understood if one notices that the reduced transport equation describes essentially the diffusion of neutrons having a power spectrum $e^{\eta u}=(v_0/v)^{2\eta}$. It is seen that when neutrons with this spectrum are scattered through any *given* angle, the scattered neutrons have again exactly the same spectrum, but owing to the change in velocity the proportionality constant in the spectrum is changed in the ratio

$$(v/v')^{2\eta}=[G(\mu)]^{2\eta}.$$

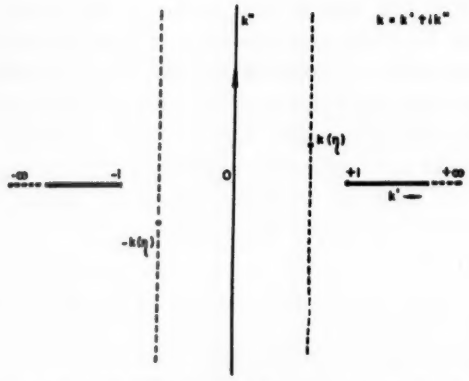

FIG. 1. The thick horizontal lines represent the "cuts" in the complex k-plane, see Eq. (13). The continuous vertical line is the integration path of Eq. (7). Two poles $k(\eta)$ and $-k(\eta)$ are indicated, the strip between the dashed lines is the convergence strip of the Fourier transform. There may be other poles outside the convergence strip.

"A") one arrives finally at the formula

$$\psi_0(z, u) = (1/2\pi i)^2 \int_{-i\infty}^{+i\infty} e^{-kz} dk \times \int_{\sigma-i\infty}^{\sigma+i\infty} e^{\eta u} \phi_0(k, \eta) d\eta, \quad (7)$$

see "M" Eq. (142a) or "A" Eq. (39). The real constant σ must be larger than the convergence abscissa of the Laplace transform; in addition we may assume $\sigma > -1$, so that condition (6) always holds true. The function ϕ_0 must be obtained from an infinite set of linear equations, "A" Eq. (24a) or "M" Eq. (141a, b). Thus the problem consists of two parts: determination of ϕ_0 and evaluation of the integrals in (7).

We are interested in the distribution of slow neutrons, i.e., large values of u. We assume for instance $u > 10$, corresponding to a reduction from an initial energy of more than 20 kev to 1 ev. On the other hand no restriction need be placed on z. (We shall see, however, that when z is large our formulae are valid under even *less* stringent conditions on u). We shall be able to eliminate one of the integrations in Eq. (7) by the method of residues. For the sake of clarity, we give first a general outline of the procedure to be followed, and fill in some of the details later.

It is clear, from the nature of ϕ_0 as a Laplace transform, that σ in Eq. (7) must be so large that all singularities of ϕ_0 in the η plane will be "to the left" of the integration path with respect to η. We may pull the integration path through the pole $\eta(k)$ having the largest real part $\Re(\eta)$ [4] and obtain a residue:

$$(1/2\pi i) \int \phi_0 e^{\eta u} d\eta = e^{\eta(k) u} R + \cdots \quad (8)$$

where

$$R \equiv R(k) = \lim_{\eta \to \eta(k)} [\eta - \eta(k)] \phi_0(\eta, k) = [\partial \phi_0^{-1} / \partial \eta]^{-1}_{\eta = \eta(k)}. \quad (9)$$

The remainder . . . is an integral running to the left of $\eta(k)$ but to the right of the next pole. We shall see that the difference $\delta\eta$ between the real parts of the two poles is at least of the order of $\frac{1}{2}$. Owing to the strong factor $e^{\eta u}$, the remainder is of the order $e^{-\frac{1}{2}u} \lesssim e^{-5}$ with respect to the first residue and can be neglected.[5] We are then left with the integral

$$\psi_0(z, u) = (1/2\pi i) \int_{-i\infty}^{+i\infty} \exp(-kz + u\eta(k)) R(k) dk. \quad (10)$$

We shall then consider k as a complex variable, and displace the integration path towards the right in the k plane. Considering the point k_0 where the path cuts the real axis, we shall see that we may choose k_0 to be a "saddle-point" for $\Re[-kz + u\eta(k)]$. At k_0 the exponential factor in (10) has a minimum along the real axis and a strong maximum along the path if this is chosen according to the prescription of "steepest descent." The exponent is then expanded in a Taylor series in the usual way

$$-kz + u\eta(k) = -k_0 z + u\eta_0 + \tfrac{1}{2} u\eta_0''(k - k_0)^2 + \cdots,$$

where

$$\eta_0 = \eta(k_0), \quad \eta_0'' = \eta''(k_0).$$

One has then

$$\psi_0(z, u) \approx (2\pi\eta_0'' u)^{-\frac{1}{2}} R(k_0) \exp(-k_0 z + u\eta_0). \quad (11)$$

We notice that the minimum condition at k_0

$$-z + u\eta'(k_0) = 0 \quad (12)$$

defines k_0 as a function of z/u. Formula (11) can be used, therefore, if we can construct a table of

[4] The position of this pole in the η-plane depends on k, as we shall see.

[5] As a matter of fact, this is an overestimate of the remainder.

$\eta(k_0)$, $\eta'(k_0)$, $\eta''(k_0)$, $R(k_0)$ as functions of the real variable k_0.

In the passage from (10) to (11) we have tacitly assumed that the path of "steepest descent" is a straight path cutting across the real axis at right angles. Actually it is not straight, but it will be shown that the validity of Eq. (12) is not affected. It will also appear, that Eq. (11) goes over into the customary "age" approximation at small distances, and at very large distances into the asymptotic formula that was reproduced in "M" Eq. (175).

2.2 The Function $\phi_0(k, \eta)$

We summarize here the main results of "A," Sections 3.1 and 4.1, concerning the determination of the function ϕ_0; in addition some relationships will be derived for later use.

Let us consider ϕ_0 as a function of the complex variable k. ϕ_0 is at first defined as a Fourier transform; as such it has a meaning only within a convergence strip $k_1 < \Re(k) < k_2$. It will appear later that k_1 and k_2 are functions of η. The definition of ϕ_0 may, however, be extended by analytical continuation; an expression of ϕ_0 as a continued fraction was given in "A," see also later, from which it was inferred that ϕ_0 is a one-valued analytic function of k in the whole k-plane provided this is cut along the real intervals

$$-\infty < k < -1 \quad \text{and} \quad +1 < k < +\infty. \tag{13}$$

In the k-plane ϕ_0 has only isolated poles. The situation is in general as sketched in Fig. 1.

In order to determine ϕ_0 one must consider it together with the remaining Legendre coefficients ϕ_1, ϕ_2, $\cdots$ of the angular distribution function $\phi(\mu)$, "A" Eq. (11). Within the convergence strip this is a regular function of the cosine μ, so that

$$\lim_{n=\infty} \phi_n = 0. \tag{14}$$

The sequence ϕ_0, ϕ_1, $\cdots$ satisfies an infinite set of equations

$$(2n+1)\gamma_n\phi_n - k(n+1)\phi_{n+1} - kn\phi_{n-1} = \delta_{n0}, \tag{15}$$

the first of which is inhomogeneous ($\delta_{00}=1$), while the remaining ones form a recurrent homogeneous relation ($\delta_{n0}=0$ if $n \neq 0$). Here

$$\gamma_n = 1 - g_n(\eta), \tag{16}$$

and it is assumed that η satisfies the conditions for Eq. (6) to be valid.

The analytical continuation of ϕ_0 outside the convergence strip may be effected by requiring (14) to be valid everywhere in the cut plane. Disregarding for a moment the first Eq. (15) (for $n=0$), one can see that the recurrent relation has two linearly independent solutions, since ϕ_0 and ϕ_1 may be chosen arbitrarily. Out of this double infinity of solutions, condition (14) selects one linearly independent solution. In fact it may be easily seen that the characteristic equation "A" Eq. (19) has a root ϵ such that $|\epsilon| < 1$, while the other root $\epsilon' = 1/\epsilon$ has $|\epsilon'| > 1$. Under such circumstances, Poincaré's theorem, see "A" Sec. 3.1, assures us that there is only one solution such that

$$\lim_{n=\infty} \phi_{n+1}/\phi_n = \epsilon. \tag{17}$$

This solution obviously satisfies Eq. (14); for all other solutions the ratio tends to ϵ', and Eq. (14) is not satisfied. The only exception occurs on the "cuts," where $|\epsilon| = |\epsilon'| = 1$; (this is the reason why ϕ_0 is not unambiguously defined on the cuts).

Turning now to the remaining inhomogeneous equation, or Eq. (15) for $n=0$, two different cases may present themselves. Either the solution satisfying (17) also satisfies the equation

$$\gamma_0\phi_0 - k\phi_1 = 0 \tag{18}$$

in which case the inhomogeneous equation cannot be satisfied; or the left hand side of (18) is $\neq 0$, and then the arbitrary multiplicative constant in the solution can be adjusted so as to make the left hand side of Eq. (18) equal to unity, i.e., so as to satisfy the whole system (15).

This is, of course, the familiar relationship: if the homogeneous system, which is obtained by replacing δ_{n0} by 0, has a non-trivial solution, then the inhomogeneous system has none, and *vice versa*. The former case will occur only for special values of the parameter k; these have been called "eigenvalues." For each value of η, there may be several eigenvalues $k(\eta)$. When k approaches an eigenvalue $k(\eta)$, the multiplicative constant tends to infinity, so that ϕ_0 has a pole singularity at $k = k(\eta)$. On the other hand it may be easily seen from the recurrent relation that the sequence $\bar{\phi}_0$, $\bar{\phi}_1$, $\cdots$, etc. where: $\bar{\phi}_0 = 1$, $\cdots$,

$\bar{\phi}_n=\phi_n\phi_0^{-1}$, $\cdots$ remains finite, so that all the coefficients ϕ_n have a pole singularity of, at most, the same degree as ϕ_0. Once the eigenvalue $k(\eta)$ is known, the behavior of the sequence ϕ_n at $k=k(\eta)$ can be computed directly from the equations

$$\bar{\phi}_0=1;\quad \gamma_0-k\bar{\phi}_1=\lim\phi_0^{-1}=0;$$
$$\gamma_1\bar{\phi}_1-2k\bar{\phi}_2-k\bar{\phi}_0=0,\ \cdots,\ \text{etc.},\qquad (19)$$

i.e., by solving the ***homogeneous*** system, with the initial conditions $\bar{\phi}_0=1$, $\bar{\phi}_1=\gamma_0/k$.

The following formulae are of use in the actual evaluation of ϕ_0. From the system (15) one easily derives an expression of ϕ_0^{-1} in terms of ϕ_1/ϕ_0, then of ϕ_2/ϕ_1, $\cdots$. One arrives finally at the continued fraction[6]

$$\phi_0^{-1}=\gamma_0-\cfrac{\beta_1}{\gamma_1-\cfrac{\beta_2}{\gamma_2-\cdots-\beta_{n-1}/(\gamma_{n-1}-\lambda_n)}}\qquad (20)$$

where

$$\beta_n=k^2n^2/(4n^2-1);$$
$$\lambda_n=[kn/(2n-1)]\phi_n/\phi_{n-1}.\qquad (21)$$

The continued fraction "A" Eq. (25) is obtained on passing to the limit for $n=\infty$.[7] The customary way of evaluation consists in breaking up the fraction at the nth denominator, i.e., setting $\lambda_n=0$ in Eq. (20). One has then

$$\phi_0^{-1}\approx U_n/V_n,\qquad (22)$$

where U_n and V_n are both solutions of the recurrent relation

$$w_{n+1}=\gamma_nw_n-\beta_nw_{n-1}\qquad (23)$$

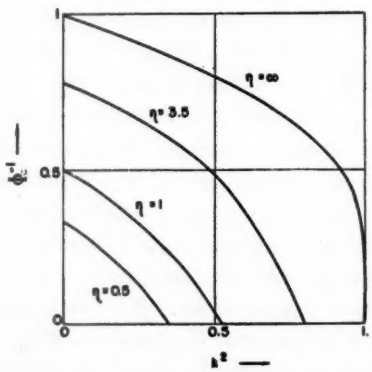

FIG. 2.

[6] See I. Waller, Arkiv f. Mat. Astron. Fysik, **34A**, No. 3, 4 and 5.

[7] It will be noticed that the equation as printed in "A" contains a slip.

with the initial values

$$U_0=1,\quad U_1=\gamma_0,\quad V_0=0,\quad V_1=1.\qquad (24)$$

The exact expression (20) can also be written

$$\phi_0^{-1}=(U_n-\lambda_nU_{n-1})/(V_n-\lambda_nV_{n-1}).\qquad (25)^8$$

A more rapidly convergent expression for ϕ_0^{-1} can obviously be obtained if instead of setting $\lambda_n=0$ in Eq. (20), we replace λ_n by the limit, that follows from Eq. (17)

$$\lambda=\lim_{n=\infty}\lambda_n=k\epsilon/2=\tfrac{1}{2}(1-(1-k^2)^{\frac{1}{2}}).\qquad (26)$$

The expression

$$\phi_0^{-1}\approx(U_n-\lambda U_{n-1})/(V_n-\lambda V_{n-1})\qquad (22')$$

was in fact found to be far more satisfactory than (22) in the numerical evaluations, see next section.

An interesting limiting case arises when for some reason the coefficients $g_m(\eta)$ are negligible for $m\geq n$. Then

$$\gamma_n=\gamma_{n+1}=\cdots=1\qquad (27)$$

and one can easily show[9] that

$$\phi_n/\phi_{n-1}=Q_n(1/k)/Q_{n-1}(1/k),\qquad (28)$$

where Q_n is the nth Legendre function of the second kind. This may be fed into Eqs. (21) and (20) or (25) to evaluate ϕ_0 in a finite form. An especially simple example of this kind occurs when $\eta\to\infty$ so that, see Eq. (6),

$$\gamma_0(\infty)=\gamma_1(\infty)=\cdots=1,$$
$$\phi_0(k,\infty)=Q_0(1/k)=\operatorname{Artanh}k/k\qquad (29)$$

as one can easily prove.

Finally we wish to derive an expression for the derivative $\partial\phi_0/\partial k$. Deriving Eq. (14) we get

$$(2n+1)\gamma_n\partial\phi_n/\partial k-k(n+1)\partial\phi_{n+1}/\partial k$$
$$-kn\partial\phi_{n-1}/\partial k=(n+1)\phi_{n+1}+n\phi_{n-1}.\qquad (30)$$

Multiplying Eq. (14) by $-\partial\phi_n/\partial k$ and (30) by $+\phi_n$ and adding, one obtains

$$A_n-A_{n+1}=n\phi_{n-1}\phi_n+(n+1)\phi_n\phi_{n+1}-\delta_{n0}\partial\phi_n/\partial k,$$

[8] We spare the reader the derivation of Eqs. (22) to (25), which are well-known in the theory of continued fractions. One can also arrive at them directly, setting:

$$\phi_n=w_nk^{-n}(n!)^{-1}1.3\cdots(2n-1),\quad w_n=\phi_0U_n-V_n$$

and inserting into Eq. (15).

[9] See for instance I. Waller, reference 6, especially the first paper.

where

$$A_n = nk(\phi_{n-1}\partial\phi_n/\partial k - \phi_n\partial\phi_{n-1}/\partial k)$$

(in particular: $A_0 = 0$). Noticing that $\lim_{n=\infty} A_n = 0$ and summing over n we have

$$\partial\phi_0/\partial k = 2\sum_{n=0}^{\infty}(n+1)\phi_n\phi_{n+1}. \quad (31)$$

2.3 Numerical Evaluation of $\phi_0(k, \eta)$

As we shall see, when k is real and within the interval $-1<k<+1$, ϕ_0 has a real pole $\eta(k)$ in the η-plane, such that $\eta>0$. This is what we call the "main pole," i.e., the pole with the largest real part, which is of paramount importance in the method of steepest descent, Eqs. (10), (11), (12). For small values of k the function $\eta(k)$ can be obtained from an expansion in powers of k^2, that will be discussed later for the general case, see Eq. (65). For the special case $M=1$ we have obtained four coefficients of the expansion, thus

$$\eta = k^2 + (11/15)k^4 + (1563/1575)k^6 + (70709/118125)k^8 + \cdots.$$

This was used for an evaluation of η, η', and η'' for $k \leq 0.5$.

When $0.5<k<1$, however, it became necessary to find the connection between η and k by a numerical investigation of the function ϕ_0 as illustrated by Fig. 2. Here ϕ_0^{-1} is plotted as a function of k^2 [10] for selected values of η, and the pole singularity of ϕ_0 appears as a zero for ϕ_0^{-1}, the position of which on the k axis varies as η varies. This gives k as a function of η, or vice versa.

The figure is qualitatively correct for any slowing down element (any M).[11] Quantitatively we have carried out the program only in the case of hydrogen ($M=1$). The calculation involves the following steps:

First, the coefficients $g_n(\eta)$ are computed for a selected value of η, by means of the relation

$$g_{n+2}(\eta) = g_n(\eta)(2\eta+1-n)/(2\eta+4+n) \quad (32)$$

and the values $g_0 = 1/(1+\eta)$, $g_1 = 1(\eta+\frac{3}{2})$. (Unfortunately a relation as simple as (32) does not exist when $M \neq 1$.)

Next a table of $\gamma_0 \cdots \gamma_n$ and $\beta_1 \cdots \beta_n$ is set up for a given k, up to a sufficiently high n, and the sequences U and V are computed by means of the homogeneous recurrent relation (23) ($n=1, 2, \cdots$) starting from the initial values (24). The expression (22′) is then found to converge satisfactorily to the value of $\phi_0^{-1}(k, \eta)$. This process is repeated for several values of k, and one of the curves in Fig. 2 is obtained.

TABLE I.

k	η	η'	η''	R	c (Eq. (48a))	$R(1-k)$
0.0	0	0	2	1		1
0.1	0.01007	0.2030	2.091	1.007		
0.2	0.04124	0.425_4	2.40_2	1.029		0.823
0.3	0.09670	0.695	3.06	1.073		0.752
0.4	0.183_2	1.05_7	4.3_1	1.15		0.696
0.5	0.314	1.60	6.5	1.26	0.534	0.655
0.5918*	0.5	2.48_3	12.8	1.45_8	0.539	0.594
0.64	0.637	3.22_3	18.4_4	1.61	0.541	0.58
0.7252*	1.0	5.58_7	41.1	2.01	0.543	0.553
0.8952*	3.5	38.615	737	4.98	0.546	0.522
1	∞	$\sim 2.36\eta^2$	$\sim 11.1\eta^3$	$\sim 1.18\eta$	$c_\infty \approx 0.548$	0.500

In practice it is only necessary to evaluate ϕ_0^{-1} crudely for a few points so as to have an idea of the position of the zero-point. Then ϕ_0^{-1} is evaluated more accurately for two or three k^2-values in the neighborhood of the zero-point, which is then obtained by interpolation. It is also possible to estimate by interpolation the derivative $\partial\phi_0^{-1}/\partial k$ at the zero point; a more accurate evaluation is obtained, however, from Eq. (31) or

$$\partial\phi_0^{-1}/\partial k = -2\sum_{n=0}^{\infty}(n+1)\phi_n\phi_{n+1}/\phi_0^2. \quad (33)$$

It may be pointed out that one has (see reference 8)

$$\phi_0^{-1}\phi_n = [1\cdot 3\cdots(2n-1)/n!]k^{-n} \times (U_n - \phi_0^{-1}V_n). \quad (34)$$

At the zero-point the term in V_n vanishes. Finally

$$\partial\phi_0^{-1}/\partial k = -2\sum_{n=0}^{\infty}[1\cdot 3\cdots(2n-1)/n!]^2 \times (2n+1)k^{-2n-1}U_nU_{n+1} \quad (35)$$

involving only known quantities. It may be easily shown that the series converges like

$$\sum_n (2\lambda/k)^{2n} = \sum_n \epsilon^{2n}.$$

The rather tedious procedure we have described was actually carried out only for three η values, indicated by an asterisk in the table

[10] It is easy to see that U_n and V_n satisfying Eqs. (23) and (24) are even functions of k, so that ϕ_0, Eq. (22), is also even.

[11] In particular it is always true that the zero-point $\eta(k)$ increases from zero to $+\infty$ while k^2 varies from 0 to $+1$.

below. It then turned out that in this region η is almost exactly linear in $(1-k)^{-1}$ so that accurate interpolation is easy. This behavior corresponds to formulae (48), (48a). As a consequence it has been possible to compute without undue labor a table of the function $\eta(k)$ and its derivatives $\eta'(k)$ and $\eta''(k)$.

In order to complete the table required by the saddle-point formulae (11) and (12), one has to evaluate R, Eq. (9).

Now the function $\eta(k)$ is defined by the equation: $\phi_0^{-1}(k, \eta)=0$, so that

$$\partial\phi_0^{-1}/\partial k+\eta'(k)\partial\phi_0^{-1}/\partial\eta=0,$$

or

$$R=-\eta'(k)/(\partial\phi_0^{-1}/\partial k) \tag{36}$$

which may be computed from the value of the expression (35). The results are summarized in the Table I, which includes the data for $k<0.5$ obtained from the series expansion for η already given and the expansion for R

$$R^{-1}=1-(2/3)k^2-(17/15)k^4 +(48176/23625)k^6+\cdots.$$

2.4 Asymptotic Formulae for $k(\eta)$ When $\eta\to\infty$

An inspection of the values in Table I, together with Eq. (12) shows that when we make the distance from the source z larger and larger (keeping the energy u constant), we are led to larger and larger values of η. At the same time $k(\eta)\to 1$, and $\epsilon\to 1$, so that the convergence of the sequence ϕ_n to zero becomes very slow (see Eq. (17)). This makes the convergence of the expressions (22) or (22′) unsuitable for numerical work.

Although the γ's are very close to unity when η is large, it is just their difference from unity that determines the difference $1-k(\eta)$, i.e., the quantity we wish to determine. In fact, as will appear from the following, the differences $g_n=1-\gamma_n$ cannot here be neglected up to a large value of n. This makes also the method based on the smallness of the g_n's (see Eqs. (27) and (28)) perfectly useless in the present case.

On the other hand, as we shall see, the recurrent system (15) takes for large η's a simple asymptotic form, that makes the problem easier than one might think.

In the first place, a simple asymptotic expression may be given for the coefficients $g_n(\eta)$, when $\eta\to\infty$. Going back to the scattering function g, Eq. (2), we make use of the known theorem, that if a function with a maximum is raised to a high power, the ensuing sharp maximum is of Gaussian shape. Setting $\mu=\cos\Theta$ in Eq. (3) and developing $\ln G(\Theta)$ for small Θ

$$\ln G(\Theta)=-\Theta^2/2M +(\Theta^4/24M)(1-3/M^2)+\cdots. \tag{37}$$

When this is substituted into Eq. (2) the Θ^2-term yields a Gaussian, which decays to a negligible value before the Θ^4-term makes itself felt. (If η is large, i.e.: $\eta\gg M$.) Within the same approximation one may replace the factor $(M^2-1+\mu^2)^{-\frac{1}{2}}$ simply by M^{-1}, so that finally

$$g(\cos\Theta, \eta)\approx(\alpha/\pi M)\exp(-\eta\Theta^2/M), \tag{38}$$

($\eta+1$ has been replaced by η in the exponent, for the same reasons). In evaluating the integrals (4) one may again make use of the fact that g, Eq. (38), decays to a negligible value as soon as $\Theta\gg(M/\eta)^{\frac{1}{2}}$, which is a small angle. The main contribution to the integral comes therefore from small Θ-values,[12] for which one may use the well known approximation

$$P_n(\cos\Theta)=J_0([n+\tfrac{1}{2}]\Theta) \tag{39}$$

where J_0 is the Bessel function of zero order. Inserting (38) and (39) into (4) one finds

$$g_n(\eta)=(\alpha/\eta)\exp[-M(n+\tfrac{1}{2})^2/4\eta]. \tag{40}$$

This expression has been compared with exact numerical values by Marshak, with very good agreement (see "M," footnote on page 231).

It may next be noticed that, η being large, the exponential in Eq. (40) is a slowly variable function of n in the whole region where it is not negligibly small. This suggests the introduction of a variable $\sigma=(M/4\eta)^{\frac{1}{2}}(n+\frac{1}{2})$, the step $\delta n=1$ corresponding to a very small step in σ: $\delta\sigma=(M/4\eta)^{\frac{1}{2}}$, so that g_n may be regarded as a

[12] It may be pointed out that this is not true if n becomes very large. One may show, however, that (provided η is large) the formula (40) represents $g_n(\eta)$ correctly up to n values such that $Mn^2/4\eta\gg 1$, so that the exponential becomes exceedingly small. In particular in the case of hydrogen it is possible to derive from Eq. (32) a closed expression for g_n when both n and η are large, no matter what the ratio n/η is. For $n\gg\eta$ the behavior of g_n as a function of n becomes oscillatory and differs radically from Eq. (40). These values are, however, so small that the difference does not matter.

smooth function of a practically continuous variable σ.

Let us now turn to the study of the system (14) when η is large and k tends to a pole $k(\eta)$. As we have seen already, the poles $k(\eta)$ may also be characterized as the "eigenvalues" of the parameter k, i.e., the values for which there exists a non-trivial solution of the completely homogeneous system

$$(2n+1)\gamma_n\phi_n - k(n+1)\phi_{n+1} - kn\phi_{n-1} = 0, \quad (n=0, 1, 2, \cdots) \tag{41}$$

subject to the condition (14). The first equation (41) is now

$$\gamma_0\phi_0 = k\phi_1. \tag{42}$$

Using the difference notation

$$\delta\phi_{n+\frac{1}{2}} = \phi_{n+1} - \phi_n, \quad \delta\phi_n = \tfrac{1}{2}(\delta\phi_{n+\frac{1}{2}} + \delta\phi_{n-\frac{1}{2}}), \quad \delta^2\phi_n = \delta\phi_{n+\frac{1}{2}} - \delta\phi_{n-\frac{1}{2}}, \tag{43}$$

the remaining equations of the system may be put into the form

$$\delta\phi_{n+\frac{1}{2}} = [n/(n+1)]\delta\phi_{n-\frac{1}{2}} + [(2n+1)/k(n+1)](\gamma_n - k)\phi_n, \tag{44}$$

or alternatively,

$$\delta^2\phi_n + (n+\tfrac{1}{2})^{-1}\delta\phi_n + (2-2k^{-1}\gamma_n)\phi_n = 0. \tag{45}$$

The difference notation emphasizes the similarity to an eigenvalue problem of the Sturm-Liouville type, and in particular to a Schrödinger equation.[13]

We assume now that η is real and >0. It may be shown later that an eigenvalue k is then necessarily real (see Appendix A). Since the intervals $-\infty < k < -1$ and $+1 < k < +\infty$ are excluded, and since the eigenvalues occur in pairs of opposite sign (ϕ_0 being an even function of k) we may limit our search to the interval $0 < k < 1$.

A further limitation is given by the fact that a positive k must be larger than *some* at least of the γ_n's.[14] In fact, if $k < \gamma_n$ for all n's, Eq. (42) shows first that (assuming for instance $\phi_0 > 0$): $\phi_1 > \phi_0$ or: $\delta\phi_{\frac{1}{2}} > 0$; subsequently Eq. (44) shows that: $\delta\phi_{3/2} > 0$, $\cdots$, etc., so that ϕ_n increases monotonically with n, and cannot tend to zero.

Since, for large η, $\gamma_n \geq \gamma_0 \approx 1 - \alpha/\eta$, we have finally to search for an eigenvalue k in the small interval

$$1 - \alpha/\eta < k < 1 \tag{46}$$

showing that $1-k$ is at most of the order of $1/\eta$.

Again using Eq. (42) and (44) we easily see that $\delta\phi_{\frac{1}{2}}$, $\cdots$ and similarly $\delta\phi_1$, $\delta\phi_2$, $\cdots$ are at most of the order of $1/\eta$. Although the argument is not valid up to indefinitely high values of n, we may see that the statement is true even there from Eq. (17), since $1-\epsilon$ is of the order of $1/\eta$ at the most.

Thus, ϕ_n is shown to be a slowly variable function of n of the same kind as $g_n(\eta)$, and we are justified in regarding it as a continuous function of the variable σ above defined. According to (46) we get $k^{-1} = 1 + k_1/\eta$ (or $k \approx 1 - k_1/\eta$). Inserting this, together with the expression (40), into (45), and dividing by $\delta\sigma^2 = M/4\eta$, we obtain

$$\delta^2\phi/\delta\sigma^2 + \sigma^{-1}\delta\phi/\delta\sigma + 8[-k_1/M + (\alpha/M)(1+k_1\eta^{-1})e^{-\sigma^2}]\phi = 0.$$

In the limit $\eta \to \infty$, $\delta\sigma \to 0$, the differences may be replaced with derivatives and the term $k_1\eta^{-1}$ may be neglected, so that, with

$$8\alpha/M = 2(M+1)^2/M^2,$$

the equation becomes

$$d^2\phi/d\sigma^2 + \sigma^{-1}d\phi/d\sigma + [-8k_1/M + 2M^{-2}(M+1)^2e^{-\sigma^2}]\phi = 0 \tag{47}$$

which was reproduced in "M" Eq. (169).[15] This equation, together with the boundary condition to be explained below, may be regarded as the radial Schrödinger equation for a two-dimensional particle, $-8k_1/M$ being the energy and $-2[(M+1)/M]^2e^{-\sigma^2}$ being the potential. σ is identified with the distance from the origin. For all values $M = 1, 2, \cdots$ the equation has only one bound level. The argument shows that k_1 approaches a finite value when $\eta \to \infty$. A more precise definition of k_1 is

$$k_1 = \lim_{\eta=\infty}[\eta(1-k)]. \tag{48}$$

[13] In the latter case we may compare the expression $2-2k^{-1}\gamma_n$ with $E - V(x)$, "2" being the energy and $2k^{-1}\gamma_n$ the potential. The eigenvalue problem then is of the type encountered when the energy level is given and a proportionality constant in the potential must be found.

[14] This is analogous to the theorem that the energy must be higher than the minimum of the potential (see reference 13).

[15] For comparison let $s = 2\sigma$. Marshak's k_1 corresponds to our k_1/M.

Now to the boundary conditions; these are

$$\phi \to 0 \text{ as } \sigma \to \infty\,; \quad \phi \text{ regular at } \sigma = 0. \tag{49}$$

The first condition does not require any comment. The second implies

$$d\phi/d\sigma = 0\,; \qquad d^2\phi/d\sigma^2 = \phi[4k_1/M - \{(M+1)/M\}^2] \tag{50}$$

for $\sigma = 0$. That these are the correct conditions may be seen on comparing them with the differences $\delta\phi_0$ and $\delta^2\phi_0$ obtained by extrapolation from $\delta\phi_{\frac{1}{2}}$ and $\delta^2\phi_1$, as computed from Eqs. (42) and (45), again neglecting terms of higher order in $1/\eta$.

Summarizing the results obtained so far, we can say that the function $k(\eta)$ for large η can be determined approximately by solving the radial Schrödinger equation for a mass-point moving with zero angular momentum in a plane under the action of a Gaussian potential. Furthermore, one can prove that even for $M=1$, when the well has its maximum depth, the equation admits only one discrete eigenvalue. For M tending to infinity the well becomes so shallow, that it is barely sufficient for binding, k_1/M tends to a very small though finite value.

Having evaluated k_1 numerically, the behavior of k for large η's is given to a first approximation by Eq. (48). Within the same approximation we easily get an expression for R from Eqs. (33) and (36). Since ϕ_n is a slowly variable function of n, we may set:

$$\sum_n \cdots \approx (\delta\sigma)^{-1} \int \cdots d\sigma,$$

and $(n+1)\phi_n\phi_{n+1} \approx (n+\frac{1}{2})\phi_n^2$ so that:

$$\partial\phi_0^{-1}/\partial k = -[8\eta/M\phi^2(0)] \int_0^\infty \phi^2(\sigma)\sigma d\sigma\,;$$

moreover $k \approx 1 - k_1/\eta$, $d\eta/dk \approx \eta^2/k_1$ so that finally

$$R = \eta M \phi^2(0) \left[8k_1 \int_0^\infty \phi^2(\sigma)\sigma d\sigma. \right]^{-1} \tag{51}$$

Thus,

$$(R/\eta)_\infty = \lim_{\eta=\infty} (R/\eta)$$

exists and may be easily evaluated once the eigenfunction $\phi(\sigma)$ is known.

2.5 Higher Approximations

In order to study the asymptotic behavior of the neutron density it is desirable to obtain some further information about $k(\eta)$ when η is large. Let us write

$$\eta = k_1(1-k)^{-1} - c, \tag{48a}$$

where c may be regarded as a function of k or alternatively of η. We shall prove that c tends to a finite value c_∞ when $\eta \to \infty$, i.e., when $k \to 1$. We can write, therefore:

$$k \sim 1 - \frac{k_1}{\eta + c_\infty} + 0(\eta^{-3}). \tag{48b}$$

In order to evaluate c_∞ we might try to improve the method of the previous section, retaining terms of a higher order in $1/\eta$. In particular, we ought to correct for the errors incurred in replacing the finite differences with derivatives, errors which are, as one easily sees, of the order of $(\delta\sigma)^2 = (M/4\eta)$. It is much easier, however, to arrive at this goal by following a different method, that we have developed and which was adopted by Marshak in his report. It consists in going back to the integral equation, of which the system (15) is the Legendre development (see "A" Eq. (24) or "M" (163)), and introducing directly into it the approximation (38). Let us use the same notation as in "A", where ω was the unit vector representing the direction of motion, and μ the cosine of the angle between ω and the z axis.

We have shown that the Legendre coefficients ϕ_n vary slowly when n varies, and are markedly different from zero over a range of n values of the order of $(4\eta/M)^{\frac{1}{2}}$. This means that the angular distribution function $\phi(\mu)$, of which the ϕ_n are the Legendre coefficients, extends over a narrow solid angle around the pole $\mu=1$, having an aperture of the order of $(M/4\eta)^{\frac{1}{2}}$. We may then use some suitable projection of the unit sphere on a plane tangent to the sphere at the pole, such that the pole is represented by the origin of a system of cartesian or polar coordinates in this plane, and such that the small area in which ϕ is different from zero is not appreciably distorted by the projection. Then arc cosμ is approximately measured by the distance s of the representative point from the origin, and the angle

$\theta = \arccos(\omega \cdot \omega')$ is approximately measured by the distance S between the representative points of ω and ω'. It is, however, convenient to choose the unit of length in the plane in such a way that it corresponds to an arc of $(M/4\eta)^{\frac{1}{2}}$ radians, so that the eigenfunction occupies an area in the plane of order unity.

Let us first preserve the same degree of approximation as in the previous section. Writing the homogeneous integral equation corresponding to the system (41)[16] in the form

$$(1-k)\mu\phi(\mu) = -(1-\mu)\phi(\mu) + \int g\phi(\mu')d\omega' \quad (52)$$

we see that all terms are of order $1/\eta$. Consequently, we may set the factor $\mu = 1$ on the left side, and $(1-\mu) = -(\arccos\mu)^2/2 = -Ms^2/8\eta$, on the right-hand side, remembering what we said about the units. Similarly, we have

$$d\omega = (M/4\eta)d\mathbf{s},$$

$d\mathbf{s}$ being the element of area in the plane; we also write $\phi(\mathbf{s})$ instead of $\phi(\mu)$. Remembering now Eqs. (38) and (48), Eq. (52) becomes

$$4k_1\phi(\mathbf{s}) + (M/2)s^2\phi(\mathbf{s}) - (\alpha/\pi)\int \exp(-\mathbf{S}^2/4)\phi(\mathbf{s}')d\mathbf{s}' = 0, \quad (53)$$

where the integral term on the right-hand side may be written also symbolically as: $\alpha e^{\Delta}\phi(\mathbf{s})$, Δ being the Laplacian operator in the plane. It is then clear that the equation can be considerably simplified by means of a two-dimensional Fourier transformation

$$\phi_\sigma = \mathfrak{F}(\phi) = (1/2\pi)\int \phi(\mathbf{s}) \exp(i\boldsymbol{\sigma}\cdot\mathbf{s})d\mathbf{s}. \quad (54)$$

We indicate the Fourier transform with the same letter ϕ, but set the variable vector $\boldsymbol{\sigma}$ as an index to avoid confusion. Owing to the fact that $\phi(\mathbf{s})$ depends only on the modulus of $\mathbf{s}$, ϕ_σ also depends only on the modulus $\sigma = |\boldsymbol{\sigma}|$. On applying the Fourier transformation the operator e becomes simply $e^{-\sigma^2}$ whilst

$$\mathfrak{F}(s^2\phi) = -\Delta_\sigma\phi_\sigma = -(d^2/d\sigma^2 + \sigma^{-1}d/d\sigma)\phi_\sigma.$$

On making these substitutions, the equation immediately reduces to Eq. (47) of the preceding section. This is indeed not surprising, as there is the following rather trivial connection between the two methods.

A development in Legendre polynomials is essentially a development in eigensolutions of the wave equation on the sphere, whilst the Fourier transformation is a development of ϕ in eigensolutions of the wave equation in the plane. On a small polar cap on the sphere, such that the curvature may be neglected, the first development is practically equivalent to the second, this being the deeper reason for the connection (39), as is well known. The inverse of Eq. (54), or

$$\phi(s) = (1/2\pi)\int \phi_\sigma \exp(-i\boldsymbol{\sigma}\cdot\mathbf{s})d\boldsymbol{\sigma} = \int_0^\infty \phi_\sigma J_0(\sigma s)\sigma d\sigma \quad (55)$$

is, in fact, the limiting form of the Legendre development "A" Eq. (11), apart from a different normalization.

We now turn to the next higher approximation. This does not present any special difficulty, and we shall only sketch the main steps. Since it is now important to consider the distortion in the projection on the plane, we must decide upon the type of projection we want to use. We choose, for instance, the homalographic projection

$$s = (4\eta/M)^{\frac{1}{2}}2\sin(\tfrac{1}{2}\arccos\mu) = [8\eta(1-\mu)/M]^{\frac{1}{2}}. \quad (56)$$

The polar angle on the plane: φ remains equal to the longitude on the sphere, of course. One has then exactly

$$1-\mu = Ms^2/8\eta; \quad d\omega = (M/4\eta)sdsd\varphi. \quad (57)$$

We must use the full expression (37) where the arc distance Θ is given by

$$(4\eta/M)\Theta^2 = S^2 + (M/4\eta)\{S^4/12 - s^2s'^2/2 + ss'\cos(\varphi-\varphi')\cdot(s^2+s'^2)/4\}, \quad (58)$$

where

$$S^2 = (\mathbf{s}-\mathbf{s}')^2 = s^2 + s'^2 - 2ss'\cos(\varphi-\varphi'). \quad (59)$$

Equation (58) is derived from the cosine theorem of spherical trigonometry. Within the same approximation we may *not* replace η by $\eta+1$ in the exponent of g, as in Eq. (38), and we must also

[16] In the same way as "A" Eq. (24) corresponds to the inhomogeneous system (15).

TABLE II.

$M=1$	2	12	16
$\eta_1=1$	0.689	2.24	2.90
$\eta_2=11/15$	0.600	1.42	1.81

use a better approximation for the factor $(M^2-\sin^2\theta)^{-\frac{1}{2}}$. Finally we find that the integral equation may be written

$$U(\phi)+\eta^{-1}\Big\{4k_1c_\infty\phi(\mathbf{s})-(Mk_1/2)s^2\phi(\mathbf{s})$$

$$+(\alpha/64\pi M)\int\exp(-S^2/4)\phi(\mathbf{s}')fd\mathbf{s}'\Big\}=0, \quad (60)$$

where $U(\phi)$ is the left hand side of Eq. (53). Moreover, terms of order η^{-2} are neglected, and k has been expanded as in Eq. (48b). Finally, f is defined by

$$f=S^4+(M^2/2)[(s^2-s'^2)^2-S^2(s^2+s'^2)]$$
$$+8(2M-1)S^2. \quad (61)$$

We can now evaluate the second-order coefficient c_∞ of the eigenvalue by means of the mean-value theorem of perturbation theory. Multiplying Eq. (60) by $\phi(\mathbf{s})$, and integrating with respect to $d\mathbf{s}$, we find as usual that the term $U(\phi)$ gives only a contribution of the order: η^{-2}.[17] Therefore, we must have

$$4c_\infty\int\phi^2(s)d\mathbf{s}=(M/2)\int s^2\phi^2(s)d\mathbf{s}$$

$$-(\alpha/64\pi k_1M)\int\exp(-S^2/4)\phi(s)$$

$$\times\phi(s')fd\mathbf{s}d\mathbf{s}', \quad (62)$$

where ϕ is now the zero-order solution.

This solves in principle the problem of computing the second order correction, i.e., the coefficient c_∞. It is also possible to apply to this formula a Fourier transformation so as to express the integrals in terms of the function ϕ_σ that can be evaluated more simply than $\phi(s)$. Numerical results for various M values will be published by Mr. Marshall.

[17] This is a consequence of the fact that ϕ differs from the zero-order solution (of Eq. (53)) only by a term of the first order, and from the fact that the kernel of Eq. (53) is symmetric.

2.6 Justification of the Method of Steepest Descent

In order to fill the gaps that were left in the derivation of the Eqs. (11) and (12), we shall now first of all collect all the available information about the poles of the function ϕ_0, i.e., the roots of the equation

$$f(k,\eta)\equiv\phi_0^{-1}(k,\eta)=0. \quad (63)$$

The integration path in the k plane, Eq. (7), passes through the origin $k=0$; this is a convenient starting point for our investigation. It was shown in "A" that when $k\to0$ any root $\eta(k)$ of Eq. (63) must tend to a root of any one amongst the equations: $\gamma_0(\eta)=0$; $\gamma_1(\eta)=0$; $\cdots$. Now $\eta=0$ is a root of the first equation, since

$$\gamma_0(0)=1-g_0(0)=1-\alpha(1-e^{-q})=0. \quad (64)$$

This indicates the existence of a function $\eta(k)$ satisfying (63) identically, such that $\eta(0)=0$. In "A" Sec. 3.2 it was indicated that this function may be expanded into a power series

$$\eta=\eta_1k^2+\eta_2k^4+\cdots. \quad (65)$$

See also "M" Eq. (142b). The first coefficients are

$$\eta_1=(3\gamma_1\gamma_0')^{-1},$$
$$\eta_2=\eta_1^2\{(4\gamma_0'/5\gamma_2)-(\gamma_1'/\gamma_1)-(\gamma_0''/2\gamma_0')\}. \quad (66)$$

The values of the γ's and their derivatives appearing in the formulae refer to $\eta=0$ and are given in "M" Eqs. (85a, b, c, d) and (147), and Table X. Some typical values are given in Table II.

The reciprocal development of k^2 in powers of η (with different notations) has been used by Waller.[6]

Let us now consider briefly the other branches of the function $\eta(k)$ in the neighborhood of $k=0$. We first examine hydrogen. In this case $\eta=0$ is the only root of $\gamma_0=0$, since $\gamma_0=1-(\eta+1)^{-1}$. The other branches of $\eta(k)$ are therefore connected with the remaining equations, $\gamma_1=0$, etc. Now for instance $\gamma_1=1-(\eta+\frac{3}{2})^{-1}$, and the root is $\eta=-\frac{1}{2}$. Assuming $\eta(0)=-\frac{1}{2}$, we get the development

$$\eta(k)=-(1/2)-(1/15)k^2+\cdots. \quad (67)$$

A numerical investigation (see "A", Fig. 1), has shown that the two solutions (65) and (67) have a very simple connection. In fact, $\eta(k)$ has two

branch-points on the imaginary axis: $k=\pm ik_b$, where $k_b^2\approx 0.4$. If we start from the origin along the imaginary axis with the branch (65) and make a loop around one of the branch points, we come back to the origin with the value (67). Both values, of course, are negative but (67) is smaller than (65) which is in fact the "main pole" of the function ϕ_0 in the η plane for these values of k. Next we ought to consider branches of $\eta(k)$ such that $\eta(0)$ is a root of $\gamma_2=0$, $\gamma_3=0$, etc. These branches lie even further to the left on the η-plane and the reader will be spared further details.

Let us now turn to the general case $M>1$. The picture is now slightly more complicated since already the equation $\gamma_0=0$ has several roots besides $\eta=0$. These lie, however, considerably to the left of the imaginary axis (see "M" Eq. (22)), and will not be investigated further. The equation $\gamma_1=0$ has no simple root such as $\eta=-\frac{1}{2}$ for $M=1$. It may be proved, however, that the roots have $\Re(\eta)<-\frac{1}{2}$; the same applies to the roots of $\gamma_2=0$, etc. (see Appendix B). The connection between the branches of $\eta(k)$ associated with these roots, and the "main" branch Eq. (65), could be investigated numerically.

It may be pointed out, however, that our main purpose in studying these secondary roots was only to show that they lie sufficiently far to the left of the main pole, to justify the approximation (8). Moreover, it is not really necessary for this to be true for all k values, but only for the points of a suitable integration path in the k-plane, or indeed for the portion of the integration path that gives a significant contribution to the integral; it does not matter at all if on the remaining portions the $\eta(k)$ poles are close together and the approximation (8) fails.

In order to make this point clear, let us examine what is perhaps the most critical case, namely $M=1$, $z=0$. Because $z=0$, the saddle-point, Eq. (12), is the origin $k=0$ and the path of steepest descent is the undeformed path of Eq. (7), i.e., the imaginary axis in the k plane. Because $M=1$, the distance $\delta\eta$ between the main pole and the next starts with a value $\frac{1}{2}$, and *decreases* with increasing $|k|$, and the approximation (8) becomes increasingly worse. On the other hand, the exponential factor is, considering Eq. (65) with $\eta_1=1$:

$$e^{u\eta(k)}\approx e^{-uy^2} \tag{68}$$

if $k=iy$. Since u is large, say $u\sim 10$, this factor becomes negligible *before* the branch point is reached, i.e., before the main pole and the one next to it come close together.[18] When now the k point moves beyond the branch-point, there will be two complex conjugate η values instead of two real ones. It is clear on physical grounds, however, that these values of the Fourier variable $k=iy$ can hardly contribute to the total intensity for small values of z, because they represent Fourier components of "wave-length" short compared to the average width $\sim u^{\frac{1}{2}}$ of the z distribution.[19]

Essentially the same considerations apply when z instead of *zero* is small, i.e., such that the expansion (65) is still rapidly convergent at the saddle-point k_0. From Eqs. (12) and (65) one finds

$$z/u=\eta'(k_0)=2\eta_1 k_0+\cdots,$$

or

$$k_0\sim z/2u\eta_1.$$

The condition is thus

$$k_0\ll 1, \quad \text{or} \quad z\ll 2u\eta_1\sim u.$$

It will be noticed that the approximation (8) becomes better as z increases, because the distance $\delta\eta$ when k is at the saddle-point k_0 becomes larger as k_0 increases (compares Eqs. (65) and (67)). It may also be pointed out that the case $M=1$, for which numerical examples have been given before, is really the most unfavorable case; for heavier elements the approximation is not good but excellent,[20] since the distance $\delta\eta$ is considerably larger than $\frac{1}{2}$ even at $k=0$.

Let us now consider what happens when z becomes $\sim u$ or larger, so that the saddle-point k_0 approaches unity. In the first place, we must prove that the integration path can be pulled to

[18] Considering only the quadratic term in Eq. (65) involves, of course, an error. The true value of $\eta(k)$ at the branch point $k^2=-0.4$ is about 0.34. This makes $e^{u\eta}\infty e^{-3.4}=0.033$ instead of $e^{-4}=0.02$.

[19] From a mathematical standpoint one would have to show that the poles $\eta(k)$ with the largest real part move further to the left as y increases.

[20] We refrained from extending our computations to this case, because we understand that work on the heavier elements is in progress elsewhere.

the right in the k-plane so as to pass through the saddle-point; to this end we first choose the abscissa σ in Eq. (7) very large. We know that when $\Re(\eta)\to+\infty$, the function ϕ_0 tends to the expression (29) for all k points outside the cuts. This is a regular analytic function in the k plane, so that all the singularities $k(\eta)$ must move toward the cuts when $\Re(\eta)\to+\infty$. Thus, when σ is sufficiently large we may deform the integration path in the k plane so as to pass through any desired point k_0 on the real axis; a suitable path, for instance, is a straight line parallel to the imaginary axis: $k=k_0+iy$ with, say, $|y|\leq 1$. From $k=k_0\pm i$ we then move to infinity on straight lines at an angle $\vartheta<\pi/2$ with the real axis. We then show that only a small portion of the central vertical path is important. On this central portion we may evaluate the η-integral by means of Eq. (8); in fact, although Eqs. (65) and (67) cannot be used when $|k|\sim k_0$ is comparable to unity, the qualitative statement that the secondary pole (67) is considerably to the left of the main pole remains true. We then expand the exponent $u\eta(k)-zk$ in powers of $k-k_0=iy$, as stated before

$$u\eta-zk=u\eta_0-zk_0-\tfrac{1}{2}u\eta_0''y^2 -(i/6)u\eta_0'''y^3+\cdots. \quad (69)$$

An estimate of the various terms can be made remembering Eq. (48a). The derivatives of the slowly variable quantity c may be neglected, if we are interested merely in orders of magnitude. Thus

$$\eta_0'\sim k_1(1-k_0)^{-2};\ \ \eta_0''\sim 2k_1(1-k_0)^{-3};\ \ \cdots. \quad (70)$$

The positive sign of η_0'' shows that the exponential of the expression (69) has indeed a maximum at $y=0$. We show, furthermore, that the exponential may be represented by a Gaussian. The condition (12) for k_0 in connection with (70) shows that $1-k_0$ is of order unity when z is comparable with u, and when $z\gg u$

$$1-k_0\approx(uk_1/z)^{\frac{1}{2}}\ll 1. \quad (71)$$

Now from (70) we have:

$$\eta_0''\approx 2\eta_0'(1-k_0)^{-1}=2z/u(1-k_0);$$

hence the quadratic term in (69) is

$$-\tfrac{1}{2}u\eta_0''y^2=-z(1-k_0)^{-1}y^2=-(y/y_0)^2, \quad (72)$$

where $y_0=[(1-k_0)/z]^{\frac{1}{2}}\ll 1$ because $z\gtrsim u\gg 1$. If only the quadratic term is retained, the exponential becomes small when $y>y_0$. Now since $\eta_0'''\approx 3\eta_0''(1-k_0)^{-1}$, the cubic term is of the order of $y/(1-k_0)$ with respect to the quadratic term; for instance, if $y=y_0$ the cubic term is

$$y_0(1-k_0)^{-1}(y/y_0)^3=y_0(1-k_0)^{-1} =[z(1-k_0)]^{-\frac{1}{2}}\ll 1. \quad (73)$$

In fact, if $z\sim u$, $1-k_0\sim 1$ and the inequality holds true. If on the other hand $z\gg u$, we may use (71) so that

$$[z(1-k_0)]^{-\frac{1}{2}}=(k_1uz)^{-\frac{1}{4}}\ll 1. \quad (74)$$

The same argument applies *a fortiori* to the higher order terms, which are of the order $[y/(1-k_0)]^n$, $n\geq 2$, with respect to the quadratic term. This proves conclusively that the gaussian approximation applies to the vertical straight part of the path. As regards the inclined parts of the path, we know from previous considerations that $\eta(k)$ moves to the left as k moves toward infinity so that $e^{u\eta(k)}$ becomes even smaller. At the same time the factor e^{-zk} tends to zero. We have thus reached a sufficient justification for the steepest descent expression (11), even though a closer investigation of upper limits might be desirable for purposes of mathematical rigor.

A few remarks remain to be made. The path we have used is not strictly speaking the path of steepest descent; as usual, it was sufficient to use a path sufficiently close to the path of steepest descent to achieve the result. It may be seen from the formula (48a), neglecting the variation of c, that the path of steepest descent in the limit of large z, or k_0 close to unity, is a small circle of equation: $(1-k')^2+k''^2=uk_1/z=(1-k_0)^2$ if $k=k'+ik''$, i.e., a circle having the center at $k=1$ and passing through the saddle-point. The significant contributions to the integral come from a small angular fraction of this circle, of the order of y_0 divided by the radius, i.e., $y_0/(1-k_0)\ll 1$ according to (73). This is why it was immaterial to replace the circle by a straight line.[21]

[21] In this limiting case of z very large, one might also present the procedure as an asymptotic expansion with respect to z, i.e., perform the integration with respect to k first by pulling the integration path in the k plane and taking the residue at $k(\eta)$, this being given by Eq. (48a). The result is, however, the same.

Another remark of interest is that when z is very large, we need no longer request $u \gg 1$, but only the weaker condition

$$uz \gg 1. \tag{75}$$

In fact, this is seen to ensure the validity of (74) and therefore of the Gaussian approximation. At the same time it is no longer necessary for u to be large in order to enable us to retain only the contribution from the main pole in Eq. (8). In fact, $\eta(k)$ at the main pole is now large, indeed of the order

$$\eta(k_0) \sim k_1(1-k_0)^{-1} \sim (k_1 z/u)^{\frac{1}{2}} \tag{76}$$

while the secondary poles are negative. Therefore, the distance $\delta\eta$ between the main pole and the one next to it is at least of the order of (76), and the factor expressing the ratio of the residues or $e^{-u\delta\eta}$ has an exponent of the order

$$u\delta\eta \gtrsim u\eta(k_0) \sim (k_1 uz)^{\frac{1}{2}}.$$

The condition for the secondary poles to be negligible is then precisely the same condition (76), ensuring the validity of the method of steepest descent.

Summarizing the conditions under which Eq. (11), (12) are expected to hold, we find

$$u \gg 1, \quad z \text{ arbitrary} \tag{77}$$

or

$$z \gg 1, \quad uz \gg 1. \tag{78}$$

2.7 Special Limiting Cases and Numerical Results for Hydrogen

If $z \ll u$ the expression (11) takes a simple form, owing to the fact that the saddle-point k_0 is close to the origin and one may neglect all the higher powers of k in the series expansions of η and R in powers of k^2. For instance,

$$R^{-1} = \gamma_0'(0) + \cdots,$$

as one can see from Eqs. (9) and (20) neglecting terms $\sim k_0^2$. Following "M" Eq. (85a) we have therefore: $R^{-1} = \xi$. Similarly we set:

$$\eta(k) = \eta_1 k^2 + \cdots,$$

and the saddle-point k_0 is given by: $z/u = \eta'(k_0) = 2\eta_1 k_0$, etc. Finally one finds

$$\psi_0(z, u) = \xi^{-1}(4\pi\eta_1 u)^{-\frac{1}{2}} \exp(-z^2/4\eta_1 u) \tag{79}$$

which coincides with the "age" approximation, "M" Eq. (145); see also "M" Eq. (85c) and our Eq. (66).

Turning now to the other extreme case: $z \gg u$, we may use Eq. (71) for the saddle-point. This follows from Eq. (48a) when we neglect the variation of c with k. Correspondingly $\eta(k_0)$ is obtained from (48a) with $c = c_\infty$, so that, using Eq. (71):

$$\eta_0 = \eta(k_0) = (k_1 z/u)^{\frac{1}{2}} - c_\infty. \tag{80}$$

Computing η_0'' in a similar way, one has finally

$$\psi_0 \sim A(zu)^{-\frac{1}{4}} \exp(-z + 2(k_1 uz)^{\frac{1}{2}} - c_\infty u),$$
$$A = (4\pi)^{-\frac{1}{2}} k_1^{\frac{1}{4}} (R/\eta)_\infty. \tag{81}$$

The constants in this formula are determined by the Eqs. (47), (51), and (62). Apart from a slightly different notation and a minor slip, Eq. (81) corresponds to "M" Eq. (175).

The range of validity of the asymptotic formula (81) depends on the accuracy with which Eq. (48a) represents $\eta(k)$ when c is regarded as a constant c_∞. If the error is of the order of $1-k$. which corresponds to the error $\sim \eta^{-3}$ in Eq. (48b), then, as one easily sees, we must expect a correction term in the exponent of Eq. (81) of the order $u^{\frac{1}{2}} z^{-\frac{1}{2}}$, which would be negligible only if $z \gg u^3$. More generally we may regard the three terms in the exponent of Eq. (81) as the

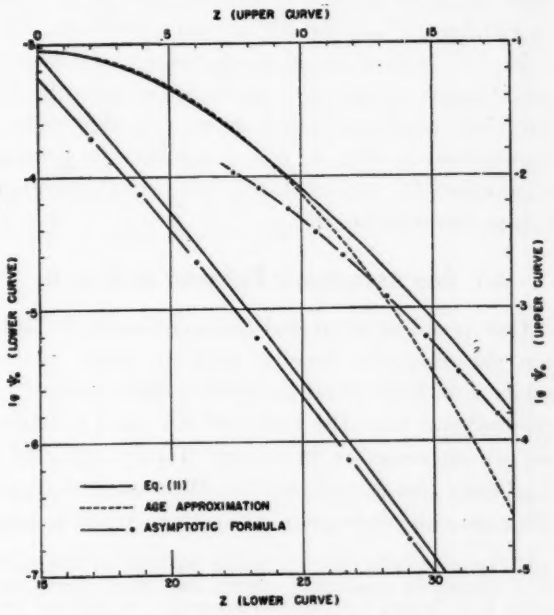

FIG. 3. The logarithm of the neutron density ψ_0 as a function of the distance z for $u = 10$ and $M = 1$.

first terms of an expansion in reciprocal powers of η_0, i.e., in powers of $(u/z)^{\frac{1}{2}}$. This will converge quite slowly, except when z is enormously large. There is not much point in computing further coefficients of the expansion.

In the particular case of hydrogen, however, the numerical data reveal a remarkable constancy of c, i.e., c approaches c_∞ sooner than one would expect in general, and as a result the asymptotic formula (81) is better than one might expect.[22]

The distribution function has been computed, as an example, for hydrogen for $u=10$, using the data of Table I. The result is plotted in Fig. 3, where the "age" approximation and the asymptotic formula are included also for comparison. The age approximation fails, as one might expect, when z becomes comparable to u, so that k_0 is no longer $\ll 1$.

3. THE CASE OF VARIABLE MEAN FREE PATH

In most practically important cases the mean free path cannot be considered constant. For many moderators, though not for all, it will decrease with decreasing velocity of the neutrons. At large distances from the source, an equilibrium between the primary and the slow neutrons is then readily established, so that the slow neutron density is determined to a large extent by the law for the primary neutrons, i.e., $r^{-2}e^{-r/l(0)}$ in the case of a point source. We shall see, however, that the asymptotic formula for the slow neutrons differs from the above-mentioned law in that it has a smaller (in general a fractional) power of the reciprocal distance before the exponential.

3.1 The Asymptotic Behavior of $\psi_0(z, u)$

Our problem is to find an asymptotic formula for the neutron density $\psi_0(z, u)$ when $z\to\infty$, while u is kept fixed at some value. It may be pointed out that the range of u values in which we are interested is finite, say: $0<u<\ln(E_0/kT)$, E_0 being the initial energy. We consider again the case of a plane primary source. Again ψ_0 may be expressed in terms of its Fourier-Laplace transform ϕ_0, Eq. (7), but ϕ_0 is given by a different set of equations.

We must, in fact, go back to "A" Eq. (2) or "M" Eq. (63) and take into account the dependence of l on the energy. Going through the same transformations as those leading to "A" Eq. (24) one finds

$$\phi(\mu)-k\mu\lambda(\mu)-\int g(\omega\cdot\omega',\eta)\phi(\mu')d\omega'=1/4\pi, \quad (82)$$

where λ is the Fourier-Laplace transform of $l(u)\psi$; the connection between λ and ϕ is thus: $\lambda=\mathfrak{L}\{l(u)\mathfrak{L}^{-1}\phi\}$ if $\mathfrak{L}$ means Laplace transform. We have to obtain ϕ from Eq. (82), and then insert $\phi_0=\int\phi d\omega$ into Eq. (7).

In order to study the asymptotic behavior of ψ_0 we may try again to pull the integration path in the k-plane, see Fig. 1, toward the right until we are stopped by a singularity; the position and character of this singularity determines the asymptotic behavior. Now we shall see that the analysis of the singularity in the k-plane when $\Re(\eta)$ is large can be made on similar lines as in Section 2.4. In order to make use of this fact we first prove that:

(a) When $\Re(\eta)>\sigma$ (this being a suitable constant) the convergence abscissae in the k-plane are independent of η[23] and precisely the convergence strip is

$$-1<\Re(k)<+1$$

if we choose the mean free path of the primary neutrons $l(0)$ as the unit of length.

(b) The convergence strip is determined by the fixed singular points $k=\pm1$, and the character of the singularity when $k\to\pm1$ is independent of η as long as $\Re(\eta)>\sigma$.

For the sake of simplicity we shall prove these statements under the assumption

$$l(u)=l_1+l_2e^{-\epsilon u}, \quad (83)$$

when l_1, l_2, ϵ are positive constants. As we said, we set

$$l(0)\equiv l_1+l_2=1. \quad (84)$$

The proof can be easily generalized to a formula containing a sum of many exponentials.

With Eq. (83) one easily expresses the connection between λ and ϕ as follows:

$$\lambda(\mu,\eta)=l_1\phi(\mu,\eta)+l_2\phi(\mu,\eta+\epsilon). \quad (85)$$

[22] This statement depends rather critically on the value of k_1 chosen in computing c from Eq. (48a). The eigenvalue k_1 is known with limited accuracy, so that the constancy of c as exhibited in the last column of Table I may be fortuitious. This, of course, does not affect the usefulness of Eq. (48a) as an interpolation formula.

[23] In sharp contrast with the constant mean free path case.

Inserting into Eq. (82) we get

$$[1-kl_1\mu]\phi(\mu,\eta)-\int g(\omega\cdot\omega',\eta)\phi(\mu')d\omega'$$
$$=kl_2\mu\phi(\mu,\eta+\epsilon)+1/4\pi. \quad (86)$$

Regarding for a moment the right-hand side of this equation as given, we notice that the left-hand side coincides with that of the integral equation "A" Eq. (24) except that k is substituted by kl_1. Hence (86) can be solved for $\phi(\mu,\eta)$ if kl_1 is different from any of the "eigenvalues" $k(\eta)$ that we studied before. Now let us choose σ in such a way that when $\Re(\eta)>\sigma$ the eigenvalue $k(\eta)$ with the smallest real part satisfies

$$l_1<\Re\{k(\eta)\}. \quad (87)$$

This is always possible since $k(\eta)\to 1>l_1$ when $\Re(\eta)\to+\infty$. Then clearly if: $-1<\Re(k)<+1$ (as we shall assume from now on), kl_1 in Eq. (86) *can not* be equal to an eigenvalue. This proves, then, that when $\Re(\eta)>\sigma$ one can use Eq. (86) to find $\phi(\mu,\eta)$ if $\phi(\mu,\eta+\epsilon)$ is known. If the latter is regular, $\phi(\mu,\eta)$ is also regular.

Now we know that when $\Re(\eta)\to+\infty$, $\phi(\mu,\eta)$ becomes the Laplace transform of the primary neutrons for which the convergence strip is $-1<\Re(k)<+1$. Thus, for a very large η, ϕ is regular within this strip. Then, according to the above statement, we can move in steps $\delta\eta=\epsilon$ toward smaller values of η and prove that ϕ remains regular, as long as $\Re(\eta)>\sigma$. On the other hand, the convergence strip of $\phi(\mu,\eta)$ cannot be wider than that for $\phi(\mu,+\infty)$,[24] which becomes singular when $k\to\pm1$. The same is expected, therefore, of $\phi(\mu,\eta)$ as long as $\Re(\eta)>\sigma$. This completes the proof of statements (a) and (b).

We are now going to investigate the properties of the Fourier-Laplace transform when η is very large. We shall find that as $k\to1$, ϕ behaves like $(1-k)^{\rho-2}$ where ρ is a constant <2. The above argument shows then that the behavior of ϕ is of the same type also for values of η that are not large, subject only to the condition $\Re(\eta)>\sigma$.

We can now drop the special assumption (83), since the discussion is equally simple in the general case, provided $l(u)$ is a decreasing function of u. Referring to the form (86) of the integral equation, we notice that the connection between ϕ and λ, in the case of large η, takes a simple form, owing to the fact that the main contribution to the Laplace integral comes from very small values of u. Therefore, omitting for simplicity the remaining variables,

$$\lambda(\eta)=\int_0^\infty e^{-\eta u}l(u)\psi(u)du$$
$$=\int_0^\infty e^{-\eta u}[l(0)+ul'(0)+\cdots]\psi(u)du, \quad (88)$$

so that, remembering Eq. (84) and setting $l'(0)/l(0)=-\gamma$, we find

$$\lambda(\eta)=\phi(\eta)+\gamma\partial\phi/\partial\eta+\cdots. \quad (89)$$

We must expect the successive terms in this development to be of decreasing order of magnitude, for large η, as can also be verified *a posteriori* on the final result. This shows, at least, that the approximation is consistent.

Since in the case of large η we are dealing mainly with neutrons that have suffered only small energy losses, the results obtained for constant m.f.p. should offer some guidance. Therefore, we surmise that we shall have to study the function ϕ for small values of $\vartheta=\arccos\mu$, and set $\mu=1-\vartheta^2/2$, then introducing approximation (38) for the scattering function and the variables $s=(M/4\eta)^{-\frac{1}{2}}\vartheta$. With this change of variable the partial derivative in Eq. (89) suffers the transformation: $\partial/\partial\eta\to\partial/\partial\eta+(s/2\eta)\partial/\partial s$. Taking this into account and introducing Eq. (89) into the integral equation, we find

$$[(1-k)+(kMs^2/8\eta)]\phi$$
$$-\gamma k\mu[\partial\phi/\partial\eta+(s/2\eta)\partial\phi/\partial s]$$
$$-(\alpha/4\pi\eta)\int\exp(-S^2/4)\phi(s')ds'=1/4\pi. \quad (90)$$

In this equation we neglect terms of higher order than η^{-1}, and thus replace $\gamma k\mu$ with γk before the square bracket. Finally, after multiplying with ηk^{-1} and remembering the abbreviation introduced after Eq. (53), the equation becomes

$$h\eta\phi-\eta\partial\phi/\partial\eta-(s/2)\partial\phi/\partial s+(M/8\gamma)s^2\phi$$
$$-(\alpha/k\gamma)e^{\Delta_s}\phi=\eta/4\pi k\gamma;\quad h=(1-k)/k\gamma. \quad (91)$$

[24] If it were, the distribution of the slow neutrons would decay faster than that of the primary ones with which they are in equilibrium, an obvious impossibility.

In order to solve this equation we consider the eigenvalue problem

$$-(s/2)dw/ds+(M/8\gamma)s^2w -(\alpha/k\gamma)e^{\Delta}w=(\rho-1)w \quad (92)$$

which is similar to Eq. (53) and can be treated in a similar manner; $\rho-1$ corresponds to k_1 in Eq. (53) and is the variable parameter. The eigenvalues of ρ form a discrete sequence ρ, ρ_1, ρ_2, $\cdots$ (see later). These eigenvalues depend on k, but when k is close to unity we may take them equal to their limiting values for $k=1$, i.e., set $\alpha/k\gamma=\alpha/\gamma$ in Eq. (92). We call ρ the lowest eigenvalue, which as we shall see is <2, when k is close to unity. Call w, w_1, w_2, $\cdots$ the corresponding eigenfunctions and develop ϕ:

$$\phi(\eta, s)=\sum_n a_n(\eta)w_n(s). \quad (93)$$

Inserting into Eq. (91) and using the orthogonality property of the eigenfunctions w_n:

$$\int w_n w_m d\mathbf{s}=\delta_{nm},$$

we find

$$(h\eta+\rho_n-1)a_n-\eta da_n/d\eta=(\eta/k\gamma)A_n, \quad (94)$$

where

$$4\pi A_n=\int w_n d\mathbf{s}. \quad (95)$$

The solution of Eq. (94) contains an integration constant that may be determined from the condition

$$a_n(+\infty)=A_n(1-k)^{-1}. \quad (96)$$

This follows from Eq. (86), remembering that $g\to 0$ when $\eta\to+\infty$. Therefore,

$$\phi(\mu, +\infty)=[4\pi(1-k\mu)]^{-1}. \quad (97)$$

Multiplying by $w_n(s)$ and integrating over $d\mathbf{s}$, and setting

$$\mu=1-\vartheta^2/2\approx 1-(M/8\eta)s^2\approx 1,$$

we get Eq. (96).

The solution of (94) is then

$$a_n(\eta)=(A_n/k\gamma)e^{h\eta}\eta^{\rho_n-1}\int_{\eta}^{+\infty} e^{-hx}x^{1-\rho_n}dx. \quad (98)$$

Examine now the behavior of this expression when $k\to 1$, t.i.: $h\to 0$, remembering that we are interested in the singularity of ϕ at this point. Now we can see that for an eigenvalue that satisfies $\rho>2$, the expression (98) remains finite when $h\to 0$, while if $\rho<2$ we can write

$$\int_{\eta}^{+\infty} e^{-hx}x^{1-\rho}dx=h^{\rho-2}\int_{h\eta}^{+\infty} e^{-y}y^{1-\rho}dy \approx(1-\rho)!h^{\rho-2}. \quad (99)$$

Hence the highest singularity will arise from the lowest eigenvalue. We consider, therefore, only the first term in the expansion (93) and drop henceforward the index n. Noticing that as $k\to 1$, $h\approx(1-k)/\gamma$, we have finally the behavior in this limit

$$\phi\sim A\gamma^{2-\rho}(1-\rho)!w(s)\eta^{\rho-1}e^{\eta(1-k)/\gamma}(1-k)^{\rho-2}. \quad (100)$$

For us the most important part of this formula is the last term or: $(1-k)^{\rho-2}$, that gives, as we have said, the singular behavior of ϕ also for finite values of η. This solves, therefore, the problem of the asymptotic behavior for large distances, for according to a well-known Tauberian theorem it is permissible, in computing the asymptotic behavior of the inverse transform, to consider all factors as constant, except the singular term of the type indicated, thus obtaining a dependence on z of the type (compare Eq. (7))

$$\cdots(1/2\pi i)\int_{-i\infty}^{+i\infty} e^{-kz}(1-k)^{\rho-2}dk =\text{const.}z^{1-\rho}e^{-z}. \quad (101)$$

For a *point* source, remembering "M" Eq. (62), we get the asymptotic dependence

$$\psi_0\sim r^{-\rho}e^{-r}, \quad (102)$$

r being the distance from the source measured in mean free paths of the primary neutrons. In order to use this law we have to solve the eigenvalue problem Eq. (92) with $k=1$. The procedure that was applied to Eq. (53) can be used here; namely, we perform a Fourier transformation (Eq. (54)) and notice that

$$\mathfrak{F}(sdw/ds)=-(\nabla_\sigma\cdot\sigma)\mathfrak{F}(w) =-(2+\sigma d/d\sigma)\mathfrak{F}(w). \quad (103)$$

Finally we set

$$U(\sigma)=e^{-\gamma\sigma^2/M}\mathfrak{F}(w) \quad (104)$$

and find

$$\{d^2/d\sigma^2+\sigma^{-1}d/d\sigma+(4\gamma/M)(2\rho-3)+2[(M+1)/M]^2e^{-\sigma^2}-(2\gamma/M)^2\sigma^2\}U(\sigma)=0 \quad (105)$$

that differs from Eq. (47) in having a different potential and a different meaning for the "energy" term. Clearly the presence of the quadratic term in the "potential" makes the eigenvalue spectrum discrete. When γ tends to zero, the lowest eigenvalue must tend to the discrete eigenvalue of problem (47), and the higher eigenvalues must crowd together, reproducing the continuous spectrum. If γ is sufficiently small the second eigenvalue must be close to the zero line, i.e., ρ must be close to $\frac{3}{2}$.

A very rough evaluation of the lowest eigenvalue has been made by the Ritz method, using the eigenfunction $e^{-\lambda\sigma^2/2}$ with λ the variable parameter. The minimum condition is

$$\alpha(1+\lambda)^{-2}+\gamma^2\lambda^{-2}/2M=M/8. \quad (106)$$

The γ term is often small, so that it is permissible to develop λ in powers of γ. As an example we find for carbon, $M=12$, the result: $\rho=1.5-0.42\gamma^{-1}+0.078_5\gamma+\cdots$. Assuming an energy dependence of the m.f.p.: $l(u)=2.75+2E$, E being the energy in Mev, the data in Table III have been obtained.

TABLE III. Variable mean free path; carbon.

Initial energy of neutrons in Mev:	0	0.5	1	2
$\gamma=0$		0.27	0.42	0.59
$\rho=-\infty$		−0.03	0.53	0.84

3.2 Remarks on the Energy Spectrum at Large Distances

Using the η-dependence of Eq. (100) and inverting the Laplace transformation, it would be easy to derive also the dependence of the neutron density on u, i.e., the spectrum. The formula, however, would hold only for very small u, or energies very near the primary one, being derived from an expression valid only for very large η.

A greater interest attaches the spectrum for large u, or in the slow neutron region. This can be derived (compare "A" Section 4.2) from the position of the first singularity that one meets as η moves to the left in the complex plane.

We must now drop the assumption $\Re(\eta)>\sigma$, that was made in Section 3.1. It is then easy to see that the singularity in the η plane must occur when kl_1 in Eq. (86) becomes equal to the eigenvalue $k(\eta)$ with the largest real part, i.e., the eigenvalue given by Eq. (65), or: $k(\eta)\approx(\eta/\eta_1)^{\frac{1}{2}}$, when η is small and by (48b) if η is large.

We write therefore

$$kl(\infty)=k(\eta)l(0) \quad (107)$$

introducing explicitly the value of the mean free paths for zero velocity: $l(\infty)$ and for the initial velocity: $l(0)$.

In order to find the spectrum, we now first keep k fixed and invert the Laplace transform (compare "A" (22a) and "A" (40)) finding an expression of the type

$$(1/2\pi i)\int_{\beta-i\infty}^{\beta+i\infty}\phi(\eta)e^{\eta u}d\eta=F(k)e^{\eta_k u}+\cdots, \quad (108)$$

where η_k is the solution of Eq. (107) and $F(k)$ is the residue of ϕ at η_k, and the terms omitted correspond to singularities further to the left in the complex η-plane. Unfortunately, it is not easy to determine $F(k)$ accurately, except by the kind of numerical work described in "A" Section 5. We know, however, that as $k\to1$, $F(k)$ behaves like $(1-k)^{\rho-2}$. For large r that is all we need, and we finally find that for large u the energy spectrum at large distances, i.e., the dependence of ψ_0 on u, is given by

$$\psi_0\sim e^{\eta_1 u} \quad (109)$$

where η_1 is the solution of

$$l_1\equiv l(\infty)=k(\eta)l(0). \quad (110)$$

The author wishes to express his gratitude to Dr. Marshak for criticism and for encouraging him to bring this work to completion. Thanks are also due Drs. Placzek, Wigner, Bethe, and Rose for some friendly advice.

APPENDIX A

Eigenvalues $k(\eta)$ when η is real and >0. We first prove that in this case: $|g_n(\eta)|<1$ for all n. Equation (2) may be written

$$g(\mu,\eta)=(\alpha/\pi)G^{2\eta+1}dG/d\mu. \quad (111)$$

One has then from Eq. (4)

$$|g_n| < 2\pi \int_{-1}^{+1} |g| d\mu = 2\alpha \int G^{2\eta+1} dG$$

$$= \alpha(\eta+1)^{-1}\{1-e^{-\alpha-\alpha\eta}\}.$$

In the interval: $0<\eta<+\infty$ the maximum of the right hand side occurs at $\eta=0$ so that

$$|g_n| < \alpha(1-e^{-\alpha}) = 1. \tag{112}$$

Multiplying now Eq. (41) by ϕ_n^* and summing over n we get

$$\sum_{n=0}^{\infty}(2n+1)\gamma_n|\phi_n|^2$$

$$= k\sum_{n=0}^{\infty}(n+1)(\phi_{n+1}\phi_n^* + \phi_n\phi_{n+1}^*). \tag{113}$$

Owing to (112): $\gamma_n \equiv 1-g_n > 0$, therefore k is the ratio of two real forms one of which is essentially positive and must be real, as stated in the text.

Needless to say, this proof assumes that the sums in (113) are convergent; according to Eq. (17) this will always be the case unless $|\epsilon|=1$, i.e., k real and $>+1$ or <-1.

It may be pointed out, however, that the latter exceptional values of k may also be regarded as eigenvalues, and more precisely as forming the continuous spectrum of eigenvalues of Eq. (41). Without going into details, we may point out that the question is entirely analogous to that about the continuous eigenvalues of a differential equation such as, for instance, Eq. (47). As is well known all positive values of the "energy" parameter $-8k_1/M$ are regarded as eigenvalues, although the corresponding eigensolutions do not satisfy the ordinary condition of quadratic integrability, but only a weaker condition. Entirely similar considerations apply here; and, needless to say, in the limit in which our system may be approximated by Eq. (47) the continuous eigenvalues of the latter equation, i.e., those with $k_1<0$, go over, according to Eq. (48b), into the continuum of real values of k with $k>+1$.

APPENDIX B

Roots of $\gamma_1=0$, $\gamma_2=0$, *etc.* It will suffice to prove that $|g_n|<1$ for $n=1, 2, \cdots$ when $\Re(\eta) \geq -\frac{1}{2}$. From Eq. (111) we have, remembering that $G \leq 1$,

$$|g| \leq (\alpha/\pi) dG/d\mu.$$

Therefore, Eq. (4) yields

$$|g_n(\eta)| < 2\alpha \int_{-1}^{+1} |P_n(\mu)|\,(dG/d\mu)d\mu. \tag{114}$$

For $n=1$ the integral is quite simple; one finds

$$|g_1| < (M+1)/2M \leq 1 \tag{115}$$

as we want. For $n>1$ we consider $M=1$ first. It is easily found that the roots of $\gamma_2=0$ are $-1\pm i2^{-\frac{1}{2}}$, those of $\gamma_3=0$ are $-(3/2)\pm i(3/2)^{\frac{1}{2}}$, etc., i.e., all these roots have $\Re(\eta)<-\frac{1}{2}$.

If $M>1$ we apply Schwartz's inequality to Eq. (114) and find

$$|g_n|^2 < (2\alpha)^2 \int P_n^2 d\mu \int (dG/d\mu)^2 d\mu.$$

Now

$$\int (dG/d\mu)^2 d\mu = \int (dG/d\mu) dG < (M^2-1)^{-\frac{1}{2}} \int G dG$$

$$= (2\alpha)^{-1}(M^2-1)^{-\frac{1}{2}}$$

by a simple majoration. Finally

$$|g_n|^2 < 2\alpha(M^2-1)^{-\frac{1}{2}} 2/(2n+1) \tag{116}$$

which is <1 for $M=2, 3, \cdots$, $n=2, 3, \cdots$.

Energy Levels in Sulfur Nuclei*

PERRY W. DAVISON**
*Sloane Physics Laboratory, Yale University,*** *New Haven, Connecticut*
(Received November 22, 1948)

A study has been made of the proton groups from the reaction of 3.22-Mev deuterons with sulfur in the form, primarily, of H_2S gas. The following Q values have been assigned to the reaction $S^{32}(dp)S^{33}$: 6.48, 5.69, 4.58, 4.31, 3.63, 3.33, 2.60, 2.33, 2.06, 1.78, 1.37, 0.85, and 0.18 Mev, corresponding to the ground state and twelve excited states of S^{33}. Four of these groups have been investigated for proton gamma-ray coincidences to confirm this assignment. The yield as a function of deuteron energy has been observed for the six highest energy groups and indication of the presence of some broad resonances found. A qualitative measurement of the variation with angle of relative yields of the groups has indicated a proton intensity distribution that is symmetric for some groups and asymmetric for others. The cross section for the reaction for 90° observation has been found to be 1.2 barns. The mass difference $S^{33}-S^{32}$ has been calculated to be 0.99963 mass unit.

Two low intensity, high energy groups have been assigned to the reaction $S^{33}(dp)S^{34}$ with Q values of 8.67 and 7.85 Mev. This, together with the above observation, leads to a value of 1.99691 for the mass difference $S^{34}-S^{32}$.

INTRODUCTION

THE existence of nuclear energy levels has been known for approximately twenty years during which period a considerable amount of information on them has been compiled.[1-3] The accumulation of evidence has been going forward in several laboratories, and in recent years the use of improved counting and bombardment techniques has enabled the extension of accurately known energy levels and mass values as far as Ne^{22}. Only a moderate amount of information is available beyond this element.

The element selected for the present investigation was sulfur which normally consists of four isotopes: S^{32}, 95.1 percent; S^{33}, 0.74 percent; S^{34}, 4.2 percent; and S^{36}, 0.016 percent. Of the several methods available for studying nuclear energy levels, the one chosen here involves the observation of proton groups from transmutations induced by deuteron bombardment. A preliminary study of this element was reported by Smith and Pollard,[4] who found six groups with an average spacing of 0.9 Mev.

Thin targets of solid sulfur are difficult to use inasmuch as this substance readily sublimes. However, gaseous H_2S is available in 99.9 percent pure form, and it was decided to use this as the target material.

EXPERIMENTAL APPARATUS

The bombardment chamber used in most of this work was one especially designed for gaseous targets. Aside from the fact that certain elements, e.g., neon and argon, can be obtained only in gaseous form, this type of target has distinct advantages to recommend it; uniform targets of any desired degree of thinness may be prepared and duplicated with ease and accuracy. This is of particular importance if the substance under study dissociates under bombardment, as does H_2S.

This bombardment chamber, illustrated in Fig. 1, consists of two sections: a chamber to

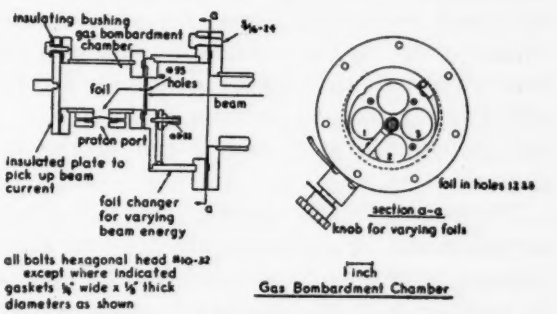

FIG. 1. A drawing showing the construction of a chamber for bombardment of gaseous targets with deuterons or alpha-particles from the Yale University cyclotron. This chamber includes a foil changer in the path of the beam for altering the bombarding beam energy.

* Part of a dissertation presented to the faculty of the Graduate School of Yale University in partial fulfillment of the requirements for the degree of doctor of philosophy.
** Now at the RCA laboratories, Princeton, New Jersey.
*** Assisted by the Office of Naval Research under Contract N6ori-44.
[1] M. S. Livingston and H. A. Bethe, Rev. Mod. Phys. 9, 245 (1937).
[2] W. F. Hornyak and T. Lauritsen, Rev. Mod. Phys. 20, 191 (1948).
[3] Ernest Pollard, Nucleonics 2, No. 4, 1 (1948).
[4] E. Smith and E. Pollard, Phys. Rev. 59, 942A (1941).

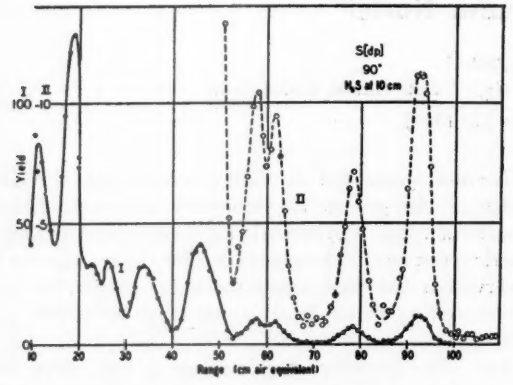

FIG. 2. The proton group spectrum for 90° observation of the reaction $S(dp)$. An H_2S target at a pressure of 10 cm Hg was used. All the groups shown have been assigned to the reaction $S^{32}(dp)S^{33}$.

contain the gas and a foil changer to alter the deuteron beam energy. The gas chamber is isolated from the cyclotron proper by means of an aluminum foil. In order to minimize the reduction in beam energy, the foil used is quite thin, approximately 2 cm of air equivalence, and cannot withstand the force due to the difference in pressure between the chamber and the cyclotron. For this reason the foil is supported on the vacuum side by a grid formed by drilling No. 55 holes in a brass plate. The protons produced in the nuclear reaction under study are observed through a "proton port" sealed by an aluminum foil. For most purposes a foil of sufficient thickness, 3 cm air equivalence or greater, may be used, and hence it need not be supported. However, for the use of thinner foils a holder has been constructed with grids on both sides of the foil. The arrangement of the foil changer is clear from the figure. The foil in the beam, and hence the beam energy reduction, may be selected, without breaking the vacuum, by means of the knob on a shaft through a Wilson seal. The foil selected is locked in position by means of a spring-operated catch on the rim of the foil changer wheel.

The bombardment chamber used for 0° observations and for proton gamma-ray coincidence measurements was constructed by Dr. Benson. It, together with the associated equipment and techniques, have been described by him elsewhere.[5] The solid target required by this bombardment chamber was prepared in the following manner. A thin layer of sulfur was deposited by evaporation on a clean gold foil. On top of this a thin layer of gold was deposited in a similar manner. The purpose of this gold coating was to inhibit the sublimation of the sulfur target. It was found that an uncoated sulfur target of 1 mg/cm² completely disappeared when in a vacuum for a period of several hours. A rough calculation using the vapor pressure of sulfur showed that this is as expected. Therefore, it was impossible to determine accurately the thickness of either the sulfur target or the gold coating, inasmuch as sulfur was lost in the process of applying the gold.

The absorption method was used to determine the proton energies. In this conjunction a mechanical foil changer was used. This instrument could be operated by remote control from the cyclotron control room and the absorption in the path of the protons could be varied in 1-cm steps to a total of 164 cm. When it was desired

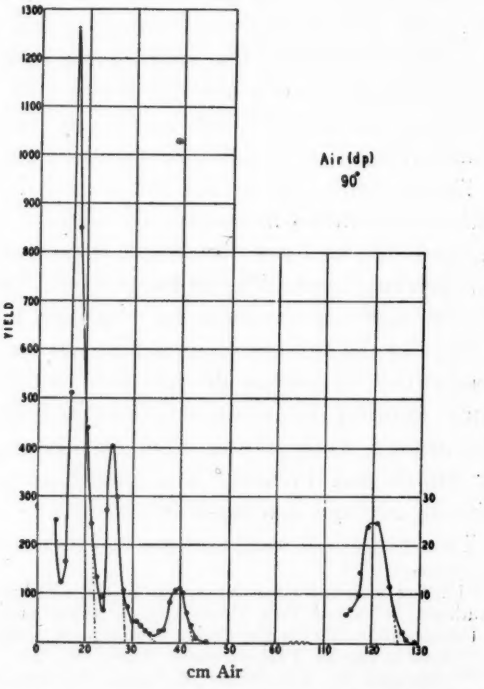

FIG. 3. The proton group spectrum for 90° observation of the reaction of deuterons with air at a pressure of 10 cm Hg. This information was obtained because of the possibility of air contamination in H_2S. The two longest range groups are due to nitrogen. The 25-cm group is due to oxygen. The 20-cm group is a composite of nitrogen and oxygen groups.

[5] B. B. Benson, Rev. Sci. Inst. **17**, 533 (1946) and Phys. Rev. **73**, 7 (1948).

to obtain increments in range of less than 1 cm, a gas absorption cell was used.

Proportional counters were used for proton detection. These were constructed under the direction of Dr. Martin.[6] The short recovery time of this type of counter allows it to be used at high counting rates. When the proper preamplifier is used, the counter pulse shape is quite good—0.1 μsec. rise time and 1.0 μsec. width, and hence short resolving-time (2×10^{-7} sec.) coincidence measurements may be made. Furthermore, the pulse amplitudes are proportional to the initial ionization produced by the particle passing through the counter. Thus, by setting the level in the counting circuits such that only pulses with an amplitude greater than a certain fixed value are recorded, one may make use of the peak in the Bragg ionization curve to restrict observations to only a small interval of range. This process is known as "peaking."

The associated electronic circuits consisted of capacity-neutralized preamplifiers, wide band (4 mc/sec.), video amplifiers, and a variable resolving time coincidence circuit. These were designed by Professor H. A. Schultz and are described elsewhere.[5-7] In addition, a modified Higinbotham scale-of-64 circuit was used when the counting rate required it.

EXPERIMENTAL RESULTS

The proton group structure as observed at 90°±5° is shown in Fig. 2. In this figure the yield, counts per minute per unit beam current, is plotted as a function of the absorption, in cm air equivalence, in the path of the protons. There are ten groups of protons which are clearly resolved. The two groups in the neighborhood of 35 and 50 cm have half-widths larger than those of longer range. This would lead one to expect that they are multiple.

IMPURITIES

As mentioned above, the H_2S used was 99.9 percent pure, the 0.1 percent impurity being due to hydrogen, water, and traces of BaCl and NaCl.[8] The hydrogen and barium would not be expected to cause complications. The reactions with Na and Cl give groups lying within the sulfur spectrum.[9,10] On the other hand, their concentrations are at most a fraction of 0.1 percent and certainly would not be responsible for groups of the intensities found. The oxygen in water was considered along with that in air, which had to be taken into account since the manometer system used to introduce the H_2S into the bombardment chamber could not be completely freed of leaks and occluded air. For this reason information on the proton groups due to air was obtained. The results are shown in Fig. 3. It will be noted that there are groups in the neighborhood of 20, 25, 40, and 120 cm. The two groups at 20 and 25 cm coincide almost exactly with groups in the sulfur spectrum. These two groups would be expected to have different excitation functions, i.e., variations of yield with beam energy, depending on whether they are due to sulfur or air. This portion of the spectrum of the two substances is shown in Fig. 4 for two different beam energies. It is clear that the yield of the longer range sulfur group increases relative to the shorter range one for a decrease in beam energy, while for air just the reverse occurs. Furthermore, it was observed that in order to account for the intensities of the H_2S groups air would have to be present to the extent of 50 percent, which was certainly not

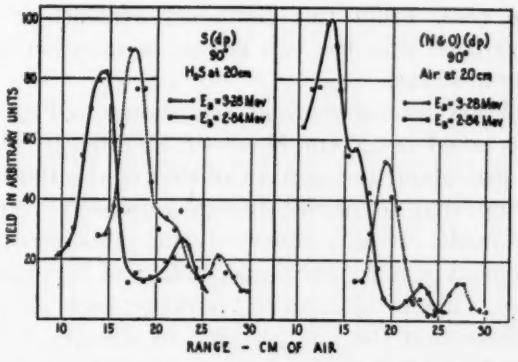

FIG. 4. The 20- and 25-cm groups from the bombardment of H_2S and air targets with deuterons of two different energies. The variation of relative intensity of the two groups with bombarding energy is not the same for the two targets. For this reason, it is concluded that the two groups from the H_2S target are not due to the presence of air.

[6] A. B. Martin, Phys. Rev. **72**, 378 (1947).
[7] H. A. Schultz and R. Beringer, Rev. Sci. Inst. **19**, 424 (1948).
[8] Matheson Company, Inc., East Rutherford, New Jersey, private communication.
[9] E. B. M. Murrell and C. L. Smith, Proc. Roy. Soc. **173**, 410 (1939).
[10] E. F. Shrader and E. Pollard, Phys. Rev. **59**, 277 (1941).

the case. From this combined evidence it is concluded that the two groups in question are due to sulfur.

A low intensity group, not shown in Fig. 2, was noted at 120 cm. However, its intensity was so low, about two percent of that of the 100-cm group, that no quantitative measurements could be made. It was observed that this group's intensity was roughly independent of H_2S pressure. This, in addition to the range, leads one to believe that the group is due to nitrogen from air. Even though this be the case, no complications would be expected from the 40-cm nitrogen group inasmuch as the H_2S groups in this region are considerably more intense than that group would be.

RESOLUTION OF MULTIPLETS

As mentioned above, the half-widths of two of the groups indicate that they may be unresolved multiplets. There are several factors that enter into the resolving power of this method; beam homogeneity, target thickness, range and angle straggling, and degree of peaking. An attempt was made to improve the largest factor, beam homogeneity, by using a system of three slits in conjunction with the field of the beam analyzer magnet. A noticeable improvement, reduction of beam half-width from 0.18 to 0.08 Mev, was obtained but with such a loss in beam intensity that satisfactory data could not be taken. The target thickness for H_2S at 10 cm pressure was 3 mm or 0.05 Mev. Range straggling is inherent in the absorption method of measuring energy and hence would not be circumvented. It amounts to 1.9 percent of the range or about 0.06 Mev at 50 cm. The angle straggling can be lessened by improving the geometry of the detection. The effect of "peaking" can be elimi-

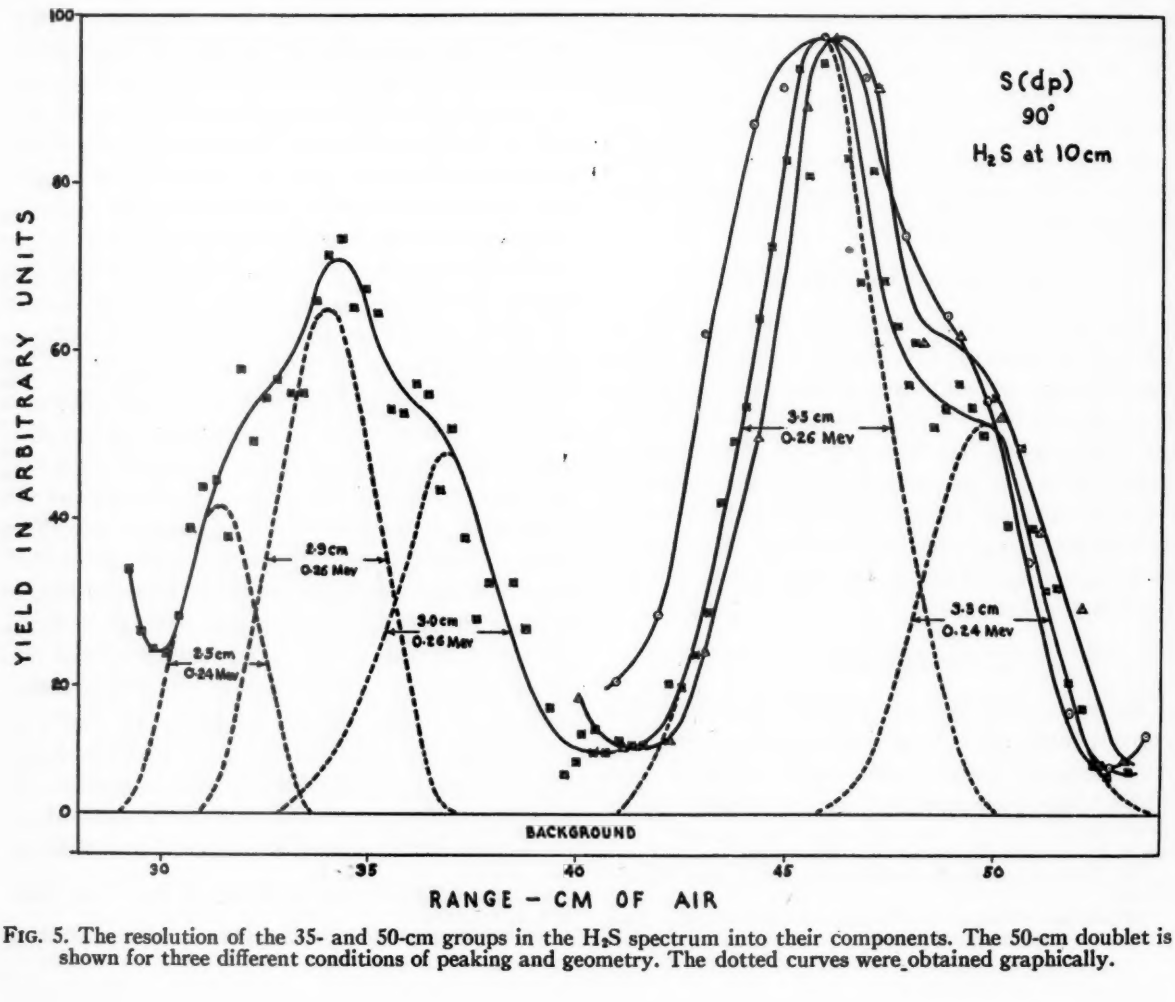

FIG. 5. The resolution of the 35- and 50-cm groups in the H_2S spectrum into their components. The 50-cm doublet is shown for three different conditions of peaking and geometry. The dotted curves were obtained graphically.

nated by setting the level at such a value that further increase causes no decrease in half-width of the group. Figure 5 shows the 50-cm multiplet for three conditions of peaking and geometry. The scatter of the observed points is explicable in terms of statistical fluctuations. The dashed curve shows the resolution into two groups. This was done in the following manner; the long-range edge of the group was reflected graphically about a vertical line, so chosen as to give the expected half-width for the resulting curve. The curve so obtained was subtracted from the observed curve to give the long-range side of the shorter range group. It will be noticed that the resulting half-widths are almost identical. Observations under the same conditions as above failed to give any clear-cut resolution of the 35-cm group into its components. There was some indication for three groups, and a graphical analysis such as just described was made and is also shown in Fig. 5. However, the identification of these three groups is not considered to be as positive as that of the two 50-cm groups.

ASSIGNMENT TO ISOTOPES

In order to check the possibility that the abrupt changes in yield at the 50-cm group (see Fig. 2) could be explained on the basis of the isotope configuration, a proton gamma-ray coincidence study was made. This technique allows the location of groups corresponding to ground states, inasmuch as no gamma-rays should be associated with such groups. The results obtained are given in Table I and in Fig. 6. In the latter is shown the group structure as observed at 0° and with large solid angle proton detection. The number of coincidences per 10^4 protons is given at the peak of the group concerned. The expected number of random coincidences, as determined from the relation $2\tau N_p N_\gamma = N_\tau$, has been subtracted from the number of observed coincidences. This method of determining the number of random coincidences was not precise, inasmuch as neither the resolving time τ nor the number of gamma-rays N_γ was very well known. τ was determined by placing a beta-ray source between two counters and observing the number of coincidences detected. The relation given above was then used and the value of τ obtained was 2×10^{-7} for the setting of the resolving time dial used in the above. N_γ was determined by means of a counting rate meter calibrated in the region used with a scaling circuit. These two factors undoubtedly account for the fact that there are residual coincidences associated with the longest range group. However, the object of prime interest was the first high intensity group and the results obtained showed that at least the prominent member of this group does not correspond to a ground state. Because of the large solid angle required, it was impossible to resolve either this group or the next longer range group into its components, and hence this method of attack was abandoned. Before leaving this subject, it might be remarked that the number of gamma-rays associated with the individual groups seems to be roughly proportional to the yield of the group. This would indicate that gamma-ray transitions in the residual nucleus are more frequently to the ground state than to intermediate states. However, it is difficult to conclude anything quantitative from these observations for the following reasons: the efficiency of the gamma-ray counter is energy dependent, the gamma-ray intensity is not likely to be spherically symmetric, and, furthermore, the

TABLE I. $S(dp)$, 0°, $P-\gamma$-coincidences.

Q* Mev	N_p Total	$N\gamma$ per sec.	T per min.	N_τ Total	N_τ per 10^4 protons	N_τ per 10^4 protons	N_τ per 10^4 protons corrected
6.48	40,000	384	83	9	2.25±0.9	1.54	0.71
	80,000	435	153.5	23	2.88±0.6	1.74	1.14
5.69	80,000	410	84.5	51	6.38±0.9	1.64	4.74
3.33	80,000	384	25.5	77	9.63±1.1	1.54	8.09
2.60	80,000	349	51.5	71	8.88±1.1	1.39	7.49

*From analysis of 90° data.

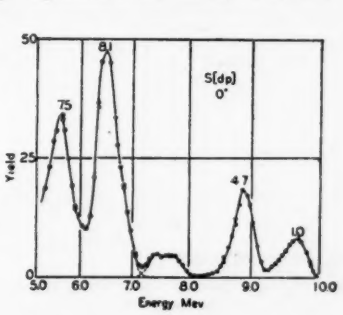

FIG. 6. The $S(dp)$ spectrum for 0° observation. The numbers at the peaks of the various proton groups give the number of proton γ-ray coincidences observed per 10^4 protons counted from that group.

TABLE II. $S^{32}(dp)S^{33}$.

Q Mev	Level Mev	Relative intensity	Level spacing Mev
6.48	0	1	
5.69	0.79	0.5	0.79
4.58	1.90	1	1.11
4.31	2.17	1.5	0.27
3.63	2.85	5	0.68
3.33	3.15	8	0.30
2.60	3.88	4	0.73
2.33	4.15	6	0.27
2.06	4.42	4	0.27
1.78	4.70	4	0.28
1.37	5.11	5	0.41
0.85	5.63	15	0.52
0.18	6.30	8	0.67

two shortest range groups studied are unresolved multiplets.

In the process of the investigation just described, it was noted that there was a small yield of protons even beyond the longest range group shown in Fig. 6. The results of a more detailed study of this region of the spectrum are given in Fig. 7. The left curve was taken with a thick solid target and shows the presence of a group ending at 148 cm. Observations were made on out to an absorption of 195 cm with no indication of further groups. The right curve given in Fig. 7 was obtained with a thin target, less than 1 mg/cm², and with moderately good geometry and peaking. There is definite indication of group structure. However, the analysis into two groups as shown cannot be considered as very reliable, inasmuch as the background count is of the same order of magnitude as that due to the groups. The longest range group has a range in the neighborhood of that that would

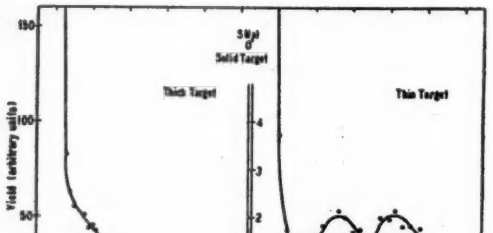

FIG. 7. Long-range, low intensity proton groups observed at 0° with thick (left curve) and thin (right curve) solid sulfur targets. The two groups observed have been assigned to the reaction $S^{32}(dp)S^{33}$.

be expected for the ground state group of nitrogen. Yet it seems unlikely that there could have been enough occluded nitrogen to account for even the low yield observed. On the basis of yield, about one percent of the longest range group in Fig. 6, and the Q value expected from existing mass values, it has been concluded that these two groups are due to the reaction $S^{33}(dp)S^{34}$.

The mass values available for S^{34} and S^{35} indicate that the ground state group from the reaction $S^{34}(dp)S^{35}$ would have a range of 67 cm for 90° observation. This is almost precisely the observed range of the long-range member of the first doublet. For this reason one is tempted to assume that the multiplet structure in the sulfur spectrum is due to the overlapping of the S^{33} and S^{35} spectra. It is regrettable that proton gamma-ray coincidence measurements could not be made on this doublet. However, the intensities of the members of each multiplet are very nearly the same, whereas the concentration of S^{32} is 23 times that of S^{34} which would require that the cross section for the $S^{34}(dp)S^{35}$ reaction be about 20 times that of the $S^{32}(dp)S^{33}$ reaction. While this is not out of the realm of possibility, it does seem unlikely. Therefore, on the basis of the existing evidence it appears that one must conclude that all except the two long-range low intensity groups (Fig. 7) are due to the reaction $S^{32}(dp)S^{33}$. This matter will have to await definite settlement until separated isotopes are available.

Q VALUES

The Q, energy change, values of the reactions may be calculated from the Q equation:

$$Q=[(M_n+M_p)/M_n]E_p-[(M_n-M_B)/M_n]E_B - 2[(M_pM_BE_pE_B)^{\frac{1}{2}}/M_n]\cos\theta,$$

obtained by applying conservation of energy and momentum to the reaction. The masses M_n, M_p, and M_B of the nucleus formed, the proton and the deuteron and the angle of observation, θ, relative to the direction of the beam, are all known. It remains to determine the beam energy, E_B, and the proton energies, E_p. The mean beam energy was found by Martin[5] to be 3.68 ± 0.05 Mev with a half-width of 0.18 ± 0.05 Mev. Recent observations by Pollard, Sailor,

and Wyly agree with these values. The value of the beam energy that must be used for the observations with gas targets must be reduced (average value used was 3.22 Mev) due to the presence of the aluminum foil and 4.22 cm of gas in the path of the beam. The latter correction involves the stopping power of H_2S, which was obtained in the following manner. It was observed that after a long run the position and amplitude of the 100-cm group were changed relative to their values at the start. The group moved out in range and down in amplitude. Both of these effects are readily explained in terms of loss of sulfur from the target due to dissociation of the H_2S by the deuteron beam. This loss was confirmed by the appearance of solid sulfur in the bottom of the bombardment chamber. The increase in range observed is due to two processes: increase in beam energy and decrease of absorption of the three cm of gas in the proton path, both of which are caused by the decreased stopping power of the gas. The effective stopping power, S, at any time can be expressed by the relation

$$(\text{fraction of } H_2S)\times S_{H_2S} + (\text{fraction of } H_2)\times S_{H_2} = S.$$

The fraction of H_2S at the end of the run can be obtained from the yield relative to that at the start of the run and the stopping power of H_2 is known to be 0.22.[11] A plot of change in range *vs.* stopping power of H_2S was calculated for an observed change in sulfur content of 75 percent. From the observed change in range, 3.5 cm for gas at a pressure of 20 cm, it was concluded that the stopping power of H_2S is 1.3 relative to air. Strictly speaking, this is a composite stopping power inasmuch as the actual stopping power is a function of the velocity of the particle and thus is different for the 10-cm deuterons and 100-cm protons. This value was used for all proton groups. However, the error thus introduced is quite small, being only 0.02 Mev for the shortest range group for a change in stopping power of 30 percent.

The values of the mean proton energies corresponding to the various groups were calculated according to the method outlined by Livingston and Bethe[1] in which corrections are made for the variation of aluminum stopping power with range, and for range and angle straggling. Refinements of this method are being worked out by Humphreys and Motz[12] in order that corrections for beam inhomogeneity and peaking level may be made. The Q values obtained are given in Table II, together with the proposed energy level scheme, the relative intensities of the levels, and the separation of the levels. In determining the relative intensities, account had to be taken of the loss of sulfur during the period of observation. Figure 8 shows the relation obtained for H_2S remaining *vs.* amount of bombardment in microampere minutes. This curve was obtained by observing the decrease in amplitude of the 100-cm proton group after a known amount of bombardment. Part of the scatter of the points is due to statistical fluctuations, which are indicated as errors. The effect of changes in counting level could not be assessed, but every attempt was made to minimize it. These data also allow

TABLE III. $S^{32}(dp)S^{33}$.

Q Mev	Level Mev	Relative intensity	Level spacing
8.67	0	1	0.82
7.85	0.82	1	

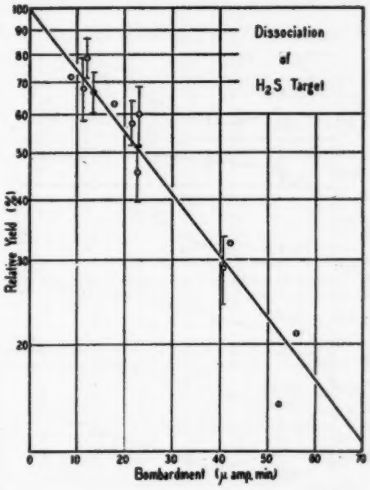

FIG. 8. A curve showing the rate of dissociation of H_2S by 3.2-Mev deuterons. This curve was used to calculate a cross section for dissociation of H_2S and to correct proton group intensities.

[11] See reference 1, p. 272.

[12] R. F. Humphreys and H. T. Motz, Phys. Rev. 74, 1232(A) (1948).

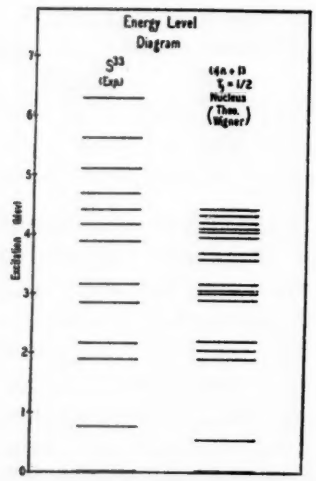

FIG. 9. Energy level diagrams comparing the experimental results given in Table II with the theoretical results obtained by Wigner. The energy scale of the theoretical diagram has been adjusted so that the ground states and second excited states agree in the two cases.

a calculation of the cross section for dissociation of H_2S by 3.2-Mev deuterons. The value obtained is

$$\sigma_{\text{diss}} = 4.8 \times 10^{-16} \text{ cm}^2.$$

It is difficult to assign an error to this figure because, in addition to the errors in the observations, there are errors in the cross-sectional area and uniformity of the beam.

The Q values for the $S^{33}(dp)S^{34}$ reaction were calculated indirectly, inasmuch as the target thickness was not precisely known. It was assumed that the longest-range high intensity group observed at 0° has a Q of 6.48 Mev. The difference in Q value between this group and the low intensity group in question was calculated using a modification of the Q equation. Then by adding this ΔQ to 6.48 Mev the values given in Table III were obtained. The remarks made above concerning the uncertainty about the excited state must be born in mind in considering this table.

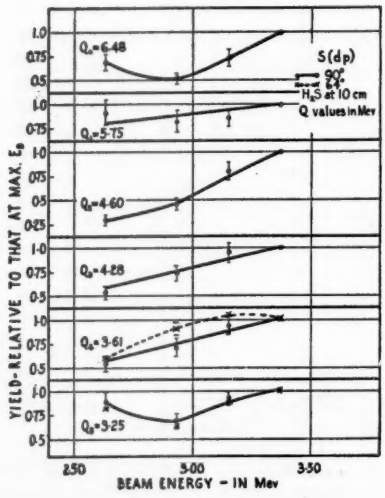

FIG. 10. The excitation functions for the ground state and first five excited states of the reaction $S^{32}(dp)S^{33}$ for 90° observation and the fourth and fifth excited states for 64° observation. The presence of broad resonances is indicated in several instances.

An analysis of the various sources of errors involved in the experimental method together with the repeatability of the data has led to an assignment of a probable error of ± 0.11 Mev to the Q values and of ± 0.05 Mev to the level spacing for the reaction $S^{32}(dp)S^{33}$. The probable error assigned to the Q values for the reaction $S^{33}(dp)S^{34}$ is ± 0.25 Mev.

The energy level scheme based on Table II is given diagrammatically in Fig. 9. Also included in that figure is an energy level diagram obtained from theoretical considerations by Wigner[13] for $4n+1$ nuclei with one more neutron than proton, to which class S^{33} belongs. In the latter diagram the energy scale is not specified and in this figure has been expanded (linearly) to fit the second excited state. Only qualitative comparison can be made with the experimental results, yet there is a striking similarity between the two.

REACTION CROSS SECTION

In order to calculate the cross section of the $S^{32}(dp)S^{33}$ reaction, an integral numbers *vs.* range curve was taken by setting the counting level as low as possible. In this manner was determined the total number of particles corresponding to the end group that were emitted within the solid angle subtended by the counter. Knowing the beam intensity, time of observation, and number of sulfur nuclei in the target volume, one may calculate the cross section for the reaction that leaves the nucleus in the ground state. This was found to be 1.9×10^{-26} cm^2 $= 1.9 \times 10^{-2}$ barn. Using the information above on the relative intensities of the various groups, one may calculate the cross sections for the total reaction. It

[13] E. Wigner, Phys. Rev. 51, 106 (1937).

was noted that for the three longest range groups there is substantial agreement between relative yields as determined from the integral curve and from the peaked curve. Hence, it is perfectly satisfactory—in fact, preferable—to obtain this information from the peaked data. The cross section obtained is

$$(\sigma S^{32}(dp))90° = 1.2 \times 10^{-24} \text{ cm}^2 = 1.2 \text{ barns},$$

which applies to 90° observation only inasmuch as the angular distribution of proton intensities is not spherically symmetric. The error in this figure is probably at least 50 percent and cannot be definitely assigned because many of the errors involved cannot be accurately estimated with the present experimental arrangement.

MASS VALUES

From the ground state Q values obtained above and the mass spectrographically determined masses of H^1 and H^2 (taken from Segrè's table) the following mass differences may be calculated.

$$S^{33} - S^{32} = 0.99963 \pm 0.00012,$$
$$S^{34} - S^{32} = 1.99691 \pm 0.00037.$$

Using the mass spectrographically determined value[14] of the mass of S^{32}, the masses of S^{33} and S^{34} may be obtained. These, together with Okuda's and Ogota's value,[14] are given in Table IV.

From the above mass differences one may calculate the mass difference ratio:

$$(S^{33} - S^{32})/(S^{34} - S^{32}) = 0.50059 \pm 0.00015.$$

TABLE IV. Mass values.

Nucleus	From $S(dp)$	From mass spectrograph[a]
S^{32}	—	31.98089±0.00007
S^{33}	32.98052±0.00020	—
S^{34}	33.97780±0.00044	33.97711±0.00033

[a] See reference 14.

This is in very good agreement with the value of 0.50066±0.00015 obtained by Townes[15] from recent measurements on the microwave spectrum of the molecule OCS.

EXCITATION FUNCTIONS

Using the bombardment chamber foil changer described above, an investigation was made of the variation of the intensity of the six longest range groups of the reaction $S^{32}(dp)S^{33}$ as a function of beam energy. The results obtained are shown in Fig. 10. The beam energies and Q values indicated are extrapolated values. The loss of target due to dissociation has been corrected for by means of the curve in Fig. 8. The errors assigned are based on those expected from statistical fluctuations and do not include the effects of changes in counting level. The latter were minimized by taking the observations in as rapid sequence as possible. Where assigned errors will allow, straight lines have been drawn. The lack of a resonance in the compound nucleus within the range of energies covered would be indicated by a nearly linear excitation function. This appears to be the case for Q_3 and Q_4 and possibly for Q_1. The curves for Q_0 and Q_5 indicate the presence of a resonance slightly below 2.6

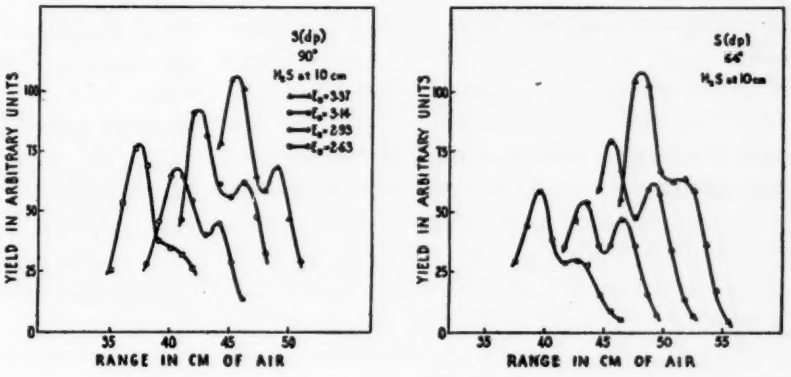

FIG. 11. The 50-cm doublet of the $S^{32}(dp)S^{33}$ reaction as observed for four beam energies and two angles of observation (90° and 64°). These results demonstrate the possibility of resolving a suspected multiplet by the proper choice of bombarding energy and angle of observation.

[14] T. Okuda and K. Ogota, Phys. Rev. 60, 690(L) (1941).
[15] C. H. Townes, private communication, June 22, 1948. C. H. Townes, A. N. Holden, and F. R. Merritt, Phys. Rev. 74, 1113 (1948).

TABLE V. Relative yields at various angles for $S^{32}(dp)S^{33}$.

Level	Yield 90° Relative to Q_6, 90°	64°	0° Relative to Q_6, 0°
Q_0	1	1.5	1
Q_1	0.5	1.2	3
Q_2	1	1	0.5
Q_3	1.5	1.5	0.5
Q_4	5	6	2
Q_5	8	9	6
Q_6	4	—	—
Q_7	6	6	4
Q_8	4	—	—
Q_9	4	5	5
Q_{10}	5	7	—
Q_{11}	15	18	15

Mev. That for Q_2 indicates the presence of a resonance above 3.4 Mev. The resonances for the various groups would not be expected to fall at the same place inasmuch as their location is dependent on the angular momentum quantum numbers of the particles involved. These resonances are expected to be broad inasmuch as the levels in the compound nucleus are believed quite closely spaced and the beam energy is not sharply defined.

Figure 10 also gives the results of a similar study for Q_4 and Q_5 at 64° observation. The curve for Q_5 is essentially identical with that obtained at 90°. However, for Q_4 the observations at 2.93 Mev differ by more than the assigned errors and the curve for 64° indicates a resonance in the neighborhood of 3.2 Mev. There is some indication of such a resonance in the 90° data but not to the same degree.

In the process of these investigations the curves shown in Fig. 11 were obtained for the 50-cm doublet. They show how the resolution of a suspected multiplet into its various components might be facilitated by the proper choice of beam energy and angle of observation. At 2.63 Mev and 90° the long-range member has been suppressed, where as at 2.93 and 64° the two components are almost equal in amplitude. This effect was also observed in conjunction with the 20-cm group in air (Fig. 4) which is composed of overlapping oxygen and nitrogen groups. This method requires, however, that the excitation functions for the components be markedly different which, in general, may not be the case.

ANGULAR VARIATIONS

As mentioned above, the intensity of a proton group is dependent on the angle of observation. This dependence is related to the angular momentum quantum numbers of the particles involved in the reaction. This effect has been studied in considerable detail for several reactions.[16] With the present equipment it was not possible to make a detailed study for this reaction. Nevertheless, observations were made at 90°, 64°, and 0°, and their results are shown in Table V. The 90° and 64° data were taken with the gas bombardment chamber, and hence it was possible to correlate the two by taking into consideration the geometrical differences involved. The 0° information was obtained with a solid target whose thickness could not be precisely determined. The results given in Table IV seem to indicate the following about the symmetry of the proton intensity patterns. Those resulting from Q_0 and Q_1 are definitely asymmetric; those from Q_2 and Q_3 are symmetric; those caused by the remaining groups are somewhat asymmetric.

ACKNOWLEDGMENTS

The author wishes to express his gratitude to Professor Ernest Pollard, who has given generously of his counsel and encouragement during the investigations described above, and to Professor R. F. Humphreys, who has been a source of many valuable discussions and suggestions.

[16] E.g., N. P. Heydenburg and D. R. Inglis, Phys. Rev. 73, 230 (1948).

On the Stability of the Isobaric Pair $In^{115}-Sn^{115}$

M. GUREVITCH*
University of California, Berkeley, California
(Received November 19, 1948)

A method employing a modified Schuler tube for the excitation of the spectral lines of milligram quantities of material is discussed. The spin of Sn^{115} is found to be one-half, and the stability of the pair $In^{115}-Sn^{115}$ to the nuclear transition $In^{115}-Sn^{115}$ is highly forbidden on the basis of a spin change of four.

INTRODUCTION[1]

AMONG the many stable isotopes there are but three known pairs of neighboring isobars: $_{48}Cd^{113}-{}_{49}In^{113}$, $_{49}In^{115}-{}_{50}Sn^{115}$, and $_{51}Sb^{123}-{}_{52}Te^{123}$. Neighboring isobars are isotopes having the same atomic mass number and differing in nuclear charge by one unit. Since all six members of these isobaric pairs occur naturally, their lifetimes must be at least of the same order as the age of the earth, about 10^9 years. The stability of these pairs against beta-decay is remarkable since we know from experience with beta-active isotopes that whenever beta-decay is energetically possible, the decay half-life of the nucleus is reasonably short, ranging up to about 10^3 years.

A possible explanation of this stability is that, although a beta-transition is energetically possible, it does not occur because the spin change from one nucleus to the other is highly "forbidden." The isobar of higher charge would decay by electron capture if it were the energetically unstable one. This decay would result in a slow disappearance of the isobar of higher charge and an increase in abundance of the isobar of lower charge. Since we do not observe this process, the best we can do is to assign a lower limit to the half-life of this isobar of about 10^9 years, the age of the earth.

Bethe and Bacher have calculated that when the isobar of lower charge is the energetically unstable member of the pair, the lifetime must be of the order of 10^{15} years if the beta-process is to be undetectable by present techniques.

From the known lifetimes of naturally occurring radioactive isotopes, a lifetime of 10^9 years seems more probable than a lifetime of 10^{15} years. Therefore, it would be more likely that, in the case of these stable neighboring isobars, it is the isobar of greater charge which is the energetically unstable one. Bethe and Bacher have calculated that if the isobar of higher charge is the unstable one and the energy of the emitted neutrino is less than 25,000 electron volts, or approximately one-twentieth of an electron mass, a change in the nuclear moment of two units would give a lifetime of 10^9 years or greater. If the change in nuclear moment is three units, the energy of the emitted neutrino could be as great as 500,000 volts, equivalent to approximately one electron mass, and the lifetime could still be 10^9 years or greater.

The purpose of the present investigation is to determine whether the nuclear spin change involved in the transition Sn^{115} to In^{115} would make this a highly "forbidden" transition.

I have been fortunate to obtain from the Manhattan District thirty-nine milligrams of tin enriched in the isotope Sn^{115}. Sn^{115} constitutes but 0.44 percent of naturally occurring tin. The major fraction of the tin sample was Sn^{116} with Sn^{115} making up most of the remainder. There were probably small percentages of the other tin isotopes also present.

DESCRIPTION OF APPARATUS

The spectrographic apparatus consisted of a one-meter, flint glass, three-prism spectrograph crossed with a Fabry-Perot interferometer. The etalon was placed between the collimator lens and the first prism. The two quartz plates of the etalon were separated by a spacer consisting of three, seventeen-millimeter, Invar pins set in equally spaced holes which were drilled in a brass ring. The plates rested on the pins, which protruded beyond the brass ring at both ends. A

* Now at University of Idaho, Moscow, Idaho.
[1] H. Bethe and R. F. Bacher, Rev. Mod. Phys. 8, 83 (1936).

silver coating was evaporated onto the plates to a reflecting power of about eighty-five percent.

The light source was a water or liquid-air cooled Schuler[2] tube through which an exciting gas was continuously circulated. The gas circulation was proposed by Schuler to decrease the rate of diffusion from the hollow cathode of the material under investigation. Obviously this precaution is important when working with milligram quantities of material. In the modification employed in this experiment the gas which leaves the Schuler tube is passed through a purifying system before it is returned.

Helium and argon were used as exciting gases. Helium was passed through the apparatus in the following order: Schuler tube; a liquid-air cooled, charcoal trap; a liquid-air trap; a single-stage mercury diffusion pump used as a circulating pump, another liquid-air trap; and, again, the Schuler tube. Argon was passed through in the following manner: Schuler tube; a calcium-coated bulb used as an argon purifier; the liquid-air trap; the circulating pump; the other liquid-air trap; and, again, the Schuler tube.

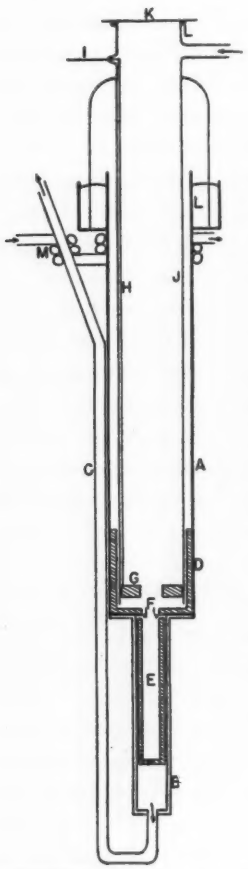

FIG. 1. The Schuler tube. *A*. Copper tube, $9\frac{1}{4}''$ long, $1\frac{3}{4}''$ diameter, $\frac{1}{16}''$ wall thickness. *B*. Copper end piece, $\frac{5}{8}''$ diameter of inside hole, $1''$ or $4''$ length, depending on Schuler tube used. *C*. Copper tube for transferring the gas from the Schuler tube to the purifier. *D*. Upper part of aluminum insert, $1\frac{3}{8}''$ inside diameter, $1\frac{3}{4}''$ height. *E*. Cathode hole of aluminum insert, $\frac{1}{8}''$ or $\frac{3}{8}''$ diameter, $\frac{1}{4}''$ to $3''$ length. *F*. Circulating holes, $\frac{1}{32}''$ diameter, closely spaced. *G*. Aluminum anode with hole $\frac{1}{4}''$ or $\frac{7}{16}''$ in diameter depending on cathode hole diameter used. *H*. Aluminum wire. *I*. Tungsten lead. *J*. Pyrex glass electrical insulator. *K*. Pyrex plate glass window. *L*. Wax seals. *M*. Water cooling tubes to prevent wax from melting when Schuler tube is run hot and freezing when it is immersed in liquid air.

The Schuler tube was constructed as shown in Fig. 1. The power supply was a 1000-volt, full-wave rectifier. The voltage drop across the tube was 200–450 volts; the current was 300–600 milliamperes.

The argon purifier consisted of a two-millimeter calcium tungsten gap in a Pyrex bulb. The purifier must be prepared in the following manner before it is ready for use. The bulb is first evacuated to a high vacuum. Then approximately two centimeters of mercury pressure of argon is introduced and the calcium arc started. The arc runs as a flame arc, depositing finely divided calcium metal over the entire inner surface of the bulb. The arc is initiated by a Tesla coil type discharge.

Now the purifier is ready for use. The finely divided calcium which has been deposited on the walls of the bulb will combine chemically with almost all gases except the noble ones and therefore keeps the argon free from contamination.

On the assumption that a glow discharge produced in the bulb increased the efficiency of the clean-up, a Tesla coil was sometimes connected to the tungsten electrode.

Although the calcium flame arc itself is a good method of purifying argon gas, it was not used in this case for two reasons: first, the gas pressures used (0.7–7 mm) were not sufficiently high to maintain a stable arc; second, there was a danger of carrying the calcium dust into other parts of the system along with the circulating gas.

EXPERIMENTAL PROCEDURE

In investigating hyperfine structure we are concerned with lines whose wave-length differences are very small. If the Doppler broadening is allowed to approach the magnitude of the separation of the lines, it is evident that the components will not be resolvable. Therefore, it is necessary to choose a source that will reduce the Doppler broadening to a minimum.

A source widely used for hyperfine structure analysis is the Schuler tube, a modification of the

[2] H. Schuler and H. Gollnow, Zeits. f. Physik **93**, 611 (1935).

Paschen hollow cathode discharge tube, which excites primarily the arc and first spark lines of the elements. The Schuler modification reduces the Doppler broadening by allowing the cathode to be cooled.

The Schuler tube operates in the following manner. The tube is filled with a noble gas at pressures varying from approximately two centimeters to less than one millimeter of mercury pressure. When the voltage is applied across the tube, the gas is excited and ionized. The major part of the discharge takes place in the cathode hole. The ionized gas atoms strike the walls of the cathode hole and sputter the material on the walls into the hole. Any material on the bottom of the cathode hole is similarly sputtered. Some of the gas atoms are in a metastable state and will undergo collisions of the second kind with atoms of the sputtered material. The atoms of the sputtered material excited by these collisions will emit light of the lower energy of the spectrum of the material when they return to the ground state.

Previous experience by the author with Pb^{208} and Fe^{57} (to be published later) has indicated that in order to obtain intense spectral lines of the element to be investigated, it is necessary that a large part of the surface of the cathode hole be covered by the element. The larger the area of the hole surface covered, the greater will be the number of atoms of the covering material sputtered into the hole and the greater the number excited.

With 50 milligrams of lead in the bottom of the cathode hole, lead lines were excited only after "conditioning" the tube by running the discharge for many hours. When the lead was plated on the walls of the cathode hole, the lines appeared immediately.

With milligram quantities of iron in the bottom of the cathode hole, iron lines could not be excited by the same "conditioning" procedure used with lead. However, when the iron was plated on the walls of the cathode hole, the iron lines appeared almost immediately.

This difference in the methods needed to excite the lead and iron lines seems to indicate that the lead eventually coated the walls of the cathode hole sufficiently sputtering from the bottom; while in the case of iron, the walls of the cathode hole remained relatively uncoated because of the slower sputtering rate of iron.[3]

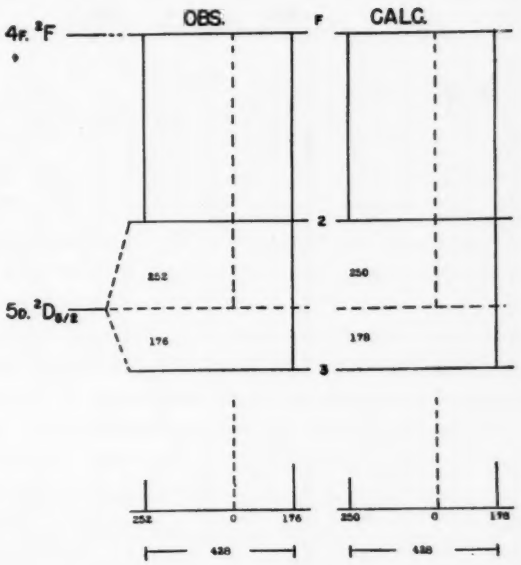

FIG. 2. Level scheme for the line Sn *II* λ5799.3 ($5d\,^2D_{5/2}-4f^2F_{7/2}$) showing the separation of the components of the odd isotope. The zero indicates the position of the even isotope component. The separations are expressed in units of 10^{-3} cm^{-1}.

Sn^{115} lines were excited very strongly from the 39 milligrams of tin placed in the bottom of a cathode hole $\frac{3}{8}''$ in diameter and 3″ long drilled in an aluminum block. Before argon or helium exciting gas was introduced the discharge was run with a charge of hydrogen for several 15-minute periods, with fresh hydrogen for each period. This procedure was adopted when the plating and conditioning methods used with lead and iron failed with tin. It was thought that the sputtering rate of tin might be improved and the binding between the sputtered tin and the aluminum walls enhanced if the surfaces were first reduced by bombardment with atomic hydrogen. After the hydrogen bombardment the exciting gas was introduced at approximately 0.7 mm of mercury pressure.

When the hydrogen bombardment was not used before the exciting gas discharge was started, no tin lines appeared and a globule of tin was found at the bottom of the cathode hole at the end of the run. When the bombardment with hydrogen was used, tin lines were obtained,

[3] J. Strong, *Procedures in Experimental Physics* (Prentice-Hall, Inc., New York, 1943), pp. 163–164.

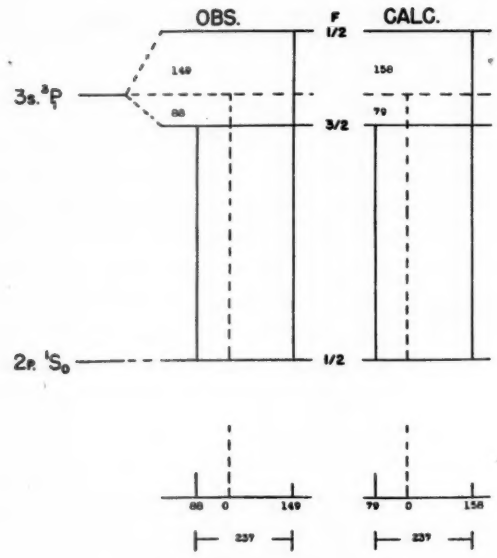

FIG. 3. Level scheme for the line Sn *I* λ5631.9 ($2p\ ^1S_0-3s\ ^3P_1$).

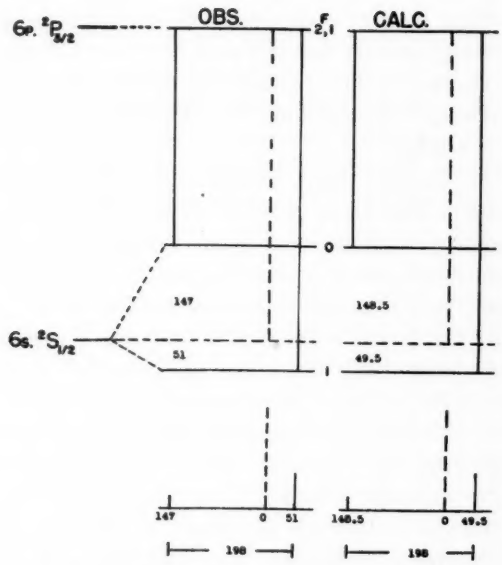

FIG. 4. Level scheme for the line Sn *II* λ6452.8 ($6S\ ^2S_{1/2}-6p\ ^2P_{3/2}$).

and there was no globule of tin found at the bottom of the hole and the walls appeared to be coated with tin.

When the discharge tube was first started, after having stood under a vacuum over-night, mercury and hydrogen lines were very strong, and tin lines were absent or very weak. In order to obtain any high intensity it was necessary to run the discharge for fifteen minutes, then pump out the exciting gas, and then repeat the process four or five times. By this time the mercury and hydrogen faded out, and the tin lines became bright.

The λλ6452.8, 5799.3, and 5631.9 lines were photographed in from one to five minutes on Super-pancropress plates. The λ6844.3 line was photographed with the same exposure on Eastman Infra-Red Plates, the best plate being the Eastman 103a-F Plate.

EXPERIMENTAL RESULTS

Sn^{115}

Three Sn *II* lines and one Sn *I* line were analyzed. The three Sn *II* lines were:[4,5]

$$\lambda 5799.3\ (5d\ ^2D_{5/2}-4f\ ^2F_{7/2}),$$
$$\lambda 6452.8\ (6s\ ^2S_{1/2}-6p\ ^2P_{3/2}),$$
$$\lambda 6844.3\ (6s\ ^2S_{1/2}-6p\ ^2P_{1/2}).$$

The Sn *I* line was

$$\lambda 5631.9\ (2p\ ^1S_0-3s\ ^3P_1).$$

None of the other lines lying within the visible spectrum and identified as belonging to tin showed any structure.

Sn *II* λ5799.3 ($5d\ ^2D_{5/2}-4f^2F_{7/2}$)

This line has three components. The very strong central component belongs to the even isotope Sn^{116}. It is approximately in the center of gravity of the two components belonging to Sn^{115}.

We know the upper term $4f\ ^2F$ is single because the line λ5589.4 ($5d\ ^2D_{3/2}-4f\ ^2F_{7/2}$) is single.[6] Therefore the structure in line λ5799.3 must be due to the lower term $5d\ ^2D_{5/2}$. For this term J is equal to 5/2. If J is smaller than I, this term would be capable of splitting into $2J+1$, or six sub-levels. Since the number of sub-levels is two, J must be greater than I, and the number of sub-levels equal to $2I+1$. Therefore I is $\frac{1}{2}$. Thus the assignment of a value of one-half to the nuclear spin of Sn^{115} is unambiguous.

The stronger Sn^{115} component of this line lies towards the violet. Since the quantum weight of a term is $2F+1$, the term value with the larger F value lies deeper. This fact indicates that the

[4] U. A. Sawyer and W. W. McCornich, Phys. Rev. **54**, 71 (1938).
[5] J. B. Green and R. A. Loring, Phys. Rev. **30**, 574 (1927).
[6] S. Tolansky, Proc. Roy. Soc. London **A144**, 574 (1934).

magnetic moment is negative. Figure 2 illustrates the level scheme for this line.

Sn *I* λ5631.9 ($2p\ ^1S_0 - 3s\ ^3P_1$)

This line also has three components. Here again the central component is due to the even isotope and lies between the two components due to the isotope Sn^{115}. The lower state $2p\ ^1S_0$ has a J value of zero. It therefore remains single no matter what the I value. Since the upper state $3s\ ^3P_1$ has a J value of unity, the value of I must be equal to one-half in order that there be only two components belonging to Sn^{115}.

Here also the larger F value lies deeper, and consequently the magnetic moment is negative. The level scheme is shown in Fig. 3.

The components in this line were not well resolved and therefore the exact values of the intervals cannot be determined by a micrometer measurement.

Together with the analysis of the preceding line λ5799.3, this analysis shows conclusively that the nuclear spin of Sn^{115} is one-half and that the magnetic moment is negative.

Sn *II* λ6452.8 ($6s\ ^2S_{1/2} - 6p\ ^2P_{3/2}$)

This line has three components. The strong central maximum belongs to the even isotope, and the two side components belong to the odd isotopes Sn^{115}. Since all $p\ ^2P_{3/2}$ terms previously investigated have shown very small structure, we may assume a similar situation in the case of the upper term. The $6s\ ^2S_{1/2}$ term has a J value of one-half. In such a case the greatest possible number of components is two, no matter what the I value. Consequently we can get no information about the nuclear spin by merely counting the components.

Careful analysis of the microphotometer trace of this line showed the intervals to be in general agreement with an I value of one-half.

The ratio of intensities of the two components of Sn^{115} is one to four and one-half. This ratio is not in as good an agreement with an I value of one-half as is the interval ratio, since such an I value should yield an intensity ratio of one to three. It does, however, correspond more closely to an I value of one-half than to any other value of I. Note that here too the terms are inverted. The level scheme is shown in Fig. 4.

Sn *II* λ6844.3 ($6s\ ^2S_{1/2} - 6p\ ^2P_{1/2}$)

This line has four components. The strong component belongs to the even isotope, and the three much weaker components belong to the odd isotope Sn^{115}. Those values which would make the ratio of the displacements from the center three to one were used as the separation of the sub-levels of the lower term. The level scheme is shown in Fig. 5.

Here also the intervals are not incompatible with an I value of one-half. Although the component that is observed to be displaced 51×10^{-3} cm^{-1} from the even isotope position should be 33×10^{-3} cm^{-1} away, it is too difficult to determine the position of this component, since it is so close to the intense even isotope component.

Thus we see that the assignment of a nuclear spin of one-half to Sn^{115} on the basis of the analyses of λ5799.3 and λ5631.9 is also given fairly good support by the analyses of λ6452.8 and λ6844.3.

To calculate the nuclear magnetic moment, the fine structure separation of the $6s\ ^2S_{1/2}$ term obtained from the analysis of the λ6452.8 line was used. From the Goudsmit[7] formula it was calculated that the nuclear magnetic moment is −0.86 nuclear magnetons.

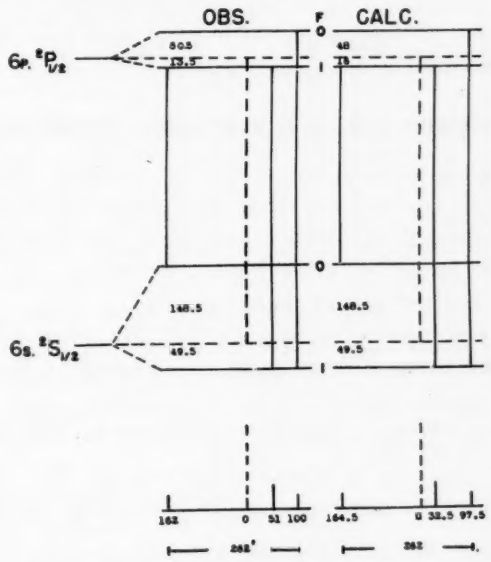

FIG. 5. Level scheme for the line Sn *II* λ6844.3 ($6s\ ^2S_{\frac{1}{2}} - 6p\ ^2P_{\frac{1}{2}}$).

[7] S. Goudsmit, Phys. Rev. **43**, 636 (1933).

TABLE I.

	Separations in units of 10^{-3} cm^{-1}*			Width of structure
5799.3				
Tolansky	152	0	−239	391
Gurevitch	176	0	252	428
5631.9				
Tolansky	158	0	82	240
Gurevitch	149	0	88	237
6844.3				
Tolansky	100 65	0	181	281
Gurevitch	100 51	0	162	262
6452.8				
Tolansky	53	0	154	207
Gurevitch	51	0	147	198

* Refers to distance from position of odd isotope component to position of even isotope component. The even isotope component is at zero.

	$g(I)$	
Tolansky	−1.78	−0.89 nuclear magnetons
Gurevitch	−1.72	−0.86 nuclear magnetons

Tolansky[6] carried out an analysis for these same four lines during an investigation of the nuclear spins of Sn^{117} and Sn^{119}. It is interesting to compare the structure which he found for these lines with that which I found in this investigation of Sn^{115} (Table I).

It may be that the lines investigated by Tolansky and myself give the same structure for all three isotopes: Sn^{115}, Sn^{117}, and Sn^{119}, and that the discrepancies noted are the result of difficulties in measuring such wide and relatively unresolved lines.

DISCUSSION OF EXPERIMENTAL RESULTS

Since we now know that the nuclear spin of Sn^{115} is one-half, and that the nuclear spin of In^{115} is nine-halves,[8] we can say that the transition from $Sn_{1/2}{}^{115}$ to $In_{9/2}{}^{115}$ is a "forbidden" one on the basis of a spin change of four.

It is interesting to note that the other stable neighboring isobaric pair whose spins we know, $Cd_{1/2}{}^{113}-In_{9/2}{}^{113}$, also has the large spin difference of four,[8,9] which makes it a "forbidden" transition. We know the spin[1,10–13] of but one of the members of the remaining stable neighboring isobaric pair $Sb_{7/2}{}^{123}-Te_{?}{}^{123}$.

There are two neighboring isobaric pairs whose spin transition is known,[14–17] which are radioactive and have very long lifetimes: $K_4{}^{40}$ to $Ca_0{}^{40}$ and $Rb_{3/2}{}^{87}$ to $Sr_{9/2}{}^{87}$. The fact that these have very long half-lives fits in well with the hypothesis that it is the large spin change that makes these transitions "forbidden."

There is another long-lived radioactive neighboring isobar whose spin difference[18,19] with its neighbor we do not know, $Os_{?}{}^{187}$ to $Re_{5/2}{}^{187}$.

All these stable and relatively stable neighboring isobars whose nuclear spins we know seem to indicate that the "forbidden" character of the transitions between neighbors is a result of their large spin differences. Finally, now that samples of elements enriched in almost any particular isotope can be obtained, it should soon be possible to complete this study on the stability of isobaric pairs.

ACKNOWLEDGMENTS

I am grateful to Dr. F. A. Jenkins for his aid and interest, and to Dr. H. E. White for suggesting the problem and for his continued encouragement and advice throughout the work.

[8] S. Millman, I. I. Rabi, and J. R. Zacharias, Phys. Rev. **53**, 384 (1938).

[9] H. Schuler and H. Bruck, Zeits. f. Physik **56**, 291 (1929).

[10] M. F. Crawford and S. Bateson, Can. J. Res. **10**, 693 (1934).

[11] J. S. Badami, Zeits. f. Physik, **79**, 206 (1932).

[12] S. Tolansky, Proc. Roy. Soc. London **A146**, 182 (1934).

[13] M. Heyden and H. Kopfermann, Zeits. f. Physik **108**, 232 (1938).

[14] J. R. Zacharias, Phys. Rev. **60**, 168 (1941).

[15] F. C. Thompson and S. Rowlands, Nature **152**, 103 (1943).

[16] H. Kopfermann, Zeits. f. Physik **83**, 417 (1933).

[17] M. Heyden and H. Kopfermann, Physik. Zeits. **38**, 960 (1937).

[18] W. F. Meggers, A. S. King, and R. F. Bacher, Phys. Rev. **38**, 1258 (1931).

[19] E. T. Lougher and S. Rowlands, Nature **153**, 374 (1944).

On the Absorption of Slow Neutrons by Rhodium

ROBERT R. MEIJER*
Cornell University, Ithaca, New York
(Received September 20, 1948)

The absorption of neutrons in rhodium as a function of their time of flight was studied with the Cornell slow neutron velocity spectrometer in the energy range of 0.0044 to 330 ev. A resonance was observed at an energy of 1.21±0.02 ev. No other resonances were observed. Values of the Breit-Wigner parameters, which best seem to fit the experimental results for a resonance energy of 1.21 ev, are 2750±200 barns for the cross section at resonance (σ_r) and 0.21±0.01 ev for the level width (Γ). The Breit-Wigner formula fits the experimental data in the low energy region. The coefficient of the $1/v$ term is 0.295±0.005 barn/μsec./m and the constant term (taken as the scattering cross section) is 6±2 barns. Values for the strength of the resonance ($\sigma_r\Gamma^2$) were computed from the minimum cross section on the low energy side of the resonance, from the $1/v$ slope, from an activity plot, and from the chosen Breit-Wigner parameters. The average of these values of $\sigma_r\Gamma^2$ is 117±8 barn-ev^2. Self-absorption measurements were made to check the results of the time-of-flight measurements. The resonance cross section obtained from the self-absorption measurements is 3120±50 barns, which is in closer agreement with the results of the spectrometer measurements than with those of previous investigators.

I. INTRODUCTION

THE absorption of slow neutrons by rhodium has been investigated by a number of workers. Experimental results were first obtained by various workers using indirect methods for determining neutron energies. These have been summarized by Bethe.[1] Values for the resonance cross section and the width of the resonance have been obtained from mutual and self-absorption measurements.[2–4] Baker and Bacher[5] measured the resonance energy by time-of-flight measurements. A recent investigation of slow neutron absorption in rhodium was undertaken with a crystal spectrometer by Sturm.[6]

This investigation of neutron absorption in rhodium with a slow neutron velocity spectrometer was conducted for two reasons. First, there were indications that rhodium has only one resonance in the energy range so far investigated and that the resonance level is wide so that the Doppler width is small compared to the resonance width. Hence the investigation of neutron absorption in rhodium should be extremely useful in determining the validity of the Breit-Wigner theory.[7] Second, the values of the resonance energy, the cross section at resonance, and the width of the resonance were in doubt since previous investigators were unable to obtain consistent results.

As a check on the results obtained from the experiments with the spectrometer, the cross section at resonance was also determined by self-absorption experiments similar to those of Hornbostel *et al.*[3]

II. APPARATUS AND EXPERIMENTAL PROCEDURE

In this investigation the transmission of neutrons by various rhodium absorbers was measured as a function of the time of flight of the neutrons. The neutron velocity spectrometer used in these time-of-flight measurements is similar to that used by McDaniel[8] and has been described in detail by Jones.[9] The timing apparatus records the number of neutrons arriving at a detector as a function of the time of flight of the neutrons from the source to the detector. In many respects, the procedure for measuring the transmission of neutrons by rhodium was similar to that described previously.[5, 8–10]

* Now at The George Washington University, Washington, D. C.
[1] H. A. Bethe, Rev. Mod. Phys. **9**, 113 (1937).
[2] Manley, Goldsmith, and Schwinger, Phys. Rev. **55**, 39 (1939); Manley, Hornbostel, and Goldsmith, Phys. Rev. **55**, 1116 (1939).
[3] Hornbostel, Goldsmith, and Manley, Phys. Rev. **58**, 18 (1940).
[4] Feeney, LaPointe, and Rasetti, Phys. Rev. **61**, 469 (1942).
[5] C. P. Baker and R. F. Bacher, Phys. Rev. **59**, 332 (1941).
[6] William J. Sturm, Phys. Rev. **71**, 757 (1947).
[7] G. Breit and E. Wigner, Phys. Rev. **49**, 519 (1936).
[8] Boyce D. McDaniel, Phys. Rev. **70**, 832 (1946).
[9] Wm. B. Jones, Jr., Phys. Rev. **72**, 362 (1947).
[10] Bacher, Baker, and McDaniel, Phys. Rev. **69**, 443 (1946).

The source-detector distance was three meters. A water moderator[8] served as the source of the slow neutrons. The detector was a BF_3 ionization chamber, whose active length was 10 cm. The repetition frequencies used were 200, 250, and 2500 c.p.s. The on-times used were 5, 10, 40, and 100 μsec.

The random background in this experiment was about three total counts per minute and amounted to about one-half percent of the recorded counts for most of the data; occasionally it was as high as two percent. Because of the collimator,[9] the fast neutron background was negligible except at high energies. For example, at energies of 30 ev the fast neutron background was only one percent of the total counting rate, whereas at energies of 100 ev it was about 10 percent.

The sum of the various time lags in the timing apparatus is obtained from the fast neutron distribution which we shall call the sensitivity function, *SF*. A typical *SF* for an on-time of 5 μsec. is shown in Fig. 1. The sensitivity function was obtained frequently, and the time delay was found to be 7.5 ± 0.2 μsec.

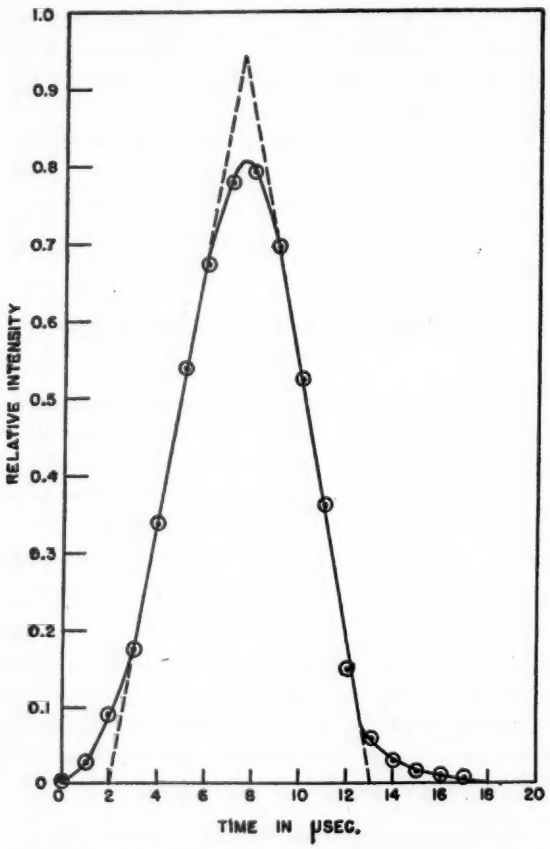

FIG. 1. Sensitivity function (*SF*) for 5-μsec. on-time. The solid curve is the measured fast neutron time distribution, or *SF*. The dashed curve shows the ideal shape of the *SF*.

As was mentioned in Section I, self-absorption measurements were made in order to check the results of the spectrometer measurements. In the self-absorption measurements the arc of the cyclotron was unmodulated and the deuteron beam was about 100 microamperes. A rhodium disk, having a thickness of 15.9 mg/cm², was used as a detector and rhodium disks, having thicknesses of 43.4 and 83.9 mg/cm², were used as absorbers. A 206-mg/cm² rhodium disk was used as a monitor. A more detailed description of the rhodium disks is given in Section III. The detector (or detector and absorber) was placed just above the monitor so that the detector (or detector and absorber) and the monitor were in the same vertical plane. Hence both detector (or detector and absorber) and the monitor received the same neutron flux. Both sides of the combination were covered with 0.9-g/cm² Cd sheet to absorb the thermal neutrons. The entire assembly was placed inside the collimator at a distance of 70 cm from the face of the water tank. The assembly was irradiated for 10 minutes to bring out the 4.2-minute period. The detector and monitor were placed in known and reproducible positions inside lead shields which housed Geiger counters. The output of each Geiger counter was connected to a discriminating amplifier which coupled into a scale-of-64 circuit and thence to mechanical counters. Data taking was started six minutes after the irradiation ended, so that the 44-second period activity was practically negligible. Counts were taken for 2 minutes for both the detector and the monitor. To guard against changes in sensitivity of the counters or the amplifiers, each foil was placed in the other shield and counts again taken for two minutes. This cycle was repeated until the background counts became as high as 1–10 percent of the total counts in a two-minute period. The background was about the same for each Geiger counter and was 0.35 scaled count/minute. A minimum of one hour elapsed between successive irradiations of the detector; hence, no correction for earlier irradiations was required.

TABLE I. Values of experimental parameters.

Condition number	On-time μsec.	Repetition frequency c/sec.	Absorber thickness g/cm²	Time of flight μsec./m	Energy ev	Moderator	Filter
1	10	2500	1.99	4–61	1.4–330	Water	0.9 g/cm² Cd
2	10	2500	1.58	24–61 70–107	1.4–9.1 0.46–1.06	Water	0.9 g/cm² Cd
3	5	2500	0.496	47–66	1.2–2.3	Water	0.9 g/cm² Cd
4	5	2500	0.0434	57–75	0.92–1.6	Water	0.9 g/cm² Cd
5	5	2500	0.206	57–75	0.92–1.6	Water	0.9 g/cm² Cd
6	10	2500	0.496	70–107	0.46–1.06	Water	0.9 g/cm² Cd
7	100	200	1.58	64–750	0.0092–1.3	Water and tray	none
8	40	250	1.58	103–245	0.087–0.49	Water and tray	none
9	100	200	0.412	720–1090	0.0044–0.010	Water and tray	none

Three runs were taken with each absorber. The entire procedure was, of course, standardized to obtain reproducible results. The consistency of the results of the three runs attests to the effectiveness of the standardization.

The following procedure was used to compute the transmission. The background counts are subtracted from the total counts. The ratio, A, of the detector-with-absorber counts to the monitor counts is obtained. The ratio, W, of detector-without-absorber counts to the monitor counts is obtained. The ratio, A/W, is the transmission. The possibility of difference between counters was taken into account by computing the transmission for each orientation and obtaining an average, weighted according to the total number of counts obtained in each orientation.

III. RESULTS

The transmission of neutrons by various thicknesses of rhodium absorbers was measured in the time-of-flight interval from 4.0 to 1090 μsec./m, corresponding to an energy range of 0.0044 to 330 ev. A resonance was found at an energy of 1.21 ev, or at a time of flight of 65.8 μsec./m. No resonances were found at higher energies. However, the resolution became progressively poorer with an increase in energy, and, hence, weak resonances probably would not be detectable at the highest energies measured.

The values of pertinent experimental param-

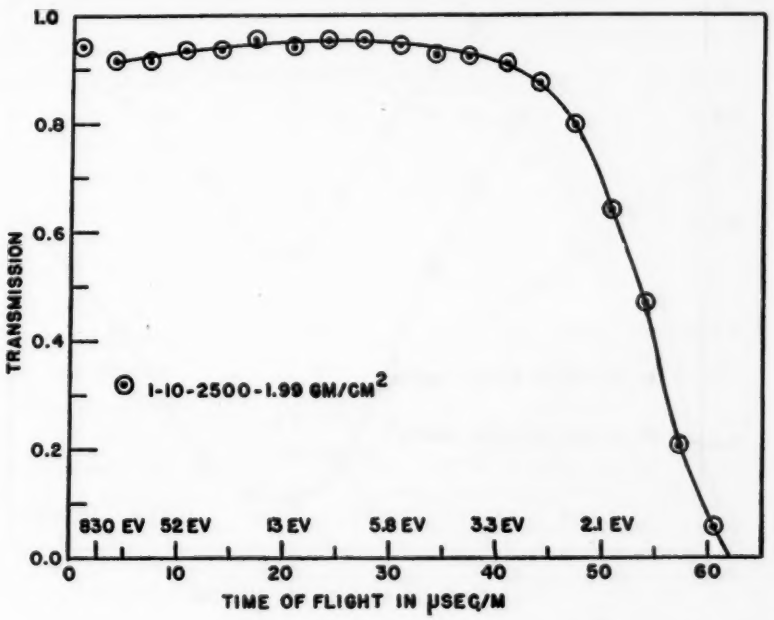

FIG. 2. Measured transmission of Rh in the energy region 1–300 ev.

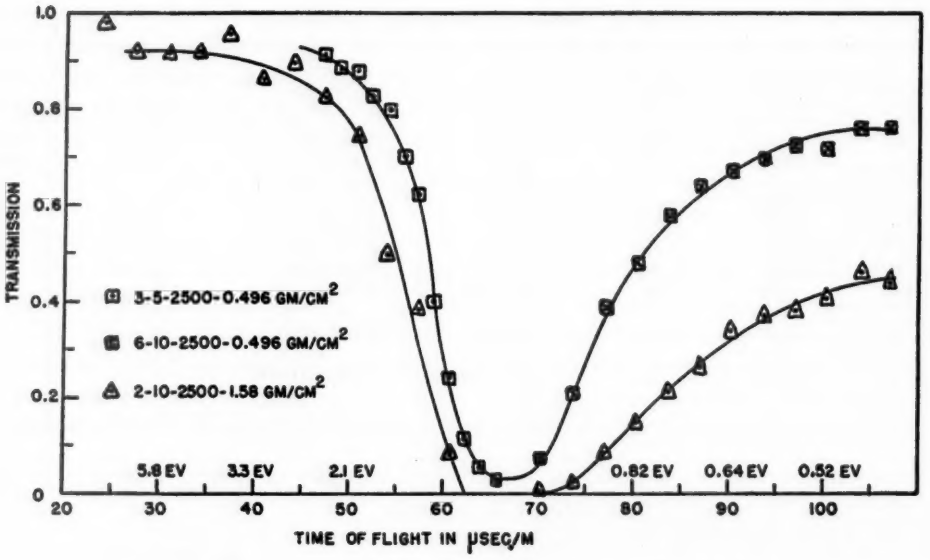

FIG. 3. Measured transmission of Rh in the energy region 0.5–10 ev.

eters used are listed in Table I. The different experimental conditions are each assigned numbers for identification purposes. A legend accompanies each graph showing experimental data. The legend indicates the condition number, the on-time, the repetition frequency, and the absorber thickness in that order. The rhodium absorbers used were uniform disks, $2\frac{1}{4}$ inches in diameter, cut from rolled sheet. The absorbers were obtained from Baker and Company, who stated that an analysis of the rhodium showed it to have a minimum purity of 99.85 percent, most of the impurities being other noble metals.

The measured transmissions of the various thicknesses of absorber are shown in Figs. 2–5. All the data have been corrected for backgrounds and time lags. The statistical error of the points is indicated by the lengths of the vertical lines

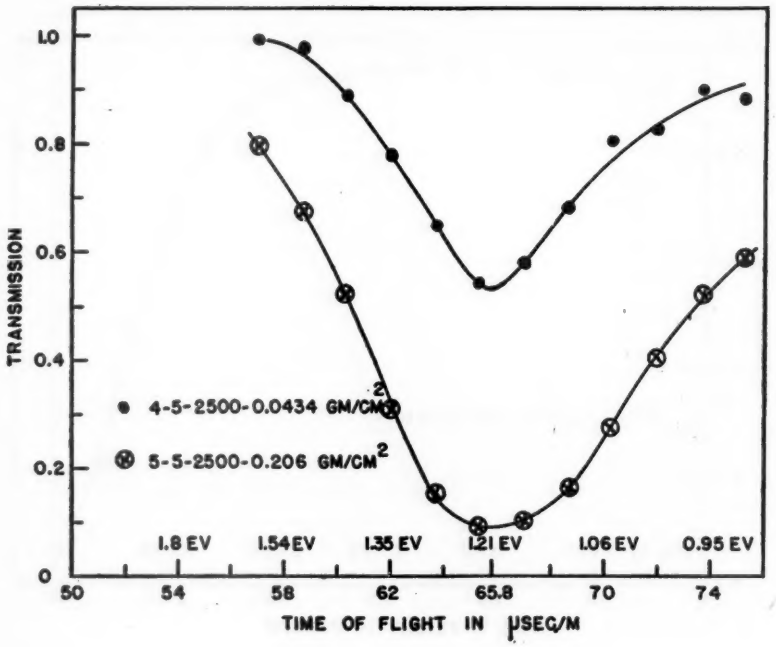

FIG. 4. Measured transmission of Rh in the energy region 0.8–1.8 ev.

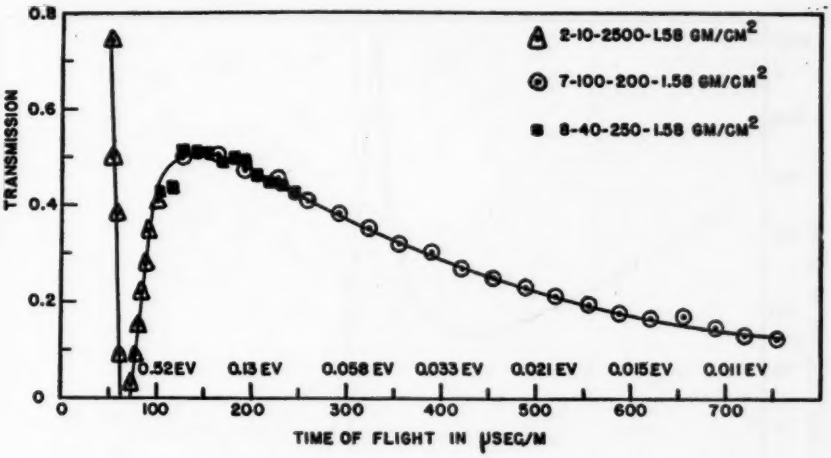

FIG. 5. Measured transmission of Rh in the energy region 0.01–1 ev.

through the points. In cases where the statistical error is less than the diameter of the plotted points, no vertical line is drawn.

The variation of the total cross section with time of flight in the low energy region is shown in Fig. 6. The cross section is obtained from the measured transmission by the relation

$$T=\exp(-\sigma n),$$

where T=transmission, σ=cross section, and n=absorber thickness. The equation of the solid curve drawn through the experimental points is

$$\sigma=(0.295\pm0.005)t(1+8650t^{-2})+(6\pm2),$$

where σ is the total cross section in barns (10^{-24} cm²/atom), t is the time of flight in μsec./m and 6 is a constant term taken to be the scattering cross section. This equation is discussed in Section IV. There are variations in the transmission at the lowest measured energies which are outside the statistical error and which may be due to the crystaline structure of rhodium. The lattice constant of rhodium metal is 3.8A. Neutrons of this wave-length have an energy of 0.0057 ev or a time of flight of 960 μsec./m.

A curve giving the total cross section as a function of the energy on logarithmic scales is shown in Fig. 7. Only those data are plotted which best represent the cross section in the regions where data are obtained with several thicknesses of absorber. The maximum measured cross section is about 2400 barns. At an energy of 0.025 ev the total cross section is about 150 barns. The minimum cross section on the low energy side of the resonance is about 73 barns and occurs at an energy of 0.25 ev, or at a time of flight of 145 μsec./m.

In the self-absorption experiments, the following transmissions were obtained: 0.710 ± 0.008 for the 43.4-mg/cm² absorber and 0.504 ± 0.012 for the 83.9-mg/cm² absorber. The errors are the r.m.s. deviations of the three separate runs with each absorber. For both absorbers the r.m.s. deviation is greater than the probable statistical error in the number of counts obtained.

IV. DISCUSSION

We are now concerned with the problem of obtaining the actual transmission (or cross section) from the measured transmission in order that the values of the parameters in the Breit-Wigner one-level formula may be obtained. The

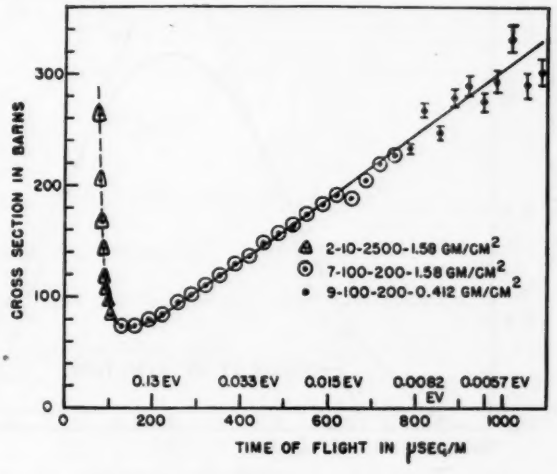

FIG. 6. Total cross section of Rh in the energy region 0.004–1 ev.

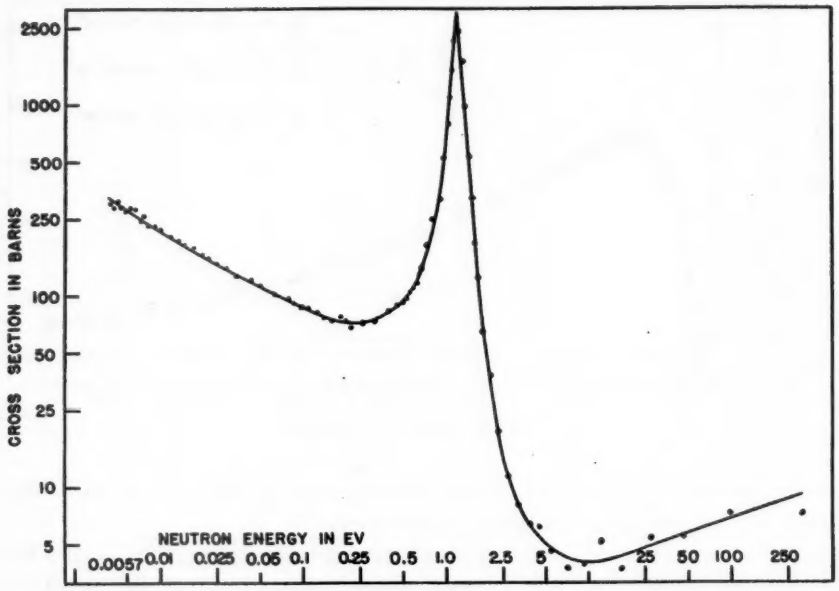

FIG. 7. Total cross section of Rh in the energy region investigated, namely, 0.004–300 ev. No correction has been made for apparatus resolution or Doppler effect. Both cross section and neutron energy are on logarithmic scales.

Breit-Wigner one-level formula is given[11] by

$$\sigma_a(E)=[E_r/E]^{\frac{1}{2}}[\sigma_r/(1+(4/\Gamma^2)(E-E_r)^2)],$$

where $\sigma_a(E)$ is the absorption cross section for neutrons of energy E, σ_r is the cross section at exact resonance, E_r is the resonance energy, and Γ is the width of the resonance level. The measured transmission can be taken as the actual transmission in regions where the transmission varies slowly with energy (e.g., in the $1/v$ region). However, in the region of a resonance, it may be necessary to make large corrections in order to obtain the actual transmission. The procedure used in the analysis of the data is similar in many respects to that used by McDaniel.[8]

Values for the parameters, σ_r and Γ in the Breit-Wigner formula, are chosen such that the experimental data in the resonance region are

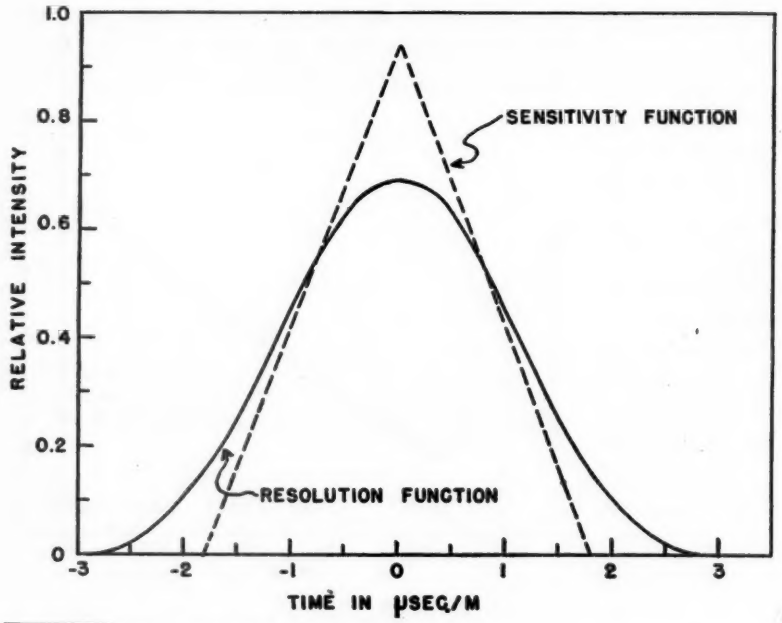

FIG. 8. Resolution function for 5.5-μsec. on-time and 1.2-ev neutrons. The solid curve is the resolution function. It is derived from the sensitivity function shown by the dashed line (and also in Fig. 5).

[11] H. A. Bethe, Rev. Mod. Phys. 9, 140 (1937).

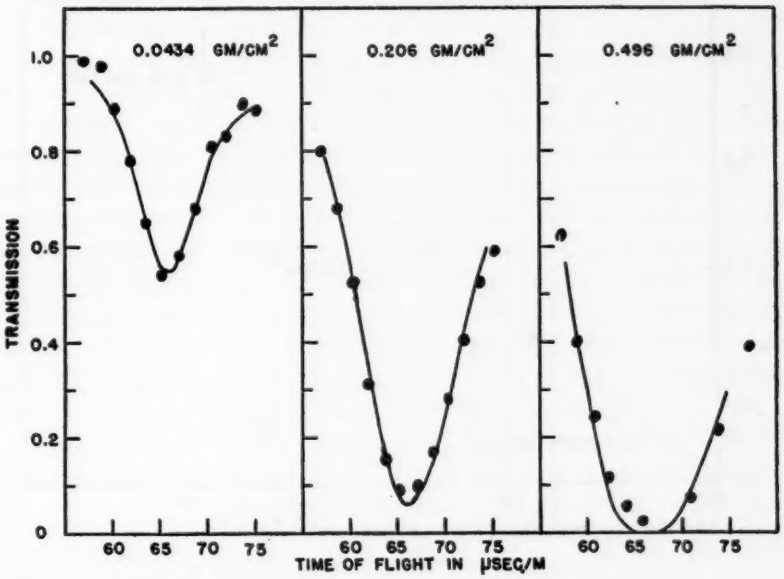

FIG. 9. Comparison of the transmissions expected from the Breit-Wigner formula with the measured transmissions. The solid curves are the expected transmissions obtained from the Breit-Wigner formula for the chosen parameters and the dots are the measured transmissions for each of three Rh absorbers.

reasonably well fitted by the formula. Since it is the total cross section that is measured, one has to subtract from it the scattering cross section to get the absorption cross section.

To obtain the scattering cross section, the procedure suggested by McDaniel *et al.*[12] was used. In the low energy region ($E^2/E_r^2 \ll 1$), the Breit-Wigner formula can be written in the approximate form $\sigma_a(E)=k(E_r/E)^1(1+2E/E_r)$, where $k=\sigma_r\Gamma^2/4E_r^2$, provided that $4E_r^2/\Gamma^2 \gg 1$. Hence, the total cross section in the low energy region is $\sigma(t)=kt/t_r(1+2t_r^2/t^2)+\sigma_s$, where t is the time of flight, t_r is the time of flight corresponding to the resonance energy, E_r, and σ_s is the scattering cross section. The constants, k and σ_s, were chosen so that the resultant curve, $\sigma(t)$ *vs.* t, fits the experimental points in Fig. 6. The values chosen are $k=19.4\pm0.3$ barns and $\sigma_s=6\pm2$ barns.

Next the Doppler effect must be taken into

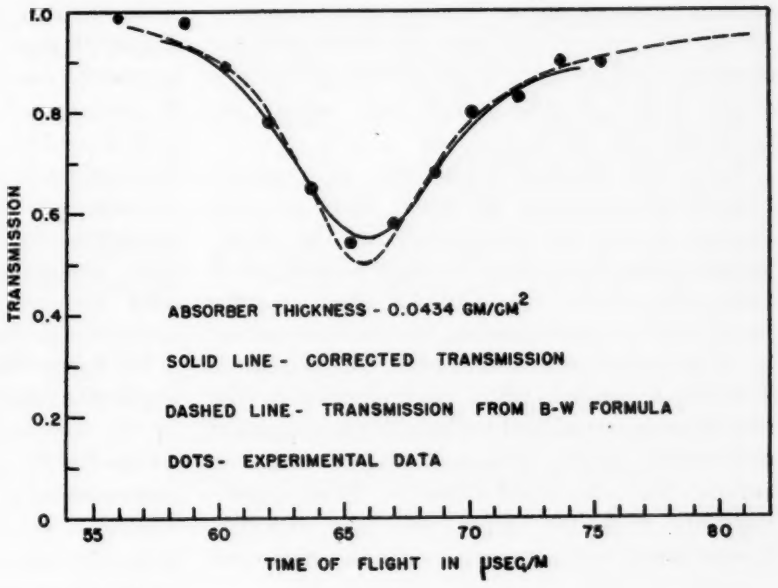

FIG. 10. Comparison of measured transmission with the transmission obtained from the Breit-Wigner formula with and without corrections. The dots are the measured transmissions. The dashed curve is the transmission obtained from the Breit-Wigner formula without any corrections. The solid curve is the (expected) transmission obtained from the Breit-Wigner formula after corrections have been made for the Doppler effect and apparatus resolution.

[12] McDaniel, Sutton, Lavatelli, and Anderson, Phys. Rev. **72**, 729 (1947).

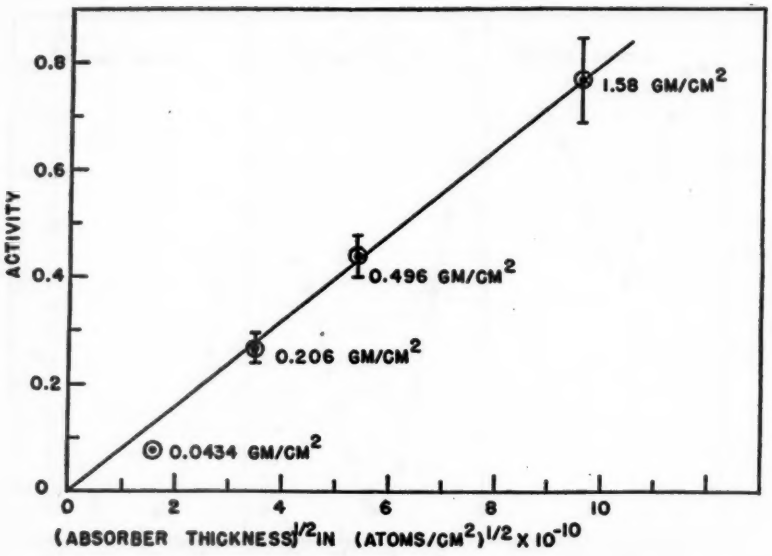

FIG. 11. Activity plot.

account. Since the Debye temperature for rhodium metal is 370°K,[13] the Doppler width, Δ, is found to be 0.038 ev for $E_r=1.21$ ev. For this value of Δ and the chosen values of σ_r and Γ, the effective cross section[11] is computed by numerical integration. The transmission, for each absorber thickness, is then computed as a function of the time of flight. The effect of the apparatus resolution of the transmission must next be considered.

The resolution function is the sensitivity of any one channel of the detector to neutrons of various times of flight. The resolution function for an on-time of 5.5 μsec., a source-detector distance of three meters, and 1.2-ev neutrons is shown in Fig. 8 (the dashed curve shows the sensitivity function).

Using this resolution function, an expected transmission curve is obtained. That is, after having chosen the parameters in the Breit-Witner formula, an effective cross section which takes into account the Doppler effect is computed, and the corresponding transmission curves for several thicknesses of absorber are obtained. These transmission curves are multiplied by the resolution function, and the product is integrated numerically to give points on the transmission curves which one would expect to obtain experimentally with the apparatus. The expected transmissions are compared with the measured transmissions and the parameters adjusted until the best fit is found between the expected and the measured transmission curves in the resonance region.

The expected transmission curves, using values for the parameters which yield the best fit to the measured curves, are shown in Fig. 9. The solid curves are the expected transmissions with the dots showing the experimental data. The values of the parameters yielding this correspondence are $E_r=1.21\pm0.02$ ev, $\sigma_r=2750\pm200$ barns and $\Gamma=0.21\pm0.01$ ev. The errors given are estimated and are based on statistical errors and resolution. Figure 10 shows the effect of the corrections. The assumed transmission obtained from the Breit-Wigner formula for the 0.0434-g/cm² absorber with $\Gamma=0.21$ ev and $\sigma_r=2750$ barns is shown by the dashed line. The solid line is the expected transmission and shows how the assumed transmission is modified by the Doppler effect and the finite resolution. The dots are the experimental data. It is interesting to note that the corrections are not very large.

No correction was made for the effect of the apparatus resolution function on the transmission in the low energy region. If the transmission varies linearly with time of flight, the measured transmission is equal to the actual transmission. Hence, a resolution correction is unnecessary, since the variation of the transmission with time of flight is almost linear within a resolution width in the low energy region.

[13] Frederick Seitz, *Modern Theory of Solids* (McGraw-Hill Book Company, Inc., New York, 1940), p. 110.

It has been pointed out by Jones[9] that a study of the behavior of the activity integral for a resonance as a function of the absorber thickness is useful in obtaining information about the values of the Breit-Wigner parameters. The activity, A, for a particular absorber thickness resulting from a resonance is defined by the relation, $A=\int(1-T)dy$, where T is the transmission of the absorber as a function of the time of flight, t, and $dy=dt/t_r$, where t_r is the time of flight corresponding to the resonance energy, E_r. The limits of the integral are taken as the values of t on either side of the resonance where $T\approx 1$. It can be shown that, for thin absorbers (i.e., $\sigma_r n\ll 1$), $A=\pi n\Gamma\sigma_r/4E_r$, and for thick absorbers

$$A=[\pi n\Gamma^2\sigma_r]^{\frac{1}{2}}/2E_r.$$

In this study the Doppler effect and apparatus resolution may be neglected in obtaining expressions for A.

A plot of the activities for the various thicknesses of absorber as a function of the square root of the absorber thickness is shown in Fig. 11. From the slope of this curve the value of $\sigma_r\Gamma^2$ is 120 ± 12 barn-ev^2. Other values of $\sigma_r\Gamma^2$, in barn-ev^2, are: 121 ± 11 computed from the chosen Breit-Wigner parameters, 114 ± 2 computed from the slope of σ_a *vs.* t in the $1/v$ region, and 112 ± 3 computed from the minimum cross section on the low energy side of the resonance.

The self-absorption data were analyzed by the method used by Hornbostel *et al.*[3] For the 43.4-mg/cm^2 absorber, the coefficient of self-indication, K_s, is found to be 9.14 cm^2/g, which gives a value of 3120 ± 50 barns for the cross section at resonance. Hornbostel found K_s to be 11.5 cm^2/g and σ_r 4100 barns. Computations were not made for the 83.9-mg/cm^2 absorber, since the approximations made in the analysis are no longer valid for such a thickness. It is of interest to note that the transmissions obtained in this experiment are higher for both absorber thicknesses than those obtained by Hornbostel.[3] The measurements above give a transmission of 0.71 and 0.50 for the 43.4- and the 83.9-mg/cm^2 absorbers, respectively, whereas the corresponding values of the transmission obtained by Hornbostel are 0.59 and 0.43. The discrepancy may be due to the fact that Hornbostel had to make a large obliquity correction since his source-detector distance was small (more than a factor of ten smaller than the source-detector distance used in this experiment). In the present experiment the maximum apparent thickness is only 1.5 percent greater than the actual thickness of the absorber.

Finally, it should be noted that, for elements in the neighborhood of rhodium, the expected spacing between energy levels is about 10 to 30 ev, for small kinetic energy of the neutron. For example, in indium[8] and in iodine[9] the spacing between levels is in this range. However, the data obtained in this investigation seem to indicate that, for rhodium, the spacing between levels is more than 300 ev.

V. ACKNOWLEDGMENTS

The author wishes to express his deep appreciation to Professor B. D. McDaniel, under whose direction this investigation was pursued, for his helpful advice and his constant encouragement. The author also wishes to express his gratitude to Professor R. F. Bacher for suggesting the problem, to Professors C. P. Baker, H. A. Bethe, P. Morrison, and Dr. W. B. Jones and to other members of the Laboratory of Nuclear Studies at Cornell University for their many suggestions.

A Cloud-Chamber Study of the Disintegration of Lithium by Slow Neutrons

J. K. BØGGILD AND L. MINNHAGEN
Institute for Theoretical Physics, Copenhagen, Denmark

(Received November 9, 1948)

The ranges of tritons and alpha-particles formed in the slow neutron reaction $^6Li(n,\alpha)\,^3H$ have been measured in a cloud chamber and found to be $R_\alpha = 10.4 \pm 0.2$ mm and $R_{^3H} = 60.0 \pm 0.6$ mm in air at N.T.P.; the corresponding Q values, derived from the blue-printed Cornell energy *vs.* range curves, disagree, and the Q derived by the proton relation is also in disaccordance with other data. The discrepancies suggest the establishment of a new point on the proton energy *vs.* range curve, *viz.*, $R_p = 20.0$ mm, $E_p = 0.88$ Mev, which means a reduction of the energy by about 6 percent.

INTRODUCTION

THE energy released when lithium reacts with slow neutrons

$$_3{}^6Li + {}_0{}^1n \rightarrow {}_2{}^4He + {}_1{}^3H + Q$$

can be determined from the mean range of either one of the released particles by means of the energy range relations for alpha-particles or protons, considering the law of conservation of momentum. The Q values reported in earlier investigations are somewhat higher than the value calculated from the isotopic weights of the nuclei involved in the reaction and do not seem to be consistent with other transmutation data. Consequently, the ranges of the two particles have now been carefully remeasured, and the results were used for a discussion of the reliability of the energy range relations.

By proper choice of the experimental conditions it was possible to select the paired tracks of the $^6Li(n,\alpha)^3H$ reaction and, therefore, a moderate number of tracks should be expected to give good values of the mean ranges. It may be added that conditions should also be favorable for finding weak groups provided that the groups are not too close to each other. We have found, however, only one group and, thus, no evidence of the existence of a ^6Li reaction by which the ^3H nucleus is left in an excited state.

EXPERIMENTAL ARRANGEMENTS

Foils carrying thin evaporated layers of lithium fluoride were suspended in the middle of a 25-cm cloud chamber, and the lithium was exposed to neutrons produced by deuteron bombardment of lithium or beryllium and slowed down by means of paraffin.

In the first part of the investigation, when studying the range of the short alpha-tracks, the support was a mica foil having a stopping power equivalent to 12 mm of air, supplied on each side with a lithium fluoride layer with a stopping power of 0.65 mm of air. The tritons could penetrate the mica foil, but the alpha-particles were stopped. Thus, only those alpha-particles gave tracks which were ejected from one of the lithium layers directly into the chamber gas. The tracks could be recognized as formed in the lithium reaction and selected from other tracks by means of the accompanying triton penetrating the mica foil in the opposite direction and giving a fainter track in the other half part of the chamber. A typical example of the paired tracks is given in Fig. 1A. The cloud chamber contained helium, ethyl alcohol, and a small amount of boric acid ethyl ester, the total pressure being about 32 cm of Hg. The stopping power of the gas was determined by measuring the tracks of the boron disintegrations produced by slow neutrons in the gas of the chamber, and were easily identified by their characteristic features.* This is a convenient method of controlling the stopping power when short range particles are studied.

The triton tracks were studied under the following conditions. On one side of an extremely thin gold foil a lithium fluoride layer was evapo-

* J. K. Bøggild, Kgl. Danske Vid. Sels. Math.-Fys. Medd **23**, No. 4 (1945). (The total mean range, 11.35 mm of air, given here for the main group of boron tracks is revised to 11.50 mm because of small corrections in the stopping power of the gas mixture and in the value of the polonium alpha-range used to control the stopping power.)

rated, having a stopping power of 1.4 mm of air. The chamber contained air and the vapors of a mixture of ethyl alcohol and water in equal portions, the total pressure being about 62 cm. The stopping power of the gas was determined by means of alpha-tracks from a thorium *C* source inside the chamber. The tritons could easily be recognized by means of the accompanying short, denser alpha-tracks, as it appears from Fig. 1B. Corrections were applied for the stopping power of the LiF layer and also of the gold foil for tritons penetrating it.

Figure 2 shows the range distribution of 95 alpha-tracks from the ^{6}Li reaction and of the tracks of boron disintegrations used as control. Figure 3 illustrates the distribution of 159 triton tracks. The mean range of the alpha-particles was found to be 10.4 ± 0.2 mm and that of the tritons 60.0 ± 0.6 mm in air at N.T.P., the maximum errors being estimated to be about 2 percent of the alpha-particle range and 1 percent of the triton range. The very few tracks shorter than the characteristic groups are supposed to be spurious—either originating in the lithium reaction, the length being reduced by some local defects, e.g., droplets on the foil, or in events in the gas accidentally resembling the tracks from the lithium reaction.

Using the energy range relations for alpha-particles (Cornell 1938[1]) and for protons (Cornell 1937 revised[2]), the following energy values are

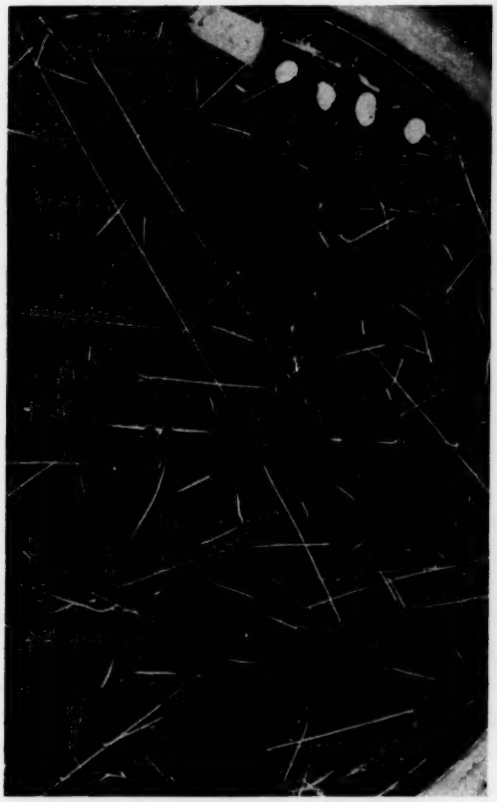

FIG. 1A. Paired tracks from a lithium disintegration. The chamber is filled with helium at low pressure in order to get alpha-tracks suitable for measurement. The dense track downward from the foil corresponds to the alpha-particle, the fainter track traversing the whole upper half part of the chamber belongs to the triton which has penetrated the mica foil carrying the lithium layers. Compare the different appearance of the track of a recoiling proton—to the right of the alpha-triton tracks and almost parallel to them—starting below the foil, penetrating it, and ending in the upper part of the chamber, the density increasing along the whole track.

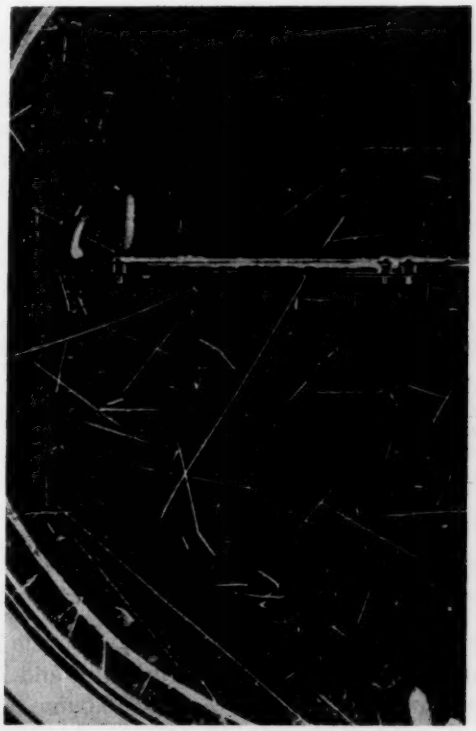

FIG. 1B. Triton track with accompanying alpha-track from a lithium disintegration. The chamber contained air with the pressure high enough to stop the triton in the gas. The obtuse-angled track intersecting the triton track near its end is to be ascribed to the fast neutron reaction $_7{}^{14}\mathrm{N}(n,\alpha)\,{}_5{}^{11}\mathrm{B}$.

[1] M. G. Holloway and M. S. Livingston, Phys. Rev. **54**, 18 (1938).
[2] H. A. Bethe, Phys. Rev. **53**, 313 (1938).

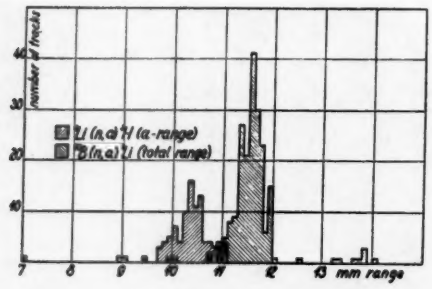

FIG. 2. Distribution of alpha-tracks from the $_3{}^6\mathrm{Li}(n,\alpha)\,_1{}^3\mathrm{H}$ reaction and of tracks from the $_5{}^{10}\mathrm{B}(n,\alpha)\,_3{}^7\mathrm{Li}^*$ reaction used to determine the stopping power of the gas in the cloud chamber. The mean range of the alpha-particles is found to be 10.4 mm; the value used for the total mean range of the main group of the boron disintegration is 11.5 mm.

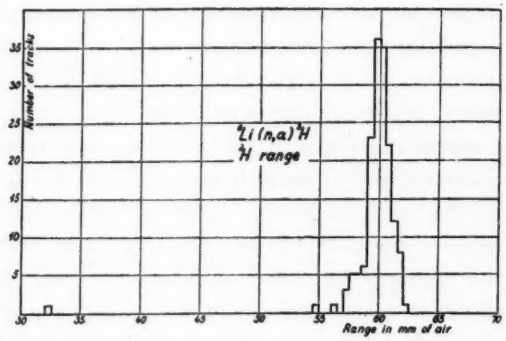

FIG. 3. Distribution of triton tracks from the $_3{}^6\mathrm{Li}(n,\alpha)\,_1{}^3\mathrm{H}$ reaction. The mean range is found to be 60.0 mm.

obtained:

$$E_\alpha = 1.955 \text{ Mev}, \quad Q' = 7/3 \cdot E_\alpha = 4.56 \pm 0.08 \text{ Mev},$$
$$E_p = 0.937 \text{ Mev}, \quad Q'' = 7/4 \cdot 3E_p = 4.92 \pm 0.03 \text{ Mev},$$

where E_α is the energy of an alpha-particle with a mean range amounting to 10.4 mm, and E_p is that of a proton having a range of 20.0 mm, which is one-third of the triton range 60.0 mm. The fact that the difference between the two values of Q obtained is larger than the estimated maximum errors, indicates that at least one of the energy range relations is somewhat incorrect.

DISCUSSION

The energy range relation for alpha-particles is considered reliable at the present time, but recent investigations on reaction cycles[3] indicate that the revised proton relation gives too high energy values, in the case of 10-mm protons by about 10 percent. It thus seems reasonable to consider our Q' value, determined from the alpha-particle range, as fairly reliable and to establish a new point on the proton relation by combining our triton range with the triton energy as calculated from Q' and by converting the values in the usual way into range and energy of a proton. The energy of a 20.0-mm proton should thus be

$$4/7 \cdot \tfrac{1}{3} \cdot (4.56 \pm 0.08) = 0.870 \pm 0.015 \text{ Mev}.$$

By substituting for Q' the Q value calculated from the isotopic weights ($Q = 4.65 \pm 0.06$ Mev, using Mattauch's[4] values and $Q = 4.64$, using those of Segrè[5]), the proton energy 0.885 ± 0.011 Mev is obtained.

Another way of determining the Q value is to combine the $^6\mathrm{Li}(n,\alpha)\,^3\mathrm{H}$ reaction with the $^6\mathrm{Li}(p,\alpha)\,^3\mathrm{He}$ reaction:

$$\left.\begin{aligned} {}^6\mathrm{Li} + n &\rightarrow {}^4\mathrm{He} + {}^3\mathrm{H} + Q \\ {}^6\mathrm{Li} + {}^1\mathrm{H} &\rightarrow {}^4\mathrm{He} + {}^3\mathrm{He} + Q_p \end{aligned}\right\}$$
$$Q = Q_p + (n - \mathrm{H}) - ({}^3\mathrm{H} - {}^3\mathrm{He});$$

here, $(n - \mathrm{H}) = 0.755 \pm 0.016$ Mev,[6] and

$$({}^3\mathrm{H} - {}^3\mathrm{He}) = 0.011 \pm 0.002 \text{ Mev}.^7$$

Thus,

$$Q = Q_p + (0.744 \pm 0.016) \text{ Mev}.$$

With Perlow's[8] $Q_p = 3.945 \pm 0.06$ Mev, as determined from the alpha-range by a method which is fairly insensitive to the alpha-relation, $Q = 4.69 \pm 0.06$ is obtained, the corresponding proton energy being 0.895 ± 0.011 Mev.

The three proton energy values given above are in reasonable agreement, and the accuracy of the mean value, 0.883 Mev, corresponding to 20.0-mm proton range, is probably better than 2 percent. This proton energy is about 6 percent smaller than that given by the revised Cornell relation, *viz.*, 0.937 Mev, and even somewhat smaller than that given by the Livingston and Bethe[9] relation from 1937, *viz.*, 0.91 Mev.

[3] I. Cornog, W. Franzen, and W. E. Stephens, Phys. Rev. **74**, 1 (1948).

[4] J. Mattauch, *Kernphysikalische Tabellen* (Berlin, 1942).
[5] E. Segrè, Atomic Energy Commission Report MDDC (1945).
[6] W. E. Stephens, Rev. Mod. Phys. **19**, 19 (1947).
[7] R. J. Watts and D. Williams, Phys. Rev. **70**, 640 (1946).
[8] G. J. Perlow, Phys. Rev. **58**, 218 (1940).
[9] M. S. Livingston and H. A. Bethe, Rev. Mod. Phys. **9**, 268 (1937).

As to previous range measurements, it appears that our triton range, 60.0±0.6 mm, is in agreement with that found by Livingston and Hoffman,[10] *viz.* 59.0±0.6 mm, and also with that found by Rumbaugh, Roberts, and Hafstad,[11] *viz.*, 61 mm (which is, however, not claimed to be very accurate). The latter authors have determined the alpha-range, too, but their value, 11.8 mm, exceeds ours by more than 10 percent and leads to $Q=4.97$ Mev, which is in serious disagreement with the data given above.

In conclusion, the authors wish to express their gratitude to Professor Niels Bohr, who placed at their disposal the facilities of the institute, for his kind interest and valuable advice regarding this investigation. Our thanks are also due Mr. O. B. Nielsen, civil engineer, and Mr. S. Holm for valuable assistance during the experiments.

[10] M. S. Livingston and J. G. Hoffman, Phys. Rev. **53**, 227 (1938).
[11] L. R. Rumbaugh, R. B. Roberts, and L. H. Hafstad, Phys. Rev. **54**, 657 (1938).

PHYSICAL REVIEW VOLUME 75, NUMBER 5 MARCH 1, 1949

Thresholds for Fast Neutron Fission in Thorium and Uranium*

W. E. Shoupp and J. E. Hill
Westinghouse Research Laboratories, East Pittsburgh, Pennsylvania
(Received November 10, 1948)

The threshold energy for fast neutron fission of thorium and uranium has been measured by using the neutrons from thin lithium films through the $Li^7(p,n)$ reaction. Neutron energy fission thresholds were found to be 1.0±0.1 Mev for U^{238} and 1.10±0.05 Mev for Th^{232}.

INTRODUCTION

THE reaction $Li^7(p,n)Be^7$ provides a convenient source of fast neutrons, the maximum energy of which is determined by the energy of the bombarding protons. These neutrons may be used to investigate the threshold of any fast neutron reaction which occurs with an observable cross section within the range of neutron energies available. Preliminary reports[1] were published for the thresholds of fast neutron fission in uranium and thorium obtained by this method. This paper gives a more complete description of these experiments, together with the results of experiments on the threshold of fast neutron fission in uranium, in which the neutrons were obtained from thin foils of lithium bombarded with protons. As a part of this problem, the yield of neutrons from thin foils of lithium was measured as a function of the energy of the bombarding protons.[2]

THICK TARGET EXPERIMENTS

In these experiments the uranium and thorium targets were bombarded with neutrons obtained from thick targets of lithium metal or lithium

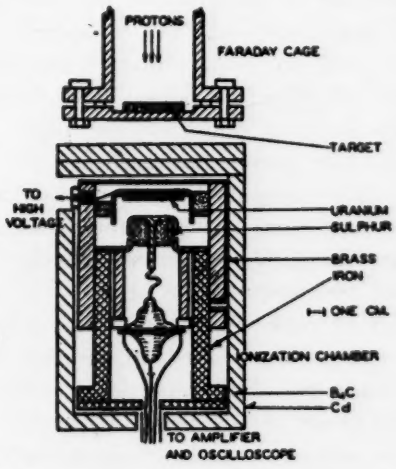

FIG. 1. Arrangement for measuring neutron fission.

* This work was completed in 1941 and has been recently declassified. Even though more accurate values may have been made since then, these results are of value due to their historical importance and may serve some use until more accurate values are made available.
[1] R. O. Haxby, W. E. Shoupp, W. E. Stephens, and W. H. Wells, Phys. Rev. **57**, 1088A (1940).
[2] J. E. Hill and W. E. Shoupp, Phys. Rev. **73**, 931 (1948).

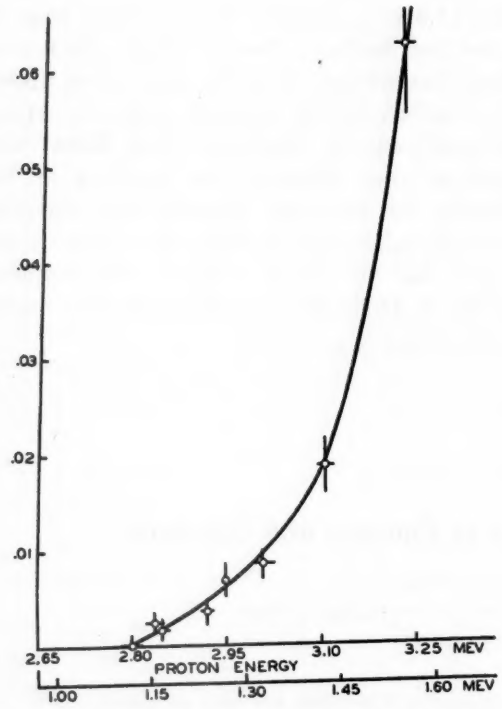

FIG. 2. Number of fissions produced in thorium per microcoulomb of protons incident on lithium as a function of the maximum energy of the neutrons.

hydride bombarded with protons, accelerated in the Westinghouse pressure electrostatic generator,[3] and analyzed magnetically. The proton current was measured by means of a current integrator and the energy of the incident protons was measured by means of a generating voltmeter. The voltmeter was calibrated before and after each run by checking the threshold for the lithium (p,n) reaction. The fission fragments were detected by means of a 1-cm deep air ionization chamber. A potential of 2000 volts was impressed on the collector plate of the chamber. The pulses produced by the fission particles were amplified by means of a linear amplifier and were either counted visually by observing the kicks on an oscilloscope screen, or—when necessary—were sent to a scale of eight circuit and a mechanical recorder. The scaling circuit was biased to respond only to fission fragments. This was easily accomplished since the fission pulses were, in general, several times the size of the pulses from natural alpha-particles. In the case of uranium fission the ion chamber was surrounded by about one cm of boron carbide and two mm of sheet cadmium, to reduce the slow neutron fission in U^{235} as much as possible. Figure 1 shows the geometrical arrangement of the apparatus as used in these experiments.

Equation (1) enables us to calculate the *maximum* energy of the neutrons, E_n, produced in the forward direction by the reaction for each value of the energy of the bombarding protons, E_p, from the relation

$$(E_n)^{\frac{1}{2}}=\tfrac{7}{8}(E_p-E_{p0})^{\frac{1}{2}}+\tfrac{1}{8}(E_n)^{\frac{1}{2}}. \qquad (1)$$

The quantity E_{p0} is the threshold proton energy which will just cause neutrons to be emitted from the lithium target and was taken as 1.85 Mev for the reaction $Li^7(p,n)Be^7$. More recent works carried out at Westinghouse Research Laboratories[4] and the University of Wisconsin,[5,6]

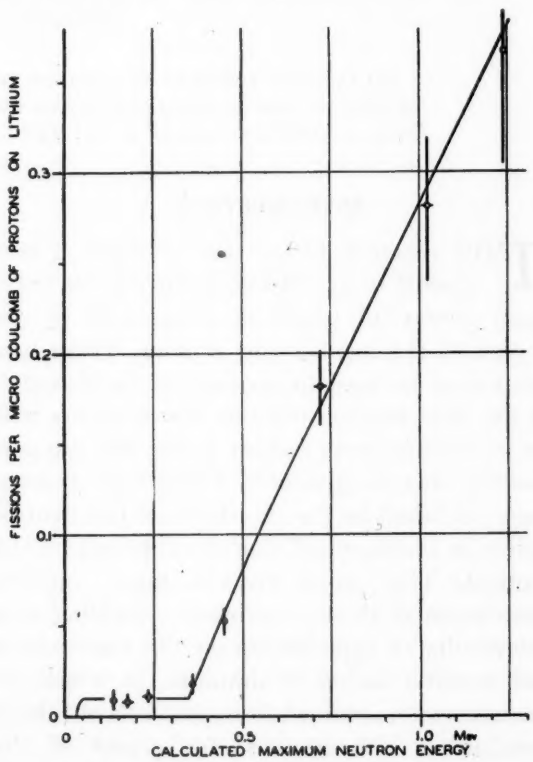

FIG. 3. Number of fissions produced in uranium per microcoulomb of protons incident on lithium as a function of the maximum energy of the neutrons.

[3] R. O. Haxby, W. E. Shoupp, W. E. Stephens, and W. H. Wells, Phys. Rev. **58**, 162 (1940).

[4] W. E. Shoupp, B. Jennings, W. Jones, and M. Garbuny, to be published.

[5] A. O. Hanson and D. L. Benedict, Phys. Rev. **65**, 33 (1944).

[6] R. G. Herb, M.I.T. Conference on Electrostatic and High Energy Accelerators, June 8, 1948.

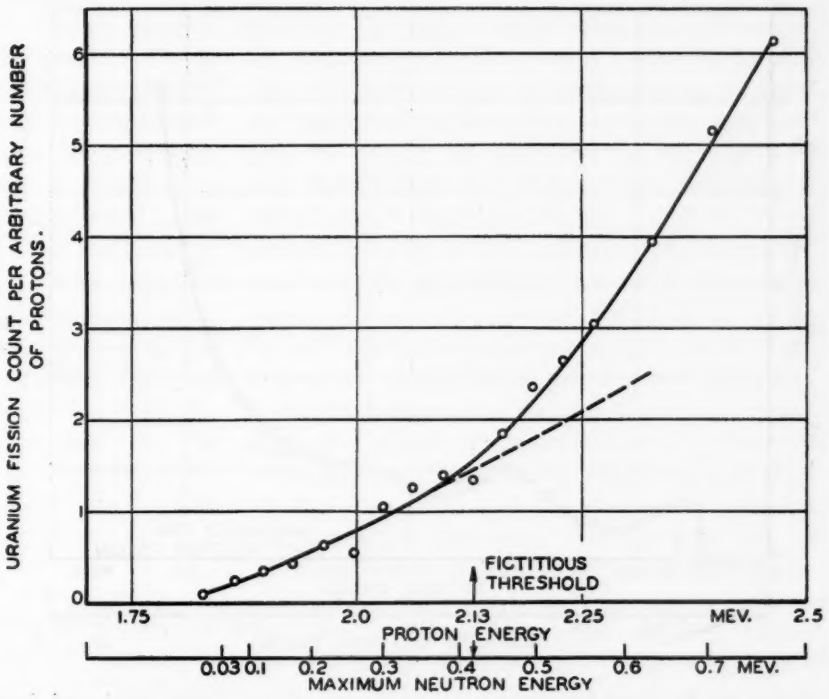

FIG. 4. Uranium fission count as a function of proton energy.

using independent methods, indicates that this threshold is in the neighborhood of 1.881 Mev.

In Fig. 2 the number of fissions produced in thorium per microcoulomb of protons incident on the lithium is plotted as a function of the maximum energy of the neutrons. This gives an upper limit for the fast neutron fission threshold for thorium of $Q_n = 1.10$ Mev± 0.05.

Figure 3 gives a similar curve for uranium. It will be noted that in this case there are always some fission pulses for all neutron energies, but that there is a sharp increase at about $Q_n = 0.35$ Mev. This break was previously interpreted as the threshold energy for the fast neutron fission in U^{238}. The fission counts obtained below this energy were observed as soon as neutrons were obtained and were attributed to slow neutron fission in U^{235}. The above data were obtained by visual observation of the pulses on an oscilloscope screen. The average counting rate for visual observation was kept less than one per second in order to avoid missing counts. Consequently, it was impractical to obtain large numbers of counts by this method. Therefore, the statistical uncertainty in the points in Figs. 2 and 3 is rather large. In the case of uranium the presence of the slow neutron fission in U^{235} makes the determination of the fast neutron fission threshold, by visual counting methods, very uncertain.

The uranium experiment was repeated using an amplifier and scale of eight biased so that only fission pulses were recorded. The resulting data thus taken are shown in Fig. 4. Again the slow neutron fission in U^{235} makes it difficult to

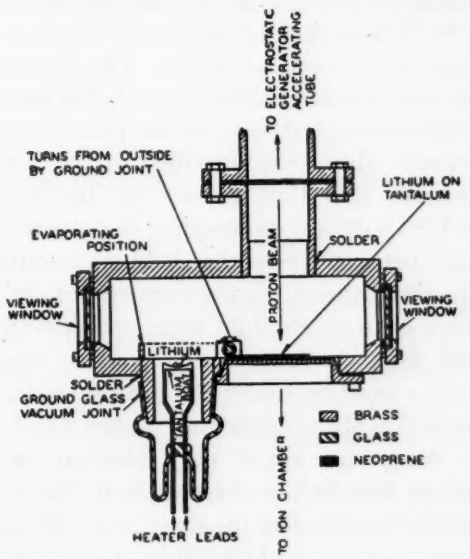

FIG. 5. Construction of lithium evaporator.

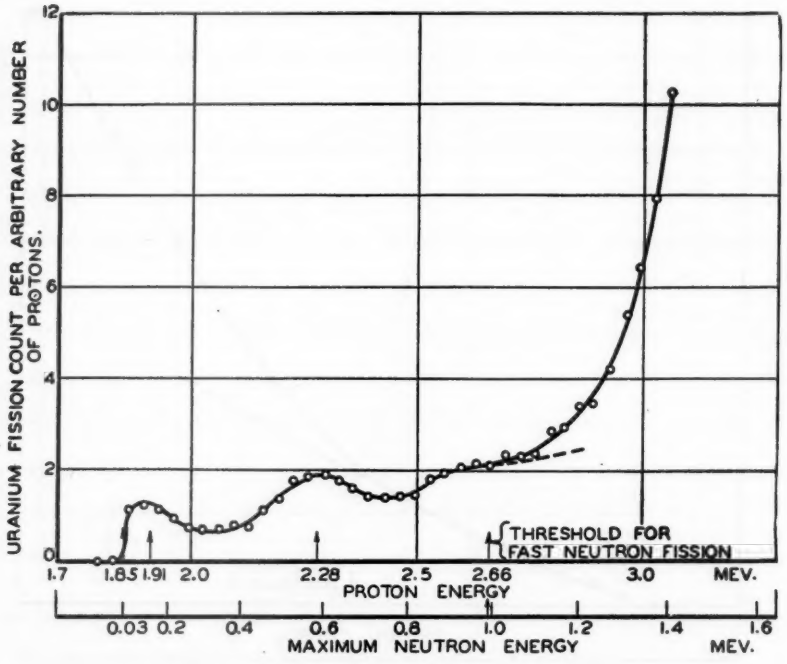
URANIUM FISSION COUNT PER ARBITRARY NUMBER OF PROTONS.
THRESHOLD FOR FAST NEUTRON FISSION
1.7 1.85 1.91 2.0 2.28 2.5 2.66 3.0 MEV.
PROTON ENERGY
0.03 0.2 0.4 0.6 0.8 1.0 1.2 1.4 1.6
MAXIMUM NEUTRON ENERGY MEV.

FIG. 6. Uranium fission count with neutrons from thin lithium target.

choose the threshold for fast neutron fission, but there is clearly an abrupt change of slope at $Q_n = 0.42$ Mev which is in fair agreement with the result of Fig. 3 considering the few points and poor statistics of the earlier experiment.

THIN TARGET EXPERIMENTS

Because of the uncertainty introduced into the determination of the fast neutron fission threshold for uranium by the slow neutron fission in U^{235}, it was decided to use a thin target of lithium as a neutron source. This procedure should give a much smaller yield of slow neutrons in proportion to fast neutrons for proton energies sufficiently above the threshold of the reaction $Li^7(p,n)Be^7$ and thus reduce the fission yield from U^{235}, with a corresponding improvement in the fast neutron fission threshold measurement.

The thin lithium targets were evaporated in a vacuum onto a tantalum sheet which could be turned from the evaporating position through 180° to a position under the proton beam. The construction of the evaporator is shown in Fig. 5. This design permitted easy cleaning of the tantalum sheet before evaporation of the lithium target, by bombarding the sheet with high energy protons, and also made possible an easy check to determine if any background of neutrons was being produced from lithium or other contamination in the tube, by merely turning the target out from under the beam. In no case was any neutron background observed.

With the exception of the above changes in the neutron source, the uranium experiment was repeated as outlined above. The result is shown in Fig. 6. The equivalent thickness of the lithium target was estimated in terms of kilovolts by

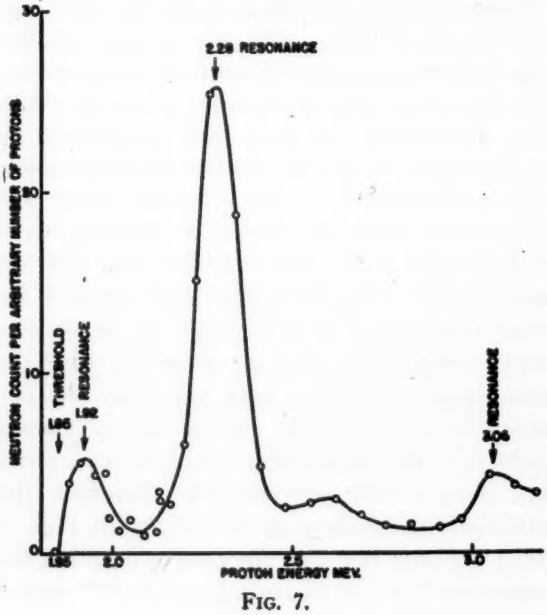

FIG. 7.

observing the half-width of the lithium gamma-ray resonance which occurs for protons of 440 kilovolts. The results of this experiment (Fig. 7) using a lithium target having an equivalent thickness of 170 kilovolts have been recently published.[2] By comparing Figs. 6 and 7, it is clear that the change of slope interpreted as the onset of fast neutron fission in the thick target experiments was in reality only the beginning of the second and the strongest neutron maximum and that the threshold for fast neutron fission is much higher. From Fig. 6, an upper limit can be set for the fast neutron fission threshold, Q_n, of about 1.0 ± 0.1 Mev. The maxima in the uranium fission yield at proton energies of 1.9 and 2.3 Mev are due to maxima in the neutron yield from the $Li^7(p,n)$ reaction.[2]

DISCUSSION

From the fast neutron fission thresholds for uranium and thorium the critical energies of fission for the nuclei U^{239} and Th^{233} may be estimated. The critical energy for fission, E_f, is the sum of the fast neutron fission threshold, Q_n, and the binding energy of the neutron, E_n. If E_n is taken equal to 5.2 Mev for U^{239} and 5.2 Mev for Th^{233}, the corresponding critical energies for fission are 6.2 Mev and 6.3 Mev. Bohr and Wheeler[7] have calculated these critical energies for fission from theoretical considerations and find the values 5.9 Mev and 6.8 Mev for U^{239} and Th^{233}, respectively. More recent and refined calculations[8] yield even higher values for these critical energies. The discrepancy, however, does not lie in the experimental determination of the thresholds, and the present results should serve as the basis for the refinement of the liquid drop theory for fission. While the experimental value of Q_n for thorium was obtained from thick target data, the value is probably very near to the true threshold since there is only one stable isotope of thorium and there is no slow neutron fission to obscure the fast neutron fission threshold as in the case of uranium. Since the experimentally determined threshold is only an upper limit to the true threshold, the fast neutron fission thresholds for thorium and possibly also U^{238} might be expected to be too high rather than too low.

[7] N. Bohr and J. A. Wheeler, Phys. Rev. **56**, 426 (1939).
[8] S. Frankel and N. Metropolis, Phys. Rev. **72**, 914 (1947).

PHYSICAL REVIEW VOLUME 75, NUMBER 5 MARCH 1, 1949

Bound Electron Creation in the Decay of Tritium

P. M. SHERK
University of Illinois, Urbana, Illinois
(Received November 19, 1948)

The relative probabilities of K creation and beta-emission are calculated for both molecular and atomic tritium. This ratio is shown to be 0.0035 for the molecule and 0.0065 for the atom, assuming the maximum kinetic energy of the beta-rays to be 16.9 kev.

WHEN beta-disintegration takes place, the electron emitted usually enters one of the continuum states of the product nucleus and is called a beta-particle; we shall refer to this process as "beta-emission." There is, however, a finite probability that the emitted electron will enter one of the discrete (bound) energy levels of the product nucleus; e.g., when atomic tritium decays, the created electron may become a bound electron of He^3. This process will be called "bound electron creation." In particular, we shall speak of "K creation" when the created electron enters the K shell of the product nucleus. The general characteristics of bound electron creation have been considered by Daudel, Benoist, Jacques, Jean, and Lecoin.[1-3] It should be emphasized that the nuclear transi-

[1] R. Daudel, P. Benoist, R. Jacques, and M. Jean, Comptes Rendus Acad. Sci. (Paris) **224**, 1427 (1947).
[2] R. Daudel, M. Jean, and M. Lecoin, Comptes Rendus Acad. Sci. (Paris) **225**, 290 (1947).
[3] R. Daudel, M. Jean, and M. Lecoin, J. de phys. et rad. **8**, Series 8, 238 (1947).

tion is the same whether the process in question is beta-emission or bound electron creation.

In this paper we shall calculate the ratio of the transition probability for K creation to that for beta-emission for molecular and atomic tritium. By "molecular tritium" we mean a hydrogen molecule one of whose nuclei has mass three; the mass of the other is immaterial. When molecular tritium undergoes beta-disintegration, the H^3 nucleus becomes a He^3 nucleus, and an electron is created. This results in a hybrid structure consisting of a hydrogen nucleus and a He^3 nucleus, surrounded by two or three electrons, depending upon whether beta-emission of bound electron creation has occurred. Loosely speaking, these electrons can be considered to occupy the familiar stationary states of H, He^+, and He. The theory shows that bound electron creation is improbable except when the created electron occupies the K shell about the He nucleus. For reasons to be explained later, the two electrons initially present in the molecule will not necessarily occupy the He K shell after beta-disintegration has occurred.

The investigators mentioned above have derived[3] an expression giving the ratio of the transition probabilities for K creation and beta-emission in the general case. If the K shell binding energy is much smaller than both the rest energy of the electron and the maximum kinetic energy of the beta-rays, this expression reduces to

$$P(N_K)/P_\beta = 0.0653(2-N_K)Z'^{3}E_\beta^{-\frac{1}{2}}, \quad (1)$$

where N_K is the number of initially present molecular electrons occupying the He K shell ($N_K=0, 1, 2$), $P(N_K)$ is the transition probability for K creation with this value of N_K, P_β is the transition probability for beta-emission, Z' is the effective charge of the product nucleus, and E_β is the maximum kinetic energy of the beta-rays in kev.

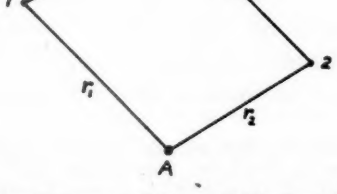

FIG. 1. Coordinates used for a "tritium molecule." The triton is at A, the other hydrogen nucleus at B. The electrons are at 1 and 2.

Let P_0 be the probability that $N_K=0$, P_1 the probability that $N_K=1$, and P_2 the probability that $N_K=2$. It is clear that if P_K is the total transition probability for K creation,

$$P_K/P_\beta = P_0[P(0)/P_\beta]+P_1[P(1)/P_\beta]. \quad (2)$$

It is not feasible to calculate P_0 directly, but it can be found from P_1 and P_2, since $P_0+P_1+P_2=1$.

The next step is the calculation of P_1 and P_2. Before the beta-disintegration occurs, the two initially present molecular electrons are in the ground state of H_2; we denote their exact wave function by $u^M(\mathbf{r}_1, \mathbf{r}_2)$, where $\mathbf{r}_1$ and $\mathbf{r}_2$ are the position vectors of the electrons. Because the disintegration takes place in a time which is short compared with atomic electron periods, it may be assumed that the wave function of the initial electrons is unchanged by the disintegration. u^M will not, however, be a stationary state wave function for these electrons after the disintegration has taken place. We denote the exact wave functions of the new stationary states by $u_\lambda(\mathbf{r}_1, \mathbf{r}_2)$. They are the solutions of the wave equation of the initial electrons in the new nuclear field, and therefore form a complete orthonormal set. To determine the probability of occupation of a given stationary state we let

$$u^M(\mathbf{r}_1, \mathbf{r}_2) = \sum_\lambda a_\lambda u_\lambda(\mathbf{r}_1, \mathbf{r}_2).$$

Here λ stands for the six quantum numbers of the two-electron system. We may disregard the spin dependence of the wave functions since only singlet states are involved. Then

$$a_\lambda = \int\int d\tau_1 d\tau_2 u_\lambda^* u^M,$$

and $|a_\lambda|^2$ will be the probability that the state λ is occupied. One of these stationary states will be similar to the He ground state $1s^2$ (both electrons in the He K shell). We denote its exact wave function by $u_{100,100}(\mathbf{r}_1, \mathbf{r}_2)$. Its occupation amplitude is

$$a_{100,100} = \int\int d\tau_1 d\tau_2 u_{100,100}^* u^M. \quad (3)$$

Since u^M and $u_{100,100}$ cannot be determined exactly, we approximate them as follows:[4]

$$u^M \cong C[u^A(\mathbf{r}_1)u^B(\mathbf{r}_2)+u^A(\mathbf{r}_2)u^B(\mathbf{r}_1)],$$

where

$$u^A(\mathbf{r}_\nu)=[1/(\pi)^{\frac{1}{2}}](Z_M/a_0)^{\frac{3}{2}}\exp[-(Z_M/a_0)r_\nu],$$

and

$$u^B(\mathbf{r}_\nu)=[1/(\pi)^{\frac{1}{2}}](Z_M/a_0)^{\frac{3}{2}}\exp[-(Z_M/a_0)s_\nu],$$

with $\nu=1, 2$. The meanings of r_ν and s_ν are as shown in Fig. 1.

$$u_{100,100}\cong u_{100}(\mathbf{r}_1)u_{100}(\mathbf{r}_2),$$

where

$$u_{100}(\mathbf{r}_\nu)=[1/(\pi)^{\frac{1}{2}}](Z'/a_0)^{\frac{3}{2}}\exp[-(Z'/a_0)r_\nu].$$

Here $C=0.586$, $Z_M=1.166$, $Z'=1.688$, and a_0 is the Bohr radius. The integral in (3) may now be evaluated using spherical coordinates, and gives the value

$$P_2=|a_{100,100}|^2=0.37.$$

The calculation of P_1 is much more complicated, because P_1 is the probability that one electron will be in the He K shell, while the other is in any other shell. The calculation of P_1 thus involves the summation of an infinite series; this is accomplished by the use of the closure theorem

$$\sum_{n=1}^{\infty} u_n^*(\mathbf{r}_1)u_n(\mathbf{r}_2)=\delta(\mathbf{r}_1-\mathbf{r}_2).$$

The result is $P_1=0.57$. From these values it follows that $P_0=0.06$. Because of the approximations used, the second decimal places in P_1 and P_2 are in doubt. Hence, the value given for P_0 represents merely the order of magnitude.

We are now in a position to calculate P_K/P_β using (1) and (2). It is important to note that in (1) Z' is the effective nuclear charge appearing in the wave function of the created electron; it will differ from two if the initial electrons exert an appreciable screening effect upon the created electron. If one of the initial electrons is in the He K shell ($N_K=1$), the wave function of the created electron resembles that of a ground state He electron, hence $Z'=1.688$ in this case. If neither of the initial electrons is in the He K shell ($N_K=0$), we can take $Z'=2$. Substituting the appropriate values in (1) and (2), we have

$$P_K/P_\beta=0.24E_\beta^{-\frac{1}{2}}.$$

Taking for E_β the recently published[5] value 16.9 kev, we have

$$P_K/P_\beta=0.0035.$$

It should be noted that the approximations made in these calculations scarcely justify the retention of two significant figures.

The calculation of P_K/P_β for atomic tritium is similar but much simpler, giving the result

$$P_K/P_\beta=0.45E_\beta^{-\frac{1}{2}}.$$

For a bare tritium nucleus P_K/P_β is simply $P(0)/P_\beta$ (see Eq. (2)), which has the value $1.04\,E_\beta^{-\frac{1}{2}}$.

Types of bound electron creation other than the K creation are, of course, possible, but it can be shown that the sum of the transition probabilities for these other processes is much less than P_K. Hence, if P is the total transition probability for beta-disintegration,

$$P\cong P_\beta+P_K=P_\beta(1+P_K/P_\beta).$$

Since P_β is fixed, P is greater for atomic tritium than for molecular tritium; in other words, the lifetime of atomic tritium is less than that of molecular tritium. This, then, is a case in which, according to present theory, the chemical state of a radioactive substance does influence its lifetime.

The author is deeply indebted to Professor A. Nordsieck for his friendly guidance and many valuable suggestions.

[4] L. Pauling and E. B. Wilson, *Introduction to Quantum Mechanics* (McGraw-Hill Book Company, Inc., New York, 1935), pp. 184, 345.

[5] S. Curran, J. Angus, and A. Cockcroft, Nature 302 (1948).

A Note on the Theory of Vibration-Rotation Interaction

RUDOLPH E. LANGER
*Department of Mathematics, University of Wisconsin, Madison, Wisconsin**

(Received November 19, 1948)

Attempts to treat the differential equation for the radial component of the *Eigenfunktion* of a rotating harmonic oscillator by the W.K.B. or alternative methods, have encountered difficulties because of the nature of the equation. The interval from $r=0$ to $r=\infty$, on which the equation has to be considered, includes both a singular point and a turning point. About these points the Stokes' phenomenon is involved, and the elementary asymptotic solutions fail to remain valid. Known theory which is applicable to the equation in intervals which contain such critical points is here called upon to yield an equation for the *Eigenwerte*, and to produce descriptions of the solutions over the complete range of the variable.

I. INTRODUCTION

THE equation for the radial component F of the *Eigenfunktion* of a rotating harmonic oscillator is, with a suitable choice of units and in familiar notation,

$$(d^2F/dr^2)+[(E-V/B_e)-(l(l+1)/r^2)]F=0,^1$$

with

$$V=(\omega^2/4B_e)(r-1)^2.$$

In terms of the symbols

$$\lambda=(E/\omega_e)-\tfrac{1}{2}, \quad \alpha=B_e/\omega_e,$$

it assumes the form

$$(d^2F/dr^2)-[((r-1)^2/4\alpha^2)-(2\lambda+1/2\alpha)+(l(l+1)/r^2)]F=0. \quad (1.1)$$

The value of the constant α is small—generally very small—and Eq. (1.1) therefore involves the "large parameter," $1/\alpha$. The point $r=1$ at which the coefficient of the highest power of this parameter becomes zero in a *turning point* for the equation, and is therefore critical, as is also the point $r=0$ at which the equation is singular. The problem to be considered is that of determining the characteristic λ-values for which the equation admits of a solution that vanishes both at $r=0$ and at $r=\infty$, and of describing the characteristic solutions which have that property.[2]

II. THE SOLUTION AROUND $r=0$

Since the function sought is to vanish at $r=0$, we begin by a consideration of Eq. (1.1) in an interval abutting this point. At $r=0$ the equation is singular (except when $l=0$) and has the exponents $(l+1)$ and $-l$. A solution of the type sought thus always exists, and is unique except for an arbitrary multiplicative factor independent of r.

* This paper was written while the author was on research leave under a grant from the Wisconsin Alumni Research Foundation.

[1] Cf. J. E. Rosenthal and L. Motz, "Application of a new mathematical method to vibration rotation interaction," Proc. Nat. Acad. Sci. **23**, 259–265 (1937). We have chosen to depart from the notation of this paper by writing r and l in the place of ρ and J, in order to avoid a later confusion of symbols.

[2] This paper was written after a reading of that by Rosenthal and Motz cited in reference 1. The authors of that paper attempted the solution of the problem here considered by a procedure which may be briefly described as follows: With v any non-negative integer, the function Y is taken to be a solution of the equation

$$(d^2Y/dr^2)-\{((r-1)^2/4\alpha^2)-(2v+1/2\alpha)\}Y=0,$$

which vanishes at $r=\infty$. The differences $(\lambda-v)$ and $(\log F-\log Y)$ are then assumed to be expressible as power series in α. Recurrence formulas for the coefficients of these series are obtained by substituting the assumed forms of λ and F into Eq. (1.1), and by taking suitable regard of the boundary conditions the coefficients are formally determined. The calculations are laborious and, unfortunately, generally futile, since the results are divergent by virtue of their involving infinite discontinuities. No reason is advanced to support any presumption that the method ever yields a usuable result, for even in the exceptional case in which the most glaring cause of failure does not manifest itself, only formal manipulations are described and no consideration is given to the rather essential matter of validity. That such a method of attack upon this problem was foredoomed to failure might well have been predicted. For, in the first place, the comparison of a solution F of an equation which is singular at $r=0$ with a solution Y of a non-singular equation might well have been appraised as unpromising. In the second place, asymptotic representations, such as the assumed power series in α would in this case be, familiarly fail to maintain their validity over intervals that contain a turning point. In the light of these facts, the title of the paper in question might well be regarded as a bit naive, rather bombastic, and, what is worst, wholly misleading.

Equation (1.1) near $r=0$ is of a type which has been considered by the author, and for which the forms of the solutions are accordingly known.[3] As it stands the equation is not of the normal form assumed in (L. '35). It may be normalized, however, by the change of variables

$$r=z^2/4, \quad F=z^{\frac{1}{2}}u, \tag{2.1}$$

which gives it the form

$$(d^2u/dz^2)+\{(z^2[(1-z^2/4)^2-2\alpha(2\lambda+1)]/-16\alpha^2) +(\tfrac{1}{4}-(2l+1)^2/z^2)\}u=0. \tag{2.2}$$

It is then of the type

$$(d^2u/dz^2)+\{\rho^2\varphi^2+(\tfrac{1}{4}-A^2/z^2)\}u=0,$$

which is basic to (L. '35), and conforms to it with

$$\begin{aligned}&\rho=i/4\alpha,\\ &\varphi=z\{(1-(z^2/4))^2-2\alpha(2\lambda+1)\}^{\frac{1}{2}},\\ &\mu=\tfrac{1}{4},\\ &\beta=l+\tfrac{1}{2}.\end{aligned} \tag{2.3}$$

It is an essential hypothesis of (L. '35) that the function φ be bounded from zero except near $z=0$ on the interval concerned. This restricts the interval in the present instance to exclude the points at which

$$(1-(z^2/4))^2-2\alpha(2\lambda+1)=0,$$

namely, the points $r=1\pm(2\alpha(2\lambda+1))^{\frac{1}{2}}$. The results which may be taken from (L. '35) are accordingly valid for r on a range

$$0\leqq r\leqq b, \text{ with } b<1-(2\alpha(2\lambda+1))^{\frac{1}{2}}. \tag{2.4}$$

In terms of the functions

$$\xi=\rho\int_0^z\varphi dz,$$

namely, in this case,

$$\xi=(i/2\alpha)\int_0^r\{(1-r)^2-2\alpha(2\lambda+1)\}^{\frac{1}{2}}dr, \tag{2.5}$$

the paper (L. '35) describes a solution u_1 of Eq. (2.2), which vanishes at $z=0$, by the formulas

$$u_1=(\xi^{\beta+\frac{1}{2}}/\rho^{\frac{1}{4}}\varphi^{\frac{1}{4}})\{\xi^{-\beta}J_\beta(\xi)+(\xi/\rho)O(1)\}, \tag{2.6}$$

when $|\xi|$ is small or of moderate magnitude, and

$$u_1=(1/\rho^{\frac{1}{4}}\varphi^{\frac{1}{4}})\{c_1e^{i\xi}[1]+c_2e^{-i\xi}[1]\}, \tag{2.7}$$

when $|\xi|$ is large. As usual J_β denotes here the Bessel function of the first kind of the order β. The symbol $O(1)$ stands for a bounded function of r and ρ, and $[x]$ is intended to denote a quantity which differs from x by at most terms of the order of $1/\xi$ or of the order of $(\log\rho)/\rho$. When $\arg z=0$, as is the case when r is on the interval (2.4), the coefficients to be used in the formula (2.7) are

$$\begin{aligned}c_1&=(1/(2\pi)^{\frac{1}{2}})\exp(-(\beta+\tfrac{1}{2})\pi i/2),\\ c_2&=(1/(2\pi)^{\frac{1}{2}})\exp((\beta+\tfrac{1}{2})\pi i/2).\end{aligned}$$

The formula (2.7) is explicit only to terms of the order of $(\log\rho)/\rho$, which means in the present instance terms of the order of $\alpha\log\alpha$. It is, therefore, clearly useless to retain in the symbols involved by it any terms of the order of α or its higher powers. We may therefore use as appropriate equivalents the following:

$$\begin{aligned}&\varphi\sim z(1-r),\\ &\xi\sim i\{(1-(1-r)^2/4\alpha)+(\lambda+\tfrac{1}{2})\log(1-r)\},\\ &(\xi/\rho)\sim\{1-(1-r)^2\}.\end{aligned} \tag{2.8}$$

The formula (2.7) thus becomes

$$\begin{aligned}z^{\frac{1}{2}}u_1=&(\exp((l+1)\pi i/2)/(2\pi)^{\frac{1}{2}}\rho^{\frac{1}{4}})\\ &\times\{(-1)^{l+1}(1-r)^{-\lambda-1}\\ &\times\exp(-1-(1-r)^2/4\alpha)[1]\\ &+(1-r)^\lambda\exp(1-(1-r)^2/4\alpha)[1]\}.\end{aligned} \tag{2.9}$$

III. THE SOLUTION AROUND $r=1$

On an interval containing the turning point $r=1$, Eq. (1.1) is of the form

$$(d^2F/dr^2)-\{\sigma^2\chi_0+\sigma\chi_1+\chi_2\}F=0, \tag{3.1}$$

with

$$\begin{aligned}&\sigma=1/\alpha, \quad \chi_0=r-1/2, \quad \chi_1=-(\lambda+\tfrac{1}{2}),\\ &\chi_2=l(l+1)/r^2.\end{aligned} \tag{3.2}$$

This is again a type which has been considered by the author, and for which the forms of the solutions are known.[4] The equation is normal,

[3] R. E. Langer, "On the asymptotic solutions of ordinary differential equations, with reference to the Stokes' phenomenon about a singular point," Trans. Am. Math. Soc. **37**, 397–416 (1935). We shall refer to this paper briefly by the notation (L. '35).

[4] R. E. Langer, "The asymptotic solutions of certain linear ordinary differential equations of the second order," Trans. Am. Math. Soc. **36**, 90–106 (1934). We shall refer to this paper briefly by the notation (L. '34).

as that is defined in (L. '34), and for it

$$k=(\lambda/2)+\tfrac{1}{4},\quad \varphi=(r-1),\quad \xi=(r-1)^2/2\alpha,$$
$$\theta=l(l+1)/r^{2}.^{5} \tag{3.3}$$

It is supposed in (L. '34) that the interval in question is one upon which the function

$$\int|(\theta/\varphi)|\,dr$$

is bounded except near $r=1$. This is readily seen to exclude the point $r=0$ in the present case, but to impose no other condition. We may therefore take r in this section to have a range

$$\alpha\leqq r<\infty,\ \text{with}\ 0<a<b. \tag{3.4}$$

A solution of Eq. (1.1) which vanishes at $r=\infty$ is denoted in (L. '34) by $u_{0,2}$. For values of r such that $(r-1)$ is positive and sufficiently large, the form of this solution is given as

$$u_{0,2}=(1/\sigma^{\frac{1}{2}}\varphi^{\frac{1}{2}})\xi^{k}\exp(-\tfrac{1}{2}\xi)[1],$$

namely, in terms of the original variables as

$$u_{0,2}=(1/\sigma^{\frac{1}{2}}(2\alpha)^{k})(r-1)^{\lambda}\times\exp(-(r-1)^{2}/4\alpha)[1]. \tag{3.5}$$

For values of r near the turning point this solution is given to be of the form

$$u_{0,2}=(1/\sigma^{\frac{1}{2}}\varphi^{\frac{1}{2}})\{(\Gamma(-\tfrac{1}{2})/\Gamma(\tfrac{1}{4}-k))M_{k,1/4}(\xi)+(\Gamma(\tfrac{1}{2})/\Gamma(\tfrac{3}{4}-k))M_{k,-1/4}(\xi)\}+\log\sigma/\sigma O(1),$$

with $M_{k,\pm 1/4}$ designating the confluent hypergeometric function usually so denoted.[6] By use of the gamma-function relations

$$\begin{aligned}&\Gamma(\tfrac{1}{2})=(\pi)^{\frac{1}{2}},\quad \Gamma(-\tfrac{1}{2})=-2(\pi)^{\frac{1}{2}},\\ &\Gamma(x)\Gamma(1-x)=\pi/\sin\pi x,\\ &\Gamma(x)\Gamma(\tfrac{1}{2}+x)=(\pi)^{\frac{1}{2}}2^{1-2x}\Gamma(2x),^{7}\end{aligned} \tag{3.6}$$

and, in terms of the original variables, it is thus found that near the turning point

$$u_{0,2}=(1/(\pi)^{\frac{1}{2}}\sigma^{\frac{1}{2}}(r-1)^{\frac{1}{2}})\times\{2\sin(\lambda\pi/2)\Gamma(\lambda/2+1)M_{k,1/4}((r-1)^{2}/2\alpha)+\cos(\lambda\pi/2)\Gamma(\lambda+1/2)M_{k,-1/4}((r-1)^{2}/2\alpha)\}+\alpha\log\alpha O(1). \tag{3.7}$$

When r is on the interval (3.4), but $r<1$, the relation $(r-1)=(1-r)\exp(\pi i)$ gives

$$\varphi=(1-r)\exp(\pi i)$$

and

$$\xi=(1-r)^{2}/2\alpha\exp(2\pi i). \tag{3.8}$$

Accordingly, $\arg\xi=2\pi$, and for values of r not too near $r=1$ it is then given that

$$u_{0,2}=1/\sigma^{\frac{1}{2}}\varphi^{\frac{1}{2}}\{[A_{2,1}{}^{(0,1)}]\xi^{-k}\exp(\tfrac{1}{2}\xi)+[A_{2,2}{}^{(0,1)}]\xi^{k}\exp(-\tfrac{1}{2}\xi)\},$$

with

$$A_{2,1}{}^{(0,1)}=-\pi\{(-i\exp(2k\pi i)/\Gamma(\tfrac{1}{4}-k)\Gamma(\tfrac{3}{4}-k))-(i\exp(2k\pi i)/\Gamma(\tfrac{3}{4}-k)\Gamma(\tfrac{1}{4}-k))\},$$
$$A_{2,2}{}^{(0,1)}=-\pi\{(i\exp(-(k-\tfrac{1}{4})\pi i)/\Gamma(\tfrac{1}{4}-k)\Gamma(\tfrac{3}{4}+k)-(i\exp(-(k+\tfrac{1}{4})\pi i)/\Gamma(\tfrac{3}{4}-k)\Gamma(\tfrac{1}{4}+k))\}.$$

These latter evaluations are easily reduced by means of the relations (3.6), and are thus found to be

$$A_{2,1}{}^{(0,1)}=\frac{\exp((2k-\tfrac{1}{2})\pi i)\sin(2k-\tfrac{1}{2})\pi\Gamma(2k+\tfrac{1}{2})}{(\pi)^{\frac{1}{2}}2^{2k-\frac{1}{2}}},$$

$$A_{2,2}{}^{(0,1)}=1.$$

In terms of the original variables, therefore,

$$u_{0,2}=\frac{\exp(-(1/4\alpha)+\lambda\pi i)}{\sigma^{\frac{1}{2}}(2\alpha)^{k}}\{-(2/\pi)^{\frac{1}{2}}\alpha^{\lambda+\frac{1}{2}}\times\exp((1/2\alpha)-\lambda\pi i)\Gamma(\lambda+1)[\sin\lambda\pi]\times(1-r)^{-\lambda-1}\exp(-1-(1-r)^{2}/4\alpha)+(1-r)^{\lambda}\exp(1-(1-r)^{2}/4\alpha)[1]\}. \tag{3.9}$$

IV. THE CHARACTERISTIC VALUES AND FUNCTIONS

Formulas (2.9) and (3.9) are both valid between 0 and 1 on the interval $a\leqq r\leqq b$. They

---

[5] It will be observed that certain symbols have here a meaning which is different from that which was assigned them in Section II. No confusion need arise from this, since the results are to be expressed promptly in terms of the original variables.

[6] Cf. E. T. Whittaker and G. N. Watson, *A Course in Modern Analysis* (Cambridge University Press, London, 1927), fourth edition, p. 337.

[7] Cf. N. Nielsen, *Handbuch der Theorie der Gammafunktion* (B. G. Teubner, Leipzig, 1906), pp. 14, 19.

describe, respectively, solutions which vanish at $r=0$ and at $r=\infty$. These solutions must be multiples of each other if the equation is to admit a characteristic solution (Eigenfunktion). This will evidently be so if and only if

$$(-1)^{l+1}=-(2/\pi)^{\frac{1}{2}}\alpha^{\lambda+\frac{1}{2}} \times\exp(1/2\alpha+\lambda\pi i)\Gamma(\lambda+1)[\sin\lambda\pi],$$

namely, if

$$[\sin\lambda\pi]=(\pi/2)^{\frac{1}{2}} \times((-1)^{l}\exp(\lambda\pi i)/\Gamma(\lambda+1)\alpha^{\lambda+\frac{1}{2}}\exp(1/2\alpha)). \quad (4.1)$$

This is, therefore, the characteristic equation whose roots are the λ-Eigenwerte.

The left-hand member of Eq. (4.1) stands for a quantity which differs from $\sin\lambda\pi$ by a term of at most the order of $\alpha\log\alpha$. Since (at least for moderate values of λ) the right-hand member is small relative to $\alpha\log\alpha$, Eq. (4.1) can be assured to give only the result

$$\sin\lambda\pi=O(\alpha\log\alpha).$$

The characteristic values thus differ from integers by terms of at most the order of $\alpha\log\alpha$, namely,

$$\lambda=v+O(\alpha\log\alpha), \quad (4.2)$$

with v an integer.

Let us designate the characteristic solution by F. It is a multiple of the function $z^{\frac{1}{2}}u_1$, of Section II, and likewise of $u_{0,2}$ of Section III. If, for convenience, we determine it by the relation

$$F=\rho^{-(\beta+\frac{1}{2})}z^{\frac{1}{2}}u_1, \quad (4.3)$$

formula (2.6) shows it to have, for values of r near $r=0$, the form

$$F=(\{1-(1-r)^2\}^{l+1}/(1-r)^{\frac{1}{2}})\{\xi^{-(l+\frac{1}{2})}J_{l+\frac{1}{2}}(\xi) +\{1-(1-r)^2\}O(1)\}, \quad (4.4)$$

with ξ as given in Section II. Although this value of ξ is purely imaginary, the term $\xi^{-(l+\frac{1}{2})}J_{l+\frac{1}{2}}(\xi)$ is real. It may be written alternatively as $|\xi|^{-(l+\frac{1}{2})}I_{l+\frac{1}{2}}(|\xi|)$. For values of r between 0 and 1, but not too near either 0 or 1, the form as obtained from (2.9) is

$$F=((4\alpha)^{l+1}/(2\pi)^{\frac{1}{2}})\{(-1)^{l+1}(1-r)^{-\lambda-1} \times\exp(-1-(1-r)^2/4\alpha)[1] +(1-r)^{\lambda}\exp(1-(1-r)^2/4\alpha)[1]\}. \quad (4.5)$$

The relation between F and $u_{0,2}$ is easily determined from (4.3) and a comparison of formulas (2.9) and (3.9). It is thus found that

$$F=((4\alpha)^{l+1}(2\alpha)^{k}\exp(1/4\alpha-\lambda\pi i)/(2\pi)^{\frac{1}{2}})u_{0,2}.$$

In accordance with (4.2) we may use in this the evaluation

$$\exp(-\lambda\pi i)=(-1)^{v}[1].$$

The formula (3.7) thus shows that for values of r near $r=1$

$$F=((-1)^{v}(4\alpha)^{l+1}(2\alpha)^{k}e^{1/4\alpha}/\pi\sqrt{2}) \times\{2\sin(\lambda\pi/2)\Gamma(\lambda/2+1)M_{k,1/4}((r-1)^2/2\alpha) +\cos(\lambda\pi/2)\Gamma(\lambda+1/2) \times M_{k,-1/4}((r-1)^2/2\alpha)+O(\alpha^{\frac{1}{2}}\log\alpha)\}, \quad (4.6)$$

with $k=\lambda/2+\frac{1}{4}$. Finally, for values of r that are larger than 1 and not too near 1, the formula (3.5) shows that

$$F=((-1)^{v}(4\alpha)^{l+1}e^{1/4\alpha}/(2\pi)^{\frac{1}{2}})(r-1)^{\lambda} \times\exp(-(r-1)^2/4\alpha)[1]. \quad (4.7)$$

PHYSICAL REVIEW VOLUME 75, NUMBER 5 MARCH 1, 1949

The Detection of Gamma-Rays with Thallium-Activated Sodium Iodide Crystals*

ROBERT HOFSTADTER
Palmer Physical Laboratory, Princeton University, Princeton, New Jersey
(Received September 27, 1948)

Thallium-activated sodium iodide crystals may be used as efficient detectors of gamma-rays and other ionizing radiations. The crystals are used in combination with a photo-multiplier after the manner of Kallmann. Curves are given which show the duration of the light emission process, the distribution of light pulse sizes, the energy discrimination possibilities, and the dependence of number of counting events on photo-multiplier voltage and amplifier gain. Comparison curves are shown for NaI(Tl) and anthracene. A description is given of the method of preparation of polycrystalline samples and single crystal specimens of the sodium iodide-thallium phosphor. A few remarks are made concerning the combination of alkali halide phosphor crystals with photographic plates.

I. INTRODUCTION

THE detection of beta-particles and gamma-rays by the combination of a luminescent crystal (phosphor) and a photo-multiplier vacuum tube has been successfully demonstrated by many investigators.[1–6] The earliest work in which large crystalline samples were used was performed by H. Kallmann.[1] Kallmann showed that large clear pieces of napththalene produced measurable scintillations when exposed to gamma- and beta-radiation from radium. Other luminescent materials have since been reported in the literature. Among these are anthracene,[5] calcium tungstate,[6] phenanthrene,** and others.

Since present-day photo-multiplier tubes have a serious "noise" background at room temperature,[7] it is important that the phosphor provide as large a light flash as possible. Other important properties of a useful phosphor are: the spectrum of the light flash, the duration and rise of the light pulse, the material density, and, finally, the chemical composition of the phosphor. The magnitude (and spectrum) and duration of the light flash are of special significance since these properties determine the signal to noise ratio.

Amplified noise pulses are, unfortunately, not small compared with light flashes in naphthalene, calcium tungstate, and anthracene. Consequently, there are important advantages in cooling the photo-multiplier tube to low temperatures at which the frequency of occurrence of noise pulses becomes insignificant compared with the signal. On the other hand, the experimental difficulties in cooling the tube may prove to be a disadvantage in some experiments.

Of those phosphors mentioned above, anthracene produces relatively large light flashes[5] in short times[8] (~0.05-microsecond duration) and matches, in its emission, the region of high spectral sensitivity of the 931 or 1P21 photo-multiplier tubes. With respect to the remaining above-mentioned characteristics of useful phosphors, anthracene has a small density (1.25 g/cm³) and is composed of elements of low atomic number (1, 6). Anthracene light flashes for, say, 1.0-Mev gamma-rays are not many times the size of photo-multiplier noise pulses, and, for a reason not yet understood, it appears that heavy particle pulses produce smaller scintillations than beta-particles of equivalent energy.[5] It is, therefore desirable to search further for a phosphor, more dense than anthracene, having constituents of higher atomic number, which provides larger light flashes than anthracene. It would also be desirable if such a phosphor would give large light flashes for heavy particles, such as alpha-particles. At the present time no phosphor has been reported which can be ob-

* The major part of these results was presented at a recent conference (July, 1948), on high speed counters, at the University of Rochester.
[1] H. Kallmann, Natur and Technik (July, 1947).
[2] J. W. Coltman and F. H. Marshall, Phys. Rev. **72**, 528 (1947).
[3] M. Deutsch, Nucleonics **2**, 58 (1948).
[4] G. B. Collins and R. C. Hoyt, Phys. Rev. **73**, 1259 (1948).
[5] P. R. Bell, Phys. Rev. **73**, 1405 (1948).
[6] R. J. Moon, Phys. Rev. **73**, 1210 (1948).
** M. Deutsch: Rochester Conference.
[7] R. W. Engstrom, J. Opt. Soc. Am. **37**, 420 (1947).
[8] L. F. Wouters, Phys. Rev. **74**, 489 (1948); G. B. Collins, Phys. Rev. **74**, 1543 (1948).

tained in large crystals, and which possesses the desirable characteristics discussed above.

It is the purpose of this article to present some of the properties of a material which is an efficient phosphor for alpha-, beta-, and gamma-radiations.[9] It has been found that sodium iodide, with a small thallium iodide impurity, possesses many desirable properties of a radiation detector. In the case of NaI(Tl) the light flashes are sufficiently large so that in most instances (e.g., 0.5-Mev gamma-rays) cooling of the photomultiplier is unnecessary. The density of NaI is 3.67 grams/cc, and a medium atomic number ($I=53$) is available in the phosphor. Large clear crystals can be prepared by relatively simple means. These features make the use of NaI(Tl) quite convenient for the counting of gamma- and beta-radiation. It is also true that heavy particle pulses are large. It cannot be said that NaI(Tl) has all the desirable properties of a phosphor which might be used for the general counting and measuring of ionizing radiation, for, as it will be shown, NaI(Tl) is not as fast as the organic phosphor materials. A practical disadvantage of NaI(Tl) is the fact that this material is highly hygroscopic, although this difficulty has been avoided by enclosure of the sample, as will be shown below. In summary, NaI(Tl), in its present form, would seem to be a useful material for alpha-, beta-, and gamma-radiations in those cases where resolving times are not required to be less than one or two microseconds.

In the following sections some experiences have been collected which concern the use of NaI(Tl) as a detector of gamma-rays. Data on the decay of luminescence of sodium iodide will be reported and some observations made on combinations of various phosphors and a photographic plate.

II. GENERAL

R. W. Pohl[10] and his co-workers have studied the alkali halide crystals with thallium impurities. In particular, this group has examined luminescence produced by ultraviolet light and the absorption of light in alkali halide phosphors. Much experimental and theoretical material on such phosphors now exists[11–15] for the significant reason that these phosphors are among the most simple now known. Nevertheless, the exact nature of the short-lived fluorescence is probably not completely understood at the present time. The thallous ion is probably responsible for the observed behavior.

In connection with the material of this paper, the experimental results of W. von Meyeren[16] and R. Hilsch[17] are of interest. These authors have studied the spectral distribution of the emitted fluorescent light, as well as absorption of light by the alkali halide-thallium phosphors. Absorption by the base materials has been studied by R. Hilsch and R. W. Pohl[18] and by E. G. Schneider and H. M. O'Bryan.[19] Unfortunately, NaI(Tl) has not been studied in emission, although its absorption is given by R. Hilsch.[11]

The experimental findings in some of the alkali halides (NaCl, KCl, RbCl, NaBr, KBr, KI) may be summarized in the following way. With a small (0.001 to 0.1 molar percent) thallium impurity these phosphors show luminescence lying in the near ultraviolet, and, in the case of KI, extending into the violet and blue region of the visible spectrum. With larger impurities (0.1 to 5 molar percent) the luminescence spectrum shifts towards the visible region.[12] With very large impurities the luminescent light

FIG. 1. Phosphor tube mounted on photo-multiplier.

[9] R. Hofstadter, Phys. Rev. **74**, 100 (1948).
[10] Bibliography in article by R. Hilsch (11).
[11] R. Hilsch, Proc. Phys. Soc. London **49**, extra part, 40 (1937).
[12] P. Pringsheim, Rev. Mod. Phys. **14**, 132 (1942).
[13] J. T. Randall and M. H. F. Wilkins, Proc. Roy. Soc. **184A**, 366 (1945).
[14] F. Seitz, J. Chem. Phys. **6**, 150 (1937).
[15] N. F. Mott and R. W. Gurney, *Electronic Processes in Ionic Crystals* (Oxford University Press, London, 1940), p. 224.
[16] W. von Meyeren, Zeits. f. Physik **61**, 329 (1930).
[17] R. Hilsch, Zeits. f. Physik **44**, 860 (1927).
[18] R. Hilsch and R. W. Pohl, Zeits. f. Physik **59**, 812 (1930).
[19] E. G. Schneider and H. M. O'Bryan, Phys. Rev. **51**, 293 (1937).

FIG. 2. Active region of tube of Fig. 1.

tends to be white. The time decay of the luminescent process varies also with the amount and kind of added impurity. There is a tendency to show a greater phosphorescent component as the amount of impurity increases. The above-mentioned emission of light is produced by stimulation by ultraviolet light lying in the absorption band or bands of the phosphors. The emitted light produced by ionizing radiation is probably, but not necessarily, the same as that produced by ultraviolet light.

The absorption of light by the alkali halide-thallium phosphors generally consists of the absorption by the base material in addition to the specific absorption bands introduced by the added impurity. The impurity absorption bands lie just beyond the emission bands on the side of shorter wave-lengths. It is fortunate that there is little overlap, and this fact makes the alkali halide phosphors quite transparent to their own fluorescent radiation. As an example, KI(Tl) absorbs in bands at 2870A and 2360A, whereas the emitted light (under ultraviolet excitation) extends from 3200A to 5000A. Such results have been stated for room temperature conditions. The emission of light has also been studied at temperatures above and below room temperature.[16] In the case of NaI(Tl), the absorption bands lie at 2930A and 2340A. The absorption of longer wave-lengths extends as far as 3200A.

Not much seems to be known of the period of decay of fluorescence in the thallium-activated alkali halide phosphors, although W. Bunger and W. Flechsig[20] have studied KCl with TlCl impurity and have found a decay at least as fast as 50 microseconds. W. Bunger[21] has observed high quantum efficiencies, of the order of 50 to 80 percent in KCl(Tl) phosphors, under excitation by ultraviolet light.

[20] W. Bunger and W. Flechsig, Zeits. f. Physik **67**, 42 (1931).
[21] W. Bunger, Zeits. f. Physik **66**, 311 (1930).

III. EXPERIMENTAL

A. Apparatus

In these experiments the photo-multiplier was mounted in a tube socket, on a small brass frame, within a light-tight galvanized iron box of $\frac{1}{32}$-inch wall thickness. The phosphor was enclosed in a quartz tube of $\frac{9}{16}$-in. outside diameter and 1-mm wall thickness. The quartz tube was placed, in a horizontal position, in contact with the photo-multiplier envelope. To prevent motion of the quartz tube, a length of adhesive tape was wrapped around the quartz tube and photo-multiplier envelope. A thin aluminum foil was placed between the sticky side of the tape and the quartz tube. In this way the phosphor tube could be removed easily and replaced easily. The aluminum foil also served as a reflector of light. Figure 1 shows the type of mounting used.

In the experiments to be described, the photo-multiplier was supplied with a stabilized negative voltage at the cathode. The anode load resistance was usually 0.1 megohm, although in some tests a 10.0-megohm resistance was employed. The combined capacitance of photo-multiplier output and amplifier input was 20 to 30 micromicrofarads. The time constant of the photo-multiplier output circuit was therefore of the order of two or three microseconds except in those cases where the 10.0-megohm load was used. The voltage divider supplying the dynodes was made up of resistances of value 33 kilo-ohms each. The anode circuit of the photo-multiplier was connected with a small lead directly to a preamplifier.

The amplifier used in most of these experiments has been the "Model 501" amplifier, designed by W. C. Elmore. It consists of a preamplifier, mentioned above, and a separate chassis containing the remaining amplifying stages and power supply. The rise time of this amplifier is about 0.15 microsecond, and the gain is about 300,000. In order to see the shape and beginning of light pulses, a Sickles delay line has been employed with delay time of one microsecond and rise time about 0.25 microsecond.***

The Model 501 amplifier has two equivalent cathode follower outputs. When counting pulses,

*** The technique employed is similar to that described in an article by W. C. Elmore, Nucleonics **2**, 16 (March 1948).

one output was brought to the scaling unit through a "T" fitting and a coaxial cable. Another cable led from the "T" fitting and was brought to an oscilloscope for routine examination of pulses while counting. The second cathode follower output was not used when such counting was studied. When the photographic studies of the rise time of pulses were made, the cable leading to the scaling unit was removed, and the short cable to the oscilloscope was the only output connection of the amplifier. The photographic studies of pulse shapes were made with the "laboratory oscilloscope" of the type described by Fitch and Titteron.[22] In other experiments, the second output was brought to a slave-sweep circuit (Model "260," designed by M. Sands) which permitted the use of a conventional oscilloscope for pulse observation.

The pulses were counted by a discriminator-scaling unit designed by M. Sands. This unit, called the "ten-channel discriminator," has ten channels into which all the incoming pulses from the amplifier are sorted. The pulses are counted in channels according to their height. For example, when 5-volt channels are used. channel 1 selects pulses from 5 to 10 volts. Channel 2 selects pulses from 10–15 volts, and so on. Channel 10 is a "surplus" channel and registers all pulses not already recorded by the other nine channels. A totalizer is available which counts all the pulses received. A cross check is therefore available to see that counts have not been missed. The totalizer is a scale of 32, the 9 channels are scales of 8, and the surplus channel is a scale of 16. A "sliding pulser," designed by M. Sands and W. A. Higinbotham, was also used to check the voltage width of the channels.

B. Preparation of the Phosphors

Most of the NaI(Tl) samples are prepared in the following way. Ten grams of NaI reagent (Baker and Adamson) are funneled into a half-inch quartz tube (closed at the lower end) to a depth of two or three inches. A constriction in the quartz tube, above the level of the NaI powder, permits subsequent sealing off of the sample while under vacuum. The quartz tube is connected to a "Hyvac" pump through a length of rubber hose and evacuated. The powder shows a tendency to "bump" and may travel rapidly throughout the vacuum system. To prevent this, a pad of glass wool is placed between the constriction and the end of the quartz tube, adjacent to the rubber hose. After evacuation, the quartz tube and contents are heated by a gas-air flame until the powder melts at about 650°C, at which the liquid NaI is pale yellow. The flame is then withdrawn and the melt allowed to cool directly. During cooling, the NaI crystals are formed and may be one or a few millimeters on a side. These crystals may be faintly luminescent. A discharge in the quartz tube, produced by the conventional "leak tester," is a good indicator of the luminescence of the phosphor. The tube is now taken away from the hose, opened to air, and 100 milligrams of Tl dropped into the tube. It is replaced on the vacuum system after the glass wool has been removed and discarded. The quartz tube and contents are reheated to melt the NaI and to mix the TlI with the NaI. After cooling and crystallization of the mixture, bright blue luminescence of the crystals can be observed with the leak tester discharge. The tube may now be sealed off for use.

Useful samples have also been made by mixing the two powders and employing a single heating process. It is probable that this method is equivalent to that described above. However, the most successful specimens were made by the process involving two meltings.

A good specimen is not always produced. The reason for this is not understood, although it is suspected that impurities, overheating, or too rapid heating before water vapor is removed may be responsible for the poorer specimens. The

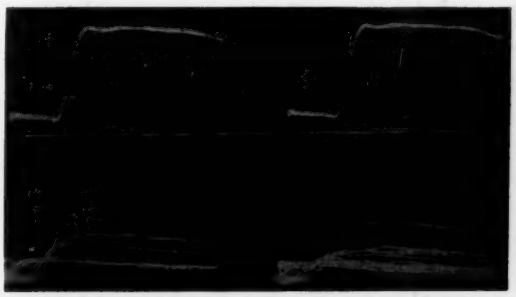

FIG. 3. "Pulser" pulses (above) and NaI(Tl) pulses (below).

[22] V. L. Fitch and E. W. Titterton, Rev. Sci. Inst. 18, 821 (1947).

poorer specimens are generally gray while the best specimens are clearer and white.

Single crystals have been prepared with surprising ease by taking the tubes as described, but with conical lower ends, suspending them in a furnace by a hook and wire, and then lowering slowly with a gear train and motor. This method of crystal formation, originally proposed by Bridgman, usually produces several large crystals. Such crystals are extremely efficient phosphors. For example, one specimen, containing about 4 grams, was made in the form of a few large crystals, one being quite large, of the order of a centimeter on one side. Even though the quartz tube was clouded by the heating process and the crystal was oblique to the walls, this specimen produced almost as many counts and nearly the same light output as a mass of 10 grams of small crystals when each tube was exposed to radium gamma-rays under the same conditions. Larger single crystal samples have been successfully grown in one-inch quartz tubes. The inner surface of such tubes apparently becomes etched in the process, and the output of light from these specimens is probably not as high as one might obtain if the surface remained clear. Large crystal specimens have been removed from the quartz tubes but rapidly "frost up" and become yellow in a humid atmosphere. Undoubtedly more successful results will be obtained when methods are developed for protecting the crystal surfaces from water vapor.

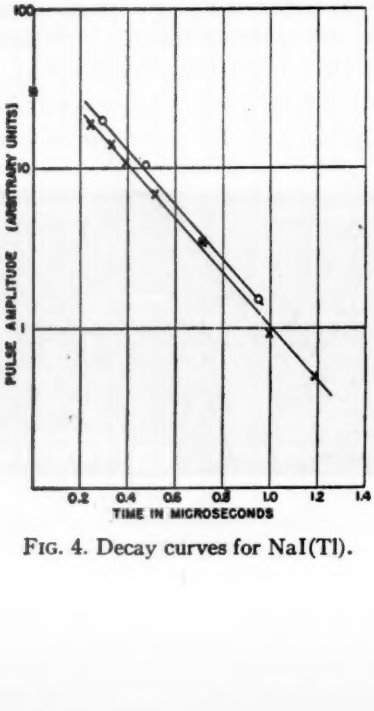

FIG. 4. Decay curves for NaI(Tl).

Figure 2 shows the active end of the first prepared phosphor tube of polycrystalline NaI(Tl). Examination of tube contents shows that the clear crystal region extends about two or three millimeters from the inside wall. Inside this region the material is more like coarse granular powder. Shorter specimens of the polycrystalline material have been prepared in tubes which, when sealed off, are 2.75 inches long.

Rough experiments have been made to find the most desirable amount of impurity. Specimens made by adding one percent of TlI seem to give the best results. Samples made with 200 mg, 50 mg, and 20 mg of TlI to 10 grams of NaI do not seem to provide as much light output as those made with 100 mg of TlI, although active samples have been prepared with as little as 0.02 percent TlI. However, the method by which these samples were made does not insure that the actual impurity content of the crystals is that determined by the amount added. The formation of gray crystals is different in different specimens and may also influence the reported findings. It has been found, however, that the single crystals are always "water white" and clear, thus indicating that the crystal is most satisfactorily prepared in a furnace under controlled temperature conditions. The torching method is probably not more than an expedient to obtain samples quickly. Counting samples have also been made with TlCl and TlBr.

IV. RESULTS

A. Counting Studies

In this section some data have been collected concerning the use of NaI(Tl) as a material in a scintillation counter. Such data may also be of interest for the theory of ionic crystals, since the alkali halide-thallium phosphors are simple fluorescent systems. Interesting topics are: (1) The duration of the light emission process. (2) The amount of light emitted per incident energy of ionizing radiation. This amount may vary for different particles of the same energy. (3) The sensitivity of the alkali halide scintillation counter in distinguishing different monoenergetic gamma-rays or beta-particles. (4) The spectral distribution of the emitted light. (5) The sensitivity to different radiations, e.g., alpha-particles, protons, neutrons, mesons, etc. (6) Mis-

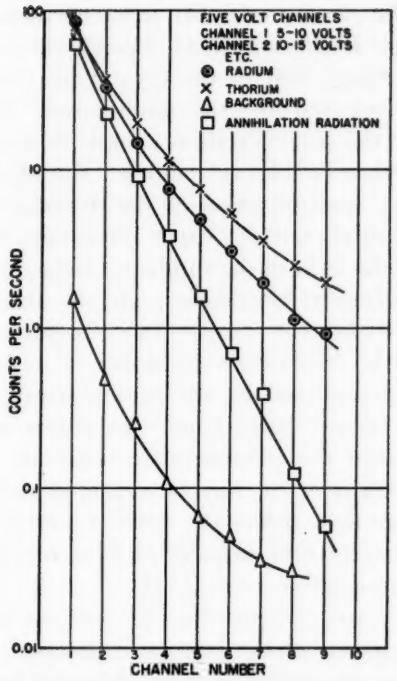

FIG. 5. Differential bias curves showing energy discrimination for various radioactive sources.

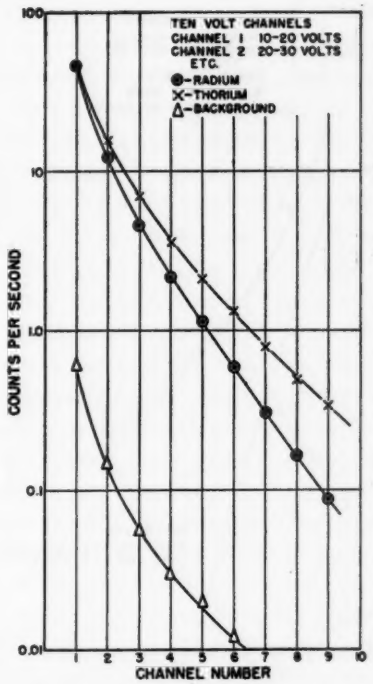

FIG. 6. Differential bias curves with ten-volt channels for radium and thorium sources.

cellaneous tests designed to see whether the alkali halide scintillation counter can serve as a general gamma-ray detector. (7) The "counting efficiency" of the crystal material, i.e., the ratio of the number of counted events to the ionizing flux passing through the crystal material.

It is not possible to present at this time complete information on all these points or on other interesting topics such as temperature effects.† However, a certain amount of information is available on almost all the topics mentioned. The points will be taken up in the above order.

(1) The emission of light, following the ionization produced in the NaI(Tl) phosphor by a gamma-ray encounter with the phosphor, has been studied by photographing the rise of the voltage pulse appearing across the anode load resistor of the photo-multiplier. In this study the anode resistor had a value of 10 megohms. The "clipping" or differentiating time constant of the amplifier was set at 40 microseconds. With this long clipping time, the height of the voltage pulse is proportional to the integral of the light emission curve and, therefore, represents the decay curve of the phosphor. This statement is true only if the phosphor decay time is several times as long as the amplifier-delay line rise time. For these experiments this is, unfortunately, not the case. Therefore, the quantitative studies must be considered, for the present, only as approximate.

To observe the effect of the amplifier-delay rise time, the phosphor pulses were compared with "artificial" repetitive pulses produced by a "Model 100" pulsing circuit. This "pulser" manufactures a step pulse with a rise time considerably smaller than that of the amplifier-delay line combination used in these experiments. Therefore, a pulser voltage pulse shows directly the rise time of amplifier and delay line. Such pulses are shown at the top of Fig. 3. Directly below are shown pulses due to gamma-rays striking the phosphor, with amplifier-delay line characteristics unchanged. The comparison between these photographs permits an approximate estimate of the decay time of the phosphor, as indicated below.

Figure 4 shows two plots which were obtained from the photographs of Fig. 3. The phosphor curves of the two largest pulses were normalized

† W. C. Elmore and R. Hofstadter, Phys. Rev. **75**, 203 (1949).

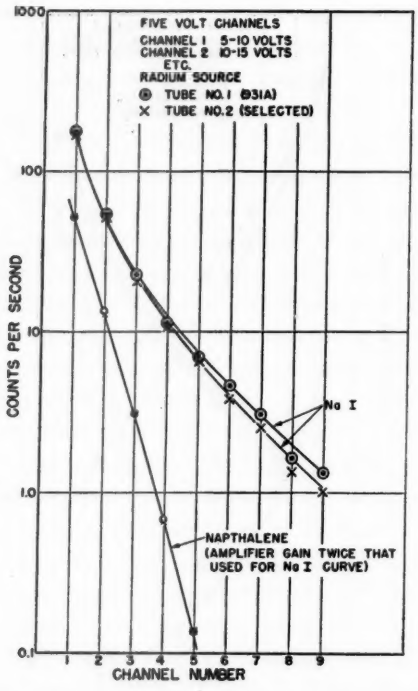

FIG. 7. Behavior obtained with different photo-multiplier tubes: amplifier rise time 0.25 microsecond; clipping time about two microseconds.

to the same maximum value. The differences between points on such normalized curves and the final saturation values of the pulses are the values plotted in the curves of Fig. 4. The figure shows that, except for the first points, both curves are fitted rather well by straight lines on semilog plots. When determined in this way, the time constants of the decays are 0.25 and 0.26 ± 0.05 microsecond. Since the 10–90 percent rise time of the "pulser" pulses is 0.27 microsecond, it can be seen that the values obtained for the phosphor will be only approximate. The phosphor measurements are probably correct to within 25 percent. The light pulse in this NaI(Tl) phosphor sample has a total duration, therefore, of the order of 0.8 microsecond. Although the decays studied appear to be exponential, other types of decay are not ruled out, particularly since only the larger pulses have been available for study.

In the experiments just described the voltage pulses measured were about 1.6 and 2.0 millivolts at the anode of the photo-multiplier.††

(2) The photo-multiplier pulse corresponding to a single ionization event depends on at least: (a) the energy lost in the crystal by the beta-particle released by the gamma-ray, (b) the region in the polycrystalline sample in which the beta-particle is released, and (c) the statistical secondary multiplication in the dynodes of the photo-multiplier. Item (b) is important since it includes the light path, number of reflections and transmissions at boundaries, and the absorption of light within the sample. The amount of light received by the photo-multiplier is, of course, further determined by the optical arrangement used to direct light from the polycrystalline sample into the photosensitive cathode of the photo-multiplier. It may be expected that with very large light pulses the voltage pulses will be proportional to the amount of light received by the photosensitive surface.†††

A very rough figure for the amount of light emitted in one of the large scintillations due to radium gamma-rays may be obtained by comparing the voltage pulses due to gamma-rays and those due to a stimulated phosphorescence in the crystal. Weak phosphorescence may be excited in the phosphor by exposing the phosphor tube to a strong ultraviolet source or by producing a discharge in it with a "leak tester." It may be expected that for weak phosphorescence indi-

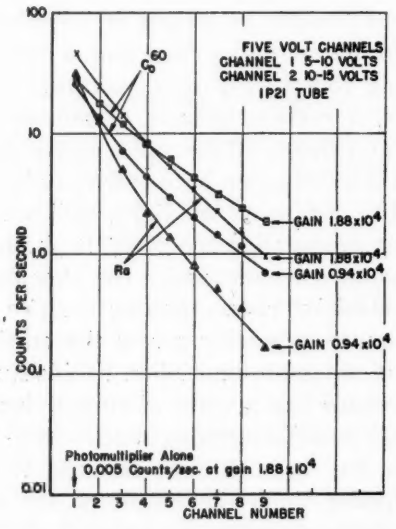

FIG. 8. Counting rates at different amplifier gain settings.

†† Larger pulses are easily obtained by increasing the photo-multiplier voltage. The pulses used are of convenient size in working with the 501 amplifier.

††† At the Rochester conference on high speed counters, Miss Rosalie C. Hoyt presented calculations on such matters.

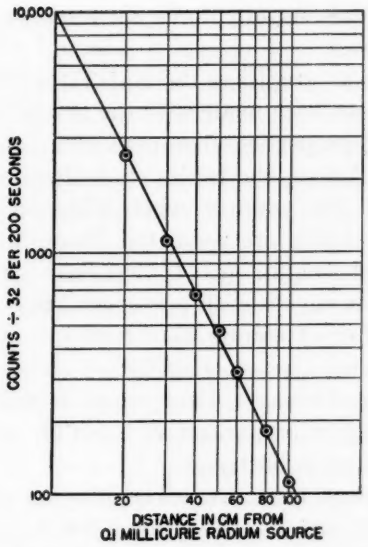

FIG. 9. Test of inverse square law.

vidual photo-multiplier counts will correspond to single electrons emitted at the photo-cathode.

Some of the large pulses due to gamma-rays are of the order of twenty-five or thirty times the height of pulses observed in phosphorescence, when the comparison is made visually on an oscilloscope screen. Since the efficiency of the photosensitive surface of the photo-multiplier lies between two and five percent, the number of photons incident on the photosensitive surface is of the order of one thousand. We may take five or ten percent as a rough estimate of the fraction of light collected by the photo-multiplier to that emitted by the crystal sample. This figure is obtained by estimating the relative aperture. We then obtain a probable figure of from 10,000 to 20,000 photons emitted by NaI(Tl) polycrystals due to an energetic gamma-ray from radium. This figure is probably a lower limit for the number of photons in such a large scintillation. Nevertheless, this figure differs considerably from the value 200,000 photons given by Moon[6] for materials which show smaller light efficiencies than NaI(Tl). It would be desirable to make more accurate determinations of the light yields from such phosphors.

(3) Deutsch[23] has shown that gamma-ray energies can be distinguished in naphthalene counters by means of bias curves, or, in other words, by the distribution pattern of pulse heights. We have shown that energy discrimination is possible with NaI(Tl) scintillations, although care must be exercised in the interpretation of the bias curves. Figure 5 shows differential bias curves taken with the ten-channel discriminator for radium, thorium (oxide), and C^{11} annihilation radiation sources. These curves were taken with channels five volts wide. Figure 6 shows curves for radium and thorium (oxide) with ten-volt channels. It can be seen that the graphs taken with the ten-volt channels show linear behavior at the higher channel numbers. It is also observed that the annihilation radiation graph is practically linear over its whole length. These facts suggest that the behavior in the higher channels may be linear (semilog plot) for homogeneous gamma-rays. The cobalt 60 curves of Fig. 8 are in reasonable agreement with this view.

It can be seen in Fig. 8 that the cobalt 60 curves show smaller slope than the radium curves in the region examined. This is probably connected with the fact that the cobalt radiation is almost homogeneous (1.2 Mev), while the

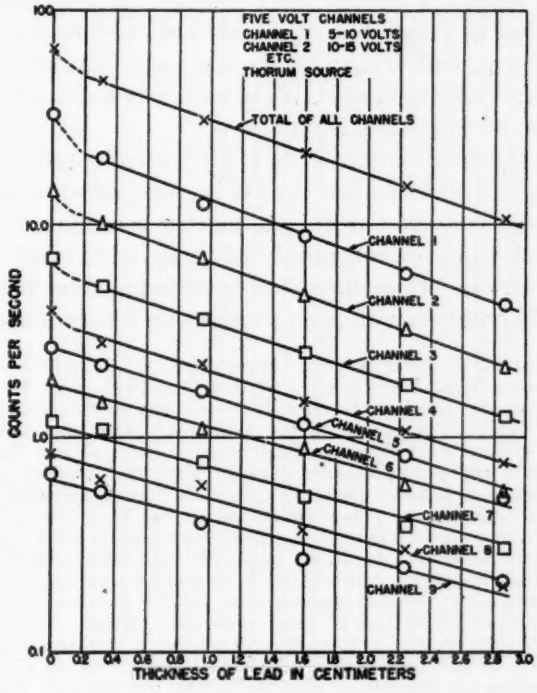

FIG. 10. Lead absorption curves taken with NaI(Tl) counter.

[23] M. Deutsch, Tech. Report No. 3, Laboratory for Nuclear Science and Engineering, M.I.T., December (1947).

TABLE I. Results of absorption measurements.

	Total	*Ch1*	*Ch2*	*Ch3*	*Ch4*	*Ch5*	*Ch6*	*Ch7*	*Ch8*	*Ch9*
Absorption coefficient (cm^{-1})	0.59	0.62	0.61	0.53	0.53	0.53	0.45	0.44	0.47	0.43

radium radiation is complex and has a strong, soft component.

Thus, while the rules of interpretation of these curves are not yet clear, it appears that the scintillation counter shows possibilities of energy discrimination in addition to its normal counting function.††††

(4) By placing a luminescent crystal or polycrystalline sample and radioactive source in front of the slit of a spectrograph, one may obtain a photograph of the spectrum of the light emitted by the sample under bombardment. Such work has been carried on by Mr. J. C. D. Milton and the author and will be reported separately. The results will merely be stated here. The light from NaI(Tl) samples, when exposed to radium gamma-rays, lies in the region 3000A to 4900A with maximum lying between 4050 and 4150A. The width at half-maximum is generally about 800A, and there is some evidence of asymmetry in regions of smaller wave-lengths. The emission band therefore has a considerable visible component. Unfortunately, the spectrum induced by ultraviolet light in NaI(Tl), with which this data can be compared, is unknown.

(5) Scintillations in NaI(Tl) caused by radium alpha-particles have already been reported to be large compared with gamma-ray scintillations, and equal in magnitude to those in ZnS(Ag).[9] There is nothing further to be added at this time. Experiments with other particles such as protons, neutrons, mesons, etc., have not been attempted in any detail.

(6) Various studies of the NaI(Tl) scintillation counter have been made with the aim of learning its general properties when used as a gamma-ray detector. Among the topics studied are: (a) Behavior of the counter when different photomultiplier tubes are used. (b) Photo-multiplier noise background. (c) Comparison of single crystal bias curves with polycrystal bias curves. (d) Number of counts as a function of source distance. (e) Use of scintillation counter with gamma-ray filters. (f) Background with NaI(Tl) counter. (g) Comparison of NaI(Tl) with anthracene and naphthalene.

(a) In these tests a NaI(Tl) phosphor tube was used both with a conventional 931A type and with a selected 931A photo-multiplier. The latter tube is the one used in most (but not all) of the experiments described in this paper. A comparison of the bias curves shown in Fig. 7 shows that the counting behavior is identical within experimental error for these two tubes. The only difference between the two cases rests in the operating voltages. The selected tube required 432 volts and the other tube 478 volts to obtain

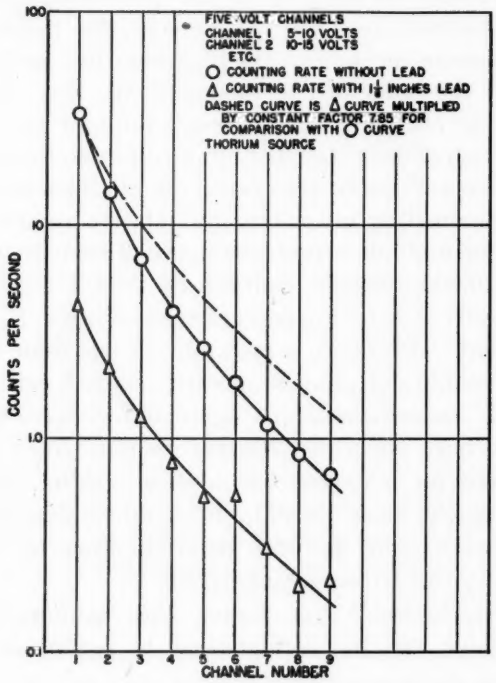

FIG. 11. Comparison of filtered with unfiltered radiation.

†††† *Note added in proof:* Hofstadter, Milton, and McIntyre (Bull. Am. Phys. Soc., No. 1, Jan. 1949, p. 16, E11 and in an article to be published) by using single crystals of NaI(Tl), cemented to the photo-multiplier tube, and a collimated Co^{60} gamma-ray source, have shown: (a) while the polycrystalline curves show the behavior of Figs. 5, 6, 8, 14(a), the single crystal Co^{60} curves show definite maxima in pulse size distributions. This fact will permit improved energy discrimination. Similar work has been carried out by P. R. Bell with anthracene crystals and beta-particle sources. (b) A very close approach to a plateau in counting gamma-rays can be obtained. For example, a variation of photo-multiplier voltage of 80 in 720 volts resulted in a change of 9 percent in total counting rate. It has been estimated that 93 percent of all Co^{60} gamma-ray encounters with the crystal are counted. The newer curves, corresponding to Fig. 14(a) drop almost to zero at higher voltages.

the results of Fig. 7. Curves taken with naphthalene are also shown in Fig. 7. It is perhaps fortuitious that the comparison is as close as has been found, for it is probable that some unselected tubes have equal noise level and lower photosensitivity than the two tubes tested.

(b) The noise level of a 1P21 photo-multiplier tube, with which the data of Fig. 8 were obtained, is too small to show as a curve in this figure. The noise pulses occurred at the rate of 1 pulse per 200 seconds and appeared in the first channel, although an occasional pulse appeared in a higher channel. The bias chosen in these tests might correspond to average operating conditions.

(c) It has already been mentioned above that a small NaI(Tl) sample (~4 grams) in the form of a few large crystals gave results comparable with a larger sample (10 grams) of polycrystalline material. Most of the inside surface of the former "single" crystal tube was frosted in the process of preparation. One clear oval portion, on the wall of the quartz tube, was not attacked. The tube was therefore mounted so that the clear portion faced the sensitive surface of the photo-multiplier. The pulse distributions obtained with this sample and with a polycrystalline sample were examined and found to be identical for equal numbers of counted pulses.††††

(d) If the observed pulses are due to direct transmission of gamma-rays from the source to the crystal specimen, the number of pulses should fall off as the inverse square of the distance. Figure 9 shows the results of making such a test. The background counting rate was subtracted for all points. At the largest distance (100 cm) the background correction amounts to 16 percent. Conformity with the inverse square law is therefor obtained, implying that counting of scattered gamma-rays can at most be a small effect for the bias and photo-multiplier voltages used.

(e) Figures 10 and 11 show the results of tests performed by placing lead absorbers of different thicknesses in front of a thorium source. From Fig. 10 one can calculate absorption coefficients from the straight lines for the different channels. The results are given in Table I.

It may be seen that, although the accuracy is not high, the transition to higher channels corresponds to measuring harder components, a result to be expected. The average value of 0.45 cm^{-1} for the last four channels compares with a calculated value of 0.47 cm^{-1} for the energy 2.62 Mev, which is the well-known thorium line. Considering the accuracy of this experiment, the measured result is in satisfactory agreement with the calculated value.

The curves of channels 1 to 4 show deviations from straight lines for zero absorber thickness, indicating that softer components probably accompany the 2.62-Mev line.

Figure 11 shows part of the data of Fig. 10 plotted in a different manner. The curves of Fig. 11 are direct differential bias curves taken without absorber (upper solid curve) and with a 1.125-inch lead absorber present (lower solid curve). For comparison, the lower curve has been shifted upwards (dashed curve) so that the first channel points coincide. It is seen that the bias curves again point to energy discrimination as discussed above in (3). The dashed curve indicates a harder gamma-ray than the upper solid curve. If extended further to the right, it is possible that the two curves would become parallel.

(f) The lower curve of Fig. 12 shows a differential bias plot of the background counts observed with an 8.6-gram mass of NaI(Tl). From

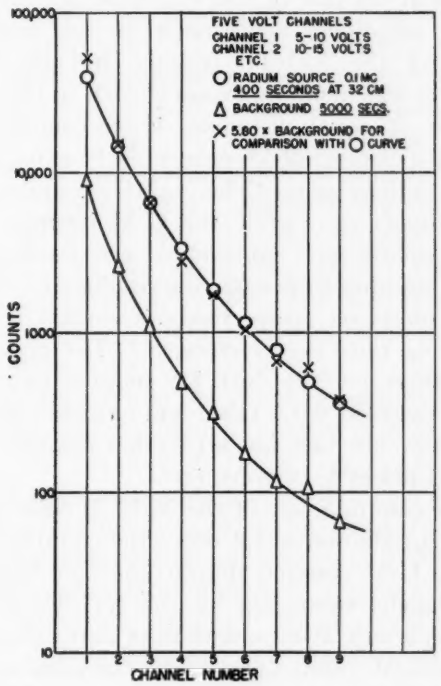

FIG. 12. Comparison of radium and background pulse distributions.

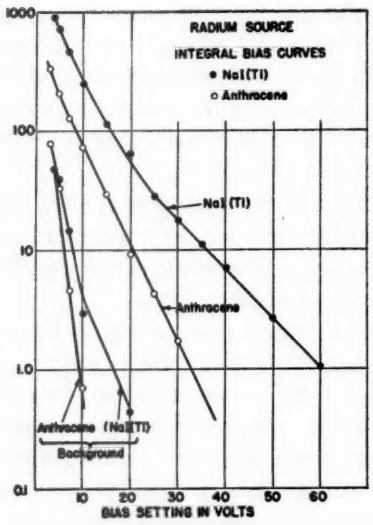

FIG. 13a. Integral bias curves for NaI(Tl) and anthracene for a radium source: amplifier rise time 0.8 microsecond; clipping time 0.8 microsecond.

this curve it can be seen that the total background counting rate is 2.8 counts per second. A comparison of this counting rate has been made with a Victoreen Geiger-Mueller type counter (diameter, $1\frac{1}{8}$-in., $2\frac{1}{2}$-in. length, $\frac{1}{32}$-in. Cu wall thickness). The G-M counter recorded pulses at the rate of 0.90 count per second.

An additional comparison of the counting rates of the NaI(Tl) counter and the G-M counter was made by exposing each to the same source at equal distances. Each counter was placed a distance of 33 centimeters from 0.1-millicurie radium source. The NaI(Tl) counter gave 168 counts/sec., while the G-M counter gave 32.5 counts/sec. Subtracting the background counting rates from each, the results are 165 and 31.6 counts/sec., respectively. The ratio of these counting rates is, therefore, 5.2. The operating conditions for the NaI(Tl) counter were 432 volts (selected 931A tube) and amplifier gain of 3.8×10^4. The bias was set so that channel 1 recorded pulses 5–10 volts, etc.

The counting rate of the NaI(Tl) counter for gamma-radiation is 5.2 times the counting rate of the G-M counter, despite the fact that the solid angle, subtended by the NaI(Tl) at the source, is only about one-third of that subtended by the G-M counter. One might, therefore, expect that the background counting rates should be in the same ratio, after correction is made for the counting of cosmic rays by the two counters. (Correction for contamination is too uncertain to be made.) The G-M counter may be corrected to read 0.63 count/sec., allowing 0.27 count/sec. for cosmic rays. The NaI(Tl) corrected background reading will be 2.71 counts/sec. The ratio of these counting rates is 4.3 instead of 5.2. Considering the rough estimates of the corrections and the neglect of other corrections, the agreement is thought to be satisfactory. One may therefore conclude that the background readings with the NaI(Tl) counter, at the bias used, have given an indication of the gamma-ray flux in the room consistent with measurements of a G-M

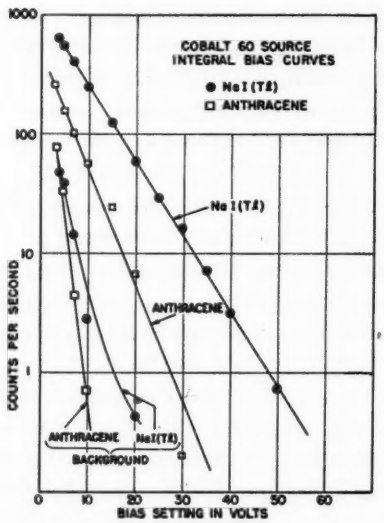

FIG. 13b. Integral bias curves for NaI(Tl) and anthracene for a Co^{60} source: amplifier rise time 0.8 microsecond; clipping time 0.8 microsecond.

counter, and therefore represent true gamma-background.

There are other indications that this conclusion is correct. These are as follows: (a) When two weak sources (0.1 millicurie each, normally kept 18 feet distant from the counter) were removed from the room, the NaI(Tl) background rate fell by 18 percent. (b) The distribution of pulse size closely resembles that of radium, which is suspected as the source of background counts in a physics laboratory. Figure 12 shows a comparison of the shape of the background curve and a curve due to a radium source. When the background curve is shifted upwards, the points of the lower curve fall rather closely on the upper

curve, due to radium. Furthermore, a closet about forty feet from the position of the NaI(Tl) counter is a storage point for radioactive sources, mostly radium, in Palmer Physical Laboratory. (c) Background counts taken with the NaI(Tl) and naphthalene counters showed the same ratio as the counting rates with a radium source present. This result may be seen in Fig. 2 of an earlier publication.[9]

(g) Integral bias curves comparing anthracene and NaI(Tl) have been taken with a Bell-Jordan amplifier and discriminator.‡ The rise and clipping times were selected as 0.8 microsecond. The sample of anthracene used was prepared by G. B. Collins and T. A. King. The anthracene sample weighed 2.0 grams and was clear except where cracked. The NaI(Tl) sample was of comparable size and polycrystalline. Figures 13(a) and (b) show the comparison. P. R. Bell previously reported similar findings at the Rochester conference on high speed counters. It should be recognized that both quantities, pulse magnitude and pulse duration, are of importance in comparing different phosphors. Anthracene and phenanthrene provide light pulses of initial height comparable with NaI(Tl) polycrystalline samples, but of smaller area when plotted against time. This behavior may be observed with a fast

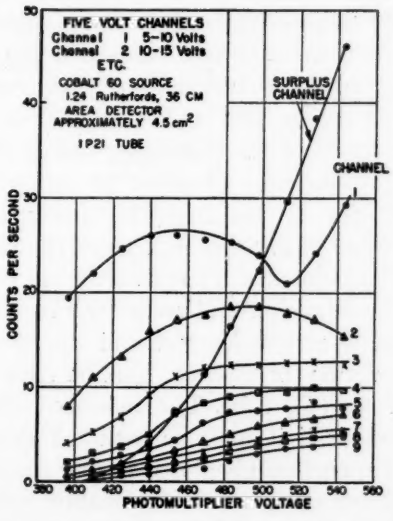

FIG. 14a. Counting rates in different channels as a function of photo-multiplier voltage for Co^{60} source. Background has been subtracted. The effective area of the counter is approximately 4.5 cm², and mass 13.0 grams.

‡ The author is indebted to Dr. H. Poss of Brookhaven National Laboratory for taking the data for these curves.

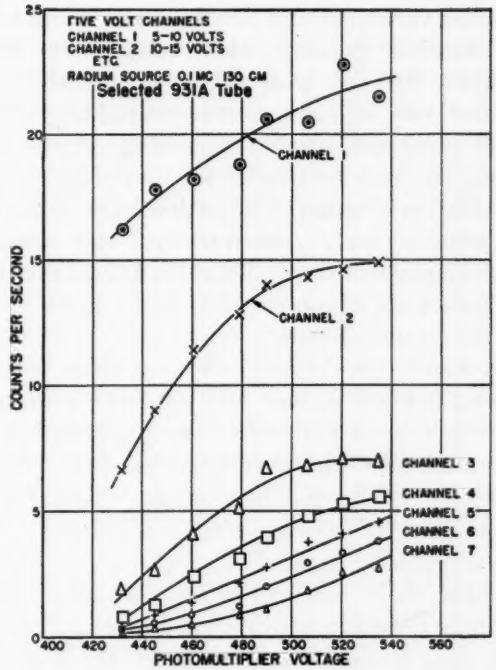

FIG. 14b. Counting rates in different channels as a function of photo-multiplier voltage for a radium source. Background has been subtracted. The effective area of the counter is approximately 3.6 cm², and mass 10 grams.

amplifier, of rise time 2×10^{-8} second.‡‡ With a slow amplifier the pulse height is proportional to the area under the light emission curves. Under these circumstances, NaI(Tl) pulses are much larger than anthracene (or phenanthrene) pulses. A single crystal of NaI(Tl) showed pulses about five times as large as a comparable anthracene sample with a slow amplifier. For fast counting, or low resolving times, phenanthrene and anthracene are definitely more suitable than NaI(Tl). A comparison of pulse size distributions for naphthalene and NaI(Tl) has been reported already.[9] There is nothing to add to these results at the present time.

(7) In this section the "counting efficiency" of the NaI(Tl) scintillation counter will be discussed. In experiments using counters a most important feature is that the counting rate should be independent, or nearly so, of counter conditions. In a Geiger-Mueller counter one has a "plateau" in counting over a certain voltage range. In this range the G-M counter is independent of other conditions if one excludes tem-

‡‡ To be described by W. C. Elmore.

perature variations and slow increase of products of chemical decomposition caused by long counting (10^9 counts or so). In the scintillation counter one encounters two variables which affect pulse magnitude, the voltage across the multiplier, and the gain of the amplifier. In the scintillation counter the pulses have variable magnitudes and, consequently, one always counts against an applied bias. In a G-M counter the pulses are of more or less uniform size, and the bias is unimportant.

In many respects the two variables, representing applied voltage and amplifier gain, are equivalent since both affect the amplification of the initial pulse. However, the noise of the photo-multiplier is changed by voltage, whereas amplifier gain, of course, does not influence the photo-multiplier noise but may bring it above the bias. (It is assumed, in this discussion, that amplifier noise is negligible.) It is possible, therefore, that different results will be obtained by separately varying photo-multiplier voltage and amplifier gain. In tests made of this point, both voltage and amplifier gain have been changed independently and the effects observed. As far as can be told, the two variables produce essentially the same results, so that the voltage region studied is that in which the noise does not increase more rapidly than the photo-multiplier gain increases as the voltage is raised. This result may be expected so long as the signal-to-noise ratio is high, as in these experiments. Figure 8 shows the results obtained when amplifier gain is changed.

The curves of Figs. 14(a) and (b) show the behavior of the NaI(Tl) scintillation counter with respect to variation of photo-multiplier voltage. These figures represent an effort to find a plateau in counting rate. It will be observed that an actual plateau has not been obtained so far, although the tendencies towards a plateau are quite clear, especially in Fig. 14(a).

It is to be expected that the counting rate will increase at low voltages because some pulses are still below the bias. At higher voltages the counting rates in the lower channels should decrease, while the higher channels, 3, 4, etc., should show evidence of saturation. With further increase of voltage the latter channels should show a decrease in counting rate. Evidence of this type is indicated by the curves of Fig. 14(a).

The second increase of counting rate in channel 1 of Fig. 14(a) is not understood, although it is quite possible that very low energy scattered gamma-rays from container, table, etc., and the overshoot of the amplifier for a large pulse may account for part of this increase. Curves 14(a) and (b) should be regarded as preliminary results. It is expected that further work will be performed employing a gamma-ray beam, a single crystal, and better shaping of the amplifier pulses. The single crystal should provide a higher signal-to-noise ratio. In Fig. 14(a) photo-multiplier noise sets in at about 520 volts, but has been subtracted as background.††††

The efficiency of the counter of Fig. 14(a) has been measured for Co^{60} gamma-rays by taking the total counting rate at 512 volts and dividing by the flux at the counter. The two figures are, respectively, 115 counts/sec. and 680 gamma-rays/sec. The measured efficiency is therefore about 17 percent. This figure is rather arbitrary since a plateau is not observed.

The efficiency for radium gamma-rays of the counter of Fig. 14(b) is more difficult to measure since the evidence of a plateau is less clear than in Fig. 14(a). It is also more difficult to find the true number of gamma-rays from radium, since there may be present some soft components difficult to measure. Using a value of 2.3 gamma-rays per disintegration of radium[24] and a counting rate of 93 counts/sec. at 538 volts (Fig. 14(b) and the totals of the remaining channels), one obtains an efficiency of about 65 percent. The effective area of the NaI(Tl) quartz tube is about 3.6 cm^2 in this case, and the 0.1-mc radium source is at a distance of 130 cm from the counter. This is a very high efficiency for the NaI(Tl), and exceeds an efficiency found by measuring the absorption of radium gamma-rays in an identical NaI(Tl) tube. The measured efficiency is 24 percent if it may be assumed that each absorbed quantum gives rise to one count. The observed counting rate is probably too high, although the figure of 2.3 gamma-rays per disintegration of radium may be too low.

Delayed pulses following alpha-particle scin-

[24] R. D. Evans and R. O. Evans, Rev. Mod. Phys. **20**, 305 (1948).

tillations have been observed by R. Sherr in ZnS counters. Such pulses were looked for in NaI(Tl), but were not found in a period of from two to ten microseconds following the main pulse. The high efficiency may be due to a longer-lived phosphorescence, although it is difficult to establish this point conclusively at the present time.

At the Rochester meeting on high speed counters, it was pointed out by several investigators that similar high efficiencies have been found in naphthalene and anthracene scintillation counters, and that the photo-multiplier itself may be producing delayed pulses. Further investigation of delayed pulses and efficiencies is clearly necessary.

B. Photographic Studies

The results of these brief studies are given at this point because of a possible application of the phosphor, photographic plate, or film technique to future experiments with gamma-rays or beta-particles and to radiation monitoring.

About a year ago the writer began a series of experiments to examine the luminescent light yield of single crystals under gamma-radiation. These experiments consisted of placing single crystal samples on top of a photographic plate. The light yield is then recorded by the photographic plate which acts as an integrating device. If a small portion of the crystal surface is masked by a piece of paper, or, better, if a metallic reflecting film is sputtered or evaporated on a portion of the crystal, the light output can be found directly as the difference between the blackening on parts of the photographic plate exposed to the light and those parts masked by the opaque film or paper. Similar early studies were made on CaF_2 by Winkelmann and Straubel,[25] with x-rays, shortly after the discovery of x-rays.

A single crystal of KI(Tl), previously described,[9] was placed on a photographic plate (Eastman 103-0) at a distance of one meter from a 1.8-millicurie radium source. A tube of NaI(Tl) was also placed on the plate. After thirty minutes of exposure, blackening under the luminescent samples was observed. The blackening under the NaI(Tl) tube was only slightly greater than that under the single crystal of KI. It appears, therefore, that the light output of KI(Tl) and NaI(Tl) are comparable, although the NaI(Tl) samples was one of only average sensitivity. The KI(Tl) sample was also favored by closer proximity to the plate.

It had previously been determined‡‡‡ that the KI(Tl) sample produced an increase of blackening, due to gamma-ray exposure, by a factor of one hundred, over the blackening resulting from direct exposure of the plate to the same radiation. Since NaI(Tl) samples have been made with twice the light output of the sample under test and since photographic film and a reflector could be wrapped around the tube for improved light reception, it seems reasonable that phosphor-film combinations could provide a factor of about four hundred in increased sensitivity of film to gamma-rays. Scattering experiments with gamma-rays might be attempted with a number of phosphor tubes placed at various angles around the scatterer.

Other tests, made with NaCl, KBr, and LiF powders to which thallium impurities were added, showed that NaI and KI powders were much more efficient as phosphors than the others.

It is interesting that KI(Tl) does not give large pulses with a photo-multiplier even though its total light output is comparable in magnitude and spectral distribution with that of NaI(Tl). One may draw the conclusion that light is emitted from KI(Tl) over a longer period of time than the light from NaI(Tl). The amplifier used in these tests had a rise time of 0.25 microsecond. It is possible that other KI(Tl) samples may behave differently; only two specimens of KI(Tl) have been studied.

ACKNOWLEDGMENTS

The author wishes to thank Mr. L. B. Harris for preparation of the quartz tubes, Mr. James Black and Mr. Howard E. Schrader for help with the drawings and photographs, and Mr. J. C. D. Milton for assistance with the equipment used in these experiments. Thanks are due Dr. P. C.

[25] A. Winkelmann and R. Straubel, Ann. d. Physik **59**, 324 (1896).

‡‡‡ Tests were made of time of exposure *versus* blackening.

Gugelot for preparation of a C^{11} sample. Kind interest in these experiments by Drs. J. A. Wheeler, M. G. White, and M. ten Bosch is gratefully acknowledged. The loan of Navy project equipment (Contract N6ori-105, Task Order I) and of equipment by Drs. R. Sherr and H. W. Fulbright is also appreciated. The author is further indebted to Mr. T. A. King for a sample of anthracene and to Dr. H. Poss for study of this specimen. Thanks are due the Office of Naval Research, the University of Rochester, and conference members, for the exchange of ideas at the recent Rochester conference on high speed counters. Finally, the author wishes to thank the Brookhaven National Laboratory for an opportunity to continue part of this work on counters.

PHYSICAL REVIEW VOLUME 75, NUMBER 5 MARCH 1, 1949

Further Experiments on Cosmic-Ray Bursts*

H. S. BRIDGE AND B. ROSSI
Physics Department and Laboratory for Nuclear Science and Engineering, Massachusetts Institute of Technology, Cambridge, Massachusetts

(Received November 29, 1948)

The paper describes further results obtained by the observation of coincidences between pulses of a Geiger-Mueller counter tray and of an ionization chamber. The experiments were carried out partly aboard a B-29 aircraft and partly on the top of Mt. Evans in Colorado. The main purpose of the experiments at Mt. Evans was an investigation of the "transition curve" in lead. The experimental data are consistent with the assumption that the coincident bursts observed with a lead shield between the Geiger-Mueller tubes and the ionization chamber are mainly produced by cascade showers initiated by electrons and photons either incident upon the lead from the atmosphere or produced in the lead by nuclear interactions. The experiments aboard the B-29 furnish information on the variation with altitude of the radiation responsible for the nuclear interactions.

I. INTRODUCTION

EXPERIMENTS made by means of a tray of Geiger-Mueller counters and an ionization chamber, arranged one above the other and separated by several inches of lead, revealed the existence of time coincident pulses, whose rate of occurrence increases rapidly with altitude.[1] This phenomenon was interpreted by postulating the existence of ionizing particles different from electrons or ordinary mesons, which are much more abundant at high altitude than at sea level and are capable of producing secondary electrons or photons of high energy after traversing moderate thicknesses of lead. The electrons or photons undergo cascade multiplication in the lead, and the resulting showers are responsible for the ionization bursts in the chamber.

In order to test this interpretation, an experiment was carried out[2] in which part of the solid lead absorber between the Geiger-Mueller tray and the ionization chamber was replaced with a cloud chamber containing a number of lead plates; the expansion was triggered by the coincident pulses of the Geiger-Mueller tray and the ionization chamber. The cloud-chamber pictures thus obtained showed that shower production by penetrating particles was indeed responsible for a large fraction of the coincidences. Furthermore, they showed that the showers usually contained electrons as well as penetrating or heavily ionizing particles. This was taken as evidence that the showers originated in nuclear, rather than in electromagnetic, interactions. The

* The work described in this paper was assisted by the joint program of the Office of Naval Research and the Atomic Energy Commission. The B-29 aircraft was provided by the U. S. Air Forces. The facilities for the work at Mt. Evans were supplied by the Inter-University High Altitude Laboratory.

[1] H. Bridge, B. Rossi, and R. W. Williams, Phys. Rev. 72, 257 (1947).

[2] H. S. Bridge, W. E. Hazen, and B. Rossi, Phys. Rev. 73, 179 (1948); H. S. Bridge and W. E. Hazen, Phys. Rev. 74, 579 (1948).

same experiments indicated, however, that air showers were probably responsible for part of the coincidences between the Geiger-Mueller counters and the ionization chamber. Also, the possibility was not ruled out that some of the coincidences might be caused by nuclear interactions resulting in the production of heavily ionizing particles, rather than in the production of electron showers.

This paper describes some further results on burst production under lead which were obtained by observation of coincidences between pulses of ionization chambers and of Geiger-Mueller counters. The chambers and the associated circuits used in this experiment were described in a recent paper by Bridge, Hazen, Rossi, and Williams,[3] to which the reader is referred for technical details. Measurements were made partly on the ground (Mt. Evans, Colorado, altitude 14,300 feet; Lexington, Massachusetts, altitude 255 feet) and partly aboard a B-29 aircraft flying at altitudes of 20,000, 25,000, and 30,000 feet.

II. EXPERIMENTS ABOARD THE B-29

1. The Experimental Arrangement

The arrangement used in the experiments aboard the B-29 is shown schematically in Fig. 1. The ionization chamber (I) had a diameter of 7.5 cm and an effective length of 52 cm. It was filled with pure argon at 7.3-atmospheres of pressure (at 25°C) and contained a polonium source of α-particles placed near the inner surface of the cylindrical wall. The pulses produced by the polonium α-particles, whose maximum size we denote by P_α, served as a standard for the measurement of the ionization bursts observed in the chamber. A pulse of size P_α corresponded to the amount of ionization produced by the passage through the chamber of 53 electrons of 10 Mev traveling perpendicularly to the chamber axis.[4]

Each of the Geiger-Mueller counters in trays A and B had a diameter of 2.5 cm and an effective length of 51 cm. The total effective area of tray C was 320 cm² in some of the experiments and 465 cm² in the others. The total effective area of tray D was 465 cm².

The lead block between tray A and the ionization chamber was 15 cm thick, 15 cm wide, and 60 cm long. The lead covering tray D was 10 cm thick.

An electronic circuit recorded events in which a pulse of the ionization chamber greater than 0.6 P_α was accompanied by one or more pulses in tray A and by two or more pulses in tray B (coincidences AIB_2). The output pulse of the electronic circuit operated a message register and, in addition, triggered a circuit which provided an intensifier pulse and a fast linear sweep for a cathode-ray oscilloscope. The pulses of the

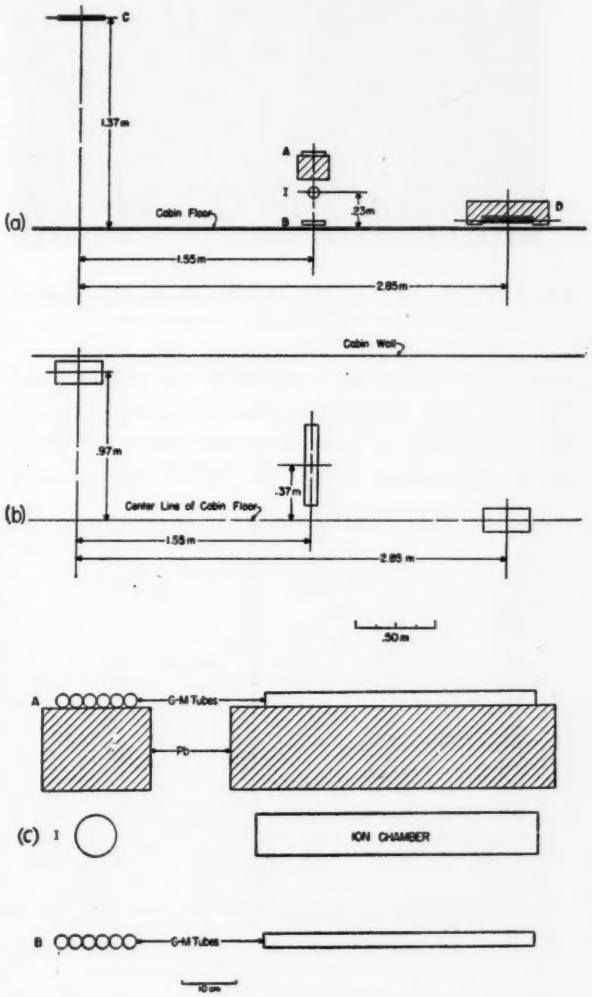

FIG. 1. Experimental arrangement used in the measurements aboard the B-29. (a) Side view; (b) top view; (c) details of the coincidence set $A\,I\,B$.

[3] Bridge, Hazen, Rossi, and Williams, Phys. Rev. **74**, 1083 (1948).

[4] See B. Rossi and K. I. Greisen, Rev. Mod. Phys. **13**, 240 (1941).

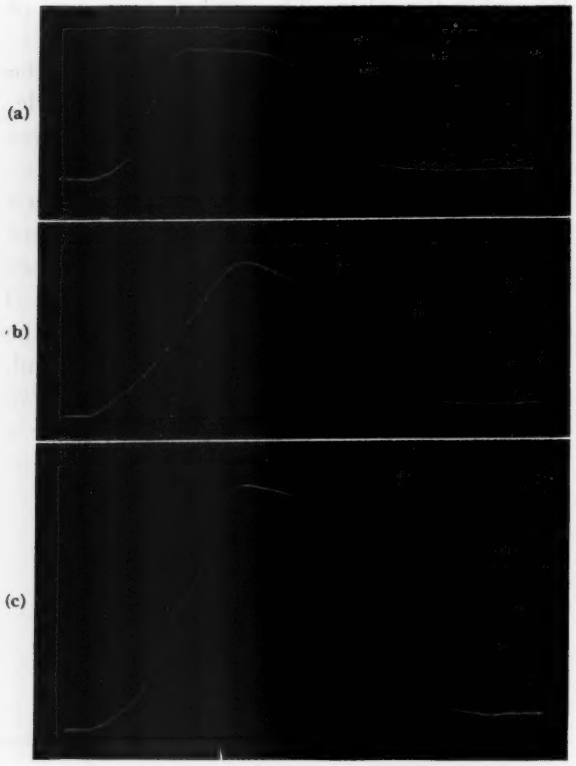

FIG. 2. Samples of pulse records. (a) α-pulse; (b) σ-pulse; (c) ν-pulse.

ionization chamber, suitably amplified and delayed, were applied to the deflecting plates of this oscilloscope. Coincidences between the (IB_2) event and pulses of the six individual tubes in tray A were recorded separately by neon bulbs which were photographed on the same film and simultaneously with the oscilloscope trace.

Two additional neon bulbs recorded discharges of the lateral trays C and D occurring simultaneously with the coincidence (AIB_2). Samples of the records obtained are shown in Fig. 2.

2. The Experimental Results

The experimental results are summarized in Figs. 3 and 4 and in Table I. Figure 3 shows a breakdown of the data obtained at the three elevations (20,000, 25,000, and 30,000 feet) according to the shape of the ionization pulse and according to the number of counters discharged in tray A, as indicated by the corresponding neon bulbs. Events in which the coincidence (AIB_2) was or was not accompanied by pulses in tray C or D are considered separately. The shapes of the ionization pulses are classified into three categories, as suggested by Bridge, Hazen, Rossi, and Williams,[3] namely: α-pulses (see Fig. 2a), σ-pulses (see Fig. 2b), and ν-pulses (see Fig. 2c). Pulses of the α- and the ν-type mark the passage through the chamber of heavily ionizing particles. Pulses of the σ-type are characteristic of showers of lightly ionizing particles, even though occasionally groups of heavily ionizing particles may give a pulse of this type.

Table I shows the total numbers of cases in which coincidences (AIB_2) were accompanied

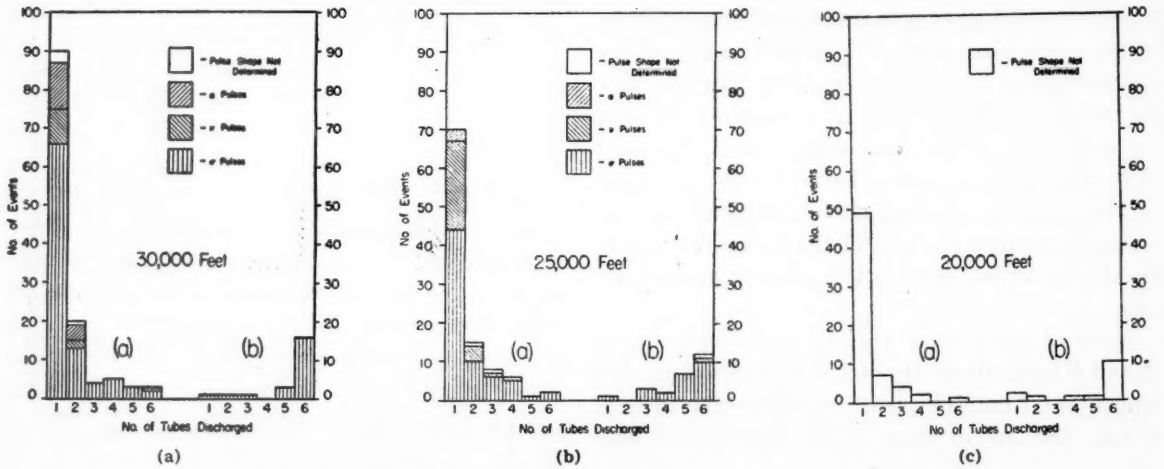

FIG. 3. Distribution of the records obtained with the instruments shown in Fig. 1, according to pulse shape and to number of tubes discharged in tray A. The area of tray C was 465 cm² for the 30,000-foot flight and for half of the 25,000-foot flight. It was 320 cm² for the rest of the flights. Histograms (a) refer to coincidences (AIB_2) unaccompanied by pulses in either C or D; histograms (b) refer to coincidences (AIB_2) accompanied by pulses in either C or D or both.

by pulses in tray C but not D (event AIB_2C-D), tray D but not C (event AIB_2D-C), both tray C and D (event AIB_2CD), and in neither tray C nor D (event AIB_2-CD).

Figure 4 summarizes the results on the variation with altitude of the rate of occurrence of coincidences AIB_2. The sea level point was obtained at Lexington, under a roof of about 12 g cm^{-2}, with the same equipment used in the B-29 flights. Figure 4 also shows the coincidence rates corrected for air showers in the manner to be discussed below.

3. Discussion

The diagrams in Fig. 3 clearly indicate that two different phenomena are responsible for the coincidences between the pulses of the ionization chamber and of the Geiger-Mueller trays A and B. We believe that these two phenomena are: (a) nuclear interactions produced in the lead block or in the chamber wall by penetrating ionizing particles. In most of these events only one Geiger-Mueller counter in tray A and none in tray C or D is discharged (see Fig. 5a). (b) Air showers incident at a large zenith angle which discharge the counter trays A and B and the ionization chamber I without traversing the entire lead block between A and I. In most of these events all of the counters in tray A are discharged, and pulses are recorded also in the lateral trays (see Fig. 5b).

In the present experiments it is not possible to establish a completely unambiguous criterion for separating events caused by nuclear interactions and by air showers, respectively. At a large zenith angle, an air shower of small density, but containing some high energy electrons or photons, could miss the lateral trays, discharge only a small number of counters in tray A, and produce a burst in the ionization chamber after undergoing some multiplication in the lead (see Fig. 5c). On the other hand, it is possible that some of the penetrating particles capable of producing nuclear interactions arrive upon the instrument accompanied by air showers which discharge several counters in tray A, as well as one or both of the lateral trays (see Fig. 5d).

Finally, we may recall that often, when a nuclear interaction of the type shown schematically in Fig. 5a occurs, penetrating particles are

TABLE I. Total number of events observed during the airplane experiments (the data obtained at the various elevations are considered all together).

Event	$(AIB-CD)$	$(AIBC-D)$	$(AIBD-C)$	$(AIBCD)$
Number of records	291	27	8	27

projected at wide angles with respect to the incident ray and even in the backward direction.[2,5-7] These particles may produce multiple discharges in the upper tray and, more seldom, strike the lateral trays. It is our belief that phenomena of this kind are responsible for most of the events in which multiple discharges in tray A are not accompanied by discharges in the lateral trays.

Provisionally we shall assume that the (AIB_2) coincidences accompanied by a discharge in tray

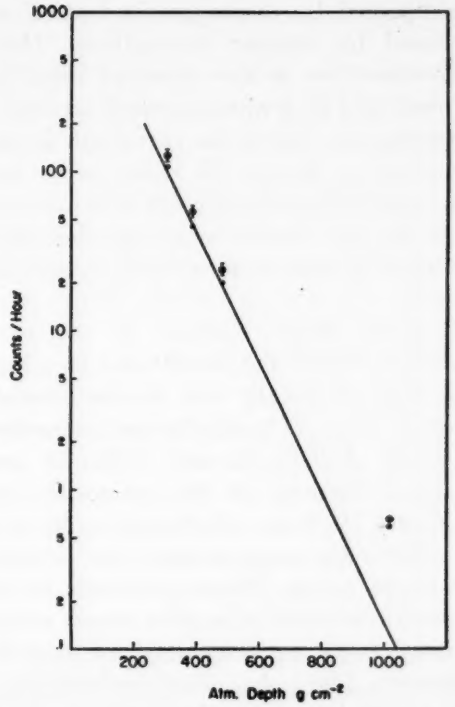

FIG. 4. Hourly rates of threefold coincidences (AIB_2) at various altitudes, as obtained with the experimental arrangement shown in Fig. 1. Minimum pulse required from the ionization chamber: 0.6 P_α. Open dots: observed rates, with corresponding statistical errors; solid dots: rates corrected for air showers. The solid line represents an exponential variation with an absorption thickness of 107 g cm^{-2}.

[5] J. G. Wilson, as quoted by D. Broadbent and L. Janossy, Proc. Roy. Soc. A190, 497 (1947).
[6] W. B. Fretter, Phys. Rev. 73, 41 (1948).
[7] C. Y. Chao, Phys. Rev. 74, 492 (1948).

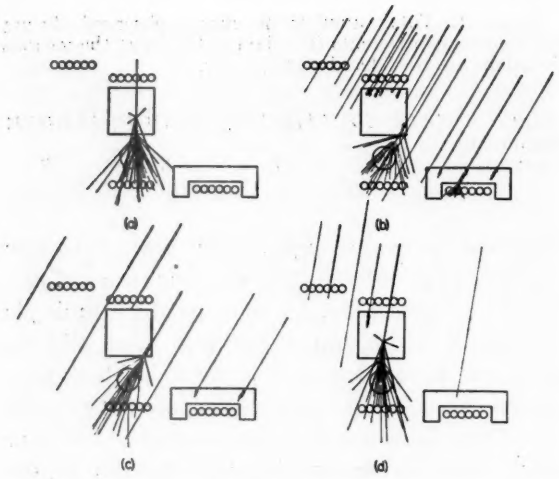

FIG. 5. Schematic representation of various cosmic-ray processes capable of producing (AIB_2) coincidences.

C or D are produced by air showers, and those unaccompanied by discharges in tray C or D are caused by nuclear interactions. The air shower correction to the observed coincidence rates made in Fig. 4 was computed according to this assumption. Since the correction is small, the uncertainty which still exists as to its accurate value does not represent a serious source of error in the determination of the altitude dependence of burst production by nuclear interactions.

The pulse shape analysis of the records obtained at 25,000 and 30,000 feet (see Fig. 3) shows that practically all of the events in which tray C or D is discharged (coincidences AIB_2C-D, AIB_2D-C, and AIB_2CD) and a substantial majority of the events in which trays C and D are not discharged (coincidences AIB_2-CD) are accompanied by ionization pulses of the σ-type. These results are in agreement with our assumption that events in which the lateral trays are discharged are caused by air showers. They also show that among the bursts caused by nuclear interactions some are produced by the passage through the chamber of a few heavily ionizing particles, but most are produced by the passage through the chamber of showers of many lightly ionizing particles. The cloud-chamber experiments mentioned previously (see references 2, 6, 7) show that these showers result from cascade multiplication of high energy electrons or photons produced in the nuclear interactions. The fact that in our experiments more pulses of the σ-type than of the α- and ν-type are observed does not mean that the production of high energy electrons or photons in nuclear interactions is a more common event than the production of heavily ionizing particles. For both types of events one can define an "effective layer" in the material above the ionization chamber where the interaction must take place in order that an observable ionization burst be produced. The thickness of this effective layer depends on the nature and on the energy distribution of the particles arising from the interaction, and is certainly greater for events leading to the production of high energy electrons or photons than for events leading to the production of heavily ionizing particles.

The very rapid increase of the coincidence rate with altitude (see Fig. 4) confirms previous results,[1] as well as the conclusion that most of the bursts observed at high altitudes are produced by particles different from ordinary mesons. It is believed that these particles are high energy protons and possibly "heavy" mesons. It is also likely that some of the coincidences (AIB_2) are produced by nuclear interactions caused by high energy neutrons and in which ionizing particles are projected backwards through the counter tray A.

In Fig. 4 the points at 30,000, 25,000, and 20,000 feet fall approximately on a straight line, but the point near sea level lies above it. This fact may be taken as an indication that radiation and collision processes of ordinary mesons, although unimportant at high altitude, contribute a large fraction of the bursts observed near sea level. It should be noted that these conclusions apply at present only to the relatively small bursts observed in our experiments.

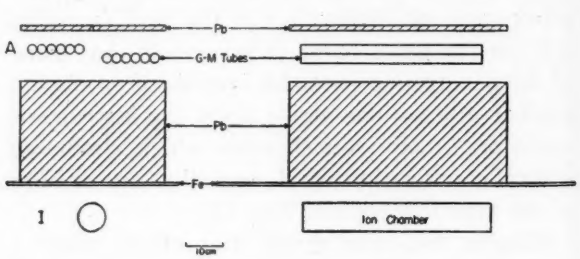

FIG. 6. Experimental arrangement used in the measurements at Mt. Evans.

TABLE II. Summary of the observations made at 14,300 feet by means of the experimental arrangement shown in Fig. 6, with different absorbers between the counter tray A and the ionization chamber I. P represents the chamber bias. $(A\ I)$ is the hourly coincidence rate between pulses of A and I. (A_2I) is the hourly rate of events in which two or more counters in A are discharged simultaneously with I. The permanent 1.27-cm lead absorber above A is *not* included in the tabulated values of absorber thickness.

Absorber	None	2.54 cm Pb	5.08 cm Pb	12.7 cm Pb	27.9 cm Pb	2.54 cm Pb 12.7 cm Fe	2.54 cm Pb 17.8 cm Fe	12.7 cm Pb 17.8 cm Fe
$P>0.6\ P_\alpha$								
$(A\ I)$ obs.	32.3±0.7	57.8±1.1	31.0±0.9	13.7±0.3	9.4±0.3	19.9±0.7	12.9±0.8	8.3±0.4
$(A\ I)$ accid.	3.2	3.3	3.5	3.6	2.4	2.6	2.4	2.4
$(A\ I)$ corr.	29.1	54.5	27.5	10.1	7.0	17.3	10.5	5.9
$P>1.1\ P_\alpha$								
$(A\ I)$ obs.	9.3±0.4	21.1±0.6	12.4±0.6	4.2±0.2	2.85±0.16	7.6±0.4	7.9±0.6	2.69±0.22
$(A\ I)$ accid.	0.4	0.7	0.6	0.25	0.20	0.2	1.8*	0.15
$(A\ I)$ corr.	8.9	20.4	11.8	3.95	2.65	7.4	6.1	2.54
(A_2I)	6.2±0.4	15.8±0.7	7.0±0.6	1.0±0.1	1.1±0.1	3.7±0.3	2.9±0.4	
$P>2\ P_\alpha$								
$(A\ I)$ obs.	3.28±0.23	8.5±0.4	5.7±0.4	1.85±0.11	1.1±0.1	3.3±0.3	2.1±0.3	1.7±0.2
$P>3\ P_\alpha$								
$(A\ I)$ obs.	1.47±0.15	4.7±0.3	3.3±0.3	0.85±0.07	0.64±0.08	1.9±0.2	1.0±0.2	

* The large accidental correction is caused by electric disturbance from a neighboring cloud chamber which affected the ionization chambe circuit, but not the Geiger-Mueller counter circuit.

III. EXPERIMENTS AT MT. EVANS

1. The Experimental Arrangement

The arrangement used in the experiments at Mt. Evans is shown schematically in Fig. 6. The ionization chamber I was the same instrument described in Part II. Each of the Geiger-Mueller counters in tray A was 51 cm long and 2.5 cm in diameter. An iron plate 0.6 cm thick was always present above the ionization chamber, and a lead plate 1.27 cm thick was always present above the counter tray. Additional absorbers of lead and iron could be placed between the ionization chamber and the Geiger-Mueller tray. When an absorber consisting partly of lead and partly of iron was used, the lead was always placed below the iron. An electronic pulse height discriminator selected pulses of the ionization chamber greater than 0.6 P_α, 1.1 P_α, 2 P_α, and 3 P_α, respectively, where P_α indicates, as before, the maximum size of pulses produced by polonium alpha-particles. Recorded were: (a) ionization pulses greater than 0.6 P_α, 1.1 P_α, 2 P_α, and 3 P_α occurring simultaneously with the discharge of at least one Geiger-Mueller tube in tray A (coincidences AI); (b) ionization pulses greater than 0.6 P_α and 1.1 P_α irrespective of whether or not simultaneous pulses occurred in the Geiger-Mueller tray; (c) ionization pulses greater than 1.1 P_α occurring simultaneously with the discharges of at least two Gieger-Mueller tubes in tray A (event A_2I); (d) all pulses of the Geiger-Mueller counter tray A.

2. The Experimental Results

The most significant results obtained with the arrangement described are summarized in Table II. The corrections for accidental coincidences indicated in the table were computed from the resolving time of the coincidence circuit (which by direct observation of the pulses was found to be approximately 50 microseconds) and from the observed rates of single pulses in the Geiger-Mueller tray and in the ionization chamber. (It may be noted that for the 0.6 P_α bias the counting rate of the ionization chamber includes a large contribution from the polonium source.)

Figure 7 shows double logarithmic plots of counting rate against chamber bias for the coincidences (AI) obtained with different lead thicknesses above the ionization chamber. In Fig. 8 the round points represent the (AI) coincidence rates obtained with a chamber bias of 1.1 P_α and with different lead thicknesses. The square dots in the same figure represent differences between (AI) and (A_2I) coincidence rates and thus refer to events in which only one Geiger-Mueller counter is discharged.

The coincidence rates plotted in Figs. 7 and 8 are corrected for accidentals. The lead thick-

nesses indicated include the thickness of the lead plate above the Geiger-Mueller counters (1.27 cm). Note that the data at 1.27 cm of lead are not directly comparable with the others because they were obtained with a much greater separation between the lead shield and the ionization chamber.

3. Discussion

From an examination of Fig. 7 it appears that power laws of the type $N(P)=\text{const.}\times P^{-\gamma}$ with $\gamma=1.5$ represent satisfactorily the integral pulse height distributions at 3.8, 14.0, and 29.2 cm of lead. The pulse height distribution at 6.35 cm seems to be somewhat flatter, and that at 1.27 cm is definitely steeper than the pulse height distributions at the other thicknesses.

The dependence of counting rate on lead thickness shown by the round dots in Fig. 8 clearly indicates that two different phenomena are responsible for the observed coincidences. It

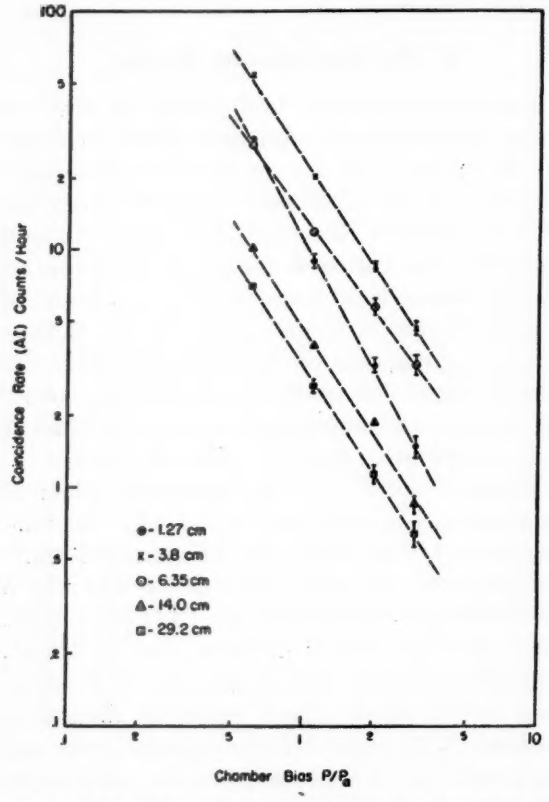

FIG. 7. Counting rate N against chamber bias P/P_0 for different thicknesses of the lead absorber in centimeters. The figures include the thickness (1.27 cm) of the permanent lead absorber above the Geiger-Mueller counters.

is natural to identify these two phenomena as shower production by high energy electrons and photons and nuclear interactions. The first phenomenon predominates at small thicknesses and explains the sharp maximum of the transition curve indicated by the experiment. The second phenomenon predominates at large thicknesses and explains the "tail" of the transition curve. From the slope of this tail one obtains the following value for the absorption thickness in lead, L_{Pb}, of the radiation responsible for nuclear interactions:

$$L_{Pb}=430\pm90 \text{ g cm}^{-2}.^{8}$$

The corresponding value for iron, as obtained by comparing the counting rates measured with 12.7 cm of lead and with 12.7 cm of lead plus 17.8 cm of iron between A and I (see Table II) is

$$L_{Fe}=320\pm70 \text{ g cm}^{-2}.$$

The above computation of L_{Pb} and L_{Fe} neglects the effect of air showers. This effect should be smaller in the experiments at Mt. Evans than in the airplane experiments because the chamber was more effectively shielded by the lead (compare Figs. 1 and 6). Also neglected is the background from radiation and collision of ordinary mesons.

The square dots in Fig. 8 show that multiple discharges of the Geiger-Mueller counters occur in a very large fraction of the coincidences observed with small lead thicknesses, most of which are due to shower production by electrons and photons from the atmosphere. This, of course, was to be expected, especially because of the 1.27-cm thick lead shield above the Geiger-Mueller counters. However, even at large thicknesses, where most of the coincidences should be caused by nuclear interactions, multiple discharges of the counter tray are found to occur in one-quarter to one-third of the cases. We believe (see Section II-3) that these multiple discharges are mainly caused by the passage through the Geiger-Mueller counters of secondary particles arising from the nuclear interactions which are also responsible for the bursts

[8] The value of L_{Pb} derived from these experiments was quoted erroneously as 280 ± 50 in Section 20 of the review article by B. Rossi in Rev. Mod. Phys. 20, 537 (1948). This was due to a mistake in the evaluation of the accidental coincidences.

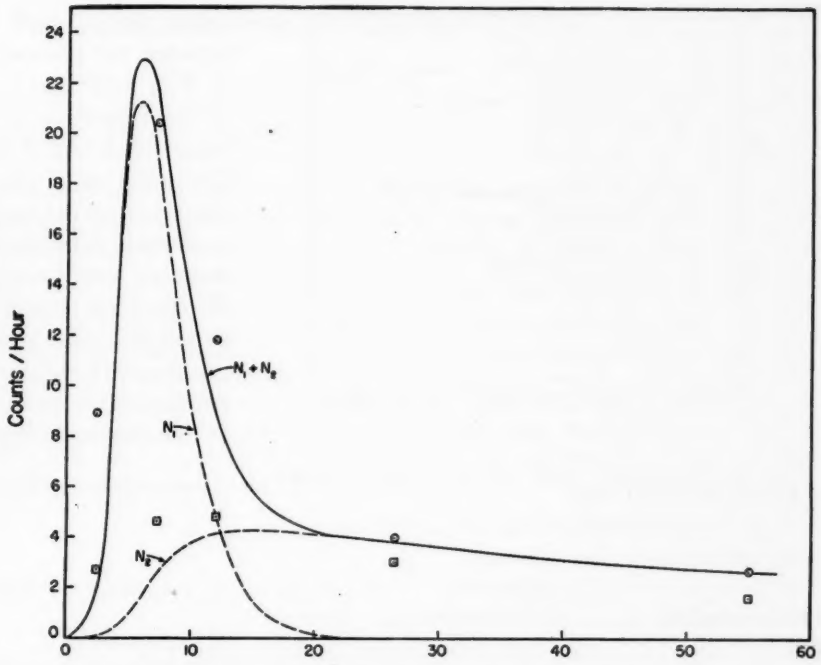

FIG. 8. The curve labeled N_1 is the theoretical transition curve for bursts produced by electrons and photons; the curve labeled N_2 is the theoretical transition curve for bursts produced by nuclear interactions. The round points represent the observed $(A\ I)$ coincidence rates, and the square points represent the difference of the coincidence rates $(A\ I)$ and $(A_2\ I)$. The abscissa represents the total thickness of lead shield above the ionization chamber in radiation lengths.

in the ionization chamber. This hypothesis may lead one to expect a decrease in the relative number of multiple discharges as the lead thickness between A and I is increased from 12.7 to 27.9 cm; such a prediction is not borne out by the observations—a fact which has not yet received a satisfactory explanation. The existence of correlated nuclear interactions indicated by various experiments may possibly furnish a clue.

We made an attempt to interpret quantitatively the observed transition curve by assuming that nuclear interactions produce bursts exclusively through the intermediary of electron showers (i.e., that the contribution of heavily ionizing particles to the ionization bursts observed under lead is negligible). We further assumed that the energy spectrum of the electrons or photons produced in the lead shield by nuclear interactions is identical to that of the electrons and photons incident upon the lead from the atmosphere and is represented by a power law. Incomplete experimental information and mathematical difficulties of the shower theory made it necessary to adopt the following additional simplifying hypotheses, all of which are very questionable: (a) the production of more than one high energy electron or photon in a nuclear interaction is a rare event; (b) the simultaneous arrival upon the instrument of more than one high energy electron or photon from the atmosphere is a rare event; (c) in the computation of cascade showers, fluctuations can be neglected, and the approximation described as approximation "B" in the review article by Rossi and Greisen can be used.[4]

Under the above assumptions, the number of showers with more than Π-electrons coming out of the lead shield and initiated by electrons or photons incident upon the shield is given by the expression

$$N_1(t)=A[E(\Pi, t)]^{-\alpha}, \qquad (1)$$

where t is the thickness of the lead in radiation lengths, $E(\Pi, t)$ is the energy of an electron or photon which produces a shower of Π-particles after traversing the thickness t, and $AE^{-\alpha}$ is the number of electrons and photons of energy greater than E incident upon the lead (the difference between showers produced by electrons or photons of the same energy in a given lead thickness is here neglected).

Similarly, the number of showers with more than Π-electrons coming out of the lead shield and initiated by electrons or photons arising from nuclear interactions in the lead is given by

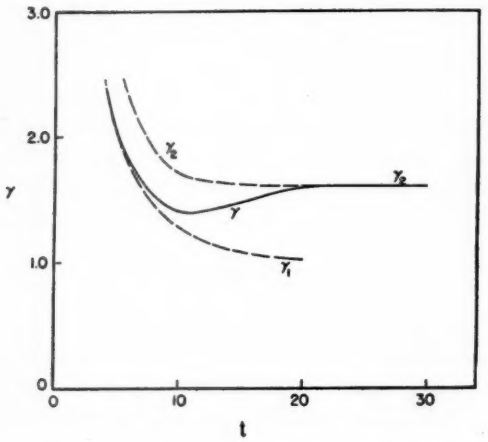

FIG. 9. Theoretical value of $\gamma_1=-d(\ln N_1)/d(\ln\Pi)$, $\gamma_2=-d(\ln N_2)/d(\ln\Pi)$, and

$$\gamma=-d(\ln N)/d(\ln\Pi)=(N_1\gamma_1+N_2\gamma_2)/(N_1+N_2)$$

at $\Pi=100$ and for various values of t.

the expression

$$N_2(t)=B\int_0^t \exp(-t'/l)[E(\Pi, t-t')]^{-\alpha}dt'/l, \quad (2)$$

where l is the absorption thickness (in radiation lengths) of the radiation producing nuclear interaction and $BE^{-\alpha}$ represents the total number of electrons or photons of energy larger than E produced by this radiation before complete absorption in lead.

The curves in Fig. 8 represent $N_1(t)$, $N_2(t)$, and $N(t)=N_1(t)+N_2(t)$ computed from Eqs. (1) and (2) with $\alpha=1.6$, $l=72$, $\Pi=100$, and such values for A and B as to obtain agreement between the theoretical and experimental values of $N(t)$ near the maximum and at the tail end of the transition curve. The ratio between the values of A and B thus determined is $A/B=0.4$. The value of Π chosen for the computation is greater than the number of electrons required to produce a pulse equal to 1.1 P_α in the ionization chamber (see Section II-1). However, many of the electrons coming out of the lead are absorbed by the iron plate placed above the chamber. Also, the shape of the theoretical transition curve does not depend critically on the value of Π.

The curves in Fig. 9 represent the quantities:

$$\gamma_1=-(d(\ln N_1)/d(\ln\Pi)),\ \gamma_2=-d(\ln N_2)/d(\ln\Pi),$$

and

$$\gamma=-d(\ln N)/d(\ln\Pi)=(\gamma_1N_1+\gamma_2N_2)/(N_1+N_2)$$

as functions of t.

Examination of Figs. 8 and 9 shows that the agreement between theoretical predictions and experimental data is as good as one can expect considering the crude approximations made. In particular, it is interesting to note that both experiment and theory indicate a minimum in the value for γ at a thickness where N_1 and N_2 have comparable values. The physical reason for this minimum is that at this thickness the relative contribution of "old showers" (i.e., of showers beyond the maximum) is greater than at either larger or smaller thicknesses.

The Radiations from 2.7-Day Au^{198}

PAUL W. LEVY* AND E. GREULING**
Oak Ridge National Laboratory, Oak Ridge, Tennessee
(Received November 3, 1948)

The radiations from the 2.7-day Au^{198} activity were investigated with a counter and photographically recording beta-ray spectrometer. The shape of the continuous beta-ray spectrum is essentially that of an allowed spectrum with some additional intensity in the region below 0.6 Mev. The maximum energy of the spectrum is 0.966 ± 0.010 Mev. Very strong conversion lines are observed from a gamma-ray of 0.408 ± 0.004 Mev, and weak conversion lines attributed to gamma-rays of 0.157 ± 0.002 and 0.208 ± 0.002 Mev were detected. These weak lines and the deviation of the spectrum from the theoretically permissable spectra suggest that the beta-ray spectrum may be complex with a component of 0.601 ± 0.016 Mev maximum energy occurring in 15 percent, or less, of the disintegrations. This suggested mode of decay is consistent with the theoretical analysis of the spectrum and half-life. In terms of this theory the 0.966-Mev transition is described by the polar-vector or pseudo-scalar interaction corresponding to a nuclear spin change of ±1, with no parity change.

I. INTRODUCTION

ONE of the first radioactive substances obtained by neutron irradiation was the 2.7-day activity of Au^{198} produced by a $n-\gamma$ reaction on the stable Au^{197} isotope. The radiations from this activity have been studied many times, and yet there is still no positive assurance that they are unambiguously known. The earliest determinations of the beta- and gamma-ray energies naturally employed absorption methods.[1-6] The energies reported for the beta-particles are in the region of ≈0.5 to ≈1.0 Mev and for the gamma-rays from ≈0.065 to 0.7 Mev with one report[2] of a gamma-ray of 2.5 Mev. Some increase in the precision of the radiation measurements was obtained by Richardson,[7] who used a cloud chamber to observe the momentum distribution of the beta-rays, and electrons ejected by quanta from a radiator. Lawson and Cork,[8] using a beta-ray spectrometer, located the internal conversion lines of a Au activity of approximately 3-day half-life. Siegbahn[9] has reported that the 2.7-day radiations consist of a single beta-ray of 0.92 Mev, followed by a gamma-ray of 0.401 Mev. Recently, Saxon[10] and Wilkinson and Peacock[11] have confirmed the 0.970 ± 0.010 Mev value for the maximum energy of the beta-rays we had previously reported.[12] They did not find evidence for the low intensity component of ≈0.6 Mev maximum energy which our work indicates may be present.

In addition to the energy measurements, many investigators[13-18] have employed coincidence absorption methods in their work on this activity. Again, in this coincidence work, there is disagreement among the various experimenters. In particular, the existence of gamma-gamma coincidences is disputed.

Considering the disagreement among the various workers, the fact that many different decay schemes for Au^{198} have been proposed is

* Present address: Physics Department, Carnegie Institute of Technology, Pittsburgh, Pennsylvania.
** Present address: Duke University, Physics Department, Durham, North Carolina.

[1] Fermi, Amaldi, d'Agostino, Rasetti, and Segrè, Proc. Roy. Soc. **A146**, 483 (1934).
[2] G. J. Sizoo and G. Ejkman, Physica **6**, 332 (1936).
[3] J. M. Cork and R. L. Thornton, Phys. Rev. **51**, 59 (1937).
[4] E. McMillan, M. Kamen, and S. Ruben, Phys. Rev. **52**, 375 (1937).
[5] J. M. Cork and J. Halpern, Phys. Rev. **58**, 201(A) (1940).
[6] R. S. Krishnan, Proc. Camb. Phil. Soc. **37**, 186 (1941).
[7] J. Reginald Richardson, Phys. Rev. **55**, 609 (1939).
[8] J. L. Lawson and J. M. Cork, Phys. Rev. **58**, 580 (1940).
[9] Kai Siegbahn, Proc. Roy. Soc. **A189**, 527 (1947).
[10] David Saxon, Phys. Rev. **73**, 811 (1948).
[11] R. G. Wilkinson and C. L. Peacock, Phys. Rev. **74**, 1250 (1948).
[12] P. W. Levy and E. Greuling, Phys. Rev. **73**, 83 (1948).
[13] F. Norling, Ark. Mat. Astr. Fys. **A27**, No. 27 (1941).
[14] Arnold Clark, Phys. Rev. **61**, 242 (1942).
[15] N. Feather and J. Dainty, Proc. Camb. Phil. Soc. **40**, 53 (1944).
[16] M. L. Wiedenbeck and K. Y. Chu, Phys. Rev. **72**, 1164, 1171 (1947).
[17] E. T. Jurney and M. R. Keck, Phys. Rev. **73**, 1220 (1948).
[18] C. E. Mandeville and M. V. Scherb, Phys. Rev. **73**, 634 (1948).

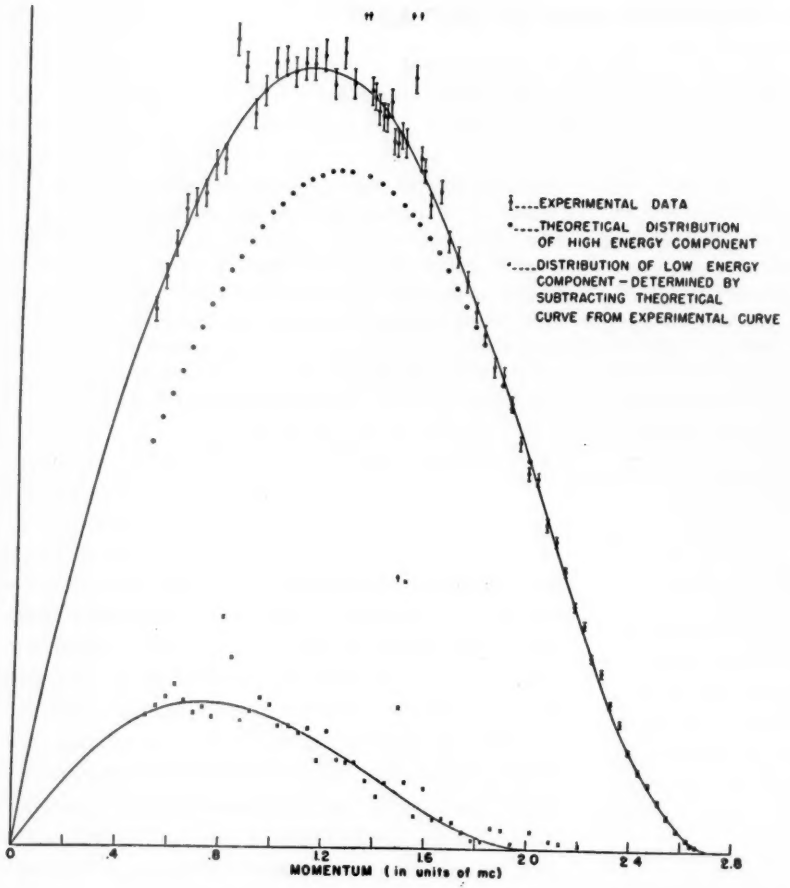

FIG. 1. Momentum distribution of Au^{198} electrons. The theoretical curve is

$$CF(W^2-1)(W_0-W)^2,$$

where W is the total electron energy in mc^2 units, W_0 is the end-point energy, 2.89_8, F is the Fermi Coulomb effect function, and C is the single component correction factor shown in curve I of Fig. 5. Arrows indicate experimental points off the figure arising from the conversion lines of the 0.41 Mev gamma-ray.

not surprising. In this paper we shall present the evidence and arguments leading to still another decay scheme.

II. EQUIPMENT

The measurements to be described below were all made with two beta-ray spectrometers.[19] One employs G-M tube recording, has a radius of 10 cm, and is similar to that constructed by Lawson and Tyler.[20] It possesses the additional feature that more than one counter can be located in the electron trajectory. With this arrangement it is possible to record coincidences between these counters, as produced by a particle in the required trajectory, with a very substantial reduction of the background due to gamma-rays from the source. This method is particularly advantageous when observing photoelectrons ejected from a radiator to determine gamma-ray energies. For measurements of continuous spectra, however, the shielding was sufficient to reduce the background to such a low level that the coincidence feature was not used. The other spectrometer employs photographic recording and is similar to those used by Ellis[21] and Valley and McCreary.[22]

The magnetic field for both of these spectrometers is provided by an electromagnet of the usual design except for the field coils. Instead of coils which have a few turns and require large currents, these coils have several thousand turns, high resistance, and require currents from 3 to 150 milliamperes. With this arrangement electronic stabilization of the field current proved to be extremly successful. All magnetic field

[19] This equipment is described in detail in Plutonium Project Report CP-3702, which is to be included in the nuclear physics section of the Plutonium Project Record.
[20] J. L. Lawson and A. W. Tyler, Rev. Sci. Inst. 11, 6 (1940).
[21] C. D. Ellis, Proc. Roy. Soc. **A138**, 318 (1932).
[22] G. E. Valley and R. L. McCreary, Phys. Rev. **56**, 581 (1947).

measurements were made with a search coil arrangement that was calibrated with a standard mutual inductance. With this equipment the total error in the energy measurements was less than one percent for particles greater than 100 kev and less than two percent for particles between 50 and 100 kev.

The sources used for the continuous spectrum and conversion electron studies consisted of gold foils mounted on Zapon films 0.05 mg/cm² thick. The thinnest foil used was 0.26 mg/cm². Thicker foils were occasionally used for conversion electron pictures, since, for energy measurements, they did not impare the precision and provided more activity. Also, thicker foils were used to determine how the foil thickness affected the shape of the continuous spectrum. Initially, it was found that usually the foils did not adhere sufficiently to the Zapon to permit handling. This situation was remedied by covering the Zapon film with extremely small droplets of water from an atomizer before placing the foils on the film. The action of the water droplets, due to surface tension, was to produce intimate contact between the foil and film. When the source was put in a vacuum, the water between the foil and film evaporated rapidly.

III. THE BETA-RAY SPECTRUM

The continuous spectrum was investigated with the 180° counter-recording spectrometer. The momentum distribution obtained with the thinnest source used, 0.26 mg/cm², is shown in Fig. 1. The Kurie plot, Fig. 2, was calculated from this data. It is apparent that this plot yields the essentially straight line theoretically attributed to allowed transitions and typical of single component beta-ray spectra. The final value for maximum energy obtained for the continuous spectrum is 0.966 ± 0.010 Mev. From the energy of the spectrum and the 2.7-day half-life, one would expect this to be a second forbidden transition for which the Kurie plot would not be linear. It was found that the curve obtained could not be fitted by any of the second forbidden correction factors predicted by theory. In particular, there was greater intensity in the region of the spectrum below 0.6 Mev than could be accounted for by a one-component theoretical spectrum. The appearance of weak conversion lines indicated that there were additional gamma-rays present other than the well-known one of 0.41 Mev.[23,24] Some of these low energy conversion lines had been reported previously by Plesset[25] and a low

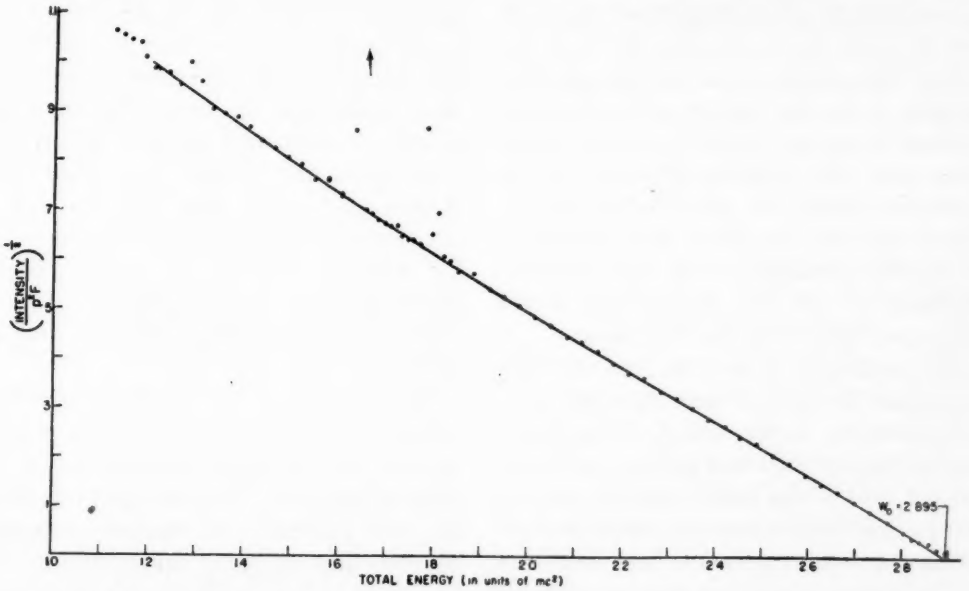

FIG. 2. Kurie plot. Arrows indicate points off the figure. The intensity is (counting rate)/$H\rho$.

[23] J. M. Cork, Phys. Rev. **72**, 581 (1947).
[24] DuMond, Lind, and Watson, Phys. Rev. **73**, 1392 (1948).
[25] E. H. Plesset, Phys. Rev. **62**, 181 (1942).

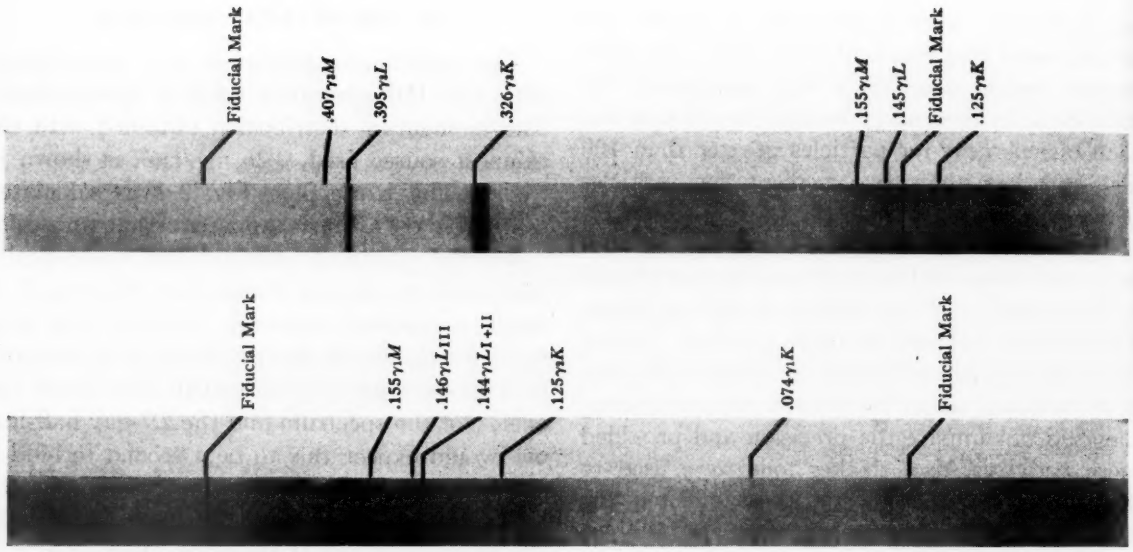

FIG. 3. Conversion electron pictures. Typical examples of the "pictures" obtained with the photographic spectrograph of the lines found in the Au spectrum. The weaker lines were lost in the process of making the reproductions.

energy gamma-ray by Richardson.[7] These weak gamma-rays could not be fitted in a decay scheme involving a single beta-ray component.

Measurements were undertaken to determine whether the additional intensity below 0.6 Mev could be attributed to source thickness effects. First the continuous spectrum was determined with sources ≈ 25.0 and 1.46 mg/cm^2 thick. It was found that the spectrum obtained from the 25.0 mg/cm^2 thick source contained considerably more intensity in the low energy region than had been obtained from the thinnest source. However, there was only a slight difference in the spectra obtained from the two thinner sources. If these were the only pertinent data, one could not exclude the possibility that the observed extra intensity in the low energy half of the spectrum is an effect of source thickness.

A second possibility is that the low intensity lines, as well as the extra intensity, could come from contamination in the source. Accordingly, the decay of this activity was followed with the spectrometer, and it was found that all parts of the spectrum, and the low intensity lines, decayed at the same rate over a period of two half-lives. The half-life observed was less than one percent lower than the reported value of 2.70 days.[26] A spectrochemical analysis of the gold foil used was made in an attempt to detect impurities. None were found which were present in quantities greater than traces except silver. Since the $K-L$ separations of the observed lines (Fig. 3) is approximately that expected for gold, these lines could not be attributed to silver. The separations could not be determined with sufficient accuracy to decide in what heavy element the conversion of the gamma-ray took place. Also, considering the large *activation* cross section of gold as compared to that of silver and the other impurities present, one is led to the conclusion that these lines are not due to contamination or impurities. Since the cross section for neutron capture is usually considerably higher than for other reactions, e.g., $n-p$ reactions, one would not expect to find activities other than the Au^{198} one.

On the basis of this evidence it is feasible to consider the possibility that there is in reality a second low intensity component in the continuous spectrum. Proceeding on this assumption, one can determine its shape by subtracting the theoretically predicted curve from the data as is indicated in Fig. 1. The maximum energy of the spectrum so obtained is approximately 0.6 Mev. This value is in good agreement with what is to be expected if this low intensity component is

[26] N. Sugarman and co-workers; unpublished Plutonium Project Work. See also reference 20.

followed by gamma-rays of 0.157 and 0.208 Mev, as the conversion electron studies described below indicate are present. However, assuming that the suggested decay scheme, Fig. 4, is correct, a more accurate procedure to determine the maximum energy of this component is to subtract the low intensity gamma-ray energies from the maximum energy, 0.966, of the intense spectrum. The value so obtained is 0.601 ± 0.16 Mev.

From the curves shown in Fig. 1 one can ascertain that the low intensity component is present in only 15 percent, or less, of the disintegrations. It is difficult to assign an error to the value of 15 percent, since, in order to determine the branching, we had to extrapolate the spectrum below the lowest momentum measured.

IV. GAMMA-RAY MEASUREMENTS

In order to obtain detailed information on the conversion lines that were found superimposed on the continuous spectra, they were studied with the photographic spectrograph. The lines from the low energy gammas were considerably weaker than the lines from the 0.41 Mev gamma. In fact, only by carefully controlling the exposure could both the K and L lines of the low intensity gammas be detected. The conversion line data and an analysis of it is contained in Table I. Figure 3 contains typical examples of the pictures obtained with the spectrograph. Considering the various factors that produce variations in the energy determinations of the lines, the best values for the gamma-ray energies are 0.408 ± 0.004, 0.157 ± 0.002 and 0.208 ± 0.002 Mev. It is to be noted that if a gamma-ray of 0.065 Mev were present with an intensity greater than a few percent, as suggested by Feather and Dainty,[15] it should have produced intense conversion lines. No such sharp lines were detected. However, there was some evidence of blackening of the negative where the Auger electrons produced by Hg and Au x-rays were focused. We have not been able to explain, at the moment, why Jnanananda[27] should have found these Auger electrons and not the lines from the 0.157 and 0.208 Mev gammas.

Most of the lines detected have been observed by Plesset, who suggests that they are due to an isomeric state of Hg^{198}, to which the 0.970 Mev beta-ray decays. If this were the case these gammas should be as intense as the 0.41 Mev gamma and would be readily detectible by absorption methods. Recently DuMond, Lind, and Watson[24] measured the energy of the 0.41 Mev gamma very accurately with a crystal spectrometer. The value they obtained, 0.4112 ± 0.001, agrees with ours, to within the experimental error. They were not able to detect the diffracted beam from the weaker gammas because of their low intensity, but by using their apparatus to obtain a finely collimated gamma-ray beam, an absorption experiment was performed that

TABLE I. Gamma-rays and conversion lines in Au^{198}.

Gamma-ray	Conversion lines observed	Estimated intensity of conversion lines	Energy of conversion lines (Mev)	Energy of gamma-rays (Mev)
1	K	Medium	0.074	0.157
	L_I+L_{II}	Weak	0.144	0.158
	L_{III}	Very weak	0.146	0.158
	M	Faint	0.155	0.157
2	K	Weak	0.125	0.208
	L	Very faint	0.193	0.207
3	K	Very strong	0.326	0.409
	L	Strong	0.395	0.407
	M	Strong	0.407	0.409

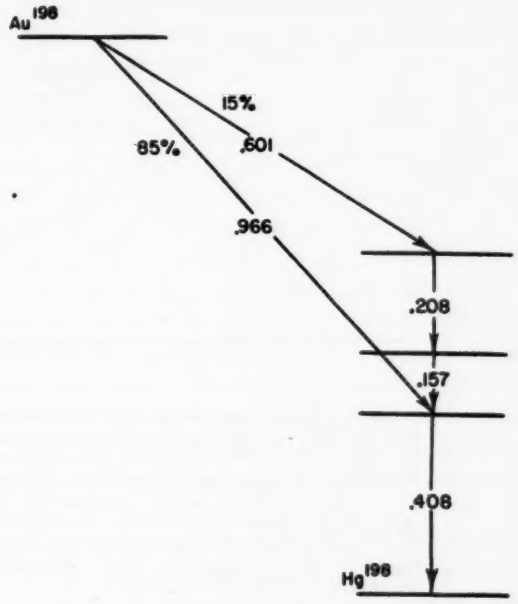

FIG. 4. Suggested decay scheme for Au^{198}. The cascade order of the two weak gamma-rays is not known.

[27] Swami Jnanananda, Phys. Rev. 70, 812 (1946).

indicates these gammas are present to about the intensity we observed.

A determination of the average gamma-ray energy has been made by Barker,[28] who gives a value of 0.366 Mev of gamma-ray energy per electron (beta-particles plus conversion electrons) emitted. This corresponds to 0.383 Mev of gamma-ray energy per disintegration, using the 4.7 percent internal conversion coefficient for the 0.41-Mev gamma-ray reported by Wiedenbeck and Chu.[16] Barker's value is consistent with a decay scheme containing only the 0.41-Mev gamma.

Using calorimetric methods, Cannon and Jenks[29] find that the total energy per disintegration for this activity is 0.788 ± 0.028 Mev. From our intensity distribution curve we find that the average energy of the beta-rays is 0.310 ± 0.01 Mev. Adding the gamma-ray and conversion electron energies to this one obtains 0.773 Mev for the average energy per disintegration. Thus our results are in agreement with those obtained by Cannon and Jenks, but not with the result of Barker.

V. COMPARISON WITH THEORY

Considering the abundance of conflicting data and proposed decay schemes published in the literature, it is obvious that the decay scheme proposed by the authors, Fig. 4, must be considered as tentative. It is worth while, however, to point out that no contradiction with the theoretically predicted spectra, half-life, or branching ratio was found.

The most obvious characteristic of the beta-spectrum measured is its close similarity with the so-called allowed type spectrum. The fact that the half-life of Au^{198} is large enough to require that it be classified as either a first or second forbidden transition prompted one of us to

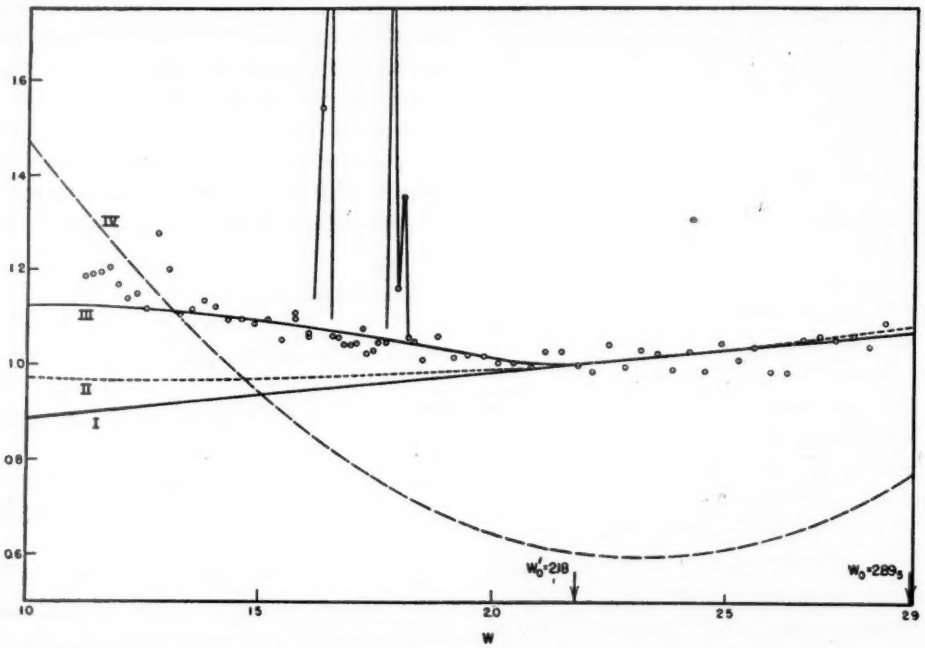

FIG. 5. Dependence of the Au^{198} correction factor on the total energy of the emitted electrons. The points are proportional to the thin source (0.26 mg/cm²) (counting rate)/$(H\rho)$ data divided by $F(W_0-W)^2(W^2-1)$. Curve I is the theoretical correction factor for a single component forbidden transition with $W_0=2.89_5$, i.e., C_{1P} with $\Delta J=\pm1$, "no" or C_{2V} with $\Delta J=\pm1$ "no" for a $0\leftrightarrow1$ transition or $|\alpha|\gg\rho$ (not $0\leftrightarrow1$). Curve II is C_{2V} with $\Delta J=\pm1$ (not $0\leftrightarrow1$) for $|\alpha|=\{W_0\rho\}$. Curve III is C_{2V} or C_{1P} obtained by adding a low energy component with end-point $W_0'=2.18$ mc² for ≈15 percent of the transitions. Curve IV shows the energy dependence of the term in C_{2V} containing $|R_{ij}|^2$. The ordinates are arbitrary. Curves I, II, III and the data normalized to 1 at $W=2.2$ mc².

[28] Edgar C. Barker, Phys. Rev. **72**, 167 (1947).
[29] C. V. Cannon and G. H. Jenks, private communication.

compute the correction factors to the allowed spectral shape one would expect according to the present theory of forbidden beta-decay transitions.[30]

All of the first forbidden correction factors are nearly independent of the electron energy if the spin and parity change for the transition is $\Delta J=\pm 1$ or 0 "yes." In the expressions for these correction factors the quantity M_0 of Konopinski and Uhlenbeck's paper[30] is essentially energy independent for high Z. This quantity M_0 containing $(\alpha Z/\rho)^2$, which is the square of the potential energy of an electron at the surface of the nucleus, predominates. $(\alpha Z/\rho)$ is much larger than the electron and neutrino energies appearing in the other terms of the correction factor. Only C_{1T} and C_{1A} for $\Delta J=\pm 2$, "yes," show such a strong variation with energy that they can be ruled out as possibilities for the Au^{198} transition upon comparison with the observed spectrum.

Of the second forbidden correction factors, the only ones that are weakly energy dependent are C_{2V}, $\Delta J=\pm 1$, "no" and C_{2T}, $\Delta J=0\rightarrow 0$, "no." The second forbidden tensor interaction with $\Delta J=0\rightarrow 0$ can be ruled out on two counts. First, the 0.41 Mev gamma-ray transition from the excited state of Hg to its ground state, which has spin zero, would be $0\rightarrow 0$ and therefore is completely forbidden. Second, if the spin of Au^{198} is zero, one would expect to find the $0\rightarrow 0$ beta-transition to the ground state of Hg out competing the $0\rightarrow 0$ transition to the Hg excited state.

That C_{2V} has essentially the same energy dependence as C_{1X} for $\Delta J=\pm 1$ is not apparent except for the $0\leftrightarrow 1$ transition, in which case only the factor containing the nuclear matrix element, $\int \boldsymbol{\alpha}\times\mathbf{r}$, enters. R_{ij} and A_{ij} appearing in C_{2V} vanish for $0\leftrightarrow 1$ transitions. For $\Delta J=\pm 1$ (not $0\leftrightarrow 1$) C_{2V} contains all three of the above nuclear matrix elements and the variation of the coefficients of $|R_{ij}|^2$ and $|A_{ij}|^2$ with energy does not resemble the experimental correction factor shown in Fig. 5. One may estimate the magnitudes of these nuclear matrix elements[31] in terms of the nuclear radius ρ (in units of the Compton wave-length) and the average value of $|\boldsymbol{\alpha}|\approx$nucleon velocity/velocity of light. Such an estimate yields, for $|\boldsymbol{\alpha}|\approx 0.1$, the following magnitudes for the three matrix elements appearing in C_{2V}:

$$\left|\int \boldsymbol{\alpha}\times\mathbf{r}\right|^2 \approx \tfrac{2}{3}|\boldsymbol{\alpha}|^2\rho^2 = 36\times 10^{-7},$$

$$\sum_{ij}|A_{ij}/2!|^2 \approx (5/9)|\boldsymbol{\alpha}|^2\rho^2 = 30\times 10^{-7},$$

$$\sum_{ij}|R_{ij}|^2 \approx \tfrac{2}{3}\rho^4 = 2.0\times 10^{-7}.$$

The term in C_{2V} containing $\sum|A_{ij}|^2$ adds less than one percent to C_{2V} for all energies as compared to that part contributed by the $|\int \boldsymbol{\alpha}\times\mathbf{r}|^2$ term, because the energy dependent factor multiplying $|A_{ij}|^2$ does not contain the Coulomb energy of the electron. Curve IV of Fig. 5 shows the term containing $|R_{ij}|^2$. Curve II is C_{2V} obtained by using a minimum estimate of the magnitude of $|\boldsymbol{\alpha}|$, i.e., $|\boldsymbol{\alpha}|=W_0\rho$, where $W_0=2.9$ is the end-point energy in mc^2 units. Curve I is proportional to the coefficient of $|\int \boldsymbol{\alpha}\times\mathbf{r}|^2$ and is thus appropriate for C_{2V} if $|\boldsymbol{\alpha}|\gg\rho$.

The only first forbidden correction factor which has the same order of magnitude as C_{2V} with $\Delta J=\pm 1$ and at the same time varies with energy just as shown in Curve I of Fig. 5 is C_{1P}. Of the correction factors which vary only slightly with energy, only C_{1P} and C_{2V} with $\Delta J=\pm 1$, "no" and C_{2T} with $\Delta J=0\rightarrow 0$, "no" have the order of magnitude 10^{-3}, which is the ratio of allowed to experimental ft value for Au^{198}. The other first forbidden correction factors with $\Delta J=\pm 1$ or 0, (not $0\rightarrow 0$), "yes" are too large by a factor of 100 because of the Coulomb energy term. C_{1T} and C_{1A} have the order of magnitude 10^{-3} for $\Delta J=\pm 2$, "yes," but cannot possibly be reconciled with the almost allowed type spectrum. All the other second forbidden correction factors are too small by a factor of 1/100 and/or do not show any similarity with the energy dependence of the experimental correction factor.

The deviation of the low energy data from the theoretical correction factors (Curves I or II of Fig. 5) can be attributed to four possible alternatives. (1) The beta-decay of Au^{198} is complex,

[30] E. J. Konopinski and G. E. Uhlenbeck, Phys. Rev. 60, 308 (1931). The notation of this paper is used throughout.

[31] E. Greuling, Phys. Rev. 61, 568 (1942).

(2) back scattering from the source and its support has not been entirely eliminated, (3) the present theory applied to low energy electrons is not correct,[32] or (4) an undetected contaminant activity may be present.

To resolve the observed spectrum into two components would be an indefensible procedure if there was no supporting evidence other than the slight deviation of the spectrum from one possibly predicted by theory. However, the existence of the two weak gamma-rays of 0.157 and 0.208 Mev and the possibility that the $\gamma-\gamma$ coincidences reported are real suggests the level scheme shown in Fig. 4. It may not be accidental that the inner end point, $W_0'=2.18$ mc^2, obtained by subtraction, coincides with the energy below which the observed spectrum is larger than predicted by the theory for a single component decay.

Curve III in Fig. 5 was obtained by assuming a branching decay for which the theoretical correction factor has the form

$$C=C_{2V \text{ or } 1P}[1+A(2.18-W)^2/(2.89_5-W)^2]$$

below 2.18 mc^2. $C_{2V \text{ or } 1P}$ is Curve I shown in Fig. 5. The parameter A is the ratio of inner end point to outer end-point correction factors which must have the order of magnitude unity. To fit the data as shown, $A=0.7$ was used. This corresponds to a maximum branching ratio of 15 percent low energy to 85 percent high energy transitions. A smaller branching ratio would be obtained if part of the rise below 2.2 mc^2 is due to source thickness effects, or if C_{2V} for the main component is between Curves I and II shown in Fig. 5.

[32] The failure of the theory at low energies is suggested by the anomalous allowed spectra observed for Cu^{64} and Cu^{61} by C. S. Cook and L. M. Langer, Phys. Rev. **73**, 601 (1948) and Phys. Rev. **74**, 227 (1948).

VI. CONCLUSIONS

It is shown that the 2.7-day Au^{198} beta-ray spectrum has a maximum energy of 0.966 ± 0.010 Mev. Measurements with the photographic spectrometer indicate that in addition to the strong 0.408-Mev gamma-ray two weak gammas of 0.157 and 0.208 Mev produce internal conversion electrons. The presence of the low energy lines suggests the possibility that the gold spectrum is complex with 15 percent, or less, of the transitions being to an excited level of Hg followed by the two weak gamma-rays in cascade to the level 0.408 Mev above the ground state. The maximum energy, 0.601 Mev, of the low intensity beta-rays is consistant with the theoretical analysis of the complete spectrum above 200 kev. In this region we believe no distortion of the spectrum, caused by counter window absorption, scattering in the source, or its backing, is present.

The theoretical analysis of the spectrum suggests that the 0.966-Mev beta-transition corresponds to a nuclear spin change of ±1 with no parity charge according to the polar vector or pseudoscalar form of interaction.

VII. ACKNOWLEDGMENT

The authors wish to acknowledge many helpful discussions with members of this laboratory too numerous to mention. Particularly appreciated is the counsel of Doctors S. DeBenedetti and E. O. Wollan. This work was done at the Oak Ridge National Laboratory under Contract W-7405 eng 26 for the Atomic Energy Commission.

The Microwave Spectrum of Carbonyl Selenide*

M. W. P. STRANDBERG, T. WENTINK, JR.,** AND A. G. HILL
Research Laboratory of Electronics, Massachusetts Institute of Technology, Cambridge, Massachusetts

(Received November 17, 1948)

The microwave absorption spectrum of carbonyl selenide, OCSe, is reported. The expected linear structure is confirmed. The spectrum includes absorptions caused by various isotopic forms of the molecule in the zero-point vibrational state and the first excited symmetrical stretching and bending vibrational states. From these data vibration-rotation interaction coefficients, mass differences and approximate interatomic distances have been determined. Values for the nuclear spins of the six stable selenium isotopes are suggested. Observations of the Stark effect lead to a determination of the dipole moment of the molecule in several vibrational states. Intensity measurements are used to determine vibrational frequencies and relative isotopic abundance.

I. INTRODUCTION

WE have previously reported measurement of the microwave absorption spectrum of carbonyl sulfide, OCS[1] (hereinafter referred to as reference 1). An obvious extension of the measurements would be the observation of the absorption spectrum of OCSe and OCTe to complete the chemically available members of the OCX series, where X is a $^3P_2$ atom from the VI_b group of the periodic table. We have observed the spectrum of OCSe, and the results of these measurements are reported in this paper.***

Carbonyl selenide, OCSe, as expected, is a linear molecule. Its preparation and chemical properties have been reported in the literature.[2] No spectroscopic data, neither vibrational nor rotational, were available at the beginning of this work. There are many isotopic forms of the molecule, since, beside the oxygen and carbon isotopes (O^{16}, O^{18}, C^{12}, C^{13}), there are six stable selenium atoms. These selenium atoms have mass numbers 82, 80, 78, 77, 76, and 74. Some packing-fraction data for these atoms are available from the work of Aston,[3] and the nuclear spins of Se^{78} and Se^{80} are tabulated by Herzberg[4] as zero.

II. EXPERIMENTAL

The sample of OCSe was prepared by passing CO over Se at approximately 500°C.[2] In setting up the microwave apparatus for a preliminary search, the $J=2\rightarrow3$ transition was calculated to be in the 1.25-cm region by using the known O−C resonant bond distance as determined in OCS, and an estimated C−Se resonant bond distance based on published single and double bond radii for selenium.[5]

The sweep spectroscope and frequency standard described in reference 1 were used in measuring the absorption frequencies. The signal generators for the $J=2\rightarrow3$ were reflex klystrons; for the $J=5\rightarrow6$ and the $J=6\rightarrow7$ absorption transitions were measured with the second harmonic power generated in silicon crystals driven by standard klystrons.

III. INTERPRETATION

As in OCS, absorptions occur for each isotopic form of the molecule, in each vibrational state. In the usual notation the absorption frequencies are given as:

$$\nu_{J\rightarrow J+1}=2(J+1)cB_v-4cD_v[(J+1)^3-(J+1)l^2]\ \text{cycles/sec.}, \quad (1)$$

where J is the total angular momentum quantum

* This work has been supported in part by the Signal Corps, the Air Materiel Command, and O.N.R.

** Now at Brookhaven National Laboratory.

[1] M. W. P. Strandberg, T. Wentink, and R. L. Kyhl, RLE Technical Report No. 59, "Rotational absorption spectrum of OCS," May 13, 1948, which appears in Phys. Rev. **75**, 270 (1949).

*** A preliminary report was given at the January, 1948, New York meeting of the American Physcial Society. Phys. Rev. **73**, 1249 (1948).

[2] T. G. Pearson and P. L. Robinson, J. Chem. Soc. (London) 652 (1932); R. H. Purcell and F. D. Zahoorbux, J. Chem. Soc. (London) 1029 (1937).

[3] F. W. Aston, Proc. Roy. Soc. **132**, 487 (1931).

[4] George Herzberg, *Atomic Spectra and Atomic Structure* (Dover Publications, New York, 1941).

[5] L. Pauling, *Nature of the Chemical Bond* (Cornell University Press, Ithaca, 1939).

TABLE I. Observed absorption frequencies.

Molecule	Transition $J\rightarrow J+1$	Vibrational state v_1 v_2 v_3	Frequency Mc/sec.	
	2→3	0 0 0		
$O^{16}C^{13}Se^{82}$			23964.50±.03	
Se^{80}			24105.98	
Se^{78}			24254.67	
Se^{77}			24331.71	
Se^{76}			24410.70	
Se^{74}			24514.67	
$O^{16}C^{13}Se^{80}$			23880.18	
Se^{78}			24030.58	
	5→6			
$O^{16}C^{13}Se^{80}$			48211.46	
Se^{78}			48508.88	
	6→7			
$O^{16}C^{12}Se^{82}$			55916.19	
Se^{80}			56246.47	
Se^{78}			56593.16	
	2→3	1 0 0		
$O^{16}C^{13}Se^{82}$			23885.76	
Se^{80}			24026.39	
Se^{78}			24174.30	
Se^{77}			24250.84	
	2→3	0 1 0 (l-doublet)		
$O^{16}C^{12}Se^{82}$			24014.97	23996.26
Se^{80}			24156.93	24138.05
Se^{78}			24305.95	24286.82
Se^{77}			24383.21	24363.97
Se^{76}			24462.42	24442.98

number, l is the angular momentum quantum number along the molecule figure axis; $|l|\leq J$, D_v is the centrifugal distortion coefficient in cm^{-1}, and B_v is the average reciprocal moment of the molecule in vibrational state v, in cm^{-1}.

The vibrational reciprocal moment is more usually represented as

$$B_v=(h/8\pi^2c)\langle 1/I\rangle_{Av}=B_e-\sum\alpha_i[v_i+(d_i/2)], \quad (2)$$

where I is the moment of inertia, B_e is the reciprocal moment of inertia of the molecule with the atoms in the minima of their vibrational potential, and α_i is a coefficient measuring the change of the equilibrium reciprocal moment when the molecule is in the v_ith excited state of the ith vibrational state which has a degeneracy d_i. This expression is useful since one may assume that the equilibrium reciprocal moment B_e depends only upon the vibrational constant potential minima, and the masses of the various atomic isotopes. The α_i depend in a complicated fashion upon an averaging of the vibrational properties, e.g., the vibration amplitudes and motions of the various atomic isotopes, and lead ultimately to a study of the binding potential of the molecule. It should be noticed that even in the ground vibrational state ($v_i=0$) the ever present half-quantum of vibrational energy enters into the calculation of $\langle 1/I\rangle_{Av}$, so that even for the ground vibrational state the reciprocal of $\langle 1/I\rangle_{Av}$ is only approximately equal to I.

The molecule OCSe has three non-degenerate vibrational states. The first is a symmetrical stretching state, v_1. The second, v_2, is a doubly degenerate bending vibration composed of an appropriate phase combination of the modes in which the atoms vibrate transverse to the figure axis in two orthogonal planes. Such a vibration can give rise to angular momentum along the figure axis which is commonly designated by the quantum number l. As in OCS, these two bending modes have different α's because of a difference in the vibration-rotation interaction for the two states. We retain the convention of calling them degenerate l states and listing the average α as α_2. The third vibration is an antisymmetrical stretching vibration v_3. In OCSe at room temperature this last vibration, v_3, has a first excited state above the ground state by about $10kT$ so that the Boltzmann factor allows only a very small population of this level. For this reason we have not observed any absorption due to the molecule in the first excited v_3 vibrational mode.

The observed absorption frequencies for various vibrational states are listed in Table I. These data may be used to deduce the term-value parameters as listed in Table II.

Some approximations must now be made to deduce molecular-structure parameters from their term-value parameters. The internuclear distances must be calculated on a rigid rotor basis since α_3 cannot be determined with the present data, and cannot be calculated since the potential constants of OCSe are not known. The rigid rotor values calculated from the zero-point B_v of $O^{16}C^{12}Se^{78}$, $O^{16}C^{13}Se^{78}$, $O^{16}C^{12}Se^{80}$, and $O^{16}C^{13}Se^{80}$ are listed in Table II. The error listed there indicates merely the consistency of the determination from both sets of data. The lack of greater internal consistency presumably results from using data uncorrected for vibration-rotation interaction. We have used the values $h=6.6242\times10^{-27}$ erg sec., 1 a.m.u. $=1.66990\times10^{-24}$ g and in atomic mass units $C^{12}=12.00382$, $C^{13}=13.00758$, $O^{16}=16.00000$, $Se^{78}=77.9424$, and

TABLE II. Derived constants for OCSe.

Molecule	cB_{000} Mc/sec.	ca_1 Mc/sec.	ca_2 Mc/sec.	cq Mc/sec.	cD_J c/sec.
	Term-value parameters				
$O^{16}C^{12}Se^{82}$	3994.009±.005	13.12±.005	−6.86±.005	3.12±.005	875±50
Se^{80}	4017.677	13.27	−6.92	3.15	755±20
Se^{78}	4042.460	13.40	−6.96	3.19	830±50
Se^{77}	4055.300	13.48	−6.98	3.21	
Se^{76}	4068.465		−7.00	3.24	
Se^{74}	4095.793				
$O^{16}C^{13}Se^{80}$	3980.045				
Se^{78}	4005.112				

	Interatomic distances		
	r_0(C=O)†	r_0(C=S)†	r_0(C=Se)†
Covalent radii	1.17A	1.54	1.69*
OCO	1.1632		
OCS	1.1637	1.5586	
OCSe	1.1588±.0001**		1.7090±.0001**

* By extrapolating for the Se triple-bond radius. See text.
** From internal consistency of data. See text.
† Rigid rotor approximation.

$Se^{80}=79.9435$. For the reasons given in reference 1, the internuclear distances may be high by 0.5 percent.

We include values from Table II of reference 1 for comparison. Since Se has no pure triple-bond structure, we have estimated a triple-bond radius by extrapolating from the Se single- and double-bond distances, being guided by the variation of the bond lengths in O and S. This triple-bond length 1.63A was used to calculate the expected CSe resonant bond length. It is interesting to note that, though the OC distance is fitted well with a resonant bond structure, the CSe distance is best approximated with a pure double-bond length, 1.72A.

Since there is an uncertainty in the selenium packing fractions, we have investigated the problem of determining the mass of the selenium isotopes from spectroscopic data. The solution of the problem is rather simple theoretically. If the equilibrium reciprocal moments for, say, $O^{16}C^{12}Se^{80}$, $O^{16}C^{13}Se^{80}$, and $O^{18}C^{12}Se^{80}$ are known, the selenium mass and the two internuclear distances may be determined from the three absorption equations. If the reciprocal moments are known to two parts in 10^6, the selenium packing fraction may be determined to 10 percent. It should be noted that the equilibrium reciprocal moments must be used, so all three α_i for the three isotopic molecules must be determined. This would be difficult to do directly from measurements unless concentrated isotopic molecules were used. The excited vibrational states are only slightly populated at room temperature, and with a rare isotope like C^{13}, present naturally in only one percent abundance, the absorption signal is reduced by another factor of 100. One could, knowing the α_i for one isotopic form, say $O^{16}C^{12}Se^{80}$, calculate the α_i for the other isotopes with a mass perturbation calculation so that the equilibrium reciprocal moment could be determined to within the generous error limits, ±2 parts in 10^6, listed above.

Mass differences, however, may be determined to fair accuracy in the following way. As we have shown in reference 1, the equilibrium interatomic distances of a linear triatomic molecule may be expressed as

$$r_{12}=\frac{[m_3^0/(m_1^0+m_2^0)]\delta_e-\delta_c}{m_1^0[[m_3^0/(m_1^0+m_2^0)]-1]},$$

$$r_{23}=(\delta_e-\delta_c)/\Sigma m^0,$$

$$\delta_e^2=\Sigma m^0\Sigma m^e(I_e^0-I_e^e)/(m_3^0-m_3^e),$$

$$\delta_c^2=\Sigma m^0\Sigma m^c(I_e^0-I_e^c)/(m_2^0-m_2^c).$$

In this notation I_e and m refer to an equilibrium moment of inertia and mass; the superscript refers to the isotopic molecule, i.e., the original molecule, (0), or the one with the end atom, number 3, isotopically substituted, (e), or the one with the central atom changed, (c). Since we assume that the vibration potential is not changed by isotopic substitutions, we may say that the equilibrium distances, i.e., the potential minima, will remain unvaried by isotopic substitutions. It can be seen, therefore, that if a series of isotopes (1, 2, 3, 4···) are substituted for an end or a central atom, all must have the same δ's or

$$\delta_c^{(1)}=\delta_c^{(2)}=\delta_c^{(3)}=\cdots \quad (3a)$$

$$\delta_e^{(1)}=\delta_e^{(2)}=\delta_e^{(3)}=\cdots. \quad (3b)$$

Townes[6] has used the relation expressed in (3b) to interpolate for the S^{33} mass from that of S^{32} and S^{34}, since it follows from (3b) that

$$\Sigma m^{(1)}(I_e^0-I_e^{(1)e})/\Sigma m^{(2)}(I_e^0-I_e^{(2)e})=(m_3^0-m_3^{(1)e})/(m_3^0-m_3^{(2)e}). \quad (4)$$

It should be noted, as Townes has indicated, that the equilibrium moment of inertia must be

[6] C. H. Townes, Phys. Rev. **72**, 513 (1947).

TABLE III. Se mass differences.

Atomic number	Mass a.m.u.	Δm a.m.u.
74	73.9550	1.9903
76	75.9453	0.9974
77	76.9427	0.9997
78	77.9424*	2.0011
80	79.9435*	1.9975
82	81.9410	

* Assumed from packing-fraction data.

used. The equilibrium values are not available at present, but the zero-point vibrational values may be used with some caution. In reference 1 we have shown that a ratio of vibrational moments of inertia is exact to zero order, and experience with OCS has shown that, in fact, such a ratio is good to better than 0.1 percent. For the present we can say no more until the change of α_3 with selenium mass is determined. Because it is interesting in any case, mass differences have been calculated by using ground vibrational data and by assuming the mass values given above for Se^{76} and Se^{82}. The results given in Table III indicate a smooth variation of selenium mass with mass number.

We have noted no anomalies in the absorption due to the isotopic forms of OCSe, either in position or intensity or line breadth. We must, therefore, conclude that the quadrupole interaction energy, i.e., eqQ in the usual notation,[7] is less than 0.5 Mc/sec. Since the selenium atom is an end atom and has a very large nucleus, one would expect the interaction energy to be considerably greater than 0.5 Mc/sec. unless the selenium 77 nuclear spin is equal to $\frac{1}{2}$, and the selenium 74, 76, 78, 80, and 82 atoms have nuclear spins of zero. For this reason we suggest a nuclear spin of $\frac{1}{2}$ for Se^{77}, and zero for $Se^{74, 76, 78, 80, 82}$. This confirms the previous assignment of zero spin to Se^{78} and Se^{80}.

IV. STARK EFFECT

We have observed the Stark effect for the $J=2\rightarrow3$ transition in OCSe in the ground vibrational state and in the first excited symmetrical stretching (v_1) and first excited bending (v_2) vibrations. The latter vibrational state has an anomalous Stark effect since there are matrix elements between the two l-split terms.

The Stark effect for the l-doublet is easily calculated, since we may assume that in the bending vibration the linear molecule is nearly a symmetric top. The Stark effect for a nearly symmetric top has been treated by Penny,[8] and his formulation may be used by the simple notation change $K\rightarrow l$.

The observed l-doublet Stark pattern is shown in Fig. 1. This is an excellent example of perturbation. When the perturbation energy of an electric dipole μ in an electric field of strength E is small compared with the level splitting, the molecule is a good asymmetric top and the Stark effect is second order as in asymmetric tops. When the perturbation energy is greater, however, than the term level splitting, then on this scale the molecule looks like a good symmetric top with degenerate K levels and the Stark effect is a first-order effect. Both conditions are readily obtained in the laboratory.

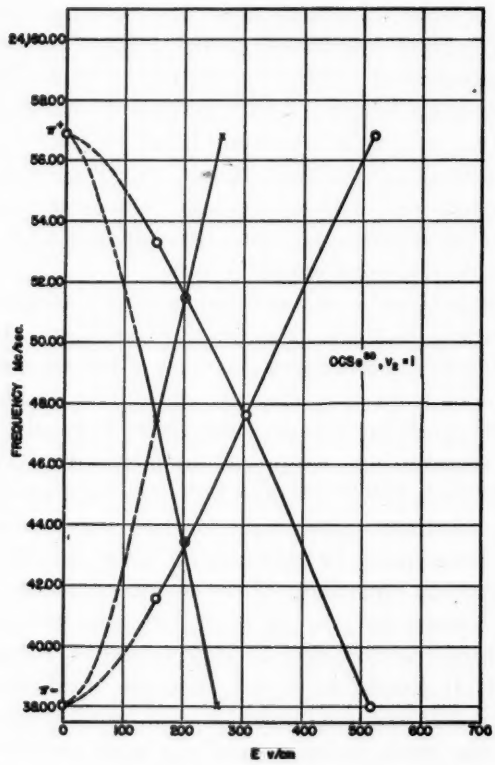

FIG. 1. Observed l-doublet Stark pattern for $OCSe^{80}$.

[7] See, for instance, B. T. Feld, Phys. Rev. 72, 1116 (1947).

[8] W. G. Penney, Phil. Mag. 11, 602 (1931).

TABLE IV. Observed electric dipole moments, OCSe.

Vibrational state			Dipole moment (e.s.u.-cm $\times 10^{18}$)
v_1	v_2	v_3	
0	0	0	0.754
1	0	0	0.728
0	1	0	0.730

One may show that if the components of the two l lines having the same magnetic quantum number, M, are made to coincide in absorption frequency in the presence of an electric field E, then in a $J \rightarrow J+1$ transition

$$\mu = J(J+1)(J+2)(J+3)\Delta\nu' h/4ME, \quad (5)$$

where $\Delta\nu'$ = absorption frequency difference of unperturbed l-doublet and h = Planck's constant.

The observed Stark shift for the ground and excited symmetrical stretching vibrations for $O^{16}C^{12}Se^{80}$ are shown in Fig. 2. As we have shown in reference 1, these data also may be used to determine the static dipole moment. These derived data are given in Table IV. Measurements on $O^{16}C^{12}Se^{78}$ yield the same dipole moment as for $O^{16}C^{12}Se^{80}$ to 0.1 percent. This lack of isotopic dependence of the dipole moment is reasonable since the Se actually moves very little in any of the vibrations, and the fractional mass change is small. This may be compared with the slight change in dipole moment when C^{13} is substituted in $O^{16}C^{12}S^{32}$, as reported in reference 1.

The strong dependence of the static dipole moment on the vibrational state is of interest for many reasons. It is obvious that this effect places a limitation on the significance of dipole moments measured in the bulk, e.g., the Debye temperature-dependent polarization method. In OCSe about $\frac{1}{6}$ of the molecules are in excited vibrational states at 20°C. Of course, the change in dipole moment with vibrational excitation is enhanced in OCSe, a molecule pictured as having a resonant bond structure in which the three forms $^{+}O \equiv C - Se^{-}$, $O = C = Se$, and $^{-}O - C \equiv Se^{+}$ participate. The static dipole moment is thus the difference between the electric moment of the molecule with the OC bond as a single- or a triple-bond structure. A vibrational state which tends to increase the OC length, for example, will make the OC single-bond structure more predominant and decrease the contribution to the state due to the triple-bond form. The actual percentage change of the resultant static moment will depend upon how nearly the contributions to the dipole moment of the two structures canceled each other initially.

J. H. Van Vleck, in a private communication, has suggested that data on the change of the dipole moment with vibrational state are of interest, indirectly, in determining vibrational intensities.[9] We measure the average value of the dipole moment in a vibrational state

$$\bar{\mu} = \int \psi_1 \mu \psi_1^* d\tau, \quad (6)$$

where ψ is the vibration wave function of state 1, whereas the vibrational intensities depend upon

$$\mu_{eff} = \int \psi_1 \mu \psi_2^* d\tau, \quad (7)$$

a quantity measuring the mixing of two vibrational states, 1 and 2, due to the dipole moment. When the vibrational potential of OCSe is known, a connection could be made between the measured dipole moments and the desired vibrational absorption intensity by a calculation of the effective charge[10] from (6), which may then be used to evaluate (7) once the wave functions are known.

With so little knowledge of the vibration

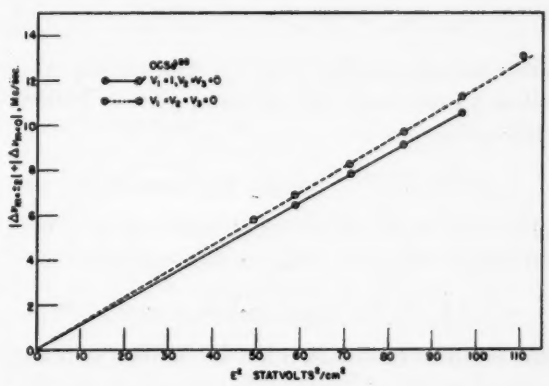

FIG. 2. Observed Stark effect for the ground and excited symmetrical stretching vibration for $O^{16}C^{12}Se^{80}$.

[9] See, for instance, G. Herzberg, *Infrared and Raman Spectra of Polyatomic Molecules* (D. Van Nostrand Company, Inc., New York, 1945), pp. 259–261.

[10] J. H. Van Vleck, *Electric and Magnetic Susceptibilities* (Oxford University Press, London, 1932).

potential available at present, we have not pursued these calculations further.

A few words regarding vibration potential are in order. R. C. Lord and R. S. McDonald of the M.I.T. spectroscopy laboratory have kindly measured the vibration frequencies of OCSe for the 0 to 1 transitions of v_1, v_2, and v_3. This information, together with the centrifugal distortion coefficient[11] allows one to solve for the four quadratic force constants. The six cubic force constants may be determined from the α_i and the change of the α_i with isotopic substitutions. We have not carried out these calculations since, at present, we lack the values of α_3 and its variation with isotopic substitution. In this way it is at least theoretically possible to determine the vibration potential to cubic terms.

Although we have the vibration frequencies as determined from infra-red studies by Lord and McDonald, it is interesting to note that these frequencies could be measured from rotational absorption studies alone. The procedure is straightforward. It is known that the absorption coefficients, γ, of a gas depends upon the number of absorbing molecules, N, and the square of the static dipole moment μ.[1] The ratio of the absorption due to molecules in the ground vibrational state to the absorption of one component of the l-doublet due to the molecules in the first excited bending state is (subscripts give vibrational quantum numbers)

$$\gamma_{000}/\gamma_{010}=(N_{000}/N_{010})(\mu_{000}/\mu_{010})^2. \qquad (8)$$

Since the populations over the vibrational states follow a Boltzmann distribution, we may immediately write

$$e^{-(W_{000}-W_{010})/kT}=(\gamma_{000}/\gamma_{010})(\mu_{010}/\mu_{000})^2,$$

where W is the vibrational term-value energy. But $W_{000}-W_{010}=-hc\omega_2$ so that we have

$$\omega_2=(kT/hc)\ \ln[(\gamma_{000}/\gamma_{010})(\mu_{010}/\mu_{000})^2]\ \text{cm}^{-1}.$$

The ratio of the absorption intensities is readily measured since the absorptions are not widely separated in frequency. We have measured the dipole moments, and so by also measuring the temperature we may determine the vibration frequency ω_2. Our measurements give ω_2 as 474 cm^{-1}. This has been measured as 464 cm^{-1} by Lord and McDonald. The two percent error is large and corresponds to an error of about five percent in measuring the absorption ratio. These measurements could be further refined to yield more precise vibration frequency data. Large ratios of intensity are best for precise determination of the vibration frequency, since the fractional error is given by

$$d\omega/\omega=(dT/T)+(dR/R\ \ln R),$$

where

$$R=(\gamma_{000}/\gamma_{010})(\mu_{010}/\mu_{000})^2.$$

T is temperature in °K, ω is a vibration frequency. The greater the ratio R is, the less will be the error contributed by the absorption measurements.

If the measurements are performed on the $v_1=1$ and $v_3=1$ states also, one can indeed, by the method described above, determine the vibration potential to cubic terms from rotational-absorption measurements alone.

As a check on our ability to measure absorption ratios, we have measured the ratio of the rotational absorption for the ground vibrational state of the molecules $OCSe^{80}$ and $OCSe^{82}$. These lines differ in frequency by about 150 Mc/sec. The measured ratio is

$$OCSe^{82}/OCSe^{80}=0.196.$$

This ratio is just the ratio of isotopic abundances since both molecules have the same dipole moment. Aston[3] and White and Cameron[12] give the isotopic ratio as

$$Se^{82}/Se^{80}=0.195 \text{ and } 0.180.$$

The latter ratio differs by more than a reasonable experimental error of ±5 percent.

[11] Theoretical expressions for D_v and α_i are available in the literature. See, for instance, A. H. Nielsen, J. Chem. Phys. 11, 160 (1943).

[12] J. R. White and A. E. Cameron, Phys. Rev. 74, 991 (1948).

Breakdown Probability of a Low Pressure Gas Discharge

ROBERT A. WIJSMAN
Department of Physics, University of California, Berkeley, California
(Received October 13, 1948)

The probability distribution of the number of electrons in an "avalanche" in a low pressure gas discharge is calculated and the result applied to the calculation of the breakdown probability. Under some simplifying assumptions the probability P_0 that the avalanche caused by one initial electron, liberated from the cathode, leads to breakdown is found to be

$$P_0=1-1/q \quad \text{if } q>1$$
$$P_0=0 \quad \text{if } q<1,$$

in which $q=\gamma\,(\exp[\int_0^d\alpha(x')dx']-1)$ is the average number of secondary electrons liberated at the cathode as a result of the avalanche of the initial electron. The calculation has been generalized to the case that the initial electron is liberated in the gas. Finally the relation between the breakdown probability P_0 and the statistical distribution of sparking time lags is discussed.

I. INTRODUCTION

A SELF-SUSTAINING gas discharge is possible only if the voltage between the electrodes exceeds a certain critical value. The transition from the non-conducting to the conducting state is called a breakdown or a spark, and the smallest value of the applied voltage at which breakdown can occur is called breakdown- or sparking-potential. The question has been raised in the past as to whether a sharp criterion for breakdown can be applied and if so, whether the breakdown potential has a theoretically well defined value. These questions have been answered in the affirmative by Braunbeck[1] and Hertz[2] for the case of a gas at low pressure, using some simplifying assumptions.

In a recent article, L. B. Loeb[3] has indicated that in general most sparking thresholds are determined by an equation of the form $\gamma\exp(\alpha d)=1$, where $\exp(\alpha d)$ represents the electron multiplication resulting from ionization by collision in the gap length d, and γ is related to the probability of liberation of secondary electrons (the definition of α and γ will be given in Sections II and III). In this article Loeb has indicated that in the prototype equation both γ and $\exp(\alpha d)$ represent the average values of quantities which are subject to considerable statistical fluctuations. The magnitude of these fluctuations has a bearing on the interpretation of breakdown-potential measurements, and a statistical treatment of the spark formation is therefore important. Such a treatment has been given previously[1,2] in an incomplete way insofar as the fluctuations from the average value $\exp(\alpha d)$ of the electron multiplication factor were neglected. In Section II it will be shown that this neglect is not justified, and it is the purpose of this paper to take these fluctuations into account.

The fact that most processes in a gas discharge, such as ionization by collision, etc., are chance phenomena, has the result that an initial electron, liberated in the gas or at the cathode by an external agency (e.g., radiation), does not invariably lead to breakdown, even when the applied voltage exceeds the breakdown potential. In order to understand this qualitatively we shall give a rough sketch of the mechanism of conduction by a gas.

The initial electron will be accelerated in the electric field and will undergo elastic and inelastic collisions with gas molecules, ionizing some of the molecules. The newly created electrons will take part in the process of ionization and thus a so-called "avalanche" of electrons and positive ions is formed. It has already been mentioned that the number of ion pairs in an avalanche is subject to considerable fluctuations. The electrons eventually reach the anode, leaving behind the positive ions, which drift back toward the cathode. In order to maintain the discharge new electrons must be liberated in the gas or at the

[1] W. Braunbeck, Zeits. f. Physik. 39, 6 (1926); 107, 180 (1937).
[2] G. Hertz, Zeits. f. Physik. 106, 102 (1937).
[3] L. B. Loeb, Rev. Mod. Phys. 20, 151 (1948).

cathode by action of positive ions, photons, or atoms in metastable states, created by the electron avalanche. Because of the statistical character of these processes it may occur at a certain stage in the development of the spark that there is no supply of new electrons, as a result of which the discharge breaks off. If the probability of interruption is denoted by Q, then $P=1-Q$ is the probability that the discharge is not interrupted, which can be defined as the breakdown probability.

Since it is not yet possible to give a rigorous calculation in which all secondary processes and the influence of space charge formation are taken into account, we limit ourselves to the case of a gas at low pressure in which (1) the principal means of maintenance of the discharge is through liberation of secondary electrons from the cathode by positive ions, and (2) the effects of space charge accumulation on the breakdown probability may be assumed to be negligible. As shown by Schade,[4] space charge does not play an appreciable role in the first and most important stage of the development of a spark in a gas at low pressure. Furthermore we restrict our treatment to cases in which the geometry of the discharge tube is such that the electric field is a function of one coordinate only, which we denote by x. This restriction is satisfied in common cases, such as a uniform field between plane parallel electrodes, and the field between coaxial cylindrical electrodes.

Within the simplifying restrictions given above the probability distribution of the number of electrons in an avalanche will be calculated in Section II, and the result will be applied to the calculation of the breakdown probability in Section III. The breakdown probability is denoted by P_0 if the initial electron is liberated at the cathode. In general, if the initial electron is liberated at some point x in the gas, the breakdown probability is denoted by P_x. Besides the dependence on x, the breakdown probability will also depend on operational conditions such as the nature and the pressure of the gas, and the voltage between the electrodes.

[4] R. Schade, Zeits. f. Physik. **104**, 487 (1937).

II. PROBABILITY DISTRIBUTION OF THE NUMBER OF ELECTRONS IN AN AVALANCHE

To every point in the discharge is assigned a coordinate x. Let the cathode be at $x=0$, the anode at $x=d$. The energy distribution of the electrons will depend in general upon x. Therefore the probability $\alpha(x)dx$ that an electron ionizes while drifting through a region between x and $x+dx$ also depends upon x. α is Townsends first ionization coefficient.

One may now ask what the probability $p(n,x)$ is that a given electron which started from the cathode has grown to an avalanche of n electrons at a distance x from the cathode. We assume that in every ionization only one additional electron is created.

The value of $p(1,x)$ is easily found. It is the probability that the electron has not ionized at all between $x=0$ and $x=x$, and is given by

$$p(1,x)=\exp[-S(x)], \tag{1}$$

in which

$$S(x)=\int_0^x \alpha(x')dx'. \tag{2}$$

In order to find an expression for $p(n,x)$ we reason as follows: the probability that the avalanche contains $n-1$ electrons at $x=x'$ is

$$p(n-1,x'). \tag{3a}$$

The probability that one and only one of these electrons will ionize in the region between x' and $x'+dx'$ is $(n-1)\alpha(x')dx'(1-\alpha(x')dx')^{n-2}$. This approaches, as $dx'\to 0$

$$(n-1)\alpha(x')dx'. \tag{3b}$$

The number of electrons in the avalanche has now increased from $n-1$ to n, and the probability that none of these n electrons will ionize in the region between $x'+dx'$ and x is

$$\exp[-n\{S(x)-S(x')\}]. \tag{3c}$$

If we take the product of the expressions (3a), (3b), and (3c) and integrate over x' we get (for $n>1$)

$$p(n,x)=\int_0^x p(n-1,x')(n-1)\alpha(x')dx' \times\exp[-n\{S(x)-S(x')\}]. \tag{4}$$

The solution of Eq. (4), in view of Eq. (1), can

easily be shown to be:

$$p(n, x) = \exp[-nS(x)](\exp[S(x)]-1)^{n-1}. \quad (5)$$

In particular, for the avalanche at the anode we have,

$$p(n, d) = \exp[-nS(d)](\exp[S(d)]-1)^{n-1}. \quad (6)$$

The expectation value of n can be obtained from Eq. (6) to be

$$\bar{n} = \sum_{n=1}^{\infty} np(n, d) = \exp[S(d)] = \exp\left[\int_0^d \alpha(x')dx'\right]. \quad (7)$$

We then can write (6) as:

$$p(n, d) = 1/\bar{n}(1-(1/\bar{n})^{n-1}.* \quad (8)$$

For $\bar{n} \gg 1$, which is the usual case, Eq. (8) can be approximated by:

$$p(n, d) \cong (1/\bar{n}) \exp[-n/\bar{n}], \quad (9)$$

which shows that $p(n, d)$ is exponentially decreasing with n. This formula also shows that the fluctuations of n from the average value $\bar{n}$ are large.

If the initial electron is not liberated at the cathode, but at some point x in the gas, the avalanche will be shorter and therefore on the average will not contain as many electrons. Let the average number in the avalanche be $\bar{n}_x$, then for the probability distribution we have by analogy to (8),

$$p_x(n, d) = \frac{1}{\bar{n}_x}\left(1-\frac{1}{\bar{n}_x}\right)^{n-1}. \quad (8a)$$

III. BREAKDOWN PROBABILITY

We may proceed to calculate the breakdown probability P. This calculation is an extension of the one given previously by Hertz.[2]

Suppose that the initial electron is liberated at the cathode. This electron creates an avalanche containing n electrons and $n-1$ positive ions. The positive ions drift back toward the cathode and liberate secondary electrons, which create new avalanches, etc. Since the liberation of electrons at the cathode is a chance phenomenon, at a certain stage in the process all the positive ions may have drifted out of the discharge without liberating any new electrons. In that case the succession of avalanches is interrupted, the probability of interruption being denoted by Q_0. The probability that the succession of avalanches goes on indefinitely is then given by

$$P_0 = 1-Q_0. \quad (10)$$

We assume that each positive ion has a probability γ of liberating an electron at the cathode, while the probability that one positive ion liberates more than one electron is assumed to be negligibly small.

The positive ions from the first avalanche liberate ν secondary electrons with a probability $u_{0\nu}$ ($\nu=0, 1, 2\cdots$). We want to investigate the probability that the discharge will break off for a certain value of ν. For $\nu=0$ it is clearly 1, for $\nu=1$ it is by definition Q_0, in general it is Q_0^ν in view of the fact that the processes caused by each secondary electron are independent of each other. Therefore it is immaterial also whether the secondary electrons are liberated at the same time or not. We then get

$$Q_0 = \sum_{\nu=0}^{\infty} u_{0\nu} Q_0^\nu. \quad (11)$$

The probability $u_{0\nu}$ can be calculated as follows. The first avalanche yields n electrons and $n-1$ positive ions with a probability $p(n, d)$, given by Eq. (8). The probability that $n-1$ positive ions liberate ν secondary electrons is

$$\binom{n-1}{\nu}\gamma^\nu(1-\gamma)^{n-1-\nu}.$$

Therefore:

$$u_{0\nu} = \sum_{n=1}^{\infty} p(n, d)\binom{n-1}{\nu}\gamma^\nu(1-\gamma)^{n-1-\nu}.$$

Making use of the relationship

$$\frac{1}{b!}\sum_{\lambda=0}^{\infty}\frac{(\lambda+b)!}{\lambda!}a^\lambda = (1-a)^{-b-1}, \quad \text{if } |a|<1$$

* After this article was written, it was kindly pointed out that Eq. (8) had previously been derived by a slightly different method by W. H. Furry, Phys. Rev. **52**, 569 (1937) in an article "On fluctuation phenomena in the passage of high energy electrons through lead." In view of the different field of application, the article had escaped our notice. The parallelism of the statistical phenomena in electron multiplication in showers and in gas discharges is interesting.

the summation in the expression for $u_{0\nu}$ can be carried out with the result:

$$u_{0\nu}=\frac{q^\nu}{(q+1)^{\nu+1}}, \tag{12}$$

in which

$$q=\gamma(\bar{n}-1), \tag{13}$$

and q has a simple interpretation. It is the average number of secondary electrons liberated at the cathode if the initial electron started from the cathode. The current in a discharge will on the average increase or decrease in time depending upon whether q is greater or smaller than unity. The equation $q=1$ represents the classical condition for a sparking threshold under the assumed conditions.

After substitution of Eq. (12) into Eq. (11), we obtain

$$Q_0=\sum_{\nu=0}^{\infty}\frac{q^\nu}{(q+1)^{\nu+1}}Q_0{}^\nu=\frac{1}{q+1-qQ_0}.$$

We can solve for Q_0 and find the two values $Q_0=1$ and $Q_0=1/q$. The corresponding breakdown probabilities are, according to Eq. (10): $P_0=0$ and $P_0=1-1/q$. From physical considerations it is clear that we must take the first solution in the case $q<1$, and the second in the case $q>1$. Mathematically this follows rigorously from a more complicated derivation, not given here,** which unambiguously gives the result

$$\begin{aligned} P_0&=0 \text{ for } q<1,\\ P_0&=1-1/q \text{ for } q>1. \end{aligned} \tag{14}$$

This solution, in contrast to the one by Hertz,[3] is simple and explicit in form. It is seen that P_0 is appreciably less than unity in a region extending far beyond the threshold $q=1$. However, P_0 as a function of the potential difference V between the electrodes is determined only if one knows q as a function of V. Since in general q increases rapidly with V in the region above the breakdown potential, P_0 may rise from zero to a value very close to 1 in a rather narrow voltage region in contrast to values of q.

Suppose now that the initial electron is liberated at a point x in the gas. In analogy to Eqs. (10), (11), (12), and (13) we have

$$P_x=1-Q_x, \tag{10a}$$

$$Q_x=\sum_{\nu=0}^{\infty}u_{x\nu}Q_0{}^\nu, \tag{11a}$$

$$u_{x\nu}=[q_x{}^\nu/(q_x+1)^{\nu+1}], \tag{12a}$$

in which

$$q_x=\gamma(\bar{n}_x-1). \tag{13a}$$

Substitution of Eq. (12a) into Eq. (11a) gives:

$$Q_x=\sum_{\nu=0}^{\infty}\frac{q_x{}^\nu}{(q_x+1)^{\nu+1}}Q_0{}^\nu.$$

For $q<1$, $Q_0=1$, so that $Q_x=1$.
For $q>1$, $Q_0=1/q$. In that case we find:

$$Q_x=\sum_{\nu=0}^{\infty}\frac{q_x{}^\nu}{(q_x+1)^{\nu+1}}q^{-\nu}=\left(q_x+1-\frac{q_x}{q}\right)^{-1}.$$

Substitution of the two values of Q_x into Eq. (10a) gives as a final result:

$$\begin{aligned} P_x&=0 \text{ for } q<1,\\ P_x&=((1-1/q)/(1-1/q+1/q_x)) \text{ for } q>1 \end{aligned} \tag{14a}$$

in which Eq. (14) is included as a special case.

Since $q_x<q$ for all values of x it follows from comparison of Eqs. (14) and (14a) that $P_x<P$ for all values of $q>1$.

The calculations can easily be extended to cases in which more than one initial electron is liberated at the same moment. For example in the case that N electrons are liberated at point x in the gas the breakdown probability is equal to $1-Q_x{}^N$. All the curves for the breakdown probability as a function of q have the feature in common that they are zero for $q<1$.

** The steps in this derivation are as follows. The probability $w(a, b)$ that a primary electrons, starting from the cathode, are succeeded by b secondary electrons can be calculated to be,

$$w(a, b)=\binom{a+b-1}{b}(q+1)^{-a-b}q^b.$$

Q_0 can be given in the following form,

$$Q_0=\sum_{a, b\cdots z=0}^{\infty}w(1, a)w(a, b)\cdots w(z, 0)$$

(infinite number of parameters a, $b\cdots z$), which can be evaluated and gives the result:

$$Q_0=(1/2q)(q+1-((q-1)^2)^{\frac{1}{2}}).$$

The cases $q<1$ and $q>1$ are distinguished by the value of the square root

$q<1$, $((q-1)^2)^{\frac{1}{2}}=1-q$ and therefore $Q_0=1$,
$q>1$, $((q-1)^2)^{\frac{1}{2}}=q-1$ and therefore $Q_0=1/q$,

which immediately leads to Eq. (14).

The breakdown potential can be defined as the potential difference between the electrodes for which $q=1$. It follows from Eqs. (14) and (14a) that below the breakdown potential $(q<1)P=0$, which means that the series of avalanches discontinues sooner or later. It must be emphasized, however, that this only holds in the case of a gas at low pressure. At higher pressure, where space charge formation is an essential element in the development of the spark,[5] the breakdown probability may be quite different, and there may be no well defined breakdown potential below which the breakdown probability is exactly zero. An alternative definition of the breakdown potential for this case is discussed by Loeb.[5]

IV. EXPERIMENTAL DETERMINATION OF BREAKDOWN PROBABILITY

There are several experimental methods by which the breakdown probability can be determined. One of these is to observe the time lag between the application of a certain voltage between the electrodes and the occurrence of a spark, while the cathode is irradiated continuously with ultraviolet light giving a known number of initiating electrons from the cathode per second. Experiments and calculations by Zuber,[6] V. Laue,[7] and Schade,[4] prove that the time lag consists of two parts. The first part gives a contribution subject to statistical fluctuations and is caused by the fact that breakdown depends first on the liberation of an initial electron by the ultraviolet light, which may occur with some delay, and second on the probability that this initial electron leads to breakdown. The second part of the time lag gives approximately a constant contribution and is due to the fact that the current has to build up from zero to a finite value, the magnitude of which is more or less arbitrarily determined by the experimental observability. This formative time lag is not appreciably influenced by the statistical fluctuations in the number of charged particles present, because these fluctuations are only important in the very early stage of the development of the spark.[4] The formative time is of course strongly dependent on the voltage between the electrodes. It should be remarked at this point that the breakdown probability, as calculated in Section III, gives the probability that the series of avalanches goes on indefinitely, whereas the result of a measurement depends on the probability that the series of avalanches is not interrupted during a finite time interval, fixed by the measurement. However, if this time interval is large compared to the time it takes for the positive ions to cross the gap, the results of Section III will give the right value for the breakdown probability to a very good approximation.

An effective method in observing the sparking time lag employs the Kerr cell optical shutter. This method has been used by Wilson[8] to observe sparking in air at atmospheric pressure. The results of measurements of this type give the probability that a spark occurs within a fixed time interval after the application of a voltage between the electrodes. This probability is called by Wilson *sparking probability*, but should be clearly distinguished from the *breakdown probability* as defined in this paper. For the relation between both probabilities the following expression can be derived.

$$R(V,T)=1-\exp[-nP_0(T-T_0)] \text{ for } T>T_0$$
$$=0 \text{ for } T<T_0, \qquad (15)$$

in which $R(V,T)$ = probability that a spark occurs within a time interval T after application of a voltage V between the electrodes, n = average number of electrons liberated per second at the cathode by an external source of radiation, P_0 = breakdown probability for each liberated electron, for a gas at low pressure given by Eq. (14), and T_0 = formative time lag. P_0 and T_0 are both functions of V.

With help of Eq. (15) the theory of breakdown probability in a gas at low pressure, as presented in this paper, can be checked experimentally. The only experiments of the type described above have been performed in air at atmospheric

[5] L. B. Loeb and J. M. Meek, J. App. Phys. **11**, 438, 459 (1940). L. B. Loeb and J. M. Meek, *The Mechanism of the Electric Spark* (Stanford University Press, California, 1941). L. B. Loeb, *Fundamental Processes of Electrical Discharge in Gases* (John Wiley & Sons, Inc., New York, 1919). H. Raether, Zeits. f. Physik. **112**, 464 (1939).

[6] K. Zuber, Ann. d. Physik **76**, 231 (1925).

[7] U. V. Laue, Ann. d. Physik **76**, 261 (1925).

[8] R. R. Wilson, Phys. Rev. **50**, 1082 (1936).

pressure, and therefore have no bearing on the theory valid for a gas at low pressure. The results of these experiments indeed seem to indicate that at high pressure the curve showing P_0 as a function of q is markedly different from the type of curve expressed by Eq. (14), especially at the foot of the curve. This is not surprising since the processes of spark formation in the two cases—high and low pressure—are quite different.

ACKNOWLEDGMENTS

The writer wishes to express his sincere thanks to Professor Leonard B. Loeb, who initiated the study of this problem and under whose stimulating interest the work was completed. The writer is also considerably indebted to the University of California whose Fellowship grants made this work possible, and to the Institute of International Education which arranged the opportunities for study in the United States.

PHYSICAL REVIEW VOLUME 75, NUMBER 5 MARCH 1, 1949

Electron Velocity Distribution Function in High Frequency Alternating Fields Including Electronic Interactions

JULIUS H. CAHN
Brace Laboratory of Physics, University of Nebraska, Lincoln, Nebraska
(Received November 22, 1948)

The Boltzmann transport equation has been solved for the electronic velocity distribution function in a high frequency gas discharge. The distribution is examined as a function of the electron density. The conductivity is computed for two electron-molecule cross sections, one, in which the cross section is inversely proportional to the electron velocity and two, in which the cross section is independent of electron energy. The results show the extension of Margenau's distribution to high densities.

THIS paper is an extension of the work of Margenau[1] in which the Boltzmann Equation

$$(e/m)\mathbf{E}\cdot\nabla f=(\partial_e f/\partial t) \tag{1}$$

was solved for high frequency fields $\mathbf{E}_s=E\cos\omega t$ for the case of low current densities. In it we will apply the results of a former paper[2] (hereinafter referred to as I) in which the Coulomb interaction term $(\partial_e f/\partial t)_1$ of the Boltzmann Equation was derived. Following the notation in I, the distribution function $f(\mathbf{v})$, normalized to the electron density n, will be expanded in the form

$$f(\mathbf{v})=f_0(v)+v_s(f_1(v)\cos\omega t+g_1(v)\sin\omega t). \tag{2}$$

The approximate collision term $(\partial_e f_0/\partial t)_1$ is given by

$$\left(\frac{\partial_e f_0}{\partial t}\right)_1=\frac{10}{s^{\frac{1}{2}}}\frac{ds^{\frac{1}{2}}}{ds}(Af_0'+Bf_0), \tag{3}$$

in which $s=v^2$, $A=\mathfrak{L}'\int_0^\infty f_0 ds$, $B=\mathfrak{L}'f_0(0)$, $\mathfrak{L}'=16\pi^2/15\cdot e^4/m^2\ln\bar{\epsilon}\rho/e^2$, $\rho=(\bar{\epsilon}_1/12\pi ne^2)^{\frac{1}{2}}$, e and m are the charge and mass of the electron; the average energy of electrons relative to electrons is $\bar{\epsilon}$, that relative to ions is $\bar{\epsilon}_1$.

We use the same electron-molecule and electron-ion collision term as in I, namely

$$\left(\frac{\partial_e f_0}{\partial t}\right)_M=\frac{\delta}{\beta s^{\frac{1}{2}}}\frac{d}{ds}\frac{s^2}{\lambda}(f_0'+\beta f_0), \tag{4}$$

where $\beta=m/2kT$, $\delta=2m/M$, T is the gas temperature, and M is the molecular mass, so that our total $\partial_e f_0/\partial t$ for electrons, molecules, and ions is the sum of (3) and (4).

We will make the same simplifications as in I in which the Coulomb interaction was neglected in the momentum balance equation. We can then use Eq. (23) in the paper by Margenau and Hartman,[3]

$$\frac{\partial_e f_0}{\partial t}=\frac{\gamma}{6v^2}\frac{d}{dv}(v^2 f_1),\quad \frac{v}{\lambda}f_1+\omega g_1=-\frac{\gamma}{v}f_0'(v),$$
$$g_1=(\omega\lambda/v)f_1. \tag{5}$$

[1] H. Margenau, Phys. Rev. 69, 508 (1946).
[2] J. H. Cahn, Phys. Rev. 75, 293 (1949).
[3] H. Margenau and L. M. Hartman, Phys. Rev. 73, 309 (1948).

After eliminating g_1 and f_1 in (5), we have finally

$$\frac{\partial_e f_0}{\partial t}=-\frac{\gamma}{3s^{\frac{1}{2}}}\frac{d}{ds}\frac{2\gamma\lambda s^2}{s+(\omega\lambda)^2}f_0'=\frac{10}{s^{\frac{1}{2}}}\frac{ds^{\frac{1}{2}}}{ds}(Af_0'+Bf_0)+\frac{\delta}{\beta s^{\frac{1}{2}}}\frac{d}{ds}\frac{s^2}{\lambda}(f_0'+\beta f_0). \tag{6}$$

As pointed out in I, (6) must be integrable because of particle conservation so that we obtain on integrating (6), a simple first order equation whose integral in turn is

$$f_0=N_0\exp\left\{-\int_0^s\frac{s^{\frac{1}{2}}+10\lambda B/\delta}{[1+\frac{2}{3}(\beta/\delta)(\gamma\lambda)^2/(s+(\omega\lambda)^2)]s^{\frac{1}{2}}+10\lambda\beta A/\delta}\beta ds\right\}, \tag{7}$$

where N_0 is the normalization constant. As a check on (7) if we let ω be zero, (7) reduces to

$$f_0=N_0\exp\left\{-\int_0^v\frac{(10B\lambda/\delta)\beta v+\beta v^2}{\frac{2}{3}[(\beta\gamma\lambda)^2/\delta]+(10\beta A\lambda/\delta)\beta v+\beta v^2}(2\beta v dv)\right\}, \tag{8}$$

which agrees with (19) in I if γ^2 is replaced by $2\gamma_{dc}^2$ because the R.M.S. value of γ is comparable to γ_{dc}.

A further check on (7) is found in Eq. (15) of Margenau[4] which reads

$$f_0=N_0\exp\left\{-\int_0^s\frac{ds}{1/\beta+[\frac{2}{3}(\gamma\lambda)^2/\delta/s+(\omega\lambda)^2]}\right\} \tag{9}$$

in our notation. Equation (7) is seen to reduce to (9) when B and A, the interaction terms, are negligible.

As was done in I, it is instructive to examine (7) for two types of electron-molecule mean free paths in which (*a*) $\tau=\lambda/v=$constant, and (*b*) λ is independent of the energy.

For case (*a*) in which the time τ between collisions is a constant, (7) reduces to

$$f_0=N_0\exp\left\{-\frac{1+10B\tau/\delta}{1+[\frac{2}{3}\beta(\gamma\tau)^2/\delta/1+(\omega\tau)^2]+10\beta A\tau/\delta}\cdot\frac{mv^2}{2kT}\right\}. \tag{10}$$

Computing A and B from (10) we obtain

$$\beta A=B\left[1+\frac{\frac{2}{3}\beta(\gamma\tau)^2/\delta}{1+(\omega\tau)^2}\right],\quad B=N_0L',$$

which when replaced in (10) give us the Maxwellian distribution

$$f_0=N_0\exp[-mv^2/2k(T+T')], \tag{11}$$

where

$$\tfrac{3}{2}kT'=\frac{M(\gamma\tau)^2}{4(1+\omega^2\tau^2)}, \tag{12}$$

and

$$N_0=[m/2\pi k(T+T')]^{\frac{1}{2}}n.$$

Distribution (11) is found to be independent of the electron density and so should be identified with (9) for the same assumption of mean free path. This is easily seen to be the case. It should be noted that at frequencies of the order of 10^{10} c.p.s., the excess electron temperature T' is independent of pressure for a large range of pressures, and is given by

$$\tfrac{3}{2}kT'=M/4(\gamma/\omega)^2. \tag{12'}$$

We next compute the drift velocity $\bar{v}_z$ from which the current density is computed. We have,

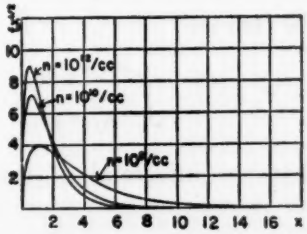

FIG. 1. Comparison of the electron distribution f_0 for three critical electron densities. The gas is assumed to have a pressure of 1 mm, atomic number of 20, temperature of 300°K. The electric field amplitude is assumed to be 1 volt/cm and the frequency, 10^{10} c.p.s. At electron densities of 10^8/cc or less, the excess electron temperature $T'=410$°K.

[4] See reference 1, p. 509.

TABLE I. Mean energies and velocities of electrons for three densities.

n/cc	$\bar{v}$	$\bar{\epsilon}$
10^8	1.825 (10)^7 cm/sec.	0.145 ev
10^{10}	1.347	0.055 ev
10^{12}	1.088	0.039 ev

from (2),

$$n\bar{v}_z=\frac{4\pi}{3}\int_0^\infty (f_1\cos\omega t+g_1\sin\omega t)v^4dv. \quad (13)$$

Making use of (5), (13) becomes

$$n\bar{v}_z=-\frac{4\pi}{3}\int_0^\infty \frac{\gamma\tau v^3}{1+(\omega\tau)^2} \times f_0'(\cos\omega t+\omega\tau\sin\omega t)dv. \quad (14)$$

When (11) is substituted in (14), $\bar{v}_z$ is found to be given by

$$\bar{v}_z=\gamma\tau(\cos\omega t+\omega\tau\sin\omega t)/1+(\omega\tau)^2.$$

The current density j is then given by

$$j=ne\bar{v}_z, \quad (15)$$

and the complex conductivity in turn by σ in the relation

$$j=\sigma\epsilon=\sigma Ee^{i\omega t}. \quad (16)$$

We then obtain for the complex conductivity,

$$\sigma=\sigma_r-i\sigma_i$$
$$=ne^2\tau(1+i\omega\tau)/m(1+(\omega\tau)^2). \quad (17)$$

When $\omega\sim10^{11}$, $\tau\sim10^{-9}$, $\omega\tau\gg1$ so that

$$\sigma=ine^2/m\omega.$$

This is the result obtained from ordinary dispersion theory when the damping is disregarded.[5] It should be pointed out that since (11) and (9) are identical for this choice of cross section, and hence independent of electron density, that (12) and (17) are special case of Margenau's results.[1]

In case (*b*) we consider the distribution (7) under the condition that the mean free path λ be independent of the electronic energy. Because the integrations must be dealt with numerically, and the frequency range for which this work is of interest is of the order of 10,000 megacycles, we choose pressures for which $\omega\lambda\gg v$ over most of the range of v and approximate (7) by

$$f_0=N_0\exp\left\{-\int_0^x \frac{x^{\frac{1}{2}}+(10B\lambda/\delta)\beta^{\frac{1}{2}}}{\left[1+\frac{2}{3}\frac{\beta}{\delta}\left(\frac{\gamma}{\omega}\right)^2\right]x^{\frac{1}{2}}+\frac{10\beta A\lambda}{\delta}\beta^{\frac{1}{2}}}dx\right\}, \quad (18)$$

where $x=mv^2/2kT$.

If we use the following notation,

$$b_1=(10B\lambda/\delta)\beta^{\frac{1}{2}},$$
$$b_2=1+\tfrac{2}{3}(\beta/\delta)(\gamma/\omega)^2,$$
$$b_3=(10\beta A\lambda/\delta)\beta^{\frac{1}{2}},$$

we can write (18) as

$$f_0=N_0\exp\left\{-\int_0^x \frac{x^{\frac{1}{2}}+b_1}{b_2x^{\frac{1}{2}}+b_3}dx\right\}. \quad (19)$$

We find that the integrand of the indefinite integral may be written in a more meaningful fashion, i.e.,

$$\frac{x^{\frac{1}{2}}+b_1}{b_2x^{\frac{1}{2}}+b_3}=\frac{B}{\beta A}+\frac{[1-(B/\beta A)b_2]x^{\frac{1}{2}}}{b_3+b_2x^{\frac{1}{2}}}. \quad (20)$$

The significance of (20) is seen from the following. When the interaction terms b_1 and b_3 are neglected in (19), we have

$$f_0=N_0e^{-x/b_2},$$

so that

$$N_0=n((\beta/\pi)b_2)^{\frac{1}{2}},$$

and

$$\beta A=b_2B.$$

Thus, at low densities, the variable term in (20) vanishes with $1-(B/\beta A)b_2$. The low density approximation to (17) is therefore the Maxwellian function

$$f_0=N_0\exp[-mv^2/2k(T+T')], \quad (21)$$

where the excess electron temperature $\frac{3}{2}kT'=M/4(\gamma/\omega)^2$, agreeing with the result in (12′) for quite a different electron-molecule cross

[5] J. A. Stratton, *Electromagnetic Theory* (McGraw-Hill Book Company, Inc., New York, 1941), First Edition, p. 327.

section. This result is of course in accord with Margenau's Eqs. (23) and (24).[1]

At high densities, (19) reduces to the Maxwellian form

$$f_0 = N_0 \exp(-mv^2/2kT). \qquad (22)$$

The transition from low to high densities is shown in Fig. 1. The mean energies and velocities at the three densities exhibited in Fig. 1 are given in Table I.

We next compute the effect of electron density on the conductivity when λ is constant. After eliminating f_1 and g_1 from (13) using (5), and making the approximation $\omega\lambda \gg v$, we find that the drift velocity $\bar{v}_z$ is given by

$$\bar{v}_z = \gamma/\omega[(4\bar{v}/3\omega\lambda)\cos\omega t + \sin\omega t],$$

showing that the in phase current is very much smaller than the out of phase current at these frequencies and pressures. The complex conductivity σ defined in (16) becomes

$$\sigma = (ne^2/m\omega)[(4\bar{v}/3\omega\lambda) + i] \doteq i(ne^2/m\omega).$$

This is identical with the result obtained for the constant τ case. The effect of varying density is here small, but of course can be readily estimated from the calculated values of $\bar{v}$ given in Table I.

In conclusion, it should be noted that whereas in the d.c. case, we noted a lowering of the entropy for increasing density, in the high frequency case, the drift velocity (in phase component) drops off with increasing density (see Table I) so that the same statement about entropy cannot be made. Since the out of phase component remains constant while the average velocity reduces for increasing density, the entropy is reduced to this extent.

PHYSICAL REVIEW VOLUME 75, NUMBER 5 MARCH 1, 1949

Ferromagnetism at Very High Frequencies
II. Method of Measurement and Processes of Magnetization*, **

M. H. JOHNSON AND G. T. RADO
Naval Research Laboratory, Washington 20, D. C.

(Received September 27, 1948)

A method for measuring the complex permeability, μ, of a ferromagnetic metal is described. The determination of both components of μ is accomplished by a simultaneous measurement of the changes in attenuation and phase velocity introduced into a conducting system by the ferromagnetism of one of its walls. An experimental technique involving pulsed magnetic fields is used. Values of μ for samples of magnetic iron at 200 and 975 Mc as a function of a polarizing magnetic field (which is parallel to the high frequency field) are compared to the static incremental permeabilities measured on the same sample. The interpretation of the experimental results indicates several characteristics of the magnetization in iron: the upper limit of domain dimensions in polarizing fields less than 500 oersteds is 10^{-4} cm; domains have different degrees of stability in the applied field; "weak-field domain" wall displacements are practically eliminated at the frequencies used; spin rotation and "strong-field domain" wall displacements are only slightly damped and contribute to the magnetization in weak as well as strong fields. Studies of hysteresis phenomena are discussed, and results on two types of permalloy presented.

I. INTRODUCTION

NUMEROUS investigations[1] have shown that two basic mechanisms are responsible for the changes in magnetization of a ferromagnetic substance placed in an external magnetic field. These mechanisms involve two different effects of the field on the configuration of the magnetically saturated regions, called domains,

* Paper I of this series, subtitled Magnetic Iron at 200 Mc, appeared in Phys. Rev. 71, 322 (L) (1947). The method and its application to iron and permalloy at 200 Mc were briefly presented at American Physical Society meetings in January and April, 1947. Phys. Rev. 71, 472 (Abstracts L4 and L5) (1947); Phys. Rev. 72, 173 (A) (1947).

** It is a pleasure to acknowledge the invaluable assistance of Matthew Maloof in carrying out the experimental work described in the present paper.

[1] R. Becker and W. Doering, *Ferromagnetismus* (Verlagsbuchhandlung Julius Springer, Berlin, 1939).

which constitute the elements of the magnetic structure in a ferromagnetic specimen. In strong fields the magnetic moment of each domain turns from the axis of easy magnetization closest to the field toward the field direction, thereby producing the changes in magnetization. This mechanism is termed spin rotation or domain rotation. Its study, which must be made close to magnetic saturation, has led to a quantitative description of magnetization curves and thus to the evaluation of phenomenological constants for the anisotropic part of the crystalline energy. In weak fields most of the changes in magnetization are due to the growth of domains oriented favorably with respect to the field at the expense of less favorably oriented domains. This mechanism, termed wall displacement, involves the motion of a thin inter-domain boundary layer and is in itself rather involved. Although it has led to useful correlations, it has not, in general, yielded a quantitative theory of the magnetization curve.

There is no reason to expect that the two mechanisms will respond to rapidly changing fields in the same way. Consequently, the possibility arises that the study of magnetization at high frequencies might yield a more detailed understanding of each mechanism. Indeed, it will be shown that, if such a study is made in the presence of a polarizing field, certain domain sizes and dynamic characteristics can be derived from the experimental results. If these conclusions are substantiated by further experiments, the existing description of domains must be substantially modified.

High frequency ferromagnetic measurements in *metals* are difficult primarily because the conductivity severely limits the penetration depth of an electromagnetic wave. Consequently, only small effects on the wave propagation in an air space bounded by conductors can be produced by the permeability and resistivity of the metallic walls. We shall see in Section II that both the real and imaginary part of the propagation vector (attenuation and phase velocity) must be measured to determine the permeability of the metallic walls.[1a] While that portion of the attenuation which is caused by ferromagnetism is not difficult to determine, measurement of the corresponding change in phase velocity requires an exacting technique. One of the essentially new experimental features in the present work is the simultaneous measurement of both these changes when the latter are caused by the ferromagnetism of a metallic substance.

A simple substitution method suggests itself. If the ferromagnetic parts of a conducting system are replaced by a non-magnetic metal, the measured changes in the propagation vector suffice to determine the permeability of the replaced metal. By this means the attenuation can in fact be determined quite accurately. However, the changes in phase velocity, unlike the attenuation, can also arise from small changes in the geometry of the conducting walls and require that the substitution be made with a mechanical exactness that is difficult if not impossible to achieve.

In surmounting this difficulty we have used the results of work done at the M.I.T. Radiation Laboratory in 1942 under the direction of O. Halpern.[2] In some of the experimental arrangements there used, a polarizing field was applied *parallel* to the high frequency field. The large decrease in the attenuation thereby produced indicated that the high frequency permeability decreased in the manner predicted by the magnetization curve. Therefore, it should be possible to bring the high frequency permeability to unity by saturating the ferromagnetic metal. The substitution of a ferromagnetic by a non-magnetic conductor can thus be effected by a parallel magnetic field sufficiently strong to saturate the ferromagnet. Since no mechanical changes are made, the geometrical conditions can be maintained with the necessary precision.

Our experiments have been made in a coaxial line resonator tuned by a dieletric bead. The ferromagnetic sample constitutes a part of the center conductor. The calculation of the resonant frequency and Q for this cavity and the relation of these quantities to the permeability of the sample are the subjects of Section II.

[1a] In the work of Arkadiew, dating back to 1913 and summarized in J. Phys. USSR 9, 373 (1945), the necessity for measuring both resistive and reactive changes in order to determine the permeability is recognized. The experimental techniques used by Arkadiew are entirely different from those used by us and his work did not include a study of the effects of a superposed polarizing field.

[2] O. Halpern, Radiation Laboratory, M.I.T., Internal Report, Nov. 4, 1942. An account of these experiments is in preparation.

The polarizing field is generated by a direct current passing through the center conductor. Currents of the order of 1000 amperes are needed to saturate the sample. To avoid heating effects in the center conductor, a pulse technique must be employed. This technique and the associated ballistic indicator are discussed in Section III, together with the method of taking and interpreting the data.

Hysteresis effects can be rapidly examined in relatively small polarizing fields by using a low frequency polarizing current through the center conductor and putting the resonator output (after rectification and "chopping") on an oscilloscope. The resulting "butterfly curves" show the changes in attenuation as a function of cyclic polarization. This type of measurement is the subject of Section IV.

In Section V values of μ for samples of magnetic iron at 200 and 975 Mc as a function of a polarizing magnetic field (which is parallel to the high frequency field) are compared to the static incremental permeabilities measured on the same sample. The interpretation of the experimental results indicates several characteristics of the magnetization in iron: the upper limit of domain dimensions in polarizing fields less than 500 oersteds is 10^{-4} cm; domains have different degrees of stability in the applied field; "weak-field domain" wall displacements are practically eliminated at the frequencies used; spin rotation and "strong-field domain" wall displacements are only slightly damped and contribute to the magnetization in weak as well as strong fields. Studies of hysteresis phenomena are discussed, and results on two types of permalloy presented.

II. THEORY

Our first task (Part *A*) is to relate the propagation constant of an electromagnetic wave in a coaxial transmission line to the permeability, conductivity, and geometrical dimensions of the walls. Next we shall show (Part *B*) how changes in the propagation constant can be expressed by the change in Q and the change in resonance frequency of a coaxial line resonator. Finally (Part *C*) the complex permeability will be discussed, and formulas for its determination in terms of experimentally measurable quantities will be given.

A. The Propagation Constant

Consider an air-filled coaxial transmission line of circular cross section and choose cylindrical coordinates r, ϕ, and z such that the z direction coincides with the axis of symmetry. Let $r=a$ and $r=b$ be the radius of the inner and outer conductor, respectively. The metal walls (located at $r\leq a$ and $r\geq b$) will be characterized by a conductivity σ and a permeability μ.

We define the permeability[3] as the ratio B/H. In the case of time-dependent fields, μ must, in general, be assumed complex, so that **B** and **H** may be out of phase. This assumption simply means that there may exist a magnetic loss, in formal analogy with the dielectric loss of an insulator characterized by a complex dielectric constant.

The problem is to find a wave solution of Maxwell's equations which satisfies the boundary conditions at the metal walls and corresponds to the principal mode of propagation. In such a solution the non-vanishing components of the field are E_r, E_z, and H_ϕ. We shall make the following assumptions:

(1) The time variation of the field components is given by the factor $\exp(i\omega t)$, where the angular frequency $\omega=2\pi\nu$ is determined by the signal generator.

(2) The permeability $\mu=B/H$, as well as $\epsilon'=D/E$, the dielectric constant not due to conduction, are uniform and independent of the field components.

(3) Ohm's law is applicable and the density of free charge is zero.

(4) For metals, the apparent dielectric constant $\epsilon=\epsilon'-2i\sigma/\nu$ is given by $-2i\sigma/\nu$. For air, $\mu=1$, $\sigma=0$, and $\epsilon=\epsilon'=1$.

If k is the unknown propagation constant, and $k_0=2\pi/\lambda_0$ is the propagation constant in free space, Maxwell's equations in Gaussian units result in

$$H=(R/r)\exp(ikz), \tag{1}$$

$$E_r=-(k/k_0\epsilon)(R/r)\exp(ikz), \tag{2}$$

$$E_z=(ik_0\epsilon)^{-1}r^{-1}dR/dr\exp(ikz), \tag{3}$$

where the unknown function $R(r)$ is the solution of

$$rd/dr(r^{-1}dR/dr)-(k^2-k_0^2\epsilon\mu)R=0. \tag{4}$$

[3] In our experiment H is sufficiently small (≤ 0.01 oersted) to make μ independent of H. Hence we are dealing with a reversible (or "incremental") permeability, and the field equations are linear.

Since E_z/H must be continuous on the air metal boundary at $r=a$ and $r=b$, the above equations make it possible to calculate k.

In solving (4) for the metal walls, we choose a solution that corresponds to an attenuation of the field components with penetration into the metal. The calculation is simplified by the fact that σ is large so that $k_0(\epsilon\mu)^{\frac{1}{2}}\gg 1$ for all but very low frequencies. In solving (4) for the air space we make the approximation that $k-k_0$, which vanishes in the case of ideal walls ($\sigma=\infty$, $\mu=1$), is small compared to k_0 for sufficiently high frequencies.

The final expression for the propagation constant may be written

$$k=k_0(1-i\alpha+\beta), \tag{5}$$

where the real numbers α and β are defined by the relation

$$\alpha+i\beta=(2k_0 \ln b/a)^{-1} \times[(1/a)(\mu_a/\epsilon_a)^{\frac{1}{2}}+(1/b)(\mu_b/\epsilon_b)^{\frac{1}{2}}], \tag{6}$$

and the subscripts on μ and ϵ identify the two conductors.

Equations (5) and (6) show that the necessary and sufficient condition for our approximation $[(k-k_0)/k_0\ll 1]$ to be valid is

$$(|\mu_a|)^{\frac{1}{2}}\ll(4\pi/c)(2\sigma\nu)^{\frac{1}{2}}a \ln b/a \tag{7}$$

with a similar condition for the outer conductor. In our experiment $a=0.159$ cm, $b/a=10$, and $\nu=2\times10^8$ sec.$^{-1}$, so that (7) becomes $(|\mu_a|)^{\frac{1}{2}} \ll 3.06\times10^{-6}\sigma^{\frac{1}{2}}$. For magnetic iron $\sigma\approx 8\times10^{16}$ sec.$^{-1}$ ($\sigma^{-1}=\rho\approx 11\times10^{-6}$ ohm-cm), and we find 100 to be a reasonable upper limit for $|\mu_a|$. These values lead to $(k-k_0)/k_0\approx 0.01$ and justify the approximation.

All three components of the electromagnetic field are seen to represent plane waves proportional to the factor

$$\exp[i(\omega t-kz)]=\exp(-k_0\alpha z)\exp[i\omega(t-z/v)],$$

where $v=c/(1+\beta)$ is the phase velocity of the waves in the transmission line. Evidently, α is a measure of the attenuation, and β is essentially the fractional deviation of the phase velocity from that in a transmission line with ideal walls.

Equation (6) shows that $\alpha=\beta$ if μ is real. Thus the permeability can be obtained either from an attenuation measurement or from a phase velocity determination. If, however, μ is complex, $\alpha\neq\beta$, and both α and β must be measured. Using the terminology of lumped electric circuits we may say that both the resistive and the reactive components of the impedance must be measured to determine the complex permeability. In general, α and β are of the same order of magnitude because $\mu\ll\epsilon$ in Eq. (6), but if μ is wholly imaginary, β is zero.

B. Resonant Frequency and Q

A half-wave resonant cavity is obtained by providing a coaxial line with metal end plates placed at $z=0$ and $z=l$, where $l\approx\lambda_0/2$. In calculating the Q of the resonator and the departure of its resonant frequency from c/λ_0 we shall assume ideal end plates (infinite σ and $\mu=1$) and use the values of the attenuation and phase velocity derived in part *A*. This procedure is justified by the fact that in our experiment, which is based on a substitution method, we are interested only in the effect of the imperfect inner conductor on the Q and resonant frequency. To find the actual Q and actual resonant frequency of the cavity, one would have to take into account the small, but measurable losses in the end plates.

In the case of perfectly reflecting end plates, the space variation of the electromagnetic field components is given by $A[\exp(ikz)-\exp(-ikz)]$, where the amplitude A is a known function of r. This expression satisfies the boundary conditions that it vanish at $z=0$, and it equal some fixed value p prescribed by the driving mechanism at $z=l$.

Since α is of the order of 10^{-3}, $k_0l\alpha\ll 1$, and we obtain, to a first approximation

$$|A|^2=(|p|^2/4)[(k_0l\alpha)^2\cos^2k_0l(1+\beta) +\sin^2k_0l(1+\beta)]^{-1} \tag{8}$$

as a measure of either the energy stored in the cavity or of the power dissipated during one cycle.

The cavity will resonate in its lowest mode if its length l is equal to $\lambda/2$, where $\lambda=\lambda_0/(1+\beta)$ is the wave-length in the resonator. This is equivalent to saying that for resonance the driving frequency ν must have a value such that

$$k_0l(1+\beta)=\pi, \tag{9}$$

which results in

$$|A|^2=|p|^2/4(k_0l\alpha)^2.$$

To reduce the energy in the resonator by one-half, the driving frequency must be changed by an amount $\Delta\nu$ which will make the denominator of Eq. (8) equal to $8(k_0l\alpha)^2$. This condition gives, to a first approximation, $(1+\beta)\Delta k_0=k_0\alpha$ so that $\nu/\Delta\nu=1/\alpha$.

For frequencies near resonance, Q is approximately constant ($Q\gg1$), and hence it may be defined by

$$Q=\nu/2\Delta\nu \tag{10}$$

which gives

$$\alpha=1/2Q \tag{11}$$

as the desired relation between α and that part of the Q which is due to the losses in the inner and outer conductor.

If $\Delta\nu'$ is the change in resonance frequency of the cavity compared to a similar cavity with ideal walls, we obtain from (9)

$$(\nu+\Delta\nu')l=c/2 \tag{12}$$

as the resonance condition for the case of ideal walls ($\beta=0$). Solving Eqs. (9) and (12) gives

$$\beta=\Delta\nu'/\nu \tag{13}$$

as the desired relation between β and that part of the resonance frequency shift $\Delta\nu'$ which is due to the losses in the inner and outer conductor.

Equations (11) and (13) lead to the following conclusions:

(1) Since β is positive, $\Delta\nu'>0$, so that the introduction of a loss decreases the resonance frequency of a cavity with ideal walls.

(2) The derivation of relations (11) and (13) merely assumes the existence of plane waves and of perfectly reflecting end plates. Thus, it is valid for certain modes in rectangular guides and other transmission lines.

(3) If we assume that all the walls of the coaxial resonator have a conductivity σ and a (real) permeability μ, Eqs. (6) and (11) lead to

$$Q=(4\pi/c)(\sigma\nu/\mu)^{\frac{1}{2}}(1/a+1/b)^{-1}\ln b/a. \tag{14}$$

Except for an additional term $[(8/\lambda_0)\ln b/a]$ in the denominator which arises from the losses in the end plates, Eq. (14) agrees with the well-known formula[4] for the Q of a half-wave coaxial resonator. If the permeability is complex ($\mu=\mu_1-i\mu_2$), our result shows that μ in Eq. (14) must be replaced by $|\mu|+\mu_2$, where $|\mu|=(\mu_1^2+\mu_2^2)^{\frac{1}{2}}$.

[4] See, for example, E. U. Condon, Rev. Mod. Phys. 14, 341 (1942), Eq. (9¹16). Condon does not use the Gaussian units employed in the present paper.

C. The Complex Permeability

According to Eq. (6), α and β are proportional to the real and imaginary parts, respectively, of the quantity $(\mu/\epsilon)^{\frac{1}{2}}$, which itself is proportional to $(i\mu\rho)^{\frac{1}{2}}$. If we assume that the existence of a permeability $\mu\neq1$ gives rise to an energy loss in addition to the ohmic loss, then $\alpha>\beta$, and the permeability is seen to be represented by a complex number of the form $\mu=\mu_1-i\mu_2$. In certain cases (resonance, apparent diamagnetism), however, the permeability is not necessarily in the fourth quadrant.

It is now possible to derive the relations which allow the evaluation of the complex permeability, in any polarizing field, from measured values of changes in resonant frequency and Q.

If the ferromagnetic inner conductor of a coaxial line resonator is magnetically saturated, the change in the attenuation caused by the disappearance of the magnetic loss is given by $\alpha-\alpha_\infty$, where the symbol α now denotes the attenuation resulting from the inner conductor in a polarizing field H_0 and α_∞ is the value of α in a polarizing field sufficiently large to saturate magnetically the specimen under investigation. This method of reducing the permeability of the inner conductor to unity avoids the necessity for replacing the specimen by a non-magnetic metal and thus it surmounts the difficulties associated with changes in the geometrical configuration of the cavity. On account of Eq. (11), we may write

$$\alpha-\alpha_\infty=(1/2)(1/Q-1/Q_\infty), \tag{15}$$

where Q is the "Q" of the cavity in a polarizing field H_0, and Q_∞ is the value of Q in a saturating field.

Similarly, the disappearance of ferromagnetism as a result of the saturation causes a change in the fractional deviation of the phase velocity from the value c. Using Eq. (13), we can write

$$\beta-\beta_\infty=(\Delta\nu'-\Delta\nu_\infty')/\nu, \tag{16}$$

where β and β_∞ refer to the inner conductor, and $\Delta\nu'-\Delta\nu_\infty'$ is the change in resonance frequency of the cavity as the value of the polarizing field on the inner conductor is changed from H_0 to a saturating field.

The constant $\alpha_\infty=\beta_\infty$ may be calculated from Eq. (6) by setting $\mu=1$ and disregarding the con-

tribution of the outer conductor. Equations (15) and (16) make it possible, therefore, to obtain α and β in terms of measurable quantities. Using Eq. (6), μ_1 and μ_2 may then be evaluated for any H_0.

In practice it is more convenient to use a magnetic rod which is shorter than the inner conductor of the resonator. The remaining part of the inner conductor may be made out of a nonmagnetic rod (e.g., brass) having the same diameter as the test specimen. This procedure has the advantage that one can work with relatively high Q values throughout the experiment, and that the range over which the receiver and indicator must be linear can be reduced. If, on the other hand, the magnetic section of the inner conductor is too short, or if it is placed too near to the center of the resonator, then the magnetic effects are too small to be measured accurately. It was found that a satisfactory compromise is obtained by making the specimen long enough to prevent end-effect errors[5] and placing it in such a position[5] that Q_∞/Q is never larger than about two or three.

By solving the appropriate boundary value problem,[5] the effect of the partially magnetic inner conductor can be predicted with sufficient accuracy. It is shown in Appendix I that the use of a magnetic section (instead of a completely magnetic inner conductor) reduces the magnetic effects $\alpha-\alpha_\infty$ and $\beta-\beta_\infty$ by a factor γ, the value of which is between zero and unity and depends exclusively on the frequency, the length of the specimen, and its position with respect to the center of the resonator.

The problem of measuring Q for large values of H_0 introduces additional difficulties. As the polarizing field H_0 has to be parallel to the high frequency magnetic field, H_0 must be generated by passing a large current through the inner conductor. To avoid excessive heating, this current and hence H_0 must be pulsed. Consequently the quantity Q can be measured directly only for small[6] values of H_0. For other values of H_0, and particularly for saturating fields, only Q ratios can be measured. If, however, the Q in zero polarizing field is chosen as the reference value, the Q ratios are found to be irreproducible because of the hysteresis effects discussed in Section IV. For this reason we have used as the reference value the $Q=Q_{\text{bias}}$ measured in a "biasing" field $(H_0)_{\text{bias}}$ which, without being too large to prevent continuous application, is yet large enough to minimize hysteresis effects. In the case of magnetic iron $(H_0)_{\text{bias}}=6.25$ oersteds was used. This value corresponds to an abscissa beyond the knee of the static magnetization curve.

On the basis of the above modifications, we can write Eqs. (15) and (16) in their final form.

Using the abbreviations

$$Q/Q_{\text{bias}}=\chi \quad \text{and} \quad Q_\infty/Q_{\text{bias}}=\chi_\infty,$$

we obtain from Eq. (15)

$$\alpha-\alpha_\infty=(2\gamma\chi_\infty Q_{\text{bias}})^{-1}[(\chi_\infty/\chi)-1]. \quad (17)$$

Using the abbreviations

$$\Delta\nu'-\Delta\nu'_{\text{bias}}=\delta \text{ and } \Delta\nu'_\infty-\Delta\nu'_{\text{bias}}=\delta_\infty,$$

we obtain from Eq. (16)

$$\beta-\beta_\infty=(1/\gamma\nu)(\delta-\delta_\infty), \quad (18)$$

where δ is the change in resonance frequency of the cavity as the value of the polarizing field on the inner conductor is changed from H_0 to $(H_0)_{\text{bias}}$, and δ_∞ is the value of δ if H_0 is a saturating field.

Using $\mu=1$ in Eq. (6) and disregarding the contribution of the outer conductor, we obtain

$$\alpha_\infty=\beta_\infty=(c/8\pi)(\rho/\nu)^{\frac{1}{2}}/a\ln(b/a), \quad (19)$$

where $\rho=1/\sigma$ is the resistivity of the magnetic specimen in electrostatic units (seconds).

As shown in Appendix I, γ may be calculated from the formula

$$\gamma=(1/\pi)[k_0L+(2\sin^2k_0D-1)\sin k_0L], \quad (20)$$

where L is the length of the magnetic specimen, D is the distance of its center from the center of the resonator, and k_0, as before, is equal to $2\pi\nu/c$.

Using $\mu=\mu_1-i\mu_2$ in Eq. (6) and disregarding the contribution of the outer conductor, we arrive at the final relations

$$\mu_1=\alpha\beta/\alpha_\infty^2, \quad (21)$$

$$\mu_2=(\alpha^2-\beta^2)/2\alpha_\infty^2 \quad (22)$$

[5] See Appendix I.

[6] In our resonator, fields up to about 6 oersteds, corresponding to about 5 amperes, can be applied continuously.

for the determination of the complex permeability.

The quantities Q_{bias}, ρ, and ν are easily measured by standard methods. Thus, the important part of our experiment consists in measuring simultaneously χ and δ as a function of H_0 by the special technique described in Section IIIB. In principle, χ_∞ and δ_∞ may also be measured by this technique. For practical reasons (see Section III), however, these quantities are sometimes obtained by extrapolating[7] the χ and δ curves to infinite fields. Equations (17) through (22) may then be used to calculate $\mu=\mu_1-i\mu_2$ for any value of H_0.

III. EXPERIMENTAL

Figure 1 shows a cross-sectional view of the coaxial cavity and a block diagram of the principal components of the apparatus.

A. Measurement of Q_{bias}

(1) *Apparatus*

In principle, Q-values were determined by measuring the voltage transmitted by the cavity as a function of frequency, and calculating the Q from several points on the resonance curve.

To obtain the required accuracy, however, it was found preferable to use a fixed frequency and to change the resonant wave-length of the cavity by means of a dielectric bead. Thus the R. F. oscillator could be left undisturbed for extended periods of time, resulting in increased frequency stability and constancy of power output. If, as in our case, the calibration of the bead (position *versus* frequency) is theoretically linear, then differences in "frequency" (actually differences in resonant wave-length) can be measured with a fractional error ($<10^{-5}$) smaller than that of commercially available crystal-calibrated heterodyne frequency meters ($\geq 10^{-4}$).

The coaxial resonator is approximately one-half wave-length long (74.5 cm) at 200 Mc and is shorted at both ends. The radii ($a=0.159$ cm, $b=1.59$ cm) were chosen so as to satisfy the following requirements: (1) Most of the resonator losses should take place in the inner conductor; (2) the radius of the inner conductor should be sufficiently large compared to the skin depth, a requirement contained in Eq. (7); (3) ferromagnetic rods having the diameter of the inner conductor should be available; (4) the Q of the cavity should be in a convenient range ($\sim$500 to 1000).

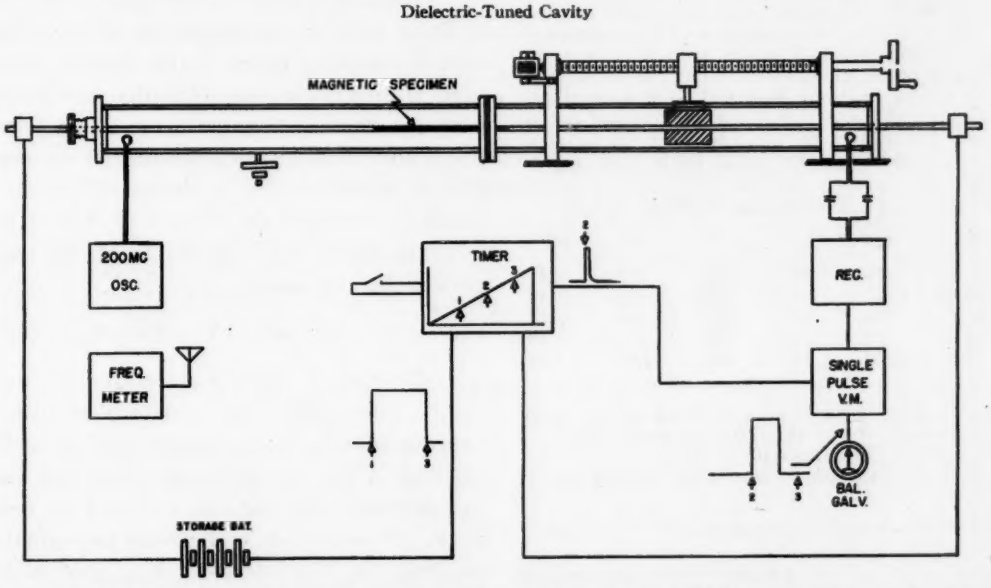

FIG. 1. Cross-sectional view of the coaxial cavity and block diagram of the principal components of the apparatus.

[7] For soft magnetic materials the fields at our disposal permitted a very close approach to saturation. Hence, the extrapolation was fairly accurate (see paper I and Section V of the present paper), especially since χ_∞ can be calculated in terms of (1) the measurable Q of a similar resonator whose center conductor is brass, and (2) the known conductivities of the magnetic specimen and brass. This calculation is presented in Appendix II.

Except for the outer conductor, which is made of copper,[8] brass is used throughout the construction of the cavity. A thin mica washer, located at the center of the cavity, prevents the polarizing current from flowing through the outer conductor. The magnetic specimen, whose diameter is that of the inner conductor, has a well-defined[9] length of 17.75 cm, and its center is located at the proper distance (two to four inches) from the center of the resonator to produce a γ-factor of the desired magnitude.[5] The inner conductor is held in the end plates of the cavity by means of set screws. In order to prevent sagging of the inner conductor it is put under a small tension (with the use of an appropriate screw arrangement) before one of the screws is tightened. This tension is approximately 0.6 kg/mm^2 and does not affect the value of Q.

Tuning of the cavity is accomplished by displacing a polystyrene bead along the axis of the cavity. The cylindrical bead (3 cm long) was attached to a rider on a calibrated screw (26 threads/in.) and its size was such that it filled the space between the inner and outer conductor without actually touching them. A sufficiently linear calibration curve of "counter units" (i.e., number of rotations of the calibrated screw) *versus* frequency is obtained by centering the motion of the bead around the $\frac{1}{4}$-length point of the cavity (see Appendix III). The deviations from linearity and the reproducibility of the calibration are smaller than one percent. A Cardwell crystal-calibrated frequency meter was used in these measurements.

The source of R. F. power is a resonant line oscillator using a 2C39 tube and working as a Hartley circuit. In order to keep the frequency constant to 0.001 percent, and the power output to 1 percent, it was found necessary to keep the output down to about 30 milliwatts.

The receiver is a standard APR-1 superheterodyne which was suitably modified to improve its stability and the linearity of its output/input voltage ratio. Output values are read on a 0–100-d.c. microammeter in series with the second detector. The remaining non-linearity (one or two percent) was corrected for by calibrating the receiver in terms of the attenuator on a type LAF-1 signal generator.

TABLE I. Typical Q-measurement. Data of 1/10/47, taken (at 200 Mc) on a 17.75-cm rod of magnetic iron whose center was at a distance of four inches from the electrical center of the cavity. The readings R and R_{res} (see text) of the output meter in microamperes are corrected for the zero-signal diode current (2.7 microamperes in this case) and for the small non-linearity of the receiver. In the first row of the table, for example, the uncorrected readings of R and R_{res} were 80.0 and 88.8, respectively. C_R and C_R' are the counter readings at two equal output readings R. The center of the resonance curve is at $(1/2)(C_R+C_R')$, and $2\Delta C$, its width at the level R, is given by $C_R'-C_R$.

R	R_{res}	C_R	C_R'	C_R+C_R'	$2\Delta C$	$q\times10^3$
77.3	86.1	427	569	996	142	3.47
67.2	85.4	387	612	999	225	3.48
56.9	85.4	336	659	995	323	3.47
47.1	85.6	279	714	993	435	3.49
37.3	85.5	200	792	992	592	3.49

Average value of $(1/2)(C_R+C_R')=497.5\pm1$ counter units.
Average value of $q\times10^3=3.48\pm0.01$ (counter units)$^{-1}$.
$Q=\nu sq=2\times10^5\times0.520\times3.48\times10^{-3}=362$.
Frequency error $\doteq\pm1$ counter unit $\doteq\pm2$ kc $\doteq0.001$ percent of ν.

[8] The type of metal used for the various parts of the cavity was determined by its availability in the proper shape. The calculations were corrected for the different resistivity of the inner and outer conductor.

[9] The difference in diameter of the brass inner conductor and of the threaded portions (≈1 cm long) on both ends of the specimen is much larger than the skin depth in brass.

(2) *Procedure*

By a suitable arrangement of the input and output coupling loops of the cavity, a considerable transmission loss (60 db) was introduced between the oscillator and receiver. Thus, the decoupling was sufficient to regard the measured Q's as unloaded Q's: a change of 12 db in the coupling changed the Q by less than 1 percent.

From the standard formula of the resonance curve, the expression

$$Q=(\nu s/2\Delta C)[(R_{res}/R)^2-1]^{\frac{1}{2}}=\nu sq \qquad (23)$$

is easily derived. Here ν is the frequency (2×10^5 kc), s the calibration constant of the cavity (approximately 0.52 counter unit/kc), R_{res} the reading of the output meter when the cavity is at resonance, and $2\Delta C$ the width of the resonance curve, in counter units, between two equal output readings R. The values of R_{max} and R are corrected for the small non-linearity of the receiver.

Using four or five pairs of points on the resonance curve extending down to the $\frac{1}{4}$-voltage point, the various Q values agreed occasionally

to ±0.2 percent and always to ±0.5 percent. Table I presents a typical example of a Q-measurement. If the inner conductor were removed from the cavity and then replaced, Q could be reproduced, over a period of several months, to better than 1 percent in the case of a brass inner conductor and to about 2 percent in the case of a partially magnetic inner conductor. The latter error is due to a hitherto unexplained magnetic effect which appears to be connected with hysteresis and often manifests itself as a slow change of the magnetic state over a period of about a day.

To obtain Q_{bias}, a constant current of 5.0 amperes was passed through the partially magnetic inner conductor. With this current flowing, the sample was demagnetized by superposing a 60-cycle a.c. on the biasing current and gradually (in approximately 3 seconds) decreasing its magnitude from a maximum value of 45 amperes RMS with the help of a variac. $Q=Q_{\text{bias}}$ was then measured as described above.

The gradual 2 percent variation of the Q with time could often be reduced, but not always eliminated, by pulsing the cavity at the beginning of a series of measurements several times with a field of about 1000 oersteds and demagnetizing between pulses.

An experimental test of the combined error resulting from the frequency instability of the oscillator and the mechanical error of the tuning mechanism presents itself in the reproducibility of the center of the resonance curve on the counter units scale. Since the center of the resonance curve, as determined by the arithmetic mean of the counter readings at two equal R values, could be reproduced to one counter unit (see Table I), the over-all frequency error of the apparatus is, as already mentioned, about 0.001 percent.

The experimental Q values for the cavity with brass inner conductor were consistently lower, by about 8 percent, than that calculated ($Q=685$) by Eq. (14) with the additional term in the denominator which arises from the losses in the end plates. Except for σ, which was measured on the inner conductor, but not on the outer conductor or on the end pieces, the parameters in this calculation are well-known. Since about 80 percent of the losses occur in the inner conductor, the theoretical Q cannot be in error by 8 percent.

As errors caused by coupling were eliminated (<1 percent), and as no radiation losses could be detected, we conclude that the "Q deficit" is due to unknown losses in the resonator. Imperfect contacts at the junctures of the inner conductor and the end pieces of the cavity appear to be the most probable locations of these losses. Since the measured Q's are reproducible, however, they may be used for the calculation of Q_∞ (see Appendix II) and no errors arise from the existence of the "Q deficit."

The validity of our permeability measurements may be questioned, of course, if our failure to realize experimentally the calculated Q is due to the non-applicability of measured σ[10] values to the surface layer of metals. Since some simple experiments (non-metallographic polishing of the surface of the inner conductor, soft soldering of the inner-conductor to the end-plate joints) did not increase the Q, the matter was not investigated further even though the limited literature on this problem appears to contain inconsistent results. As the theoretical value of Q_∞, which depends on σ (see Appendix II), was checked experimentally, and as some of the final results (the equality of μ_{stat} and μ_1 for iron over a large range of H_0) are so readily interpretable, it was assumed that no anomalies in σ exist. It should be stated, however, that in the case of 45 Permalloy (the extrapolated) experimental value of Q_∞ is 3 percent smaller than the calculated value.

B. Measurement of χ and δ

(1) *Apparatus*

The quantities χ and δ were determined by measuring, with two values (H_0 and $(H_0)_{\text{bias}}$) of an applied polarizing field, the voltage transmission of the cavity as a function of resonant wave-length. From the ratio of the two resonance

[10] The results of the well-known Hagen-Rubens experiment make it appear extremely unlikely that the value of σ at UHF differs from the static value.
The variation of σ with a magnetic field (magnetoresistive effect) should, in principle, be taken into account. For the substances used in our investigation, however, this effect is about ten times too small to cause noticeable errors.

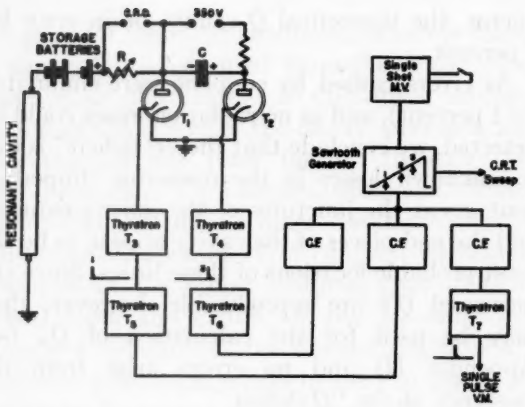

FIG. 2. Schematic diagram of the 1000-ampere pulser and block diagram of the timing circuit. The tubes T_1 and T_2 are ignitrons (GL-415).

curves thus obtained (see inset, Fig. 3), χ and δ are easily calculated.

The purpose of the circuits to be described is twofold. First, a direct current (i.e., the polarizing current which generates H_0) must be applied to the inner conductor for a short time interval Δt_p. Second, the high frequency transmission of the cavity must be measured during an interval Δt_v located within Δt_p, and during an equal interval $\Delta t_v'$ located outside of Δt_p.

In order to eliminate errors caused by the transient skin effect, it is obviously necessary for H_0 to be constant (or at least to have penetrated into the inner conductor a distance of several skin depths) at the time the "viewing pulse" measures the high frequency transmission of the cavity. By observing the shape of the current pulses on an oscilloscope it was found that the inductive transients die out in about one[11] millisecond. Nevertheless, a pulse length Δt_p of about 8 milliseconds was adopted in all measurements. This arrangement made it possible to "move" Δt_v within Δt_p, and thus it provided a means of checking on the flatness of the top of the current pulses by comparing measurements of the cavity transmission at different times within Δt_p. The same technique was used and found to be invaluable in investigating heating effects. It was shown that even in the highest fields the transmission is independent of the viewing time if the front edge of Δt_v is moved between the limits of 1 msec. and 5 msec. from the beginning of Δt_p.

To obtain reproducible data in spite of the hysteresis effect, it proved necessary to demagnetize the sample after every current pulse before the "unpulsed transmission" could be measured during the interval $\Delta t_v'$. The heating of the inner conductor as a result of the combined effect of the demagnetizing a.c. and the high current pulse necessitated a waiting period of $\frac{1}{2}$ to 3 minutes between the Δt_p pulses. It is evident, therefore, that a system employing regularly repeated pulses would not have any advantages over the "single pulse system" (SPS) adopted here.

Figure 1 shows the general function of the circuits. Between the instants denoted by "1" and "3" a current pulse Δt_p is applied to the inner conductor of the cavity. At the instant denoted by "2" a trigger activates the single pulse voltmeter (SPVM) which measures the transmission of the cavity during the viewing pulse Δt_v starting at "2."

Figure 2 shows a more detailed schematic diagram of the pulser and a block diagram of the timing circuit. The high currents are obtained from 14 low resistance storage batteries (Navy Type No. 17-B-9536) connected in series.[12] The pulses are started and stopped by firing the ignitrons T_1 and T_2, respectively. Tube T_1 (the "starter") is turned off at the end of Δt_p by applying to its plate a negative pulse from the large (3200-μf) condenser through tube T_2, the latter being extinguished automatically as the condenser discharges. The magnitude of the current pulses is controlled by means of an appropriate series resistor R. For low currents, commercially available non-inductive resistors of high wattage are used. For high currents, the resistors were made of manganin wire. The size of the voltage pulse across R, as determined on a calibrated cathode-ray oscilloscope with a long persistence screen (Type P7), provides a measurement of the polarizing current with an accuracy of ± 2 percent. For the cavity described in this

[11] A rigorous theoretical solution of this transient problem is hardly possible as the permeability is unknown. Furthermore, the field equations become non-linear since the effective permeability to the applied square wave field depends (in an unknown manner) on H_0. By assuming a constant permeability of 1000 (upper limit), however, a penetration time of the order of milliseconds was calculated.

[12] In view of the relatively long duration of Δt_p and the requirement of reasonably flat pulses, the use of a condenser would involve prohibitively large capacities. The problem of pulsing a generator was not explored.

paper, the value of H_0 on the surface of the inner conductor ($2i/10a$) is $1.25i$, where i is the polarizing current in amperes.

The timing circuit is largely conventional. By adjusting the bias on the three 2050 thyratrons it is possible to vary the length of Δt_p, its position on the linear sweep, and the starting time of the viewing pulse Δt_v. The length of Δt_v (2 milliseconds) is also adjustable and is determined by the time constant of a one-shot multivibrator which is a part of the single pulse voltmeter (SPVM).

To determine the transmission of the cavity during Δt_v, one might measure the output pulse of the receiver (i.e., the voltage drop across the load resistance of the second detector) on an oscilloscope. This method, however, does not have the required precision (<0.5 percent) during a single pulse. Instead, we developed the SPVM, which consists of a pulsed cathode follower bridge in conjunction with a ballistic galvanometer[13] and measures ballistically the output current of the receiver during Δt_v. Since the pulses are flat and Δt_v is constant, the galvanometer deflection is proportional to the receiver output.

The apparatus described here has been operating satisfactorily since September, 1946. Among the important practical problems that were encountered are the elimination of interference (the cavity and receiver were situated in separate screen rooms) and the minimizing of pick-up due to the large pulse currents by properly locating the ground points.

(2) *Procedure*

The transmission V_{bias} of the cavity in the biasing field ($(H_0)_{\text{bias}}=6.25$ oersteds is continuously applied to the inner conductor) is measured on the SPVM by disconnecting the igniters of T_1

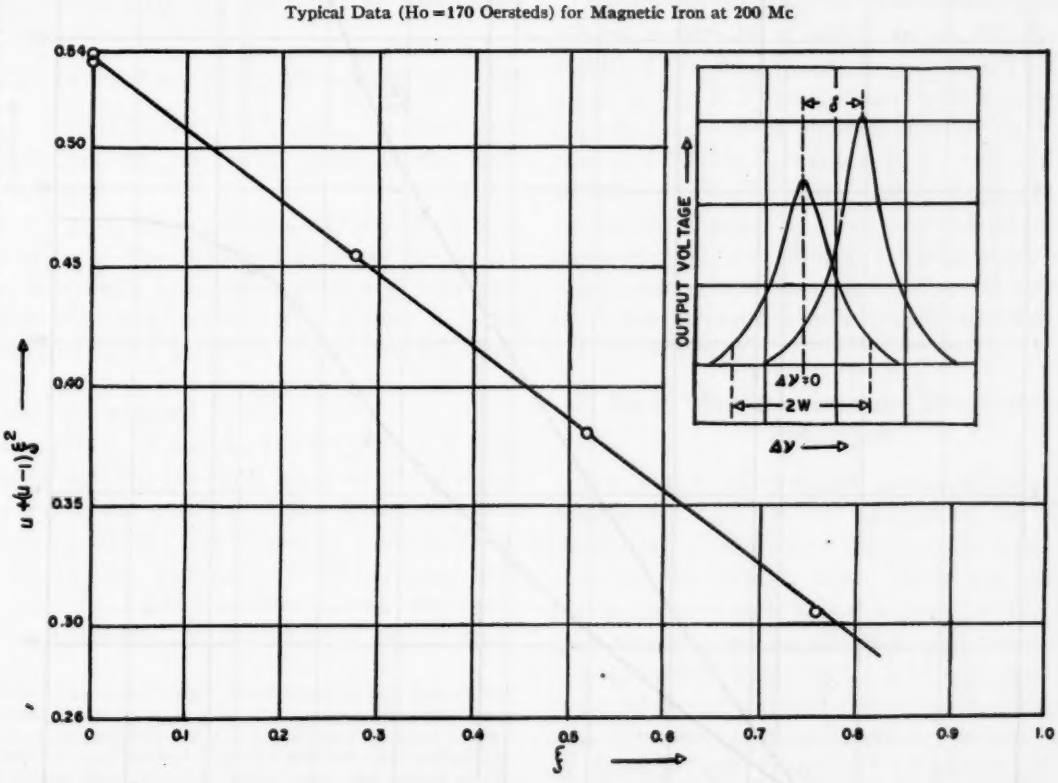

FIG. 3. Typical experimental curve used for the determination of χ'' and δ at a given polarizing field and frequency. Inset: Schematic representation of resonance curves for $(H_0)_{\text{bias}}$ (left), and H_0 (right), illustrating the increased Q and increased resonant frequency obtained by pulsing the cavity.

[13] G. T. Rado, M. H. Johnson, and M. Maloof, "A single pulse voltmeter," paper to be submitted to The Review of Scientific Instruments.

and T_2 from the circuit. About $\frac{3}{4}$ minute later (the period of the galvanometer is about 30 seconds) the cavity is "pulsed," and the transmission V corresponding to H_0 is measured. Then the sample is demagnetized, and after it has cooled off, both V_{bias} and V are checked twice. Starting from the center of the "unpulsed" resonance curve (corresponding to $(H_0)_{bias}$), the ratio $u=(V_{bias}/V)^2$ is measured at various counter settings, i.e., various resonant wave-lengths. The

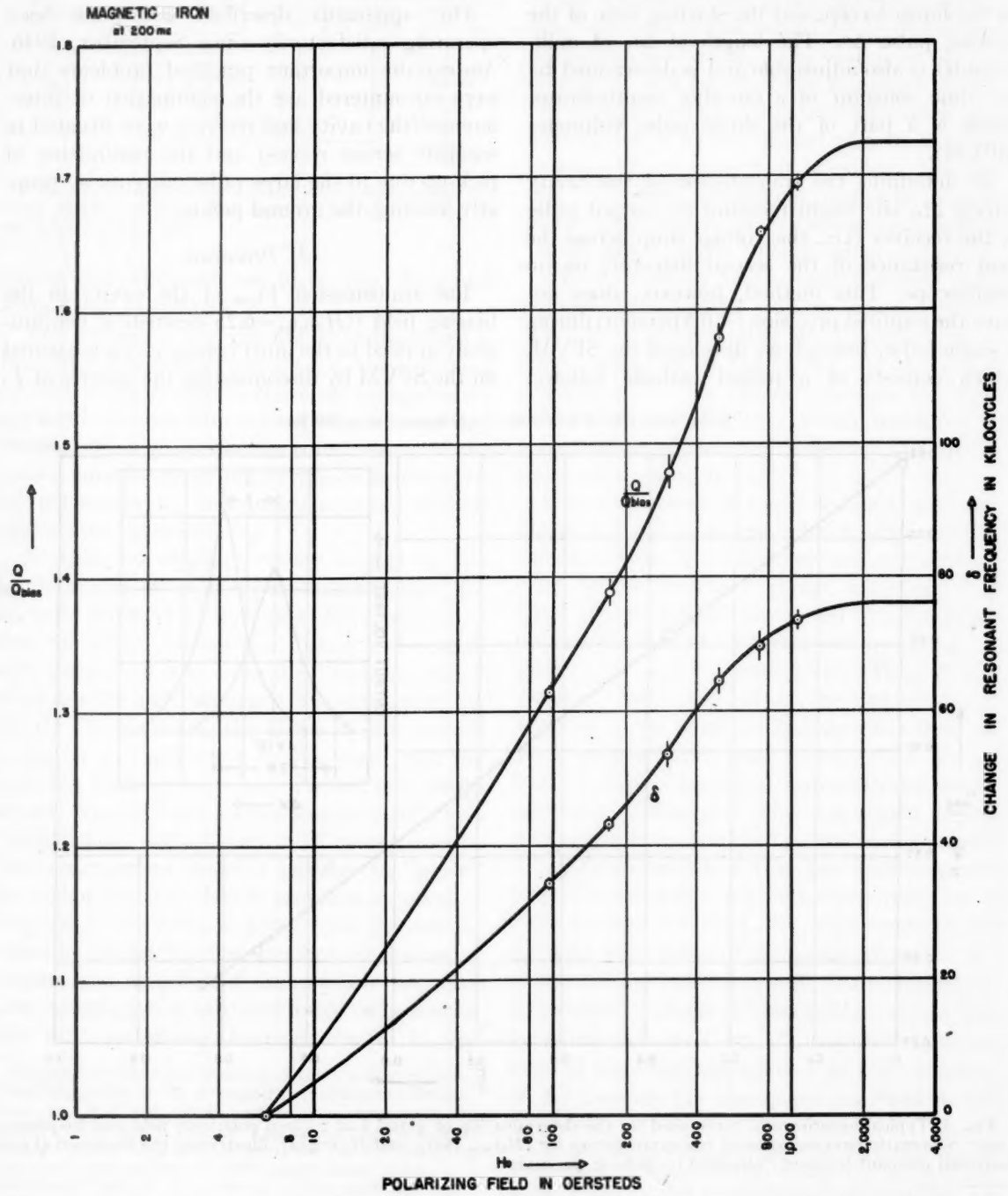

FIG. 4. Q ratio and change in resonant frequency as a function of the polarizing field H_0 for magnetic iron at 200 Mc.

values of χ and δ for any given H_0 are determined as follows:

From the standard formula of the resonance curve one obtains

$$(V_{\text{bias}}/V)^2=(V_{\text{bias}}'/V')^2 \times[1+4Q^2(\delta-\Delta\nu)^2/(\nu+\delta)^2] \times[1+4Q_{\text{bias}}^2(\Delta\nu/\nu)^2]^{-1}, \quad (24)$$

where $\Delta\nu$ is the change in resonance frequency measured from the center ν of the unpulsed resonance curve, and the primed quantities denote maximum (i.e., resonant) values. On the basis of Section II, the shift δ in Eq. (24) must clearly be positive: the center $(\nu+\delta)$ of the pulsed resonance curve (which corresponds to relatively small magnetic losses) must occur at a higher frequency than the center of the unpulsed resonance curve (which corresponds to relatively large magnetic losses).

Since $\delta\ll\nu$, and since for a decoupled resonator $V_{\text{bias}}'/V'=Q_{\text{bias}}/Q$, Eq. (24) may be rearranged to yield

$$u+(u-1)\xi^2=\chi^{-2}+(\delta/W)^2-(2\delta/W)\xi, \quad (25)$$

where $\xi=\Delta\nu/W$, and $2W=\nu/Q_{\text{bias}}$ is the width of the unpulsed resonance curve at the half-power point.

Plotting the measured quantity $u+(u-1)\xi^2$ as a function of the measured quantity ξ, one obtains a straight line whose slope and intercept furnish δ and χ, respectively. Figure 3 is an example of such a graph. It is seen that the slope of the straight line is negative so that δ is positive, as expected.

In practice, of course, the frequency is held constant and the resonant wave-length changed by varying the position of the dielectric bead. Expressing all the frequencies in counter units, we obtain the expressions[14] $W=1/2q_{\text{bias}}$ and $\xi=-(\Delta C)2q_{\text{bias}}$ which involve only directly measurable quantities. As the terms of Eq. (25) are dimensionless, we obtain

$$\delta=(\text{slope})W/2s \text{ kilocycles}, \quad (26)$$

and

$$\chi=[\text{intercept}-(\text{slope}/2)^2]^{-\frac{1}{2}}, \quad (27)$$

where s and q were defined in connection with Eq. (23), and q_{bias} is the value of q for $H_0=(H_0)_{\text{bias}}$.

If the response of the apparatus were perfectly linear, $u=(V_{\text{bias}}/V)^2$ would be given by $(G_{\text{bias}}/G)^2$, where G and G_{bias} are the galvanometer deflections corresponding to the voltage transmissions V and V_{bias}. Actually the combined errors resulting from the small non-linearity of the receiver and the SPVM, as well as from the flat scale on the galvanometer, happen to lead to a rather accurate proportionality between the deflections and the ηth power of the voltage. Thus $u=(G_{\text{bias}}/G)^{2/\eta}$, where the value of $\eta(\approx 1.02)$ is determined by an over-all calibration of the system with an R.F. signal generator.

The procedure described above leads to experimental curves of χ and δ *versus* H_0. Typical results of this kind (magnetic iron at 200 Mc) are given in Fig. 4. The saturation values χ_∞ and δ_∞ are obtained either experimentally, as in the case of 4–79 Mo-Permalloy, or by extrapolation to infinite fields, as in the case of magnetic iron. As stated in paper I, χ_∞ can be calculated (see Appendix II), and thus it is much more accurately determined than δ_∞, which must be found by a measurement or an extrapolation that cannot be verified.

C. Static Measurements and Preparation of Specimens

The static incremental permeabilities were measured by Mr. E. A. Gaugler of the Naval Ordnance Laboratory on the identical specimens used for the 200-Mc tests. These samples are $\frac{1}{8}$-inch diameter rods having a length of 17.75 cm (plus threads) and an effective axial ratio of 57. A longitudinal magnetizing field was produced in an oil-cooled solenoid coaxial with the specimen. The demagnetization correction was based on Bozorth and Chapin's[15] tabulation of the demagnetizing factor of rods as a function of the apparent static permeability and the axial ratio. Both the induction and its increment were

[14] Since the correct sign determination for δ is rather important, it seems appropriate to mention that the minus sign in the expression for ξ is not erroneous even though the cavity is constructed in such a manner that a displacement of the dielectric bead away from the center of the cavity, which causes an increase in the cavity's resonance frequency, happens to be accompanied by an increase in the counter reading. The minus sign results from the fact that we obtain what is in effect a positive $\Delta\nu$ not by increasing the applied frequency, which is actually constant, but by decreasing the counter reading and thus decreasing the resonance frequency of the cavity.

[15] R. M. Bozorth and D. M. Chapin, J. App. Phys. **13**, 320 (1942).

measured ballistically. The thin search coil was placed near the center[15] of the rod and the correction for the flux in the air space was obtained experimentally. Since the incremental changes of the magnetic field were sufficiently small, their magnitude did not affect the measurements of μ_{stat}. With the exception of the early part of the magnetization curve, where the demagnetization correction is somewhat uncertain, Gaugler's values of μ_{stat} are at least as accurate as our high frequency permeabilities. Fortunately, however, the exact value of the large static incremental permeabilities at very small polarizing fields is of little interest (Section V) for our purposes. In the coaxial line measurements, of course, the demagnetizing field is zero for both the static and the high frequency lines of force. The static measurements refer to the initial magnetization curve rather than to the particular method of traversing the magnetization curve used in the high frequency case. At polarizing fields of several oersteds the difference between these two procedures has a negligible effect on μ_{stat}.

All specimens were made from rods[16] that had been annealed before we received them. The process of threading the samples did not significantly change their magnetic properties. This conclusion was reached by re-annealing the iron specimen (in an H_2 atmosphere at 1100°C) after the static and 200 Mc measurements were completed, and then re-measuring μ_{stat}. The results agreed with the original static measurements even at small polarizing fields where the effect of any appreciable stresses would be most pronounced. Since the static results could be reproduced on two specimens of equal length made from adjacent portions of the iron rod, it was unnecessary to attempt static measurements on the short (4-cm) specimen, used for our 975 Mc[17] work, which was cut from the original rod. In the case of the permalloys the above mentioned verifications were omitted so that residual stresses due to the threading may have caused μ_{stat} to be too low in the relatively unimportant region of small polarizing fields. For large values of H_0, however, the static results are in satis-

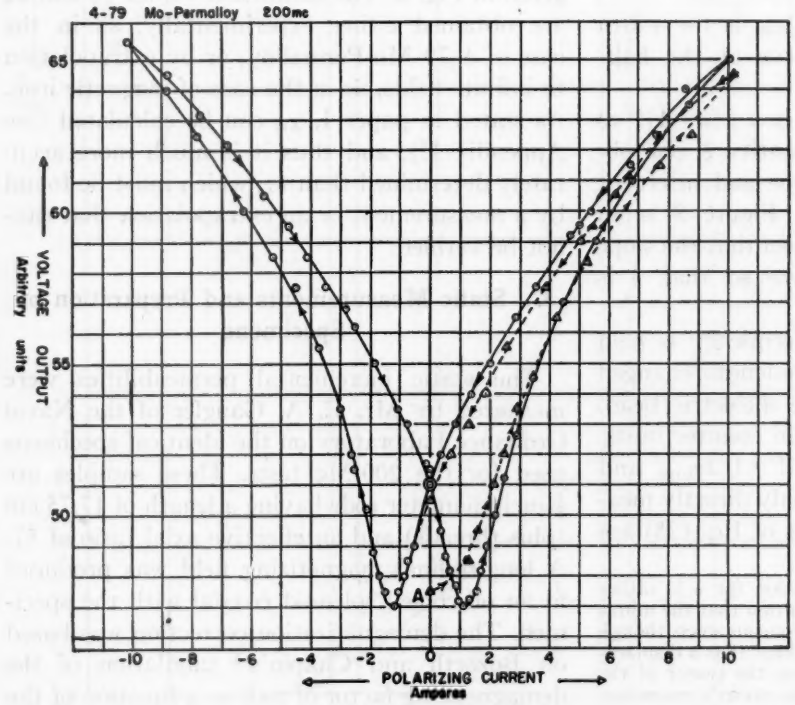

FIG. 5. Typical butterfly curve (4–79 Mo Permalloy at 200 Mc) obtained by using a d.c. polarizing current. The starting point (marked "A") represents the demagnetized state.

[16] We are indebted to Mr. R. A. Chegwidden of the Bell Telephone Laboratories for samples of the magnetic materials used in this work.

[17] The 975-Mc measurements were made in a special resonator by a method practically identical with the one described in the present paper. We wish to thank Mr. H. Rosenblatt for his help in taking some of the data. Further results, including the effect of surface treatments on the complex permeability, will be reported in a later publication.

TABLE II. Summary of butterfly data.

I Material	II ν in Mc	III H_0 at max μ	IV μ_0	V μ/μ_0 at $H_0=18$ oersteds	VI μ/μ_0 at max μ
Iron	0	1.0	55 (198)	0.5	2.5
	200	2.7	95	0.68	1.10
	975	3.5	66	0.87	1.01
Mo Permalloy	0	0.05	7,000 (11,700)	$\sim 10^{-4}$	1.5
	200	2.2	64	0.41	1.32
45 Permalloy	0	0.3	1,200 (2,700)	0.06	1.9
	200	~4.0	81	0.87	1.03

Column I: The materials used by Elmen (see reference 22) for his static measurements were Armco iron, 3.8–78.5 Mo Permalloy, and 45 Permalloy, whereas the high frequency results refer, of course, to magnetic iron, 4–79 Mo Permalloy, and 45 Permalloy. Any comparison of the static and high frequency data of this table must thus be qualitative. Only the data of Figs. 9, 11, and 12 may be used for a quantitative comparison of static and high frequency results.
Column II: The data quoted for $\nu=0$ are Elmen's (see reference 22) results at 200 cycles/sec. Presumably these data apply to the static case.
Columns III–VI: At the high frequencies, the permeabilities listed in these columns are apparent permeabilities (μ_R) and were measured (Section IV) by the brass substitution method in conjunction with the butterfly technique. At zero frequency the permeabilities are static incremental permeabilities (μ_{stat}). In either case the subscript zero indicates that $H_0=0$. Except for the data in parentheses, which refer to the demagnetized state, all values of μ_0 (including those in the ratios of columns V and VI) refer to the cross-over point of the butterfly and are thus characteristic of remanence. The high frequency results were obtained from butterfly curves whose maximum value of H_0 was taken as 17.7 oersteds in the case of magnetic iron and 4–79 Mo Permalloy, and as 35.4 oersteds in the case of 45 Permalloy.

factory agreement with representative values published by Legg.[18]

The surface of each specimen is reasonably smooth, only a few fine ridges in the direction of the axis being visible to the unaided eye. Microscopic examination revealed additional irregular striations and pitted regions.

The purity of our magnetic iron is listed as 99.94 percent, and a spectrochemical analysis at this laboratory showed that the metallic impurities total less than 0.03 percent. It seems reasonable to assume, therefore, that the accepted value[1] of the anisotropy constant of iron agrees closely with that of our particular material. The pertinent conclusions of Section V remain valid as long as the discrepancy between these two values does not exceed a factor of three.

IV. HYSTERESIS EFFECTS

The measured quantities Q_{bias}, χ, and δ, and hence the high frequency permeability, were found to be independent of the R. F. field strength for values around 0.01 oersted. This shows that for sufficiently small fields ordinary hysteresis is absent at 200 Mc so that all our results refer to *reversible* magnetization processes. In fact, the trend of the data of Kreielsheimer[19] indicates that even for fields of several oersteds, ordinary hysteresis is no longer present at 200 Mc.

The static (or low frequency) magnetization, however, is subject to ordinary hysteresis with respect to the polarizing field H_0. For this reason, the R.F. permeability is a double valued function of H_0 if the latter, instead of being applied in pulses starting from a uniquely magnetized state (as in Section III), is applied cyclically to the magnetic specimen. It is this dependence that will be referred to as "hysteresis effect" throughout the present paper. The double valued function mentioned above has the form of the "butterfly" curve which will be discussed later. This curve represents the combined effect of those reversible processes which are still effective at 200 Mc; the independent variable is essentially the state of static magnetization of the specimen.

Hysteresis effects of this kind can be rapidly examined in relatively small polarizing fields by using a direct or low frequency current through the center conductor and measuring the high frequency transmission of the cavity as a function of cyclic polarization. Although this method yields only the apparent permeability μ_R[20] rather than μ_1 and μ_2, it does have the advantage of not requiring the complicated pulse technique which was developed primarily for the accurate measurement of resonance frequency changes. On the typical "butterfly" curve shown in Fig. 5,

[18] V. E. Legg, Bell Sys. Tech. J. 18, 438 (1939).
[19] See reference 1, pp. 234–237.
[20] As shown in Appendix IV, $\mu_R=|\mu|+\mu_2$.

the voltage transmission of the cavity, as determined by the rectified current output of the receiver, is plotted against the polarizing current in amperes. The dielectric bead, which is adjusted to resonate the cavity at $H_0=0$, remains fixed throughout the experiment.

To interpret the butterfly curves we use an equation similar to (24) and obtain

$$(V_0/V)^2=(V_0'/V')^2[1+4Q^2(\delta'-\Delta\nu)^2/(\nu+\delta')^2]\times[1+4Q_0^2(\Delta\nu/\nu)^2]^{-1}, \quad (28)$$

where the subscript zero refers to the demagnetized state ($H_0=0$) and δ' is the change in resonance frequency corresponding to a change in polarizing field from zero to H_0. Since $V_0'/V'=Q_0/Q$, $\delta'\ll\nu$, and $\Delta\nu=0$, Eq. (28) becomes

$$(V_0/V)^2=(Q_0/Q)^2[1+(\delta'/W')^2], \quad (29)$$

where $2W'=\nu/Q$ is the width, at the half-power point, of the resonance curve corresponding to a polarizing field H_0. From the measurements of δ *versus* H_0 we know that $\delta'\ll W'$ for all but very high fields. In the case of magnetic iron, for example, the maximum value of δ, which is almost as large as δ', is about 80 kc, whereas the corresponding W' is about 167 kc ($\nu=2\times10^5$, $Q=600$), so that $(\delta'/W')^2$ never exceeds 0.23. Thus, we may use

$$V_0/V=Q_0/Q \quad (30)$$

instead of Eq. (29) for low and intermediate H_0.

If the inner conductor of the cavity consisted completely of the magnetic material under investigation, and if the rest of the cavity had infinite conductivity in addition to being non-magnetic, then the measured Q's, and hence the ordinates of the butterfly curve, would be inversely proportional to the corresponding α's and to the square root of the apparent permeabilities.[21]

In the actual case of an imperfect cavity with a partially magnetic inner conductor, we have, analogously to Eqs. (15) and (17),

$$\alpha_0-\alpha=(1/2\gamma)(1/Q_0-1/Q),$$

which may be rewritten by using Eq. (30) to yield

$$(\alpha_0-\alpha)/\alpha_0=(1/2\gamma Q_0\alpha_0)(V-V_0)/V=\mathfrak{N}, \quad (31)$$

where the measurable quantity $\mathfrak{N}$ equals[21] the fractional change of the square root of the apparent permeability as the polarizing field is changed from zero to some value H_0.

From Eq. (31) we obtain[21] the expression

$$\mu_R/(\mu_R)_0=(1-\mathfrak{N})^2, \quad (32)$$

used for the interpretation (Table II, Section V) of the butterfly curves. To determine $\mathfrak{N}$ and to find the actual value of $(\mu_R)_0$ the quantity α_0 must be measured. This is accomplished with a fair degree of accuracy ($\leq$15 percent) by actually substituting a brass inner conductor for the partially magnetic inner conductor. Simple Q measurements may then be used (without pulsing)

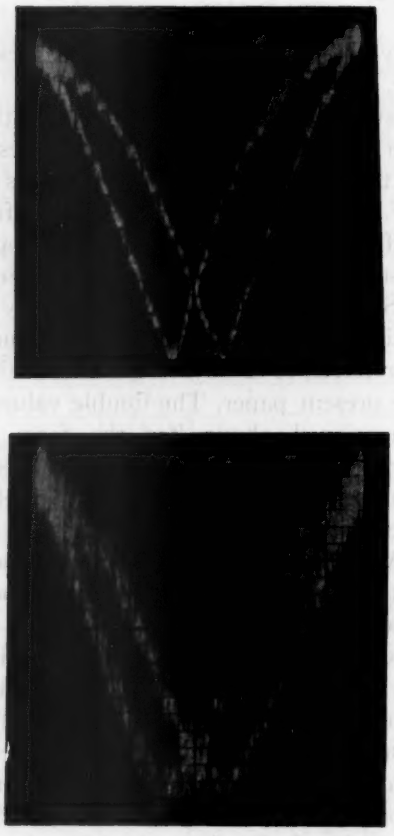

FIGS. 6 and 7. Oscillograms of butterfly curves for magnetic iron at 200 Mc (Fig. 6), and at 975 Mc (Fig. 7), using a 60-c.p.s. polarizing field of 17.7-oersted amplitude. The ordinates represent the modulated part of the cavity transmission and the abscissae are proportional to the polarizing field. The noise signals appearing in Fig. 7 are a result of the larger gain used at 975 Mc, where the dependence of the permeability on a polarizing field is less pronounced than at 200 Mc.

[21] As shown in Appendix IV, $\alpha/\alpha_\infty=(\mu_R)^{\frac{1}{2}}$.

to obtain α_0 from the equation

$$\alpha_0-\alpha_{Br}=(1/2\gamma Q_{Br})[(Q_{Br}/Q_0)-1], \quad (33)$$

where the subscript Br refers to brass. The attenuation α_{Br} is calculated from Eq. (19) by using ρ_{Br} in place of ρ.

The butterfly curve shown in Fig. 5 was taken on 4–79 Mo Permalloy (at 200 Mc) by using a continuous direct current to generate the polarizing field. Starting from the demagnetized state, marked "A," the dashed line corresponds to the initial magnetization curve and merges into the butterfly curve (solid line) when the cyclic state is reached. The slight unsymmetry of the curve is due to heating effects caused by the application of the polarizing current for a relatively long time. These effects may be avoided by using a polarizing current of low audiofrequency and displaying the rectified cavity output on an oscilloscope where the butterfly curve may be photographed. The curve corresponding to the initial curve, of course, does not appear when an alternating polarizing field is used. Figures 6 and 7, taken on magnetic iron at 200 and 975 Mc, respectively, provide examples of such photographs. A further refinement is introduced by "chopping" the receiver output by means of an electronic switch. This method allows the zero level of the cavity transmission to be included in the photograph as a horizontal straight line that can be used for reference purposes. The typical example of Fig. 8 shows this type of presentation for 4–79 Mo Permalloy (at 200 Mc) where the permeability, and consequently the modulation of the cavity output, are relatively large, so that details of the butterfly curve are discernible. In those cases where the modulation is small compared to V_0, the cavity transmission for $H_0=0$, the determination of $\mathfrak{N}$ requires a scope calibration. The latter involves measuring the number of divisions on the screen of the cathode-ray tube which would be equivalent to V_0 if the gain were equal to that used in connection with the butterfly photograph.

The general results of the butterfly investigations may be summarized as follows:

(1) As expected, the shape and size of the butterfly curves is independent of the frequency of the polarizing field. Experiments in support of this statement were carried out on the same specimen at frequencies of zero, 60, 400, and 800 cycles/sec.

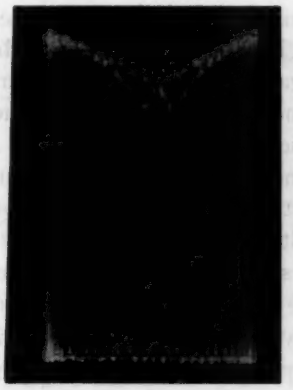

FIG. 8. Oscillogram of a typical butterfly curve (4–79 Mo Permalloy at 200 Mc) obtained by using an electronic switch; the ordinates represent the total cavity transmission.

(2) The butterfly curves do depend, to a small extent, on the maximum value of the polarizing field that is used in traversing the hysteresis cycle.

(3) There seems to be a superficial resemblance between our butterfly curves and the butterfly curves obtained by plotting the incremental static[22] permeability as a function of a polarizing field. In detail, however, these two types of curves differ in two important respects:

(*a*) As the polarizing field is changed from zero to several oersteds, the apparent high frequency permeability, as computed from the butterfly curve, changes by a much smaller fraction than the incremental static permeability.

(*b*) The positions of the minima on the high frequency butterfly curve, which correspond to a maximum apparent permeability, often occur at larger values of H_0 than those on the static curve for the same substance.

Numerical data (Table II) on the statements "*a*" and "*b*," as well as their interpretation, are given in Section V.

V. RESULTS AND DISCUSSION

As the penetration depth of a 200-Mc electromagnetic wave in iron or permalloy is less than 10^{-3} cm, the measured permeabilities are surface properties of the metal under investigation. In any interpretation of the data consideration must therefore be given to the effect of surface conditions on the processes of magnetization as well as to the response of these processes to high frequency excitation. Static measurements deter-

[22] G. W. Elmen, Bell Sys. Tech. J. 15, 113 (1936), published such curves for several magnetic substances. The frequency of the small alternating field was 200 cycles/sec., and its amplitude was of the order of 0.001 oersted. Presumably, however, the results would have been the same if a static incremental field had been used.

mine the magnetization in the interior of the metal and give some indication of the processes of magnetization taking place at various points on the magnetization curve. Consequently, when made on the same sample of metal as the high frequency measurements, they are an invaluable aid in disentangling the different effects.

Our results for magnetic iron at 200 Mc and 975 Mc are shown in Fig. 9. Curves are given for the in-phase and out-of-phase components of the permeability, μ_1 and μ_2, the static incremental permeability, μ_{stat}, and the loss tangent of the susceptibility, $\mu_2/(\mu_1-1)$. The latter are the two topmost curves whose ordinate scale is on the right-hand side of the figure.

The most striking feature of our experimental results is the equality of μ_{stat} and μ_1 at both frequencies for all values of the polarizing field, H_0, greater than 50 oersteds. It is evident from Fig. 10, in which a typical[23] magnetization curve for magnetic iron is shown, that these fields are well beyond the knee of the magnetization curve. Consequently, we may conclude that the processes giving rise to changes in magnetization close to saturation respond fully (only weakly damped) to the high frequency excitation and that they differ in no way on the surface and in the interior of the samples we used.

The process known to be present, and usually assumed to be wholly responsible for magnetization changes close to saturation, is termed domain or spin rotation. According to this conception,[1] developed by Akulov and Gans, the metal is divided into domains in which the spins of the individual ions are ridigly coupled by the Heisenberg exchange force so that each domain is magnetized to saturation. The direction of the domain spin is fixed by the balance between the torque of the applied field and the torque from the anisotropy in the crystalline field. Changes in

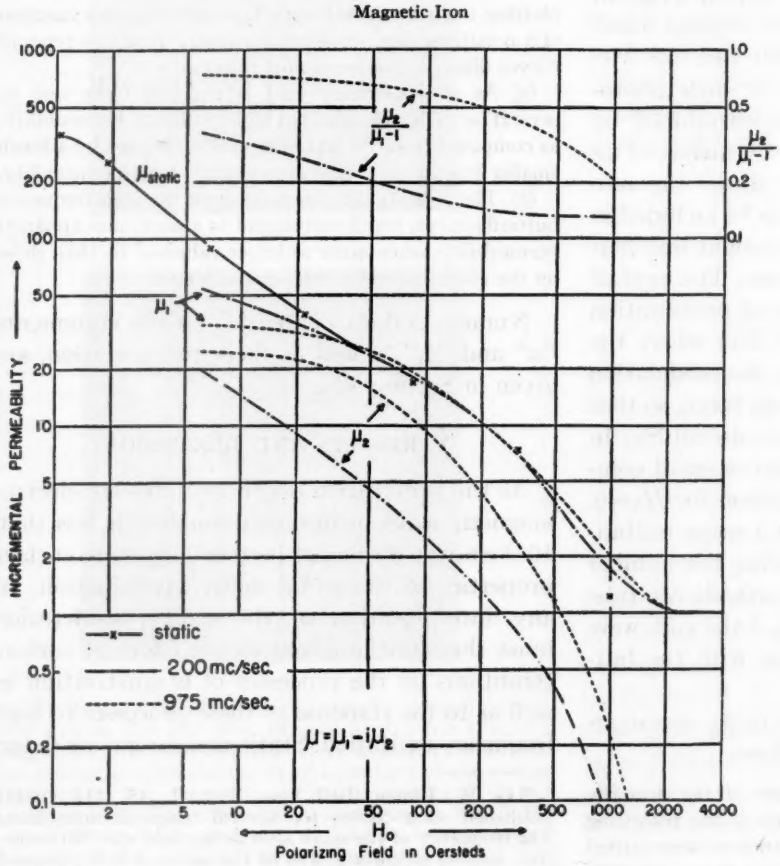

FIG. 9. Experimental permeabilities as a function of the polarizing field H_0 for magnetic iron at 0, 200, and 975 Mc.

[23] The typical magnetization curves of Figure 10 were taken from Legg's paper (see reference 18).

magnetization are produced by disturbing this balance when the applied field is altered. Saturation occurs when the torque of the applied field is so large that the crystalline field has a negligible influence on the direction of the domain spin.

The fact that $\mu_1=\mu_{stat}$ implies that domain rotation, at least for $H_0>50$ oersteds, responds fully to 975-Mc excitation. If the penetration depth of the 975-Mc field were smaller than the domain size, this would not be possible. The torque exerted on the spin would then be smaller, and since the rigid spin coupling causes the whole domain to rotate, the induced magnetization in the region of the applied field would be diminished. As the experimental result shows that the response is not diminished, and as the penetration depth of a 975-Mc wave in iron for $\mu=25$ is 1.0×10^{-4} cm, we can conclude[24] that the domains whose spins rotate are smaller than 10^{-4} cm for polarizing fields between 50 and 500 oersteds. It should be noted that the entire volume in which the high frequency field exists must be partitioned by domains to this size. If this were not so, the contribution to μ_{stat} of spin rotation, which takes place throughout the metal, would be larger than to μ_1.

The question arises as to whether 10^{-4} cm is the largest possible domain size. Recent experiments on the depolarization of slow neutrons[25] by the magnetic discontinuities in iron in a field of 10,000 oersteds have shown that the ultimate domain size is certainly greater than 7×10^{-4} cm and is probably the size of the microcrystal itself. Microphotographs of the samples used in the present experiments show a grain size[26] of 1.4×10^{-2} cm$\pm$20 percent. Consequently, the ultimate domain size in our samples is at least a hundred times the limit (10^{-4} cm) set above.

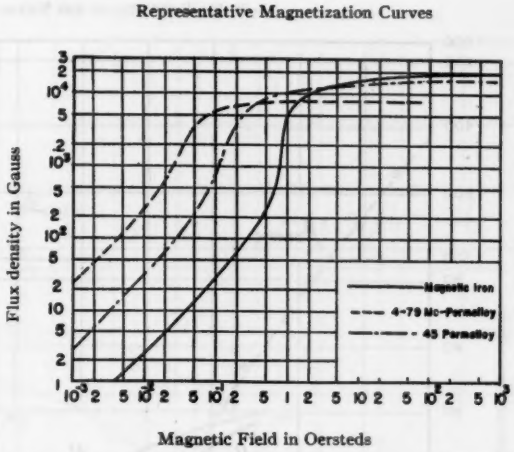

FIG. 10. Typical magnetization curves (reproduced from Leggs' (see reference 18) paper) for magnetic iron, 4–79 Mo Permalloy and 45 Permalloy.

The fact of a larger domain size at fields above 500 oersteds means that the domains existing in fields below 500 oersteds (which must be smaller than the skin depth for $\mu=4$, and thus smaller than 2.5×10^{-4} cm) are not stable, and that in higher polarizing fields they coalesce to form the larger domains. Therefore, above 500 oersteds wall displacements still occur and must contribute to changes in magnetization. We are, therefore, led to the idea of domains that are far more stable than those commonly supposed to exist at low fields and to disppear at the knee of the magnetization curve. It is most unlikely that wall displacements should contribute to magnetization above 500 oersteds and not below it. Consequently in the region $50<H_0<500$ oersteds wall displacements should also be contributing to the magnetization.

The existence of wall displacements for $H_0>50$ oersteds is confirmed by the quantitative results of the spin rotation theory. According to Gans'[27] formulae, which give the permeability in terms of the applied field, the saturation moment per unit volume, and the anisotropy constant, the permeability from spin rotation in zero field for polycrystalline iron is 14. As μ_1 (or μ_{stat}) is not reduced to this value until a polarizing field of 140 oersteds is applied, the actual permeability

[24] This is contrary to the assumption used by C. Kittel, Phys. Rev. **70**, 281 (1946), who attributed the decrease of the permeability at high frequencies to the smallness of the skin depth compared to the domain size. (The Barkhausen effect leads to estimates (see reference 1) of domain dimensions ranging from 10^{-3} to 10^{-4} cm.)

[25] D. J. Hughes, J. R. Wallace, and R. H. Holtzman, Phys. Rev. **73**, 1277 (1948). See also O. Halpern and T. Holstein, Phys. Rev. **59**, 960 (1941) and F. Bloch, M. Hammermesh, and H. H. Staub, Phys. Rev. **64**, 47 (1943).

[26] Even if iron oxide occlusions, clearly visible in the microphotographs, should determine the ultimate domain size, it would be greater than 3×10^{-3} cm. This seems a very unlikely possibility because such occlusions must have been present in the iron used in the neutron experiments and furthermore the hydrogen annealing had reduced most of the oxygen in the surface of our samples.

[27] R. Gans, Ann. d. Physik **15**, 28 (1932).

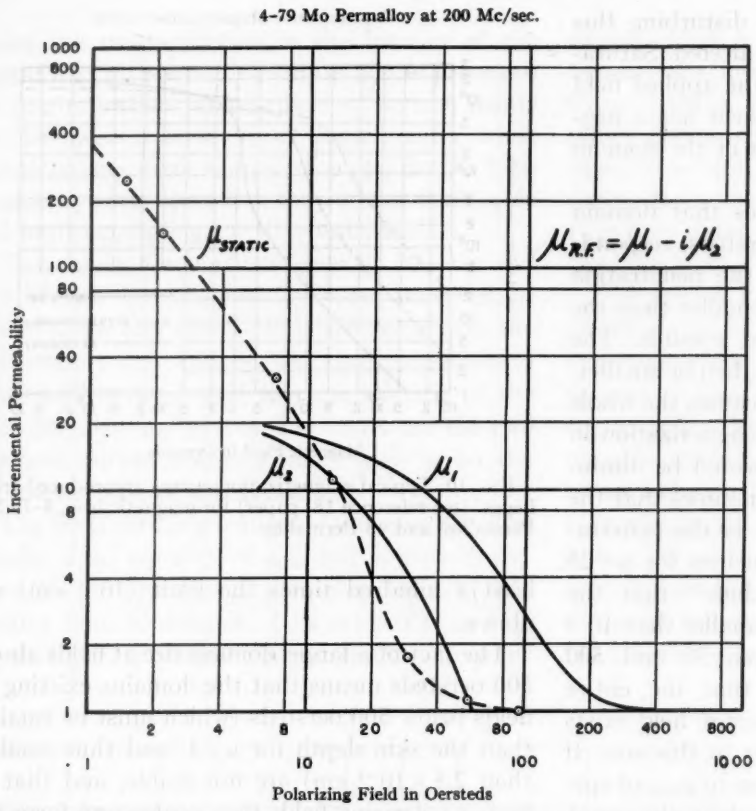

FIG. 11. Experimental permeabilities as a function of the polarizing field H_0 for 4–79 Mo Permalloy at 0 and 200 Mc.

exceeds[28,29] the calculated value by a large amount throughout this region. Since the conditions for the applicability of Gans' theory are well satisfied in our samples, this excess in the permeability can be attributed to changes in magnetization by wall displacements.

Let us next consider how the "50-oersted processes" of magnetization may behave at lower fields. The domains involved certainly cannot become larger; hence the contribution of spin rotation should still be present in accordance with Gans' formula. The domain walls, however, must contribute much more in order to account for the high values of μ_{stat} at low fields. This may occur either because of the motion of additional walls obtained by subdivision of the 50-oersted domains (the notation H_0-domain is used to designate a domain that exists in a field of H_0 oersteds) or because of the increased mobility and perhaps increased length of 50-oersted domain walls at lower fields. The first alternative means that magnetization (at any frequency) in lower fields occurs not only by processes active in higher fields but also by *additional processes* which come into being at the lower fields. The second alternative means that the larger magnetization changes in lower fields are the results of *altered characteristics* in the process active at higher fields.

The damping forces on domain walls are presumably the result of eddy currents induced by the change in magnetization when the walls are displaced. While the damping forces depend on the velocity of the wall, they do not depend directly on the polarizing field or on the stability

[28] H. Lawton and K. H. Stewart, Proc. Roy. Soc. **A193**, 72 (1948), have calculated magnetization curves for iron single crystals of simple shape for the case where the field is applied in an arbitrary direction with respect to the crystal axes. Their theory (which takes into account demagnetization effects on the surface of the sample) is based on spin rotation and the results are in good agreement with experiment down to relatively small fields. It therefore appears that the magnetic behaviour of polycrystals and single crystals is fundamentally different.

[29] It may be noted that microscopic observations of magnetic powder patterns on unstrained surfaces of single crystals indicate magnetic inhomogeneities of about 10^{-2} cm. See H. J. Williams, Phys. Rev. **70**, 106 (A) (1946); also **71**, 646 (1947); **72**, 529 (A) (1947); **73**, 1246 (A) (1948). If magnetic structures smaller than 10^{-4} cm existed in a single crystal, they could not be detected with the resolving power of a microscope utilizing visible light.

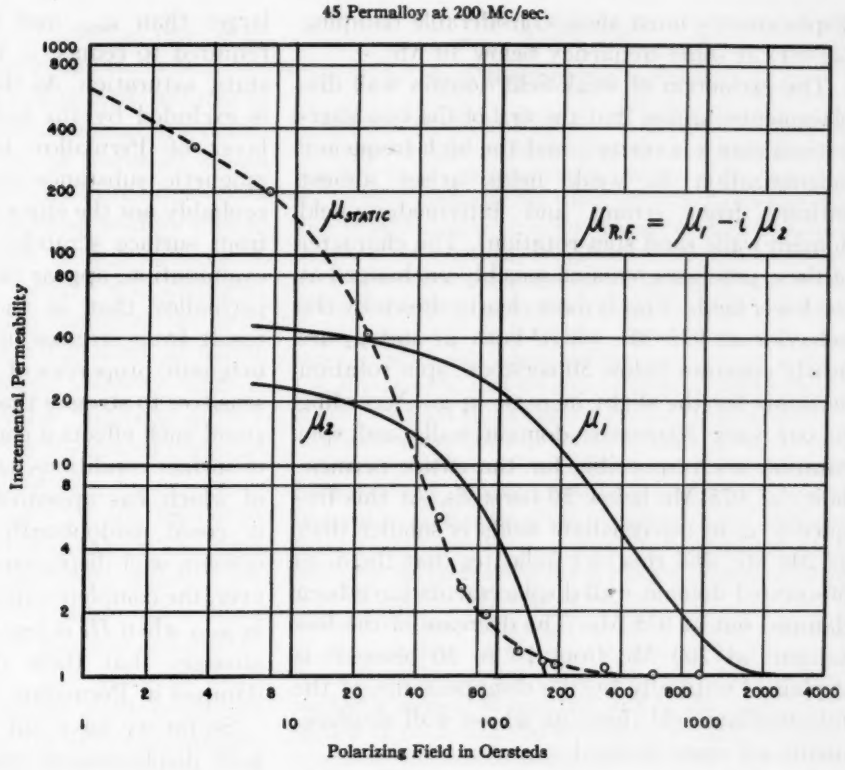

FIG. 12. Experimental permeabilities as a function of the polarizing field H_0 for 45 Permalloy at 0 and 200 Mc.

of the wall. On the other hand, the restoring force should be larger for the domain walls in higher fields because only the domains of greater stability exist in the higher fields. It is thus easily shown[30] that the induced magnetization, and hence $\mu-1$, has the form

$$\mu-1=(\mu_{stat}-1)(1-i\omega\tau)(1+\omega^2\tau^2)^{-1}, \quad (34)$$

where τ is a relaxation time that is smaller for the more stable domains. When the walls are highly damped, $\omega\tau\gg1$, and the out-of-phase component of magnetization, μ_2, is much larger than the in-phase component, μ_1-1.

Examination of Fig. 9 shows that μ_{stat} increases by a factor of four in passing from 6.25 oersteds to zero fields. Since μ_1 at 200 Mc is but a fifth of μ_{stat} at $H_0=0$, these weak-field domain walls must be highly damped[31] and do not contribute to μ_1. Furthermore, nothing like the fourfold increase in μ_{stat} is reflected in μ_2 so that the contribution of weak-field domain walls to μ_2 must also be small. As H_0 is reduced from 6.25 oersteds to zero, the increase in μ_2 amounts to about 18.[32] This figure sets an upper limit on the contribution of weak-field domain wall displacements to μ_2. Since $\mu_{stat}\approx360$ at $H_0=0$, Eq. (34) gives $\omega\tau\geq20$ at 200 Mc so that weak-field wall

[30] R. Becker, see reference 1, pp. 237–242. The general reasoning given by Becker may be applied individually to the walls of all the domains characterized by a given degree of stability. All such walls have a relaxation time which depends on the degree of domain stability; their displacements contribute a portion (according to their number) to the total static and high frequency susceptibility.

[31] The extinction of wall displacements mentioned in paper I refers to the weak-field domains.

[32] Our permeability data for $H_0<6.25$ oersteds (not shown in Figs. 9, 11, and 12) are uncertain because of the hysteresis effect, and only approximate values can be given for the permeability at $H_0=0$. These are $\mu_1=78$ and $\mu_2=38$ at 200 Mc, and $\mu_1=36$ and $\mu_2=25$ at 975 Mc. To compare these results with those given in the literature we note that C. Kittel, Phys. Rev. 70, 281 (1946), has summarized the experimental values of the apparent permeabilities μ_R and μ_L of "iron" and drawn a smooth curve through the most reliable data. Using this experimental curve, and the equations of Appendix IV, we find $\mu_1=80$ and $\mu_2=39$ at 200 Mc, and $\mu_1=\mu_2=34$ at 975 Mc. The good agreement between the two sets of data is largely accidental because the mean values derived from previous measurements refer to different materials (even in the case of μ_R and μ_L at the same frequency) and are subject to considerable variations. This statement is supported by recent results of G. Eichholz and G. F. Hodsman, Nature 160, 302 (1947), on the apparent permeability μ_R in various types of iron and steel. A comprehensive review of past work on apparent permeabilities at high frequencies was given by J. T. Allanson, J. Inst. Elec. Eng. 92, Part III, 247 (1945).

displacements must show considerable damping ($\omega\tau \approx 1$) at some frequency below 10 Mc.

The extinction of weak-field domain wall displacements implies that the *first* of the two alternatives above is correct, and the high frequency magnetization in weak fields arises almost entirely from strong and intermediate-field domain walls (and spin rotation). The character of these processes remains sensibly unchanged at the lower fields. This is most clearly shown by the behavior at 975 Mc where both μ_1 and μ_2 are nearly constant below 50 oersteds; spin rotation accounts for the slight increase in μ_1. According to our view 50-oersted domain walls and spin rotation are responsible for the entire permeability at 975 Mc below 50 oersteds. At this frequency μ_1 in intermediate fields is smaller than at 200 Mc, and this fact indicates that the 6- to 50-oersted domain wall displacements have been damped out at 975 Mc. The decrease of the loss tangent at 200 Mc from 10 to 50 oersteds is explained naturally by the disappearance of the intermediate-field domains whose wall displacements are more damped.

One difficulty occurs in the use of Eq. (34). The loss tangent of 0.65 at 50 oersteds for the 975-Mc permeability implies that μ_1 should be about 30 percent smaller than μ_{stat}, a discrepancy which is definitely outside the experimental error.[33] Consequently there is some doubt as to the meaning of the experimental values of μ_2 or as to the applicability of Eq. (34). There are some indications (which will be reported in a later paper) that the experimental values of μ_2 depend on surface conditions much more sensitively than those of μ_1.

Our results for 4–79 Mo Permalloy (4-percent Mo, 79-percent Ni) and for 45 Permalloy (45-percent Ni) are shown in Figs. 11 and 12. As in the case of magnetic iron, relatively small damping is indicated at high polarizing fields. Contrary to the situation in iron, μ_1 becomes larger than μ_{stat} and higher values of H_0 are required to reduce μ_1 to unity than to produce static saturation. As the possibility of resonance is excluded by the behavior of μ_2, the surface layer of Permalloy behaves like a "harder" magnetic substance than the interior. This is probably not the effect of a demagnetizing factor from surface scratches, which, on microscopic examination, appear no more pronounced in the permalloy than in the iron samples. It could result from stresses in the surface because the magnetic properties of Permalloy are much more sensitive to stresses than those of iron. To understand such effects a comprehensive investigation of surface conditions has been undertaken, a part of which has appeared.[34] Whatever the effect, it could undoubtedly change the weak-field domain wall displacements in Permalloy. However, the complete extinction of the large changes in μ_{stat} when H_0 is less than 0.5 oersted indicates strongly that these displacements are highly damped in Permalloy also.

So far we have not discussed the irreversible wall displacements that take place when one domain configuration changes to another configuration of lower energy, which is not obtained from the first by infinitesimal displacements. The high frequency changes in magnetization are necessarily reversible (see Section IV). Nevertheless, the response depends on the domain configurations and will reflect changes in these configurations whether they are reversible or irreversible. This is clearly demonstrated by the results of the technique described in Section IV which are summarized in Table II.

In general the hysteresis effects shown in the oscillograms of Figs. 6, 7, and 8 are smaller at 200 Mc and much smaller at 975 Mc than might be expected from the corresponding changes in static fields. This is illustrated in columns V and VI of Table II in which the permeability at zero field in the remanent[35] state is compared to the permeability in a polarizing field of 18 oersteds and to the maximum permeability reached in the

[33] The error in μ_1 is estimated as less than ± 5 percent but the values of μ_2 are considerably less certain. Since μ_2 depends on the small difference $\alpha - \beta$ (Eq. 22), it is difficult to determine at fields close to saturation. This is especially true in iron, where δ_∞ could not be measured directly and was found by an extrapolation (as in Fig. 4) that is subject to an error of about ± 2 percent. Nevertheless, the error in μ_2 is estimated as less than ± 10 percent for small values of H_0 and as less than ± 50 percent at $H_0 = 500$ oersteds.

[34] G. T. Rado, M. Maloof, and H. Rosenblatt, Phys. Rev. 74, 1206 (A) (1948).

[35] The effects indicated by these comparisons would appear more pronounced had the ratios in columns V and VI of Table II referred to the demagnetized state rather than to the remanent state.

hysteresis cycle. This result follows at once from the extinction by damping of the weak-field domain wall displacements which contribute most to the static changes in magnetization at low fields.

Inspection of column III of Table II shows that the maximum permeability in the hysteresis cycle occurs at a higher polarizing field for higher frequencies. As the changes in permeability in low fields at 200 Mc are mostly wall displacements of the 6- to 50-oersted domains, the coercive force for these domains is greater, as might be expected from their greater stability, than it is for the weak-field domains. Similarly at 975 Mc the wall displacements of 50-oersted domains give a still greater coercive force.

Another interesting feature of the results is that the hysteresis loops indicated by the high frequency measurements (butterfly curves) are wider than the corresponding static ones. Since at 975 Mc the permeability changes are due to the most stable domains, the ratio of high field hysteresis changes to low field hysteresis changes will be greatest for 975 Mc in accordance with observation. Indeed the existence of wall displacements at 500 oersteds implies that irreversible changes can take place in this strong a field.

The absence of any hysteresis effects reflecting irreversible changes in weak-field domains requires an explanation when it is remembered that we have already indicated why spin rotation in these domains must contribute a considerable fraction of the high frequency permeability. Of course at low frequencies the relative contribution of spin rotation to the weak field permeability is very small. Since the induced magnetization in spin rotation depends on the magnitude of the angle between the spin direction and the applied field, an irreversible change that alters this angle will be reflected in the spin rotation permeability. However, if the irreversible displacement is simply a reversal in sign of the spin direction ("180-degree wall") along the crystal axis, there will be no change in spin rotation permeability. It seems plausible that the irreversible changes occurring when the direction of the applied field is reversed are of this kind and should be the predominant type for weak-field domain hysteresis.

APPENDIX

I. Theory of the γ-Factor

In this appendix we calculate the change of the propagation constant (or refractive index) in a coaxial cavity resulting from a replacement of a *section* of the inner conductor by a similar section which differs in its conductivity and/or permeability from the original section. The result applies if one metal (A) is replaced by another metal (B), as in the substitution method of Section IV, or if the electromagnetic properties of a given metal are altered by a static magnetic field (Section II) or other means. For the purpose of this calculation we may assume, without loss of generality, that the outer conductor and end plates of the cavity are perfect conductors and non-magnetic.

The refractive index ($n=k/k_0$) is given by $n_A=1-i\alpha_A+\beta_A$ and its deviation from unity is now due to the inner conductor only. If the whole inner conductor (A) were replaced by another metal (B), the change of the refractive index would be $\Delta n=-i(\alpha_B-\alpha_A)+(\beta_B-\beta_A)$, but if only a section of the inner conductor is replaced, the value of Δn must be modified as shown below.

The cavity may be divided into three sections according to the properties of the inner conductor. In Sections I ($z=0$ to $z=z_1$) and III ($z=z_2$ to $z=z_3\approx\lambda_0/2$) the inner conductor consists of metal A, and in the intermediate Section II ($z=z_1$ to $z=z_2$) it is made of metal B. As the tangential components E_r and H of the field must be continuous at the boundaries (z_1 and z_2), the impedance $Z=E_r/H$ must also be continuous, and the solution of the boundary value problem may be carried out in terms of Z. Since $Z=-n$ in a coaxial line (Eqs. (1) and (2)), the expression

$$Z_m=n_m(e^{\theta}-c_m'e^{-\theta})(e^{\theta}+c_m'e^{-\theta})^{-1}$$

is consistent with the field equations and describes the reflection of the waves in the cavity. Here θ is an abbreviation for in_mk_0z, the reflection coefficients c_m' are undetermined constants, and the subscript m ($m=$I, II, III) identifies the three sections of the cavity. Writing the constants in exponential form ($c_m'=\exp(-2c_m)$) the expression for Z_m is equivalent to

$$Z_m=n_m\tanh(in_mk_0z+c_m).$$

The value of the refractive index in the various sections of the cavity is given by $n_{\mathrm{I}}=n_{\mathrm{III}}=n_A$ and $n_{\mathrm{II}}=n_B=n_A+\Delta n$. Since $c_{\mathrm{I}}'=1$ (E_r vanishes at $z=0$), $c_{\mathrm{I}}=0$, and only the two constants c_{II} and c_{III} are unknown. These constants may be evaluated from the two equations resulting from the boundary conditions $Z_{\mathrm{I}}=Z_{\mathrm{II}}$ at z_1, and $Z_{\mathrm{II}}=Z_{\mathrm{III}}$ at z_2. The calculation is based on the same approximation ($k-k_0\ll k_0$, or $n-1\ll 1$) which was used in Section II, and the result shows that both c_{II} and c_{III} may be treated as small quantities of the order of Δn ($\Delta n\ll 1$). It is convenient to introduce the quantity γ defined by

$$\gamma=(1/\pi)[k_0L+(2\sin^2k_0D-1)\sin k_0L], \qquad \text{(A-1)}$$

where $L=z_2-z_1$ is the length of the replaced section (metal B) and $D=|\lambda_0/4-(z_1+z_2)/2|$ is the distance of its center from the center of the resonator. Using this

abbreviation, we obtain $c_{III}=i\pi\gamma\Delta n$, and the value of Z_{III} at the end of the cavity ($z=z_2\approx\lambda_0/2$) is thus given by $n_A\tanh[i\pi(n_A+\gamma\Delta n)]$. Since $\gamma=1$ if the whole inner conductor is replaced ($L\approx\lambda_0/2$), the result of the calculation is that the change of the refractive index due to a replacement of a *section* of the inner conductor is given by $\gamma\Delta n$.

The foregoing calculation neglects the end-effects existing at z_1 and z_2; if L is sufficiently large, however, these effects may be shown to be negligible. Measurements of the cavity Q for several positions D of a given magnetic rod permitted several independent determinations of the attenuation α_0. Since these determinations made use of Eq. (33), which contains γ, the observed agreement (within the experimental error) of the various values of α_0 constitutes an experimental verification of the formula (A-1) for γ. In this connection we note that D must be measured from the electrical center of the cavity rather than from the mechanical center. The electrical center was found experimentally by determining the position corresponding to maximum Q on a symmetrical curve of cavity Q *versus* position of the magnetic rod. Other experiments showed that at 200 Mc $L=17.75$ cm is sufficiently large, and $L=4$ cm too small, for the γ-formula to be applicable; for $L\geq 10$ cm, deviations caused by end-effects appear to be negligible. In all the 200 Mc measurements we used $L=17.75$ cm and obtained a convenient value for Q_{bias} ($Q_\infty/Q_{bias}\approx 2$) by adjusting the distance D.

II. Calculation of Q_∞

Let us compare a cavity with brass inner conductor and a similar cavity whose inner conductor consists of a section of magnetic material and two sections of brass, as described in Section II. In analogy with Eqs. (17) and (33) we have

$$(1/2)(1/Q_\infty-1/Q_{Br})=\gamma(\alpha_\infty-\alpha_{Br}). \qquad \text{(A-2)}$$

The difference in losses represented in Eq. (A-2) is *independent* of any attenuation in the outer conductor and end plates, as well as of unknown losses in the cavity. In calculating α_∞ and α_{Br}, which refer to the inner conductor, we use Eq. (19) with suitable values for the resistivity. Substituting the resulting expressions into Eq. (A-2), one obtains

$$1/Q_\infty=\gamma c(\rho^{\frac{1}{2}}-\rho_{Br}^{\frac{1}{2}})/4\pi\nu^{\frac{1}{2}}a\ln(b/a)+1/Q_{Br}, \qquad \text{(A-3)}$$

where the resistivities ρ (of the magnetic material) and ρ_{Br} (of brass) are in e.s.u. (seconds). Equation (A-3) allows the calculation of Q_∞ from the *measured* value (Q_{Br}) of the cavity Q with brass inner conductor. The resistivities are measured on the actual rods used for the inner conductor and the remaining quantities are determined by the dimensions of the cavity and the frequency.

III. Theory of the Dielectric Tuner

In considering the effect of the dielectric tuner on the resonant wave-length of the cavity, we may assume, without loss of generality, that the cavity has ideal walls. Thus the refractive index in the cavity is unity except in the region occupied by the dielectric bead; in this region $n=\epsilon_d^{\frac{1}{2}}$, where ϵ_d is the dielectric constant (assumed to be a real number) of the polystyrene bead. By solving a boundary value problem similar to that involved in the theory of the γ-factor, and assuming that the length L_d of the bead is small ($L_dk_0\ll 1$), one obtains the following expression for the increase of the resonant wave-length ($\Delta\lambda_0$) of the cavity as a result of the presence of the bead:

$$\Delta\lambda_0=2L_d(\epsilon_d-1)\sin^2k_0L_d', \qquad \text{(A-4)}$$

where L_d' is the distance of the bead from either end of the cavity. Equation (A-4) shows, in agreement with experiment, that the calibration of the cavity ($\Delta\lambda_0$ *versus* position of the bead) is sensibly linear over an appreciable part of the range between one end of the cavity ($L_d'=0$) and its center ($L_d'\approx\lambda_0/4$). Because of the effect of the bead, the electrical center of the cavity (Appendix I) is moved slightly from the mechanical center to that side of the cavity which contains the bead. The changes in the cavity Q caused by displacements of the low loss polystyrene bead are negligible.

IV. Significance of Apparent Permeabilities

Assuming that the permeability μ is *real*, Eqs. (6) and (19) lead to the relations $\alpha/\alpha_\infty=\mu^{\frac{1}{2}}$ and $\beta/\beta_\infty=\mu^{\frac{1}{2}}$, where $\alpha_\infty=\beta_\infty$ is the value of α (or β) if the permeability is unity. Since, in general, α and β are not equal, the assumption of a real μ is contrary to experimental facts. Contradictions of this kind are well known (see reference 1, pp. 233–237) and led to a distinction[1] between a *real* permeability, μ_R, determined from a resistance measurement, and a *real* permeability, μ_L, determined from a reactance measurement. As pointed out by Becker[1] and particularly by Kittel (Phys. Rev. **70**, 281 (1946)), however, these two types of measurements reveal different aspects of the same fundamental phenomena. Experimental data may be expressed either in terms of the two apparent permeabilities μ_R and μ_L ($\mu_R\neq\mu_L$), or in terms of the complex permeability employed in the theory of W. Arkadiew (Physik. Zeits. **14**, 928 (1913)).

In our experiment the measured attenuation is due to resistive losses and the measured change of phase velocity is due to reactive changes. Thus, the definition of the apparent permeabilities leads to

$$\alpha/\alpha_\infty=\mu_R^{\frac{1}{2}} \quad \text{and} \quad \beta/\beta_\infty=\mu_L^{\frac{1}{2}}. \qquad \text{(A-5)}$$

Substituting the relations (A-5) into Eqs. (21) and (22), we obtain

$$\mu_1=(\mu_R\mu_L)^{\frac{1}{2}}, \qquad \text{(A-6a)}$$

and

$$\mu_2=(1/2)(\mu_R-\mu_L). \qquad \text{(A-6b)}$$

Using $|\mu|=(\mu_1^2+\mu_2^2)^{\frac{1}{2}}$, these equations result in

$$\mu_R=|\mu|+\mu_2, \qquad \text{(A-7a)}$$

and

$$\mu_L=|\mu|-\mu_2. \qquad \text{(A-7b)}$$

Equations (A-6) and (A-7), first given by Arkadiew [Zeits. f. Physik **27**, 37 (1924)], relate the complex permeability to the apparent permeabilities and are valid whenever a strong skin effect occurs.

Electrical Properties of Pure Silicon and Silicon Alloys Containing Boron and Phosphorus

G. L. PEARSON AND J. BARDEEN
Bell Telephone Laboratories, Murray Hill, New Jersey
(Received November 29, 1948)

Electrical resistivity and Hall measurements have been made over the temperature range from 87° to 900°K on pure silicon and on silicon alloys containing from 0.0005 to 1.0 percent boron (p-type impurity) or phosphorus (n-type impurity). X-ray measurements indicate that both elements replace silicon in the lattice. It is shown that each added boron atom contributes one acceptor level, and it is likely that each added phosphorous contributes a donor level.

The temperature variation of the concentrations of carriers, electrons and holes, and of their mobilities, are determined from the resistivity and Hall data for the different samples. In the intrinsic range, at high temperatures, conductivity results from electrons thermally excited from the filled band to the conduction band. The energy gap is about 1.12 ev. The product of electron and hole concentration at any temperature is

$$n_e n_h = 7.8\times 10^{32} T^3 \exp(-12{,}900/T).$$

In the saturation range, which occurs just below the intrinsic range, the concentrations are independent of temperature. All donors (or acceptors) are ionized and the concentration of carriers is equal to the net concentration of significant impurities (P or B).

The energy, E_A, required to ionize an acceptor by exciting an electron from the filled band, as determined from the temperature variation of concentration at lower temperatures, decreases with increasing impurity concentration and vanishes for concentrations above 5×10^{18}/cm³. The value of E_A at high dilution, 0.08 ev, is about what is expected for a hole moving in a hydrogen-like orbit about a substitutional B^- ion. The decrease in E_A with increase in concentration is attributed to a residual potential energy of attraction between the holes and impurity ions. The ionization energy of donors is less than that of acceptors, probably because conduction electrons have a smaller effective mass than holes. In samples with large impurity concentrations the carriers form a degenerate gas at low temperatures, and the resistivity and Hall coefficient become independent of temperature.

At high temperatures the mobilities of electrons and holes approach the values

$$\mu_e = 3.0\mu_h = 15\times 10^8 T^{-\frac{3}{2}} \text{ (cm}^2\text{/volt sec.)}.$$

These values are determined by lattice scattering and are independent of impurity concentration. At lower temperatures scattering by both ionized and neutral impurity centers contribute, and the mobility is largest for the more pure samples. Impurity scattering increases rapidly with decrease in temperature and the mobility passes through a maximum which depends on impurity concentration. Theories of impurity scattering of Conwell and Weisskopf, of Johnson and Lark-Horovitz, and of Mott give mobilities which agree as to order of magnitude with the observed.

I. INTRODUCTION

ELECTRICAL resistivity and Hall measurements have been made over a temperature range from 87°K to 900°K on a number of silicon samples to which known amounts of boron and phosphorus have been added.[1] Both enter substitutionally, boron acting as an acceptor impurity and phosphorus as a donor. The data are analyzed to determine the variation of concentration of current carriers and mobility with impurities and temperature. The results are interpreted in terms of existing theories of conduction in semiconductors. The analysis is similar to that applied by Lark-Horovitz and Johnson to the conductivity in germanium.[2] Our results are more complete, particularly as regards the wide range of impurity concentrations, than previous measurements on silicon made at the Universities of Pennsylvania[3] and Purdue.[4]

1.1 Energy Levels in Silicon

Silicon is an element of the fourth group of the periodic table, with the same crystal structure as diamond. Each silicon atom has four near neighbors with which it forms covalent bonds in a tetrahedral configuration. The specific gravity is about 2.4 and the melting point 1420°C. The

[1] A preliminary account of this work was presented by the authors at the Am. Phys. Soc. meeting in New York, January, 1948. See Phys. Rev. **73**, 1256A (1948). Earlier measurements are described by G. L. Pearson and W. Shockley, Phys. Rev. **71**, 142A (1947).

[2] K. Lark-Horovitz and V. A. Johnson, Phys. Rev. **69**, 258A (1946).

[3] F. Seitz, *The Electrical Conductivity of Silicon and Germanium* (NDRC 14–110, University of Pennsylvania, November 3, 1942).

[4] Unpublished measurements of W. W. Scanlon and others.

dielectric constant is about 13. The conductivity at room temperature depends on the presence of impurities. It is estimated that ideally pure silicon would have a resistivity of about 10^6 ohm cm.

Considerable progress was made in understanding the nature of the significant impurities by research done during the war in connection with the development of rectifiers for radar uses.[5] Scaff, Theuerer, and Schumacher[6] of the metallurgical group of the Bell Laboratories have found that elements of the third group, such as boron and aluminum, give defect or *p*-type conductivity. Elements from the fifth group, such as phosphorus, antimony, and arsenic, give excess or *n*-type conductivity. Impurities which give *p*-type conductivity are called acceptors; those which give *n*-type conductivity, donors. We shall give x-ray evidence that boron and phosphorus enter substitutionally into the lattice. Probably the other significant impurities also occupy substitutional rather than interstitial positions.

A substitutional impurity atom from the fifth group has one more valence electron than is required to fill the four valence bonds with neighboring silicon atoms. In its lowest energy state, this extra electron is weakly bound by the extra charge on the nucleus of the impurity atom. The electron moves in a hydrogen-like orbit,[7] but the electrostatic attractive force is reduced by the dielectric constant, κ, of the crystal. The effect is to reduce the binding energy by a factor κ^2, which brings it down to the range of thermal energies ($\sim$0.08 ev). This means that a large fraction of the impurity atoms are thermally ionized at room temperature, and the electrons thus freed contribute to the conductivity.

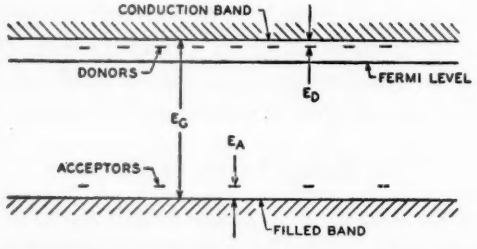

FIG. 1. Schematic energy level diagram for silicon.

A trivalent impurity atom, such as boron, has one less electron than is required to fill the valence bonds.[8] The position from which the electron is missing may shift from one valence bond to another in the crystal by motion of an electron in the opposite direction. The missing electron, or hole, behaves in all respects like a particle with a positive charge equal in magnitude to the electron charge. It has inertia, momentum, and energy corresponding to a mass of the same order as the mass of an electron. Thus one speaks of the velocity, mobility, and kinetic energy of a hole moving through the crystal in just the way one speaks of the corresponding quantities for excess or conduction electrons. The only essential difference is in the sign of the mobile charge.

The extra electron required to fill the valence bonds about the trivalent impurity gives the atom an effective negative charge, so that it becomes in effect a negative ion. In its lowest state, the positive hole will be weakly bound by the electrostatic field of the negative ion and will move in a hydrogen-like orbit similar to that of the excess electron discussed above. The ionization energy, that is, the energy required to free the hole from the negative ion so that it is free to contribute to the conductivity, is likewise of the order of thermal energy. At room temperature the majority of the acceptor impurities will be dissociated into holes and negative ions.

If sufficient energy is available, an electron can be removed from a normal valence bond to a distant place in the crystal. Both the electron so freed and the place of the missing electron, or hole, left behind are free to take part in conduction. The energy required is about 1.12 ev in silicon.[9] Electrons and holes may be so produced by light quanta of sufficient energy, or by thermal excitation at high temperatures. In the intrinsic

[5] J. H. Scaff and R. S. Ohl, Bell Sys. Tech. J. 26, 1 (1947). A comprehensive review of the work done during the war under the NDRC is given by H. C. Torry and C. A. Whitmer, *Crystal Rectifier* (McGraw-Hill Book Company, Inc., New York, 1948). This book will be referred to as T-W.

[6] J. H. Scaff, H. C. Theuerer, and E. E. Schumacher, "*P*-type and *N*-type silicon and the formation of the photovoltaic barrier in silicon" (to be published in Trans. A.I.M.E.).

[7] See N. F. Mott and R. W. Gurney, *Electronic Processes in Ionic Crystals* (Oxford University Press, London, 1940), p. 166. For application to silicon, see T-W, p. 66.

[8] See T-W, p. 65.

[9] This value, derived from the present experiments, agrees with earlier values of Seitz (reference 3) and of G. K. Teal, J. R. Fisher, and A. W. Treptow, J. App. Phys. 17, 879 (1946).

conductivity range there are equal concentrations of electrons and holes determined by a balance between those formed by thermal excitation and those recombining. The recombination, of course, corresponds to excess or conduction electrons dropping back into vacant valence bond positions. The intrinsic conductivity range occurs at temperatures so high that the numbers of electrons or holes arising from impurities is small compared with the total number present.

The energy relations are illustrated in the energy level diagram[10] shown schematically in Fig. 1. The diagram shows the allowed energy levels for the valence electrons in a silicon crystal. There is a continuous band of levels, the filled band, normally occupied by the electrons in valence bonds, an energy gap of 1.12 ev in which there are no levels of the ideal crystal, and then another continuous band of levels, the conduction band, normally unoccupied. There are just sufficient levels in the filled band to accommodate the four valence electrons per atom. The acceptor impurity levels lie just above the filled band and the donor levels just below the conduction band. The donors are normally neutral, but become positively charged when ionized by excitation of an electron to the conduction band. The acceptors are normally neutral, but become negatively charged when occupied by electrons excited from the filled band.

1.2 Preparation of Samples

The silicon used in these studies was obtained from E. I. du Pont de Nemours Company. It is in the form of long needles and was prepared from silicon tetrachloride by pyrolytic reduction with zinc.[11] The purity is very high—about 99.97 percent with some variation between lots as shown by spectroscopic analysis. The subsequent forming with the addition of known amounts of boron or phosphorus was done by J. H. Scaff and H. C. Theuerer of the metallurgical group of the Bell Telephone Laboratories. The steps which have been described in detail[6] include (1) careful determination of the weights of the raw materials, (2) melting the charge in a silica crucible by means of an induction furnace in an atmosphere of helium, and (3) solidifying into an ingot by a precisely controlled temperature cycle.

The ingot was cut into thin slabs approximately 2 cm×0.5 cm×0.1 cm with a diamond wheel and the surfaces smoothed by lapping with 600 mesh carborundum and water. Metallic electrodes were applied by means of the electrolytic deposition of rhodium. The entire surface was usually plated and, after protecting the desired sections, the excess was removed with an air blast containing 180-mesh carborundum grains. By this process non-rectifying electrodes as small as 0.02 cm in diameter were prepared which remained intact over the entire temperature range from 87 to 900°K in an atmosphere of air.

Using the methods described above, samples having the compositions listed in columns 1–5 of Table I were prepared.

TABLE I. Composition of silicon alloys.

I	II	III	IV	V	VI	VII
Sample	Solute	Weight percent of solute	Atomic percent of solute	Atoms of solute per cc of melt	Carriers/cc of melt in saturation range	Carriers/atoms of solute
1	——	0.0	0.0	0.0	8.0×10^{18}	α
2	Boron	0.0005	0.0013	6.7×10^{17}	6.0×10^{17}	0.90
3	Boron	0.001	0.0026	1.3×10^{18}	1.3×10^{18}	1.00
4	Boron	0.002	0.0052	2.7×10^{18}	2.5×10^{18}	0.93
5	Boron	0.005	0.013	6.7×10^{18}	5.3×10^{18}	0.79
6	Boron	0.01	0.026	1.3×10^{19}	1.4×10^{19}	1.08
7	Boron	0.1	0.26	1.3×10^{20}	1.2×10^{20}	0.93
8	Boron	1.0	2.6	1.3×10^{21}	4.8×10^{20}	0.37
A	Phosphorus	0.001	0.00091	4.7×10^{17}	1.05×10^{17}	0.22
B	Phosphorus	0.0057	0.0072	2.7×10^{18}	1.25×10^{18}	0.46
C	Phosphorus	0.1	0.091	4.7×10^{19}	1.7×10^{19}	0.36
D	Phosphorus	1.0	0.91	4.7×10^{20}	2.6×10^{20}	0.55

1.3 Lattice Spacings of Silicon Alloys Containing Boron and Phosphorus

In order to determine whether boron and phosphorus enter the silicon lattice in a sub-

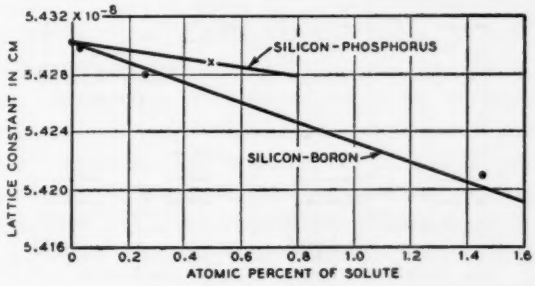

FIG. 2. Lattice constants of silicon-phosphorus and silicon-boron alloys at 25°C as determined from x-ray data.

[10] Cf. T-W, p. 49. A quantum-mechanical calculation of the energy bands in silicon is given by J. F. Mullaney, Phys. Rev. 66, 326 (1944).

[11] The method used by du Pont for purifying silicon is described in T-W, p. 301.

stitutional or an interstitial manner, a study was made of the lattice spacing of these alloys as a function of the impurity content. Since the atomic radii of silicon, boron, and phosphorus are 1.17, 0.89, and 1.10×10^{-8} cm, respectively, it is predicted by Vegard's law that if the process is by substitution the addition of boron should shrink the lattice appreciably, while phosphorus should produce only a slight shrinkage. If these atoms enter the interstices between the silicon atoms, however, both should expand the lattice with phosphorus having a greater effect.

The lattice spacing measurements, performed by E. S. Greiner of the metallurgical group of the Bell Telephone Laboratories, were obtained by back reflection x-ray diffraction from powdered samples containing varying amounts of boron or phosphorus. The results, given in Fig. 2, show that both impurities contract the silicon lattice and that boron has the greater effect. Microscopic examination of alloys containing more than 0.5 percent boron by weight showed that a second phase appears and deposits on crystal grain boundaries.

The results of this study indicate, therefore, that for small concentrations a substitutional solid solution of either boron or phosphorus is formed in silicon. That each added boron atom contributes an acceptor level is shown by a comparison of columns V and VI of Table I. There is evidence that not all the phosphorus added goes into solution, which accounts for smaller numbers of carriers for these samples.

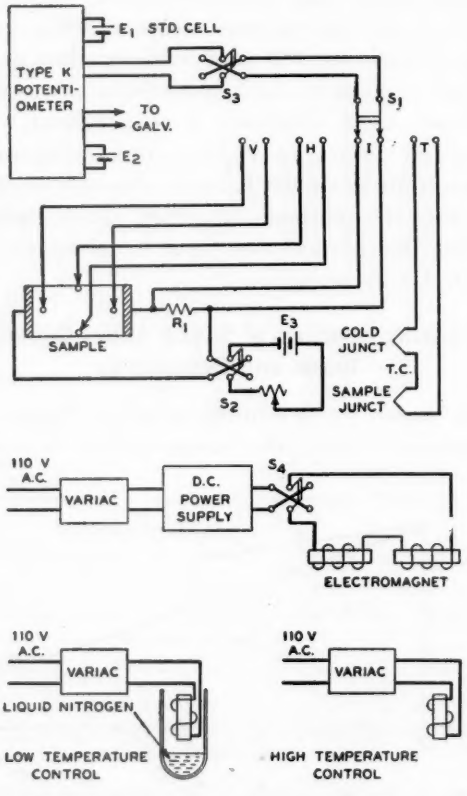

FIG. 3. Circuit diagram of equipment for measuring resistivities and Hall coefficients at different temperatures.

II. EXPERIMENTAL PROCEDURE

The fundamental experimental data obtained in this study are the resistivity and Hall voltage as a function of temperature for each of the several alloy samples. Resistivity was measured by the potential probe method, Hall effect from the transverse voltage in a magnetic field, and temperature by the thermoelectric voltage of a Chromel-Alumel thermocouple.

A Leeds and Northrup Type K potentiometer in conjunction with a selector switch was used to measure all of these d.c. voltages. A rotating coil driven by a synchronous motor was used for measuring the magnetic field strengths. The indicating instrument for the a.c. measurement was a Weston model 622 voltmeter, and the system was calibrated with a permanent magnet whose field strength had been measured at the National Bureau of Standards. The desired temperatures were obtained by heating coils operating either in a thermos bottle containing liquid nitrogen for the low values, or in an electrically heated ceramic tube for the high values. Temperature gradients were avoided by placing the samples in good thermal contact with a non-magnetic metal block.

Figure 3 is a circuit diagram of the entire measuring circuit. The electrode arrangement of the sample is as shown, with contact being made to the rhodium by platinum-rhodium springs which held their tensile strength over the entire temperature range. The current through the sample is determined from the voltage drop across the fixed resistor R_1. The sample current, as well as the magnetic field polarity, may be reversed by switches S_2 and S_4. Measurements for both directions of these quantities are required to eliminate spurious thermal effects.

After showing the Hall effect to be a linear function of magnetic field strength over a wide range, a field strength of 4000 gauss was chosen for most of the measurements. The current through the sample was regulated to give the most advantageous voltage readings and was usually between 0.1 and 10 milliamperes. At low temperatures this current was reduced to avoid Joule heating and at high temperatures, especially in the high impurity samples, it was increased in order to raise the Hall voltage to a detectable level. It was the reduction of the Hall voltage at high temperatures which limited our Hall measurements to temperatures below 800°K for the high purity silicon and to still lower temperatures for the samples to which large amounts of boron or phosphorus had been added.

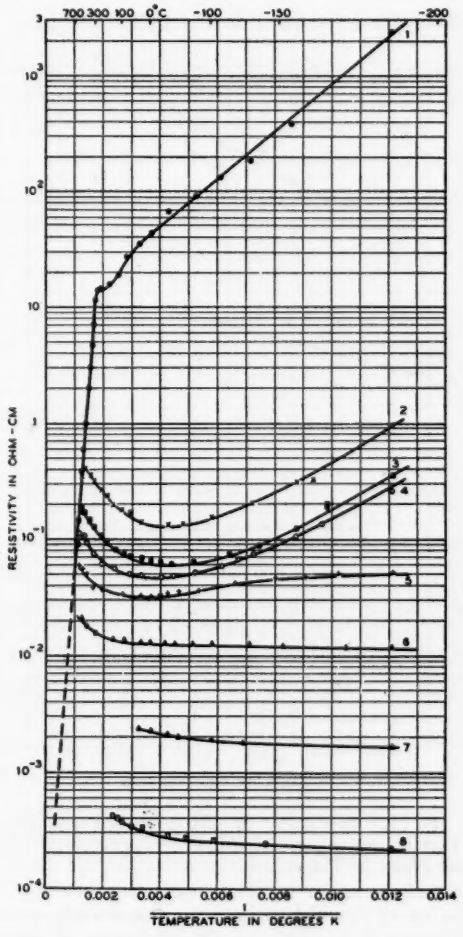

FIG. 4A. Resistivity of silicon-boron alloys as a function of the inverse absolute temperature. Compositions are given in Table I.

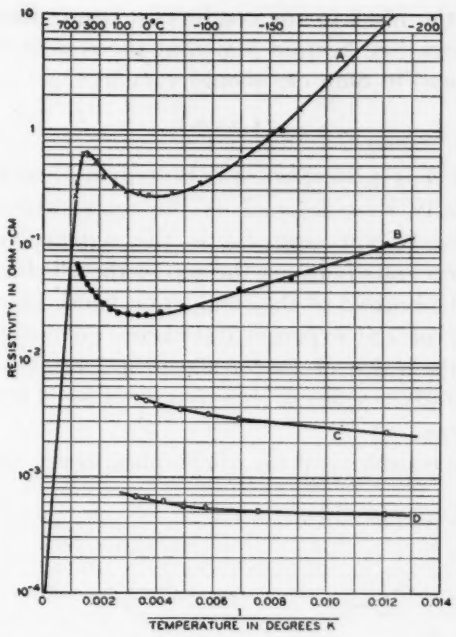

FIG. 4B. Resistivity of silicon-phosphorus alloys as a function of the inverse absolute temperature. Compositions are given in Table I.

III. EXPERIMENTAL RESULTS

The resistivities of the silicon-boron alloys are shown as a function of temperature in Fig. 4A. Curve 1 is for the high purity du Pont silicon to which no impurity was deliberately added and curves 2–8 are for silicon to which the specified amounts of boron (expressed in weight percents) had been introduced in the melt. The temperature range is from 700°C to −190°C, and the resistivity limits are from 2×10^{3} ohm cm for the high purity silicon to 2×10^{-4} ohm cm for the one percent boron alloy.

At high temperatures the resistivities all fall on the same straight line. This is the intrinsic region in which there are approximately equal concentrations of electrons and holes. At lower temperatures the resistivity depends on the impurity content, increasing amounts of boron giving lower resistivity. Since sample No. 1 does not follow the intrinsic line at the lower temperatures, it is concluded that residual impurity atoms of unknown elements are present in the melt. The rapid decrease of resistivity with temperature in the intrinsic range results from the increase in concentration of electrons and holes which arise from thermal excitation of electrons

from the filled to the conduction band. Theory indicates (see Section 5.3) that the resistivity ρ expressed in ohm cm should vary as

$$\rho = A\epsilon^{E_G/2kT}, \tag{1}$$

where A is a constant, k is Boltzman's constant (8.69×10^{-5} ev/deg.), T is the temperature in degrees Kelvin, and E_G is the separation in electron volts between the top of the filled band and the bottom of the conduction band. From a fitting of the experimental data, we conclude that the value of E_G for silicon is 1.12 electron volts and the value of the constant A is 1.1×10^{-4} ohm cm.

The resistivity of the silicon-phosphorus alloys is shown as a function of temperature in Fig. 4B. These curves have the same general shape as those for the silicon-boron series and the intrinsic line is identical.

Hall voltages of the various samples were measured as a function of temperature and the Hall coefficient R, in cm³/coulomb, calculated from the relation

$$R = 10^{-8}\, V_H t/HI, \tag{2}$$

where V_H is the measured Hall voltage in volts, t the thickness of the sample in cm, H the magnetic field in gauss, and I the current in amperes.[12] As stated above, the measurements were taken with the field first in one direction and then in the other to eliminate false thermoelectric effects. The sign of the Hall coefficient was determined from the polarities of I, H, and V_H.

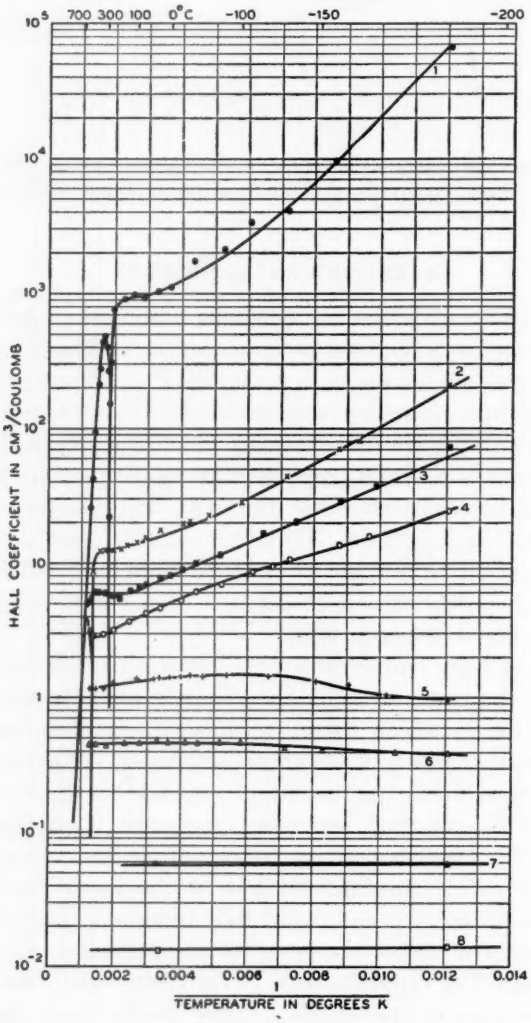

FIG. 5A. Hall coefficient in silicon-boron alloys as a function of the inverse absolute temperature. Compositions are given in Table I.

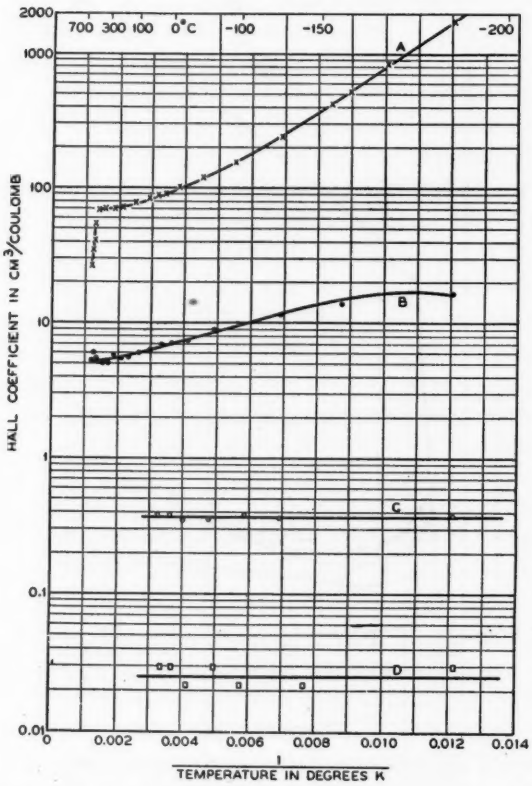

FIG. 5B. Hall coefficient in silicon-phosphorus alloys as a function of the inverse absolute temperature. Compositions are given in Table I.

[12] The length to width ratio of our samples was around 4. This is sufficient to eliminate the errors due to short circuiting of the current electrodes as described by I. Isenberg, B. R. Russell, and R. F. Greene, Phys. Rev. **74**, 1255(A) (1948).

Figure 5A is a plot of Hall coefficient as a function of temperature for the boron-silicon alloys. In each case the sign of the coefficient was positive in the low temperature or impurity conduction region, which indicates that boron is an acceptor impurity in silicon. For the purer samples No. 1 and No. 2 the coefficient reduced to zero and went negative in the intrinsic range. This negative sign in the region where electrons and holes are present in comparable numbers arises from the fact, as will be discussed in more detail in a following section, that electrons have a greater mobility than the holes.

Figure 5B is a plot of Hall coefficient as a function of temperature for the silicon-phosphorus alloys. The sign of the coefficient is negative at all temperatures, indicating that phosphorus is a donor impurity in silicon.

IV. CONCENTRATIONS AND MOBILITIES

Having measured the resistivity and Hall coefficient as a function of temperature for the two silicon alloy systems, it is now possible to calculate the following additional quantities as a function of temperature for either holes or electrons: (1) the number n per cm^3, (2) the mobility μ in cm^2/volt-sec., and (3) the mean free path l in cm. In Section 4.1 we deal only with non-degenerate cases, i.e., low densities of holes or electrons at medium and high temperatures. The degenerate cases are considered in Section 4.2.

The following notation is used:

e = magnitude of electronic charge $= 1.6\times10^{-19}$ coulomb.
n_e = concentration of conduction electrons (no./cm^3).
n_h = concentration of holes (no./cm^3).
N_D = concentration of donor impurities (no./cm^3).
N_A = concentration of acceptor impurities (no./cm^3).
μ_e = mobility of conduction electrons (cm^2/volt sec.).
μ_h = mobility of holes (cm^2/volt sec.).
$c = \mu_e/\mu_h$ = ratio of mobilities.
σ = conductivity (ohm^{-1} cm^{-1}).
$\rho = 1/\sigma$ = resistivity (ohms cm).
R = Hall coefficient (cm^3/coulomb).
l_e = mean free path of electrons (cm).
l_h = mean free path of holes (cm).
E_G = energy gap between filled and conduction bands.
E_D = energy difference between donor level and conduction band.
E_A = energy difference between acceptor level and conduction band.
m = mass of electron in free space $= 9.03\times10^{-28}$ grams.

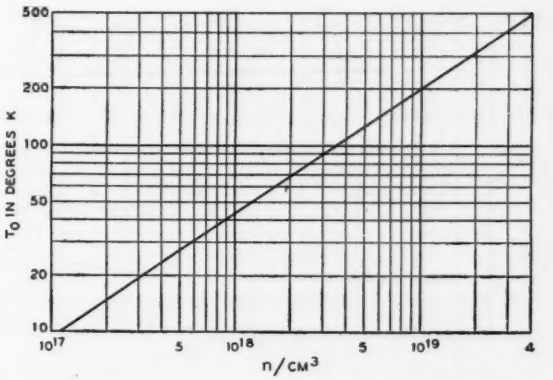

FIG. 6. Degeneracy temperature in degrees absolute as a function of electron density.

m_e = effective mass of conduction electrons (grams).
m_h = effective mass of holes (grams).
k = Boltzman's constant $= 1.37\times10^{-16}$ erg/degree.
T = absolute temperature (°K).
h = Planck's constant $= 6.55\times10^{-27}$ erg-sec.
$n_s = |N_A - N_D|$ = saturation concentration of holes or electrons (no./cm^3).
κ = dielectric constant.
$E_0 = (h^2/8m)(3n/\pi)^{\frac{2}{3}}$ = kinetic energy of electron (or hole) at the surface of the Fermi distribution.

4.1. Non-Degenerate Electron Gas

The basic equations required for the calculation of the mobility and concentration from measurements of the conductivity and Hall coefficient follow:[13]

(a) Impurity range:

$$\sigma = ne\mu, \tag{3}$$

$$R = \pm 3\pi/8en = \pm 7.4\times10^{18}/n, \tag{4}$$

$$n = \pm 7.4\times10^{18}/R, \tag{5}$$

$$\mu = \pm(8/3\pi)\sigma R = \pm 0.85\sigma R. \tag{6}$$

The positive signs apply to p-type and the negative to n-type conductivity.

(b) Intrinsic range:

$$\sigma = n_e e\mu_e + n_h e\mu_h, \tag{7}$$

$$R = -(3\pi/8e)([n_e c^2 - n_h]/[n_e c + n_h]^2). \tag{8}$$

If $n_e = n_h = n$,

$$\sigma = ne(\mu_e + \mu_h), \tag{9}$$

$$R = -(3\pi/8ne)([c-1]/[c+1]), \tag{10}$$

$$n = -7.4\times10^{18}([c-1]/[c+1])/R. \tag{11}$$

[13] For methods of deriving the equations, see, for example, F. Seitz, *The Modern Theory of Solids* (McGraw-Hill Book Company, Inc., New York, 1940), Chapter IV. Cf. T-W, pp. 53–55.

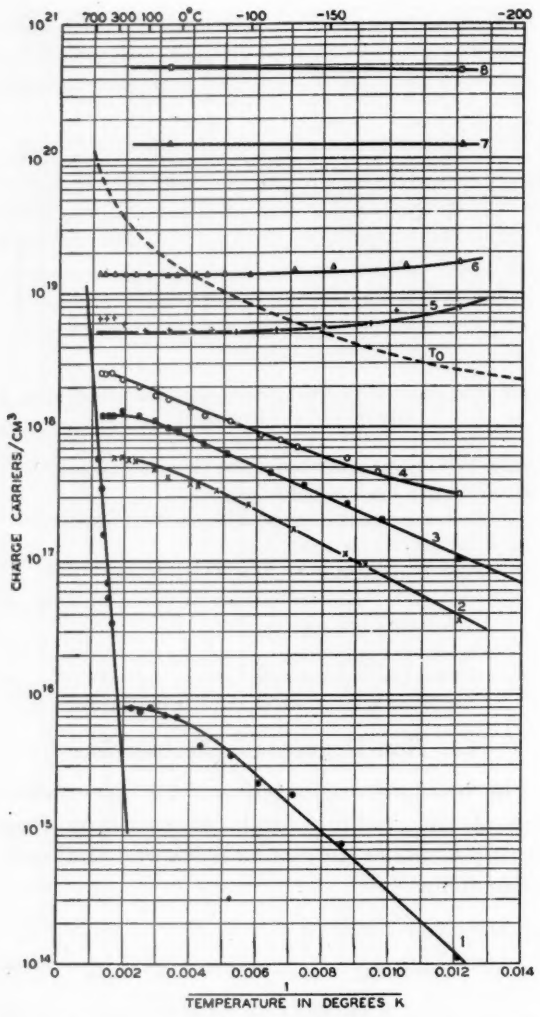

FIG. 7A. Number of charge carriers per unit volume in silicon-boron alloys as a function of the inverse absolute temperature. Compositions are given in Table I. T_0 is the degeneracy temperature.

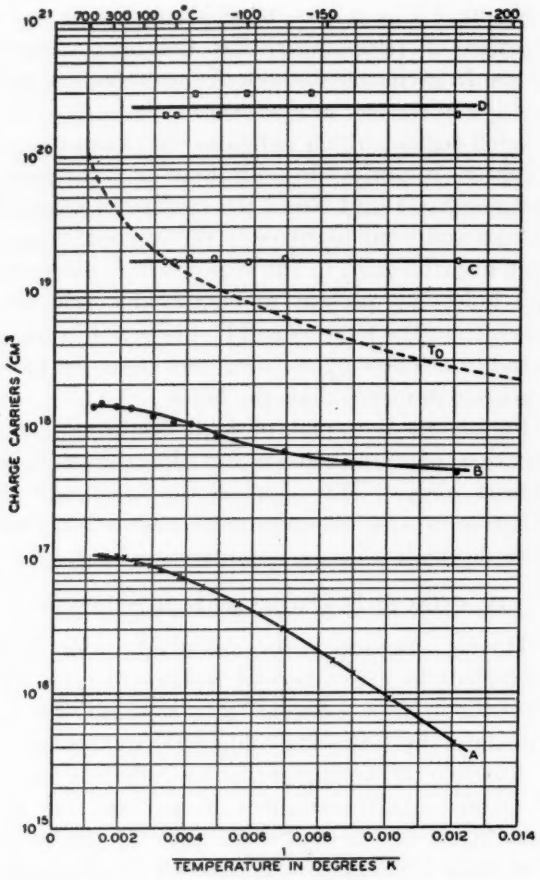

FIG. 7B. Number of charge carriers per unit volume in silicon-phosphorus alloys as a function of the inverse absolute temperature. Compositions are given in Table I. T_0 is the degeneracy temperature.

The numerical factor $3\pi/8$ which occurs in the expressions for R, μ, and n is based on the assumption that the mean free path is independent of velocity. While this is true for scattering by lattice vibrations (thermal scattering), it is not true for scattering by impurities, which predominates at low temperatures. A different numerical factor should be used in the impurity scattering range[14] and intermediate values used when both lattice and impurity scattering are important. For simplicity, we neglect these variations and use the factor $3\pi/8$ throughout.

The equation relating the moboility μ, the mean free path l, and the effective mass m_e is

$$\mu=(4/3)el(2\pi m_e kT)^{-\frac{1}{2}}(\text{e.s.u.}). \quad (12)$$

If $m_e=m$, the mass of an electron in free space,

$$\mu=2.43\times10^{9}lT^{-\frac{1}{2}}(\text{cm}^2/\text{volt-sec.}), \quad (13)$$

$$l=4.12\times10^{-10}\mu T^{\frac{1}{2}}\ (\text{cm}). \quad (14)$$

Equations (12), (13), and (14) may be applied to either electron or hole mobility, provided that the proper effective mass is used.

4.2. Degenerate Electron Gas

At low temperatures and high densities the electron gas becomes degenerate, i.e., Fermi-Dirac rather than Boltzmann statistics must be

[14] If the mean free path varies with electron velocity as v^p, the factor is $3\pi^{\frac{1}{2}}\Gamma(p+3/2)/4(\Gamma(p/2+2))^2$, which reduces to $3\pi/8$ for $p=0$. For scattering by impurity ions, $p\sim4$ and the factor is 1.93 in place of 1.18.

used. The limiting temperature, T_0, is that for which the energy of an electron (or hole) corresponding to the energy at the surface of the Fermi distribution is equal to kT_0. This gives

$$T_0=(h^2/8km)(3/\pi)^{\frac{1}{3}}n^{\frac{1}{3}}=4.2\times10^{-11}n^{\frac{1}{3}}. \quad (15)$$

A plot of T_0 as a function of the concentration, n, is given in Fig. 6. For $T\gg T_0$, the electron gas is non-degenerate, and Eqs. (3) to (14) applicable to Boltzmann statistics should be used. For $T\ll T_0$ the electron gas is completely degenerate, and the equations generally applied to conduction in metals may be used. Some of these are listed below. The intermediate case, for $T\sim T_0$, has been discussed by Johnson and Lark-Horovitz.[15] The equations are much more complicated than for the two limiting cases, and we will not attempt to interpret the curves in this region.

The expression for the Hall coefficient is slightly different for a degenerate electron gas in that the numerical factor is unity instead of $3\pi/8$. The basic equations are:[13]

$$\sigma=ne\mu, \quad (16)$$

$$R=\pm1/en=\pm6.25\times10^{18}/n, \quad (17)$$

$$n=\pm6.25\times10^{18}/R, \quad (18)$$

$$\mu=\pm\sigma R, \quad (19)$$

where the plus signs apply to hole conductors and the minus signs to electron conductors.

The relation between the mean free path, l, and the mobility, μ, is

$$l=(h/2e)(3n/\pi)^{\frac{1}{3}}\mu(\text{e.s.u.}). \quad (20)$$

If μ is expressed in cm²/volt-sec.,

$$l=2.02\times10^{-15}n^{\frac{1}{3}}\mu(\text{cm}). \quad (21)$$

4.3 Calaculation of n, μ, and l

Using Eqs. (5) and (18), the density of holes for the silicon-boron alloys was calculated and plotted in Fig. 7A as a function of temperature. It can be seen that n varies from 10^{14} to 5×10^{20} and is a function of temperature and boron content. The degeneracy temperature T_0 is plotted for reference in this figure. Samples 1 to 4 are non-degenerate, and log$n$ increases linearly with temperature until saturation is reached just before entering the intrinsic range. In samples 5 to 8, which are degenerate over most of the

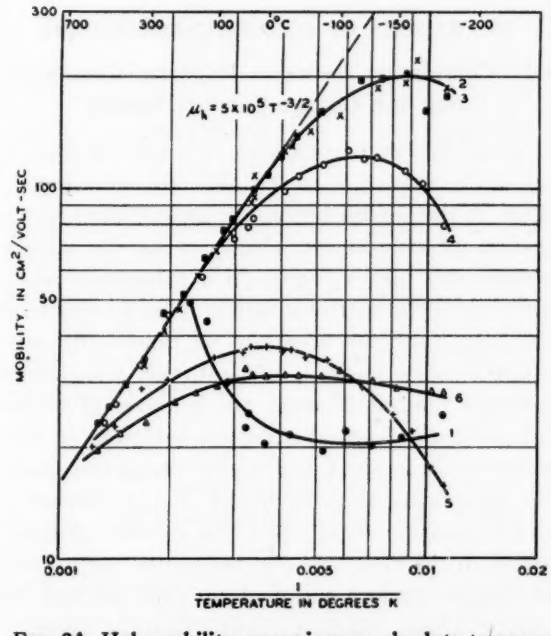

FIG. 8A. Hole mobility *versus* inverse absolute temperature for silicon-boron alloys. Compositions are given in Table I.

[15] V. A. Johnson and K. Lark-Horovitz, Phys. Rev. 71, 374 (1947); 72, 531A (1947).

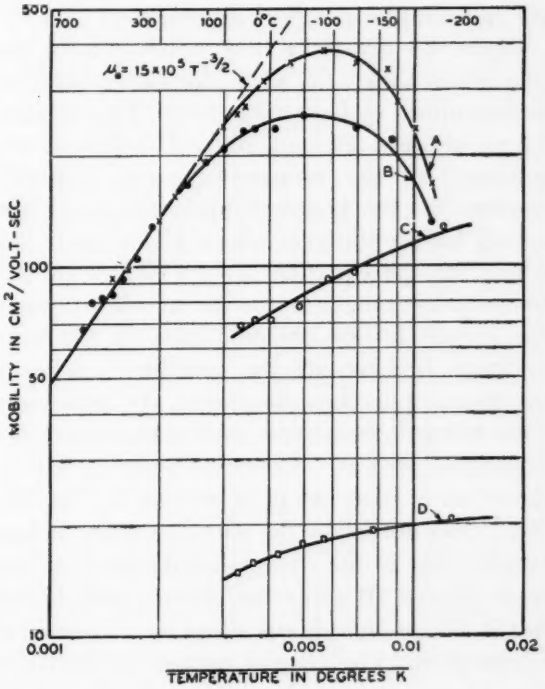

FIG. 8B. Electron mobility *versus* inverse absolute temperature for silicon-phosphorus alloys. Compositions are given in Table I.

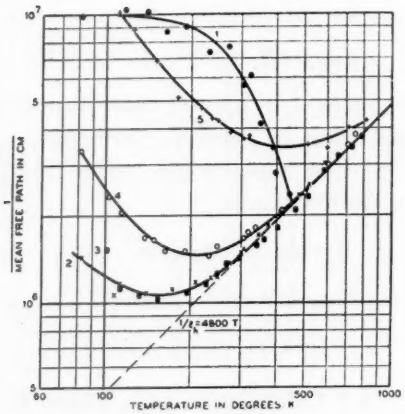

FIG. 9A. Reciprocal of the mean free path of conduction holes in silicon-boron alloys *versus* the temperature in degrees absolute. Compositions are given in Table I.

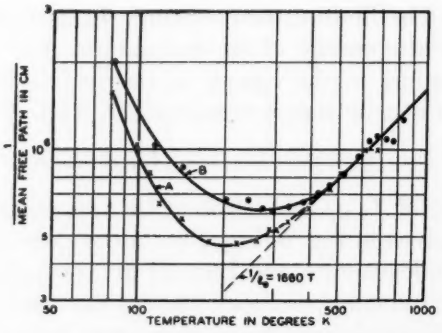

FIG. 9B. Reciprocal of the mean free path of conduction electrons in silicon-phosphorus alloys *versus* the temperature in degrees absolute. Compositions are given in Table I.

temperature range, n is approximately constant with temperature. The intrinsic line on the left was calculated by substituting the high temperature Hall data for sample No. 1 into Eq. (11) using a value $c=3.0$ as derived below.

Figure 7B gives the density of conduction electrons as a function of temperature for the silicon-phosphorus alloys as calculated from Eqs. (5) and (18). Samples A and B are non-degenerate and samples C and D degenerate.

Figure 8A gives the hole mobility μ_h in the silicon-boron alloys as a function of temperature as determined by Eqs. (6) and (19). The mobility varies between 20 and 200 cm²/volt-sec., depending on the temperature and impurity content. In the higher temperature range the curves for the different alloys join a single line which fits the equation $\mu_h=5\times10^5T^{-\frac{3}{2}}$. In this temperature range, scattering by vibrations of the crystal lattice predominates. As the temperature is lowered, the mobility reaches a maximum and then decreases, the maximum value being dependent on the number of acceptor impurities present. Impurity scattering will be described in more detail in Section 6.1. Sample No. 1 does not follow the normal pattern and we believe this is due to non-homogeneity of this melt. Figure 8B gives the electron mobility μ_e in the silicon-phosphorus alloys as a function of temperature. The general pattern is similar to Fig. 8A except that the ratio of the electron to hole mobility in the lattice scattering range is about 3.

Figures 9A and 9B give the reciprocal of mean free path for holes and electrons in the silicon alloys as computed from Eqs. (14) and (21). In the lattice scattering range there is a linear inverse relationship between mean free path and absolute temperature just as found in metals. The mean free path of the electrons in the lattice scattering range is three times that of the holes. In the impurity scattering range the mean free path decreases with increasing impurity content and at a given impurity content decreases with decrease in temperature.

V. ANALYSIS OF CONCENTRATION DATA

5.1. Correlation between Impurity Concentration and Charge Carrier Density

It can be seen from Figs. 7A and 7B that as the temperature is raised the concentration of holes in the silicon-boron alloys and the concentration of conduction electrons in the silicon-phosphorus alloys approach a saturation value just below the intrinsic range. This results from the fact that all acceptor or donor impurity atoms become ionized, and a further rise in temperature cannot increase the number of charge carriers until thermal energy is sufficient to raise electrons from the filled to the conduction band. By comparing the density of charge carriers in this saturation region with the density of solute atoms in the melt, one can determine the number of charge carriers supplied by each ionized impurity atom. Such a comparison is given in columns V, VI, and VII of Table I for each of the samples under study. The silicon-boron samples numbered 2 to 7 have a ratio of hole density to boron atom density close to unity,

which shows that each donor impurity atom contributes one hole. In sample 8, to which 1.3 atomic percent of boron had been added, the ratio dropped to 0.36. A microscopic examination of this melt indicated that only a part of the boron atoms went into solid solution with the remainder forming a second phase at crystalline grain boundaries. Although the ratio obtained for each of the four silicon-phosphorus melts is appreciably less than unity, we believe that each ionized donor atom produces one conduction electron and that the small ratio is due to loss of phosphorus atoms during the processing of the melt. Such a loss is to be expected since the vapor pressure of phosphorus is much higher than that of silicon. A spectroscopic analysis has verified this conclusion.

5.2 Calculation of Impurity Ionization Energies

As the equations which determine the variation of electron concentration with temperature in the impurity range of an n-type semiconductor are similar to those which give the hole concentration in p-type material, we will discuss explicitly only the case of electrons.[16] We assume that the concentrations of conduction electrons, donors, and acceptors are n_e, N_D, and N_A. In an n-type semiconductor, N_D is larger than N_A and all acceptor levels are occupied (ionized). The energy required to raise an electron from a donor level to the conduction band is E_D. The equilibrium concentration of electrons, n_e, at any temperature is determined by a balance between the rate at which electrons are thermally excited from neutral donors to the conduction band and the rate at which electrons recombine with ionized donors. The equation governing the reaction may be written

$$e^- + D^+ \leftrightarrow D.$$

The concentration of ionized donors is N_A+n_e, since N_A electrons go from the donor levels to ionize the acceptors and n_e to the conduction band. The concentration of neutral donors is $N_D-N_A-n_e$. The law of mass action for the reaction may be written in the form

$$n_e(n_e+N_A)/(N_D-N_A-n_e)=K_e. \quad (22)$$

The equilibrium constant, K_e, determined from statistical considerations, is

$$K_e=(2\pi m_e kT/h^2)^{\frac{3}{2}} \exp(-E_D/kT), \quad (23)$$

in which m_e is the effective mass of the electron. Equation (22) may be expressed in the form

$$(n_e+N_A)(n_e+K_e)=N_D K_e, \quad (24)$$

which is a quadratic equation for the electron concentration n_e.

If N_A is greater than N_D, the semiconductor is p-type. The same equations apply with n_h, N_A, and N_D replacing n_e, N_D, and N_A. The corresponding equilibrium constant is

$$K_h=(2\pi m_h kT/h^2)^{\frac{3}{2}} \exp(-E_A/kT), \quad (25)$$

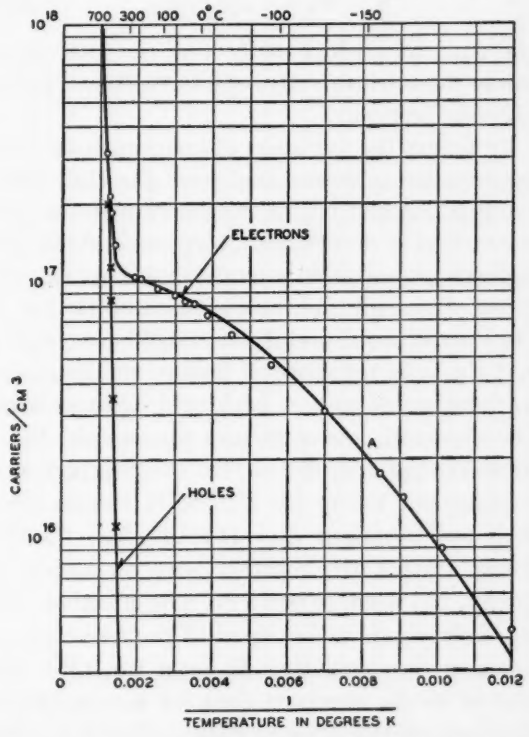

FIG. 10. Concentrations of conduction electrons and holes in sample A, Si+0.001 percent P *versus* inverse absolute temperature. Above room temperature, points are derived from resistivity using lattice scattering mobility as discussed in Section 5.3. Solid lines are derived from semi-empirical Eq. (45), using saturation concentration $N_s=10.5\times10^{16}$. For fit of Hall data in this range, see Table III. Below room temperature, points are derived from Hall data, solid line from semi-empirical theory using Eq. (22), with $N_D=12\times10^{16}$, $N_A=1.5\times10^{16}$, $E_D=0.045$ ev, and $m_e=0.33m$.

[16] The equations to be presented in this section were first derived by J. H. de Boer and W. C. van Geel, Physica 2, 286 (1935). See N. F. Mott and R. W. Gurney, *Electronic Processes in Ionic Crystals* (Oxford University Press, London, 1940), Chapter V.

TABLE II. Concentrations and ionization energies of donors and acceptors as determined from Hall data at low temperatures.

Sample	N_A	N_D	E_A or E_D
1— ——	15×10^{15}	9×10^{15}	0.075 ev
2—Si+0.0005%B	6×10^{17}	——	0.048 ev
3—Si+0.001%B	1.3×10^{18}	——	0.037 ev
4—Si+0.002%B	2.2×10^{18}	——	0.027 ev
5—Si+0.005%B	5.3×10^{18}	——	0
A—Si+0.001%P	1.5×10^{16}	12×10^{16}	0.045 ev
B—Si+0.0057%P	——	1.25×10^{18}	0

in which m_h is the effective mass of a hole and E_A is the energy required to excite an electron from the filled band to an acceptor level.

The saturation concentrations, attained at temperatures so high that all donors and acceptors are ionized, are

$$n_e = N_D - N_A (n\text{-type}), \tag{26a}$$

$$n_e = N_A - N_D (p\text{-type}). \tag{26b}$$

The equations which determine the concentration in the intrinsic range will be discussed in the following section.

By fitting the variation of concentration with temperature as determined from the Hall effect (see Figs. 7A and 7B) to the theoretical, the concentrations of donors and acceptors and the corresponding ionization energies have been determined. It is only for the purest samples, No. 1, "du Pont silicon," and A, "Si+0.001 percent P," that the concentrations of donors and acceptors are comparable so that both need be considered. The observed concentrations for sample No. 1 are somewhat irregular, so that the interpretation is uncertain. Values for $T<250°$K can be fitted fairly well by taking $N_A=15\times10^{15}$, $N_D=9\times10^{15}$, giving $n_e=6\times10^{15}$, together with an ionization energy, E_A, equal to 0.075 ev. The effective mass of a hole, m_h, is taken equal to the free electron value, m, in calculating K_h from Eq. (25). The best fit to the observed data for sample A was obtained with $N_D=12\times10^{16}$, $N_A=1.5\times10^{16}$, giving $n_e=10.5\times10^{16}$, together with an ionization energy for donors, E_D, equal to 0.045 ev. It was found that a better fit could be obtained by taking a value for m_e less than m, and a value $m_e=0.33m$ was adopted. This value for m_e is only about half that estimated from other considerations. Because of the number of adjustable parameters involved, these values are uncertain. A comparison of calculated and observed values of n_e is given in Fig. 10. The concentration of holes is also shown.

The remaining non-degenerate p-type samples, Nos. 2, 3, 4, and 5, contain sufficient added boron so that the concentration of acceptors is large compared with any small residual concentration of donors. Accordingly, the observed data were fitted by setting $N_A=n_h$ and $N_D=0$. Taking $m_h=m$, the only remaining parameter is the ionization energy, E_A, which was determined in each case to give the best fit. The values obtained are listed in Table II and are plotted in Fig. 11. Figure 12 gives a comparison of the theoretical and experimental values of n_h. The solid lines were calculated using the constants listed in Table II and the points are those derived from Hall measurements. The agreement is satisfactory.

There is a continuous decrease in E_A as N_A increases. Sample 5, with $N_A=6.5\times10^{18}$, exhibits relatively little change in concentration with temperature, so we have set $E_A=0$. The degeneracy temperature for this sample is about 150°K. Similarly, the variation of n_e with temperature is small at low temperatures in sample B, which is n-type with $N_D=1.25\times10^{18}$. We have set $E_D=0$ for this sample, although this may be a borderline case as n_e changes by a factor of about two between 150 and 300°K. The degeneracy temperature for this sample is about 50°K for $m_e=m$, or about 150°K if $m_e=0.33m$.

In a neutral donor, the electron moves in a hydrogen-like orbit about the ion. Similarly, in a neutral acceptor, a hole moves in a hydrogen-like

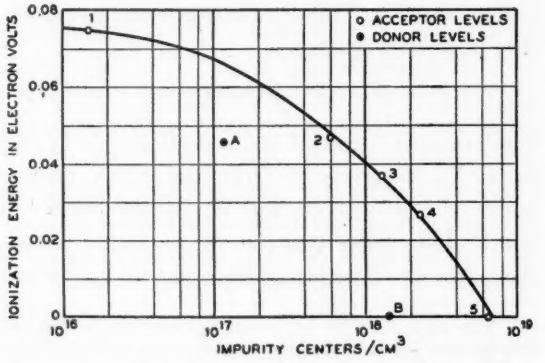

FIG. 11. Variation of ionization energy of impurity centers with concentration.

orbit about the negative acceptor ion. In each case, the force acting on the mobile charge is reduced by the dielectric constant, κ, of the medium. The ionization energy is reduced by κ^2 and the radius of the orbit is increased by κ. Since the radius of the orbit is large compared with the radius of the ion, only the Coulomb field of the ion is important in determining the energy. The ionization energy for a mass m^* and dielectric constant κ is given by the Bohr formula,

$$E_I = 2\pi^2 m^* e^4/\kappa^2 h^2. \tag{27}$$

For the case of holes in silicon we set $m^* = m_h = m$ and $\kappa = 13$, which gives

$$E_A = 13.5/13^2 = 0.08 \text{ ev}. \tag{28}$$

This value is close to that observed for the limit of high dilution.

The decrease in activation energy with increase in concentration probably results from a decrease in the average potential energy of an electron or of a hole.[17] If an isolated atom or impurity center is ionized, the electron is removed to infinity so that there is no resultant potential energy of attraction between the ion and the electron. In a semiconductor the conduction electrons will tend to shield the ions, so that on the average any small region of the crystal will be electrically neutral. There will be a resultant potential energy of attraction which will be greater the higher the concentration. Other things being equal, this energy will be inversely proportional to the average distance of separation between impurities, or, for the case of p-type samples, to $N_A^{\frac{1}{3}}$. Thus, on theoretical grounds one might expect the ionization energy to vary with concentration as

$$E_A = E_I - aN_A^{\frac{1}{3}}, \tag{29}$$

where E_I is the ionization energy for an isolated impurity center, about 0.08 ev in silicon, and a is a constant.

The values of E_A determined by experiment can be fitted closely by an expression of this form. The solid line in Fig. 11 is plotted from

$$E_A = 0.08 - 4.3\times 10^{-8} N_A^{\frac{1}{3}} (\text{ev}). \tag{30}$$

The value 0.08 for E_I is in agreement with Eq. (28). The value of a was determined by an empirical fit of the data. A theoretical discussion of the factor a is given below.

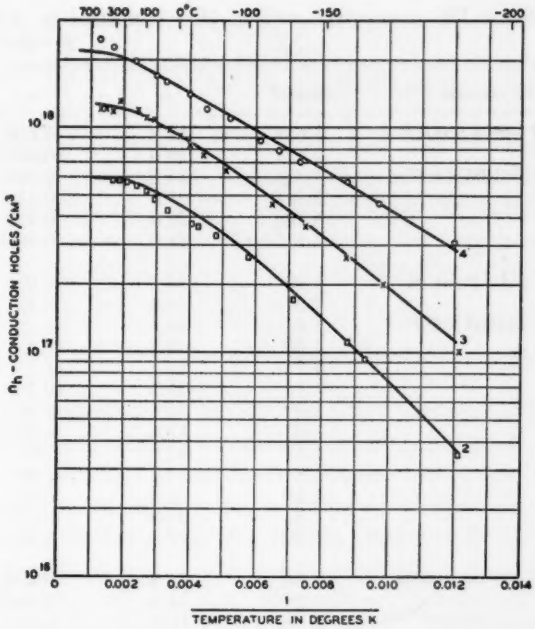

FIG. 12. Concentration of holes in samples 2, 3, and 4 *versus* inverse absolute temperature. Points are derived from Hall data, solid lines from semi-empirical theory using concentrations, and ionization energies listed in Table II.

Also shown in Fig. 11 are two points, labelled A and B, which give the ionization energies for the donor levels determined from the Hall data on samples A and B. They lie below the curve for acceptors. It is probable that the effective mass of the conduction electrons is less than the free electron value, m, so that E_I is less than 0.08 ev for donors. A value

$$m_e = 0.67m \tag{31}$$

gives

$$E_D = 0.054 \text{ ev}, \tag{32}$$

which is in reasonable agreement with the observations.

An accurate calculation of the potential energy term is difficult. We will attempt only very rough considerations to see whether or not the empirical value is of reasonable magnitude. The impurities are probably distributed more or less at random. The mobile charges are probably distributed in such a way as to shield the ions from one another. Following the method of Wigner

[17] For a similar suggestion, see T-W, p. 66.

TABLE III. Concentrations and Hall coefficient in intrinsic range as determined from conductivity and mobility, $\mu_e = 3\mu_h = 15\times 10^{15} T^{-\frac{3}{2}}$.

Sample	1000/T	μ_h	ρ	$n_e\times 10^{-17}$	$n_h\times 10^{-17}$	R(calc.)	R(obs.)
A−Si+0.001P	1.628	32.8	0.600	1.06	0.01	−69.5	−70
	1.472	28.0	0.620	1.16	0.11	−59	−68.5
$n_s = 1.05\times 10^{17}$	1.386	25.8	0.534	1.40	0.35	−44	−45
	1.314	23.7	0.410	1.88	0.83	−29.5	−27
	1.285	23.0	0.350	2.18	1.13	−23	−20
	1.215	21.0	0.264	3.06	2.01	−15	−14
1−du Pont Si	1.99	53.5	14.9	0.0035	0.0835	+495	+750
	1.87	44.0	14.1	0.0070	0.0870	+151	+310
$n_s = 0.08\times 10^{17}$	1.82	40.3	13.1	0.0105	0.0905	−22	−22
	1.80	38.7	12.3	0.0140	0.0940	−132	−151
	1.78	37.5	11.5	0.0162	0.0962	−178	−262
	1.75	36.5	10.2	0.0215	0.1015	−248	−400
	1.69	34.6	7.12	0.0435	0.1235	−310	−489
	1.63	32.6	4.65	0.120	0.201	−206	−434
	1.57	31.0	3.05	0.145	0.225	−183	−276
	1.51	28.7	2.00	0.252	0.332	−120	−212
	1.40	26.0	0.98	0.592	0.672	−58	−93
	1.32	23.8	0.69	0.925	1.005	−31	−43
	1.26	22.3	0.385	1.80	1.88	−20	−25
2−Si+0.0005B	1.34	24.8	0.408	0.07	5.97	+10.4	+8.45
	1.26	22.5	0.340	0.58	6.48	+1.4	+3.04
$n_s = 5.9\times 10^{17}$	1.12	18.8	0.164	3.60	9.50	−4.1	——

and Seitz,[18] it should be possible to draw a roughly spherical region about each ion which is electrically neutral. The average radius, r_s, of such a sphere is given by

$$4\pi r_s^3/3 = N_A^{-1}, \tag{33}$$

or

$$r_s = 0.62 N_A^{-\frac{1}{3}}. \tag{34}$$

If it is assumed that the mobile charges are uniformly distributed throughout the sphere, the potential energy of attraction is

$$-1.5e^2/\kappa r_s. \tag{35}$$

The self-energy of the uniform charge distribution in the sphere is

$$+0.6e^2/\kappa r_s. \tag{36}$$

This calculation assumes no correlations between the positions of the mobile charges. Actually, there is probably a large correlation energy resulting from the fact that these charges tend to keep apart. The most stable arrangement, which will be approached when the kinetic energy is small compared with the potential, is body-centered cubic. The reduction in potential energy relative to a random distribution is

$$-0.746e^2/\kappa r_s. \tag{37}$$

The sum of these three contributions is

$$-1.646e^2/\kappa r_s. \tag{38}$$

Substituting for r_s from Eq. (34), and putting in numerical values, this becomes

$$-3\times 10^{-8} N_A^{\frac{1}{3}} \text{ (ev)}, \tag{39}$$

which is about $\frac{2}{3}$ of the empirical value. The mobile charges may be concentrated more in the vicinity of the ions than we have assumed, increasing the energy of attraction.

If this is the correct picture, the assumption of a single ionization energy independent of the degree of ionization of the impurities can be considered to be only an approximation.

5.3. Concentrations in the Intrinsic Range

The expressions (7) and (8) for the conductivity and Hall coefficient in the intrinsic range involve four quantities, two concentrations, n_e and n_h, and two mobilities, μ_e and μ_h. As there are only two measured quantities, σ and R, additional relations are required. One may be obtained from the requirement of electrical neutrality. The difference between n_h and n_e must

[18] See reference 3, Chapters 9 and 10. The theory of a metallic modification of hydrogen, which is similar to our problem, has been discussed by E. Wigner and H. B. Huntington, J. Chem. Phys. **3**, 764 (1935).

be equal to the net concentration of impurity ions, which in turn is equal to the saturation concentration, n_s, in the impurity range. Thus

$$n_s = n_e - n_h \ (n\text{-type}), \tag{40a}$$

$$n_s = n_h - n_e \ (p\text{-type}). \tag{40b}$$

At high temperatures the mobilities of electrons and holes in all samples approach the values corresponding to lattice scattering, which are approximately

$$\mu_e = 15\times 10^5 T^{-\frac{3}{2}} (\text{cm}^2/\text{volt sec.}), \tag{41a}$$

$$\mu_h = 5\times 10^5 T^{-\frac{3}{2}}. \tag{41b}$$

The mobilities of holes in samples 2, 3, and 4 and of electrons in sample B lie on the lattice scattering line over the same temperature range for which the conductivity of samples 1 and A become intrinsic. Thus there is every reason to believe that the lattice scattering mobilities will apply in the intrinsic range.

Assuming Eqs. (41a) and (41b) for the mobilities, and using Eqs. (40a) and (40b) expressing electrical neutrality, the concentrations n_e and n_h in the intrinsic range can be found from either the conductivity or the Hall coefficient. We have determined n_e and n_h from the conductivity and used these values to calculate the Hall coefficient to compare with the observed. The conductivity may be expressed in the form

$$\sigma = e\mu_h(cn_e + n_h). \tag{42}$$

For a p-type sample we set $n_e = n_h - n_s$ and find

$$n_h = ((\sigma/e\mu_h) + cn_s)/(c+1). \tag{43}$$

For an n-type sample, we set $n_e = n_h + n_s$ and find

$$n_h = ((\sigma/e\mu_h) - cn_s)/(c+1). \tag{43a}$$

Using these equations, both n_e and n_h were determined in the intrinsic range for samples 1, 2, and A. The values are listed in Table III.

Statistical theory indicates that the product of the electron and hole concentrations at any temperature is independent of impurity concentration and is given by:[19]

$$n_e n_h = 4(2\pi mkT/h^2)^3 (m_e m_h/m^2)^{\frac{3}{2}} \exp(-E_G/kT)$$
$$= 2.4\times 10^{31} (m_e m_h/m^2)^{\frac{3}{2}} T^3 \times \exp(-E_G/kT). \tag{44}$$

A plot of $\log(n_e n_h/T^3)$ *versus* $1/T$ should then give a straight line. Such a plot is shown in Fig. 13. Values of $n_e n_h/T^3$ calculated from the values of n_e and n_h determined as above for the three samples all lie on the same straight line whose equation is:

$$n_e n_h/T^3 = 7.8\times 10^{32} \exp(-12{,}900/T). \tag{45}$$

This equation is of the correct form, but the numerical factor is considerably larger than the theoretical. The difference seems too large to account for by the term involving the effective mass. In fact, the mass term operates in the wrong direction, as the evidence is that m_e is only about two-thirds of m. Neglecting the difference in effective mass, the discrepancy is a factor of about 32.5. It is most likely accounted for by a variation of E_G with temperature. If there is

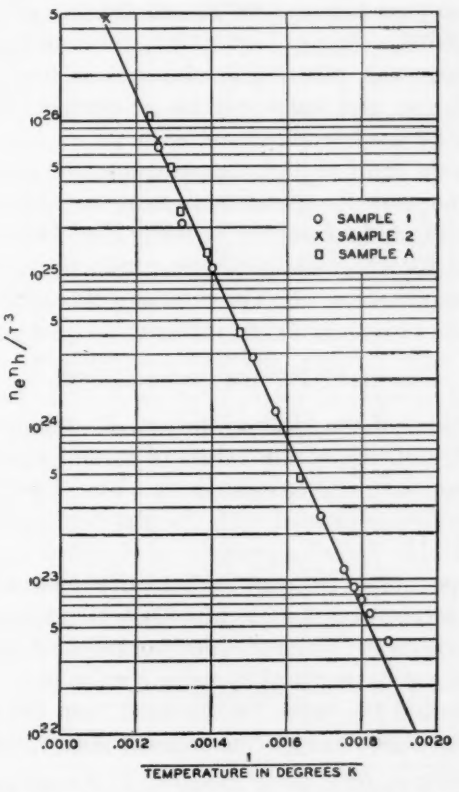

FIG. 13. Plot of $n_e n_h/T^3$ *versus* inverse absolute temperature for samples 1, 2, and A. Equation of straight line is $n_e n_h/T^3 = 7.8\times 10^{32} \exp(12{,}900/T)$.

[19] See, for example, R. H. Fowler, *Statistical Mechanics* (Cambridge University Press, London, 1936), second edition, Chapter 11. While not given explicitly, Eq. (44) can be derived readily from the relations expressing n_e and n_h in terms of the Fermi level.

TABLE IV. Fit of mobility data by $1/\mu = aT^{-\frac{3}{2}} + bT^{\frac{1}{2}}$.

Sample	Impurity centers/cm³	$1.8\times 10^{-16}N_I$	a	b
2−Si+0.0005B	0.6×10^{18}	1.1	3.1	2×10^{-6}
3−Si+0.001B	1.3×10^{18}	2.3	3.1	2×10^{-6}
4−Si+0.002B	2.5×10^{18}	4.5	8.3	2×10^{-6}
A−Si+0.001P	1.0×10^{17}	0.19	3.1	0.67×10^{-6}
B−Si+0.0057P	1.25×10^{18}	2.3	5.5	0.67×10^{-6}

linear variation, we may write

$$E_G(T) = E_G(0) - \beta T. \tag{46}$$

The empirical equation for $n_e n_h/T^3$ can be brought into agreement with the theoretical by taking

$$E_G(0) = 12{,}900/11{,}600 = 1.115 \text{ ev}, \tag{47}$$

and

$$\beta = k \log 32.5 = 3.0\times10^{-4} \text{ ev/degree}. \tag{48}$$

The value of $E_G(0)$ is in close agreement with photoelectric studies of a silicon $p-n$ junction at low temperatures.[20] These studies also indicate a shift in response corresponding to a change in $E_G = 0.1$ ev between 90°K and 290°K, a range of 200°K, giving $\beta = 5\times10^{-4}$. The difference between this value of β, obtained at low temperatures, and ours may be accounted for, in part, by the effective mass term.

In the limit of high temperatures, the concentration may be found by setting $n_e = n_h = n$ in Eq. (45) and solving for n. Using Eqs. (41a) and (41b) for the mobilities, the conductivity may be found for Eq. (9). The corresponding equation for the resistivity in the intrinsic range is

$$\rho = 1.1\times10^{-4} \exp(6450/T) \text{ ohm}.$$

Values of the Hall coefficient, R, were calculated with use of the values of n_e and n_h determined from the conductivity. The calculated values are compared with the observed values in Table III. Good agreement is obtained for the n-type sample (A), but there are discrepancies for the p-type samples, (1) and (2), which appear to be outside the limits of experimental error. Agreement can be obtained by using a value of $c = 3.75$ instead of the value 3.0 obtained from the ratio of the mobilities in the sub-intrinsic range of other samples. This would correspond to an electron mobility of about $19\times10^5 T^{-\frac{3}{2}}$ for the intrinsic range of p-type samples as compared with $15\times10^5 T^{-\frac{3}{2}}$ for electrons in n-type samples. A real difference of this sort would be surprising. If the higher value is used to compute n_e and n_h for the p-type samples, it is found that values of $n_e n_h/T^3$ for the different samples do not lie on the same line. It is possible that the theory for the Hall coefficient in the intrinsic range requires modification.

[20] F. S. Goucher, H. B. Briggs, G. L. Pearson and W. Shockley, "Photoelectric and electric studies of P-N junctions in silicon and germanium," to be published in Phys. Rev.

VI. LATTICE AND IMPURITY SCATTERING: ANALYSIS OF MOBILITY DATA

6.1. Lattice Scattering

We have seen that the mobilities of electrons and holes in all samples approach the same limiting curves at high temperatures, independent of impurity concentration. The mobility in this temperature range is determined by scattering by vibrations of the crystal lattice. It has been shown by Wilson,[21] and later more generally by Seitz,[22] that in a non-polar material such as germanium or silicon the mean free path is independent of velocity. Above a few degrees absolute, the scattering by lattice vibrations is isotropic, and energy is conserved during collisions. The mean free path varies as T^{-1} and in the non-degenerate case the mobility varies as $T^{-\frac{3}{2}}$. These theoretical predictions agree well with the experimental results for silicon, and, as pointed out by Seitz,[22] the observed values are of the expected order of magnitude.

The difference in electron and hole mobility (Eqs. (41a) and (41b)), a factor of three, may result at least in part from the fact that the effective mass of a conduction electron is less than that of a hole. Theory indicates that the mobility varies as $(m_{eff.})^{-5/2}$. A factor of three would require that

$$(m_h/m_e)^{5/2} = 3,$$

or

$$m_e/m_h = 0.65. \tag{49}$$

This ratio is about the same as that required to explain the difference in ionization energies between donors and acceptors, but is about

[21] A. H. Wilson, *Theory of Metals* (Cambridge University Press, Cambridge, 1936), p. 211.
[22] F. Seitz, Phys. Rev. **73**, 549 (1948).

twice as large as that derived in Section 5.1 from concentration data for sample A. The larger value is probably more nearly correct.

6.2 Impurity Scattering—Non-Degenerate

At lower temperatures impurities contribute to the scattering, so that the mobilities are higher in the purer samples. The impurity centers which give the largest scattering are the donors and acceptors. Scattering by both ionized and neutral centers is large at low temperatures. It is not possible to make anything like an exact calculation of the way the mobility should change with temperature when both lattice and impurity scattering is involved for the following reasons:

(1) The theory of the scattering, particularly by neutral centers, is complicated, and only rough approximations are available.

(2) Scattering by the lattice, ionized centers, and neutral centers are not additive because they depend in different ways on the velocities of the carriers.[23]

In this section we attempt to give only a brief outline of theoretical considerations involved in impurity scattering, and to indicate roughly the correlation between theory and experiment. We discuss first the case of a non-degenerate gas and then the degenerate case.

Conwell and Weisskopf[24] have given an expression for the resistivity of a semiconductor which is based on scattering by ions which are present with a total concentration N_I. The expression for the reciprocal of the mobility, which applies for a non-degenerate gas, may be written in the form

$$1/\mu=(N_I\pi^{3/2}e^3m^{1/2})/(2^{7/2}\kappa^2(kT)^{3/2}) \times\log(1+x^2)(\text{e.s.u.}), \quad (50)$$

where

$$x=6\kappa dkT/e^2. \quad (51)$$

In these equations d is the average distance the field of any one ion extends, so that $2d$ is something like the average distance between near neighbors. For the purpose of numerical calculation, we take

$$d=0.5N_I^{-\frac{1}{3}}. \quad (52)$$

The choice of the numerical factor is somewhat arbitrary. Inserting numerical values for the fundamental constants and converting to practical units, Eqs. (50) and (51) may be written for application to silicon in the form

$$1/\mu=1.8\times10^{-18}N_IT^{-\frac{3}{2}}\log(1+x^2), \quad (53)$$

$$x=2.3\times10^4N^{-\frac{1}{3}}T. \quad (54)$$

A neutral donor or acceptor consists of an electron or hole moving in a hydrogen-like orbit about the corresponding ion. The calculation of the scattering by such a center is mathematically the same as that of the scattering of an electron by a hydrogen atom, which problem has been treated theoretically by Massey and Mohr.[25] An exact calculation is difficult, particularly for incident energies less than the ionization energy, for which exchange effects are important. In the limit of zero velocity of the incident particle, the cross section for scattering is 124 times that of the Bohr orbit. The cross section decreases rapidly with increasing velocity, but is still large when the kinetic energy of the incident particle is less than about 25 percent of the kinetic energy of an electron in a Bohr orbit. The radius of the orbit about an ion in a semiconductor is increased by the dielectric constant and the cross section by the square of the dielectric constant.

To compare the scattering by neutral and ionized centers, we write down an expression for the mobility in a semiconductor containing N_n neutral scattering centers. The reciprocal of the mobility is related to the effective scattering cross section, A, by

$$1/\mu=(m/e)N_nvA \text{ (e.s.u.)}, \quad (55)$$

where v is an average thermal velocity for the carrier. We may set

$$A=124\pi\kappa^2A_0^2\alpha(T), \quad (56)$$

where $\alpha(T)$ is a numerical factor which equals unity at $T=0$ and decreases with increasing

[23] W. Shockley (unpublished) has made calculations of the resistivity when both lattice scattering, with l_L independent of velocity, and scattering by ions, with $l_I\sim v^4$, are present. Large deviations from simple additivity are found.

[24] E. Conwell and V. F. Weisskopf, Phys. Rev. **69**, 258A (1946). The problem is mathematically identical with that of the scattering of electrons in an ionized gas which has been solved to the same approximation by S. Chapman, Monthly Notices, R.A.S. **82**, 294 (1922).

[25] H. S. W. Massey and C. B. O. Mohr, Proc. Roy. Soc. **A132**, 605 (1931); **A136**, 289 (1932).

TABLE V. Limiting low temperature resistivities and mobilities for degenerate samples.

Sample	n	μ	ρ	$1.87\times10^{17}/n$
6−Si+0.01B	1.4×10^{19}	31	1.25×10^{-2}	1.33×10^{-2}
7−Si+0.1B	1.2×10^{20}	30	1.62×10^{-3}	1.56×10^{-3}
8−Si+1.0B	4.8×10^{20}	54	2.21×10^{-4}	3.9×10^{-4}
C−Si+0.1P	1.7×10^{19}	130	2.5×10^{-3}	1.1×10^{-3}
D−Si+1.0P	2.6×10^{20}	50	5.0×10^{-4}	7.2×10^{-4}

temperature. Putting $\kappa=13$ for silicon, substituting in Eq. (55), and converting to practical units gives

$$1/\mu=7.6\times10^{-22}N_nT^{\frac{1}{2}}\alpha(T). \tag{57}$$

This equation may be compared with Eq. (53) which applies to ionized centers. The effective scattering cross sections will be equal for a temperature such that

$$T^2=2.4\times10^8\log(1+x^2)/\alpha(T).$$

It is not unreasonable to expect that the effective scattering cross section for neutral centers is as large or is larger than the cross section for ionized centers at temperatures above about 100°K.

The mobilities of the p-type samples are shown in Fig. 8A and the n-type in Fig. 8B. Of the p-type samples, numbers 1, 2, 3, and 4 are nondegenerate and number 5 is borderline, as the degeneracy temperature is about 150°K. The mobility values for sample 1 are anomalously low. It is thought that in this case the sample is not homogeneous so that the method does not give reliable results. The mobilities of the remaining p-type samples, numbers 2, 3, and 4, and of the n-type samples, A and B, can be approximated over the temperature range by an expression of the form

$$1/\mu=aT^{-\frac{1}{2}}+bT^{\frac{3}{2}}. \tag{58}$$

This form is suggested by assuming additivity of lattice and impurity scattering, and by the form of Eq. (53) for impurity scattering. The first term represents impurity scattering and the second term lattice scattering. The coefficient b is equal to 2×10^{-6} for the p-type samples and to 0.67×10^{-6} for the n-type samples. Values of a which give the best fit to the observed data are listed in Table IV.

The empirical values of a are of the same order as expected from theory. Equation (53) gives

$$a=1.8\times10^{-18}N_I\log(1+x^2). \tag{59}$$

The factor multiplying the logarithm is listed in Table IV for the different samples. The logarithm is slowly varying with concentration and temperature, and may be expected to increase a by a small factor. The order of magnitude is about the same as the observed. Actually, a large fraction of the impurity centers are neutral over the temperature range, the concentration of ions decreasing with decrease in temperature, so that the comparison is not significant except as to general order of magnitude. The empirical values of a do not decrease as rapidly as expected with decreasing concentration. The discrepancy is particularly large for sample A.

6.3. Impurity Scattering—Degenerate

In the degenerate cases, the concentrations and resistivities approach constant values at low temperatures. The resistivity is determined by impurity scattering. Because of Fermi-Dirac statistics, the effective velocities of the carriers and thus the mobilities and resistivities become temperature independent. The constancy of ρ and R over a wide temperature range for samples 6, 7, 8, and D is striking.[26]

When degeneracy applies, it may be assumed that there are impurity centers of only one type and that these are all ionized. The concentration of ions is then equal to that of the electrons (or holes). Johnson and Lark-Horovitz[15] have extended the calculations of Conwell and Weisskopf to cover this case. the problem is mathematically identical with that of the calculation of the resistivity of dilute solutions of metals of higher valency in monovalent solvents such as Cu, Ag, and Au. This latter problem has been discussed by Mott.[27] He assumes that the impurity ions are screened by the electrons, so that the poten-

[26] G. L. Pearson and W. Shockley (reference 1) have found that the resistivity and Hall coefficient of a sample of silicon similar in composition to sample 6 remain constant to 10°K. Similar results were obtained for a germanium sample with added impurities. I. Esterman, A. Foner, and J. A. Randall [Phys. Rev. 72, 530A (1947)] have reported that the resistivity and Hall coefficient of a sample of germanium with 0.04 atomic percent Al added remained substantially constant between 20°K and 200°K.

[27] N. F. Mott, Proc. Camb. Phil. Soc. 32, 281 (1936).

tial of an ion is of the form

$$V(r)=(Ze^2/r)e^{-qr}, \tag{60}$$

where Z is the difference in valency between the solute and solvent atoms, and q depends on the screening. To apply to our case we replace Z by $1/\kappa$, where κ is the dielectric constant.

Both Mott's theory and that of Johnson and Lark-Horovitz lead to an expression for the reciprocal of the mobility of the form:

$$1/\mu=(8\pi e^2m^2/3\kappa^2h^3)f(y)(\text{e.s.u.}). \tag{61}$$

The parameter y is a measure of the ratio of the kinetic energy of an electron at the surface of the Fermi distribution, E_0, to the potential energy in the field of the ion:

$$y=\kappa E_0/e^2n^{\frac{1}{3}}=(\kappa h^2/8me^2)(3/\pi)^{\frac{1}{3}}n^{\frac{1}{3}}. \tag{62}$$

The form of the function $f(y)$ is discussed below. Putting in numerical values for silicon gives

$$y=3.4\times10^{-7}n^{\frac{1}{3}}. \tag{63}$$

Inserting constants for silicon into Eq. (61) and converting to practical units gives

$$\rho=1/ne\mu=(1.87\times10^{17}/n)f(y)(\text{ohm cm}). \tag{64}$$

The function $f(y)$ depends on what is assumed for the field of an ion. Johnson and Lark-Horovitz assume a cut-off distance

$$d=n^{-\frac{1}{3}}/2\pi^{\frac{1}{3}}=0.28n^{-\frac{1}{3}}, \tag{65}$$

which, using an extension of the Conwell-Weisskopf theory, gives

$$f(y)=\log(1+y^2/\pi). \tag{66}$$

In the limiting case of y^2 small compared with unity, the logarithm can be replaced by y^2/π, giving

$$1/\mu=(\pi h/4e)(3/\pi)^{\frac{1}{3}}n^{\frac{1}{3}}\ (\text{e.s.u.}). \tag{67}$$

The mobility and thus the resistivity are in this approximation independent of the dielectric constant and effective mass, and so should depend only on the concentration. The resistivity is inversely proportional to the cube root of the concentration. In practical units

$$\rho=6270n^{-\frac{1}{3}}\ (\text{ohm cm}). \tag{68}$$

This is the formula as given by Johnson and Lark-Horovitz.

Mott's expression for $f(y)$ may be written in the form

$$f(y)=\log(1+ay)-ay/(1+ay). \tag{69}$$

The numerical factor a is inversely proportional to the square of the screening constant, q, and is equal to $2(\pi/3)^{\frac{1}{3}}$ if the Thomas-Fermi method is used to evaluate q. Mott believes that this method yields a value for q which is too large. The best value for a may therefore be several times larger than $2(\pi/3)^{\frac{1}{3}}$. In the derivation of Eq. (69) the Born approximation is used to determine the collision cross sections. This approximation is valid in the limit of large ratios of kinetic to potential energy, that is, for large values of y. This condition is not well satisfied in our case, and it is probable that the actual cross sections are larger than given by the formula.

We would expect a formula based on screening to be more accurate than one based on a cut-off distance for the ion field, so that Mott's formula is to be preferred. The use of the Born approximation limits the accuracy that can be attained.

The experimental results do not agree well with either formula except as to order of magnitude. In Table V we have listed the limiting resistivities and mobilities and have also listed the values of the factor multiplying $f(y)$ in Eq. (64). It can be seen that these values are in fair agreement with the observed values of ρ, indicating that $f(y)\sim1$. Both Lark-Horovitz's and Mott's expressions yield values for $f(y)$ which are smaller than unity. It appears likely, however, that appropriate modifications of Mott's theory would yield agreement.

ACKNOWLEDGMENTS

The authors are indebted to J. H. Scaff and H. C. Theuerer for the preparation of the samples, to E. S. Greiner for the x-ray measurements, to P. W. Foy for assistance with the electrical measurements, and to W. van Roosbroeck for aid with some of the calculations on impurity scattering. The research program on the electrical properties of silicon was carried out under the direction of W. Shockley, who made many suggestions and was himself responsible for much of the analysis in the early stages of the work.

Letters to the Editor

PUBLICATION of brief reports of important discoveries in physics may be secured by addressing them to this department. The closing date for this department is five weeks prior to the date of issue. No proof will be sent to the authors. The Board of Editors does not hold itself responsible for the opinions expressed by the correspondents. Communications should not exceed 600 words in length.

On the Theory of Superfluidity

L. LANDAU
Institute for Physical Problems Academy of Sciences of the U.S.S.R., Moscow, U.S.S.R.
November 19, 1948

SINCE my paper on the theory of the superfluidity of helium *II* was published in 1941[1] and in later papers,[2,3] this problem has been repeatedly discussed in scientific literature. I should like to express my opinion on some of the statements which have been put forward, especially in connection with the last paper by L. Tisza.[4] *

It follows unambiguously from quantum mechanics that for every slightly excited macroscopic system a conception can be introduced of "elementary excitations," which describe the "collective" motion of the particles and which have certain energies ϵ and momenta p (leaving aside the question as to the actual dependence $\epsilon(p)$, i.e., the actual form of the energy spectrum). It is this assumption, indisputable in my opinion, which is the basis of the microscopical part of my theory. On the contrary, every consideration of the motion of individual atoms in the system of strongly interacting particles is in contradiction with the first principles of quantum mechanics.**

As to the actual form of the energy spectrum, the general principles allow one merely to assert[1] that for small energies the dependence $\epsilon(p)$ must be of the "phonon" type, i.e., $\epsilon=cp$, c being the velocity of sound. This fact is in itself sufficient to deduce strictly the superfluidity of the liquid at sufficiently low temperatures (reference 1, § 5). It is useful to note that N. N. Bogoliubov[5] has succeeded recently, by an ingenious application of second quantization, in determining the general form of the energy spectrum of a Bose-Einstein gas with a weak interaction between the particles. As it should be, the "elementary excitations" appear automatically, and their energy ϵ as a function of the momentum p is represented by a single curve, which has a linear initial part. Although the model of such a gas does not have any direct bearing on the actual liquid helium *II*, it shows the manner in which the quantum-mechanical mathematical formalism leads, in fact, from a macroscopical body to an energy spectrum with the indicated properties.

The further trend of the ϵ *vs.* p curve cannot be established in a general form by purely theoretical considerations. The spectrum with two branches ($\epsilon=cp$ and $\epsilon=\Delta+p^2/2\mu$), which I originally postulated, consisted of two intersecting curves; the latter fact alone makes this spectrum unsatisfactory. These considerations, together with an elaborate investigation of the new experimental data, lead[3] to a spectrum consisting of a single curve; after a linear initial part, the function $\epsilon(p)$ passes through a maximum, then has a minimum and increases again.***

Apart from the microscopic theory and the calculation of the thermodynamic quantities based on this theory, my paper of 1941 contained also the derivation of the hydrodynamic equations for helium *II*. This part of the theory does not depend on the assumptions concerning the energy spectrum and the equations can be deduced starting merely from the conservation laws and the Galilean relativity principle. From these hydrodynamic equations the formula which determines the velocity of the "second sound" in terms of the thermodynamic quantities of helium *II* was deduced. I would like to emphasize that, at present this formula can be directly checked by the experimental data on the entropy and the specific heat of helium *II* and the values of ρ_n directly measured by E. Andronikashvilli.[6] Such a comparison shows excellent agreement between the theory and the experiment well inside the limits of the experimental error. Therefore, one must consider as a mere misunderstanding Tisza's assertion that this formula is in conflict with experiment.

The hydrodynamic equations given by Tisza are, in my opinion, quite unsatisfactory. It is easy to see that in their exact form they even violate the conservation laws!**** If one tries to obtain my results starting from these equations, it can be done only as far as equations of the first approximation are concerned, in which the terms of the second order in the velocities are neglected. In this case Tisza's equations can be readily reduced to my equations by means of a suitable definition of the arbitrary quantity p_n, which enters Tisza's theory; this is exactly what he does in his recent paper. Unfortunately, however, he obtains the correct result by using an incorrect assumption of the proportionality between the entropy and the normal part of the density ρ_n of helium *II*. Tisza's effort to give a thermodynamical foundation for this assumption is quite unconvincing and the formulas given[1,3] actually show that such a proportionality is absent.†

Tisza excludes phonons from the "normal part" of the liquid, the argument being that the phonons are "associated with the liquid as a whole," contrary to the "elementary excitations" which "correspond to helium atoms in translational Bloch-type states." Such exclusion of the phonons evidently presumes either that (1) the phonons penetrate freely through narrow slits, without scattering by the walls (I do not mention their mutual collisions, which can be calculated hydrodynamically and turn out to be by no means improbable), or (2) the moving phonon gas has no momentum, whereas the opposite ("the sound wind"!) is well known. Both alternatives are so obviously incorrect that I can hardly imagine which is the one adopted by Tisza. It should also be noted that the part of the density ρ_n which is due to phonons can be strictly calculated.[1] †† The experimental data which are available at present are yet insufficient to disprove Tisza's assertion, because of the comparatively small role of the phonons in the temperature region explored. But I have no doubt

whatever that at temperatures of 1.0–1.1°K the second sound velocity will have a minimum and will increase with the further decrease in temperature. This follows from the values of the thermodynamic quantities of helium *II* calculated by me.

Tisza's paper contains also some considerations concerning the viscosity of helium *II*. These considerations are, however, confined to some unconvincing remarks on the necessity of distinguishing the "liquid-type viscosity" from the "gas-type or transport viscosity," and as a result Tisza concludes that the viscosity must decrease with decreasing temperature. Actually, this problem is theoretically rather complicated, and its solution requires an elaborate investigation of different elementary collision processes of phonons and rotons with each other. Such an investigation shows that the viscosity coefficient of helium *II* can be represented as a sum of two parts—the "roton part" and the "phonon part." The first one turns out to be independent of the temperature, whereas the second increases experimentally with decreasing temperature (a temperature region which is not too near to the λ-point is implied, thus allowing one to consider the phonons and rotons as a "perfect gas"). These results are entirely in accord with the recent viscosity measurements by E. Andronikashvilli,[7] which correspondingly are in conflict with Tisza's considerations.

Finally, I should like to dwell upon the question of behavior of foreign atoms dissolved in helium *II* (e.g., atoms of the isotope He^3). In a recent paper by I. Pomeranchuk and the author,[8] it was shown by considering the energy spectrum of a quantum liquid, together with a foreign atom that the presence of such atoms gives rise to the appearance of a new kind of "elementary excitation" connected with these atoms. These atoms enter the "normal part" of the liquid together with the phonons and rotons and thus cannot penetrate narrow slits (a fact actually observed by Daunt *et al.*[9]). It is to be emphasized that this fact has nothing to do with the question as to the superfluidity of the substance of the admixture in itself (in particular of the pure He^3), contrary to the opinion expressed in the literature (J. Franck[10] and Tisza[4]).

* I am glad to use this occasion to pay tribute to L. Tisza for introducing, as early as 1938, the conception of the macroscopical description of helium *II* by dividing its density into two parts and introducing, correspondingly, two velocity fields. This made it possible for him to predict two kinds of sound waves in helium *II*. [Tisza's detailed paper (J. de phys. et rad. 1, 165, 350 (1940) was not available in U.S.S.R. until 1943 owing to war conditions, and I regret having missed seeing his previous short letter (Comptes Rendus 207, 1035, 1186 (1938)).] However, his entire quantitative theory (microscopic as well as thermodynamic-hydrodynamic) is in my opinion, entirely incorrect.

** Such reasonings are also present in Tisza's recent paper. No quantum meaning can be given to such assertions, as, e.g., "every vortex element can be associated with a definite mass contained in the volume in which the vorticity is different from zero" (reference 4, p. 852).

*** Tisza's remark that this assumption "tends to modify the theory in the wrong direction" (reference 4, p. 852) can hardly be justified.

**** For instance, the time derivative of the total momentum $\int(\rho_n \mathbf{V}_n + \rho_s \mathbf{V}_s)dV$ is not equal to zero.

† Accidentally, the temperature dependences of the roton parts of ρ_n and of the entropy are very similar (the only difference being the factor $1+3T/2\Delta$). It is this circumstance that enabled Tisza to attain a good agreement with the experimental data on the second sound velocity in the region of not too low temperatures, where the rotons prevail over the phonons.

†† Tisza remarks that the argument given in reference 1 "is not convincing as it tends to obtain information on a kinetic coefficient (viscosity) from equilibrium considerations" (reference 4, p. 852). However, this is a mere misunderstanding. It is generally known that the uniform rotation admits a thermodynamic consideration, and the argumentation given[1] uses such considerations only for the calculation of that part of the helium mass which rotates together with the rotating vessel, whereas no conclusions on the magnitude of the helium viscosity can be obtained in such a way. Of course, my paper does not make an attempt of this kind.

[1] L. Landau, J. Phys. U.S.S.R. **5**, 71 (1941).
[2] L. Landau, J. Phys. U.S.S.R. **8**, 1 (1944).
[3] L. Landau, J. Phys. U.S.S.R. **11**, 91 (1947).
[4] L. Tisza, Phys. Rev. **72**, 838 (1947).
[5] N. Bogoliubov, J. Phys. U.S.S.R. **11**, 23 (1947).
[6] E. Andronikashvilli, J. Exper. Theor. Phys. **16**, 780 (1946); **18**, 424 (1948).
[7] E. Andronikashvilli, J. Exper. Theor. Phys. **18**, 429 (1948).
[8] L. Landau and I. Pomeranchuk, Comptes Rendus Acad. Sci. U.S.S.R. **59**, 669 (1948).
[9] Daunt, Probst, Johnston, Aldrich, and Nier, Phys. Rev. **72**, 502 (1947).
[10] J. Franck, Phys. Rev. **70**, 561 (1946).

On the Theory of Superfluidity*

L. Tisza
Massachusetts Institute of Technology, Cambridge, Massachusetts
December 20, 1948

IN order to appreciate the relation of Landau's theory[1,2] of superfluidity to ours[3–5] one has to keep in mind a fundamental difference in attitude. We started from the conviction that the present techniques of handling the quantum-mechanical many-body problem are inadequate for a theory of liquid helium and formulated a few assumptions which enabled us to correlate and predict experimental facts.

On the other hand Landau attacked the helium problem from a more fundamental point of view and tried to derive the properties of this system from the principles of quantum mechanics. Landau criticizes our ideas not so much because of their internal inconsistency but because they do not follow from his theory of phonons and rotons. We are frankly impressed by the audacity and power of Landau's approach but we feel that he has introduced into his theory more or less disguised assumptions which cannot claim the same degree of certainty as the principles of quantum mechanics. These assumptions need an experimental verification no less than the assumptions formulated by ourselves.**

There are essentially two issues awaiting experimental decision. The first is whether or not the Bose-Einstein statistics is essential for the superfluidity of He*II*. We have pointed out[5] that the macroscopic effects cannot decide either for or against this assumption, since their interpretation depends only on certain general features of the two-fluid model. Landau is right in pointing out that the experiments with He^3, He^4 mixtures are not quite conclusive in this respect either. Recently, however, the liquefaction of pure He^3 has been reported[6] and the question is likely to be decided before long.

The second group of experiments concerns the low temperature behavior of helium *II*. In contrast to Landau, we predicted that somewhere between 0.6 and 1°K, helium *II* gradually becomes a homogeneous liquid and the thermomechanical effect vanishes. Thus heat transfer should occur by the conventional mechanism and not by second sound. Also the cooling method based on the thermomechanical effect[3,7] should fail in this temperature range.

The origin of this divergence is in a rather subtle difference in the interpretation of the two-fluid concept. We

consider the "normal flow" as a drift of elementary excitations possessing rest masses (postulate c^5) whereas for Landau the normal flow is that of the whole excitation energy. Thus Landau *includes* and we *exclude* phonons. We doubt that this issue can be conclusively decided theoretically at the present time and we would await the outcome of the low temperature experiments.

We would like to make a few remarks on Landau's criticism of our hydrodynamic equations. These equations appear as direct consequences of the two-body problem in point mechanics; hence the conservation laws are automatically satisfied. Since we were mostly interested in wave propagation, the quadratic terms in the velocity were not always considered.

The osmotic pressure P_n is not an arbitrary quantity; it is directly observed as the fountain pressure. The possibility of its definition follows from the existence of semi-permeable capillaries.

Landau questions the validity of our relation (11) of of reference 5, which is the basis for the proof of equivalence of the two expressions for the velocity of second sound. Equation (11) is valid for adiabatic processes (such as the propagation of sound) provided our postulate c^5 is valid. Thus the use of (11) is legitimate within the framework of our assumptions.

On the other hand, the validity of Eq. (12) and consequently of Eq. (28)[5] giving the explicit temperature dependence of the second sound velocity have only an approximate nature.[8] The approximation should be better for lower temperatures and in fact Peshkov's[9] measurements between 1.2° and 1.6°K show that they are satisfied to a very great accuracy. Therefore we concluded[5] that experiment is in favor of our postulate c. Since that time Pellam[10] has extended Peshkov's measurements to nearly 1°K. At the lowest temperatures he does not completely check Peshkov's measurements; thus it seems justified to consider this question to be open until the measurements have been carried out well below 1°K.

The situation can be summed up as follows: (1) The two macroscopic theories are essentially equivalent. The actual overlapping is not complete. E.g. Landau obtained several particular solutions of the hydrodynamic equations. On the other hand we discussed questions such as what is responsible for the difference in behavior of He*I*, a quantum liquid, and hydrogen, a classical liquid, which is hard to understand from Landau's point of view. (2) Landau and ourselves have formed somewhat different intuitive pictures of the two-fluid model. Since this concept is no doubt in need of further clarification, it seems rather fortunate that several variants could be developed leading to different experimental predictions. The results of these crucial experiments are bound to render the theory more definite and thus prepare the ground for a satisfactory quantum-mechanical foundation.

* We would like to express our thanks to the Editor for making it possible for us to comment on Landau's paper before its publication.

** A few examples will suffice to explain our point: (1) The form (1.10) of reference 1 for the Hamiltonian is hardly obvious. The assumption of a potential energy dependent on the density alone is probably related to our assumption of the vanishing of the microscopic rigidity. (2) It is tacitly assumed that the energy gap Δ is independent of the size of the system. First, this is not obvious; second, it seems to be in conflict with the observation that the critical velocity is dependent on the geometry of the system. Also the observed critical velocity may be as much as 100 times smaller than the one computed by Landau. (3) It is assumed that the symmetrization of the wave function according to the Bose-Einstein statistics is unimportant. (4) In the experiment on the rotating vessel it is assumed that the relaxation time is short compared with the duration of real experiments. Assumptions (3) and (4) are at present open questions.

[1] L. Landau, J. Phys. U.S.S.R. **5**, 71 (1941).
[2] L. Landau, J. Phys. U.S.S.R. **11**, 91 (1947).
[3] L. Tisza, Comptes Rendus **207**, 1035, 1186 (1938).
[4] L. Tisza, J. de phys. et rad. **1**, 165, 350 (1940).
[5] L. Tisza, Phys. Rev. **72**, 838 (1947).
[6] S. G. Sydoriak, E. R. Grilly, and E. F. Hammel, Phys. Rev. **75**, 303 (1949). Announced by Grilly at Chicago Am. Phys. Soc. meeting, Nov. 1948.
[7] P. Kapitza, J. Phys. U.S.S.R. **5**, 59 (1941).
[8] This was pointed out to us by Dr. Dingle. See R. B. Dingle, Proc. Phys. Soc. **61**, 9 (1948).
[9] V. Peshkov, J. Phys. U.S.S.R. **10**, 389 (1946).
[10] J. R. Pellam, Phys. Rev. (in press).

The Viscosity of Mixtures of He_3 and He_4

D. TER HAAR AND H. WERGELAND
Department of Physics, Purdue University, Lafayette, Indiana
January 10, 1949

IF one may accept Tisza's phenomenological picture[1] of the viscosity of He_4, it is not difficult to estimate the influence of an admixture of He_3 to the He_4 liquid. In Tisza's picture the viscosity consists of two parts, the kinetic and the dynamic viscosity:

$$\eta=\eta^{\text{kin}}+\eta^{\text{dyn}}. \tag{1}$$

The first part, η^{kin}, is given by the well-known formula from kinetic gas theory

$$\eta^{\text{kin}}=\tfrac{1}{3}\rho\bar{c}l, \tag{2}$$

where l is the mean free path, $\bar{c}$ the average velocity, an ρ the density. For the He_4 liquid below the λ-point, the dynamic viscosity should be zero and the kinetic viscosity will be decreasing rapidly with decreasing temperature, thus accounting for the superfluidity of He*II*.

If a fraction x of the liquid is changed from He_4 to He_3, the dynamic viscosity will presumably not change appreciably since it is determined by the forces between the atoms. The same applies for the spacing of the atoms in the liquid, and we shall assume

$$\rho_3/m_3=\rho_4/m_4, \tag{3}$$

where m is the mass of one atom.

Because of the difference in statistics, the kinetic viscosity of He_3 will be much larger than that of He_4. It will not decrease for decreasing temperature but approach to a constant value corresponding to the zero-point momentum in a Fermi-Dirac gas. Since the kinetic viscosity of a mixture should be additive in high approximation, we can write for the increase in viscosity due to a fraction x of He_3 in the He_4 liquid:

$$\Delta\eta=\eta_{\text{mix}}-\eta_4=x(\eta_3^{\text{kin}}-\eta_4^{\text{kin}})\approx x\eta_3^{\text{kin}}, \tag{4}$$

where we have neglected the kinetic viscosity of He_4 as compared to the kinetic viscosity of He_3.

It is easy to get an estimate for η_3^{kin}. The mean zero-point energy of a particle in a Fermi-Dirac gas and the corresponding mean velocity are given by

TABLE I.

T in °K:	1.6°	1.8°	2.0°	2.1°	2.2°	2.4°	3°	4°
η_4 in μP:	0.18	0.35	0.80	1.5	15	22	25	28
$\Delta\eta/\eta_4$:	0.35	0.18	0.079	0.042	0.0042	0.0029	0.0025	0.0022

$$\bar{E}=(3h^2/10m)(3\rho/8\pi m)^{\frac{1}{3}},$$
$$\bar{c}=(2\bar{E}/m)^{\frac{1}{2}}=(h/m)(3/5)^{\frac{1}{2}}(3\rho/8\pi m)^{\frac{1}{3}}. \quad (5)$$

For ρ/m we may take the value given by Eq. (3) since we should take for the volume available per He_3 atom the free volume of one atom in the liquid. The density of liquid He_4 does not change appreciably over the whole range of possible temperatures. We shall assume $\rho_4=0.145$ g/cm³. Since the mean free path l is equal to $m/\sqrt{2}\pi\rho d^2$, where d is the diameter of the atoms involved, we have for η_3^{kin} from Eqs. (2), (3), and (5):

$$\eta_3^{kin}=(h/\pi d^2)(30)^{-\frac{1}{2}}(3\rho_4/8m_4)^{\frac{1}{2}}=6.3\mu P, \quad (6)$$

with $d=2.9$A.[2]

Using Eq. (6), expression (4) for the change in viscosity and the experimental values of ρ_4 given in Keesom's monograph,[3] it is possible to calculate the percentage changes in viscosity. For $x=0.01$, these changes are for different temperatures (see Table I).

It must be remarked that the values in the table are lower estimates. There are two reasons why the effect may well be higher. Firstly, the Maxwell tail of the Fermi distribution may give rise to a slightly higher value of $\bar{c}$. Secondly, He_3 may well have a dynamic viscosity below 2.2°K since its λ-point, if it exists, will probably occur for a lower temperature. The higher viscosity of the mixture, however, might perhaps under certain conditions of flow be partly concealed by a lubricating effect of the He_4. Finally, we must remark that even if He_3 should show a λ-transition, which could, e.g., be observed in the specific heat curve, no superfluidity or large heat conductivity would be present due to the Fermi-Dirac viscosity, given by Eq. (6)

[1] L. Tisza, Phys. Rev. **72**, 838 (1947).
[2] W. H. Keesom, *Helium* (Elsevier Publishing Company, Amsterdam, 1942), p. 50 and following pages.
[3] See reference 2, p. 267, Fig. 6.03; p. 271, Table 6.02.

On the Nuclear Electric Quadrupole Moment of Li^6

P. KUSCH
Columbia University, New York, New York
January 24, 1949

THE line observed in the molecular beam magnetic resonance method, and which results from the reorientation of the nuclear spin with respect to an applied magnetic field, is the envelope of a large number of closely spaced lines arising in the rotational states, J, m_J. Feld and Lamb[1] have shown that the effect of a quadrupole moment of one of the nuclei in a heteronuclear diatomic molecule at sufficiently high fields is to introduce into this envelope 2I equally spaced maxima, each maximum corresponding to a particular transition m_I to $m_I\pm1$. The maxima are symmetrically disposed about the frequency $g_I\mu_0H/h$. From the separation of the maxima it is possible to determine the quadrupole interaction energy, e^2qQ.

Whether or not the maxima are observable depends on a number of factors which include the inherent width of the maxima as determined by the interaction of the quadrupole moment with the molecular rotation, the interaction of the magnetic dipole moment with the molecular rotation, and the resolution of the molecular beam apparatus.

The spectra of all the lithium halides have been observed at a field of about 11,000 gauss. At this field the Li^7 line occurs at a frequency of about 9.6 mc/sec. and all second- and higher order terms in the quadrupole interaction energy may be ignored. The line of Li^7 in all of the lithium halides shows the characteristic structure predicted by Feld and Lamb. Three peaks occur, and the frequency separation of the two extreme peaks, $e^2qQ_7/2h$, is given for the case of the four lithium halides in the second column of Table I. The width of the central maximum, which is a measure of the interaction of the nuclear moment with the magnetic field of the molecular rotation, is given in the third column of Table I.

The line of Li^6, where $I=1$, should consist of two components whose separation is $3e^2qQ_6/4h$. Evidently, since the same value of q occurs for either isotope in a given molecule, and since the separation of the peaks is substantially the same for Li^7 in LiCl, LiBr, and LiI, it is to be expected that the separation of the two peaks in the molecules containing Li^6 should also be the same. However, the line of Li^6 in three lithium halides appears as a single line whose width is given in Table I. The lack of resolution occurs either because of the extremely small quadrupole interaction or because the widths of lines resulting from other interactions and instrumental limitations preclude resolution. The fact that the widths are not constant can be attributed to the rather large differences which occur in the interaction energy of the nuclear moment with the molecular rotation.

In the case of LiI, where the Li^6 line has the least width, the maxima of the intensity distribution must lie somewhere within the observed pattern. Accordingly an upper limit for the quantity $3\,e^2qQ_6/4h$ is 2.85 kc/sec. The quantity $e^2qQ_7/2h$ for the same molecule is 43 kc. Hence it is possible to state at once that $Q_6/Q_7\leqslant 1/23=0.044$.

It is to be emphasized that no experimental evidence exists and that the quadrupole moment of Li^6 is other than zero. In the absence of a quadrupole moment of Li^6, the ratio of the width of the observed line to that of the central

TABLE I. The first column lists the molecule; the second column, the frequency separation in kc/sec. between the extreme peaks of the Li^7 lines; the third column, the half-width in kc/sec. of the central component of the lines of Li^7; and the fourth column, the half-width of the Li^6 lines.

I	II	III	IV
LiF	102	37.0	
LiCl	48	15.5	5.5
LiBr	46	12.3	4.4
LiI	43	8.5	2.85

component of the line of Li^7 should be the ratio of the nuclear g-values. The observed ratio is about 2.85, while the ratio of the g-values is 2.64. The resolution of our apparatus is somewhat variable, depending on the velocity of the molecules in the beam. The best resolution occurs, in these experiments for LiI, where, for a perfectly homogeneous magnetic field, the resolution half-width is about 1.2 kc/sec. It is thus evident that the entire width of the observed Li^6 line can be accounted for without any broadening due to the electric quadrupole moment of Li^6.

By use of a Hartree Model, Weisskopf[2] has calculated the quadrupole moment of the Li^7 nucleus to be -2.2×10^{-26} cm^2. Nordheim[3] has proposed a model which assumes that all nuclear properties are derivable from the last odd particle in the nucleus. Mr. Vernon Hughes of this laboratory has used the model to determine the appropriate mixture of wave functions necessary to give the observed spin and magnetic moment of the nucleus. From this wave function, the quadrupole moment of the nucleus may be calculated and it is found that $Q_7=-2.0\times10^{-26}$ cm^2. If Q_7 is taken to be -2×10^{-26} cm^2, then $Q_6\leqslant\pm0.88\times10^{-27}$ cm^2. The quadrupole moment of the deuteron is known[4] to be 2.73×10^{-27} cm^2, and this arises because of a small admixture of a D state into the S state of the deuteron. Evidently since the quadrupole moment of Li^6 is at most one-third as great as that of H^2, the Li^6 nucleus is in very nearly a pure S state.

I wish to acknowledge my indebtedness to Professor I. I. Rabi for his interest in the experiments and their interpretation.

[1] B. T. Feld and W. E. Lamb, Phys. Rev. **67**, 15 (1945).
[2] V. F. Weisskopf, private communication to I. I. Rabi.
[3] L. W. Nordheim, Bull. Am. Phys. Soc., **2**, No. 1 (January 1947), and a privately circulated prepublication copy of a paper.
[4] J. M. B. Kellog, I. I. Rabi, N. F. Ramsey, and J. R. Zacharias, Phys. Rev. **57**, 677 (1940).

The Absorption Spectrum of Neodymium Bromate Crystals

A. Benton and E. L. Kinsey
University of California, Los Angeles, California
January 13, 1949

THE visible absorption spectrum of neodymium bromate crystals with polarized light was studied by Kinsey and Krueger.[1] By the use of the theory of group representations, they obtained a quantum-mechanical explanation of the observed polarization effects and assigned quantum numbers to many of the energy levels of the neodymium ion in the crystal. We extended their work to the ultraviolet region of the spectrum. One interesting result of this work is that spectra obtained with thin (0.32 mm) crystals of $Nd(BrO_3)_3\cdot9H_2O$ and $Nd(BrO_3)_3\cdot9D_2O$ are identical in all respects except one. The strong line which appears in the former at 3469A (28826 cm^{-1}) is displaced toward higher frequencies by 17 cm^{-1} in the latter, appearing at 3467A (28843 cm^{-1}). This shift of one and only one strong line, which occurs in both polarizations, is so remarkable that a photograph of it made on a large Littrow type Bausch and Lomb spectrograph is reproduced in this preliminary note (Fig. 1). The shift appears to be in some way connected with an interaction between electronic energy levels of the Nd^{+++} ion and those of curtailed rotations of the water molecules in the crystal lattice.

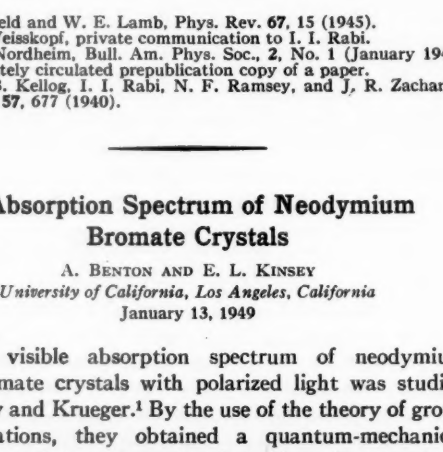

FIG. 1. The figure shows the absorption spectra of $Nd(BrO_3)_3\cdot9H_2O$ (labeled H_2O) and $Nd(BrO_3)_3\cdot9D_2O$ (labeled D_2O) taken with polarized light (π and σ denote E vector parallel and perpendicular, respectively, to the optic axis of the crystal). The πD_2O spectrum is omitted because it bears the same relationship to the σD_2O spectrum as does the πH_2O to the σH_2O.

The ultraviolet absorption spectrum of neodymium bromate was found to have only one group of very strong, fairly sharp lines. The five lines of this group occur at 3562, 3552, 3538, 3509, and 3469A. By following an analysis similar to that employed by Kinsey and Krueger in their work on the visible spectrum of neodymium bromate, these lines were shown to be the result of electronic transitions from the $^4I_{9/2}$ ground state of Nd^{+++} to each of the five component levels into which the $^2G_{7/2}$ upper state is split by the crystal field. The analysis also furnished the M quantum numbers associated with each level.

After completion of the work in the ultraviolet, the spectra of $Nd(BrO_3)_3\cdot9H_2O$ and $Nd(BrO_3)_3\cdot9D_2O$ in the visible region were compared. No shift of any strong line of the type found in the ultraviolet was observed. Differences, however, in the two spectra appeared when very thick (4 mm) crystals were used. It was found that several very weak lines, present only with thick crystals, were displaced in the one spectrum relative to the other. A detailed analysis showed these lines to result from a coupling of the 3μ-vibrational terms of the water molecules in the crystal lattice with electronic terms of the Nd^{+++} ion.

[1] E. L. Kinsey and R. W. Krueger, Phys. Rev. **62**, 82 (1942).

On The Compressibility of Metallic Cesium

R. M. Sternheimer
Department of Physics, University of Chicago, Chicago, Illinois,
and
*Department of Physics, Yale University, New Haven, Connecticut**
January 20, 1949

THE volume discontinuity of cesium[1] at 45,000 kg/cm^2 is too large (about 11 percent) to be accounted for by a change of crystal structure. The probable explanation is that the free electrons which normally occupy the 6*s* band are forced into the empty 5*d* band at higher pressures. A Wigner-Seitz[2] calculation shows that the energy *versus* volume curves for the bottom of the 5*d* band and the top of the 6*s* band cross at approximately the volume where

the phase transition begins. As the metal is further compressed, electrons from the top of 6*s* move into 5*d*. The energy of the lattice does not increase as rapidly with decreasing volume as it would in the absence of 5*d*. This effect is pronounced, because the energy of the bottom of the 5*d* band decreases while the energy of the bottom of the 6*s* band increases with decreasing volume in this region, and because the 5*d* band is narrower than the 6*s* band. When a reasonable correction is made for the change in the energy of the inner electrons, the resulting total energy *versus* volume curve has a region of downward curvature near the volume for which the phase transition is found experimentally. The volume changes discontinuously between the two points with common tangent. This gives a discontinuity of the right order of magnitude at a pressure of about 52,000 kg/cm².

The potential on which the Wigner-Seitz calculations are based is described and tabulated in a forthcoming paper. The essential quantitative agreement with the experimental pressure *versus* volume curve is partly caused by an empirical parameter in the energy of the inner electrons.

I would like to express my thanks to Professor E. Fermi, who suggested the line of approach to this problem and to Professor E. Teller for many helpful discussions.

* Assisted by the O.N.R.

[1] P. W. Bridgman, Phys. Rev. **72**, 533 (1947); Proc. Am. Acad. **76**, 55 (1948). I am very much indebted to Professor Bridgman for a table of the volume compression before publication.

[2] E. Wigner and F. Seitz, Phys. Rev. **43**, 804 (1933); **46**, 509 (1934).

Search for Nuclear Isomers with Half-Lives between a Millisecond and a Second

J. E. R. Holmes, J. Y. Mei,* and R. S. Turgel
Physics Department, University of Birmingham, Birmingham, England
January 13, 1949

A SEARCH has been made for short-lived isomers with half-lives in the range of 10^{-3} to 1 sec. A rotating wheel method was employed similar to that of Nahmias and Walen.[1]

The sample, placed along the inside of a steel hoop 18 in. in diameter, was irradiated with slow neutrons from a 230-millicurie Ra–Be source surrounded by 2 in. of paraffin wax. Diametrically opposite the source and facing the sample was a thin-window Geiger-Müller counter, well shielded from γ-radiation from the neutron source.

Any short-lived activity produced in the sample would give a rate of counting depending upon the speed of rotation of the hoop.

The sensitivity of the experiment was limited by the γ-ray background from the neutron source (about 65 counts/min.) and by any β-activity produced in the sample. It was also dependent upon the internal conversion coefficient of the isomeric transition. The least cross section of formation of an isomer required to detect the isomer could thus not be simply stated, but in typical cases would be of the order of 5 or 10×10^{-24} cm². Therefore, the search had to be restricted to elements having fairly large slow neutron capture cross sections.

In the 16 elements examined (Li, B, Cl, Ni, Cu, Rh, Ag, Cd, In, Sm, Eu, Gd, Dy, Ir, Au, Hg) no isomers were found.

The above method applies only to metastable states formed as the immediate consequence of slow-neutron capture, in contrast to the delayed coincidence method[2] which detects metastable states formed by β-decay.

For half-lives greater than 10 sec., the known isomeric transitions are distributed roughly uniformly with respect to the logarithm of the half-life.[3] If the same were true for shorter-lived isomers, about as many could be expected between 10^{-3} and 1 sec. as between 10^{-6} and 10^{-3} sec. Within this latter range the delayed coincidence method has yielded four isomers out of the 62 isotopes investigated.[2]

* Now at the University of Indiana, Bloomington, Indiana.

[1] M. E. Nahmias and R. J. Walen, J. de phys. et rad. **8**, 153 (1937).

[2] S. De Benedetti and F. K. McGowan, Phys. Rev. **74**, 728 (1948).

[3] M. L. Wiedenbeck, Phys. Rev. **69**, 567 (1946), see Fig. 1.

Second-Order Stark Effect of Methyl Chloride

Robert Karplus* and A. Harry Sharbaugh
General Electric Research Laboratory, Schenectady, New York
January 19, 1949

THE first rotational transition, $(J, K)=(0, 0)\rightarrow(1, 0)$, of $C^{12}H_3Cl^{35}$ and $C^{12}H_3Cl^{37}$ has been measured and analyzed by Gordy, Simmons, and Smith.[1] We have re-examined these lines, using the square wave Stark Effect modulation technique[2,3] and find these lines to exhibit a second-order Stark Effect. This is expected, because that part of the Hamiltonian,

$$H_{K=0}=-\mu\cdot E+H_Q+H_0^{**} \qquad (1)$$

(μ=electric dipole moment, E=electric field, H_Q=quadrupolar interaction between nuclear spin I, and molecular

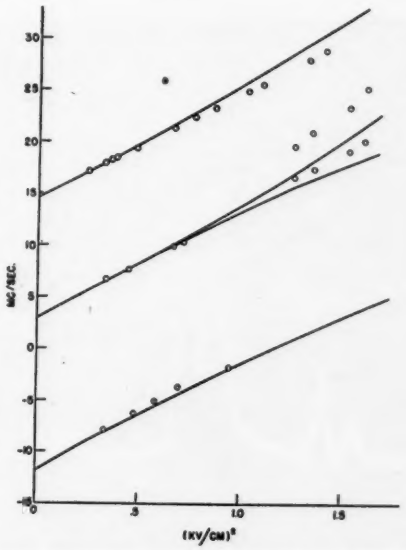

FIG. 1. Stark splitting for $J=0\rightarrow1$ transition of $C^{12}H_3Cl^{37}$. Solid lines—theoretical calculation for $\mu_0=1.70$ D and $eQ(\partial^2V/\partial z^2)=-59.0$ Mc/sec. Circles—experimentally observed values.

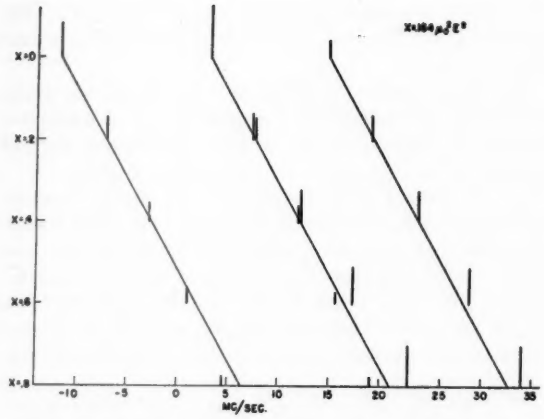

FIG. 2. Stark effect of $C^{12}H_3Cl^{37}$; $J=0\rightarrow1$ transition; $x=0.164\ \mu_0^2E^2$; μ_0 = permanent electric moment in debye units; E = electric field in kv/cm.

angular momentum J, H_0 = rigid rotor Hamiltonian), which depends on the electric field, has a vanishing expectation value in the initial and final rigid rotor states. Because of this fact, however, one can transform to a set of wave functions which take into account, to first order, the presence of the electric field. In this representation, the appropriate Hamiltonian is

$$H'_{K=0}=-i/2[S,\mu\cdot E]+H_Q+H_0, \qquad (2)$$

where $[S,H_0]=-i\mu\cdot E$, and where terms too small to be of interest for methyl chloride have been omitted. The first term describes the second-order Stark Effect; the other operators have the same meaning as in Eq. (1).

Now one must find the wave functions which diagonalize $H'_{K=0}$. They are intermediate between the wave functions which diagonalize the interaction with the electric field (M_I, M_J quantum numbers) and those which diagonalize the quadrupole interaction ($F=I+J$; $M_F=M_I+M_J$ quantum numbers) [4] The eigenvalues of $H'_{K=0}$ and the transformation matrix to the correct wave functions have been obtained as a function of the applied electric field. By means of these quantities, the field dependence of the positions of the absorption lines (Fig. 1 shows the most intense ones) and of their intensity (Fig. 2) has been calculated for $C^{12}H_3Cl^{37}$, with the quadrupole coupling reported in reference 1.

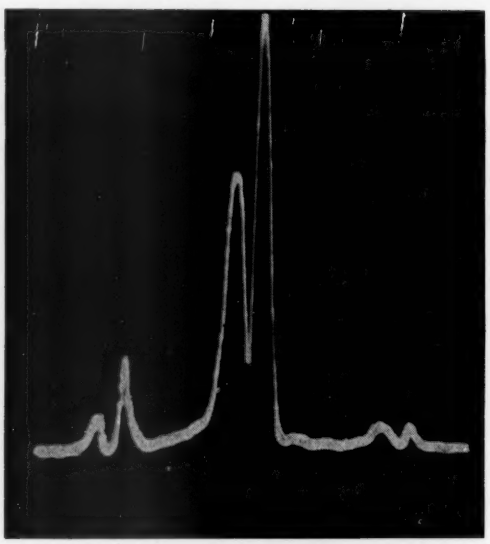

FIG. 3. The Stark pattern for the $C^{12}H_3Cl^{37}$ triplet for the $J=0\rightarrow1$ transition.

The straight lines in Fig. 2 indicate the limiting weak field behavior. Interestingly enough, this is almost identical for the three components. Experimentally, such a similarity is also found. In fact, the most accurate measurements which were made with fields between one-half and one kilovolt per centimeter, can be summarized by the equation

$$\Delta\nu/E^2=10.5\pm0.2\ \text{mc/(kv/cm)}^2. \qquad (3)$$

At lower fields, the lines and their Stark effect images could not be resolved.[3] Figure 3 shows the three pairs of lines found for $C^{12}H_3Cl^{37}$, the right member of each pair being the unperturbed line. Equation (3) should be compared to the theoretical weak field behavior (Fig. 2),

$$\Delta\nu/E^2=(3.70\pm0.02)\mu_0^2\ \text{mc/(kv/cm)}^2, \qquad (4)$$

which leads to a value

$$\mu_0=1.70\pm0.03\ \text{debye}, \qquad (5)$$

considerably lower than the value of 1.86 debye given by Smyth;[5] a value of 1.65 debye was reported by Sircar.[6] At high fields the agreement with theory is not so good (Fig. 1). Nevertheless, the close doublet predicted for the central line was resolved.

Incidental to this study, the quadrupole coupling constants $eQ(\partial^2V/\partial Z^2)$ were measured for the two isotopic species, and were found to be in substantial agreement with those reported by Gordy *et al.*[1]

	$eQ(\partial^2V/\partial z^2)$(Gordy)	$eQ(\partial^2V/\partial z^2)$(this paper)
CH_3Cl^{37}	−75.13	−75.50 mc
CH_3Cl^{37}	−59.03	−58.03

* Present address, The Institute for Advanced Study, Princeton, New Jersey.
[1] W. Gordy, J. W. Simmons, and A. G. Smith, Phys. Rev. **74**, 243 (1948).
[2] E. B. Wilson, Jr. and R. H. Hughes, Phys. Rev. **71**, 562 (1947).
[3] Robert Karplus, Phys. Rev. **73**, 1027 (1948).
** The diagonal block of the Hamiltonian corresponding to $K=0$ is relevant alone, because the perturbations do not produce transitions between different values of this quantum number.
[4] U. Fano, J. Research Nat. Bur. Stand. **40**, 215 (1948).
[5] C. P. Smyth, *Dielectric Constant and Molecular Structure* (Reinhold Publishing Company, New York, 1931).
[6] S. C. Sircar, Ind. J. Phys. **3**, 197 (1928).

A Note on the Arc Spectrum of Lithium

B. EDLÉN AND K. LIDÉN
Department of Physics, University of Lund, Lund, Sweden
January 3, 1949

IN a study of the arc spectrum of fluorine, using a hollow cathode lamp charged with LiF, the lines of LiI in the visible and photographic infra-red were recorded with various grating and prism spectrographs. When comparing

our results with the interferometer measures recently published by Meissner, Mundie, and Stelson,[1] we found agreement within our limits of error for all lines except one, *viz.*, λ4132. For this double line MMS give the center of gravity wave-length 4132.173A, while we find from several plates, consistently within ±0.02A, the value 4132.60. The difference of 0.43A is at least 10 times in excess of our limits of error.

As an explanation for this discrepancy, we suggest that the inaccuracy of the wave-length data available in the literature[2] has led MMS to choose an incorrect order number in the interpretation of the Fabry-Perot patterns of this line. It turns out that a correction of 4, 5, 10, and 18 fringes for the 8-, 10-, 20-, and 36-mm spacers, respectively, would bring the interferometer values in close agreement with our observations. This change would decrease the wave numbers given by MMS for $2\,^2P-5\,^2D$ by 2.500 cm^{-1}, a correction which is confirmed by applying a Ritz formula to the series $n\,^2D$. In fact, after fixing the series limit of the sharp and the diffuse series at $2\,^2P_{3/2}=28583.19\pm0.02\ cm^{-1}$, the four levels 3, 4, 5, $6\,^2D_{5/2}$ are reproduced by the formula

$$T=109728.6(n-0.0019350+0.3762\cdot10^{-7}T)^{-2},$$

with an accuracy of ±0.002 cm^{-1}.

As a consequence of the above observation, the figures given in *Atomic Energy Levels*[3] for $5d\,^2D_{3/2}$, $5d\,^2D_{5/2}$, and the limit, should be changed to 39094.93, 39094.94, and 43487.19, respectively.

[1] K. W. Meissner, L. G. Mundie, and P. H. Stelson, Phys. Rev. **74**, 932 (1948). Hereinafter referred to as MMS.
[2] It should be noted, however, that a higher value, 4132.66A, was given by S. Werner, Dissertation (Copenhagen, 1927).
[3] Circular of the National Bureau of Standards 467, Washington D. C., 1948.

Erratum: Structure of the ^2D Terms of the Arc Spectrum of Lithium

[Phys. Rev. **74**, 932 (1948)]

K. W. Meissner, L. G. Mundie, and P. H. Stelson
Purdue University, Lafayette, Indiana

A COPY of the foregoing letter to the editor was kindly sent to us by Dr. Edlén. Thus I am able to comment without delay on the origin of the discrepancy they found.

The authors are quite right in their assumption that the wave-length data available in the literature has led us to select incorrect order numbers for the line 4132A. I should like to point out that the order numbers we employed were the only feasible ones if one assumed that the wave-length values given in the literature were correct within one- to two-tenths of an angstrom.

Two wave-length values were at our disposal, namely, Fowler's value given in the MIT tables, 4132.16A, and Datta's value, 4132.244A. These values suggested that the true wave-length was approximately 4132.2A. With this assumption the comparison of the different possible values obtained with 8-mm and 10-mm spacers, the smallest employed with the atomic beam source, was sufficient to select the only permissible value. The different possible values of the strong component resulting from Perot-Fabry patterns are given in Table I.

TABLE I. Possible values for the strong components resulting from Perot-Fabry patterns.

8 mm	10 mm
4132.6176	4132.6173
2.511	2.532
2.405	2.447
	2.362
2.298	2.277
4132.1917	4132.1919
2.085	2.107
1.979	2.022
	1.937
1.872	1.852
4131.7658	4131.7666

As one sees, only three pairs of these values agree with each other, namely 4132.617A and 4131.766A. Considering the close mutual agreement of the two values of the literature, we had to choose, consequently, the value 4132.192A and to discard the two other ones. If we had known the greater wave-length reported by Werner, the first one would have been possible too and a definite decision could have been obtained by employing another properly chosen spacer, e.g., a 3-mm.

Unfortunately, we were not able to carry out grating measurements of sufficiently high accuracy when we started our work since the Purdue Concave Grating mounting was not ready yet. After the receipt of Dr. Edlén's information, Mr. Wannlund and the writer carried out measurements with this instrument employing a lithium vacuum arc as light source. The grating employed is a concave grating with 15,000 lines per inch and a 30-ft. radius. The wave-length values obtained confirm the greater wave-length given by Edlén and Lidén. The average value of our grating measurements (center of gravity of the unresolved doublet) is 4132.61±0.01A, in close agreement with the value obtained by Edlén and Lidén with the hollow cathode source.

The interferometric wave-length values of the two components of 4132A reported in our paper for the atomic beam source and the vacuum arc have to be changed accordingly. The average values obtained from patterns with 8-, 10-, 20-, 36-, and 66-mm spacers are:

strong component: $\lambda=4132.618A$, $\nu=24\,190.940\ cm^{-1}$;
weak component: $\lambda=4132.562A$, $\nu=24\,191.268\ cm^{-1}$.

It may be stated that the conclusion regardingthe structure of the D terms is not affected by this change.

A Note on the Determination of the Rates of Energy Loss of H^1 and H^2 Nuclei in Gold and Aluminum

T. A. Hall and S. D. Warshaw
Institute for Nuclear Studies, The University of Chicago, Chicago, Illinois
January 24, 1949

OUR laboratory is extending the previously reported measurements[1] of the energy loss of slow nuclear particles passing through thin metallic foils. In these ex-

periments the nuclear particles are accelerated by a Cockroft-Walton set, magnetically selected and then scattered at 90° from a thin film of gold on a beryllium button to produce the monoenergetic beam incident on the foils. The beam energy is then measured by an electrostatic analyzer, once with the foil in the beam path, and twice with the foil withdrawn.

At present the accuracy of the measurements is limited by two factors: non-uniformity of the foils, and deposition of diffusion pump oil on the foil and on the target as was noted by Wilcox. In the newer measurements, we have given these factors more attention, using more efficient dry ice, acetone traps in an attempt to freeze out the oil before it could reach the foil, and measuring the loss through more foils in an attempt to average out the non-uniformity. Some of Wilcox' conclusions[1] must be changed.

Protons and deuterons of the same velocity were reported by Wilcox as having different rates of energy loss in gold, although he could find no such effect in aluminum. To check this point closely, we have admitted a mixture of hydrogen and deuterium gases to our ion source; the H_2^+ and the D^+ components are selected together magnetically from the accelerated beam and, after scattering from the target button, give a beam of mono-velocity H^+ and D^+. It is possible to study these protons and deuterons separately and almost simultaneously, since the analyzer selects each at a different voltage.[2]

The pairs of values obtained in this way never differed by more than 3 percent, and the difference was never consistently either more or less for the deuterons over the protons. This deviation is less than the dispersion of the proton points over the whole curve. Therefore, it can be concluded that the deuterons and protons both have the same rate of energy loss.

Wilcox suggested that "hard" atomic collisions might have accounted for his observed difference at low energies. However, Bohr[3] gives a formula for this effect:

$$\left.\frac{dE}{dx}\right|_{\text{"hard"}} = N\frac{4\pi e^4 Z_1^2 Z_2^2}{M_2 v^2}\log\left[\frac{M_1 M_2}{M_1+M_2}v^2\frac{a_{12}^{\text{scr}}}{Z_1 Z_2 e^2}\right]\text{erg/cm},$$

where N=atoms/cm³ in the foil, M_1=mass of incident nucleus, Z_1=effective charge, M_2=mass of foil nucleus, Z_2=charge, v=velocity of incident nucleus, a_{12}^{scr}=internuclear distance: the distance where the electronic screening cancels the nuclear force, taken to be just the Bohr radius (a_0=0.53A) in this calculation. Actually a_{12}^{scr} is smaller than a_0 and the effect is even more negligible. Direct substitution shows that protons incident on gold at 100 kev would lose only 0.6 kev/mg/cm² or less due to hard sphere collisions, while deuterons would lose only about 20 percent more from the same cause. This mechanism could, therefore, hardly account for a 10 percent difference in the total loss rates, which are about 80 kev/mg/cm².

Preliminary results indicate that the rate of loss in aluminum is somewhat less (about 25 percent) than that reported by Wilcox, while the shape of the curve is substantially the same. The rather large discrepancy is presumably due to local non-uniformities in the foils used, and an attempt will be made to eliminate this source of error.

We hope to publish a complete report of these measurements soon, including beryllium as a stopping substance, and possibly including other incident nuclei. In acknowledgement, we would like to thank S. K. Allison for suggesting the work and for his help in its progress.

[1] H. A. Wilcox, Phys. Rev. **74**, 1743 (1948).
[2] One objection to this procedure is that the counted beam consists of deuterons or protons alone, while the input monitor beam contains both deuterons and protons so that a fluctuation in beam composition would affect the data. However, this could produce only random effects, and the consistency of our results makes it certain that no error has been introduced by this possibility. It is also possible to use the HD^+ beam obtained when our ion source is run on commercial deuterium gas; on scattering from the target, this beam breaks up into mono-velocity H^+ and D^+. While the use of this convenient two-component, mono-velocity beam would eliminate any monitoring question, we have not, because of technical difficulties, been able to run with it successfully.
[3] N. Bohr, Phys. Rev. **59**, 270 (1941).

Erratum: The Cosmic-Ray Intensity Above the Atmosphere

[Phys. Rev. **75**, 57 (1949)]

A. V. GANGNES, J. F. JENKINS, JR., AND J. A. VAN ALLEN
Applied Physics Laboratory, Johns Hopkins University, Silver Spring, Maryland

ON pages 67 and 68 the name of Pomerantz should be substituted for Primakoff. Inasmuch as Dr. Pomerantz' work appeared in the same issue of the Physical Review, reference 20 may be revised as follows:

[20] M. A. Pomerantz, Phys. Rev. **75**, 69 (1949).

On the Origin of Cosmic Rays

H. ALFVEN
Royal Institute of Technology, Stockholm, Sweden
AND
R. D. RICHTMYER
The Institute for Advanced Study, Princeton, New Jersey
AND
E. TELLER
Institute for Nuclear Studies, University of Chicago, Chicago, Illinois

December 29, 1948

THE discovery of highly charged nuclei among cosmic rays makes it appear probable that cosmic rays are due to electromagnetic acceleration processes. The great total energy present in cosmic rays would require very efficient methods for the production of these rays if one assumes that cosmic rays are spread uniformly throughout the galaxy,[1] and even more so if they are spread uniformly throughout intergalactic space. One way out of this difficulty is to assume that cosmic rays are generated on or in the neighborhood of the sun and are kept near the solar system by extended magnetic fields. These fields could also account for the isotropy and constancy of cosmic rays by repeatedly reflecting and homogenizing the charged particles. The assumption of the presence of such a field considerably simplifies the problem of the generation of cosmic rays.

Feenberg and Primakoff[2] have shown that Compton scattering processes eliminate the faster electrons from cosmic rays that are evenly distributed through inter-

galactic space. If one assumes that the cosmic rays are confined to the planetary system, the intense solar radiation will give rise to a sufficient number of Compton scatterings to account for the absence of electrons including those of low energy.

During magnetic storms, cosmic-ray variations of up to 20 percent are sometimes observed. These variations cannot be explained as effects of disturbances of the earth's magnetic field. The only phenomenon that can account for these variations seems to be the electric field of the storm-producing beams. According to the corpuscular theory of magnetic storms, beams are emitted from the sun with a very high velocity. During their passage through the solar magnetic field these beams are polarized and the electric field generated in this way is probably responsible for the variations of cosmic ray intensity during magnetic storms.

It seems plausible to assume that cosmic rays are produced by repeated passages of particles through beams of the kind described above. During such passages the particles may be accelerated or decelerated by the electric fields in these beams. Further changes in the energy of the particles may occur as a result of the changes in the solar magnetic field connected with the storm-producing beams. On the average, the acceleration processes predominate and the particle may be accelerated to cosmic-ray energies.

A detailed discussion of these points will be published shortly.

[1] We are indebted to Professor E. Fermi for telling us of such an efficient method of cosmic-ray production. This work of Professor Fermi is now in press.
[2] E. Feenberg and H. Primakoff, Phys. Rev. 73, 449 (1948).

Domain Interactions in the Theory of Ferromagnetic Resonance

GEORGE T. RADO
Naval Research Laboratory, Washington 20, D. C.
January 20, 1949

THE application of Kittel's theory[1] of ferromagnetic resonance to the experimental data obtained at microwave frequencies yields values of the Landé splitting factor, g, considerably larger than the value $g=2$ associated with a free electron spin. This apparent gyromagnetic anomaly has not yet been explained. In view of recent and relatively accurate experiments,[2–4] a deficiency in the theory is indicated. It will be shown that the g-values resulting from the application of the theory proposed below are smaller than two, and that they agree satisfactorily with those measured by the Barnett effect.

In his treatment of polycrystals, Kittel neglects magnetic anisotropy and assumes implicitly that the whole *sample* is a single domain.[5] This assumption does not seem justifiable for the relatively small fields ($H\approx 10^3$ oersteds) used in the experiments. Each *crystallite*, however, is known to be a single domain in these fields. Since the crystallites are oriented at random, the additional field arising from the magnetic interaction of the crystallites (i.e., domains) *cannot be parallel* to the magnetic moment of a given domain. Thus there must be an additional torque acting on the moment of each domain so that the g-factor derived from a resonance experiment at a fixed frequency should be smaller than that derived from the same experiment on the assumption of a single domain or non-interacting domains.

Although the quantitative determination of the local field is difficult, Néel[6] has solved just this problem in his ingenious theory of the approach to saturation in cubic, polycrystalline substances. He finds, *in effect*, that (to the order of $1/H^2$) the lining-up of the domains proceeds as if they were independent of each other but subject to a field

$$H'=H(2/P)^{\frac{1}{2}}, \tag{1}$$

where

$$P=1+\tfrac{1}{2}(r+1)+[\tfrac{1}{2}(r+1)^2][(r+1)/r]^{\frac{1}{2}}\tanh^{-1}[r/(r+1)]^{\frac{1}{2}}. \tag{2}$$

Here $r=4\pi M_s/H$, and M_s is the saturation value of the magnetization, M.

Since the microwave component of the magnetization is very small, the equations of motion show that the domain interactions in ferromagnetic resonance absorption may be accounted for by simply using the local field H', instead of the applied field H, in the equations of Kittel and Larmor. Thus the resonance conditions become

$$\omega=\gamma[H'(H'+4\pi M)]^{\frac{1}{2}} \tag{3}$$

for a plane sample, and

$$\omega=\gamma H' \tag{4}$$

for a sphere small compared to the skin depth. Here ω is the circular frequency at resonance and $\gamma(=ge/2mc)$ denotes the gyromagnetic ratio.

Table I compares the g-factors calculated by means of Eqs. (3) and (4) with those calculated on Kittel's theory. It is seen that the g-factors for nickel (Griffiths' new[4] experiment) and for Supermalloy now differ by only 2.6 percent from Barnett's[7] experimental values, whereas Kittel's theory leads to discrepancies of 12 and 14 percent. For zinc-manganese ferrite no Barnett-effect values are

TABLE I. Comparison of the g-factors calculated from Eqs. (3) and (4) with those calculated from Kittel's theory.

Material	Shape: plate thickness cm	Shape: sphere diam. cm	Resonant frequency c.p.s. $\times 10^{-10}$	Value of the Landé g-factor: calculated Kittel's theory	calculated present theory	measured Barnett[d] effect
Supermalloy[a]	0.01	—	2.41	2.17	1.86	1.91
Nickel[b]	$>8\times10^{-5}$	—	2.44	2.14	1.86	1.91
	$<5\times10^{-5}$	—	2.44	2.00	1.75[e]	
Ferrite[c]	0.03	—	2.40	2.12	1.96	—
	—	0.15	2.37	2.16	1.98	—

[a] See reference 2.
[b] See reference 4. $M=M_s=500$ was assumed in the calculation.
[c] See reference 3. The material was (ZnO) (MnO) $\cdot 2Fe_2O_3$. The calculation for the spherical sample is based on the value $M_s=200$ given for the plane sample.
[d] See reference 7. Barnett's value for Supermalloy refers to an alloy of similar composition.
[e] See text for comment.

available, but the proposed theory leads to reasonable g-values ($g<2$). The difficulty in the case of Griffiths' very thin sample ($<5\times10^{-5}$ cm) may well be due to a lack of randomness in the crystallite orientations so that Eq. (1) may not apply.

Since P, and especially $(2/P)^{\frac{1}{2}}$, is a slowly varying function of r in the range of interest, the remarkable constancy of Kittel's g-values (≈2.2) is easily understandable. It is also interesting that for large fields ($r\ll1$) the local field becomes $H'=H+(4\pi M_s)/3$, which is just the Lorentz cavity field. Thus $H'=H$ for fields large compared to the ferric induction, and Kittel's theory is seen to represent the limiting case corresponding to the hypothesis of a single-domain sample.

[1] Charles Kittel, Phys. Rev. **71**, 270 (1947); **73**, 155 (1948).
[2] W. A. Yager and R. M. Bozorth, Phys. Rev. **72**, 80 (1947).
[3] W. H. Hewitt, Jr., Phys. Rev. **73**, 1118 (1948).
[4] J. H. E. Griffiths, Program of the Oxford Conference of the Physical Society, July 23 and 24, 1948.
[5] On pp. 160 and 161 of his 1948 paper, Kittel considers a space-dependent magnetization (and hence a multi-domain model) but the result is the same as that of his 1947 paper because the interactions between domains are neglected. Incidentally, the left side of his Eq. (30) should be $-$ curl curl $\mathbf{H}$ instead of $\nabla^2\mathbf{H}$.
[6] L. Néel, J. de phys. et rad., [VIII], **9**, 193 (1948).
[7] For a review, see S. J. Barnett, Am. J. Phys. **16**, 140 (1948).

Differential Cross Section for Reaction D(d,n)He^3 for 10-Mev Bombarding Energy*

K. W. Erickson, J. L. Fowler, and E. J. Stovall, Jr.
Los Alamos Scientific Laboratory, Los Alamos, New Mexico
January 10, 1949

THE subject reaction was produced in a thin gas target by the deuteron beam focused 15 ft. away from the Los Alamos cyclotron. He^3 particles, emitted at laboratory angles from 16° to 40° (to the direction of the beam) were detected by a proportional counter and the resulting pulses were fed through an amplifier and into a ten-channel pulse amplitude analyzer where they were separated and counted according to energy lost in the counter. The deuteron beam current was measured by means of a Faraday cup and current integrator. The accuracy of the current measurement was checked by the temperature rise of a copper block placed in the beam.

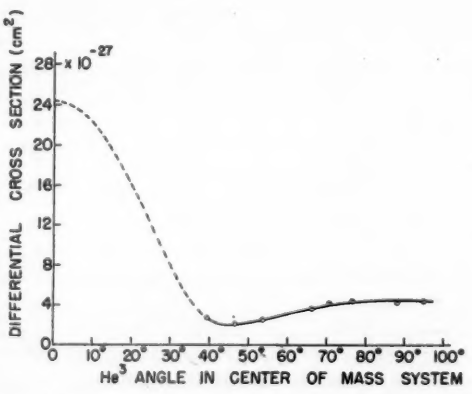

FIG. 1. Differential cross section for D(d,n)He^3 for 10-Mev deuterons.

The energy of the deuteron beam was measured by magnetic deflection immediately after the data for each angular point was taken. The cross section for all points was corrected to 10.3 Mev.

Preliminary results on this work have been previously reported;[1] however, since the time of that report several improvements have been made in equipment and technique which permit more accurate data to be taken. These include better angular definition of the beam (±0.5°), use of a palladium valve and deuterium gas of higher purity (99.3 percent), improved counter design, and better control over the energy lost by the He^3 in the counter. This last improvement was realized by placing a remote controlled foil system between the counter and the target.

Since, for any one angle, the foil system was adjusted to allow the He^3 particles to just traverse the counter, these particles lost considerably more energy in the counter than the other particles involved, and therefore resulted in a well resolved peak located (on curves from the ten-channel analyzer) well above the background. The minimum between the peak and background for most points was about one percent of the peak. These curves have been analyzed for possible excited states of the He^3 nucleus, and this analysis indicates that no such states exist up to three-Mev energy above the ground state. If a group of He^3 particles corresponding to such excited states were present to two percent of the main group, they would have been detected.

The cross section at zero degrees was obtained from the neutrons emitted by this reaction in the vicinity of zero degrees. This yield was determined by use of Cu^{63}(n,$2n$)Cu^{62} detectors. Thus the D(d,n)He^3 cross section was obtained in terms of the 10-min. activation cross section of Cu^{63} which in turn was estimated from results of several unpublished measurements made at Los Alamos.

Figure 1 shows the differential cross section obtained as a function of angle in the center of mass system. The curve is dotted below 39° because of uncertainties in the determination of the cross section at zero degrees. The total cross section (obtained by integrating this curve through 360°) was found to be 0.07×10^{-24} cm^2.

* This document is based on work performed at Los Alamos Scientific Laboratory of the University of California under Government Contract W-7405-eng-36.
[1] B. R. Curtis, L. Rosen, and J. L. Fowler, Phys. Rev. **73**, 648 (1948).

Neutron Production by Cosmic Rays at Sea Level*

A. R. Tobey**
*Sloane Physics Laboratory, Yale University, New Haven, Connecticut****
January 7, 1949

THE rates of production of neutrons in paraffin, lead, and aluminum by cosmic rays at sea level have been measured. A cylindrical ionization chamber ten inches long and three inches in diameter filled with boron tri-

fluoride served as a detector. The chamber was embedded in a block of paraffin of dimensions 25×25×36 inches for the pure paraffin measurement. In the lead and aluminum experiments, the metal was distributed through the block of paraffin in lattice or laminar arrangements. In the latter experiments, the paraffin served as a moderator for neutrons produced in the metals.

A slow-neutron detector placed in a medium of short diffusion length acts as a sink toward which neutrons diffuse. For mathematical simplicity, the cylindrical chamber filled with BF_3 was extended to 37 inches over all, the detector itself comprising the central section. Under these conditions, a solution of the diffusion equation for slow neutrons in cylindrical coordinates leads to a rigorous relation in closed form between the rate of production in the medium (assumed uniform throughout the block) and the number of neutrons captured per unit time in the chamber.

The lattice and laminar structures used in the investigation of lead and aluminum were treated mathematically as homogeneous mixtures. This procedure is justified by the fact that the spacing between blocks or layers of the metal was always less than the root-mean-square distance traveled by a neutron slowing to thermal velocity from a few Mev. Since it is generally assumed that neutrons are produced with energies comparable to those observed in other nuclear processes in the laboratory, the diffusion accompanying their slowing down to thermal energies thus results in a fairly homogeneous distribution of thermal neutrons. The rate of production of neutrons in each mixture was measured, and the contribution from the metal calculated using the measured value for pure paraffin.

The over-all size of the block or "pile" was large enough to assure a negligible effect at the detector of diffusion in or out at the outer boundaries. This fact was verified by (a) surrounding the block with borax, and (b) varying the size of the block. The assumption that the rate of production was constant throughout the block is equivalent to the assumption that the neutron-producing radiation is not appreciably absorbed in the thickness used.

The background, consisting of alpha-particles from the walls of the chamber and large cosmic-ray bursts of ionization, was determined by immediately surrounding the chamber with about 1 inch of borax and then by the paraffin. The rates of neutron production so determined are:

2.0×10^{-5} neutron per second per gram of paraffin,
6.1×10^{-5} neutron per second per gram of lead, and
2.3×10^{-5} neutron per second per gram of aluminum,

with an estimated error of about 10 percent. If one assumes that the production of neutrons in paraffin is entirely the results of the carbon, the calculated rate of production for carbon is 2.3×10^{-5} neutron per second per gram.

The details of this work and further measurements conducted at Denver and Climax, Colorado, are being prepared for publication.

* This work is part of a dissertation presented for the degree of Doctor of Philosophy in Yale University.
** Now at the Department of Physics, State College of Washington, Pullman, Washington.
*** Assisted by the joint program of the ONR and AEC.

The Scattering of Slow Neutrons by Paramagnetic Crystals*

I. W. Ruderman, W. W. Havens, Jr., T. I. Taylor, and L. J. Rainwater
Columbia University, New York, New York
January 17, 1949

A PARAMAGNETIC ion such as Mn^{++}, which has a large magnetic moment in virtue of its five unpaired $3d$ electrons, should scatter neutrons because of the interaction of the ionic and neutron magnetic moments. This phenomenon has been treated theoretically in detail by Halpern and Johnson,[1,2] but the experimental evidence for paramagnetic scattering has thus far been inconclusive.[3-5] In this paper are presented preliminary results of an investigation of the slow neutron transmission of 0.5-mm crystals of pure, anhydrous manganous fluoride. The existence of a large paramagnetic cross section, σ_{pm}, is clearly indicated.

For an isolated paramagnetic ion having a total electron spin quantum number, S, σ_{pm} is given[2] by:

$$\sigma_{pm}=[(8\pi/3)(e^2\gamma/mc^2)^2S(S+1)]F, \qquad (1)$$

where γ is the neutron magnetic moment in nuclear magnetons and F is the form factor integrated over all scattering angles. When F is unity, then σ_{pm} for Mn^{++} becomes equal to 21.2 barns; the order of magnitude of paramagnetic scattering is thus seen to be large enough for the effect to be measurable.

F has been computed on the basis of Halpern's model which assumes *elastic* scattering, and is shown in Fig. 1 for various values of $\alpha/k=6\pi/r_0\lambda$, where r_0 is the most probable radius of the paramagnetic ion and λ is the neutron wave-length. When there is strong spin coupling of the paramagnetic ions, the scattering is predominantly inelastic; in this case, Van Vleck has shown[6] that the form factor may be much smaller than it would be for elastic scattering. Exchange coupling should be important for those compounds having a large Δ in the Weiss-Curie formula $\chi=C/(T+\Delta)$. Since Δ for MnF_2 is 113[7] (while

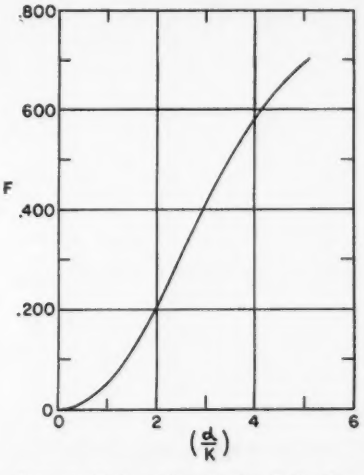

FIG. 1. The theoretical integral form factor, F, for the paramagnetic scattering of a free paramagnetic ion as a function of (α/K), assuming elastic scattering.

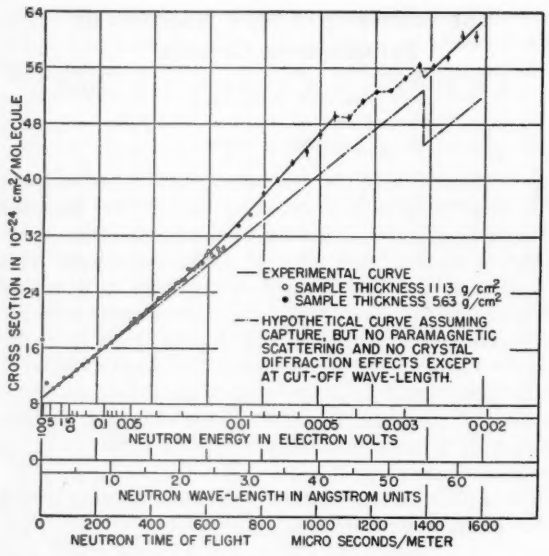
CROSS SECTION IN 10^{-24} cm²/MOLECULE
EXPERIMENTAL CURVE
○ SAMPLE THICKNESS 1113 g/cm²
● SAMPLE THICKNESS 563 g/cm²
HYPOTHETICAL CURVE ASSUMING CAPTURE, BUT NO PARAMAGNETIC SCATTERING AND NO CRYSTAL DIFFRACTION EFFECTS EXCEPT AT CUT-OFF WAVE-LENGTH.
NEUTRON ENERGY IN ELECTRON VOLTS
NEUTRON WAVE-LENGTH IN ANGSTROM UNITS
NEUTRON TIME OF FLIGHT MICRO SECONDS/METER

FIG. 2. The observed slow neutron total cross section of manganous fluoride compared with a hypothetical curve which neglects paramagnetic scattering.

$\Delta = 827$ for MnS which Van Vleck used as an example in his calculations), F for MnF_2 may not be too badly represented by the curve in Fig. 1.

The Columbia neutron velocity spectrometer[8] was used to obtain the transmission data shown in Fig. 2. For $\lambda > 3$A Be and BeO filters were used to eliminate perturbing effects caused by faster neutrons. Since paramagnetic scattering is incoherent with respect to nuclear scattering, we may separate the two types of scattering in regions where there are no interfering crystal diffraction effects. To aid in such a separation, the hypothetical curve shown in Fig. 2 was constructed by extending to 5.46A the experimental curve between 0 and 1.0A. The equation

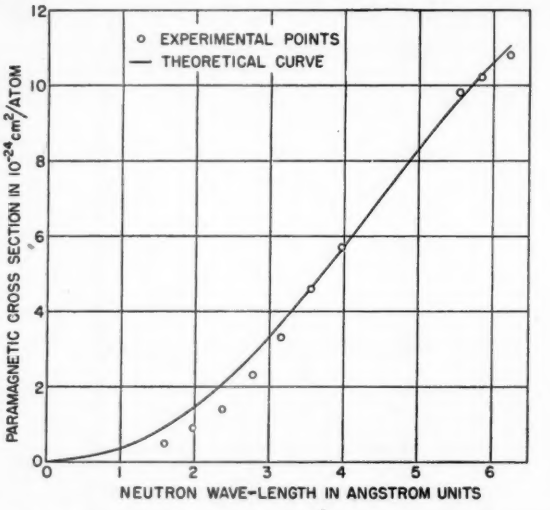
○ EXPERIMENTAL POINTS
— THEORETICAL CURVE
PARAMAGNETIC CROSS SECTION IN 10^{-24} cm²/ATOM
NEUTRON WAVE-LENGTH IN ANGSTROM UNITS

FIG. 3. Experimental values of the paramagnetic scattering cross section of Mn^{++} in manganous fluoride compared with a theoretical curve calculated on the basis of elastic scattering.

of the line so obtained is given by $\sigma = (8.7 + 2.31E^{-\frac{1}{2}})$, which agrees well in slope and intercept with reported data[8,9] for Mn and F. For simplicity, we assume that there is no loss of coherent scattering in the hypothetical curve up to 5.46A, the cut-off wave-length for Bragg reflections for MnF_2.[10] Beyond the cut-off the equation of the curve is given by $\sigma = (1.0 + 2.31E^{-\frac{1}{2}})$; the assumed residual incoherent scattering cross section of 1.0 barn appears to be a justifiable approximation on the basis of other studies carried out here. The difference between the experimental and hypothetical curve (Fig. 2) in the regions 0 to 4.2A and 5.5 to 6.2A was taken as the paramagnetic cross section. No analysis was made in the intermediate region, where the experimental curve indicates marked crystal diffraction effects. Figure 3 shows the values of σ_{pm} obtained in this way, as well as a theoretical curve calculated from Eq. (1) using values of F taken from Fig. 1 with r_0 set equal to 0.82A so as to give the best fit. The dependence of σ_{pm} on λ is seen to have the predicted form.

A similar investigation of the paramagnetic scattering of MnO, MnS, $MnBr_2$, MnI_2, and $MnSO_4$ is now under way. It is hoped that the variation of σ_{pm} with λ observed for this series of compounds of different magnetic dilution will shed some light on the nature of exchange coupling forces between ions in paramagnetic solids.

The authors wish to express their appreciation to Professor O. Halpern, who suggested this problem, for his valuable advice and criticism. They are also indebted to Professor F. Seitz for helpful discussions and to Professor J. R. Dunning for his interest and encouragement.

* This letter is based on work performed under Contract AT-30-1-Gen 72 with the AEC at Columbia University. Publication assisted by the Ernest Kempton Adams Fund for Physical Research at Columbia University.

[1] O. Halpern and M. H. Johnson, Jr., Phys. Rev. **51**, 992 (1937); **52**, 52 (1937).
[2] O. Halpern and M. H. Johnson, Phys. Rev. **55**, 898 (1939).
[3] Martin D. Whitaker, Phys. Rev. **52**, 384 (1937).
[4] M. D. Whitaker, H. G. Beyer, and J. R. Dunning, Phys. Rev. **54**, 771 (1938).
[5] M. D. Whitaker and W. C. Bright, Phys. Rev. **60**, 280 (1941).
[6] J. H. Van Vleck, Phys. Rev. **55**, 924 (1939).
[7] H. Bizette and B. Tsai, Comptes rendus **209**, 205 (1939).
[8] Rainwater, Havens, Jr., Wu, and Dunning, Phys. Rev. **71**, 65 (1947).
[9] Rainwater, Havens, Jr., Dunning, and Wu, Phys. Rev. **73**, 733 (1948).
[10] The 110 plane reflects at 6.92A, but because the Mn and F scatter in opposite phase the crystal structure factor is small, and this reflection is so weak that it may be neglected. See E. O. Wollan and C. G. Shull, Phy. Rev. **73**, 830 (1948).

The Theory of Statistical and Isotropic Turbulence

S. CHANDRASEKHAR
Yerkes Observatory, University of Chicago, Williams Bay, Wisconsin
January 24, 1949

IN two recent papers Heisenberg[1] has developed the theory of locally isotropic turbulence (in the sense of Kolmogoroff) by incorporating the idea that the energy dissipated by the eddies of the various sizes is constant along the hierarchy of eddies which is present in a turbulent fluid. Analyzing the velocity field in a Fourier series, Heisenberg obtains the expression

$$S_k = 2\left\{\mu + \kappa\rho \int_k^\infty dk'' k''^{-3/2} \sqrt{F(k'')}\right\} \int_0^k dk' k'^2 F(k'), \quad (1)$$

for the loss of energy of that part of the spectrum that is contained between the wave numbers $k=0$ and k. In (1), μ is the coefficient of viscosity, ρ is the density, κ a number of order unity (~ 0.8), and $\rho F(k)dk$ is the energy contained between the wave numbers k and $k+dk$.

Under stationary conditions S_k is independent of k and this constancy of S_k determines the spectrum of turbulence, $F(k)$. Heisenberg discusses the condition

$$S_k = \text{constant}, \tag{2}$$

and derives the correct asymptotic behaviors of $F(k)$. However, it can be shown that the condition (2) leads to the following explicit solution for $F(k)$:

$$F(k) = F(k_0)\left(\frac{k_0}{k}\right)^{5/3} \frac{(1+C)^{4/3}}{[C+(k/k_0)^4]^{4/3}}, \tag{3}$$

where c is a constant given by

$$3/4c(1+c)^{\frac{1}{2}} = \mu/\kappa\rho[k_0/F(k_0)]^{-\frac{1}{2}}. \tag{4}$$

For large Reynolds numbers (to which, alone, this theory is applicable) c is a very large member. Accordingly, defining

$$k_s = k_0 c^{\frac{1}{4}}, \tag{5}$$

we can rewrite the solution (3), to a sufficient accuracy, in the form

$$F(k) = F(k_0)(k_0/k)^{5/3}[1+(k/k_s)^4]^{-4/3}. \tag{6}$$

This solution is to be contrasted with the expression

$$F(k) = F(k_0)(k_0/k)^{5/3}[1+(k/k_s)^{8/3}]^{-2},$$

suggested by Heisenberg as a suitable "interpolation" formula. The use of (6) modifies some of the numerical results of Heisenberg, but the physical picture is, of course, unaltered.

[1] W. Heisenberg, Zeits. f. Physik **124**, 628 (1948) and Proc. Roy. Soc. **A195**, 402 (1948).

Some Characteristics of Antimony (125)*

C. E. Mandeville and E. Shapiro
Bartol Research Foundation of the Franklin Institute, Swarthmore, Pennsylvania
January 7, 1949

THE radiations of the 2.7-year Sb^{125} have been investigated by Stanley and Glendenin[1] who report two beta-ray spectra having end points at 0.3 and 0.7 Mev, the intensity ratio being 65:35. Friedlander, Goldhaber, and Scharff-Goldhaber[2] have found a 60-day daughter activity, emitting conversion electrons and x-rays, which they have assigned to an isomer of the stable tellurium (125).

The activities discussed in this letter were obtained when metallic tin was irradiated by slow neutrons in the Oak Ridge pile. After aging for four months, the irradiated tin was dissolved in aqua regia and carrier antimony and tellurium in $3N$ HCl solution were added to the tin solution. Metallic tellurium was precipitated from a hot 10 percent HCl solution with SO_2 and removed by filtration. Metallic antimony was precipitated from the filtrate with iron powder after the excess SO_2 was removed. To insure high purity, both the tellurium and antimony precipitates were dissolved in aqua regia and reprecipitated with SO_2 and iron powder as before.

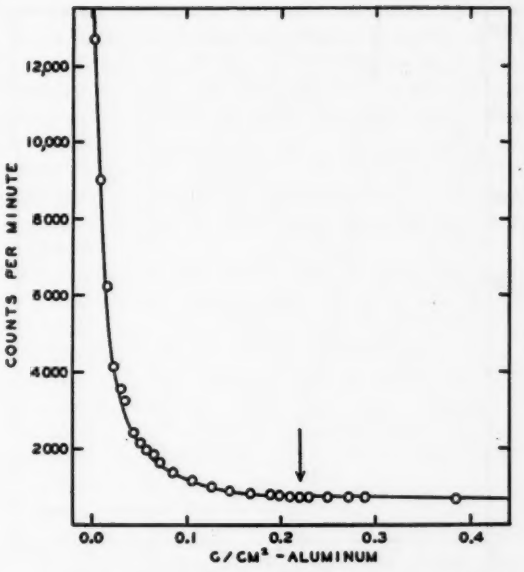

FIG. 1. Absorption in aluminum of the beta-rays of Sb^{125}.

The beta-rays of the 2.7-year antimony were absorbed in aluminum as shown in Fig. 1. The end point, 220 mg/cm², corresponds to a maximum energy of 0.704 Mev as calculated by Feather's equation. The beta-gamma-coincidence rate of Sb^{125} is plotted in Fig. 2 where it seems to be independent of the beta-ray energy. This would suggest a simple spectrum. However, there is evidence to the contrary.[3] Since the coincidence rate of Fig. 2 is constant out to the end point of the 0.704-Mev beta-ray group, it

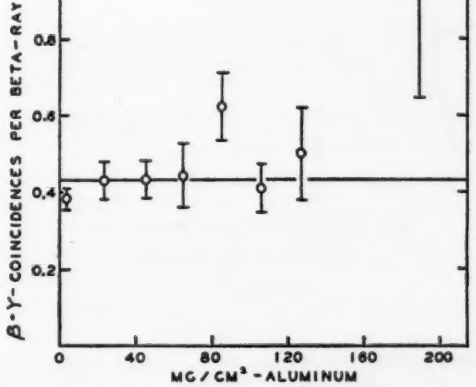

FIG. 2. Beta-gamma-coincidence rate of Sb^{125} as a function of the surface density of aluminum placed before the beta-ray counter.

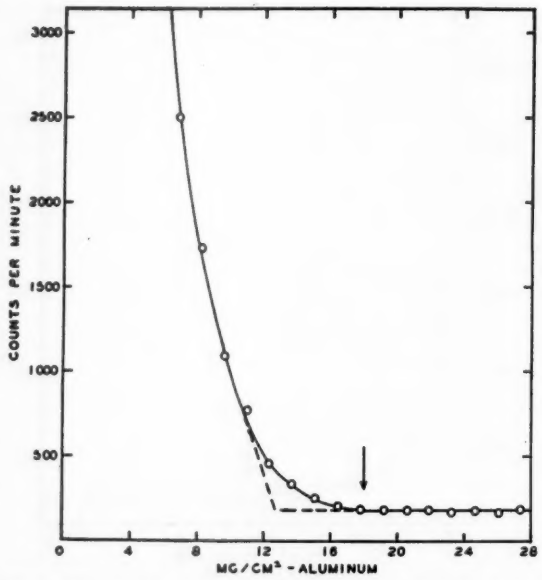

FIG. 3. Absorption in aluminum of the conversion electrons of *Te^{125}

can be concluded that the high energy beta-rays do not go directly to the 60-day tellurium level but are followed by gamma-rays which then lead to the tellurium isomer. The beta-gamma-coincidence rate, 0.42×10^{-3} coincidence per beta-ray, suggests that the beta-rays of the high energy group are followed by 0.31 Mev of "immediate" gamma-ray energy.

The conversion electrons of *Te^{125} were absorbed in aluminum as shown in Fig. 3. The end point, shown by the arrow, occurs at 18 mg/cm², 120 kev, in exact agreement with the earlier measurement.[2] On the other hand, extrapolation of the curve as indicated by the broken line, gives an end point at 12.7 mg/cm² or 93 kev. Either value, together with the half-life, corresponds to a 2^5-pole isomeric transition.

All measurements were completed within five days after the chemical separations. It should also be mentioned that a coincidence absorption experiment disclosed the presence of the 1.7-Mev gamma-ray of Sb^{124} in the antimony fraction.

* Assisted by the joint program of the ONR and the AEC.
[1] C. W. Stanley and L. E. Glendenin, Plutonium Project Report, "Nuclei formed in fission," Rev. Mod. Phys. **18**, 513 (1946).
[2] G. Friedlander, M. Goldhaber, and G. Scharff-Goldhaber, Phys. Rev. **74**, 981 (1948).
[3] A. C. G. Mitchell, verbal communication. Spectrometric data of the Indiana group indicate the presence of soft spectra in Sb^{125} in addition to the principal group at 0.704 Mev.

On Radiative Corrections to Electron Scattering

JULIAN SCHWINGER
Harvard University, Cambridge, Massachusetts
January 21, 1949

RADIATIVE corrections to the electromagnetic properties of the electron produce energy level displacements and modify electron scattering cross sections. Although the high accuracy of radiofrequency spectroscopy facilitates the measurement of energy level displacements, as in the Lamb-Retherford experiment[1] and the evidence on the anomalous magnetic moment of the electron,[2] nevertheless the correction to the cross section for scattering of an electron in a Coulomb field is not without interest, since it permits a comparison between theory and experiment in the relativistic region, as compared to the non-relativistic domain to which the energy level measurements pertain.

The radiative correction to the cross section for essentially elastic scattering of an electron by a Coulomb field has been computed with the form of quantum electrodynamics developed in several recent papers.[3] In addition to the emission and absorption of virtual quanta, we include the real emission of quanta with maximum energy ΔE, which is small in comparison with $W=E-mc^2$, the initial kinetic energy of the electron. In other words, we treat only those inelastic events in which a small fraction of the original energy is radiated. The contribution of the remainder of the inelastic processes can be derived from the well-known bremsstrahlung cross section, and is not of principal interest. The result, expressed as a fractional decrease in the differential cross section for scattering through an angle ϑ, is

$$\delta=2\alpha/\pi\left[\left(\log\frac{E}{\Delta E}-1\right)(K_0+K_1)+\tfrac{1}{2}K_0-K_1+\tfrac{1}{3}K_2-L+\tfrac{1}{2}\frac{(mc^2/E)^2}{1-\beta^2\sin^2\vartheta/2}K_0\right], \quad (1)$$

where

$$K_0=[\lambda/(1+\lambda^2)^{\frac{1}{2}}]\log[(1+\lambda^2)^{\frac{1}{2}}+\lambda],\ \lambda=(p/mc)\sin(\vartheta/2),$$
$$K_1=[(1+\lambda^2)/\lambda^2]K_0-1, \quad (2)$$
$$K_2=[(1+\lambda^2)/\lambda^2]K_1-\tfrac{1}{3}$$

and

$$L=(\lambda^2+\tfrac{1}{2})\frac{(mc^2/E)^2}{\beta}\int_0^1\left[\frac{\log\frac{1}{2}(1-\beta x)}{1+\beta x}-\frac{\log\frac{1}{2}(1+\beta x)}{1-\beta x}\right]\frac{dv}{x}$$
$$-\tfrac{1}{2}\frac{(mc^2/E)^2}{\beta}\left[\frac{\log\frac{1}{2}(1-\beta)}{1+\beta}-\frac{\log\frac{1}{2}(1+\beta)}{1-\beta}\right]. \quad (3)$$

Here

$$x=[1-\sin^2(\vartheta/2)(1-v^2)]^{\frac{1}{2}} \quad (4)$$

and $\beta=pc/E$. Note that δ diverges logarithmically in the limit $\Delta E\to0$. It is well known that this difficulty stems from the neglect of processes involving more than one low frequency quantum.[4] Actually the essentially elastic scattering cross section approaches zero as $\Delta E\to0$; that is, it never happens that a scattering event is unaccompanied by the emission of quanta. This is described by replacing the radiative correction factor $1-\delta$ with $e^{-\delta}$, which has the proper limiting behavior. The further terms in the series expansion of $e^{-\delta}$ express the effects of higher order processes involving the multiple emission of soft quanta. However, for practical purposes such a refinement is unnecessary. The accuracy with which the energy of a particle can be measured is such that the limit $\Delta E\to0$ cannot be realized, and δ will be small in comparison with unity under presently accessible circumstances.

In the non-relativistic limit, $\beta \ll 1$,

$$K_n=[1/(2n+1)]\beta^2\sin^2(\vartheta/2),$$
$$L=[(4/3)(\log 2-1)-\tfrac{1}{5}]\beta^2\sin^2(\vartheta/2), \quad (5)$$

and

$$\delta=(8\alpha/3\pi)\beta^2\sin^2(\vartheta/2)[\log(mc^2/2\Delta E)+(19/30)], \quad (6)$$

which increases linearly with the kinetic energy of the particle. For a slowly moving particle, it is an elementary matter to include the additional scattering produced by the real emission of quanta with energies in the interval from ΔE to W. One thereby obtains the following fractional decrease in the differential cross section for scattering through an angle ϑ, irrespective of the final energy:

$$\delta=(8\alpha/3\pi)\beta^2\sin^2(\vartheta/2)[\log(mc^2/8W)+(19/30)+(\pi-\vartheta)\tan(\vartheta/2)+[\cos\vartheta/\cos^2(\vartheta/2)]\log\csc(\vartheta/2)]. \quad (7)$$

We may remark, parenthetically, that in the same non-relativistic approximation, the radiative correction to the energy of a particle moving in an external field with potential energy $V(r)$ is[5]

$$\delta E=(\alpha/3\pi)[\log(mc^2/2\Delta w)+(31/120)](\hbar/mc)^2\langle\nabla^2V\rangle+(\alpha/2\pi)(\hbar/2mc)\langle-i\beta\boldsymbol{\alpha}\cdot\nabla V\rangle$$
$$=(\alpha/3\pi)(\hbar/mc)^2[(\log(mc^2/2\Delta W)+(19/30))\langle\nabla^2V\rangle+\tfrac{3}{4}\langle\boldsymbol{\sigma}\cdot\mathbf{L}(1/r)(dV/dr)\rangle], \quad (8)$$

where $\mathbf{L}$ is the orbital angular momentum operator in in units of $\hbar$, and ΔW is an average excitation energy of the system.[6] Applied to the relative displacement of the $2^2S_{\frac{1}{2}}$ and $2^2P_{\frac{1}{2}}$ levels of hydrogen, this formula yields 1051 mc/sec., to be compared with the experimental value[7] of 1062 ± 5 mc/sec.

The extreme relativistic limit of (1) is

$$\delta=(4\alpha/\pi)[(\log(E/\Delta E)-(13/12))\times(\log(2E/mc^2)\sin(\vartheta/2)-\tfrac{1}{2})+(17/72)+\phi(\vartheta)], \quad (9)$$

where

$$\phi(\vartheta)=\tfrac{1}{2}\sin(\vartheta/2)\int_{\cos(\vartheta/2)}^{1}\left[\frac{\log\frac{1}{2}(1+x)}{1-x}-\frac{\log\frac{1}{2}(1-x)}{1+x}\right]\times\frac{dx}{(x^2-\cos^2(\vartheta/2))^{\frac{1}{2}}}. \quad (10)$$

The integral can be performed analytically for $\vartheta=\pi$, $\phi(\pi)=\pi^2/24$, but must be evaluated numerically for other angles. An approximation in excess, which has the correct asymptotic form at small angles, is provided by

$$\phi(\vartheta)\sim\frac{1-\cos(\vartheta/2)}{[2\cos(\vartheta/2)(1+\cos(\vartheta/2))]^{\frac{1}{2}}}\times\left[\log\frac{1}{2(1-\cos(\vartheta/2))}+\frac{1-\cos(\vartheta/2)}{2}+1\right]. \quad (11)$$

This approximation is reasonably accurate even at $\vartheta=\frac{1}{2}\pi$, where the value yielded by (11) exceeds by only 8.6 percent the following result of a numerical calculation, $\phi(\pi/2)=0.292$.

The asymptotic formula (9) is quite accurate for even moderate energies. Thus, with $\vartheta=\frac{1}{2}\pi$, $\Delta E=10$ kev, and $W=3.1$ Mev, which corresponds to $(E/mc^2)\sin(\vartheta/2)=5$, the value of δ computed from (9) differs from the correct value, $\delta=8.6\ 10^{-2}$, by only a few tenths of a percent. It is evident from this numerical result that radiative corrections to scattering cross sections can be quite appreciable. For the particular conditions chosen, ΔE can be materially increased (but still subject to $\Delta E \ll W$), without seriously impairing δ. Thus, with $\Delta E=40$ kev, $\delta=6.3\ 10^{-2}$, while $\Delta E=80$ kev yields $\delta=5.1\ 10^{-2}$. As to the energy dependence of δ, we remark that with a given accuracy in the determination of the energy, say $\Delta E/E=0.04/3.6=1.1\ 10^{-2}$, an increase in the total energy by a factor of four produces an addition of $4.4\ 10^{-2}$ to δ. Thus, for a kinetic energy of 14 Mev, $\delta=11\ 10^{-2}$.

The variation of δ with angle, at moderate energies, cannot be studied with the asymptotic formula (9) alone, for at small angles the condition $(p/mc)^2\sin^2(\vartheta/2)\gg1$, which underlies this formula, will not be maintained. It is evident from (1) that δ is proportional to $\sin^2(\vartheta/2)$ at angles such that $(p/mc)^2\sin^2\frac{1}{2}\vartheta\ll1$. However, for $W=3.1$ Mev, $\Delta E=40$ kev, and $\vartheta=\pi/4$, which corresponds to $(p/mc)\sin(\vartheta/2)=2.7$, the correct value of δ, $4.2\ 10^{-2}$, exceeds that deduced from (9) by only 2 percent. For the same choice of W and ΔE, the value of δ associated with $\vartheta=3\pi/4$ is $\delta=7.2\ 10^{-2}$.

The verification of these predictions would provide valuable conformation for the relativistic aspects of the radiative corrections to the electromagnetic properties of the electron.

[1] W. E. Lamb and R. C. Retherford, Phys. Rev. **72**, 241 (1947).
[2] J. E. Nafe, E. B. Nelson, and I. I. Rabi, Phys. Rev. **71**, 914 (1947); D. E. Nagle, R. S. Julian, and J. R. Zacharias, Phys. Rev. **72**, 971 (1947); P. Kusch and H. M. Foley, Phys. Rev. **72**, 1256 (1947); **73**, 412 (1948).
[3] J. Schwinger, Phys. Rev. **74**, 1939 (1948); **75**, 651 (1949).
[4] F. Bloch and A. Nordsieck, Phys. Rev. **52**, 54 (1937).
[5] This result agrees with that obtained by an earlier method [J. Schwinger, Phys. Rev. **73**, 416 (1948)], and announced at the January 1948 meeting of the American Physical Society. However, in the previous method the contribution of the additional magnetic moment to the energy in an electric field had to be artificially corrected in order to obtain a Lorentz invariant result. This difficulty is attributable to the incorrect transformation properties of the electron self-energy obtained from the conventional Hamiltonian treatment, and is completely removed in the covariant formulation now employed. Independent calculations by J. B. French and V. F. Weisskopf [Phys. Rev. **75**, 338 (1949)], as well as N. M. Kroll and W. E. Lamb, Jr. [Phys. Rev. **75**, 388 (1949)], are also in agreement with Eq. (8).
[6] H. A. Bethe, Phys. Rev. **72**, 339 (1947).
[7] R. C. Retherford and W. E. Lamb, Jr., Bull. Am. Phys. Soc. **24**, No. 1, (1949).

Measurements of Behavior and Mobility of Polyatomic Ions

P. B. Weisz and W. P. Kern
Socony-Vacuum Laboratories, Research and Development Department, Paulsboro, New Jersey
December 27, 1948

A TECHNIQUE capable of tracing continuously in time the motion of a body of ions in an electric field is desirable for the measurement of mobility and could indicate changes of mobility occurring due to changes in the nature of the moving charges (due to transfer of charge in ion-molecule collision, dissociation to smaller, or association to larger ionic masses, etc.).

The technique used by H. G. Stever[1] in obtaining a "recovery curve" for Geiger-Mueller tube discharges has been extended to give information concerning the actual progress of the sheath $r=r(t)$ by simultaneously performing three experiments:

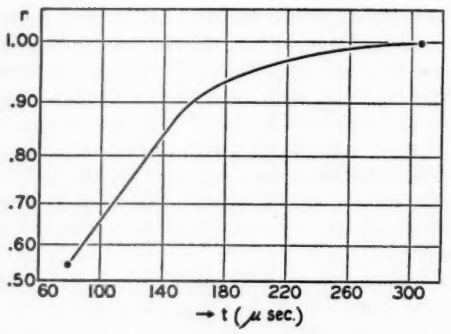

FIG. 1. Plot of r^2 vs. the dead-time t, showing linear relation up to $r=0.9$.

1. The "recovery curve," i.e., pulse-size of subsequent discharge pulses S as a function of time elapsed since the previous discharge pulse t, at an applied potential V_0.
2. The pulse-size S *versus* applied potential V for ordinary space-charge free operation.
3. The space-charge density q developed per pulse at $V=V_0$.

These three measurements together with the relationship

$$V=V_0-2q\log(b/r),$$

which defines the effect of the ionic sheath of space-charge q on the field condition near the wire by comparing it to the effect of an equivalent potential V in absence of space-charge is used to derive the progress of the sheath $r=r(t)$. In the case of the cylindrical geometry at hand, the mobility k can then be shown to be

$$k=\tfrac{1}{2}(C/V_0)(d/dt)(r^2),$$

so that the slope of a r^2 *versus* t plot will reveal the effective mobility at each point.

For a tube in which $r_{max}=b=1.0$ cm, plots of r^2 *versus* t obtained from mixtures of 5.0 cm Hg of argon and 2.5 cm Hg of polyatomic component P, for the six normal hydrocarbons C_nH_{2n+2} from ethane (C_2H_6) to heptane (C_7H_{16}), straight lines were obtained between the dead-time radius (at which the measurement becomes possible) to about $r=0.9$. Thereafter, a "tail" is observed for all experiments which is believed to be caused mainly by electrical end-effect and by eccentricity. Figure 1 is an example.

Figure 2 indicates relative mobility figures derived from the respective straight-line slopes.

Mass spectrometer research together with calculations of fields in the G-M tube would indicate that in the discharge-avalanche process large concentrations of fragment ions are to be expected having masses considerably smaller than those of the parent molecules. The rather straightforward trend of mobility with parent mass, however, seems to indicate that the bulk of ionic masses consists of ionized parent molecules.

The observations made concern ions over a path of some 10^4 collisions but are also *begun* only after elapse of some 10^4 collisions since their creation (because of the "dead-time" phenomenon). Charge transfer from initial "fragment" ions to ultimate parent ions may have occurred, therefore.

It can be shown that a transfer mechanism to the complete parent such as $C_3H_7^+ + C_6H_{14} \rightarrow C_3H_7 + C_6H_{14}^+$ requires additional energy, about 2.6 ev in this case, while the type of transfer exemplified by

$$C_3H_7^+ + C_6H_{14} \rightarrow C_3H_8 + C_6H_{13}^+$$

can proceed "exothermally" as is probably true generally for the latter type of transfer, namely:

$$(C_fH_{2f+1})^+ + (C_pH_{2p+2}) \rightarrow (C_fH_{2f+2}) + (C_pH_{2p+1})^+,$$

as long as $f<p$ which is true by definition of fragment and parent.

However, there is a region in the G-M discharge in which kinetic energies of the order of 2.6 ev can be obtained[2] so that the first type of exchange may also proceed.[3]

Incidentally, the measurement on ethyl alcohol demonstrates that a relationship of mobility with molecular mass is applicable only to a homologous series of molecules.

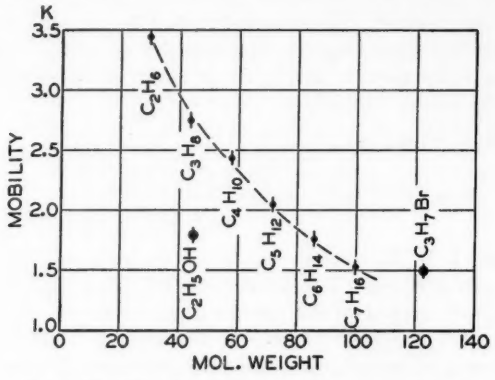

FIG. 2. Mobilities of various molecular ions as a function of molecular weight.

The transfer of ionic charge from one type of parent ion such as ethane to parent molecules of lower characteristic ionization potentials by admixing a controlled impurity of the latter molecules has also been demonstrated by the same technique of measurement.

While the experimental work is as yet incomplete, it seemed worth pointing out that the technique employed may well aid in studying a number of aspects of polyatomic ion behavior in a perhaps unique manner.

[1] H. G. Stever, Phys. Rev. 61, 38 (1942).
[2] Serge A. Korff, Phys. Rev. 72, 477 (1947).
[3] A. O. Allen pointed out to us that the experiment on C_3H_7Br would be indicative of the first-mentioned type of transfer reaction.

Scintillation Counting with Chrysene

EDWIN J. SCHILLINGER, JR.,* BERNARD WALDMAN, AND WALTER C. MILLER
Department of Physics, University of Notre Dame, Notre Dame, Indiana
January 19, 1949

TO extend the range of response of scintillation counters to low energy beta-particles, various organic phosphors have been investigated. Chrysene has proved to be at least as efficient as anthracene for crystals of comparable size. However, with respect to ease of crystallization of relatively large size crystals, chrysene is superior to anthracene. Slow cooling of a heated solution of toluene and

chrysene in a Dewar flask precipitated colorless rhombic crystals averaging 5×5×0.5 millimeters. Preliminary tests with one- and two-thickness layers of these crystals and with smaller crystals showed that the originals were about optimum size for low energy beta-counting; i.e., 150 kev and less. No attempt was made to make larger crystals although it is assumed that it could be accomplished by the method of Feazel and Smith.[1]

Anthracene crystals were precipitated in the same manner as above but large size crystals were not obtained. A comparison was made between the small anthracene crystals so obtained and chrysene crystals of comparable size. The counting rates, using C^{14} as a source, showed chrysene to be slightly more efficient than anthracene. A one-layer screen of the large chrysene crystals gave appreciably greater counting rates than for the small anthracene crystals.

The scintillation counter employed a 1*P*21 photomultiplier tube with 75 volts on each of the first two dynode stages and 100 volts on each of the last seven. A gain of from 5 to 10 percent in the signal-to-noise ratio was found by decreasing the voltage between dynode nine and ground from 50 to 5 or 10 volts. The pulses were fed into a cathode follower and then into a Los Alamos model 501 amplifier, using a gain of about four hundred. All data were taken at room temperature.

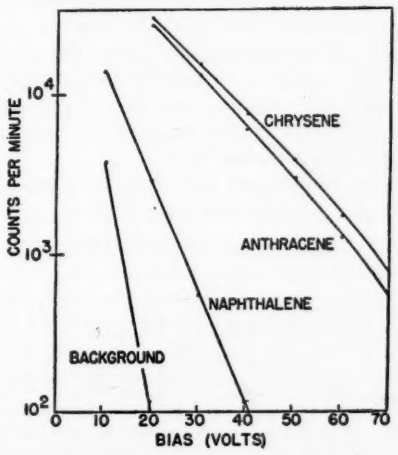

FIG. 1. Comparison of Koppers naphthalene, small anthracene crystals, and large chrysene crystals using an uncollimated C^{14} source. Counts per minute are plotted against bias. All rates are with background subtracted.

With the same values of the circuit parameters as above, efficiency tests were made. The C^{14} source, roughly collimated, when placed next to the window (1.93 mg/sq. cm) of a Tracerlab G-M counter, produced two thousand counts per minute. The chrysene scintillation counter, using the same collimated source, had the same efficiency when the counter bias was adjusted to admit a background of sixty counts per minute. Lowering the bias to admit four hundred background pulses per minute gave a counting rate (with background subtracted) 1.4 times the G-M rate (see Fig. 1).

Efficiency tests were also made on the beta-rays of Co^{60}. A screen two crystals deep was found to be the optimum thickness for this source, but the efficiency of the scintillation counter could not be made equal to that of the G-M counter unless a background of 450 pulses per minute was admitted. This high rate is undesirable especially since the actual counting rate was only one thousand counts per minute over background. The apparent inefficiency of the scintillation counter for these energies (300 kev and less) is undoubtedly due to loss of light by reflection from the crystal faces. Crystals of about one millimeter thickness should bring the efficiency of the scintillation counter to a more practical value.

The chrysene scintillation counter was used to detect the internally converted electrons from Rh^{103*} (about 40 kev). A weakly activated sample (x-ray excited) gave counting rates slightly greater than twice background at an optimum bias setting.

This work was supported by the joint program of the ONR and the AEC.

* AEC Predoctoral Fellow.

[1] C. E. Feazel and C. D. Smith, Rev. Sci. Inst. 19, 817 (1948).

Neutron Yield from $Li^7(p, n)Be^7$

G. FREIER, E. E. LAMPI, AND J. H. WILLIAMS
University of Minnesota, Minneapolis, Minnesota
January 13, 1949

SINCE the reaction $Li^7(p, n)Be^7$ is used extensively as a monochromatic source of fast neutrons, we have studied the yield from the threshold, 1.88 Mev to 3.66 Mev to determine whether there exists more than one group of neutrons. It has been reported[1] that a resonance occurs at 3.06 Mev with the possibility that this is due to an excited state of Be^7.

The Minnesota Van de Graaff generator was used to accelerate protons up to 3.66 Mev with an energy control of ±5 kev. The lithium target was evaporated on a 0.010-inch thick rotating backing. The target was measured to be 24 kev thick.[2] The measurements of the neutron yield

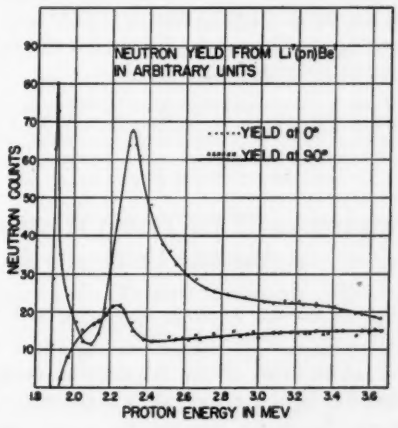

FIG. 1. The neutron yield at 0° and 90° as measured with a flat energy response detector. The statistical deviations are ±2.5 percent at 2.8 Mev in the 0° curve and +4.0 percent in the 90° curve.

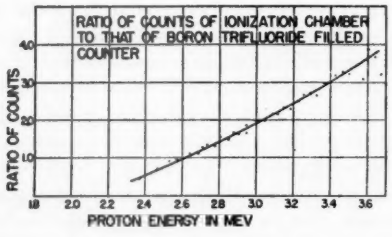

FIG. 2. The ratio of counts in an ionization chamber to those in a boron trifluoride counter covered with paraffin. The statistical deviations are ±6.4 percent at 2.8 Mev.

at 0° and 90° were taken with a flat energy response detector similar to the one described by A. O. Hanson and J. L. McKibben.[3]

The yield at 0° was measured with the counter 13½ inches from the target. In this position it subtended a solid angle of 0.28 steradian. At 90° the counter was placed 31 inches from the target. Figure 1 shows the yield at 90° and 0° as measured with the flat energy response counter. The large solid angle at 0° distorts the first peak in the curve. The results agree fairly well with those of Taschek and Hemmindinger.[2] No evidence for additional resonances as reported by Hill and Shoupp[1] were found.

In an attempt to find more than one group of neutrons, a comparison was made of the yield at 20° as measured simultaneously with an ionization chamber and a boron trifluoride-filled counter surrounded with a two-inch layer of paraffin. The argon-filled ionization chamber with a thin paraffin radiator was designed to detect only fast neutrons of energy greater than 0.6 Mev. Since the ionization chamber efficiency increases with neutron energy and the boron counter decreases with neutron energy, it was felt that an excited state of Be^7 would result in a discontinuity in the ratio of counts in these two detectors at an incident proton energy just sufficient to produce this excited state. Figure 2 shows the ratio between the neutron counts in the ionization chamber and the boron trifluoride counter as a function of the proton energy. No anomalies were found. We conclude that to within the accuracy of our measurements there is only one group of neutrons emitted in this reaction up to a proton energy 3.66 Mev.

This research was done under the partial support of the ONR, Contract N5ori-147.

[1] J. E. Hill and W. E. Shoupp, Phys. Rev. **73**, 931 (1948).
[2] R. Taschek and A. Hemmindinger, Phys. Rev. **74**, 373 (1948).
[3] A. O. Hanson and J. L. McKibben, Phys. Rev. **72**, 673 (1947).

Measurement of the Proton Moment in Absolute Units

HAROLD A. THOMAS, RAYMOND L. DRISCOLL, AND JOHN A. HIPPLE
National Bureau of Standards, Washington, D. C.
January 10, 1949

THE absolute value of the magnetic moment of the proton has been determined by measuring the magnetic field and frequency required for nuclear resonance absorption in a proton sample. The nuclear resonance technique is similar to that developed by Purcell[1] and his collaborators but has a modified circuit design. The sample is water with the relaxation time adjusted to an optimum value by the addition of ferric oxalate.

An electromagnet having auxiliary coils in addition to the main exciting windings was used to produce a field of about 5000 gauss in a 2-inch gap having approximately rectangular pole pieces 8½ inches by 12½ inches. The field distribution in the gap was obtained by using two nuclear resonance probes, one to plot the field and the other to regulate the field by means of a phase detector and power amplifier supplying the auxiliary coils. After shimming, field variations throughout the volume used did not exceed one part in 10,000 and they were accurately plotted. By means of a balance the value of the field at the center of the gap was measured from the force produced on straight conductors 10 cm long which carried a known current. These conductors form one side of a rectangular coil whose opposite side is 70 cm above the center of the gap. The stray field at the upper end of the coil was reduced to zero by a pair of large diameter Helmholtz coils. The accuracy of the measurement of the field by this means was limited principally by the uncertainty in the length of the conductors which was one part in 20,000.

During the measurement, the field was regulated to within 0.02 gauss by one resonance probe which had a local field bias such that the field at the center of the gap where the conductors were located was the exact value required for proton resonance. This could be checked before and after each field measurement by using the other probe. Both resonance probes were supplied from a 20-mc crystal oscillator, and the frequency was measured to a few parts per million by heterodyning the oscillator with the NBS standard frequency station WWV.

The values of field and frequency thus measured give a value for the gyromagnetic ratio of the proton of

$$\gamma_p = (2.6752 \pm 0.0002) \times 10^4.$$

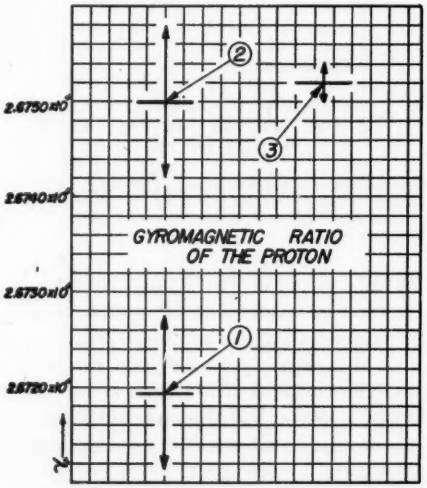

FIG. 1. (1) indicates the value of the gyromagnetic ratio of the proton reported by Millman and Kusch (reference 3). (The error does not include any uncertainty in the value of m/M); (2) shows the value of Millman and Kusch with the radiative correction to the electron moment (see references 4 and 5); (3) is the value reported here.

The magnetic moment of the proton is known less accurately than this because of the greater uncertainty in the value of h. Using a value[2] of

$$h=(6.6234\pm0.0011)\times10^{-27}\text{ erg sec.},$$

the magnetic moment of the proton is

$$\mu_p=(1.4100\pm0.0003)\times10^{-23}\text{ gauss cm}^3.$$

The figure shows the value of γ_p from this measurement compared with a value given by Millman and Kusch[3] which was obtained by determining the magnetic field from radiofrequency spectra of the alkali atoms and thus depends on the electron moment. If the radiative correction[4,5] for the electron moment is applied to their value, excellent agreement, well within the experimental error, is noted.

[1] N. Bloembergen, E. M. Purcell, and R. V. Pound, Phys. Rev. 73, 679 (1948).
[2] J. W. Dumond and E. R. Cohen, Rev. Mod. Phys. 20, 82 (1948).
[3] S. Millman and P. Kusch, Phys. Rev. 60, 91 (1941).
[4] P. Kusch and H. M. Foley, Phys. Rev. 72, 1256 (1947); 73, 412 (1948).
[5] Julian Schwinger, Phys. Rev. 73, 415 (1948).

Coincidence Measurement of Neutron Energy

DONALD C. WORTH*
*Sloane Physics Laboratory, Yale University, New Haven, Connecticut***
January 10, 1949

A TECHNIQUE for measurement of neutron energy has been developed in which use is made of a coincidence-absorption arrangement. Protons which originate as recoils from the incident neutrons in a hydrogen-filled proportional counter pass through a variable amount of absorption into a second proportional counter. Coincidences between the two counters are registered on the output of a medium resolution coincidence circuit and are normalized to the counting rate in the first counter. A plot of coincidence rate as a function of absorption gives the extrapolated range and energy of the scattered protons, hence of the neutrons.

Figure 1 gives an idea of the physical setup used for gas-target bombardment. The proportional counters have a grounded cathode of one-inch inner diameter, the center wire being maintained at a positive (above ground) potential. The associated preamplifiers are of the type standard to this laboratory,[1] modified to allow for the positive center-wire voltage by means of a high voltage blocking condenser. The video amplifiers[2] and resolution circuit[3] are of conventional type. The first counter (where recoils originate) is at low bias and the second counter is "peaked." When peaking is great enough, separate neutron groups may be seen.

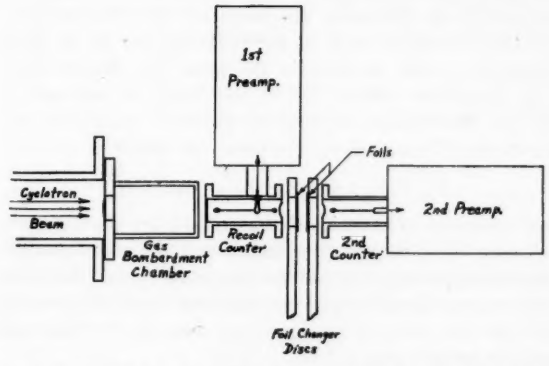

FIG. 1. Sketch of arrangement used. The foil changer disks are remotely operated by synchros, with provision on the disk for infinite absorption.

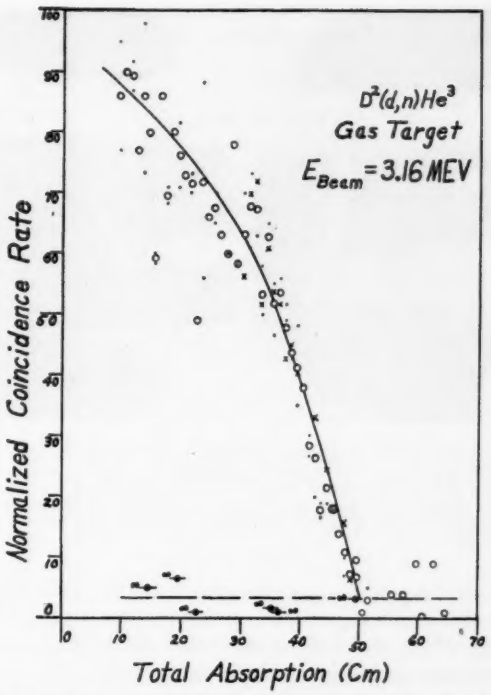

FIG. 2. Composite plot of several runs. The filled-in circles are infinite absorption points and represent the background yield.

A first test of the method is seen in the $H^2(dn)He^3$ reaction tried which was chosen for its homogeneous neutron yield. A composite plot of results is shown in Fig. 2. The Q-value determined by the extrapolated range is $Q=3.08\pm0.18$ Mev, with most of the uncertainty connected with the energy of the cyclotron beam after passing through a gold foil into the bombardment chamber.

* AEC Fellow.
** Assisted by the joint program of the ONR and the AEC.
[1] H. L. Schultz and R. Beringer, Rev. Sci. Inst. 19, 424 (1948).
[2] Bruce B. Benson, Rev. Sci. Inst. 17, 533 (1946).
[3] H. L. Schultz and E. C. Pollard, Rev. Sci. Inst. 19, 617 (1948).

A Cosmic-Ray Particle of Charge Two or Greater*

R. W. SAFFORD** AND A. M. THORNDIKE
Brookhaven National Laboratory, Upton, New York
January 17, 1949

A CLOUD-CHAMBER photograph has been obtained at an altitude of 93,000 feet*** which shows a heavily ionized track penetrating a 1.25-cm lead plate. Stereoscopic views are given in Fig. 1. The track appears to have

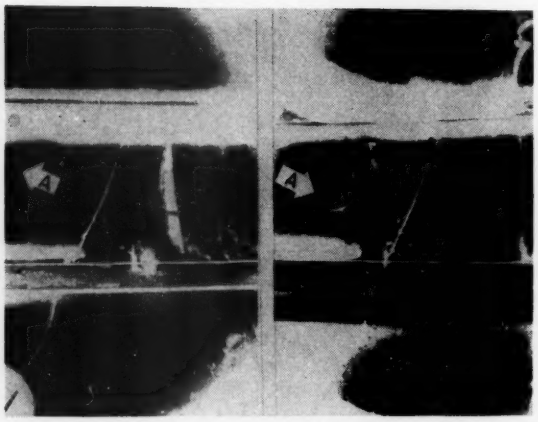

FIG. 1. Pair of stereoscopic photographs of heavily ionizing penetrating track taken at 93,000 feet. Lightly ionizing tracks are barely visible at "A." Because of temperature changes during the flight the cloud chamber is rather foggy, especially near the lead plates. Parts of the right-hand picture are doubly exposed because of failure of the film advance.

passed through the upper 0.63-cm lead plate as well but is not well illuminated above the plate. The track is somewhat old, so that it is not sharp and the bottom section is much distorted, presumably by turbulence.

On the assumption that the tracks marked "A" have minimum ionization, it is estimated that between the two plates the heavily ionizing track has a density of ionization between 10× and 100× minimum ionization. There is no marked change in ionization density on passing through the bottom plate. The ionization density above the top plate cannot be determined. The extent of scattering is unknown since the tracks are certainly distorted by turbulence.

Comparison of these observations with curves for range and energy loss[1] shows that the particle causing the track must be heavier than a proton. A proton with ionization density of 10× minimum or greater would have a range not greater than 2 g/cm², whereas the particle actually passes through 16 g/cm² in the bottom plate. An alpha-particle with ionization 10× the minimum for a particle of unit charge would, however, have a range of about 28 g/cm² of lead and could penetrate our lead plate. A lithium nucleus could also cause such a track, but a particle of charge 4 would cause ionization at least 16× minimum. If the ionization is considered to be as high as 100× minimum, then the particle must have $7 \leqslant Z \leqslant 10$, assuming that its mass is $2Z$. Thus the estimate of ionization between 10× and 100× the minimum for a particle of unit charge implies a charge not less than two nor more than ten, with higher charges resulting from higher estimates of the ionization. In the absence of an accurate determination of the density of ionization of the track, it seems most probable that it was caused by an alpha-particle since alpha-particles have been reported to be much more numerous than heavier nuclei.[2] To cause the observed track an alpha-particle would require energy of the order of 400 Mev; a heavier particle would have to be more energetic. The high energy and approximately vertical incidence make it probable that a primary particle is involved, similar to those found by Freier, Lofgren, Ney, and Oppenheimer.[2]

* Research carried out at Brookhaven National Laboratory under the auspices of the AEC.
** Now at Laboratory for Nuclear Science and Engineering, Massachusetts Institute of Technology, Cambridge, Massachusetts.
*** Equipment was flown by General Mills, Inc. Project "Skyhook" balloon from Camp Ripley, Minnesota.
[1] B. Rossi and K. Greisen, Rev. Mod. Phys. 13, 240 (1941).
[2] Freier, Lofgren, Ney, and Oppenheimer, Phys. Rev. 74, 1818 (1948).

The Mass of the Cosmic-Ray Mesotrons*

ROBERT B. BRODE
Department of Physics, University of California, Berkeley, California
January 10, 1949

IN a paper by W. B. Fretter[1] measurements were reported on the range (R) and the momentum ($B\rho$) of 26 mesotrons. There is a unique relation between mass, range, and momentum so that the knowledge of range and momentum enables one to determine the mass of the mesotrons. The 26 mass values observed by Fretter were treated by him as a set of linear measurements, and the mean value ($\bar{m}$) was found by weighting each value (m_i) in inverse proportion to the square of the probable error (Δm_i) assigned to that value, i.e.,

$$\bar{m} = \{\Sigma[m_i/(\Delta m_i)^2]/\Sigma[1/(\Delta m_i)^2]\}.$$

This calculation gave a value, in units of the electrons' mass, for m of 202 with a probable error of ±5. The probable error of the individual measurements was of the order of 15 percent of the mass values.

Since the range of the mesotron was measured by observing the lead plate in which it stopped, the mean value of the range is taken as the distance to the middle of the plate with a probable error in this estimate of one-quarter of the plate thickness. This probable error is independent of the range of the particle. The curvature (C) of the particle in the magnetic field determines its momentum. The scattering of the particle and turbulence in the cloud chamber introduces spurious curvatures which with equal probability increase or decrease the true curvature. The principal cause of error in curvature is the turbulence which introduces an error that is independent of the magnitude of the curvature. In a plot which uses range and curvature to determine the mass of the mesotron, the probable errors in both of the variables are nearly independent of their position in the plot. The choice of the best parameter curve, that is the curve of constant m, for the distribution of observed values of range (R) and curvature (C) is given by the curve for which

$$\Sigma\{[V_R^2/(\Delta R/R)^2]+[V_C^2/(\Delta C/C)^2]\}$$

is a minimum. The residuals V_R and V_C are the difference between the observed coordinates and the coordinates of the corresponding point on the parameter curve.[2] With this more accurate method of treatment of the data given by Fretter the value of the mesotron mass in electron mass units is found to be 212±5.

If the percent probable errors in range and curvature are equal, the observed point will be on the orthogonal to

the parameter curve that passes through the corresponding point on the parameter curve. An inspection of the curves of constant m in the range, curvature coordinates shows that the linear measure orthogonal to the parameter curves is closely proportional to log m. The change of the variable from m to log m with appropriate change in weight makes an appreciable change in the mean value of the mass. When each value of log m is weighted inversely as a square of $\Delta m/m$ the value of m corresponding to the mean is found to be 212 in agreement with the more accurate method.

* Assisted by the joint program of the ONR and AEC.
[1] W. B. Fretter, Phys. Rev. **70**, 625 (1946).
[2] A detailed discussion of the adjustment of a parameter curve to two Gaussian variables is given by Demming, *Statistical Adjustment of Data* (John Wiley and Sons, Inc., 1943), pp. 141–144.

Interaction of Mesons with Nucleons and Light Particles

T. D. LEE, M. ROSENBLUTH, AND C. N. YANG
Institute for Nuclear Studies, University of Chicago, Chicago, Illinois
January 7, 1949

WE have been making a phenomenological study of the various experiments which have been done in recent years on the interaction between the various types of particles. In the course of this investigation two interesting points have come to light.

First, we found that if the decay of the μ-mesons and the capture of the μ^--mesons by nuclei are described by the reactions[1]

$$\mu \to e+\nu+\nu \qquad (e=\text{electron},\ \nu=\text{neutrino})$$
$$\mu^-+P \to N+\nu \qquad (P=\text{proton},\ N=\text{neutron}),$$

and that the Fermi type interactions are assumed to be responsible for these processes, the coupling constants would have the values

$$g_{\mu e} \sim 3\times 10^{-48} \text{ erg cm}^3$$

and

$$g_{\mu P} \sim 2\times 10^{-49} \text{ erg cm}^3,$$

respectively. These values are so determined as to fit the experimental lifetime[2] of the μ-mesons and the capture probability of the μ^--mesons by nuclei.[3] It is remarkable that the three independent experiments: the β-decay of the nucleons and the μ-mesons and the interaction of the nucleons with the μ-mesons lead to coupling constants of the same order of magnitude.

One can perhaps attempt to explain the equality of these interactions in a manner analogous to that used for the Coulomb interactions, i.e. by assuming these interactions to be transmitted through an intermediate field with respect to which all particles have the same "charge." The "quanta" of such a field would have a very short lifetime and would have escaped detection.

Second, if we assume the π-mesons to have integral spin and assume direct couplings for the processes

$$\pi \to \mu + \text{anti } \nu$$
$$N \to P + \pi^-$$

with coupling constants determined from the lifetime of the π-mesons[4] and the strength of nuclear forces,[5] the interaction between the μ-mesons and the nucleons can be *quantitatively* explained as a second-order interaction through the virtual creation and annihilation of π-mesons.

After the completion of our work Mr. A. Ore has kindly informed us that similar considerations have been carried out by J. A. Wheeler and J. Tiomno.

[1] The masses of the π- and μ-mesons are taken to be

$$m_\pi = 286 m_e, \qquad m_\mu = 212 m_e.$$

[2] B. Rossi, Rev. Mod. Phys. **20**, 537 (1948).
[3] B. Rossi, Rev. Mod. Phys. **20**, 537 (1948). In the calculation for the capture process the Fermi model for the nucleus is assumed and only single particle excitations are considered. See M. Rosenbluth, Phys. Rev. **75**, 532 (1949).
[4] J. R. Richardson, Phys. Rev. **74**, 1720 (1948).
[5] H. Bethe, Phys. Rev. **57**, 390 (1940).

Some Preliminary Cloud-Chamber Photographs of Artificial Mesons

WALTER HARTSOUGH, EVANS HAYWARD, AND WILSON M. POWELL
Radiation Laboratory, University of California, Berkeley, California
January 24, 1949

THE 184-inch cyclotron has recently been converted so that it accelerates protons up to an energy of 350 Mev. A cloud chamber has been operated in the neutron beam which is produced when the 350-Mev protons are allowed to strike a two-inch copper target. The first run has yielded several tracks that may be definitely classified as meson tracks though we are not able to distinguish between light and heavy mesons.

The cloud chamber was operated in a magnetic field of 21,700 gauss and contained 1½ atmospheres of argon with water vapor. The neutron beam was six inches in diameter and was allowed to strike the chamber so that it traversed

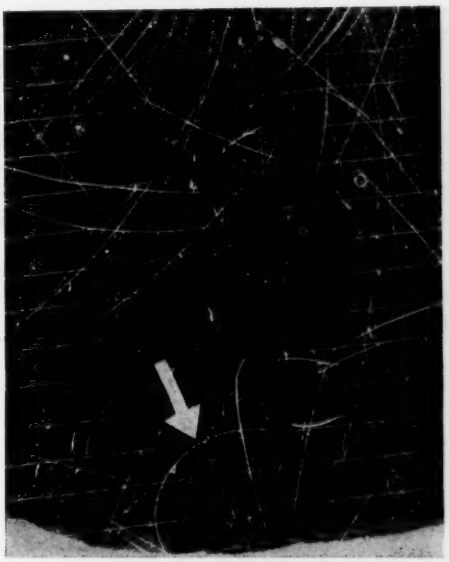

FIG. 1. Meson track produced in a cloud chamber, operated in a beam of neutrons from a copper target bombarded by 350-Mev protons. Its radius of curvature corresponds to a π-meson of 2.3 Mev or a μ-meson of 3.0 Mev.

FIG. 2. Capture of a negative meson by a nucleus, presumably an argon nucleus. A star with two prongs may be seen.

both the top glass and the Lucite at the bottom of the chamber. Out of 100 photographs, seven examples have been found that are definitely the tracks of mesons of two or three Mev. They were all produced in either the top or bottom of the chamber; and in all cases but one, they were observed only to traverse the illuminated region. They have been identified by the fact that their radii of curvature are ~5 cm whereas a proton stops while its radius is larger than 10 cm. The meson tracks show ionization comparable to that of a slow proton. Figure 1 is a photograph of the first meson observed; its radius of curvature corresponds to a π-meson of 2.3 Mev or a μ-meson of 3.0 Mev. Figure 2 shows the capture of a negative meson by a nucleus, presumably by an argon nucleus. The resulting star has two heavy fragments.

Another interesting group of tracks has been observed in the same film. They are particles that ionize near the minimum but are curved too much to be protons. They may be either fast electrons or fast mesons. Their curvatures correspond to electrons of about 150 Mev or mesons of about 70 Mev. If electrons, they may result from the bremsstrahlung of suddenly accelerated protons though there is no reason for not expecting to see mesons of this energy.

We wish to thank Professor E. O. Lawrence for his interest and encouragement. This work was done under the auspices of the AEC.

Upper Limit for the (d,H^3) Reaction in Phosphorus*

DAVID KAHN AND GERHART GROETZINGER
Institute for Nuclear Studies, University of Chicago, Chicago, Illinois
January 10, 1949

SEVERAL cases of (d,H^3) reactions have been reported. In spite of the fact that such a reaction is energetically possible, L. B. Borst mentioned in an abstract that he could not find it in P^{31} with 7.5-Mev deuterons, but made no quantitative statement about the smallest cross section that could have been observed.[1] The search for this reaction has been repeated by bombarding elemental red phosphorus for periods of one minute with 7.5-Mev deuterons with an arrangement which would allow the detection of this process if the cross section were larger than 5×10^{-30} cm^2.

The product nucleus which would occur in such a reaction is P^{30}, a positron emitter with a half-life of 150 seconds. Using a magnetic field to separate the positive and negative electrons only a positron radiation of approximately 72-second half-life was observed after bombardments. The major impurities in our samples determined by the manufacturer were approximately 130 p.p.m.SiO_2, 8 p.p.m.S, and a few p.p.m.Fe.[2] The oxidation in the form of phosphates which might have been incurred in handling before bombardment was determined by a phosphate-molybdate colorimetric test[3] to be less than 5 p.p.m. The bombardment of the impurities leads only in the case of oxygen to a positron-emitting product nucleus decaying with a half-life between one and three minutes, namely F^{17} with a half-life of 70 seconds. The observed activity is thus due to the oxygen impurity. Assuming a cross section of $\approx1\times10^{-26}$ cm^2 for the $O^{16}(d,n)F^{17}$ reaction,[4] and assuming that a P^{30} activity one-tenth as strong at the end of the bombardment could have been detected (especially in view of the fact that activity measurements were begun approximately 2.5 minutes afterwards) the above mentioned upper limit can be given. A rough check using the observed strength of the 72-second half-life activity leads to approximately the same amount of oxygen in the sample as specified by the manufacturer.

* Assisted by the joint program of the ONR and the AEC.
[1] L. B. Borst, Phys. Rev. 61, 106A (1942).
[2] We wish to thank Dr. G. A. Stiegman of the Oldbury Electro-Chemical Company for the specially prepared sample of phosphorus and the above impurity analysis.
[3] This determination was made by Mr. George Herz using the method described in Snell's *Colorimetric Methods of Analysis*.
[4] H. W. Newson, Phys. Rev. 51, 620 (1937).

Cascade Theory*

HARTLAND S. SNYDER
Brookhaven National Laboratory, Upton, New York
January 20, 1949

IN a recent paper[1] and in earlier papers, Bhabha and Chakrabarty have questioned the validity of the solutions of the diffusion equations as given by Serber[2] and myself.[3] Their objections were twofold. First, we used graphical interpolation methods for evaluating a function $K_\mu(y,s)$ which satisfies a difference equation of the form

$$K_\mu(y,s)=g(y,s-1)K_\mu(y,s-1). \qquad (1)$$

The function $K_\mu(y,s)$ satisfies the condition $K_\mu(y,0)=1$. It is easy to compute the values of $K_\mu(y,s)$ for integral values of s. From the values of $K_\mu(y-y)$ for integral y the values of this function were estimated for non-integral values of y by interpolation. All the uncertainties thus engendered are overcome by a suitable solution of (1), namely

$$K_\mu(y, s) = K_\mu(y, t)g(y, t)^{s-t} \times \prod_{n=0}^{\infty}\left(\frac{g(y, t+n)}{g(y, s+n)}\left(\frac{g(y, t+n+1)}{g(y, t+n)}\right)^{s-t}\right). \quad (2)$$

The conditions that (2) shall be a solution of (1) are: (a) the infinite product in (2) converges; (b) $\lim_{N\to\infty}[g(y, s+N)/g(y, N)]=1$. Both of these conditions are satisfied for the particular $g(y, s)$ that comes from cascade theory.

Their second objection was that our solution did not satisfy the correct boundary conditions. This is true, but if $\beta \ll E_0$ the error introduced is negligible. In a paper which will be submitted for publication soon, a solution will be given which does satisfy the correct boundary conditions, a solution which can be reduced to the forms given by Bhabha and Chakrabarty. Also, the form of the energy spectrum will be given for low energies ($E<\beta$). My results do not agree with those of Bhabha and Chakrabarty[1] as given by their Eqs. (37), but do agree with those given earlier by Carlson and Oppenheimer[4] in their Eqs. (34).

* Research carried out at Brookhaven National Laboratory under the auspices of the Atomic Energy Commission.

[1] H. J. Bhabha and S. K. Chakrabarty, Phys. Rev. **74**, 220 (1937).
[2] R. Serber, Phys. Rev. **54**, 317 (1938).
[3] H. Snyder, Phys. Rev. **53**, 960 (1938).
[4] J. F. Carlson and J. R. Oppenheimer, Phys. Rev. **51**, 220 (1937).

Electro-Disintegration of Nuclei

J. S. BLAIR
Department of Physics, University of Illinois, Urbana, Illinois
January 10, 1949

IN recently reported experiments[1] the electron beam from the 22-Mev betatron activated a stack of thin, uniform foils by the reaction $A^z(e; e', n)(A-1)^z$. The activity in a foil was the sum of the activity from electro-disintegration, which was constant in each foil, and from photo-disintegration by bremsstrahlung produced by the incident electrons, which was a linear function of foil position.

The relative activities due to these two processes were estimated using the virtual quanta method[2] to obtain the electro-disintegration cross section and agreed closely with experiment. But since the virtual quanta method is not valid for energy transfers comparable to the incident electron energy, we have calculated the relative activities using more accurate expressions for the electro-disintegration cross section.

We assume that neither the electron beam nor the bremsstrahlung lose appreciable numbers or energy in traversing the foil and the bremsstrahlung is predominantly in the forward direction. Then we find

$$w_{pd} = Z^2 r_0^2 N a (n-\tfrac{1}{2}) F w_{el},$$

where w_{pd} and w_{el} are the activities in the nth foil from the photo- and electro-disintegration, respectively, due to the excitation of a single level, Z is the atomic number, N is number of nuclei/cc, $r_0=2.8(10^{-13})$ cm, a is thickness of foil in cm, F is a function only of the initial and final energies of the electron and of the kind of transition to the excited level, i.e., electric dipole, magnetic dipole, or electric quadrupole. The expression for F involves the cross section for bremsstrahlung production,[3] the transition probabilities for photo-excitation, and the cross sections for electro-excitation.[4] At very low energy transfers, F for electric and magnetic dipole transitions converges to the virtual quanta result, $8\pi/3$, while it vanishes for electric quadrupole transitions.

In the above equation we can interpret w_{pd} and w_{el} as the total activities, found by summing over-all excited levels leading to disintegration, if we replace F by its average for energy transfers above disintegration threshold, $\bar{F}$. We find that F is almost constant for energy transfers between disintegration threshold and 16 Mev, the incident electron energy, for the three reactions studied. Thus the manner in which F is averaged is not very critical.

The comparison (Fig. 1) between calculated values of F as a function of energy transfer and the experimental values of $\bar{F}$, seems to indicate that electric dipole transitions do not predominate. Theoretical and experimental uncertainties, however, make this judgment tentative. Further experiments with higher incident electron energies would be very informative, particularly with respect to the presence of electric quadrupole transitions.

The quadrupole curve was computed assuming that the invariant moment $(a|\Sigma r_i^2|b)$, discussed by Wick, vanishes. Since this moment contributes to electro-, but not to photo-transitions, its presence would further lower the quadrupole curve.

The angular distribution of inelastically scattered electrons is a marked function of the kind of nuclear transition. The presence, however, of electrons inelastically scattered in producing bremsstrahlung will make it necessary to use special techniques to investigate this effect.

We wish to thank Professor S. M. Dancoff for his guidance and Professors A. T. Nordsieck, A. O. Hanson, D. W.

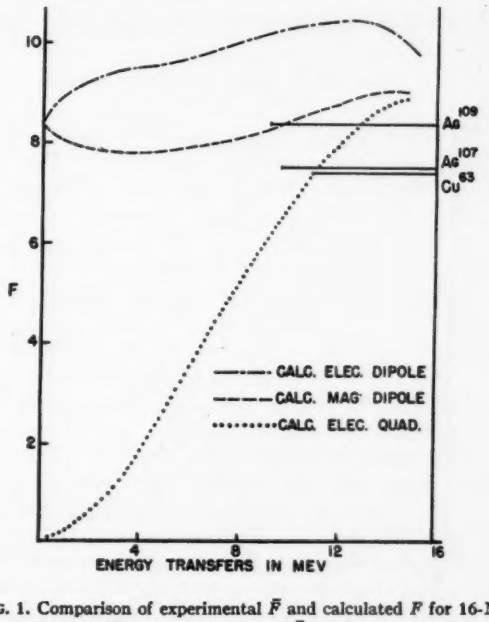

FIG. 1. Comparison of experimental $\bar{F}$ and calculated F for 16-Mev incident electrons. Experimental values of $\bar{F}$ are drawn as straight lines extending over energy transfers above disintegration threshold.

Kerst, Dr. L. S. Skaggs, and Mr. S. P. Lloyd for helpful discussions. This investigation was assisted by the joint program of the ONR and the AEC.

[1] Skaggs, Laughlin, Hanson, and Orlin, Phys. Rev. **73**, 420 (1948).
[2] E. J. Williams, Kgl. Danske Vid. Selskab Math.-Fys. Medd. **XIII**, 4 (1935).
[3] Heitler, *The Quantum Theory of Radiation*, (Oxford University Press, London, 1944), second edition, Chapter 17, Eq. (20).
[4] G. C. Wick, Ric. Sci. **XI**, 49 (1940); B. Peters and C. Richman, Phys. Rev. **59**, 804 (1941); I. N. Sneddon and B. F. Touschek, *Proc. Roy. Soc.* **193**, 344 (1948); See also H. Bethe and R. Peierls, *Proc. Roy. Soc.* **148**, 146 (1935). There is a discrepancy in the electron excitation cross section for electric quadrupole transitions between Sneddon and Touschek, who obtain essentially the same result for both electric quadrupole and magnetic dipole transitions, and Wick. We have also calculated this and agree with Wick's result.

On the Nature of Mesons in Penetrating Showers

H. A. MEYER, G. SCHWACHHEIM, A. WATAGHIN, AND G. WATAGHIN
Departamento de Fisica, Universidade de São Paulo, São Paulo, Brasil
January 6, 1949

THE present experiment was performed at an altitude of 1750 meters at Campos do Jordão in order to obtain some information on the nature of the particles produced in penetrating showers. The penetrating showers were detected by a Geiger-Müller counter arrangement as shown in Fig. 1. The counter trays had an area of 500 cm² each and were connected in fourfold coincidence. The experiment consisted in comparing the penetrating power of showers produced in the atmosphere and showers produced in 21 g/cm² of gasoline located above the counters (see Fig. 1). The absorption of the penetrating showers was

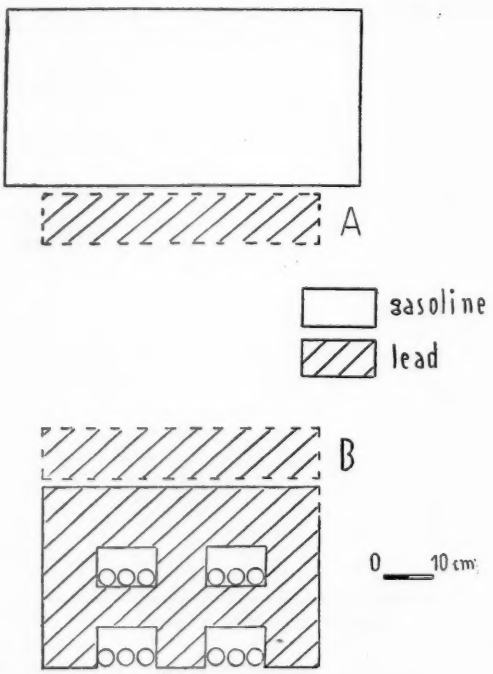

FIG. 1. Arrangement of Geiger-Müller counters.

TABLE I. Hourly rate of coincidences.

No material	3.37±0.16
Pb in position *A*	4.10±0.24
Pb in position *B*	3.35±0.22
Gasoline	4.16±0.19
Gasoline with Pb in position *A*	4.07±0.19
Gasoline with Pb in position *B*	3.50±0.19

obtained by 110 g/cm² of lead alternatively situated in position *A*, just below the gasoline, and in position *B*, just above the permanent shielding of the telescopes. Our results are shown in Table I. The frequency of the showers produced in the air is given in the first line. The lead placed in position *B* did not alter this frequency. This indicates that showers produced in the air are not appreciably absorbed in an additional protection of 10 cm of lead. This result has been checked by several independent experiments (to be published shortly—see also Cocconi and Greisen,[1] and Sazepin and Eydus[2]), so that it seems difficult to explain the constant frequencies by a compensation of production and absorption in the additional lead. When the lead was placed in position *A*, we noticed a production of 0.73±0.29 hr.⁻¹. Probably the production in *B* was not registered due to an unfavorable geometrical arrangement.[3]

The frequency of showers produced in gasoline alone is 0.79±0.25 hr.⁻¹, whereas the rate due to the compound effect of gasoline and lead in *A* is 0.70±0.25 hr.⁻¹. This effect is much smaller than the one we should expect due to the production in gasoline plus the production in lead, taking into account the reduction of the intensity of the shower-producing radiation in gasoline. On the basis of previous results we assume that nucleons responsible for penetrating showers are absorbed in gasoline with a coefficient ~60 g/cm².[4] Thus it seems to us that 76±41 percent of the showers produced in gasoline are absorbed in the additional layer of lead. Similarly we noticed that 84±31 percent of the production in gasoline is absorbed by the lead in position *B*.

We conclude that some of the shower particles produced locally above the counter arrangement are much softer than those of the penetrating showers produced in the atmosphere, the former being absorbed in 28 cm of lead. This result cannot be explained by theoretical arguments, since showers produced in gasoline should be more energetic than those produced in air.[5]

We are led to explain the experimental results by the following considerations based on some recent ideas about the properties of different types of mesons. The mesons produced initially in the penetrating showers are mainly π-mesons.[6] These mesons, responsible for the nuclear forces, should interact strongly with matter and in consequence be appreciably absorbed by the lead layer near to their production center. As the π-mesons are unstable with a mean life of ~10^{-8} sec.,[7] they should after a path of a few meters decay into μ-mesons, which are the usual mesons observed in cosmic radiation and which have a great penetrating power. Now, the main part of the penetrating showers produced in air have their production centers at a

greater distance than, e.g., 10 meters so that the particles constituting the showers are unaffected by the additional layer of 10 cm of lead.

We acknowledge our indebtness to Professor H. Stammreich and Mr. R. Salmerón for some helpful assistance with our experimental equipment.

[1] G. Cocconi and K. Greisen, Phys. Rev. **74**, 62 (1948).
[2] G. Sazepin and L. Eydus, J. Exper. Theor. Phys. **18**, 259 (1948).
[3] L. Jánossy and G. D. Rochester, Proc. Roy. Soc. **A183**, 181 (1944).
[4] H. A. Meyer, G. Schwachheim, and A. Wataghin, Phys. Rev. **74**, 846 (1948).
[5] Gleb Wataghin, Phys. Rev. **74**, 975 (1948).
[6] C. M. G. Lattes, G. P. S. Occhialini, and C. F. Powell, Nature **160**, 453 and 486 (1947).
[7] Camerini, Muirhead, Powell, and Ritson, Nature **162**, 433 (1948).

On the Beta-Particle Spectrum from the Decay of Tritium

W. J. Byatt,
The University of North Carolina, Chapel Hill, North Carolina
F. T. Rogers, Jr.,
Oak Ridge National Laboratory, Oak Ridge, Tennessee
and
Arthur Waltner
North Carolina State College of Engineering, Raleigh, North Carolina
January 21, 1949

IN an earlier letter we presented[1] unreduced data relative to the beta-particle spectrum from the decay of tritium; these data, taken from tracks of the beta-particles in a cloud chamber, were in the form of a differential distribution of plane-projected track lengths. A reduction of these data has now been completed, with the following interesting results.

By numerical solution of the rather complicated relevant integral equation, a differential distribution of true track lengths was obtained; this, after consideration of the small effects of straggling, was converted to a differential energy-distribution; finally, this last distribution was compared in the standard way with the theory of Fermi.[2] Extrapolation of the linear portion of the Fermi plot indicated an end-point energy which is 1.222 times that shown by the initial distribution of projections; this extrapolation was based upon the statistically satisfactory portions of the data, so the extrapolated end-point can be determined by the energy-range relation of von Droste.[3] Thus the cloud-chamber data now lead to an extrapolated end-point energy of $14.0\times1.222=17.0$ kev, which is in extremely good agreement with the 16.9 kev recently obtained[4] by Curran, Angus, and Cockcroft.

Figure 1 shows the distribution of energy in the decay of tritium, as determined by both experiments, on the assumption that both experiments indicate the same end-point energy. Although there are statistical limitations to the precision of the cloud-chamber data at energies near the end point, and observational limitations at very short ranges (both of which could be considerably reduced by obvious means), the agreement between the results of the two experiments, at energies between 6 and 13½ kev, is remarkably good. This agreement, incidentally, has a significant bearing upon the results reported recently[5] on the low energy portion of the beta-particle spectrum from the decay of RaE, for the RaE data were obtained with the same apparatus and the same detailed techniques, except that $Bi^{210*}(CH_3)_3$ was the molecule instead of tritiated water.

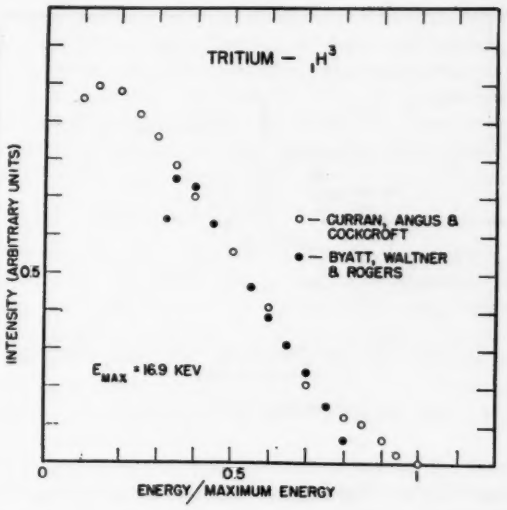

FIG. 1. Distribution of energies in the beta-decay of tritium.

[1] W. J. Byatt, F. T. Rogers, Jr., and Arthur Waltner, Phys. Rev. **74**, 699 (1948). In this reference is an expression of the authors' indebtedness to the Carnegie Institution of Washington for the gift of tritiated water.
[2] See E. J. Konopinski, Rev. Mod. Phys. **15**, 209 (1943).
[3] Von Droste, Zeits. f. Physik **84**, 33 (1933).
[4] S. C. Curran, J. Angus, and A. L. Cockcroft, Nature **162**, 302 (1948).
[5] Arthur Waltner and F. T. Rogers, Jr., Phys. Rev. **74**, 699 (1948).

The Gamma-Rays Following Au^{198} β-Decay

D. Saxon and R. Heller
Argonne National Laboratory, Chicago, Illinois
January 20, 1949

THE question whether the decay of Au^{198} is simple or complex has been pointed up by much recent work in the literature. Levy and Greuling,[1] from spectrometer measurements, have proposed a complex decay scheme wherein ~15 percent of the transitions emit a β of 0.605 Mev, and γ's of 0.157 and 0.208 Mev. DuMond, Lind, and Watson,[2] by absorption in Sn, found low energy γ's in ~15 percent ratio to the precisely measured 0.4112-Mev γ-ray. These low energy γ's could explain the γ-γ coincidences of many recent measurements.[3,4]

In a spectrometer measurement of the β-shape Saxon[5] found the spectrum allowed down to 0.2 Mev, but no systematic search for the low energy γ's was made. Wilkinson and Peacock[6] also report a simple spectrum, while Jurney and Keck[7] found no γ-γ coincidences.

In view of the above conflicting measurements, it was decided to rerun the Au spectrum, with particular care in looking for low energy internal conversion lines from the 0.157- and 0.208-Mev γ's. The same source material used previously[5] was reactivated in the Argonne heavy water

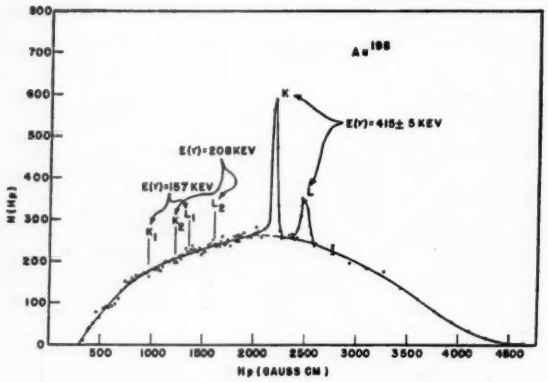

FIG. 1. The β-ray spectrum of Au^{198}.

pile. The final source was ~3 mg/cm², mounted on 0.5-mg/cm² Nylon. The counter window, as before, was 0.3-mg/cm² Nylon, while the resolution $\Delta H\rho/H\rho$ was 2 percent.

The momentum plot of the resulting spectrum is given in Fig. 1. The K and L lines of the high energy γ give 415±5 kev, close to the precision value of DuMond *et al.*[2] From the areas under the peaks and curve we get the following conversion coefficients, correction having been made for the window absorption at low energies:

$$\frac{E(\gamma)}{415\text{ kev}}\ \frac{K}{3.50\%}\ \frac{L+M}{1.30\%}\ \frac{K+L+M}{4.80\%}\ \frac{K/(L+M)}{2.69}.$$

The spin change of the γ can be estimated from the K/L ratio, assuming the M contribution to be a small part of the L peak. Extrapolating the theoretical curves of Hebb and Nelson[8] to high Z, for electric multipole radiation, the spin change is found to be $\Delta l=3$. The value of 4.80 percent for the total conversion coefficient agrees well with that of 4.70±0.24 percent determined by Wiedenbeck and Chu[3] using an entirely different method. As to the 0.157- and 0.208-Mev γ-rays, there is no sign of a conversion line at either the K or L positions. From the statistical errors in this region of the spectrum, it is possible to estimate an upper limit for the presence of the low energy γ's, after making some reasonable assumptions as to their conversion properties. If both γ's were electric dipole, then conversion coefficients of ~5 percent would be expected from Hulme's[9] theoretical data. This leads to an upper limit of ~4 percent for the presence of the γ-rays. Similarly, for electric quadrapole radiation, using the theoretical curve of Taylor and Mott,[10] this upper limit is decreased to ~1 percent. It is clear that γ's present in 15 percent ratio to the β's, would be easily detected even with conversion coefficients as low as 1 percent.

The only reasonable conclusion seems to be that the low energy γ's are associated with an impurity. Mitchell, in a communication to DuMond,[2] has suggested that this impurity is mercury. An analysis of our samples by F. Tompkins' group shows <0.01 percent Hg and Pt.

Jnanananda[11] found a conversion line at 58.4 kev, $H\rho=837$ gauss cm, which was interpreted as an Auger electron due to the 70.3 kev Hg Kα x-ray converting in the L_{III} shell of Au^{198}. We do not find this line in our curve, even though the window is thin enough to let most of the continuous β's through at the line energy. If we use our value of 3.50 percent for the K conversion coefficient of the 411-kev γ-rays, and assume a value of ~0.9 for the fluorescence yield of the Hg K level, the expected yield of the Auger line is ~0.35 percent of the continuous β-spectrum. This value is about the limit of our sensitivity, indicating why the line was not found.

The previous value for the Au^{198} half-life,[5] 2.66±0.01 days, has been raised slightly, after recalculating some of the background corrections. Our final value is 2.69±0.02.

[1] P. W. Levy and E. Greuling, Phys. Rev. **73**, 83 (1948).
[2] J. W. M. DuMond, D. A. Lind, and B. B. Watson, Phys. Rev. **73** 1392 (1948).
[3] M. L. Wiedenbeck and K. Y. Chu, Phys. Rev. **72**, 1171 (1947).
[4] C. E. Mandeville and M. V. Scherb, Phys. Rev. **73**, 634 (1948).
[5] D. Saxon, Phys. Rev. **73**, 811 (1948); Phys. Rev. **74**, 297 (1948).
[6] R. G. Wilkinson and C. L. Peacock, Phys. Rev. **74**, 1250 (1948).
[7] E. T. Jurney and M. R. Keck, Phys. Rev. **73**, 1220 (1948); E. T. Jurney, Phys. Rev. **74**, 1049 (1948).
[8] M. H. Hebb and E. Nelson, Phys. Rev. **58**, 486 (1940).
[9] H. R. Hulme, Proc. Roy Soc. **A138**, 643 (1932).
[10] H. M. Taylor and N. F. Mott, Proc. Roy Soc. **A138**, 665 (1932).
[11] S. Jnanananda, Phys. Rev. **70**, 812 (1946).

Coherent Scattering of Radiation and Negative Energy States

OTTO HALPERN
University of Southern California, Los Angeles, California
AND
HARVEY HALL
U. S. Navy Department, Washington, D. C.
January 7, 1949

FOLLOWING Dirac,[1] it has been generally[2] accepted that in the absence of real pairs, the theoretical expressions for the scattering cross section are identical, whether negative energy states are assumed to be free or occupied. On the basis of this reasoning Waller[2] calculates the scattering cross section of neutral atoms assuming the negative energy states to be unoccupied, and then claims that his results apply equally to the case of occupied negative energy states (hole theory proper). Heitler[2] reports in detail the proof originally given by Dirac that the matrix elements in both versions of the theory are identical; for every matrix element of a transition leading from a state of positive energy through an intermediate occupied state of negative energy to a final state of positive energy, there exists an *identical* matrix element of a transition starting from the (previously intermediate) occupied state of negative energy and leading to the final state of positive energy, while the second part of the transition leads from the initial state of positive energy to the vacated state of negative energy.

This theorem is obviously true for phenomena like the Comptom effect, where the final state differs from the initial state of positive energy. But it is equally obvious, though so far overlooked, that the theorem cannot apply, e.g. to coherent scattering processes in which the initial and final state are the same. In this latter case, the transition from the negative energy state to the final state is as impossible as the transition from the initial state of posi-

tive energy to the not yet vacated state of negative energy. Somewhat similar remarks can be made concerning incoherent scattering processes leading to final bound states, but the discussion of them would not add anything new to the principal question.

It is therefore certain that no matrix elements exist in the hole theory proper which are *identical* with the matrix elements calculated by Waller that are proportional to Z, and give the main contribution to the coherent scattering of x-rays by atoms. One has, therefore, to turn to a closer study of those matrix elements which are characteristic for the hole theory, and have no direct analog in the other version of the theory. These new matrix elements correspond to transitions from a state of negative energy to an intermediate state of positive energy and back to the vacated state of negative energy. The intermediate states of positive energy can be either bound or free states; they, as well as the states of negative energy, have eigenfunctions which are determined by the combined potential of the nucleus and the atomic electrons.

If the quantum of incident radiation is large compared to the ionization energy of the atom but small compared to mc^2, then the Waller terms which give the main contribution to x-ray scattering are replaced by two groups of terms of the following character. The first group is of the same form as the Waller term with the characteristic difference that the form factor of the atom is not that of the real scattering atom but that of a "substitute atom." The substitute atom is defined as an assembly of electrons which occupy (as far as these solutions exist) states with the same quantum numbers as the electrons in the scattering atom. But the eigenfunctions of these electrons are the solutions of a *one-electron problem* in the field of the nucleus modified by the potential produced by all the electrons in the *scattering* atom.[3] The form factor of these terms is, therefore, in principle, different from the Waller terms.

In addition there exist terms of the type

$$\Sigma[(\psi_-^*(\alpha\cdot\mathbf{A}_0)\psi_+)(\psi_+^*(\alpha\cdot\mathbf{A})\psi_-)/E]$$

where the notation is customary, and the sum is to be extended over *all positive and negative* energy states. Here again the eigenfunctions of the positive and negative energy states are defined by the "substitute potential" which is, as before, the sum of the nuclear and electronic potential of the scattering atom. This additional sum over positive and negative energy states requires special treatment to avoid divergences.

The results obtained indicate that not only the proof concerning the equivalence of the two versions of the theory is erroneous, but also that the two theories lead to different predictions concerning experimental results; it is of course to be hoped that after elimination of the pseudo-divergences the hole theory proper will be confirmed by observation.

We shall in the near future present the calculations leading to the results quoted, as well as extensions to the case of large quanta and bare nuclei.

[1] P. A. M. Dirac, Proc. Roy. Soc. **126**, 360 (1930).
[2] I. Waller, Zeits. f. Physik **61**, 837 (1930); W. Heitler, *Quantum Theory of Radiation* (Oxford University Press, London, 1936), p. 189.
[3] Atoms with incomplete shells require a slightly modified treatment.

THE AMERICAN INSTITUTE OF PHYSICS

INCORPORATED

57 East 55 Street New York 22, N.Y.

MEMBER SOCIETIES:

American Physical Society
KARL K. DARROW, *Secretary*, Columbia University, New York 27, New York.

Optical Society of America
ARTHUR C. HARDY, *Secretary*, Massachusetts Institute of Technology, Cambridge 39, Massachusetts.

Acoustical Society of America
WALLACE WATERFALL, *Secretary*, 57 East 55th Street, New York 22, New York.

Society of Rheology
EARL K. FISCHER, *Secretary*, Institute of Textile Technology, Charlottesville, Virginia.

American Association of Physics Teachers
C. J. OVERBECK, *Secretary*, Northwestern University, Evanston, Illinois.

AFFILIATED SOCIETIES:

American Society for X-Ray and Electron Diffraction
Electron Microscope Society of America
Physical Society of Pittsburgh
Physics Club of Chicago
Physics Club of Philadelphia
Cleveland Physics Society
Physics Club of the Lehigh Valley

ASSOCIATES:

Over seventy-five leading industrial enterprises and other institutions which contribute to the support of the Institute.

JOURNALS:

The Physical Review
JOHN T. TATE, *Editor*, University of Minnesota, Minneapolis, Minnesota.

Reviews of Modern Physics
J. W. BUCKEE, *Editor*, University of Minnesota, Minneapolis, Minnesota.

Journal of the Optical Society of America
GEORGE R. HARRISON, *Editor*, Massachusetts Institute of Technology, Cambridge, Massachusetts.

The Journal of the Acoustical Society of America
FLOYD A. FIRESTONE, *Editor*, 3318 Forrester Street, N.W., Washington, D. C.

American Journal of Physics
THOMAS H. OSGOOD, *Editor*, Michigan State College, East Lansing, Michigan.

The Review of Scientific Instruments
GAYLORD P. HARNWELL, *Editor*, Randal Morgan Laboratory of Physics, University of Pennsylvania, Philadelphia, Pennsylvania.

The Journal of Chemical Physics
JOSEPH E. MAYER, *Editor*, Kent Chemical Laboratory, University of Chicago, Chicago 37, Illinois.

Journal of Applied Physics
ELMER HOUSTON, *Editor*, Case Institute of Technology, Cleveland 6, Ohio.

Physics Today
DAVID A. KRASNOW, *Editor*, American Institute of Physics, 57 East 55 Street, New York 22, New York.

OFFICERS

GEORGE R. HARRISON, *Chairman*
Massachusetts Institute of Technology
WALLACE WATERFALL, *Secretary*
The Celotex Corporation
GEORGE B. PEGRAM, *Treasurer*
Columbia University
JOHN T. TATE,
Adviser on Publications
University of Minnesota

GOVERNING BOARD

LUIS W. ALVAREZ
ROBERT B. BRODE
E. U. CONDON
A. J. DEMPSTER
W. F. FAIR, JR.
HARVEY FLETCHER
R. C. GIBBS
GEORGE R. HARRISON
W. V. HOUSTON
PAUL E. KLOPSTEG
F. W. LOOMIS
PHILIP M. MORSE
GEORGE B. PEGRAM
A. H. PFUND (*deceased*)
JOHN T. TATE
WALLACE WATERFALL
M. W. WHITE
A. G. WORTHING
Consultant on Printing
MELVIN LOOS

ADMINISTRATIVE STAFF

HENRY A. BARTON, *Director*
CLEVELAND NORCROSS,
General Manager
THEODORE VORBURGER,
Business Manager
RUTH F. BRYANS,
Publication Manager
BETTY HOFSTADTER, *Office Manager*
EILEEN B. NEUBERGER,
Circulation Manager

THE American Institute of Physics was founded in 1931 as a federation of leading societies in the field of Physics. It combines into one operating agency those functions on behalf of physics which can best be done by the Societies jointly. Its purpose is the advancement and diffusion of physics and its applications to human welfare. To this end it publishes for itself or the Societies the nine journals listed on this page; promotes unity and effectiveness of effort among all who are interested in physics; renders numerous direct services to physicists and to the public; and cooperates with government agencies, national associations, educational institutions, technical industries, and others in such manner as to realize the opportunities and fulfill the responsibilities of physics as an important and constructive human activity.

CONTENTS

THE PHYSICAL REVIEW SECOND SERIES, VOL. 75, NO. 5 MARCH 1, 1949

Neutron-Proton and Neutron-Neutron Scattering at High Energies . . . . . F. ROSELIUS AND J. [illegible]
Particle Groups from the Disintegration of Aluminum by Deuterons . . . . . E. C. POLLARD, V. L. SAILOR, AND L. D. [illegible]
Emission of Radiation in the Disintegration of Mesons . . . . . DANIEL B. [illegible]
Interaction of Nuclear Electric Quadrupole Moments with Molecular Rotation in Asymmetric Top Molecules. II. Approximate Methods for First-Order Coupling . . . . . J. K. BRAGG AND S. [illegible]
On the Space Distribution of Slow Neutrons . . . . . G. C. [illegible]
Energy Levels in Sulfur Nuclei . . . . . PHILIP W. DEVINE
On the Stability of the Isobaric Pair $Ti^{50}-Sc^{50}$ . . . . . M. [illegible]
On the Absorption of Slow Neutrons by Rhodium . . . . . ROBERT E. [illegible]
Cloud-Chamber Study of the Disintegration of Lithium by Slow Neutrons . . . J. K. BRIGGS AND L. [illegible]
Thresholds for Fast Neutron Fission in Thorium and Uranium . . . . . W. E. STEPP AND J. E. [illegible]
Bound Electron Capture in the Decay of Tritium . . . . . P. M. [illegible]
Note on the Theory of Vibration-Rotation Interaction . . . . . RUDOLPH E. LANGER
Detection of Gamma-Rays with Thallium-Activated Sodium Iodide Crystals . . . . . ROBERT HOFSTADTER
Further Experiments on Cosmic-Ray Bursts . . . . . H. S. BRIDGE AND B. [illegible]
Radiations from 2.3-Day Ag^{108} . . . . . PAUL W. LEVY AND E. [illegible]
Microwave Spectrum of Carbonyl Selenide . . . . . M. W. P. STRANDBERG, T. WENTINK, JR., AND A. G. [illegible]
Breakdown Probability of a Low Pressure Gas Discharge . . . . . ROBERT A. [illegible]
Electron Velocity Distribution Function in High Frequency Alternating Fields Including Electronic Interactions . . . . . JULIUS H. [illegible]
Ferromagnetism at Very High Frequencies. II. Method of Measurement and Processes of Magnetization . . . . . M. H. JOHNSON AND G. T. [illegible]
Electrical Properties of Pure Silicon and Silicon Alloys Containing Boron and Phosphorus . . . . . G. L. PEARSON AND J. [illegible]

Letters to the Editor

On the Theory of Superfluidity . . . . . L. LANDAU
On the Theory of Superfluidity . . . . . L. TISZA
Viscosity of Mixtures of He_3 and He_4 . . . . . D. TER HAAR AND H. WERGELAND
On the Nuclear Electric Quadrupole Moment of Li^6 . . . . . P. KUSCH
Absorption Resonance of Neodymium Bromate Crystals . . . . . A. BENTON AND E. L. KINSEY
On the Compressibility of Metallic Cesium . . . . . R. M. SUTHERLAND
Search for Neutron Isomers with Half-Lives between a Millisecond and a Second . . . . . J. E. R. HOLMES, J. Y. MEI, AND R. S. TWOMEY
Second-Order Stark Effect of Methyl Chloride . . . . . ROBERT KARPLUS AND A. HARRY SHARBAUGH
Note on the Arc Spectrum of Lithium . . . . . B. EDLÉN AND K. LUDEN
Erratum: Structure of the ^3D Terms of the Arc Spectrum of Lithium . . . . . K. W. MEISSNER, L. G. MUNDIE, AND P. H. STERLING
Note on the Determination of the Ratio of Energy Loss of H^1 and H^2 Nuclei in Gold and Aluminum . . . . . T. A. MALL AND S. D. WARSHAW
Erratum: The Cosmic-Ray Intensity above the Atmosphere . . . . . A. V. GANGES, J. F. JENKINS, JR., AND J. A. VAN ALLEN
On the Origin of Cosmic Rays . . . . . H. ALFVÉN, R. D. RICHTMYER, AND E. TELLER
Domain Interaction in the Theory of Ferromagnetic Resonance . . . . . GEORGE T. RADO
Differential Cross Section for Reaction $D(d, n)He^3$ for 10-Mev Bombarding Energy . . . . . K. W. ERICKSON, J. L. FOWLER, AND E. J. STOVALL, JR.
Neutron Production by Cosmic Rays at Sea Level . . . . . A. R. TOBEY
Scattering of Slow Neutrons by Paramagnetic Crystals . . . . . W. RUDERMAN, W. W. HAVENS, JR., T. I. TAYLOR, AND L. J. RAINWATER
Theory of Statistical and Isotropic Turbulence . . . . . S. CHANDRASEKHAR
Some Characteristics of Antimony (125) . . . . . C. E. MANDEVILLE AND E. SHAPIRO
On Radiative Corrections to Electron Scattering . . . . . JULIAN SCHWINGER
Measurements of Detection and Mobility of Polyatomic Ions . . . . . P. B. WEISZ AND W. P. KERR
Scintillation Counting with Chrysene . . . . . EDWIN J. SCHELLINGER, JR., BERNARD WALDMAN, AND WALTER C. MILLER
Neutron Yield Ratio $T^3(p, n)He^3$ . . . . . G. FREIER, E. E. LAMPI, AND J. E. WILLIAMS
Measurement of the Proton Moment in Absolute Units . . . . . HAROLD A. THOMAS, RAYMOND L. DRISCOLL, AND JOHN A. HIPPLE
Coincidence Measurement of Neutron Energy . . . . . DONALD C. WORTH
Cosmic-Ray Particles of Charge Two or Greater . . . . . R. W. SAFFORD AND A. M. THORNDIKE
Mass of the Charged Mesotrons . . . . . ROBERT B. BROOKE
Interaction of Mesons with Nucleons and Light Particles . . . . . T. D. LEE, M. ROSENBLUTH, AND C. N. YANG
Some Preliminary Results Obtained by Photographic Plates of Artificial Mesons . . . . . WALTER HARTSOUGH, EVANS HAYWARD, AND WILSON M. POWELL
Upper Limit for the $(p, 2p)$ Reaction in Phosphorus . . . . . DAVID KARN AND GERHART GROETZINGER
Cascade Theory . . . . . HARTLAND S. SNYDER
Electro-Disintegration of Nickel . . . . . J. S. BLAIR
On the Nature of Showers in Penetrating Showers . . . . . H. A. MEYER, G. SCHWACHHEIM, A. WATAGHIN, AND G. WATAGHIN
On the Beta-Particle Spectrum from the Decay of Tritium . . . . . W. J. BYATT, F. T. ROGERS, JR., AND ARTHUR WALTHER
Gamma-Rays Following Alpha-Particle Decay . . . . . D. SAXON AND R. HELLER
Coherent Scattering of Radiation and Negative Energy States . OTTO HALPERN AND HARVEY HALL

LANCASTER PRESS, INC., LANCASTER, PA.